Sajal Kumar Das
Md. Rabiul Islam
Wei Xu *Editors*

Advances in Control Techniques for Smart Grid Applications

Springer

Advances in Control Techniques for Smart Grid Applications

Sajal Kumar Das · Md. Rabiul Islam · Wei Xu
Editors

Advances in Control Techniques for Smart Grid Applications

Springer

Editors
Sajal Kumar Das
Department of Mechatronics Engineering
Rajshahi University of Engineering
and Technology
Rajshahi, Bangladesh

Wei Xu
School of Electrical and Electronic
Engineering
Huazhong University of Science
and Technology
Wuhan, Hubei, China

Md. Rabiul Islam
Faculty of Engineering and Information
Sciences
School of Electrical, Computer
and Telecommunications Engineering
University of Wollongong
Wollongong, NSW, Australia

ISBN 978-981-16-9855-2 ISBN 978-981-16-9856-9 (eBook)
https://doi.org/10.1007/978-981-16-9856-9

This Springer imprint is published by the registered company Springer Nature Singapore Pte Ltd.
The registered company address is: 152 Beach Road, #21-01/04 Gateway East, Singapore 189721, Singapore

Contents

About the Editors

Dr. Sajal Kumar Das is Head of the Department of Mechatronics Engineering of Rajshahi University of Engineering & Technology, Bangladesh, and Director of Control System Research Group of RUET. He served as President of the Robotic Society of RUET and is Advisor of the Robotics and Automation Society, IEEE RUET SB, Bangladesh. He earned a Ph.D. degree from the University of New South Wales (UNSW), Australia, and worked as Research Engineer at the National University of Singapore (NUS), Singapore. He was Visiting Academic at the University of Newcastle, Australia, and Faculty Member of the Department of Electrical and Electronic Engineering of American International University, Bangladesh. He is Member of IEEE and serves as Guest Associate Editor in *IET Renewable Power Generation* and Guest Editor in *Sustainability and Energies*. His research interest includes robust control and applications, renewable energy generation and control, microgrid, smart grid, virtual power plant, cyber-security and nano-positioning control. He has published more than 100 peer-reviewed journal and conference papers.

Dr. Md. Rabiul Islam received the Ph.D. degree from University of Technology Sydney (UTS), Sydney, Australia, in 2014 in Electrical Engineering.

He was appointed as Lecturer at RUET in 2005 and promoted to Full Professor in 2017. In early 2018, he joined the School of Electrical, Computer, and Telecommunications Engineering (SECTE), University of Wollongong (UOW), Wollongong, Australia. He is Senior Member of IEEE. His research interests are in the fields of power electronic converters, renewable energy technologies, power quality, electrical machines, electric vehicles and smart grid. He has authored or co-authored more than 310 papers including 86 IEEE Transactions/IEEE Journal papers. He has written or edited seven technical books published by Springer and Taylor & Francis. He has received several Best Paper Awards including two Best Paper recognitions from the *IEEE Transactions on Energy Conversion* in 2020. He is serving as Associate Editor for the *IEEE Transactions on Industrial Electronics*, *IEEE Transactions on Energy Conversion*, *IEEE Power Engineering Letters*, and *IEEE Access*. He is also editing a special issue entitled "Advances in High-frequency Isolated Power Converters" for the *IEEE Journal of Emerging and Selected Topics in Industrial Electronics*. He is Editor of the Book Series entitled "Advanced in Power Electronic Converters" for CRC Press, Taylor & Francis Group. He has received several funding from government and industries including in total $5.48 million from Australian Government through Australian Research Council (ARC), e.g. Discovery Project (DP) 2020 entitled "A Next Generation Smart Solid-State Transformer for Power Grid Applications".

Dr. Wei Xu (M'09-SM'13) received the double B.E. and M.E. degrees from Tianjin University, Tianjin, China, in 2002 and 2005, and the Ph.D. from the Institute of Electrical Engineering, Chinese Academy of Sciences, in 2008, respectively, all in Electrical Engineering. His research topics mainly cover design and control of linear/rotary machines.

From 2008 to 2012, he was Postdoctoral Fellow in the University of Technology Sydney, Vice Chancellor Research Fellow in Royal Melbourne Institute of Technology and Japan Science Promotion Society Invitation Fellow in Meiji University, respectively. Since 2013, he has been Full Professor with State Key Laboratory of Advanced Electromagnetic Engineering in Huazhong University of Science and Technology, China. He has more than 110 papers accepted or published in IEEE Journals, two edited books published by Springer Press, one monograph published by China Machine Press and more than 150 Invention Patents granted or in pending, all in the related fields of electrical machines and drives. He is Fellow of the Institute of Engineering and Technology (IET). He is General Chair for 2021 International Symposium on Linear Drives for Industry Applications (LDIA 2021) and 2023 IEEE International Conference on Predictive Control of Electrical Drives and Power Electronics (PRECEDE 2023) in Wuhan, China, respectively. He has served as Associate Editor for several leading IEEE Transactions Journals, such as *IEEE Transactions on Industrial Electronics*, *IEEE Transactions on Vehicular Technology*, *IEEE Transactions on Energy Conversion* and so on.

List of Figures

A Robust Controller for Multilevel Distributed Generation Based Islanded Microgrid

Multi-source Microgrid Frequency Stability Control Using Learning-Based Technology

Hybrid Renewable Energy Systems for Future Power Grids

Operation of Renewable Energy and Energy Storage-Based Hybrid Remote Area Power Supply Systems: Challenges and State-of-the-Arts

A Symbolic Aggregate Approximation-Based Data Mining Tool for the Detection and Classification of Power Grid Voltage Events

Identifying Hosting Capacity of Renewable DG Units in Smart Grids Considering Protection Systems

Management of Distributed Generation for Smart Buildings

Smart Inverters and Controls for Grid-Connected Renewable Energy Sources

Transformerless Three-Phase Solar Photovoltaic Power Conversion Systems

Sensorless Control Technologies for Stand-Alone and Grid-Connected Operation of Brushless Doubly-Fed Induction Generators in Smart Grid

Control and Observation of Induction Motors Based on Full-Order Terminal Sliding-Mode Technique

List of Tables

Management of Distributed Generation for Smart Buildings

Smart Inverters and Controls for Grid-Connected Renewable Energy Sources

Transformerless Three-Phase Solar Photovoltaic Power Conversion Systems

Sensorless Control Technologies for Stand-Alone and Grid-Connected Operation of Brushless Doubly-Fed Induction Generators in Smart Grid

Control and Observation of Induction Motors Based on Full-Order Terminal Sliding-Mode Technique

A Robust Controller for Multilevel Distributed Generation Based Islanded Microgrid

Sadia Afrin Dola, Md. Faisal Rahman Badal, Sajal Kumar Das, Md. Rabiul Islam, and Wei Xu

Abstract The power requirement throughout the world is continuously increasing due to the technological development and change in human life. The unplanned uses of the fossil fuel to fulfill the electric demand hampers the future resources that will make resource threat for the future generation. Non-renewable energy sources are the alternative of fossil fuel that increases the possibility of the microgrid (MG) technology that not only reduces the excess pressure on fossil fuel but also produces clean energy. The control of proper operation of the MG is essential for maintaining stable voltage, current and power delivery. The stable profile of the performance of MG may be greatly hampered due to the presence of load dynamics as well as uncertainties that is responsible to damage the system. This chapter represents an improved design of fuzzy logic control approach to regulate the stable and tracking performance of the MG against different faults and uncertainties.

Keywords Islanded microgrid · Multilevel generation units · Fuzzy logic controller · Fault analysis

S. A. Dola · M. F. R. Badal (✉) · S. K. Das
Rajshahi University of Engineering & Technology, Rajshahi 6204, Bangladesh
e-mail: faisalrahman@mte.ruet.ac.bd

S. K. Das
e-mail: sajal.das@mte.ruet.ac.bd

M. R. Islam
School of Electrical, Computer and Telecommunications Engineering, University of Wollongong (UOW), Wollongong, NSW 2522, Australia
e-mail: mrislam@uow.edu.au

W. Xu
Huazhong University of Science and Technology (HUST), Wuhan 430074, China
e-mail: weixu@hust.edu.cn

S. K. Das et al. (eds.), *Advances in Control Techniques for Smart Grid Applications*,
https://doi.org/10.1007/978-981-16-9856-9_1

List of Symbols

f_{s}	System frequency (Hz)
f_{b}	Base frequency (Hz)
V_s	Location voltage (V)
V_{b}	Base voltage (V)
P	Active power (W)
P_{b}	Base active power (W)
Q	Reactive power (VAR)
Q_{b}	Base reactive power (VAR)
α	Duty cycle
L_t	Inductance (H)
I_L	Inductor current (A)
$\tilde{V}_L$	Inductor voltage (V)
$\tilde{V}_{\mathrm{sw}}$	Switching voltage (V)
$\tilde{V}_{\mathrm{dc}}$	DC source voltage (V)
V_{g}	Grid voltage (V)
C_t	Capacitor (F)
$\tilde{I}_c$	Capacitor current (A)
$\breve{V}_{t,\mathrm{abc}}$	Three-phase terminal voltage (V)
$\breve{I}_{t,\mathrm{abc}}$	Three-phase terminal current (A)
R_t	Terminal resistor (Ω)
V_{abc}	Three-phase base voltage (V)
$\breve{I}_{t,dq}$	Three-phase terminal current in dq frame (A)
$\breve{V}_{dq}$	Three-phase terminal voltage in dq frame (V

List of Acronyms

CoS	Case of system
DER	Distributed energy resource
DG	Distributed generation
DSC	Distributed secondary control
ESS	Energy storage system
FLC	Fuzzy-logic controller
MG	Microgrid
MIMO	Multi-input multi-output
PCC	Point of common coupling
PFSRC	Parallel structure fractional repetitive control
PSO	Particle swarm optimization
pu	Per unit
PV	Photovoltaic

PWM	Pulse width modulation
RE	Renewable energy
VSC	Voltage source converter
VSI	Voltage source inverter

1 Introduction

Fossil fuels are the major choice for generating electricity that are the main cause of the reduction of the fossil fuels as well as the tremendous growth of the greenhouse gases that adversely effects the world environments [1, 2]. These greenhouse gases have an adverse effect on our environment and health of the mass population. Again, once these fossil fuels are finished, they are gone forever.

The procedure of electricity generation, distribution and transmission solely depends on the economical, technical and environmental inducements, which are known as common phenomena in the field of power generation unit. The larger disconnection between the fuel production location and consumption area faces a great challenge due to lack of proper transportation and transmission system [1].

The delivery of the proper power to any location by adjusting the use of fossil fuels, the development of microgrids has been pursued [3–7]. Microgrids are a good means to meet the consumer demand as they are able to supply power by disconnecting the main grid during disturbances. Moreover, the dependency of the world on MG is growing rapidly due to the higher reliability, sustainability, and utility and lower required investment of microgrids [8–13].

Microgrid refers to the small scaled power grid that have its own loads and energy sources and capable to combine and separate itself from the utility grid [1]. It is used to meet the increasing demand for the low-cost electric power. Electrification in remote places and developing countries becomes easier by implementing microgrid [2]. To deliver necessary power to any particular location, the MG concept is emerged including various load dynamics and micro sources functioning in islanded mode which is considered as a single controllable system [2]. The MG concept has created a revolutionary era when distributed generation unit captures the major focus. The MG surrounds a wide variety of distributed energy resources (DER) to develop distribution system of electric power at local downstream [3]. That is why, MG has gained high demand in competitive energy trading market [4]. The idea of generating power from the islanded MG plays an innovative role as electricity delivery system from producers to consumers [5].

1.1 Mode of Operation of Microgrid

The operation of MGs can be divided into two modes. One of them is called grid-connected mode where there is a direct connection between utility grid and MG and the whole performance of the MG can be directly maintained from the utility grid. The connection between the utility grid and MG is termed as point of common coupling (PCC).

Another type is called islanded mode in which the connection of the PCC is kept open that is used in case of fault or disturbance. The main grid has no control over the MG and the profile of the MG voltage or current may be easily hampered at the presence of load dynamics or uncertainties. The control structure of grid-connected and islanded MGs is quite different [12, 14].

1.2 Components of Microgrid

A microgrid generally comprises of some major components such as distributed generation units (DG), loads, immediate storage, power conversion device, controller and point of common coupling as shown in Fig. 1 [3, 4].

1.2.1 Distributed Generation Units

Power generation units are termed as DG units which are mainly renewable energy (RE) sources such as wind, solar, water, biogas etc. RE sources come from nature and these sources are not affected by use. Also, due to their availability, sustainability, ease of use and connection with the MG, low cost and effect on the environment, the use of these RE sources in power systems is growing [15–18]. The lack of the fossil

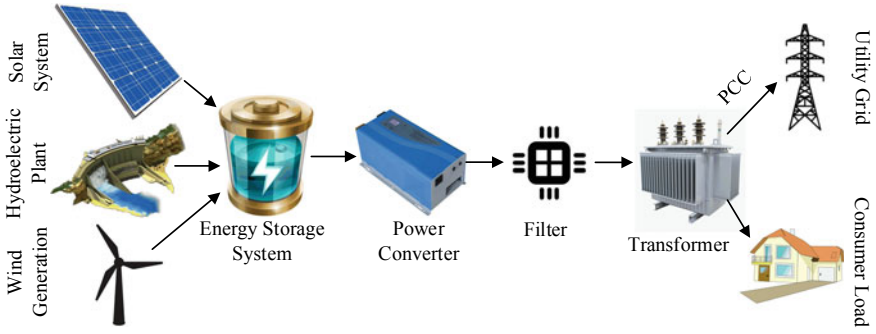

Fig. 1 Typical microgrid system

fuels and easy maintenance of the RE accelerate the dependency of the people on the RE sources and growing interest to make energy farm [19–23].

Standalone solar photovoltaic (PV) resource is used in MG plant to provide basic electricity to the rural residents, even though AC power system is capable enough to transfer efficient amount of voltage by carrying power from producer to consumer with minimum line losses [11]. The disadvantage of wind-turbines and solar parks is they fail to retain balanced position during the time of natural calamity and they cannot compensate the losses [13]. The primary energy source of DG unit can be DC or AC [12]. However, DC zones become more widely distributed and shared over time among customers than AC zones [12]. DG resources must have the characteristics of improved facilities, such as, service and safety reliability, better power supply quality, greater energy efficiency by making use of accessible dissipate heat from power propagation unit [12]. So, DG source will be determined in such a way where major concern will be given to the energy management system to avoid any kind of uncertainties [13].

1.2.2 Power Distribution System

Different types of power distribution system of MG such as DC power distribution microgrid, AC power distribution microgrid and Hybrid DC and AC power distribution microgrid are used to manage electricity demand from RE sources. Figure 2 shows different power distribution systems of MG.

The voltage source converter (VSC), voltage source inverter (VSI), DC/DC and DC/AC converter are used for conversion between AC and DC as per needed by the energy distribution system. Figure 2a represents the AC MG system whose whole control structure is responsible to produce AC power. Large power generating, long distance travelling and power transforming capability increase the popularity of the AC MG [24].

The operation of most telecommunication system, industrial components as well as many home appliances require DC power to maintain their operation which increases the requirement of the DC MG as shown in Fig. 2b. The benefits of both types of MG can be achieved from the AC–DC hybrid MG as shown in Fig. 2c that efficiently regulate the feeder loss, voltage sag and voltage harmonic [24].

Energy storage system (ESS) is used to store the energy for further use. After conversion, the voltage is needed to be stepped up or down as per required by the loads. Step-up and step-down transformers are used for converting the voltage in higher and lower ratings respectively. The loads get connected to the transformer for consuming the electricity [24].

1.2.3 Power Conversion System

Most of the RE sources produces DC power while the loads require AC power to operate that employs the implementation of voltage source converter, voltage source

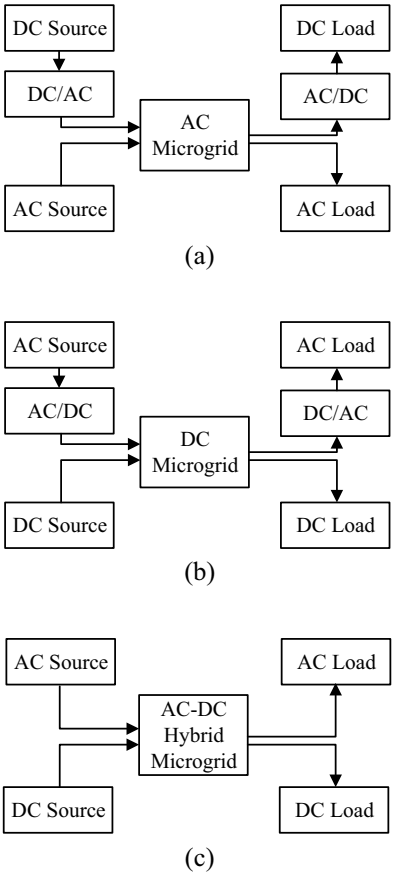

Fig. 2 Power distribution systems of microgrid **a** AC, **b** DC and **c** AC–DC hybrid microgrid

inverter, DC/DC or AC/DC conversion system. Different types of transformer or transformerless inverter with different modulation technique has been employed to control the gate signal of the converter so that it can efficiently produce the AC power and feed it to the load through filter [24].

1.2.4 Filter

The signal may be disturbed by different types of noise and disturbance that makes the signal unstable. To stabilize the voltage and current, a proper filter design is required. The parameter selection of this filter is very important to minimize the higher frequency component from the signals [24].

1.3 Challenges of Controlling Microgrid

In islanded mode, the microgrid system needs to be operated separately from the utility grid. Grid mode is converted into islanded mode at the presence of fault in the transmission line and voltage collapse. Again, the prime mover of the islanded MG is RE sources whose behavior are largely depended on the nature that is responsible for voltage and power profile disturbance. So, the MG system is needed to have its own voltage and power control system. Some technical challenges occur while controlling the voltage of islanded MG. It seems that control and protection become the primary challenge during operation of islanded microgrid [24–26]. The challenging sections of an islanded microgrid are:

(1) As MG uses weather dependent energy sources, the generation of electricity is challenging. Moreover, the design of a hybrid system becomes complicated [10].
(2) In islanded mode, the active and reactive power control become a problem in controlling the MG. So, PQ control is an important consideration in MG [11].
(3) Voltage fluctuation control is another major issue in MG, which is caused due to the non-uniform voltage output from RE sources [12]. The harmonics caused by power electronics devices are also a prime cause of voltage fluctuations [13, 27].
(4) Addition of different load dynamics can cause unstable operation of an islanded MG [14]. So, it is needed to control the operation under the application of different load dynamics.
(5) Uncertainties and faults can degrade the performance of the MG which are major issues in controlling the operation of the MG [28].

2 Control Approaches for Voltage Regulation of Islanded Microgrid

There are different types of MG system having different generation units and architectures [3]. The MG is considered as a case of system (CoS) [18] and control system should be applied to overcome the technical challenges which appear during the operation of MG [19, 20]. Some significant controllers are described in the next section.

2.1 Distributed Secondary Control (DSC)

DSC can be defined as the system where the control elements are distributed throughout the system [21]. It is a system where an auxiliary control system is established along with the primary control system, as shown in Fig. 3 where the DG

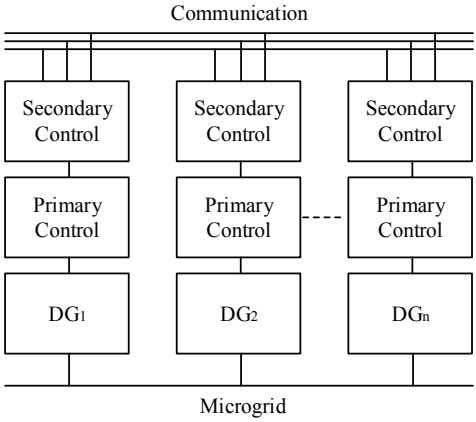

Fig. 3 Illustration of distributed secondary control

units are separately controlled by primary control and secondary control afterwards. After that the DG units are merged at the communication section. This ensures the distribution of the DG units. The main features of this controller are [22, 23, 29]:

- Restoring capability of frequency; and
- Controlling the bus voltage and reactive power.

2.2 *Droop Control*

Commonly used method for controlling the generator's frequency and voltage is droop controller, as shown in Fig. 4, whose governing equations are [26, 30],

$$f_s = f_b + r_p(P - P_b)$$
$$V_s = V_b + r_q(Q - Q_b)$$

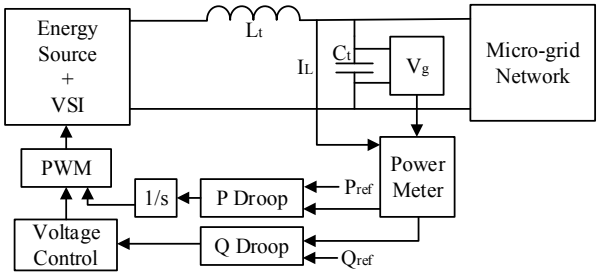

Fig. 4 Illustration of droop control

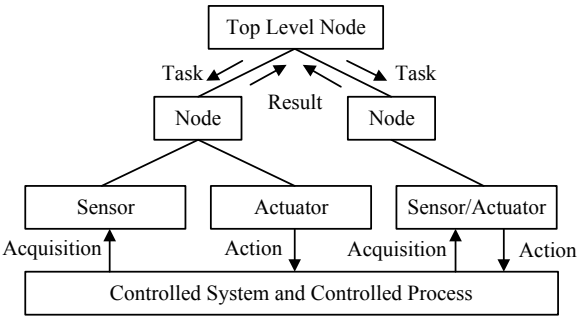

Fig. 5 Illustration of hierarchical control

where f_s and f_b is the system and base frequency, P and P_b represents active and base active power, V_s and V_b represents the voltage at the measurement location and base voltage, Q and Q_b is the reactive power and base reactive power.

Droop controllers are used to coordinate between different DG units. It provides stabilized voltage and frequency output during disturbance in MG. Particle swarm optimization (PSO), inverter output controller optimization, droop controller optimization are some of the optimization techniques used to find the droop control parameters. The major disadvantage of the control method is that it limits the power sharing accuracy due to voltage deviation.

2.3 Hierarchical Control

Hierarchical control arranges the hardware and software hierarchically, as shown in Fig. 5 that enhances the system's bandwidth [31, 32]. The hierarchical control scheme is more feasible. It is a multi-level control method.

2.4 Parallel Structure Fractional Repetitive Control (PSFRC)

PSFRC is a control scheme that gets the tracking error of the system, filters it ith times with a finite of control gains, sums them and gives the best output, shown in Fig. 6. From Fig. 6, Q_i can be represented as [33],

$$Q_i = e^{\frac{ji2\pi\sigma}{n}} * Z^{-\text{round}\left(\frac{N}{n}\right)}$$

where σ is the correction factor, N is the ratio of sampling and fundamental frequency and $i \leq n$.

The controller works in a parallel structure and the filter compensates the error repetitively. The control scheme facilitates more flexibility and substantive selection

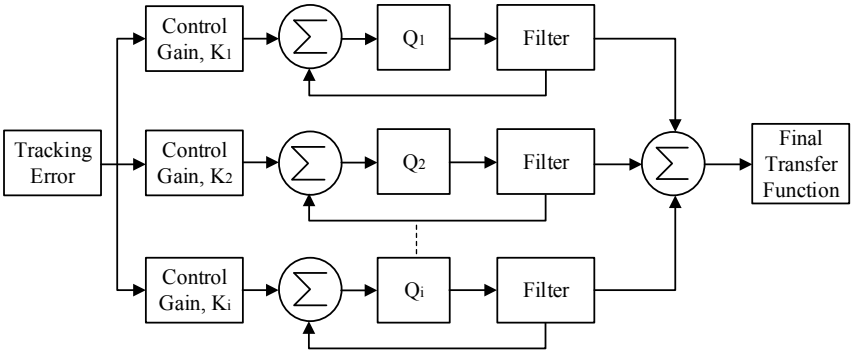

Fig. 6 Block diagram of parallel structure fractional repetitive controller

for different harmonics. Thus, the PSFRC scheme provides improved tracking accuracy for grid simulators. The controller is also faster, more flexible and more accurate than the conventional repetitive control approach. Although the PSFRC gives the MG system flexibility and faster output, the controller has not been tested for uncertainty, fault occurrence and under different loads that are so much important for tracking the performance of a MG [33].

3 Microgrid Modelling

Figure 7 represents the control structure of the single-phase islanded MG where the switching action of the VSI can be represented as $\tilde{V}_{sw} = \propto (s)\tilde{V}_{dc}$, which has impact on the faster action of the MG. Large amount of noise is produced in the VSI side that is diminished by implementing a LC filter. The voltage across the filter capacitor is the grid voltage [26].

Figure 8a, b represents the control structure of three-phase MG with single- and two-phase energy source. Distribution line connects the DG units and transformer

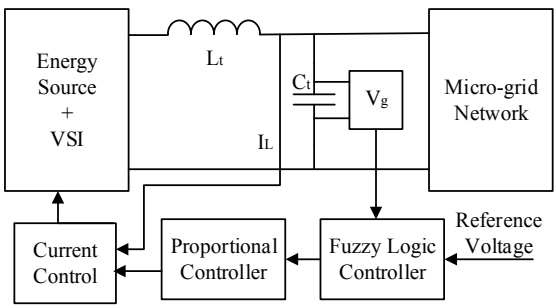

Fig. 7 Closed-loop control strategy for single-phase MG system with a single energy source

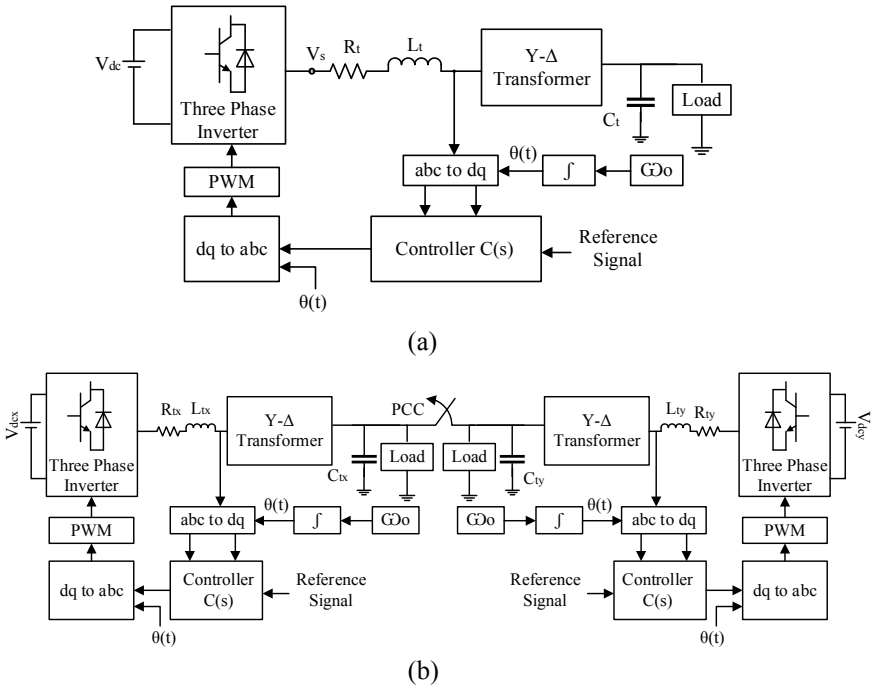

Fig. 8 Closed-loop control strategy for **a** three-phase microgrid system with a single energy source **b** three-phase microgrid systems with dual energy sources

in $Y-\Delta$ connection. The unidentified parameters create undesired noise and disturbances due to the load dynamics. The harmonics and oscillatory behavior may harm the MG systems which is controlled by C_t [34].

3.1 Voltage, Frequency, Current and Power Control Method

The system consists of one basic control structure based on fuzzy logic. First of all, the activation of the current controller is activated for controlling the duty ratio $\propto$ of VSI by using pulse width modulation (PWM) that is responsible to enhance the system's response. The reference signal's parameters are modified with the help of the modulation index. The falsification of the parameters of the reference signal and the modulated unstable state appeared from the carrier signal can be taken into account by characterizing the modulation index [34–36].

The voltage controller finds the grid voltage error with the help of reference voltage and produces an inductor current (I_L) to generate duty ratio $\propto$. The proper regulation of the duty ratio is responsible to stabilize the MG performance against different faults and uncertainties.

3.2 Single-Phase MG Modelling

The inductor voltage $\tilde{V}_L$ can be calculated based on the single-phase MG as shown in Fig. 7 as [34–36],

$$\tilde{V}_L = L_t \frac{\mathrm{d}I_L}{\mathrm{d}t} \tag{1}$$

where L_t is the inductance and I_L is the inductor current. The inverter's switching voltage $\tilde{V}_{\mathrm{sw}}(s)$ is given by,

$$\tilde{V}_{\mathrm{sw}}(s) = \propto (s)\tilde{V}_{\mathrm{dc}}(s) \tag{2}$$

where $\tilde{V}_{\mathrm{dc}}(s)$ is the voltage of the DC source and $\propto (s) \in \{-1, 1\}$.

Hence,

$$\frac{\mathrm{d}I_L}{\mathrm{d}t} = \frac{\tilde{V}_L}{L_t} = \frac{\tilde{V}_{\mathrm{sw}} - V_{\mathrm{g}}}{L_t} \tag{3}$$

The Laplace transformation of these equation can be represented as,

$$\tilde{V}_L(s) = sL_t I_L(s) \tag{4}$$

And

$$I_L(s) = \frac{\tilde{V}_L(s)}{sL_t} = \frac{\tilde{V}_{\mathrm{sw}}(s) - V_{\mathrm{g}}(s)}{sL_t} \tag{5}$$

And the voltage across the capacitor C_t is the output or MG voltage V_{g} that can be given from Fig. 7 as,

$$\frac{\mathrm{d}V_g}{\mathrm{d}t} = \frac{1}{C_t}\tilde{I}_C = \frac{1}{C_t}\left(I_L - \tilde{I}_g\right) \tag{6}$$

where $\tilde{I}_c$ is the capacitor current having capacitance C_t. For linear conversation,

$$\frac{\mathrm{d}x}{\mathrm{d}t} = Ax + Bu \tag{7}$$

$$y = Cx + Du \tag{8}$$

where $x = \begin{bmatrix} I_L \\ V_g \end{bmatrix}$, $y = \begin{bmatrix} 0 \\ V_g \end{bmatrix}$, $A = \begin{bmatrix} 0 & -\frac{1}{L_t} \\ -\frac{1}{C_t} & 0 \end{bmatrix}$, $B = \begin{bmatrix} \frac{1}{L_t} \\ 0 \end{bmatrix}$, $C = \begin{bmatrix} 0 & 1 \end{bmatrix}$, $D = 0$ and $u = \tilde{V}_{sw}$. Then it can be written,

$$\frac{d}{dt}\begin{bmatrix} I_L \\ V_g \end{bmatrix} = \begin{bmatrix} 0 & -\frac{1}{L_t} \\ -\frac{1}{C_t} & 0 \end{bmatrix}\begin{bmatrix} I_L \\ V_g \end{bmatrix} + \begin{bmatrix} \frac{1}{L_t} \\ 0 \end{bmatrix}\begin{bmatrix} \tilde{V}_{sw} \end{bmatrix} + \begin{bmatrix} 0 \\ -\frac{1}{C_t} \end{bmatrix}\begin{bmatrix} \tilde{I}_g \end{bmatrix}$$

and

$$y = \begin{bmatrix} V_g \end{bmatrix} = \begin{bmatrix} 0 & 1 \end{bmatrix}\begin{bmatrix} I_L \\ V_g \end{bmatrix}.$$

3.3 Three-Phase MG Modelling

The mathematical representation of three-phase MG based on Fig. 8a can be given as [34–36],

$$\breve{V}_{t,abc} = L_t \frac{d\breve{I}_{t,abc}}{dt} + R_t \breve{I}_{t,abc} + \breve{V}_{abc} \tag{9}$$

And

$$\frac{d\breve{I}_{t,abc}}{dt} = -\frac{R_t}{L_t}\breve{I}_{t,abc} + \frac{1}{L_t}\breve{V}_{t,abc} - \frac{1}{L_t}\breve{V}_{abc} \tag{10}$$

Hence,

$$\frac{d\breve{V}_{abc}}{dt} = \frac{1}{C_t}\breve{I}_{t,abc} \tag{11}$$

The dq frame of these equations are,

$$\frac{d\breve{I}_{t,dq}}{dt} = -j\omega_o \breve{I}_{t,dq} - \frac{R_t}{L_t}\breve{I}_{t,dq} + \frac{1}{L_t}\breve{V}_{t,dq} - \frac{1}{L_t}\breve{V}_{dq} \tag{12}$$

And

$$\frac{d\breve{V}_{dq}}{dt} = -j\omega_o \breve{V}_{dq} + \frac{1}{C_t}\breve{I}_{t,dq} \tag{13}$$

By separating the d and q part, we can write,

$$\frac{\mathrm{d}}{\mathrm{d}t}\breve{V}_d = \omega_o \breve{V}_q + \frac{1}{C_t}\breve{I}_{t,d} \tag{14}$$

$$\frac{\mathrm{d}}{\mathrm{d}t}\breve{V}_q = -\omega_o \breve{V}_d + \frac{1}{C_t}\breve{I}_{t,q} \tag{15}$$

$$\frac{\mathrm{d}}{\mathrm{d}t}\breve{I}_{t,d=} - \frac{1}{L_t}\breve{V}_d - \frac{R_t}{L_t}\breve{I}_{t,d} + \omega_o \breve{I}_{t,q} + \frac{1}{L_t}\breve{V}_{t,d} \tag{16}$$

$$\frac{\mathrm{d}}{\mathrm{d}t}\breve{I}_{t,q=} - \frac{1}{L_t}\breve{V}_q + \omega_o \breve{I}_{t,d} - \frac{R_t}{L_t}\breve{I}_{t,q} + \frac{1}{L_t}\breve{V}_{t,q} \tag{17}$$

Now using (16) and (17), we consider $G_p(s) = C_p(sI - A_p)^{-1} B_p + D_p$ where

$$A_p = \begin{bmatrix} 0 & \omega_0 & \frac{1}{C_{pt}} & 0 \\ -\omega_0 & 0 & 0 & \frac{1}{C_{pt}} \\ -\frac{1}{L_{tt}} & 0 & \frac{R_{st}}{L_{tt}} & \omega_0 \\ 0 & \frac{1}{L_{tt}} & \omega_0 & \frac{R_{st}}{L_{tt}} \end{bmatrix};\ B_p = \begin{bmatrix} 0 & 0 \\ 0 & 0 \\ \frac{1}{L_{tt}} & 0 \\ 0 & \frac{1}{L_{tt}} \end{bmatrix};\ C_p = \begin{bmatrix} 1 & 0 & 0 & 0 \\ 0 & 1 & 0 & 0 \end{bmatrix};\ \text{and } D_p = 0$$

where the state vector $x = \begin{bmatrix} \breve{V}_d & \breve{V}_q & \breve{I}_{t,d} & \breve{I}_{t,q} \end{bmatrix}^{\mathrm{T}}$; input vector $u = \begin{bmatrix} \breve{V}_{t,d} & \breve{V}_{t,q} \end{bmatrix}^{\mathrm{T}}$ and the output vector $y = \begin{bmatrix} \breve{V}_d & \breve{V}_q \end{bmatrix}$.

4 Controller Design

The nonlinear and uncertain behavior of the RE sources hamper the activities of MG. With the change of environment such as, the direction and speed of wind flow, light intensity, the presence of fog etc., the production of MG is greatly hampered with the fluctuation of the voltage and frequency which requires a proper control design to reduce these impacts.

4.1 Fuzzy-Logic Control

Fuzzy-logic control (FLC), proposed by Lotfi Zadeh in1965, is a rule based powerful tool that can handle any complex problem. This control approach has the capability to deal with the system whose behavior is unknown or ill-defined. Fuzzy logic takes the available dates and controls the system based on the decision-making approach.

4.1.1 Fundamentals of Fuzzy-Logic Control

The fuzzy-logic controller consists of main four part such as, fuzzification, rule-base, interface mechanism, and defuzzification. Fuzzification is the process that makes the system input acceptable for the controller. The system input may be some crisp or algebraic value which is measured from sensors. This crisp input is converted into fuzzy set by the fuzzification approach.

Rule-base is used to make different decision-making condition based on IF–THEN rule. A set of IF–THEN rules are constructed by the expert to deal with the system behavior. The fuzzy input and the rules are fed into the interface mechanism to make the decision based on the system and environment requirement. The mechanism finds the matching percentage between the fuzzy input and rules provided by the expert and produces fuzzy output to feed the system. The processed data of the controller is fed to the practical system through the defuzzification process that converts the fuzzy set into crisp or algebraic value.

4.1.2 Input Membership Functions for Single-Phase FLC

The first step of the FLC is to select the membership function of the input and output of the system. For the single-phase MG, the input membership function has been selected within the range [−500 3000] and triangular membership function has been chosen for the fuzzy input and output where the centroid is used for defuzzification process.

The chosen membership function of the fuzzy inputs has been shown in Fig. 9. Eight membership functions have been considered for the input variables that are labeled as LN = large negative; SP3 = small positive-3, SP2 = small positive-2, SP1 = small positive-1, MP = medium positive, LP1 = large positive-1, LP2 = large positive-2, LP3 = large positive-3 respectively. These functions have the following ranges,

- LN [−500 −250 0];
- SP3 [0 400 800];
- SP2 [400 800 1200]
- SP1 [800 1200 1600];
- MP [1200 1600 2000];
- LP1 [1600 2000 2400];
- LP2 [2000 2400 2800]; and

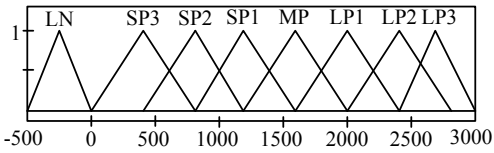

Fig. 9 Input membership functions for single-phase MG based FLC

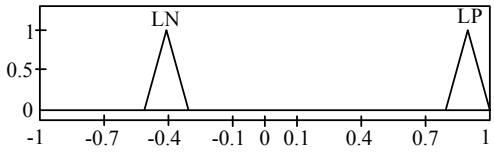

Fig. 10 Output membership functions for single-phase MG based FLC

- LP3 [2400 2700 3000].

4.1.3 Output Membership Functions for Single-Phase FLC

In case of output variable, the membership functions have been chosen within the range [−1 1] in which two triangular membership functions have been selected as, LN = large negative and LP = large positive that is shown in Fig. 10. These functions have the following ranges,

- NB [−0.5 −0.4 −0.3] and
- PB [0.8 0.9 1].

4.1.4 Rule-Set and Rule Viewer for Single-Phase FLC

The next step is to generate the IF–THEN rule based on the input and output variables to meet the requirements of the system. The generated rules between the input (IN) and output (OUT) are given below whose value is represented in Fig. 11,

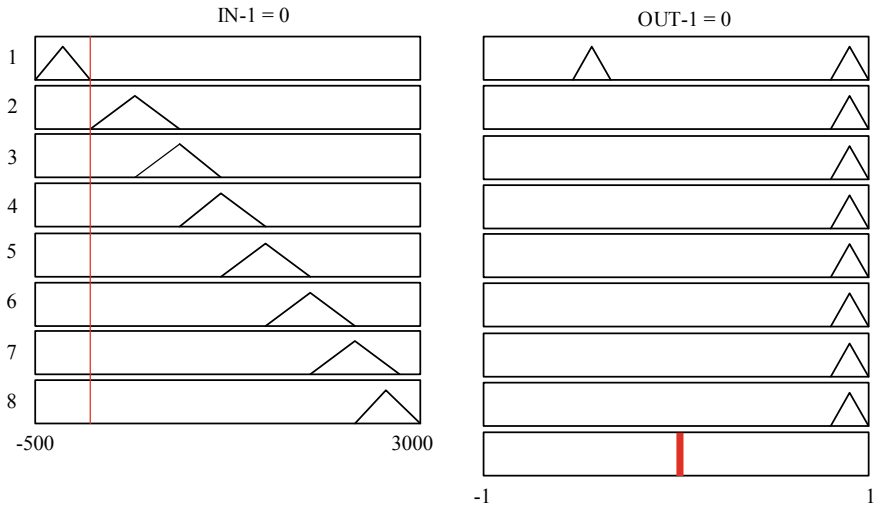

Fig. 11 Rule-set and rule viewer for single-phase MG based FLC

- IF (IN is LN) THEN (OUT is LN);
- IF (IN is SP3) THEN (OUT is LP);
- IF (IN is SP2) THEN (OUT is LP);
- IF (IN is SP1) THEN (OUT is LP);
- IF (IN is LP1) THEN (OUT is LP);
- IF (IN is LP2) THEN (OUT is LP);
- IF (IN is LP3) THEN (OUT is LP); and
- IF (IN is LP1) THEN (OUT is LP).

4.1.5 Graphical User Interface of Three-Phase Fuzzy Controller Design

.

In case of three-phase MG as shown in Fig. 8 that is a MIMO (multi-input multi-output) system, three triangular membership functions have been chosen for the input variable of the three-phase MG system having range [−600 600]. Due to the MIMO system, the three-phase MG has two input and two output. For the input variables, similar membership functions of both the inputs have been selected that is represented in Fig. 12. The three membership functions are chosen as S = small, M = medium and L = large and their ranges are given below,

- S [−600 −450 −300];
- M [−300 0 300]; and
- L [300 450 600].

Similarly, three membership functions have been chosen for both output variables as S = small, M = medium and L = large within the range [−2 2] and the corresponding values are given below as shown in the Fig. 13,

- S [−2 −1.4 −0.8];
- M [−0.8 0 0.8]; and
- L [0.8 1.4 2].

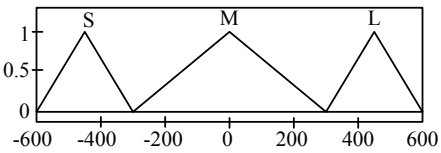

Fig. 12 Membership functions for both IN-1 and IN-2 of three-phase MG

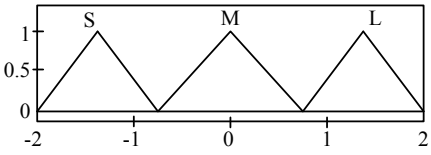

Fig. 13 Membership functions for both OUT-1 and OUT-2 of three-phase MG

After completing the fuzzification of the input and output variables, a rule base has been constructed to interface between the input and output variables. The rules are selected as,

- IF (IN-1 is S) THEN (OUT-1 is S);
- IF (IN-1 is M) THEN (OUT-1 is M);
- IF (IN-1 is L) THEN (OUT-1 is L);
- IF (IN-2 is S) THEN (OUT-2 is S);
- IF (IN-2 is M) THEN (OUT-2 is M); and
- IF (IN-2 is L) THEN (OUT-2 is L).

Figure 14 exhibits the rule base of the FLC for three-phase MG. To test the performance of the designed FLC, the inputs are taken as 0 and the outputs are taken as 1.77e−17 that regulates the MG voltage at stable region based on the constructed rule base.

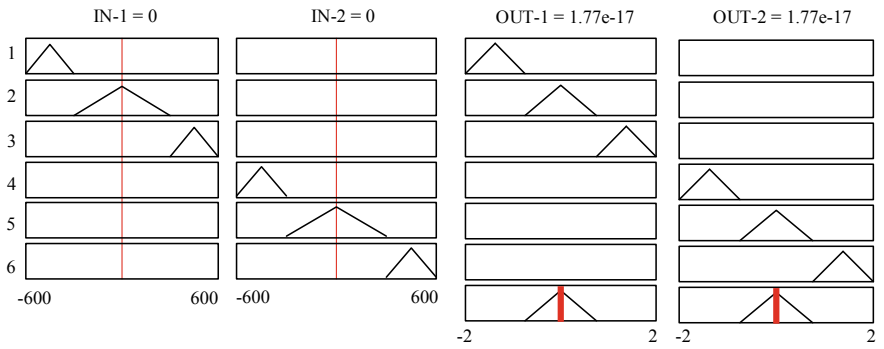

Fig. 14 Rule view

Table 1 Single-phase MG parameters

Parameter	Magnitude
Voltage of the DC bus $\left(\tilde{V}_{\mathrm{dc}}\right)$	300 V
Capacitive type filter (C_t)	15×10^{-9} F
Inductive type filter (L_t)	2×10^{-3} H
Resistance type load (R_L)	0.45 Ω
Consumer type load (R)	40 Ω

5 Performance Evaluation

The proficiency of the proposed controller with both single- and three-phase MG has been investigated here with the help of MATLAB Simulation Software. Tables 1 and 2 represent the parameters for single- and three-phase islanded microgrid.

5.1 Performance Evaluation of the Single-Phase Islanded Microgrid

The performance of the FLC based single- and three-phase MG has been investigated based on the parameters listed in Tables 1 and 2 with load dynamics and uncertainties. The performance has been investigated against different loads such as consumer load, harmonic load, induction load, dynamic load as well as unknown load. Due to the variation of the load, system performance has been changed that will hamper the voltage, current and the power profile of the system.

Figures 15 and 16 show the simulation results for single-phase MG system for current control against dynamic load, harmonic load, induction load and unknown load respectively. The results have been collected without any fault condition where closed-loop responses are quite similar to that of the open-loop responses. Dynamic, harmonic, induction and unknown load provide closed-loop responses of 153 A, 15 A, 100 A and 100 A respectively.

Figures 17 and 18 show the simulation results for single-phase MG power control against dynamic load, harmonic load, induction load and unknown load. The reactive power is always at zero level. It means no generated power is at loss. Dynamic,

Table 2 Three-phase MG parameters

Parameter	Magnitude
Voltage of the DC bus (V_{dc})	2000 V
Voltage of the VSC	600 V
Voltage ratio of the transformer	8.28
Frequency of the PWM carrier	1980 Hz
Frequency of the system (f_0)	60 Hz
Resistance of the VSC filter (R_t)	$1.5 \times 10^{-3}\Omega$
Rated power of DG	3×10^6 VA
Inductance of the VSC filter (L_t)	100×10^{-9} H
Capacitance of the VSC filter (C_t)	100×10^{-9} F
Resistance type load (R)	4.33 Ω
Capacitance type load (C)	100×10^{-3} H
Inductance type load (L)	1×10^{-12} F

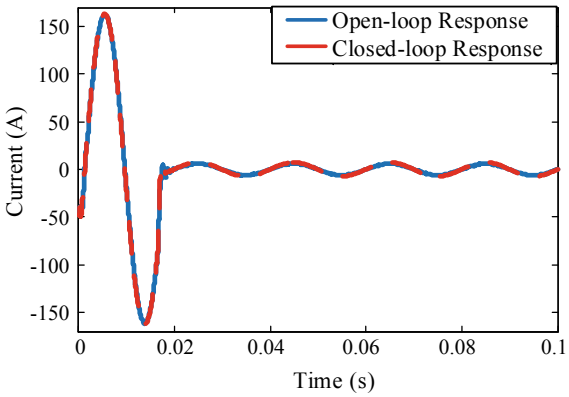

Fig. 15 Single-phase MG response of current control for dynamic load

harmonic, induction and unknown load provide active power responses of 1650 W, 95 W, 1500 W and 280 W respectively.

The voltage control of the single-phase MG under different load dynamics has been investigated in Figs. 19 and 20. The load change is the responsible to fluctuate the voltage profile of the open-loop system as shown in Figs. 19 and 20 that may hamper the MG system and load completely or permanently. The regulation of the MG voltage has been done by employing FLC controller that reduces the fluctuations of the voltage and tracks the reference signal efficiently by maintaining desired frequency and phase. Dynamic, harmonic, induction and unknown load provide closed-loop responses of 300 V voltage respectively.

5.1.1 Performance of Single-Phase MG Against Dynamic Load

The stability and effectiveness of the MG largely depends on the characteristics of the dynamic load. Dynamic load such as a current source having 50 MW active and 25 MW reactive power has been connected with MG to investigate the voltage and power profile. Due to the changing of the load, the system exhibits variable voltage profile which disgraces the power and current stability. The effective control of current, power and voltage are shown in Figs. 15, 17a and 19a, which prove the robust performance of the proposed controller with high bandwidth and stability.

5.1.2 Performance of Single-Phase MG Against Harmonic Load

Computer, television, battery etc. are the examples of harmonic load which produce undesirable harmonics in the MG voltage and current that are responsible for excessive current flow in the system by making a complex current waveform. This excessive current may produce overheating in the system and unsafe the nominal operation of the MG. A third-order parallel harmonic load has been connected with MG having

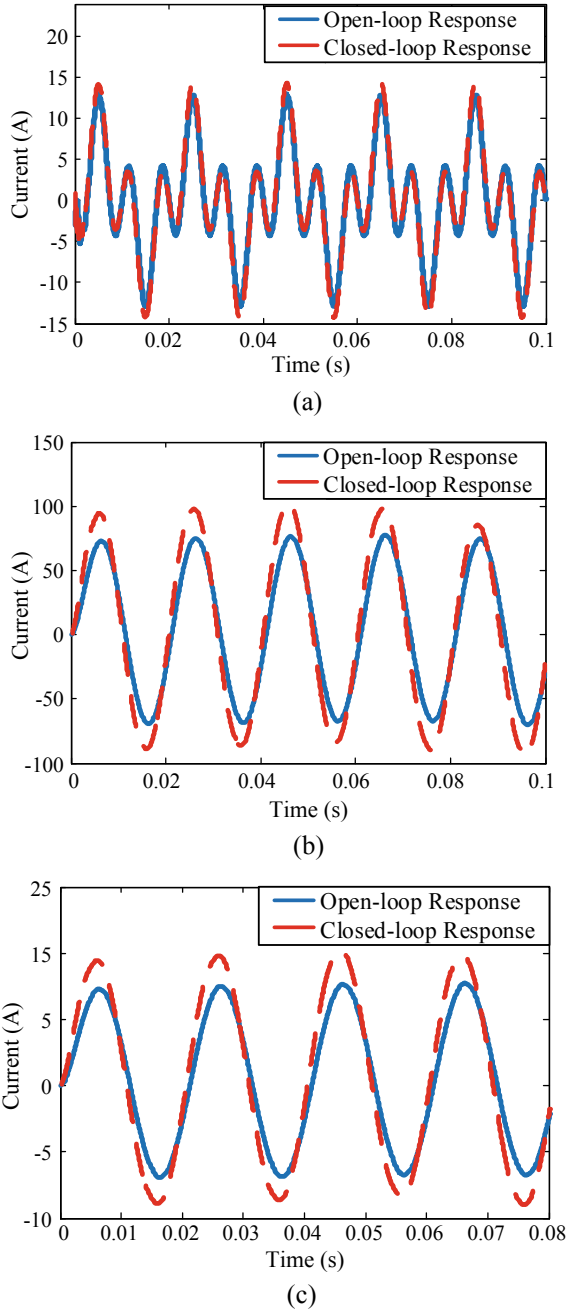

Fig. 16 Single-phase MG responses of current control for **a** harmonic load, **b** induction load and **c** unknown load

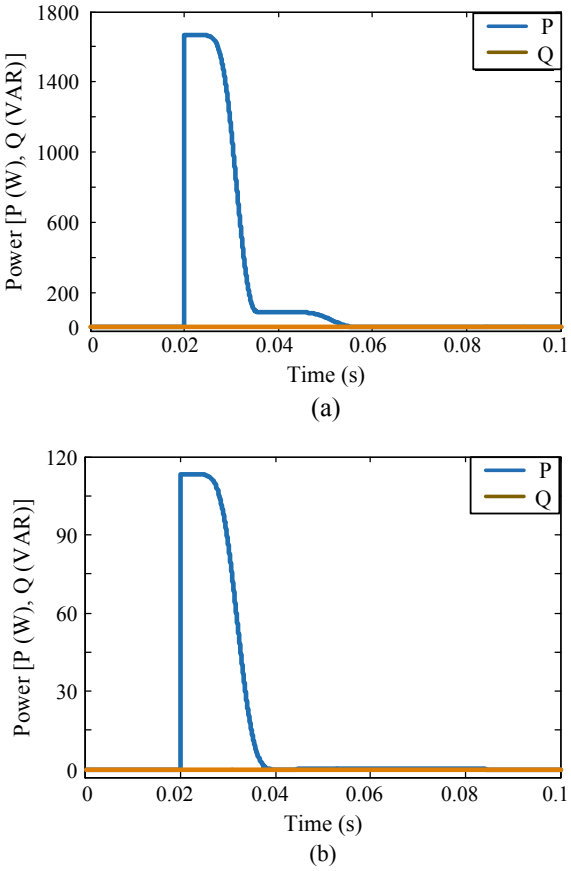

Fig. 17 Single-phase MG responses of power control for **a** dynamic load and **b** harmonic load

7 A current source and 150 Hz frequency. Figures 16a, 17b and 19b present the effective current, power and voltage control of the system using the controller that ensures the effectiveness of the proposed controller.

5.1.3 Performance of Single-Phase MG Against Induction Load

Induction or asynchronous load such as induction motor may hamper the voltage, current and power profile of the MG. An induction motor has been connected with MG in parallel whose steady-state condition has been made zero by using dq frame. The open-loop performances of the system are hampered while using this type of load as shown in Figs. 16b, 18a and 19c. The closed-loop response of the Figs. 16b, 18a and 19c ensure the high performance of the controller that enhances the robustness and stability of MG against asynchronous load.

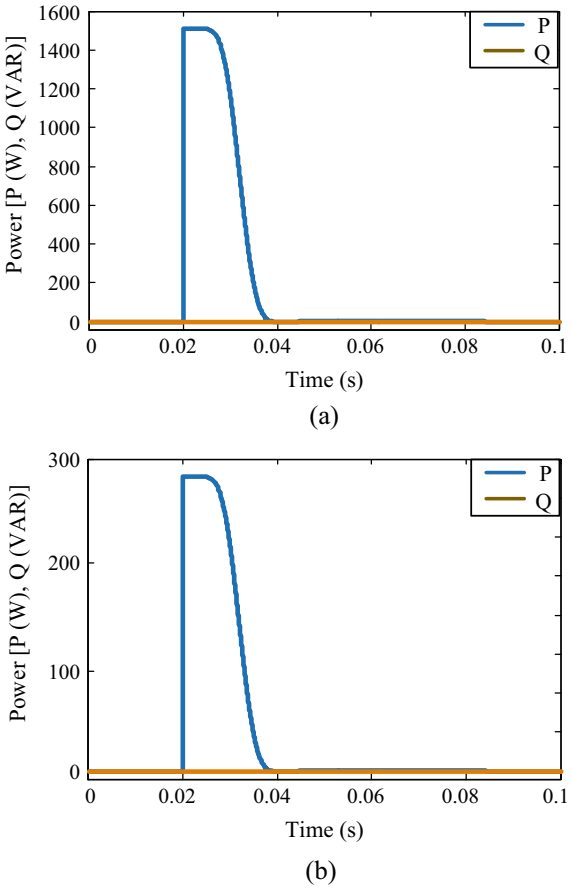

Fig. 18 Single-phase MG responses of power control for **a** induction load and **b** unknown load

5.1.4 Performance of Single-Phase MG Against Unknown Load

The load which is not considered while modeling the system is known as unknown load. The certain presence of the unknown load is responsible to change the system parameters and deviate the system performance. An unknown load is connected with the MG in parallel at 0.02 s which hampers the steady-state of the system and generates undesirable peek in the performance profile. The proposed control algorithm efficiently reduces the peeks and provides a stable performance of the current, power and voltage as shown in Figs. 16c, 18b and 20.

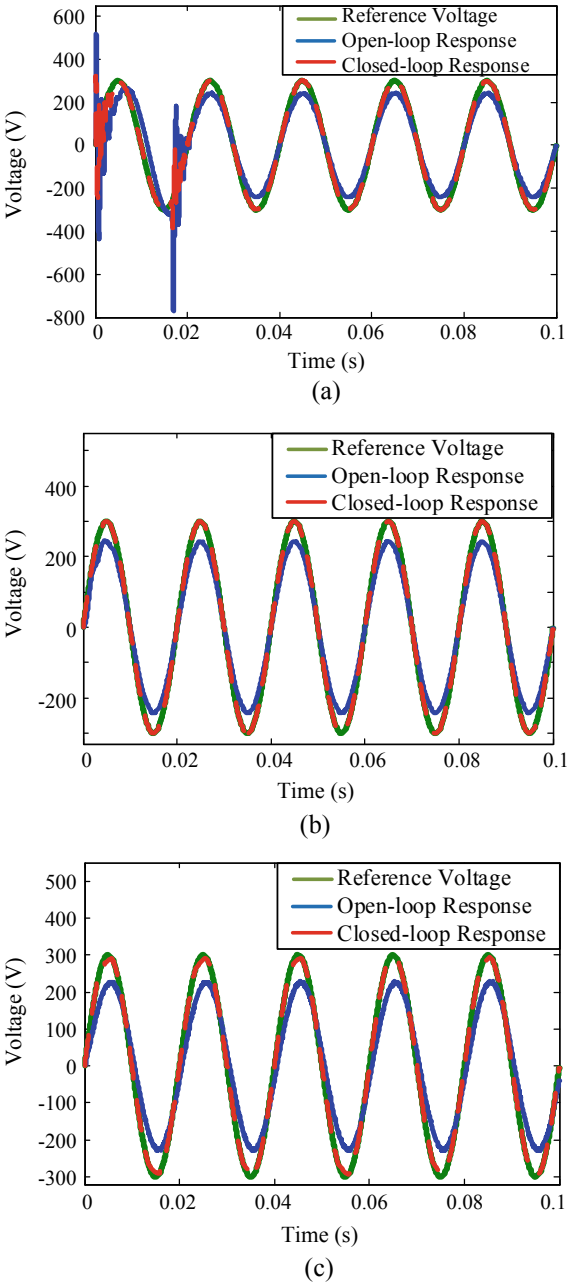

Fig. 19 Single-phase MG responses of voltage control for **a** dynamic load, **b** harmonic load and **c** induction load

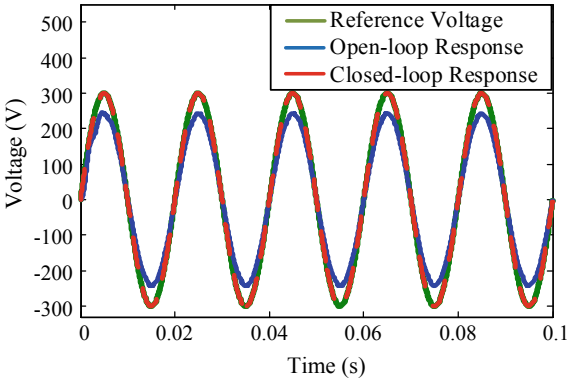

Fig. 20 Single-phase MG response of voltage control for unknown load

5.2 Fault Condition Analysis of Single-Phase MG

To analysis the robust performance of the designed FLC, a mimic environment of the fault has been created on the system and investigates its performance under different loads. The fault has been established in the system between $t = 0.03$ and 0.05 s. During the fault, the system exhibits distorted signal as shown in Figs. 21 and 22 that analyze the simulation results for single-phase MG current control against different loads. The closed-loop responses have shown high tracking performance with respect to reference signal. Dynamic, harmonic, induction and unknown load provide closed-loop responses of 500 A current respectively.

The power analysis of Figs. 23 and 24 are used to ensure the robust performance of the FLC. During the fault, the active power is reduced that is regained its peak value within a short period of time. The reactive power is always zero just like the previous ones. Dynamic, harmonic, induction and unknown load provide active power of 2000 W, 1600 W, 1900 W, 1950 W, respectively.

Figures 25 and 26 show that the open-loop voltage of the single-phase MG is largely distorted during the fault condition that may hamper the load and system permanently or partially. The restoration of the MG voltage is essential within a short period of time for a safe and stable operation of the power system. The closed-loop response of the Figs. 25 and 26 efficiently tracks the reference signal with same frequency and phase that ensures higher tracking and robust performance of the proposed fuzzy-logic controller.

5.3 Performance Investigation of Three-Phase MG

This section has been used to analysis the performance of the three-phase islanded MG against different load dynamics and uncertainties to validate the performance of the proposed control structure. The output results have been shown as per unit (pu)

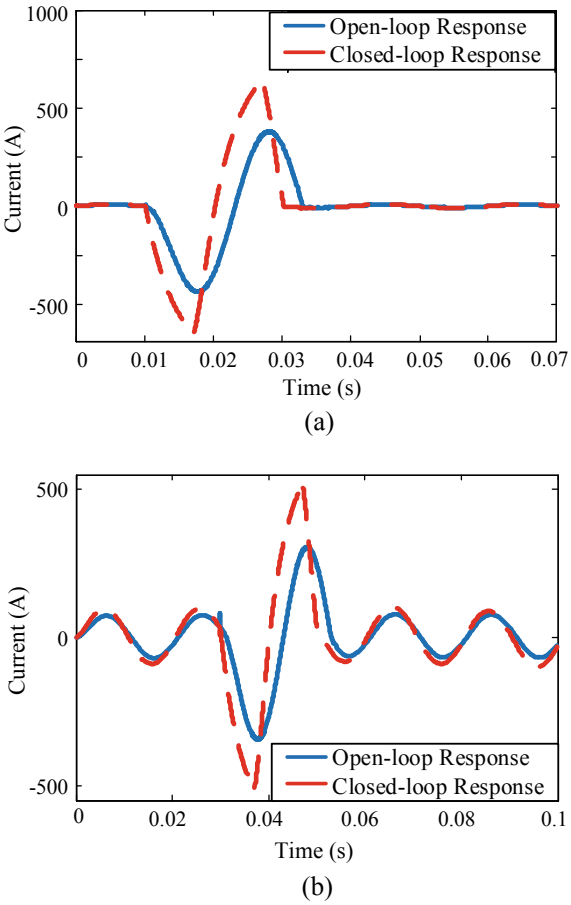

Fig. 21 Single-phase MG fault condition responses of current control for **a** dynamic load and **b** harmonic load

though the phase-to-phase nominal voltage has been set to 600 V. To investigate the performance of the three-phase MG, different loading conditions such as balanced load, consumer load, nonlinear load and unknown load have been used.

5.3.1 Performance Investigation of Three-Phase MG Against Balanced Load

A three-phase balanced load is one whose load impedance and phase angle are equal in each phase. To construct a three-phase balanced load, a resistive load having 3 kW active power and 60 V phase-phase voltage is considered that is connected with the system from 0.3 to 0.31 s to analyze the current, power and voltage profile of the three-phase MG. At this time the performance of the three-phase MG is greatly

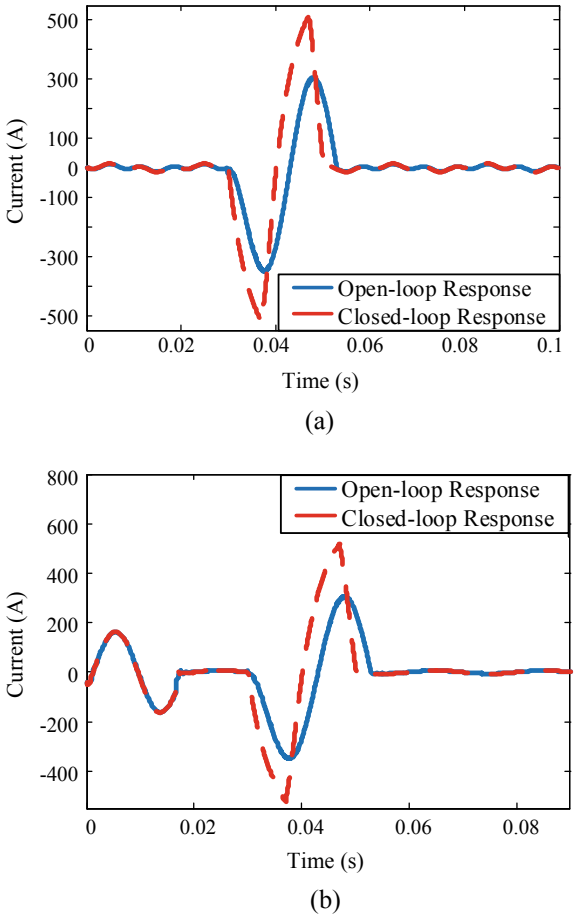

Fig. 22 Single-phase MG fault condition responses of current control for **a** induction load and **b** unknown load

hampered which is regulated properly by the proposed controller as shown in Figs. 27 and 28 that ensure the high performance of the system.

5.3.2 Performance Investigation of Three-phase MG against Consumer Load

The increase of the energy source rises the control parameter of three-phase MG that makes it difficult to control as compared to single-phase MG. The efficiency of the proposed controller against consumer load is shown in Fig. 29 with d and q frame voltage 0.81 and 0.59 pu respectively which ensure the high performance of the proposed controller.

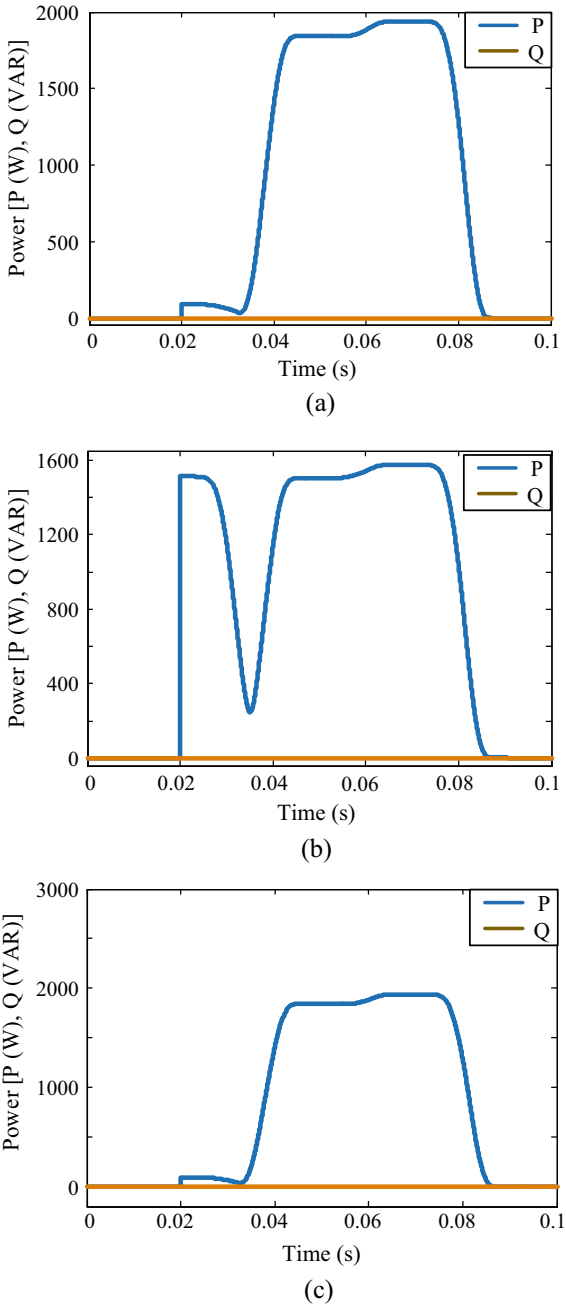

Fig. 23 Single-phase MG fault condition responses of power control for **a** dynamic load, **b** harmonic load and **c** induction load

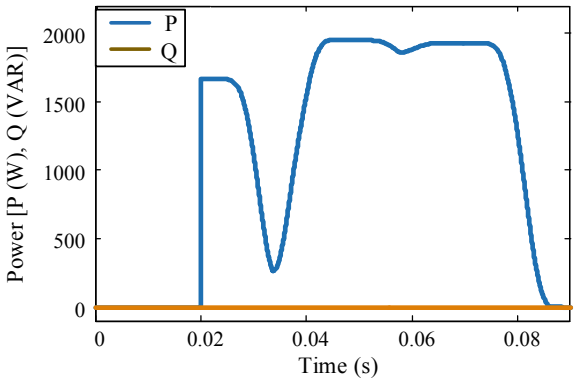

Fig. 24 Single-phase MG fault condition response of power control for unknown load

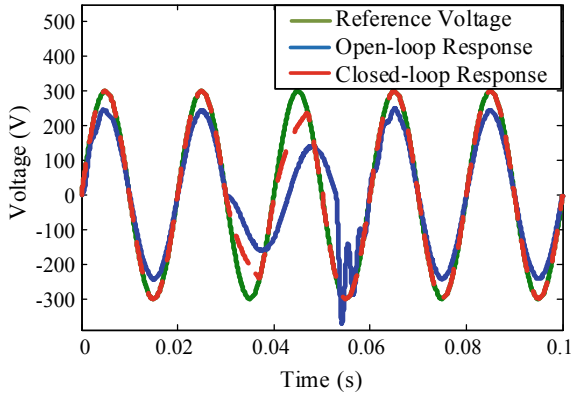

Fig. 25 Single-phase MG fault condition response of voltage control for dynamic load

5.3.3 Performance Investigation of Three-Phase MG Against Nonlinear Load

Electronic lighting, input from the rectifier etc. are the examples of nonlinear load that is responsible to produce third-order harmonic current and voltage in the system and increase the neutral current. This excessive current is responsible for heat generation in the system that may damage the load and power system. To investigate the performance of the designed FLC, a diode rectifier having six pulse is used as nonlinear load which is attached to the system from 0.35 to 0.36 s. The insertion of the nonlinear load into the system is responsible to produce undesirable noise in the system which is diminished by the proposed controller, shown in Figs. 30 and 31.

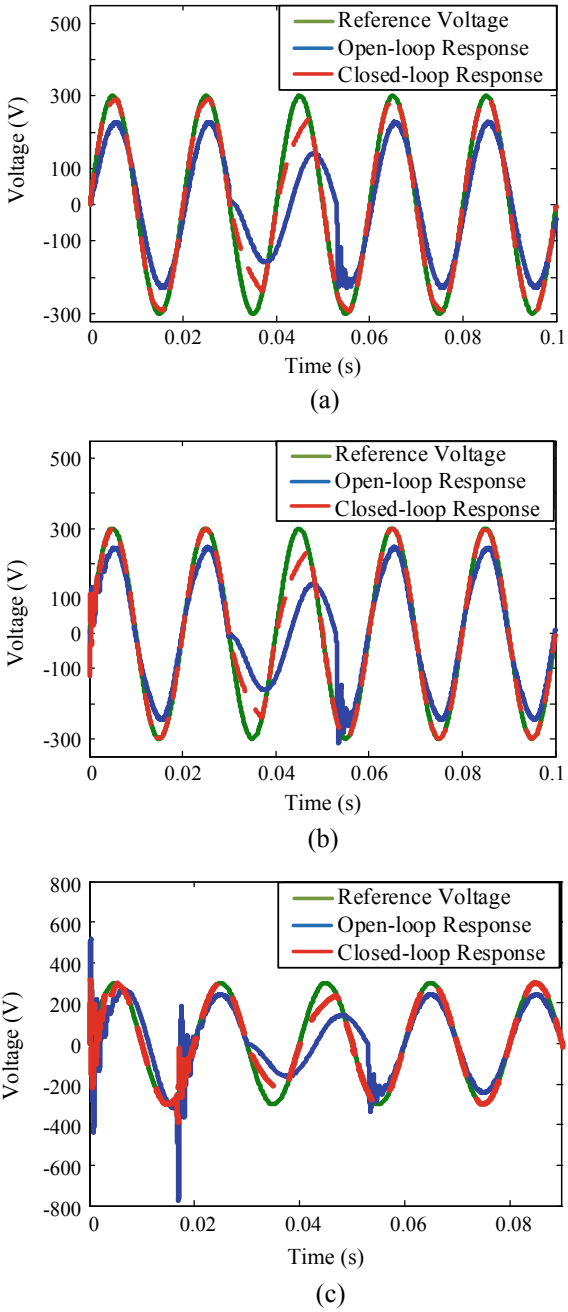

Fig. 26 Single-phase MG fault condition responses of voltage control for **a** harmonic load, **b** induction load and **c** unknown load

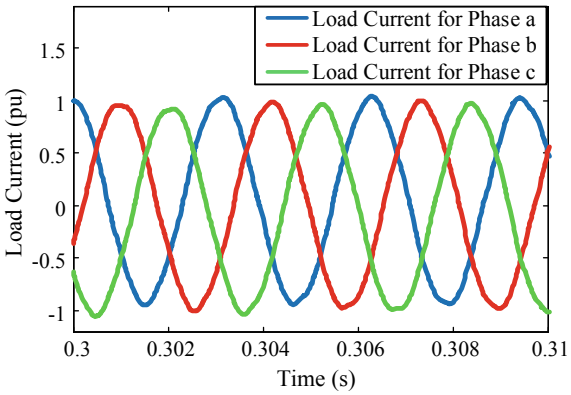

Fig. 27 Control of three-phase MG current under balance load

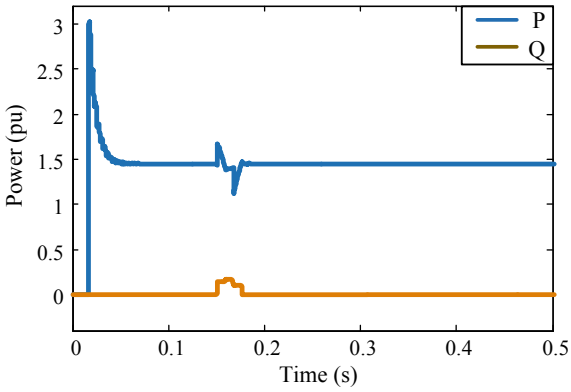

(a)

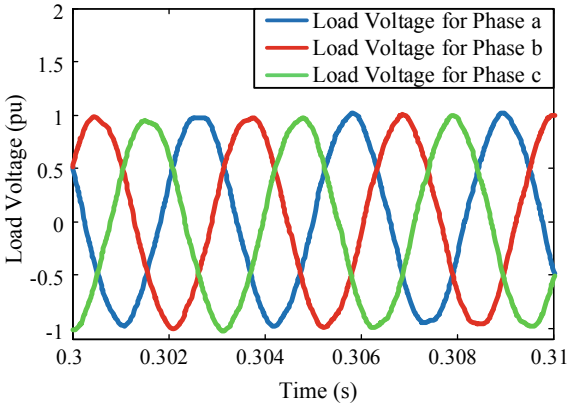

(b)

Fig. 28 Control of three-phase MG **a** power and **b** voltage under balance load

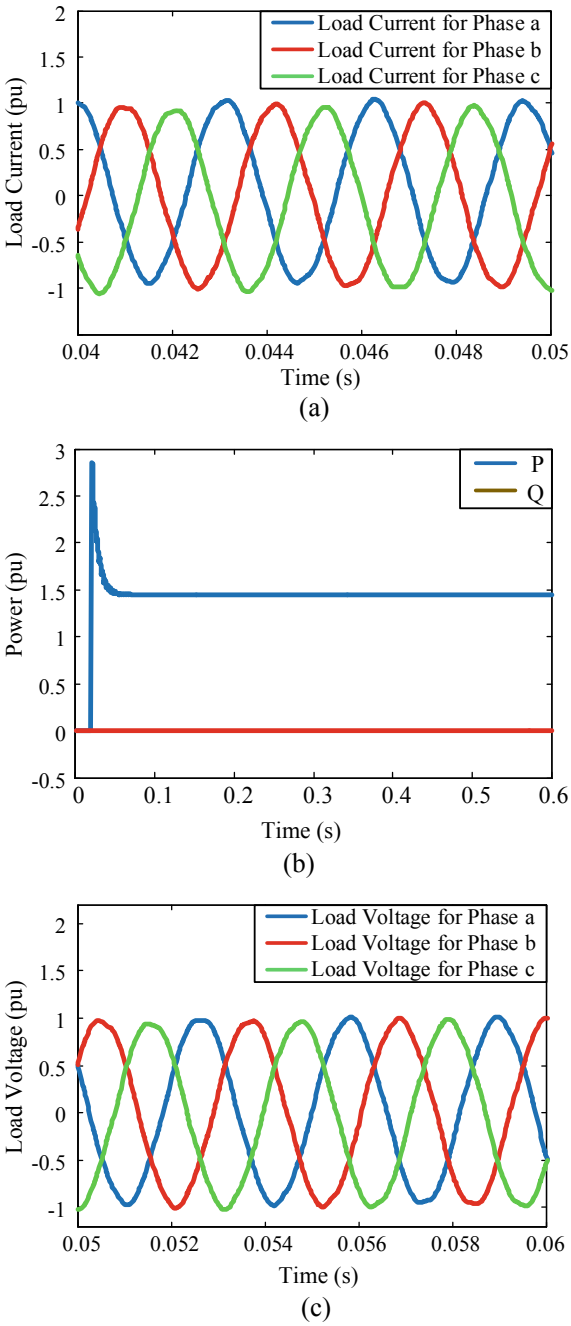

Fig. 29 Control of three-phase MG **a** current **b** power and **c** voltage under consumer load

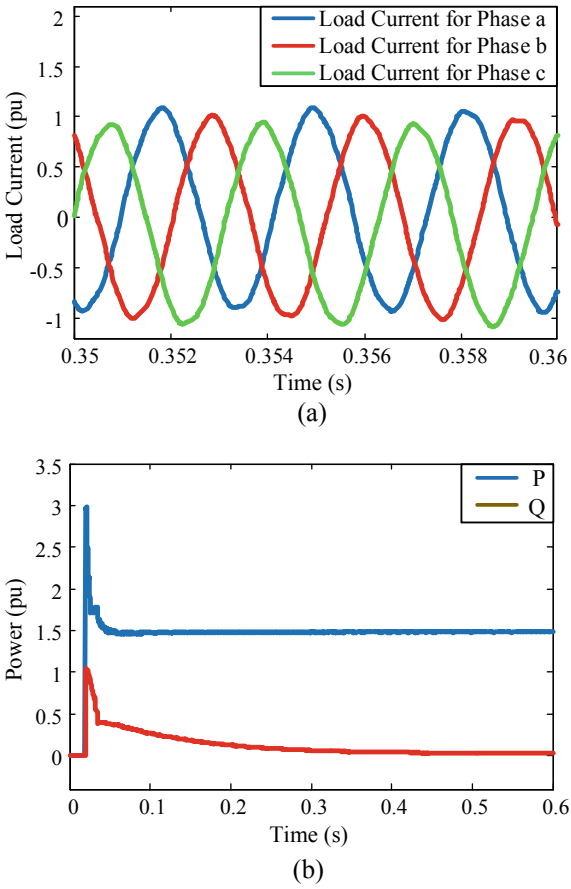

Fig. 30 Control of three-phase MG **a** current and **b** power under nonlinear load

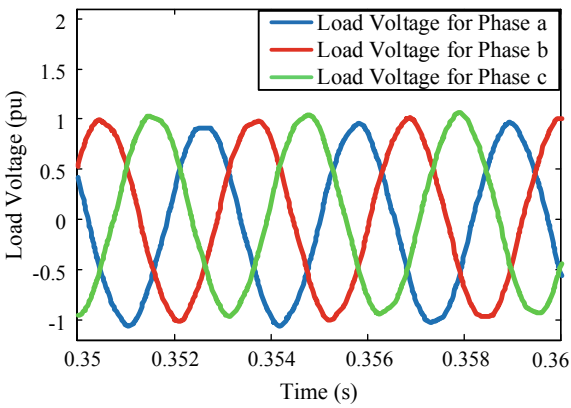

Fig. 31 Control of three-phase MG voltage under nonlinear load

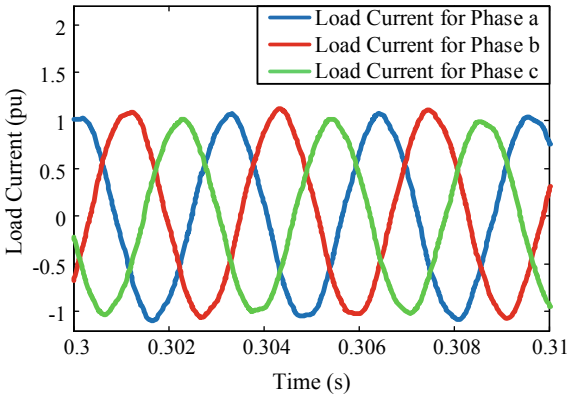

Fig. 32 Control of three-phase MG current under unknown load

5.3.4 Performance Investigation of Three-Phase MG Against Unknown Load

A three-phase unknown load having RLC and switch whose function is to regulate the load after a fixed time such as 0.5 s is connected with three-phase MG. Figures 32 and 33 have been investigated to have the adverse effect of the current, power and voltage of the system against unknown load. The closed-loop performance of the Figs. 32 and 33 ensure the efficient and high performance of the proposed controller.

5.4 Fault Condition Analysis of Three-Phase System

The robustness analysis of the designed FLC controller is ensured by investigating the fault impact on the three-phase MG. The proper control of the MG current at the presence of fault has been analyzed in Figs. 34 and 35. The output results have been shown as per unit (pu) though the phase-to-phase nominal voltage has been set to 600 V. This zoom view of the simulation results declare that current is controlling perfectly as all the three-phases are within value 1 (pu) but during the fault occurrence the current gets higher from 0.36 to 0.38 s and restores the current profile within a short period of time.

Figures 36 and 37 have been investigated for the power control of the three-phase MG at the presence of fault against different loads such as balance load, consumer load, nonlinear load and unknown load. The reactive power is no more at the level zero. Therefore, some power loss occurred here for the three-phase systems. The active power is 1.5 according to the per unit calculation but during the fault condition power gets higher as the current rises.

Figures 38 and 39 analyzed the three-phase MG voltage control for having different load with fault condition. The output results have been shown as per unit (pu) though the phase-to-phase nominal voltage has been set to 600 V. This zoom

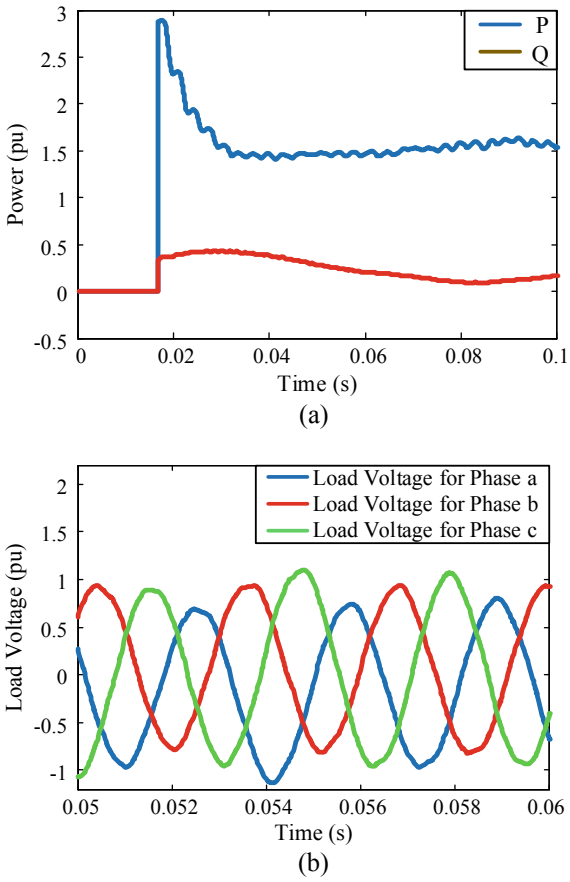

Fig. 33 Control of three-phase MG **a** power and **b** voltage under unknown load

view of the simulation results declare that current is controlling perfectly as all the three-phases are within value 1 (pu) but during the fault condition voltage gets zero as there remains no voltage difference between the source and grid voltage.

5.5 Performance of Multi-level Generation Units

The system design and control complexity will increase with the increasing number of DG unit connected with the power system due to the increased parameters. The effectiveness of the designed FLC controller has been examined in this section in case of multi-level generation system having generation unit DG1 and DG2 against balance load, consumer load, nonlinear load and unknown load. The current profile of the multi-level generation system as shown in Figs. 40 and 41 which ensures that the

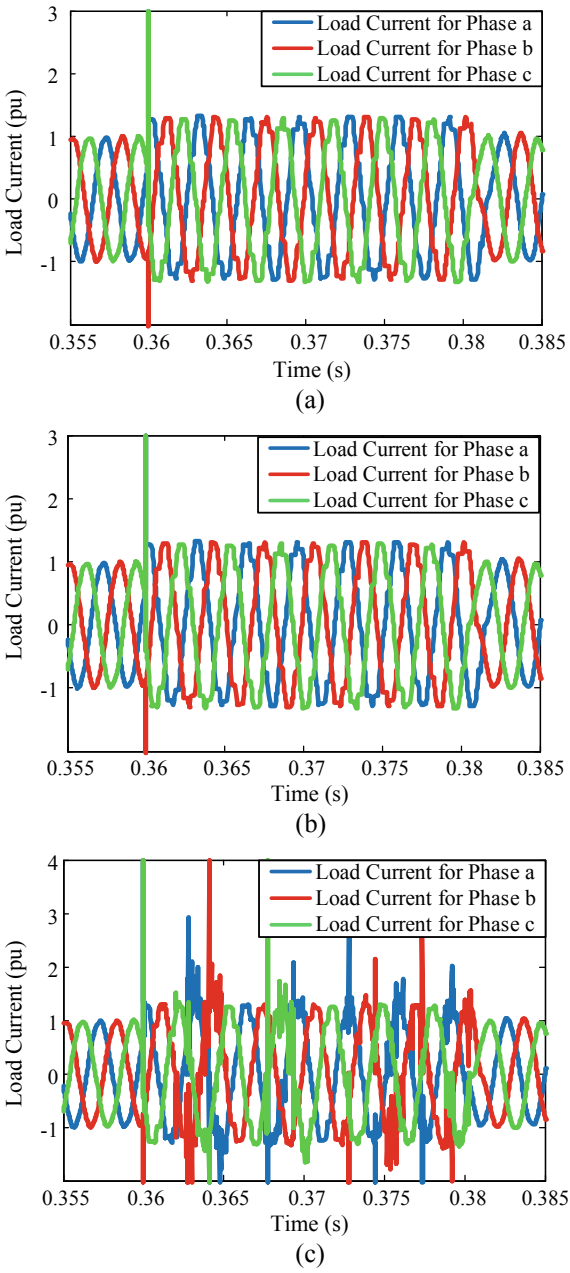

Fig. 34 Three-phase fault condition responses of current control for **a** balance load, **b** consumer load and **c** nonlinear load

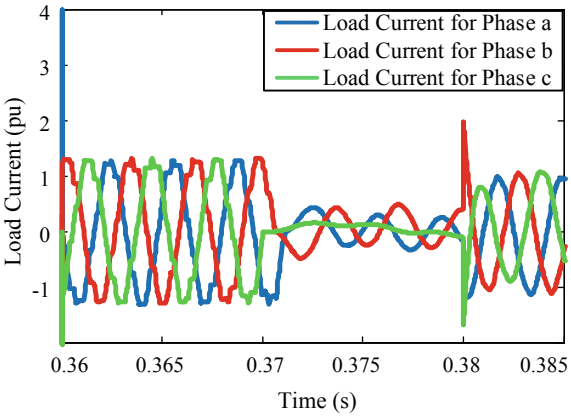

Fig. 35 Three-phase fault condition response of current control for unknown load

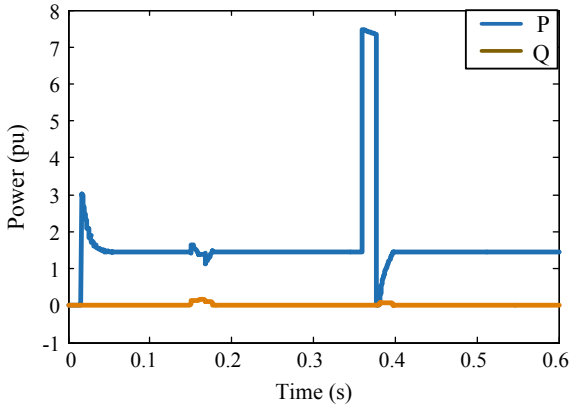

(a)

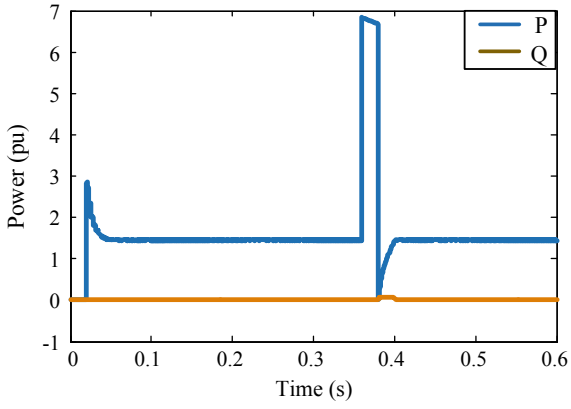

(b)

Fig. 36 Three-phase fault condition responses of power control for **a** balanced load and **b** consumer load

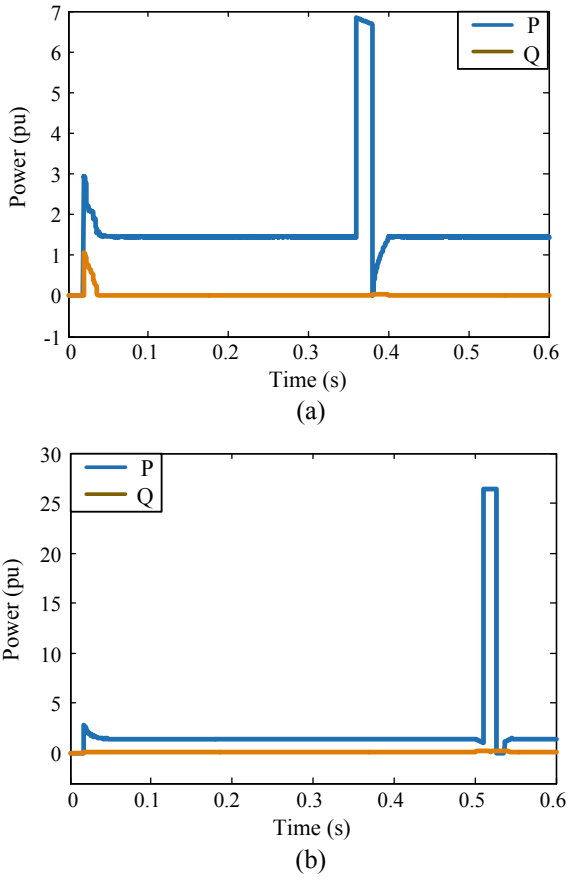

Fig. 37 Three-phase fault condition responses of power control for **a** nonlinear load and **b** unknown load

proposed controller efficiently regulates the closed-loop performance against load dynamics and maintains a reliable and stable operation of the system.

The phase-to-phase nominal voltage has been set to 600 V. The regulation of MG active and reactive power as well as MG voltage as shown in Figs. 42, 43, 44 and 45 shows the higher effectiveness and stable performance of the proposed control algorithm.

6 Conclusion

The thrust of electricity throughout the world can be overcome with the proper implementation of MG. The higher demand of electricity increases the DG units that not only increases the control parameters but also reduces the stability of the MG by increasing its complexity. Again, different noise and harmonics may be

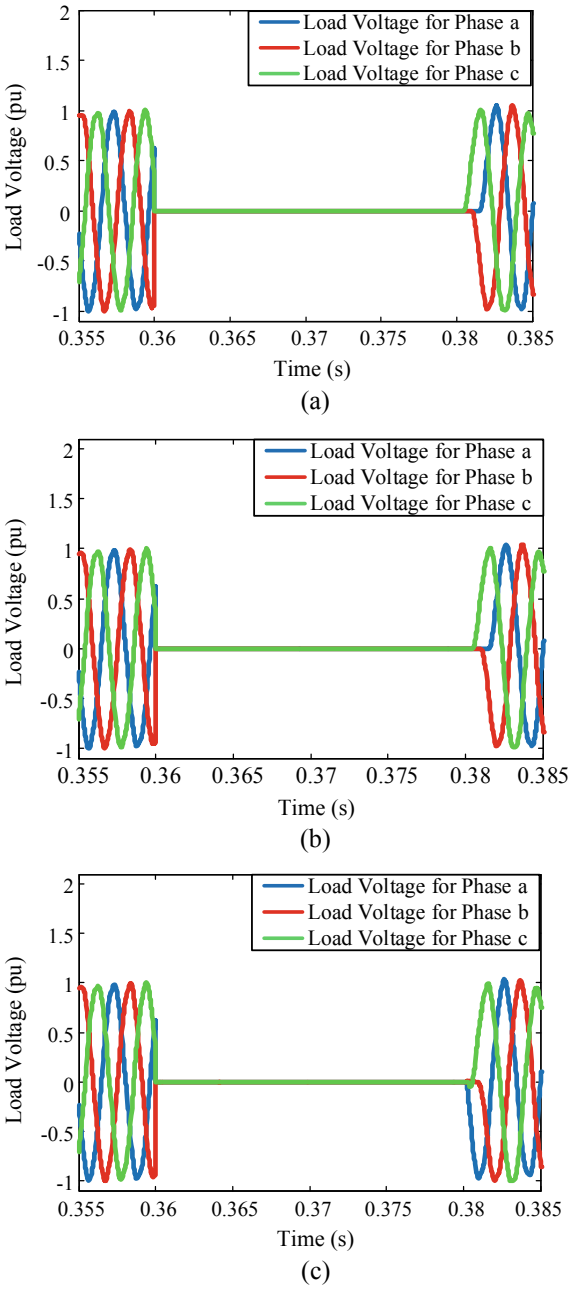

Fig. 38 Three-phase fault condition responses of voltage control for **a** balance load, **b** consumer load and **c** nonlinear load

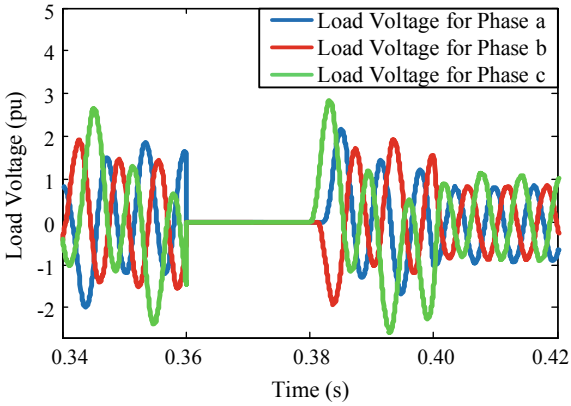

Fig. 39 Three-phase fault condition response of voltage control for unknown load

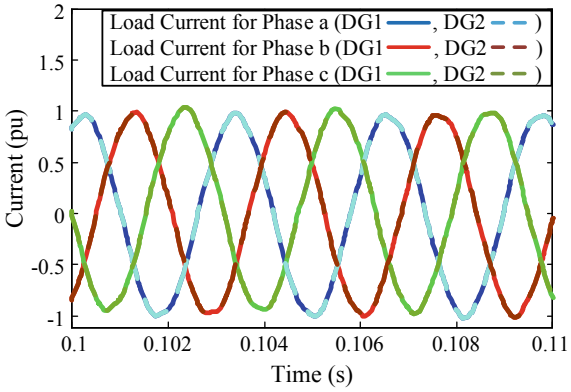

Fig. 40 Three-phase response for multi-level generation unit of current control for balance load

produced in the system at the presence of any fault or uncertainty. The adverse effect of these disturbance has been overcome by designing a robust FLC controller that regulates the frequency, power as well as voltage and current of both single and three-phase MG. Different loads have produced different effect on the performance of MG which is enabled to unstabilize the nominal operation of MG. The proposed controller efficiently minimizes these adverse effects and exhibits high tracking and robust performance for both single and three-phase MG.

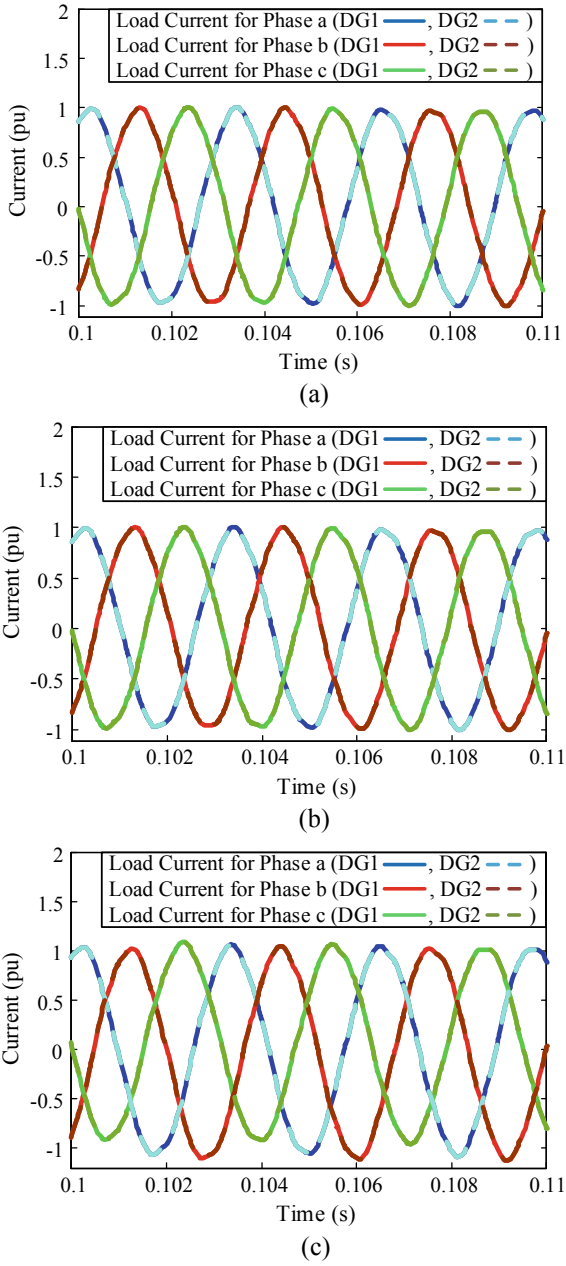

Fig. 41 Three-phase responses for multi-level generation unit of current control for **a** consumer load, **b** nonlinear load and **c** unknown load

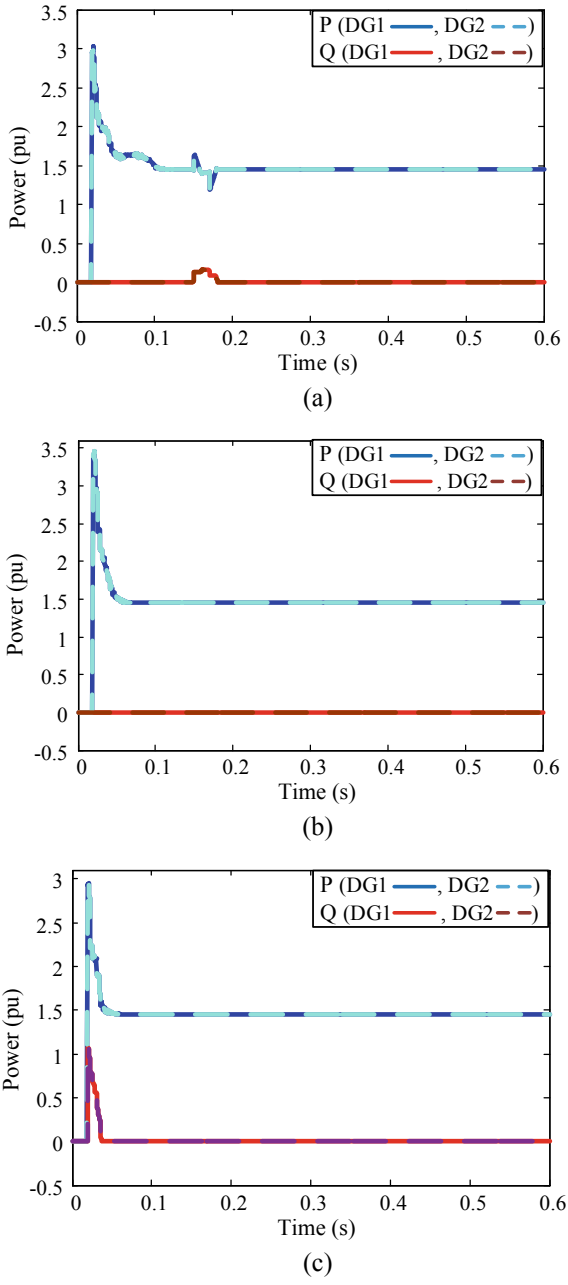

Fig. 42 Three-phase multi-level distributed generation responses of power control for **a** balance load, **b** consumer load and **c** nonlinear load

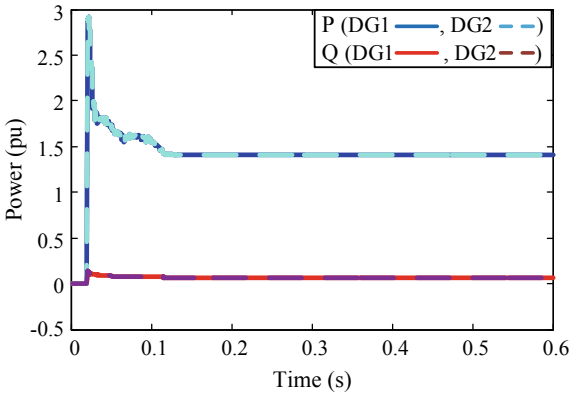

Fig. 43 Three-phase multi-level distributed generation response of power control for unknown load

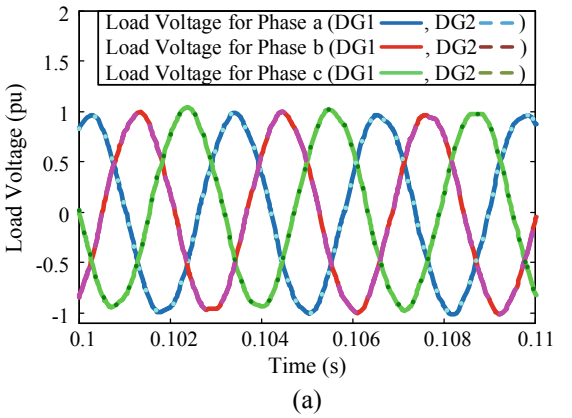

(a)

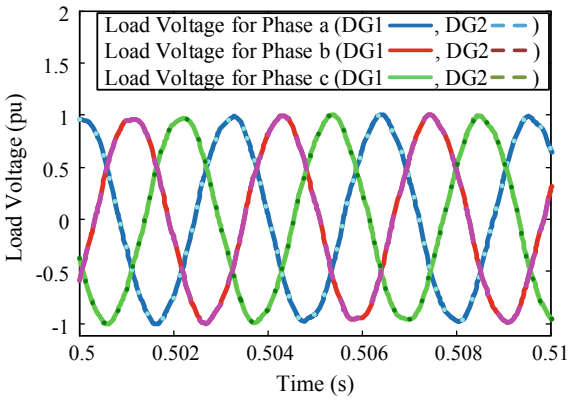

(b)

Fig. 44 Three-phase multi-level distributed generation responses of voltage control for **a** balance load and **b** consumer load

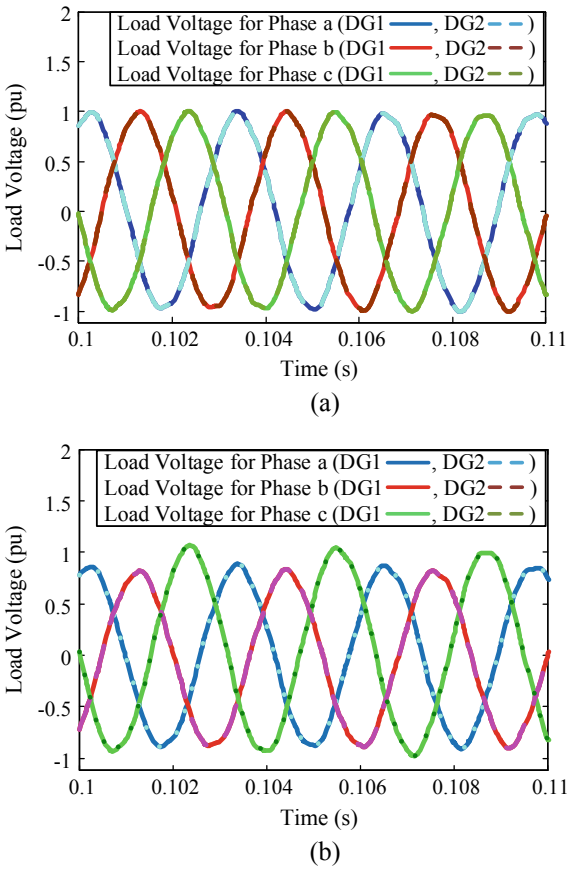

Fig. 45 Three-phase multi-level distributed generation responses of voltage control for **a** nonlinear load and **b** unknown load

References

1. K. Strunz, E. Abbasi, D.N. Huu, DC microgrid for wind and solar power integration. J. IEEE. J. Emerg. Sel. Top. Power Electron. **2**(1), 115–126 (2014)
2. M. Marzband, E. Yousefnejad, A. Sumper, J.L. Domínguez-García, Real time experimental implementation of optimum energy management system in standalone microgrid by using multi-layer ant colony optimization. Int. J. Electr. Power Energy Syst. **75**, 265–274 (2016)
3. F. Katiraei, R. Iravani, N. Hatziargyriou, A. Dimeas, Microgrids management. IEEE Power Energ. Mag. **6**(3), 54–65 (2008)
4. J. Lee, J. Guo, J.K. Choi, M. Zukerman, Distributed energy trading in microgrids: a game-theoretic model and its equilibrium analysis. IEEE Trans. Industr. Electron. **62**(6), 3524–3533 (2015)
5. M. Sechilariu, B. Wang, F. Locment, Building-integrated microgrid: advanced local energy management for forthcoming smart power grid communication. Energy and Buildings **59**, 236–243 (2013)
6. J.M. Guerrero, J.C. Vasquez, J. Matas, L.G. De Vicuña, M. Castilla, Hierarchical control of droop-controlled ac and dc microgrids-a general approach toward standardization. IEEE Trans. Industr. Electron. **58**(1), 158–172 (2011)

7. U.K. Kalla, B. Singh, S. Sreenivasa Murthy, C. Jain, K. Kant, Adaptive sliding mode control of standalone single-phase microgrid using hydro, wind, and solar PV array-based generation. IEEE Trans. Smart Grid **9**(6), 6806–6814 (2017)
8. P. Li, Z.Q. Zheng, Robust adaptive second-order sliding-mode control with fast transient performance. IET Control Theory Appl. **6**(2), 305–312 (2012)
9. M.A. Hossain, H.R. Pota, Voltage tracking of a single-phase inverter in an islanded microgrid. Int. J. Renew. Energy Res. (IJRER) **5**(3), 806–814 (2015)
10. T. Logenthiran, D. Srinivasan, A.M. Khambadkone, Multi-agent system for energy resource scheduling of integrated microgrids in a distributed system. Electric Power Syst. Res. **81**(1), 138–148 (2011)
11. M. Nasir, H.A. Khan, A. Hussain, L. Mateen, N.A. Zaffar, Solar PV-based scalable DC microgrid for rural electrification in developing regions. IEEE Trans. Sustain. Energy **9**(1), 390–399 (2018)
12. Z. Jiang, R.A. Dougal, Hierarchical microgrid paradigm for integration of distributed energy resources, in *2008 IEEE Power and Energy Society General Meeting-Conversion and Delivery of Electrical Energy in the 21st Century* (IEEE, 2008), pp. 1–8
13. J.L. Mirez, H.R. Chamorro, C.A. Ordonez, R. Moreno, Energy management of distributed resources in microgrids, in *2014 IEEE 5th Colombian Workshop on Circuits and Systems (CWCAS)* (IEEE, 2014), pp. 1–5
14. J. Mongkoltanatas, D. Riu, X. LePivert, H infinity controller design for primary frequency control of energy storage in islanding microgrid, in*, 2013 15th European Conference on Power Electronics and Applications (EPE)* (IEEE, 2013), pp. 1–11
15. M. Ge, M.-S. Chiu, Q.G. Wang, Robust PID controller design via LMI approach. J. Process Control **12**(1), 3–13 (2002)
16. M. Armin, P.N. Roy, S.K. Sarkar, S.K. Das, Lmi-based robust pid controller design for voltage control of islanded microgrid. Asian J. Control **20**(5), 2014–2025 (2018)
17. M. Liserre, R. Teodorescu, F. Blaabjerg, Multiple harmonics control for three-phase grid converter systems with the use of PI-RES current controller in a rotating Rrame. IEEE Trans. Power Electron. **21**(3), 836–841 (2006)
18. R. Teodorescu, F. Blaabjerg, M. Liserre, P.C. Loh, Proportional-resonant controllers and filters for grid-connected voltage-source converters. IEEE Proc-Electr. Power Appl. **153**(5), 750–762 (2006)
19. X. Li, Y.-J. Song, S.-B. Han, Frequency control in micro-grid power system combined with electrolyzer system and fuzzy PI controller. J. Power Sources **180**(1), 468–475 (2008)
20. Q. Salem, J. Xie, Transition from grid-connected to islanded drooped microgrid based on islanding detection scheme. Int. J. Power Energy Syst. **36**(3), 112–118 (2016)
21. J.M. Guerrero, M. Chandorkar, T.-L. Lee, P.C. Loh, Advanced control architectures for intelligent microgrids-part I: decentralized and hierarchical control. IEEE Trans. Industr. Electron. **60**(4), 1254–1262 (2013)
22. Q. Shafiee, J.M. Guerrero, J.C. Vasquez, Distributed secondary control for islanded microgrids-a novel approach. IEEE Trans. Power Electron. **29**(2), 1018–1031 (2014)
23. J.M. Wassick, P.S. McCroskey, J.J. McDonough, D.K. Steckler, Model predictive controller. US Patent, vol. 5740033 (1998)
24. F.R. Badal, P. Das, S.K. Sarker, S.K. Das, A survey on control issues in renewable energy integration and microgrid. Protect. Control Modern Power Syst. **4**(1), 1–27 (2019)
25. S.K. Sarkar, F.R. Badal, S.K. Das, A comparative study of high performance robust PID controller for grid voltage control of islanded microgrid. Int. J. Dynam. Control **6**(3), 1207–1217 (2018)
26. S.K. Sarkar, F.R. Badal, S.K. Das, Y. Miao, Discrete time model predictive controller design for voltage control of an islanded microgrid, in *2017 3rd International Conference on Electrical Information and Communication Technology (EICT)* (IEEE, 2017), pp. 1–6
27. Q.L. Lam, A.I. Bratcu, D. Riu, J. Mongkoltanatas, Multi-variable h-infinity robust control applied to primary frequency regulation in microgrids with large integration of photovoltaic energy source, in *2015 IEEE International Conference on Industrial Technology (ICIT)* (IEEE, 2015), pp. 2921–2928

28. M. Ghafouri, U. Karaagac, H. Karimi, S. Jensen, J. Mahseredjian, S.O. Faried, An lqr controller for damping of subsynchronous interaction in dfig-based wind farms. IEEE Trans. Power Syst. **32**(6), 4934–4942 (2017)
29. N. Yang, D. Li, J. Zhang, Y. Xi, Model predictive controller design and implementation on FPGA with application to motor servo system. Control Eng Pract. **20**(11), 1229–1235 (2012)
30. T.L. Vandoorn, B. Renders, L. Degroote, B. Meersman, L. Vandevelde, Voltage control in islanded microgrids by means of a linear-quadratic regulator, in *Proceedings IEEE Benelux Young Researchers Symposium in Electrical Power Engineering (YRS10),* 2010
31. C.E. Garcia, D.M. Prett, M. Morari, Model predictive control: theory and practice-a survey. Automatica **25**(3), 335–348 (1989)
32. Y.A.R.I. Mohamed, A.A. Radwan, Hierarchical control system for robust microgrid operation and seamless mode transfer in active distribution systems. IEEE Trans. Smart Grid **2**(2), 352–362 (2011)
33. T. Liu, D. Wang, Parallel structure fractional repetitive control for PWM inverters. IEEE Trans. Industr. Electron. **62**(8), 5045–5054 (2015)
34. S.K. Sarker, F.R. Badal, P. Das, S.K. Das, Multivariable integral linear quadratic Gaussian robust control of islanded microgrid to mitigate voltage oscillation for improving transient response. Asian J. Control **21**(4), 2114–2125 (2019)
35. S.K. Das, D. Datta, S.K. Sarker, S.R. Fahim, M.R.I. Sheikh, F.R. Badal, Improved voltage oscillation damping and tracking of subgrid of a hybrid ac/dc microgrid using robust integral linear quadratic gaussian control, in *2020 2nd International Conference on Smart Power & Internet Energy Systems (SPIES)* (IEEE, 2020), pp. 299–304
36. M.A. Rahman, S.K. Sarkar, F.R. Badal, S.K. Das, Optimal design of integral linear quadratic Gaussian controller for controlling of islanded microgrid voltage, In *2018 International Conference on Advancement in Electrical and Electronic Engineering (ICAEEE)* (IEEE, 2018), pp. 1–4

Multi-source Microgrid Frequency Stability Control Using Learning-Based Technology

Chaoxu Mu, Yong Zhang, Weiqiang Liu, and Wei Xu

Abstract Due to stochastic power generations and uncertainties, the high penetration rate of renewable energy makes frequency control very difficult. Therefore, for the photovoltaic (PV)-integrated multi-source microgrid, the load frequency control (LFC) problem is investigated. A learning-based frequency control strategy is developed including thermal controller, hydro controller, and auxiliary power controller when the power mismatches occur. The proportion-integral (PI) controller are used for thermal and hydro generation, and auxiliary power controller is designed based on Adaptive dynamic programming (ADP) to improve the adaptability. With the maximal PV power, the auxiliary power controller regulates the PV power to realize the frequency regulation or to be stored by charging electric vehicles (EVs). For the studied benchmark microgrid, several numerical cases are applied to verify the proposed control strategy, which demonstrates the superiority for stabilizing the frequency and fully using solar energy. Further, a model-based intelligent frequency control strategy is designed to adjust the power outputs of micro-turbine and energy storage system (ESS) in the expansion and prospect, which is no longer an auxiliary control strategy.

Keywords Microgrid · Load frequency control · Photovoltaic power · Neural network · Adaptive dynamic programming

List of Symbols

R_s	Series resistance (Ω)
R_{sh}	Parallel resistance (Ω)
I_{ph}	Current source (A)

C. Mu · Y. Zhang · W. Liu
Tianjin University, Tianjin 300072, China
e-mail: cxmu@tju.edu.cn

W. Xu (✉)
Huazhong University of Science and Technology, Wuhan 430074, China
e-mail: weixu@hust.edu.cn

S. K. Das et al. (eds.), *Advances in Control Techniques for Smart Grid Applications*,
https://doi.org/10.1007/978-981-16-9856-9_2

R	External resistance (Ω)
I_{ph}	Current of PV module (A)
I_{pv}	Output current (A)
U_{pv}	Output voltage (V)
I_{d}	Reverse saturation current of diode (A)
K	Boltzmann constant
T	Temperature (°C)
q	Electronic charge of an electron
A	Diode ideality factor
U_{oc}	Open-circuit voltage (V)
U_{m}	MPP output voltage (V)
I_{m}	MPP output current (A)
I_{sc}	Short-circuit current (A)
P_{pv}^{*}	Maximum power of PV module (W)
$\delta_1, \delta_2, \delta_3$	Distribution coefficients
u_{t}	Thermal control signal
u_{h}	Hydro control signal
u_{pv}	PV control signal
u_{e}	EV control signal
Δf	Frequency deviation (Hz)
ΔP_{d}	Power mismatch from load change (p.u.)
ΔP_{pv}	Power mismatch from PV power generation (p.u.)
ΔP_{e}	Output power change of EV aggregator (p.u.)
ΔP_{h}	Output power change of hydro generation (p.u.)
ΔP_{t}	Output power change of thermal generation (p.u.)
ΔX_{hg}	Governor position change of hydro generation
ΔX_{tg}	Governor position change of thermal generation
K_{a}	Changing/discharging coefficient
K_{p}	Microgrid gain
K_{r}	Steam turbine reheat constant
N_{e}	Number of EVs in a EV aggregator
R_{h}	Speed regulation coefficient of hydro generation
R_{t}	Speed regulation coefficient of thermal generation
T_{t}	Steam turbine time constant
T_{e}	Time constant of EV
T_{lg}	Reset time of hydro turbine speed governor
T_{p}	Time constant of microgrid
T_{rh}	Time constant of hydro turbine speed governor transient droop
T_{r}	Steam turbine reheat time constant
T_{tg}	Time constant of speed governor
J	Cost function
U	Utility function
x	State vector
γ	Discount factor
μ	Adaptive power control signal

x_{a}	Input vectors of action networks
x_{c}	Input vectors of critic networks
ψ	Activation function
$\iota_{\mathrm{c}}/\iota_{\mathrm{a}}$	Number of neurons in the input-layer of critic/action network
τ_c/τ_{a}	Number of neurons in the hidden-layer of critic/action network
w_{ij}^{c1}/w_{ij}^{a1}	Weights in input-to-hidden layer of critic/action network
w_j^{c2}/w_j^{a2}	Weights in hidden-to-output layer of critic/action network
q_j^c/q_j^a	Output of jth hidden-layer neuron of critic/action network
p_j^c/p_j^a	Input of jth hidden-layer neuron of critic/action network
$E_{\mathrm{c}}/E_{\mathrm{a}}$	Approximate error of critic/action network
r	Reinforcement learning signal
Q, M	Positive definite matrixes with proper dimensions
$\lambda_{\mathrm{c}}/\lambda_{\mathrm{a}}$	Learning rate of critic/action network
u_{m}	Maximum value of PV reserve power
$\mathcal{F}$	Performance index
ΔP_{mt}	Output power change of micro-turbine (p.u.)
ΔP_{mg}	Governor position change of micro-turbine (p.u.)
ΔP_{ess}	Output power change of ESS (p.u.)
T_{mg}	Time constant of micro-turbine governor
T_{mt}	Time constant of micro-turbine
T_{ess}	Time constant of ESS
σ_{mg}	Uncertain parameter of micro-turbine governor
R_{mt}	Speed regulation coefficient of micro-turbine
u_{mg}	Control signal of micro-turbine
u_{ess}	Control signal of ESS
θ_1, θ_2	Positive constants designed in the cost function
Ω_{c}	Admissible control set
Ess1	Electrical changes of ESS due to frequency control (p.u.)
Ess2	Electrical changes of ESS due to PV power dispatch (p.u.)
Soc^0	Initial electrical energy of ESS (p.u.h)
$\mathrm{Soc}^m/\mathrm{Soc}^M$	Lower/upper bound of SOC (p.u.h)
$\Delta P_{\mathrm{ess}}^m/\Delta P_{\mathrm{ess}}^M$	Lower/upper bound of ESS power output (p.u.)
β	Charging/discharging coefficient of ESS
Bias	Power deviation of load demands and PV
Φ	Regulation coefficient

List of Acronyms

A	Ampere
AC	Alternating current
ADP	Adaptive dynamic programming
DC	Direct current

ESS	Energy storage system
EVs	Electric vehicles
GRC	Generation rate constraint
HJB	Hamiltonian-Jacobi-Bellman
Hz	Hertz
LFC	Load frequency control
MPP	Maximum power point
MPPT	Maximum power point tracker
PI	Proportion-integral
PID	Proportion-integral-derivative
PV	Photovoltaic
PWM	Pulse width modulation
SMC	Sliding mode control
SOC	State of charge
V	Voltage
V2G	Vehicle-to-grid

1 Introduction

In the past few decades, smart grids have rapidly developed and renewable energies have been widely incorporated into the microgrid. In particular, solar energy, as a clean and abundant renewable energy, has attached much attention of many research communities and power industries [1, 2]. However, the available solar energy should be fully used due to the high cost of infrastructure construction [3]. As the photovoltaic (PV) maximum power is easily affected by solar insulation and temperature, it usually requires the PV power generation to track the maximum power point (MPP) [4–9]. PV power generation is very sensitive to weather conditions, and even fluctuates greatly in cloudy days [10–12]. For microgrid, when integrating renewable energy such as PV power generation, there is always power mismatch and random uncertainty.

Although renewable energy has the advantages of low pollution and large reserves, but stochastic and intermittent power generation may cause system instability [13, 14]. For example, PV power varies with weather conditions rather than a constant value, and frequency oscillation would occur as the PV power is injected into the power grid. By using vehicle-to-grid (V2G) technique, EVs have been integrated into the microgrid which can be considered as the mobile energy storage devices and controllable loads [15–17]. EVs can provide power by discharging, or absorb power from generation through charging, which has been widely integrated into the microgrid. The frequency stability is an indispensable factor for the transient stability of microgrid [18]. Therefore, the security of microgrid cannot be guaranteed when the frequency deviation is not stabilized in time. Thus, the frequency regulation is necessary when the power mismatches occur, especially for a multi-source microgrid.

Without considering generator dynamics, a linear model near the operation point is usually applied to the power system [19]. The purpose of frequency regulation is to maintain the frequency convergence in a specified range, and many load frequency control (LFC) methods have been consulted to deal with this problem. For example, the traditional proportion-integral-derivative (PID) control is the earliest used method [20]. After the offline tuning of parameters, the PID controller can have good performance around the designed operating point [21, 22]. In addition, several advanced control methods have also been applied, such as sliding mode control (SMC) [23–25], fuzzy logic control [26–29], robust control [30], intelligent control [31], and so on. Although these controls can reduce the frequency oscillation in some decent, considering the randomness and diversity of load and power generation in the microgrid, it is still an open problem to propose a frequency strategy which is able to deal with more randomness of modern microgrid.

To enhance the adaptivity of frequency regulation for the multi-source microgrid, adaptive dynamic programming (ADP) method has been developed to get the approximate solution for solving optimal control problem, which can be implemented by neural networks [32–34]. This method has been widely used in many fields, such as manipulators [35], spacecrafts [36], quadrotors [37], games [38], navigations [39], as well as in the power systems [40–46]. For example, in [40], the action dependent heuristic dynamic programming was used for the static compensator controller design in a multimachine microgrid. The decentralized control of large-scale power system using ADP method has been studied in [41]. Compared with PID and fuzzy logic control, ADP has an advantage in the optimality and adaptability of the algorithm. This is particularly prominent in dealing with uncertainties, such as the uncertain PV power generation, and it is also the motivation for us to use this method.

At the same time, model parameters such as governor time constant may fluctuate in a small range of nominal values during microgrid operation [47, 48]. The stochastic uncertainties may bring frequency fluctuations for the microgrid [49, 50]. In order to adjust the stochastic uncertainty more effectively, some energy storage devices may be needed, such as energy storage system (ESS), electric vehicles (EVs), etc. [51]. The ESS has excellent charging and discharging performance, which can be applied to improve the controllability and flexibility. Many ESSs have been studied in recent years, such as flywheel ESS [52], battery energy storage station [53–55], and electrolyzer/fuel cell hybrid system [56, 57]. Besides, the state of charge (SOC) is necessary to be regarded as the constraints [58–61]. Therefore, an expansion and prospect is added in this chapter. A model-based intelligent frequency control strategy is designed to adjust the power outputs of micro-turbine and energy storage system (ESS). The stochastic PV power generation, generation rate constraint (GRC) and parameter uncertainties, SOC constraints and ESS power constraints have been considered. Meanwhile, a regulation strategy is proposed for the full utilization of ESS and PV power generation, where the recycling of ESS can be realized. It is worth noting that due to the use of model information, the model-based strategy is completely based on the ADP method but not an auxiliary control strategy, which has much different to the previous works [25, 41, 62].

Based on the aforementioned discussions, a learning-based multi-source frequency control strategy including thermal controller, hydro controller, and power controller is designed for the frequency regulation of a multi-source microgrid composed of reheat-turbine thermal generation, hydro generation, PV system and EVs. It is noted that the three controllers are separately designed and are used to cope with the frequency oscillations simultaneously. The maximum PV power generation is obtained based on the mathematical PV model, and a benchmark multi-source microgrid system with the connection of PV power and EV aggregator is formulated. The multi-source frequency control strategy is composed of thermal controller and hydro controller based on the PI control, and the power controller is designed by using an ADP auxiliary controller to deal with the uncertain PV power generation. The power controller is adopted for managing the PV reserve power and regulating the charging and discharging power of EV aggregator to improve the utilization of solar energy, and the LFC problem under different PV generation scenarios is discussed in detail with comparative case analysis. In the expansion and prospect, a model-based intelligent frequency control strategy is developed to regulate the power output of micro-turbine and ESS, which is completely based on the ADP but not an auxiliary control strategy.

The rest of this chapter is organized as the following sections. In Sect. 2, the studied multi-source microgrid system and the associated mathematical models are introduced. In Sect. 3, three controllers are presented to deal with the frequency oscillations. Section 4 carried out the benchmark microgrid to verify the proposed control strategy in the simulation. For the microgrid with stochastic model uncertainties, a model-based intelligent frequency control strategy is developed in the expansion and prospect in Sect. 5. Some conclusions are given in Sect. 6.

2 Multi-source Benchmark Microgrid

2.1 The Mathematical Model of PV Module

The PV module is made up of semiconductor materials that directly converts the solar irradiance into electrical energy. Figure 1 shows the equivalent circuit of PV module, which is composed of reverse diode, series resistance R_s, parallel resistance R_{sh}, current source I_{ph} and external resistance R.

I_{ph} is the generated current of PV module under the given solar radiation and temperature. I_{pv} and U_{pv} are the output current and voltage, respectively, which can be calculated by

$$I_{pv} = I_{ph} - I_d\left[\exp\left(\frac{q\left(U_{pv} + I_{pv}R_s\right)}{AKT}\right) - 1\right] - \frac{\left(U_{pv} + IR_s\right)}{R_{sh}}, \tag{1a}$$

$$U_{pv} = I_{pv}R, \tag{1b}$$

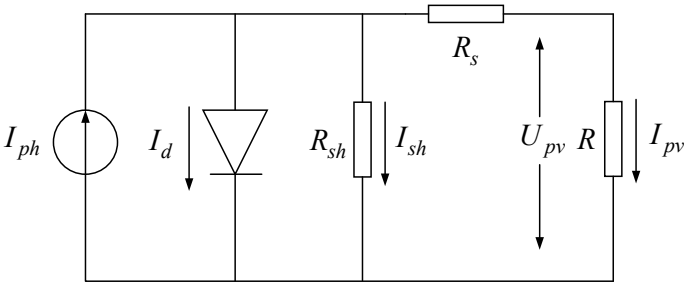

Fig. 1 Equivalent circuit of PV module

where I_{d} is defined as the reverse saturation current of diode, q represents electronic charge of an electron, A is the diode ideality factor, K is the Boltzmann constant, and T is the temperature.

To simplify this model, we do the following simplification. Because R_{s} is very small, and R_{sh} is far greater than R_{s}, so $(U_{\mathrm{pv}} + I_{\mathrm{pv}}R_{\mathrm{s}})/R_{\mathrm{sh}}$ in (1a) can be ignored. Let the short-circuit current I_{ph} be equal to I_{sc}. Then (1a) can be simplified as follows

$$I_{\mathrm{pv}} = I_{\mathrm{sc}}\left\{1 - \alpha_1\left[\exp\left(\frac{U_{\mathrm{pv}}}{\alpha_2 U_{\mathrm{oc}}}\right) - 1\right]\right\}, \tag{2}$$

where U_{oc} is open-circuit voltage. α_1 and α_2 can be expressed as

$$\alpha_1 = \left(1 - \frac{I_{\mathrm{m}}}{I_{\mathrm{sc}}}\right)\exp\left(-\frac{U_{\mathrm{m}}}{\alpha_2 U_{\mathrm{oc}}}\right), \tag{3a}$$

$$\alpha_2 = \left(\frac{U_{\mathrm{m}}}{U_{\mathrm{oc}}} - 1\right)/\ln\left(1 - \frac{I_{\mathrm{m}}}{I_{\mathrm{sc}}}\right), \tag{3b}$$

where U_{m} is the output voltage and I_{m} is the output current when system works at the MPP of PV module. Then the output power can be calculated as

$$P_{\mathrm{pv}}(U_{\mathrm{pv}}) = U_{\mathrm{pv}} I_{\mathrm{sc}}\left\{1 - \alpha_1\left[\exp\left(\frac{U_{\mathrm{pv}}}{\alpha_2 U_{\mathrm{oc}}}\right) - 1\right]\right\}. \tag{4}$$

Therefore, Eqs. (2)–(4) are used to simulate generation process of PV module. When the temperature $T = 25\ ^{\circ}\mathrm{C}$, under different irradiance, Fig. 2 displays the output characteristic curves of PV module. It can be observed that when the temperature is constant, as the radiation decreases, the maximum power of PV module P_{pv}^{*}, the short-circuit current I_{sc} and the open-circuit voltage U_{oc} are reduced. However, ideal conditions may not exist, so in this Chapter, the frequency response of different PV generation scenarios including constant, decreasing and uncertain PV power is investigated in the case analysis.

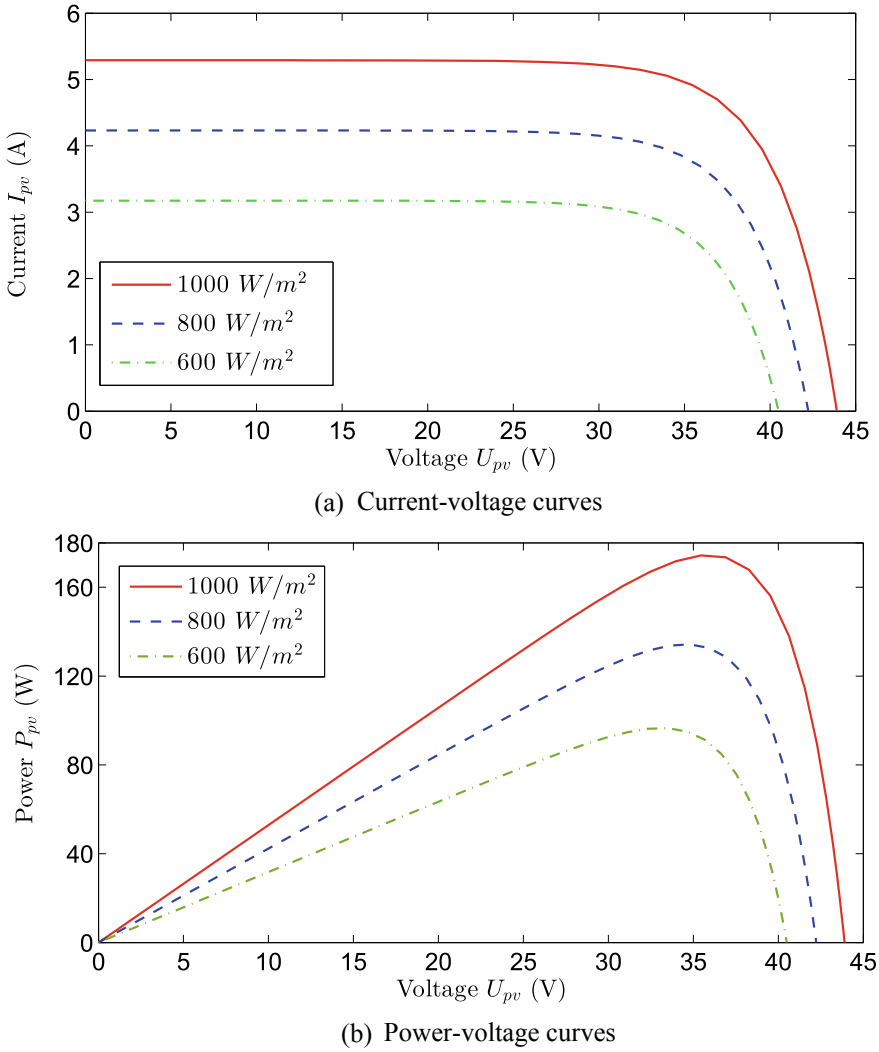

Fig. 2 Output characteristics of PV module

2.2 PV-Integrated Microgrid Description

The studied PV-integrated multi-source microgrid is a single area system containing reheat-turbine thermal generation, hydro generation, PV system, equivalent governor, EV aggregator and loads, and other electrical components. The model of reheat-turbine thermal generation and hydrogeneration can refer to [63]. In this section, the multi-source off-grid benchmark microgrid is investigated, which is shown in Fig. 3. The notations in Fig. 3 can be referred to Table 1.

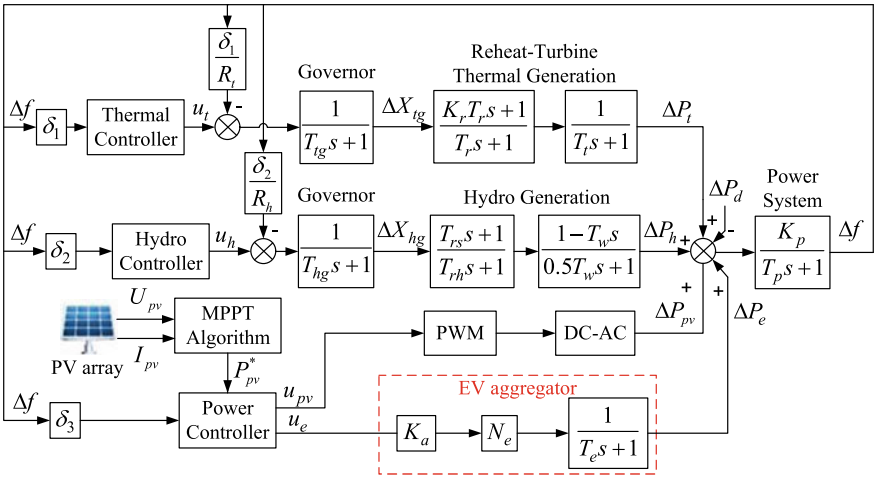

Fig. 3 Schematic diagram of the PV-integrated microgrid

Table 1 Notations in the PV-integrated microgrid

Variables	Meaning of notations
Δf	Frequency deviation
ΔP_{d}	Power mismatch from load change
ΔP_{e}	Output power change of EV aggregator
ΔP_{h}	Output power change of hydro generation
ΔP_{t}	Output power change of thermal generation
ΔX_{hg}	Governor position change of hydro generation
ΔX_{tg}	Governor position change of thermal generation
K_{a}	Changing/discharging coefficient
K_{p}	Microgrid gain
K_{r}	Steam turbine reheat constant
N_{e}	Number of EVs in a EV aggregator
R_{h}	Speed regulation coefficient of hydro generation
R_{t}	Speed regulation coefficient of thermal generation
T_{t}	Steam turbine time constant
T_{e}	Time constant of EV
T_{hg}	Reset time of hydro turbine speed governor
T_{p}	Time constant of microgrid
T_{rh}	Time constant of hydro turbine speed governor transient droop
T_{r}	Steam turbine reheat time constant
T_{tg}	Time constant of speed governor

Furthermore, δ_1, δ_2 and δ_3 are the distribution coefficients of frequency deviations which are defined for the thermal controller, hydro controller and power controller, respectively, and the sum of three distribution coefficients equals to 1. u_t, u_h, u_{pv} and u_e are control laws of different controllers to restrain the frequency deviation.

Compared with the traditional microgrid, the benchmark system in Fig. 3 is integrated PV system and EV aggregator. When the microgrid is stable, we inject most of the PV power generation in microgrid, and the rest PV reserve power is stored in the EV aggregator. When the frequency fluctuations occur, thermal controller, hydro controller, and power controller according to the measured frequency and distribution factor to generate appropriate control signals, so that the frequency deviation can be adjusted quickly and effectively.

3 Frequency Control Strategy for Multi-source Microgrid

In this Section, reheat-turbine thermal generation, hydro generation, PV system and EV aggregator all participate into frequency regulation. Thermal controller and hydro controller are used to adjust reheat-turbine thermal generation and hydro generation, respectively. Based on the collected microgrid data, power controller is adopted for managing the PV reserve power and regulating the charging and discharging power of EV aggregator. Considering that PV system and EVs are faster response than reheat-turbine thermal generation and hydro generation for the power mismatch, the distribution coefficient δ_3 should be much larger than δ_1 and δ_2. In addition, three controllers are designed separately and are used to deal with the frequency deviation at the same time.

3.1 Thermal Controller and Hydro Controller

In the studied microgrid, the reheat-turbine thermal generation and hydro generation are two important power generations, so it is necessary to regulate their output power for reducing the power mismatches. In this Section, both thermal controller and hydro controller are designed by the PI control method for highlighting the role of power controller.

In the proposed strategy, PI controller is used for thermal and hydro control. On the one hand, PI control is a relatively mature and simple method, and there are many work foundations, such as [20–22]. From the perspective of application, this is conducive to engineers' understanding and recognition of the proposed method. On the other hand, the application of relatively complex control methods will not be conducive to highlight the advantages caused by which factors.

3.2 Adaptive Learning Design of Power Controller Based on ADP

To improve PV energy efficiency and eliminate frequency fluctuation, the power controller is proposed to manage the power output of PV system and control the charging or discharging of the EVs. Since an EV only can charge the limited power, so a great number of EVs are controlled as the EV aggregators. Then, the power controller gives the control signal to the pulse width modulation (PWM) to generate a suitable PV reserve power output, and provides a control signal to charge and discharge of EV aggregator. Considering the PV power integration and load disturbances, a controller with strong adaptive ability is needed. In addition to the PI controller, an ADP auxiliary controller is contained in the power controller design by using ADP-based auxiliary control approach.

In the ADP-based auxiliary control approach, the frequency deviations of multiple time instants and the auxiliary control signal will be used to construct the cost function. Based on the reinforcement learning mechanism, through the interaction between the microgrid and the network environment, the goal is to minimize the cost function, corresponding to the physical system, that is, to minimize the frequency fluctuation. Through iterative learning, the approximate optimal control strategy will be obtained. Therefore, under this proposed strategy, the frequency fluctuation of microgrid can be suppressed and the stability will be improved.

Then, the cost function for the frequency regulation of PV-integrated multi-source microgrid can be formulated as

$$J(t) = \sum_{\varepsilon=t}^{\infty} \gamma^{\varepsilon-t} U(x(\varepsilon), \mu(\varepsilon), \varepsilon), \tag{5}$$

where $U(x(t), \mu(t), t)$ is the utility function. $x(t)$, $\mu(t)$ and γ are state vector, control signal and discount factor, respectively. To obtain the approximate optimal control, ADP method is applied for solving the Bellman equation

$$J^*(t) = \min_{\mu(t)} \left\{ U(x(t), \mu(t), t) + \gamma J^*(t+1) \right\}, \tag{6}$$

where $J^*(t)$ represents the current minimum cost function and $J^*(t+1)$ is the minimum cost in the future. With the optimal control law $\mu^*(t)$, the optimal cost function $J^*(t)$ can be achieved. Generally, the optimal control law $\mu^*(t)$ is difficult to be directly solved, since $J^*(t+1)$ is unknown. Therefore, neural networks as the functional approximation method are applied to approximately solve the Bellman equation and implement the ADP-based algorithm.

The ADP algorithm is implemented in a heuristic action-critic structure in this Section, which contains an action network and a critic network. Therein, the control structure is used to approximate the optimal control and the optimal cost by using

action and critic networks, respectively. Specifically, we will give the detailed mathematical basis and calculation principle of the ADP algorithm below.

The input of critic network contains $x_{\mathrm{a}}(t)$ and $\hat{\mu}(t)$, and the output is the approximate cost function $\hat{J}(t)$. For the action network, $x_{\mathrm{a}}(t)$ is the input vector which demonstrate the frequency deviations of multiple time instants, and the output vector $\hat{\mu}(t)$ is defined as the adaptive auxiliary control law. The input vectors of these two networks can be expressed as

$$x_{\mathrm{a}}(t) = [\delta_3 \Delta f(t), \ldots, \delta_3 \Delta f(t - \iota_{\mathrm{a}} + 1)]^{\mathrm{T}} \in \mathbb{R}^{\iota_{\mathrm{a}}},$$
$$x_{\mathrm{c}}(t) = \left[\hat{\mu}(t), \delta_3 \Delta f(t), \ldots, \delta_3 \Delta f(t - \iota_{\mathrm{c}} + 2)\right]^{\mathrm{T}} \in \mathbb{R}^{\iota_{\mathrm{c}}}.$$

In this Section, the sigmoid function $\psi(z) = \left(1 - e^{-z}\right)/\left(1 + e^{-z}\right)$ is used as the activation function of both action and critic networks. Then we can calculate the approximate cost value $\hat{J}(t)$ as follows

$$\hat{J}(t) = \sum_{j=1}^{\tau_{\mathrm{c}}} w_j^{c2}(t) q_j^c(t), \quad j = 1, \ldots, \tau_{\mathrm{c}}, \tag{7a}$$

$$q_j^c(t) = \left(1 - e^{-p_j^c(t)}\right)/\left(1 + e^{-p_j^c(t)}\right), \tag{7b}$$

$$p_j^c(t) = \sum_{i=1}^{\iota_{\mathrm{c}}} w_{ij}^{c1}(t) x_{\mathrm{c}}(t), \quad i = 1, \ldots, \iota_{\mathrm{c}}, \tag{7c}$$

where ι_{c} and τ_{c} represent the number of neurons in the input-layer and hidden-layer of critic network, respectively. $w_{ij}^{c1}(t) \in \mathbb{R}, i = 1, \ldots \iota_{\mathrm{c}}, j = 1, \ldots, \tau_{\mathrm{c}}$ and $w_j^{c2}(t) \in \mathbb{R}$ represent the weight vectors used in the input-to-hidden layer and hidden-to-output layer, respectively. $q_j^c(t) \in \mathbb{R}$ and $p_j^c(t) \in \mathbb{R}$ represent the output and input of jth hidden-layer neuron, respectively.

The back-propagation algorithm is used in the process of weight updating. Then, define the approximate error of critic network as

$$E_{\mathrm{c}}(t) = \frac{1}{2} e_{\mathrm{c}}^2(t), e_{\mathrm{c}}(t) = \gamma \hat{J}(t) - \left(\hat{J}(t-1) - r(t)\right). \tag{8}$$

In order to approximate the minimum value of $\hat{J}(t)$, $r(t)$ is used as the reinforcement learning signal during the algorithm implementation. Using a properly positive definite matrix Q, $r(t)$ is formulated as

$$r(t) = -x_{\mathrm{a}}^T(t) Q x_{\mathrm{a}}(t). \tag{9}$$

When disturbances occur in the microgrid, the weights of neural networks will be adjusted by using $r(t)$, and the adaptivity of proposed method is greatly improved. By using (8) and (9), the weight updating rule of critic network is designed as

$$\Delta\omega_j^{c2}(t) = -\lambda_c \frac{\partial E_c(t)}{\partial \hat{J}(t)} \frac{\partial \hat{J}(t)}{\partial w_j^{c2}(t)}, \tag{10}$$

$$\Delta\omega_{ij}^{c1}(t) = -\lambda_c \frac{\partial E_c(t)}{\partial \hat{J}(t)} \frac{\partial \hat{J}(t)}{\partial q_j^c(t)} \frac{\partial q_j^c(t)}{\partial p_j^c(t)} \frac{\partial p_j^c(t)}{\partial w_{ij}^{c1}(t)}, \tag{11}$$

where λ_c is the learning rate used in the critic network.

Then, based on the forward calculation of action network, define $\hat{\mu}(t)$ as the adaptive auxiliary controller and it is formulated as follows

$$p_j^a(t) = \sum_{i=1}^{\iota_a} w_{ij}^{a1}(t) x_a(t), \quad i = 1, \ldots, \iota_a, \tag{12a}$$

$$q_j^a(t) = (1 - e^{-p_j^a(t)})/(1 + e^{-p_j^a(t)}), \quad j = 1, \ldots, \tau_a, \tag{12b}$$

$$\hat{\mu}(t) = \left(1 - e^{-\sum_{j=1}^{\tau_a} w_j^{a2}(t) q_j^a(t)}\right) / \left(1 + e^{-\sum_{j=1}^{\tau_a} w_j^{a2}(t) q_j^a(t)}\right), \tag{12c}$$

where $w_{ij}^{a1}(t) \in \mathbb{R}, i = 1, \ldots \iota_a, j = 1, \ldots, \tau_a$ and $w_j^{a2}(t) \in \mathbb{R}$ represent the weight vectors corresponding to input-to-hidden layer and hidden-to-output layer of action network. ι_a and τ_a are the number of neurons in the input-layer and hidden-layer. The output and input of the jth hidden-layer neuron are defined as $p_j^a(t) \in \mathbb{R}$ and $q_j^a(t) \in \mathbb{R}$, respectively.

Similarly, for the action network, define the approximate error as

$$E_a(t) = \frac{1}{2} \hat{J}^2(t). \tag{13}$$

Then the weights of action network can be updated by using the back-propagation algorithm,

$$\Delta\omega_j^{a2}(t) = -\lambda_a \frac{\partial E_a(t)}{\partial \hat{J}(t)} \frac{\partial \hat{J}(t)}{\partial \hat{\mu}(t)} \frac{\partial \hat{\mu}(t)}{\partial \psi(t)} \frac{\partial \psi(t)}{\partial \omega_j^{a2}(t)}, \tag{14}$$

$$\Delta\omega_{ij}^{a1}(t) = -\lambda_a \frac{\partial E_a(t)}{\partial \hat{J}(t)} \frac{\partial \hat{J}(t)}{\partial \hat{\mu}(t)} \frac{\partial \hat{\mu}(t)}{\partial \psi(t)} \frac{\partial \psi(t)}{\partial q_j^a(t)} \frac{\partial q_j^a(t)}{\partial p_j^a(t)} \frac{\partial p_j^a(t)}{\partial \omega_{ij}^{a1}(t)}, \tag{15}$$

where the learning rate λ_a is used in action network.

3.3 Power Controller Design Based on PV System and EVs

Based on the adaptive auxiliary control, Fig. 4 shows the design mechanism and structure of power controller. The ultimate control $u(t)$ consists of auxiliary control $u_a(t)$ and PI control $u_0(t)$. Once the adaptive control signal $\hat{\mu}(t)$ is generated, it is outputted through a limiter to obtain auxiliary control signal $u_a(t)$, which guarantees the stability of the power controller.

Once the control signal $u(t)$ is generated by the power controller, $u_{pv}(t)$ and $u_e(t)$ can be calculated. The details of control signal distribution are illustrated in the flowchart of Fig. 5, where $u_m(t)$ is the maximum value of the PV reserve power.

It is necessary to judge the sign of $u(t)$ in the control signal distribution process. $u(t) < 0$ indicates that the total demand is less than the total power generation, and it should decrease the power generation. In this case, the power generation of reheat-turbine thermal generation and hydro generation should be reduced, while EVs absorb the extra power. Note that the PV reserve power is used for EVs charging but not for frequency regulation.

On the contrary, $u(t) > 0$ indicates that the power generation is insufficient. Then, the PV reserve power will quickly inject into microgrid, and both reheat-turbine thermal generation and hydro generation increase. The injected amount of PV reserve power is determined by the value of $u(t)$. If $u(t) > u_m(t)$, all PV reserve power is injected into the microgrid, and EVs discharge to compensate the rest power. Otherwise, the power mismatch can be eliminated by only injecting the PV power and adjusting the reheat-turbine thermal generation and hydro generation, then the

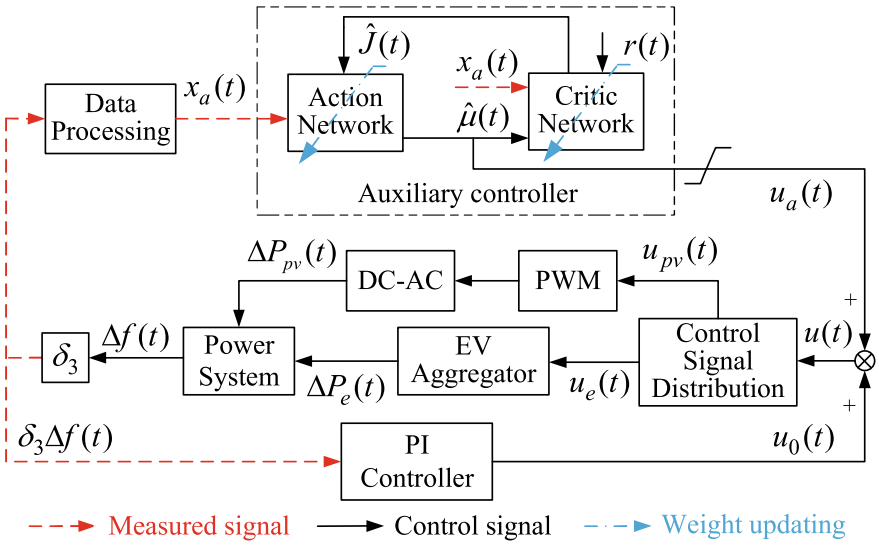

Fig. 4 Schematic diagram of power controller

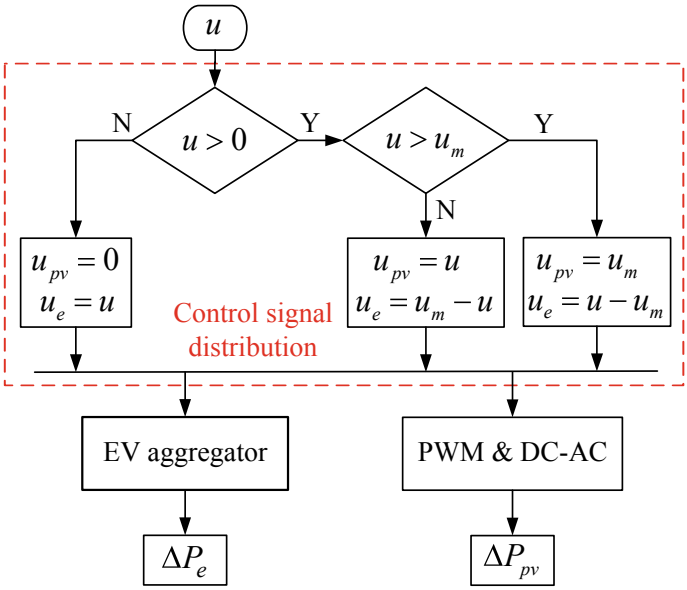

Fig. 5 Operation flowchart of the control signal distribution

rest PV reserve power is still used for charging the EVs. Under this control strategy, the frequency fluctuation can be eliminated effectively and the PV power can be fully utilized.

4 Cases Analysis with Uncertain PV Power Generation

In this section, the influence of PV system and EVs integrating into the microgrid is first studied. Then the frequency response using different control strategies is comparatively studied in different kinds of PV reserve power.

4.1 Frequency Response with and Without PV and EVs

The microgrid with and without PV reserve power and EVs is investigated, and the PV reserve power is set as 0.15 p.u. The parameters of microgrid are set as follows, $T_{tg} = 0.08$, $T_r = 10$, $T_t = 0.3$, $K_r = 3$, $T_{hg} = 0.2$, $T_{rh} = 28.75$, $T_{rs} = 5$, $T_w = 1$, $T_e = 0.035$, $K_A = 2.4 \times 10^{-3}$, $N_e = 2500$, $T_p = 10$, $K_p = 1$ and $R_t = R_h = 0.05$. The distribution coefficients $\delta_1 = \delta_2 = 0.2$ and $\delta_3 = 0.6$. The thermal controller, hydro controller and power controller are all designed by PI method, and the proportion

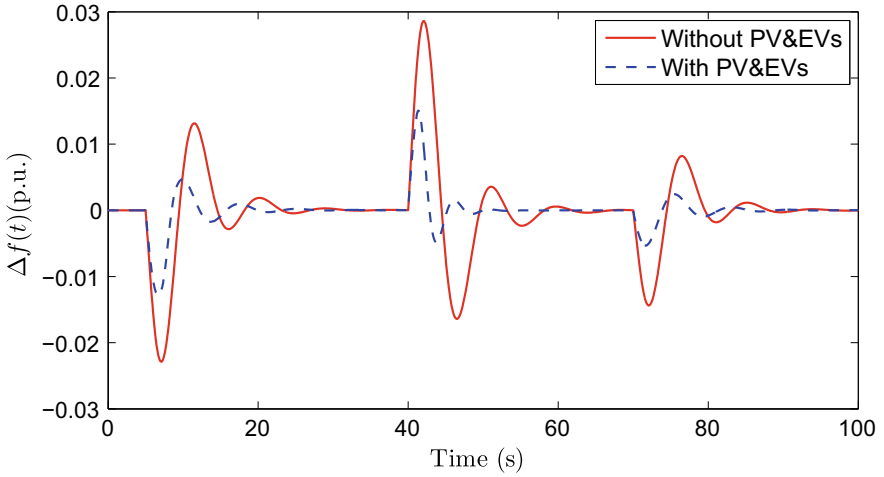

Fig. 6 Frequency response with and without PV and EVs

and integral coefficients of three controllers are given as follows: $K_{\mathrm{P}}^{t} = 17$ and $K_{\mathrm{I}}^{t} = 10$, $K_{\mathrm{P}}^{h} = 35$ and $K_{\mathrm{I}}^{h} = 4$, $K_{\mathrm{P}}^{p} = 5$ and $K_{\mathrm{I}}^{p} = 10$, respectively.

The frequency fluctuation does not exist at the initial moment. Then three active power disturbances occur at 5 s, 40 s and 70 s, where + 0.16 p.u., − 0.20 p.u. and + 0.10 p.u. step disturbances are applied, respectively. Then, the frequency response with and without PV reserve power and EVs is shown in Fig. 6. We can find that the system inertia has been increased when the PV reserve power and EVs are integrated, such that the frequency stability of microgrid is significantly improved. According to Figs. 4 and 5, only PV reserve energy is involved in frequency regulation during 5–40 s and 70–100 s, while PV reserve energy and EVs are involved in frequency regulation in 40–70 s. In the following case, both PV reserve power and EVs are integrated into the microgrid.

The performance index $\mathcal{F}$ is defined to quantify the comparison of frequency deviation, which refers to the integral absolute value of total frequency deviation during regulation process,

$$\mathcal{F} = \int_{0}^{\Gamma} \|\Delta f(t)\| \mathrm{d}t, \tag{16}$$

where Γ represents the whole frequency regulating time. By applying the performance index $\mathcal{F}$, the results of microgrid with and without PV reserve power and EVs are presented in Table 2, which are 11.1719 and 3.5417, respectively. This also

Table 2 Influence of PV and EVs on the values of $\mathcal{F}$

	Without PV and EVs	With PV and EVs
$\mathcal{F}$	11.1719	3.5417

illustrates that integrating PV reserve power and EVs into the microgrid helps to stabilize the frequency.

4.2 Frequency Response of Constant PV Power

The PV reserve power is set as constant value of 0.15 p.u. in this case. The thermal controller and hydro controller are still designed by PI method, and all controller parameters are the same as Case A. The power controller is designed by the supplemented ADP control method with PI thermal and hydro controllers, which is recorded as adaptive control in all figures. The three controllers are designed by PI method, recorded as multi-PI control in all figures. During the weight updating process of ADP auxiliary control, relevant parameters are selected as $\lambda_c = \lambda_a = 0.05$, $\iota_c = 3$, $\iota_a = 2$, $Q = \text{diag}\{1, 0.5\}$, $\tau_c = \tau_a = 6$ and $\gamma = 0.95$. Figure 7 shows the frequency response by using multi-PI control and adaptive control under same disturbances as before. The output of reheat-turbine thermal generation, hydro generation, PV reserve power and EV aggregator are shown in Fig. 8. Figure 9 is the control signals of power controller. Taking the third input node as an example, the weight updating process of critic network is as shown in Fig. 10, and the weights can be adaptively adjusted when facing with different power mismatch. Note that the ADP auxiliary controller is constrained within $[-0.01, 0.01]$.

It can be concluded from Fig. 7 that the adaptive control method performs better than the multi-PI control with only two obvious frequency fluctuations during the regulation process. From Fig. 8, the response ability of PV system and EVs to power mismatch is faster than reheat-turbine thermal generation and hydro generation. When the power generation is insufficient, the PV reserve power is quickly injected

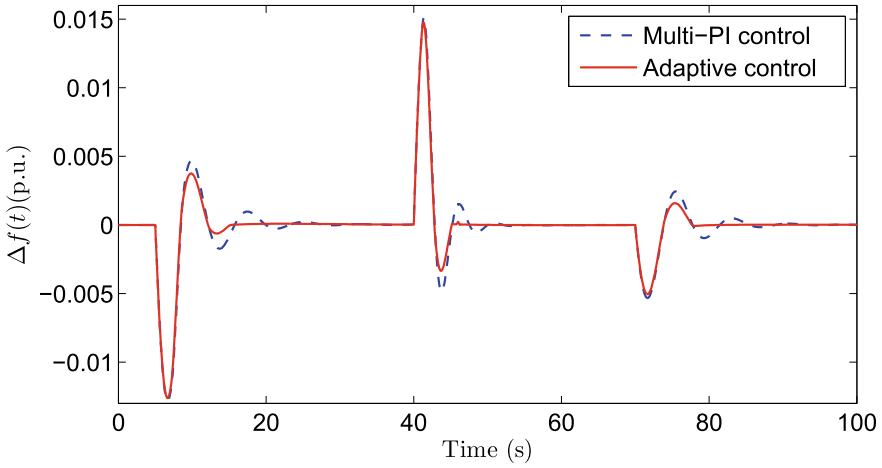

Fig. 7 Frequency deviation of PV at constant power

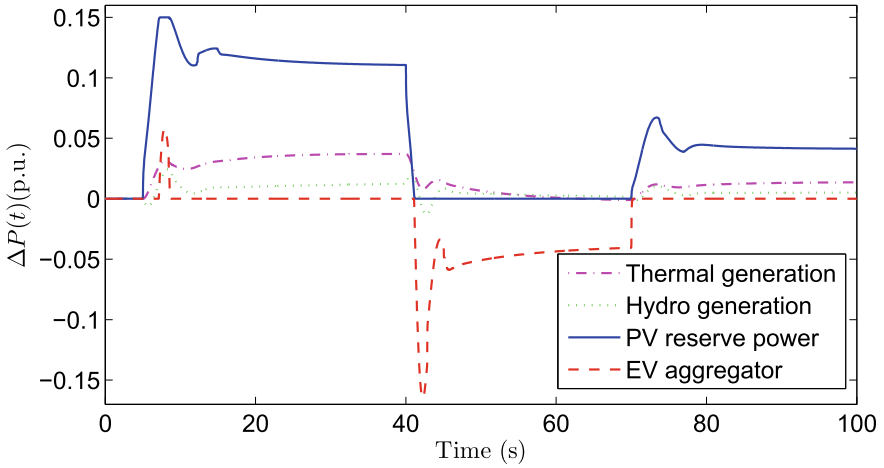

Fig. 8 Output power changes with the different control strategy

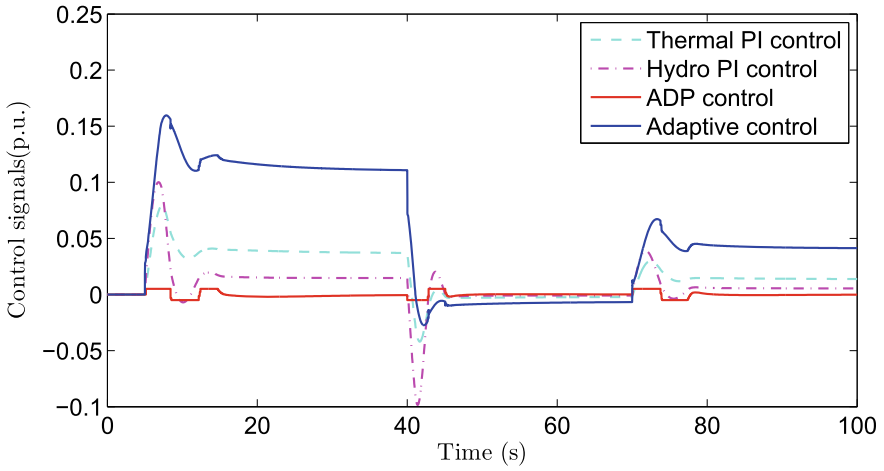

Fig. 9 Control signals of power controller

into the microgrid, and meanwhile both reheat-turbine thermal generation and hydro generation increase the power generation. If the gap between generated power and load demand is greater than the maximum PV reserve power, EVs are discharged to provide power compensation for the load consumption, such as 5–40 s in Fig. 8. Otherwise, one part of the PV reserve power is injected into the microgrid, and the other part is used for EV charging, such as 70–100 s in Fig. 8. On the contrary, it is necessary to reduce the generation power and absorb the extra power when power generation is too much. The power generation of reheat-turbine thermal generation and hydro generation needs to be reduced, while EVs absorb the extra power by

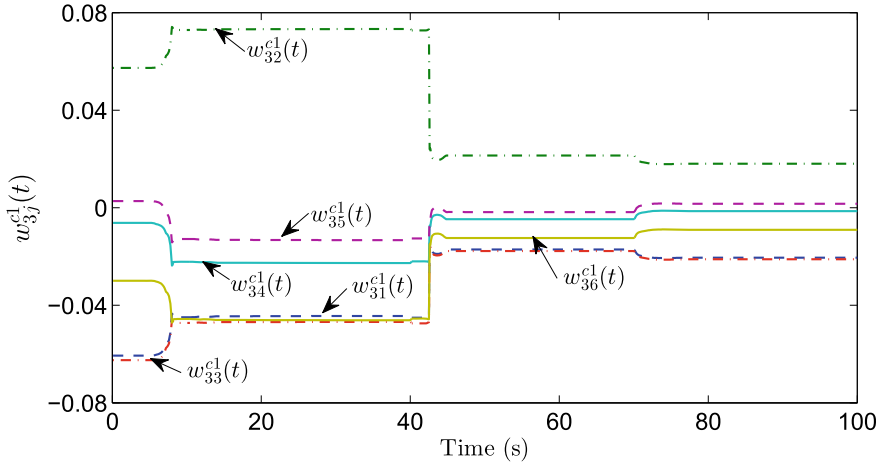

Fig. 10 Weight updating process of critic network

charging, such as 40–70 s in Fig. 8, and the PV reserve power is only used for charging EVs.

To better illustrate the relationship between PV reserve power and EVs, the PV reserve power used to charge EVs is shown in Fig. 11. During 0–5 s, the PV reserve power is fully used to charge EVs because the microgrid is stable. A disturbance is applied during 5–40 s, then the PV power is first injected into the microgrid to eliminate power mismatches and the remaining part of PV reserve power is used for charging EVs. Although there are also disturbances during 40–70 s, but the PV reserve power does not need to be involved in frequency regulation, so the PV reserve

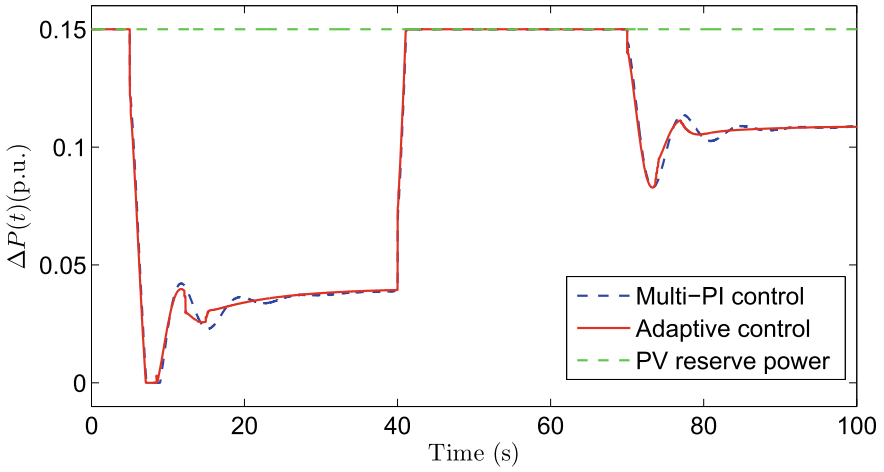

Fig. 11 Power of the PV for charging the EVs (constant PV reserve power)

Table 3 Values of $\mathcal{F}$ under different power controller: Case 4.2

	Multi-PI control	Adaptive control
$\mathcal{F}$	3.5417	2.8614

power is all used for charging EVs. Due to the small disturbance during 70–100 s, only a small portion of the PV reserve power is required to inject into the microgrid, while the majority is still used for charging EVs. Under this control strategy, the frequency fluctuation can be eliminated effectively and the PV power can be fully utilized.

The performance index $\mathcal{F}$ is defined to measure the control effect of proposed strategy, which is shown in Table 3. Obviously, the proposed adaptive control is more effective than the multi-PI control.

4.3 Frequency Response of Decreasing PV Power

In this case, the PV power is decreasing. By applying three above disturbances, the frequency response under different power controller is shown in Fig. 12, and the PV reserve power used to charge EVs is shown in Fig. 13. Figure 14 gives the control signals of power controller. Using the third input node as an example, the weight updating process of critic network is shown in Fig. 15.

From Figs. 12 and 13, by using the proposed ADP auxiliary control during the frequency regulation, it is obvious that the frequency response has shorter adjustment time and smaller fluctuation, and the charging power change of PV reserve power is also earlier to be stable. Since the auxiliary controller has the learning ability, the

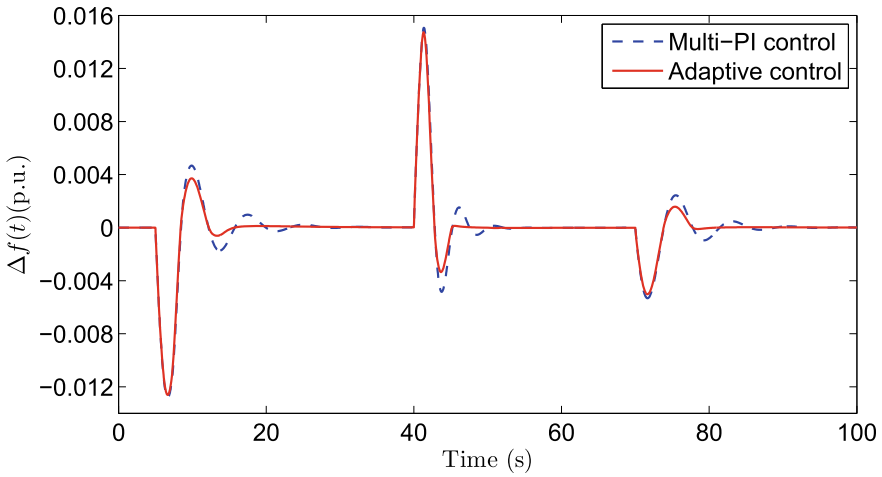

Fig. 12 Frequency deviation with decreasing PV reserve power

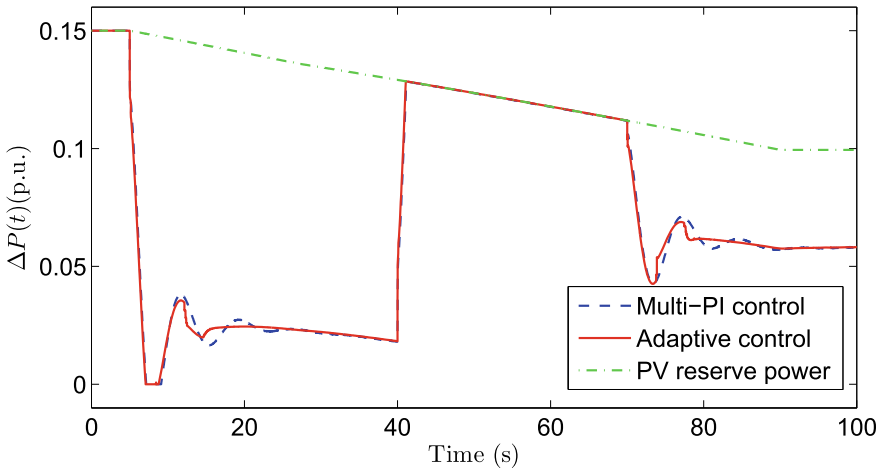

Fig. 13 Power of the PV for charging the EVs (decreasing PV reserve power)

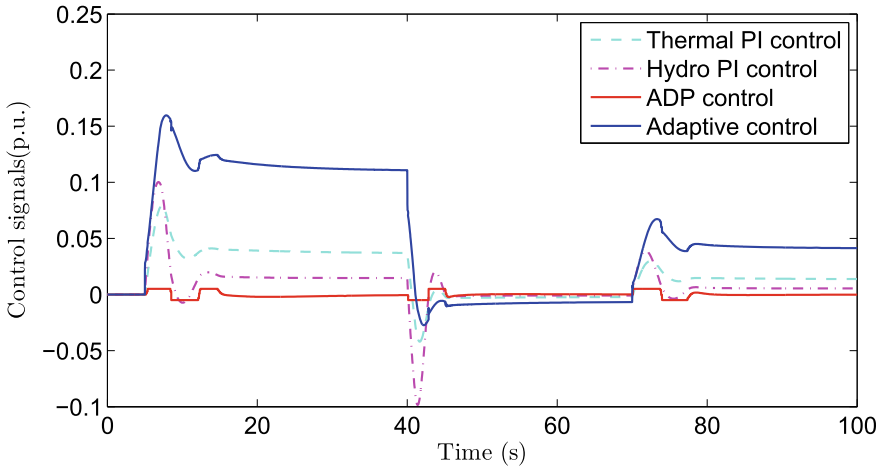

Fig. 14 Control signals of power controller

frequency tends to stabilize faster in the latter two disturbances. The ADP auxiliary controller can be adjusted to the disturbances and it is shown in Fig. 14. Although the ADP auxiliary control signal is limited into a suitable range, but it still can effectively improve the performance of power controller.

In addition, the values of performance index $\mathcal{F}$ are shown in Table 4, which are 3.4889 and 2.8294 under the multi-PI control and the adaptive control, respectively. Similarly, the proposed adaptive control can perform better than the multi-PI control under the condition of decreasing PV power.

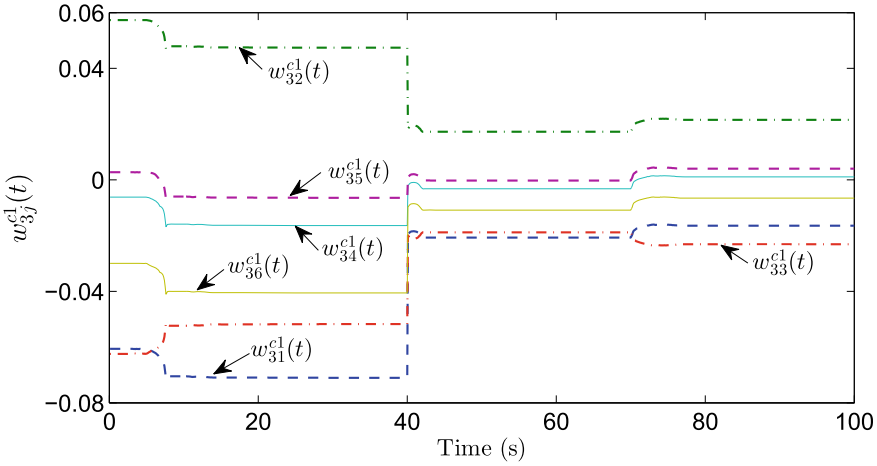

Fig. 15 Weight updating process of critic network

Table 4 Values of $\mathcal{F}$ under different power controller: Case 4.3

	Multi-PI control	Adaptive control
$\mathcal{F}$	3.4889	2.8294

4.4 Frequency Response of Uncertain PV Power

The PV power is randomly selected in this case. Then under different control strategies, Fig. 16 displays the frequency derivation. The PV reserve power used to charge

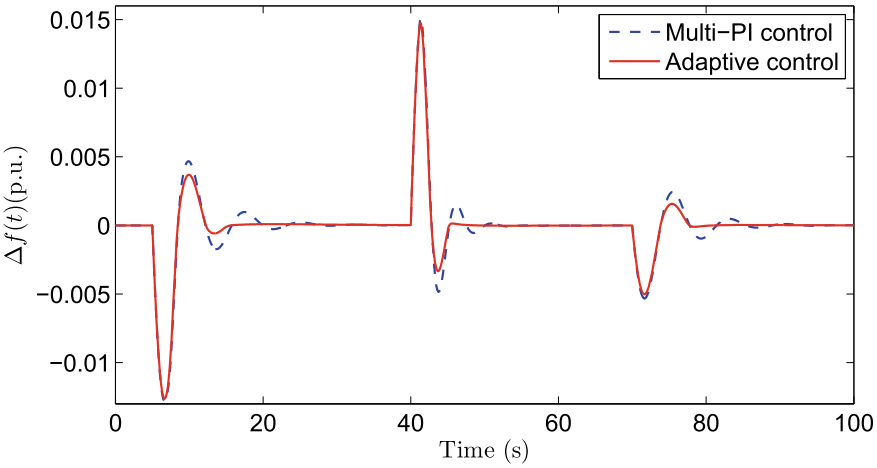

Fig. 16 Frequency deviation of uncertain PV reserve power

EVs is shown in Fig. 17. Figure 18 shows the detail of power control signals during the frequency regulation and Fig. 19 is the weight updating process of critic network, where we take the third input node as an example.

In the current strategy, both PV and EV are used to alleviate the power disturbances. The excess PV power will be directly used for EV charging, with little impact on the frequency response. In the cases analysis, the power disturbances in the four scenarios are the same. Therefore, under the same strategy, the frequency response in Figs. 7, 12, 16 and control signals in Figs. 9, 14, 18 are similar. The EV charging process reflected in Figs. 11, 13 and 17 are quite different.

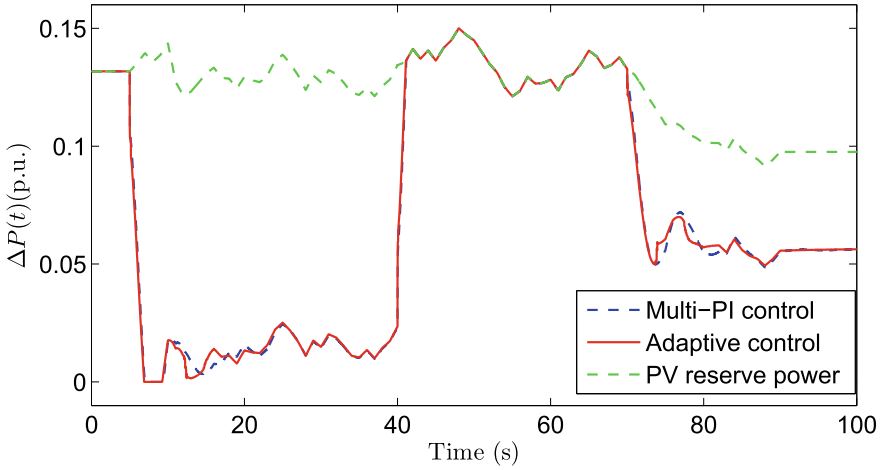

Fig. 17 Power of the PV for charging the EVs (uncertain PV reserve power)

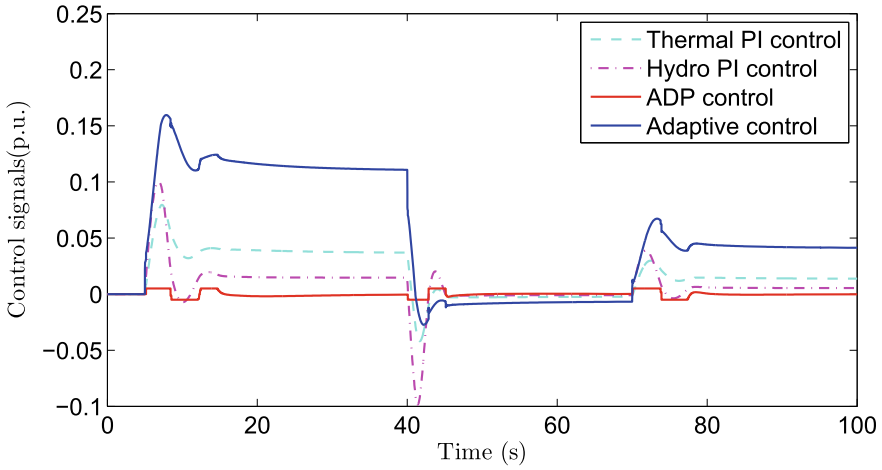

Fig. 18 Control signals of power controller

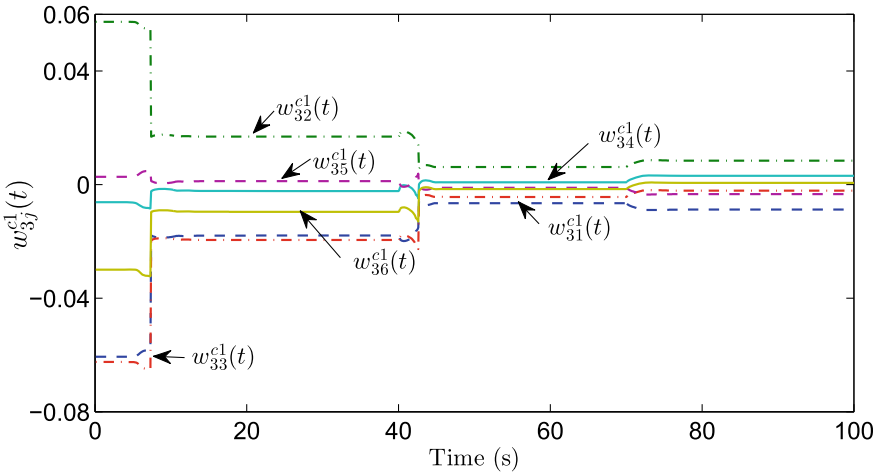

Fig. 19 Weight updating process of critic network

Table 5 Values of $\mathcal{F}$ under different power controller: Case 4.4

	Multi-PI control	Adaptive control
$\mathcal{F}$	3.4939	2.8370

From Fig. 16, the frequency response of power controller designed by ADP auxiliary control is still better than PI control. The performance index values of two control methods are shown in Table 5, which are 3.4939 and 2.8370, respectively.

From the above cases, the frequency stability of microgrid can be significantly improved by integrating PV reserve power and EVs. Both frequency response and performance index also demonstrate that the proposed adaptive control strategy has the better control performance to restrain the frequency derivations compared with the multi-PI control. Furthermore, the PV power can be fully utilized by participating in frequency regulation and charging EVs.

5 Expansion and Prospect

In this section, a model-based intelligent frequency control strategy is expanded and used to deal with uncertain problems in microgrids. The uncertain PV power generation and load demands, GRC and parameter uncertainties of governor, the ESS power constraints and SOC constraints are all considered. The model-based controller is used to adjust the power outputs of micro-turbine and ESS. A regulation strategy is proposed for the full utilization of PV power generation, and the recycling of ESS can be realized.

The model information is applied in the controller design, so the robustness of this controller is better than the data-based controller in Sect. 3. The model-based strategy is completely based on the ADP method but not an auxiliary control strategy. This is an innovative expansion and prospect for the application of learning-based algorithm in LFC of microgrid.

5.1 Mathematical Model and Model-Based Intelligent Frequency Control

In this section, the uncertainties arising from load demands, PV power generation and time constant of governor are considered in the modeling process of benchmark microgrid. The basic structure of ESS-based microgrid is given in Fig. 20. Then, the mathematical model of microgrid is as follows.

$$\begin{aligned}
\Delta \dot{f}(t) &= \frac{K_{\mathrm{p}}}{T_{\mathrm{p}}}\left[\Delta P_{\mathrm{mt}}(t) + \Delta P_{\mathrm{ess}}(t) + \Delta P_{\mathrm{pv}}(t) - \Delta P_{\mathrm{d}}(t)\right] - \frac{1}{T_{\mathrm{p}}}\Delta f(t), \\
\Delta \dot{P}_{\mathrm{mt}}(t) &= -\frac{1}{T_{\mathrm{mt}}}\Delta P_{\mathrm{mt}}(t) + \frac{1}{T_{\mathrm{mt}}}\Delta P_{\mathrm{mg}}(t), \\
\Delta \dot{P}_{\mathrm{mg}}(t) &= -\frac{1}{R_{\mathrm{mt}}T_{\mathrm{mg}}}\Delta f(t) - \frac{1}{T_{\mathrm{mg}}}\Delta P_{\mathrm{mg}}(t) + \frac{1}{T_{\mathrm{mg}}}u_{\mathrm{mg}}(t) \\
&\quad + \frac{\sigma_{\mathrm{g}}(t)}{T_{\mathrm{mg}}\left(T_{\mathrm{mg}} + \sigma_{\mathrm{mg}}(t)\right)}\left[\frac{1}{R_{\mathrm{mt}}}\Delta f(t) + \Delta P_{\mathrm{mg}}(t) - u_{\mathrm{mg}}(t)\right],
\end{aligned}$$

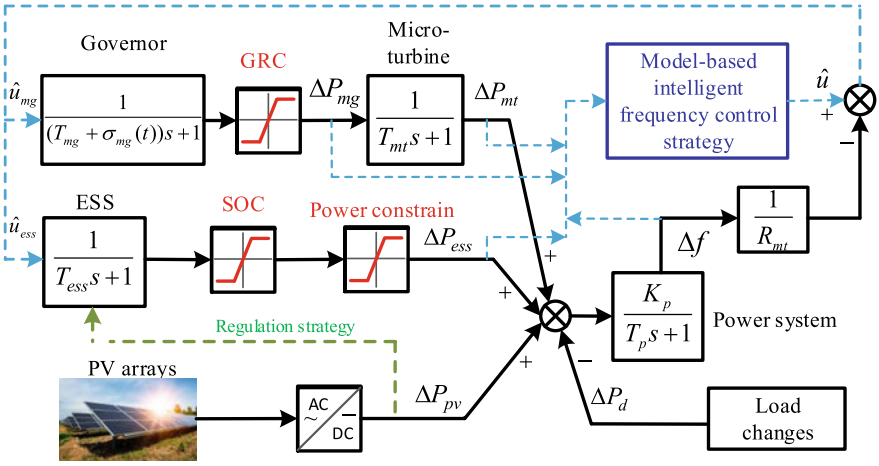

Fig. 20 Basic structure of ESS-based microgrid

$$\Delta \dot{P}_{\mathrm{ess}}(t) = -\frac{1}{R_{\mathrm{mt}} T_{\mathrm{ess}}} \Delta f(t) - \frac{1}{T_{\mathrm{ess}}} \Delta P_{\mathrm{ess}}(t) + \frac{1}{T_{\mathrm{ess}}} u_{\mathrm{ess}}(t), \tag{17}$$

where $\Delta f(t)$ represents the frequency fluctuation, $\Delta P_{\mathrm{mt}}(t)$, $\Delta P_{\mathrm{mg}}(t)$ and $\Delta P_{\mathrm{ess}}(t)$ are the power output of micro-turbine, position value of governor and power output of ESS, respectively. T_{mg}, T_{mt}, T_{ess} and T_{p} are the time constants. $\sigma_{\mathrm{mg}}(t)$ represents the uncertain parameter of governor. R_{mt} is the speed regulation coefficient. $\Delta P_{\mathrm{pv}}(t)$ is the uncertain PV power, and $\Delta P_{\mathrm{d}}(t)$ represents the uncertain load change. $u_{\mathrm{mg}}(t)$ and $u_{\mathrm{ess}}(t)$ are the controller to be designed for micro-turbine and ESS, respectively.

Further, to facilitate the design process, the compact form of the mathematical model can be expressed as

$$\dot{x}(t) = Ax(t) + G(u(t) + \Lambda(t)) + \Pi(t), \tag{18}$$

$$A = \begin{bmatrix} -\frac{1}{T_{\mathrm{p}}} & \frac{K_{\mathrm{p}}}{T_{\mathrm{p}}} & 0 & \frac{K_{\mathrm{p}}}{T_{\mathrm{p}}} \\ 0 & -\frac{1}{T_{\mathrm{mt}}} & \frac{1}{T_{\mathrm{mt}}} & 0 \\ -\frac{1}{R_{\mathrm{mt}} T_{\mathrm{mg}}} & 0 & -\frac{1}{T_{\mathrm{mg}}} & 0 \\ -\frac{1}{R_{\mathrm{mt}} T_{\mathrm{ess}}} & 0 & 0 & -\frac{1}{T_{\mathrm{ess}}} \end{bmatrix}, \quad G = \begin{bmatrix} 0 & 0 \\ 0 & 0 \\ \frac{1}{T_{\mathrm{mg}}} & 0 \\ 0 & \frac{1}{T_{\mathrm{ess}}} \end{bmatrix},$$

$$\Lambda(t) = \begin{bmatrix} -T_{\mathrm{mg}} \lambda_{\mathrm{g}}(t) u_{\mathrm{mg}}(t) \\ 0 \end{bmatrix}, \quad \Pi(t) = \begin{bmatrix} \frac{K_{\mathrm{p}}}{T_{\mathrm{p}}} \left(\Delta P_{\mathrm{pv}}(t) - \Delta P_{\mathrm{d}}(t) \right) \\ 0 \\ \lambda_{\mathrm{mg}}(t) \left(\frac{1}{R_{\mathrm{mt}}} \Delta f + \Delta P_{\mathrm{mg}}(t) \right) \\ 0 \end{bmatrix}.$$

where $x(t) = \left[\Delta f, \Delta P_{\mathrm{mt}}, \Delta P_{\mathrm{mg}}, \Delta P_{\mathrm{ess}} \right]^{\mathrm{T}} \in \mathbb{R}^m$ is the state variable of microgrid. $\lambda_{\mathrm{mg}}(t) = \sigma_{\mathrm{mg}}(t) / \left[T_{\mathrm{mg}} \left(T_{\mathrm{mg}} + \sigma_{\mathrm{mg}}(t) \right) \right]$ is about the parameter uncertainties. $u(t) = \left[u_{\mathrm{mg}}, u_{\mathrm{ess}} \right]^{\mathrm{T}} \in \mathbb{R}^n$ corresponds to the control strategy.

The model-based intelligent frequency control strategy $u(t)$ is developed by using the nominal system

$$\dot{x}(t) = Ax(t) + Gu(t). \tag{19}$$

Then, the cost function for the nominal system is designed as

$$J(x) = \int_t^{\infty} (U(x(\tau), u(\tau)) + \Theta(\tau)) \mathrm{d}(\tau), \tag{20}$$

and $U(x(t), u(t)) = x^{\mathrm{T}}(t) Q x(t) + u(t)^{\mathrm{T}} M u(t)$ is the utility function. Appropriate positive definite symmetric matrices Q and M need to be selected.

$$\Theta(t) = \theta_1^2 \Gamma_{\Lambda}^2(t) + \theta_2^2 \Gamma_{\Pi}^2(t) + \frac{\theta_1^2 + \theta_2^2}{4 \theta_1^2 \theta_2^2} \| \nabla J(x) \|^2. \tag{21}$$

$\Theta(t)$ is the perturbed term which reflects the cost of disturbances. $\nabla J(x) = \partial J(x)/\partial x$. θ_1 and θ_2 are two positive constants. Then, the Hamiltonian function and Hamiltonian-Jacobi-Bellman (HJB) function can be formulated as

$$H(x(t), u(t), \nabla J(x)) = (\nabla J(x))^{\mathrm{T}} \dot{x}(t) + U(x(t), u(t)) + \Theta(t), \tag{22}$$

and

$$0 = \min_{u \in \Omega_c} H\big(x(t), u(t), \nabla J^*(x)\big). \tag{23}$$

respectively. Ω_c represents the admissible control set. Then, the optimal control strategy can be expressed as

$$u^*(t) = -\frac{1}{2} M^{-1} G^{\mathrm{T}} \nabla J^*(x). \tag{24}$$

Then, substitute (24) in to (23), we can get the partial differential HJB equation

$$\begin{aligned} 0 &= (\nabla J(x))^{\mathrm{T}} \dot{x}(t) + U(x(\tau), u(\tau)) + \Theta(t) \\ &= (\nabla J(x))^{\mathrm{T}} A x(t) - \frac{1}{4} (\nabla J(x))^{\mathrm{T}} G M^{-1} G^{\mathrm{T}} \nabla J(x) + x(t)^{\mathrm{T}} Q x(t) + \Theta(t), \end{aligned} \tag{25}$$

which is difficult to be directly solved [37, 64]. Therefore, in this section, the model-based ADP method is used to get the approximate optimal solution through iterative learning.

In the proposed model-based intelligent frequency control strategy, $\nabla J(x)$ in (24) will be approximated based on critic NNs, and G is the model information needed in the control strategy. Then, the approximate form of optimal cost function $\hat{J}^*(x)$ is expressed as

$$\hat{J}^*(x) = \hat{w}_c^T(t) \psi(x), \tag{26}$$

where $\hat{w}_c \in \mathbb{R}^j$ is estimated weight parameter and j is the dimensionality of the hidden layer neuron. $\psi(x)$ represents the activation function of critic NNs. The partial derivative of cost function is

$$\nabla \hat{J}^*(x) = \nabla \psi^{\mathrm{T}}(x) \hat{w}_c(t). \tag{27}$$

Therefore, the model-based frequency controller can be formulated as

$$\hat{u}^*(t) = -\frac{1}{2} M^{-1} G^{\mathrm{T}} \nabla \psi^{\mathrm{T}}(x) \hat{w}_c(t). \tag{28}$$

For the iteration process, the estimated Hamiltonian function based on (22) is deduced as

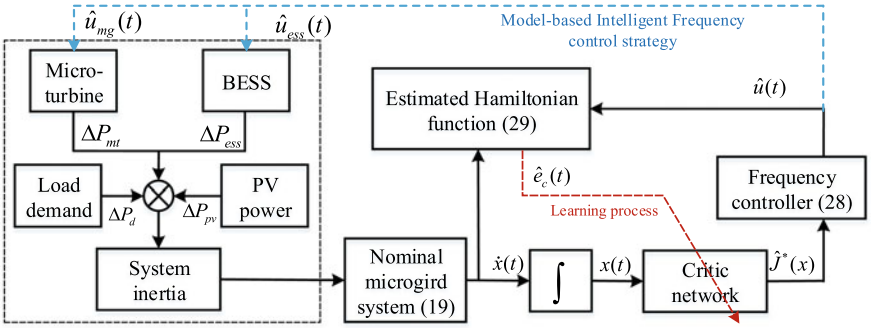

Fig. 21 Flow chart of model-based intelligent frequency control strategy

$$\begin{aligned} H\left(x(t), u^*(t), \hat{w}_c(t)\right) &= \left(\nabla\psi^{\mathrm{T}}(x)\hat{w}_c(t)\right)^{\mathrm{T}}\dot{x} + U\left(x(t), u^*(t)\right) \\ &\quad + \theta_1^2\Gamma_\Lambda^2(t) + \theta_2^2\Gamma_\Pi^2(t) + \frac{\theta_1^2+\theta_2^2}{4\theta_1^2\theta_2^2}\left\|\nabla\psi^{\mathrm{T}}(x)\hat{w}_c(t)\right\|^2 \\ &= \hat{e}_c(t). \end{aligned} \tag{29}$$

To minimize $E_c(t) = 0.5\hat{e}_c^{\mathrm{T}}(t)\hat{e}_c(t)$, the weight update law of $\hat{w}_c(t)$ can be defined as

$$\begin{aligned} \dot{\hat{w}}_c(t) &= -\gamma_c\frac{\partial E_c(t)}{\partial \hat{w}_c(t)} + \gamma_a\nabla\psi(x)GM^{-1}G^{\mathrm{T}}\nabla J_s(x) \\ &= -\gamma_c\hat{e}_c(t)\nabla\psi(x)Ax(t) + \gamma_a\nabla\psi(x)GM^{-1}G^{\mathrm{T}}\nabla J_s(x) \\ &\quad - \gamma_c\hat{e}_c(t)\frac{\theta_1^2+\theta_2^2}{2\theta_1^2\theta_2^2}\nabla\psi(x)\nabla\psi^{\mathrm{T}}(x)\hat{w}_c(t) \\ &\quad + \frac{1}{2}\gamma_c\hat{e}_c(t)\nabla\psi(x)GM^{-1}G^{\mathrm{T}}\nabla\psi^{\mathrm{T}}(x)\hat{w}_c(t), \end{aligned} \tag{30}$$

where $\gamma_c > 0$ and $\gamma_a > 0$ are the learning rate of proposed intelligent frequency control strategy. Based on Lyapunov theorem, $J_s(x) = 0.5x^{\mathrm{T}}(t)x(t)$ can be selected.

Therefore, the mathematical principles and basis of the model-based intelligent frequency control strategy have been given in detail. Further, the flow chart of the control strategy is shown in Fig. 21.

5.2 *Regulation Strategy for ESS and PV Power Generation*

In this subsection, the regulation strategy is developed for the full utilization of ESS and PV power generation. In Sect. 5.1, the proposed frequency control strategy will be used to adjust the power output of ESS and micro-turbine. Therefore, the electrical energy that changes due to the frequency control is defined as Ess*1*(t). The initial

electrical energy of ESS is Soc^0. Then, we have the following SOC limit

$$\mathrm{Soc}(t+1) = \begin{cases} \mathrm{Soc}(t) - \int_0^t \mathrm{Ess1}(\tau)\mathrm{d}\tau, & \mathrm{Soc}^m < \mathrm{Soc}(t) < \mathrm{Soc}^M, \text{ or} \\ & \mathrm{Soc}(t) = \mathrm{Soc}^M \text{ and } \mathrm{Ess1}(t) > 0, \text{ or} \\ & \mathrm{Soc}(t) = \mathrm{Soc}^m \text{ and } \mathrm{Ess1}(t) < 0, \\ \mathrm{Soc}(t), & \text{else}, \end{cases} \tag{31}$$

$$\mathrm{Ess1}(t) = \begin{cases} \Delta P_{\mathrm{ess}}^M/\beta, & \Delta P_{\mathrm{ess}}(t) > \Delta P_{\mathrm{ess}}^M, \\ \Delta P_{\mathrm{ess}}(t)/\beta, & 0 < \Delta P_{\mathrm{ess}}(t) \le \Delta P_{\mathrm{e}}^M, \\ \beta \Delta P_{\mathrm{ess}}(t), & \Delta P_{\mathrm{ess}}^m \le \Delta P_{\mathrm{ess}}(t) \le 0, \\ \beta \Delta P_{\mathrm{ess}}^m, & \Delta P_{\mathrm{ess}}(t) < \Delta P_{\mathrm{ess}}^m, \end{cases} \tag{32}$$

where Soc^m is the lower bound of SOC and Soc^M is the upper bound. The lower bound of power output is and the upper bound is. represents the charging/discharging coefficient of ESS.

Generally, for the load demand and PV power generation, the day-ahead dispatch curves are available data resource for the power sector. At the same time, in this regulation strategy, the requirements for the accuracy of the day-ahead dispatch curve are not strict, which is conducive to the realization of the control strategy. Take a commercial building as an example, its day-ahead dispatch curve is given in Fig. 22.

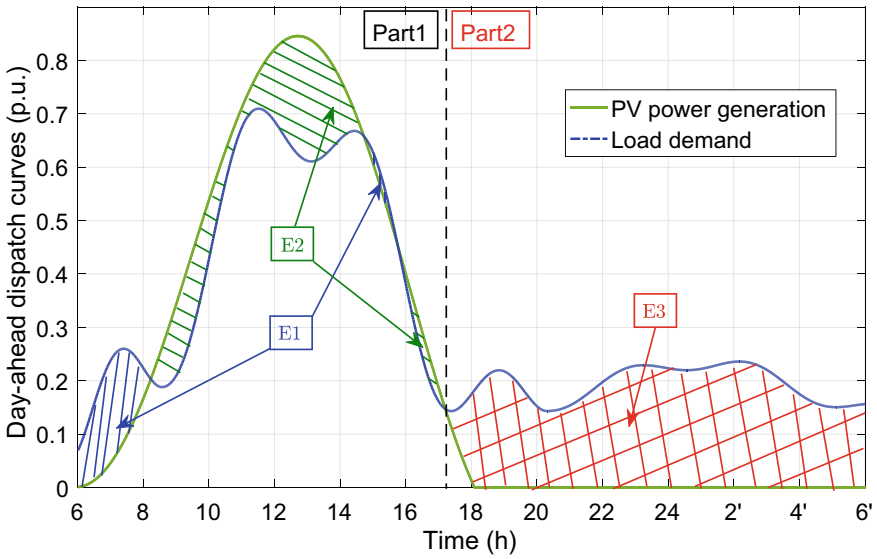

Fig. 22 Day-ahead dispatch curves

It should be noted that $2'$, $4'$, and $6'$ represent the moment of the next day. For the microgrid powered by PV power generation, there is a moment after which the power of PV cannot meet the load demand. Based on this moment, the regulation strategy is divided into two parts in the Fig. 22. In Part 1, E1 represents the consumed energy of ESS, and E2 is the excess PV power which will be stored in ESS. In Part 2, some of the electrical energy stored by the ESS will be used to compensate for the insufficient load demand. Bias(t) is the power deviation of load demands and PV. The electrical energy changes of ESS are defined as Ess2(t), and the SOC limit can be formulated as

$$\mathrm{Soc}(t+1) = \begin{cases} \mathrm{Soc}(t) - \Phi(t)\int_0^t \mathrm{Ess2}(\tau)\mathrm{d}\tau, & \mathrm{Soc}^m < \mathrm{Soc}(t) < \mathrm{Soc}^M, \text{ or} \\ & \mathrm{Soc}(t) = \mathrm{Soc}^M \text{ and } \mathrm{Ess2}(t) > 0, \text{ or} \\ & \mathrm{Soc}(t) = \mathrm{Soc}^m \text{ and } \mathrm{Ess2}(t) < 0, \\ \mathrm{Soc}(t), & \text{else}, \end{cases} \tag{33}$$

where

$$\mathrm{Ess2}(t) = \begin{cases} \Delta P_{\mathrm{ess}}^M/\beta, & \mathrm{Bias}(t) > \Delta P_{\mathrm{ess}}^M, \\ \mathrm{Bias}(t)/\beta, & 0 < \mathrm{Bias}(t) \le \Delta P_{\mathrm{ess}}^M, \\ \beta\mathrm{Bias}(t), & \Delta P_{\mathrm{ess}}^m \le \mathrm{Bias}(t) \le 0, \\ \beta\Delta P_{\mathrm{ess}}^m, & \mathrm{Bias}(t) < \Delta P_{\mathrm{ess}}^m, \end{cases} \tag{34}$$

Part 1: $\Phi(t) = 1$.
Part 2:

$$\Phi(t) = \begin{cases} (\mathrm{E2} - \mathrm{E1})/\mathrm{E3}, & \mathrm{E3} > (\mathrm{E2} - \mathrm{E1}), \\ 1, & \mathrm{E3} \le (\mathrm{E2} - \mathrm{E1}). \end{cases} \tag{35}$$

$\Phi(t)$ is the regulation coefficient. Through the regulation, the excess energy of PV can be stored during the day and properly released at night. Therefore, the full utilization of ESS and PV power generation can be realized. Meanwhile, ESS can also be recycled through reasonable discharge at night, which is meaningful for engineering practice.

In this Section, a model-based intelligent frequency control strategy is expanded and prospected. Different from Sects. 2–4, the proposed strategy uses part of the dynamic model of microgrid, which makes it more robust. Meanwhile, the model-based strategy is not used as an auxiliary control in the microgrid. More complex uncertain problems are considered, and the dispatch of PV power generation can be well achieved through the ESS-based regulation strategy. The content of this section is mainly to provide a model-based LFC strategy for the stochastic modeling of the microgrid. At the same time, the proposed strategy can increase the utilization rate of PV power generation and ensure the recycling of ESS.

6 Summary

An improving adaptive frequency regulation strategy is proposed for a PV-integrated multi-source microgrid in this Chapter. The thermal controller and hydro controller based on PI control, and adaptive auxiliary controller based on ADP auxiliary control are simultaneously applied for the frequency regulation. Then, case analysis shows the improvement in the frequency regulation by using PV and EVs. Under different PV scenarios, without PV, constant PV, decreasing PV and uncertain PV, comparative results demonstrate the superiority of proposed adaptive control method for restraining frequency fluctuations with the full utilization of PV power. At the same time, under the defined frequency stability performance index, the proposed method also has great advantages. Further, a model-based intelligent frequency control strategy is extended and prospected to deal with more complex uncertainties in microgrid. Meanwhile, based on the regulation strategy, the solar energy can be effectively utilized by dispatching ESS and PV power generation.

References

1. V.C. Gungor, D. Sahin, T. Kocak, S. Ergut, C. Buccella, C. Cecati, G.P. Hancke, A survey on smart grid potential applications and communication requirements. IEEE Trans. Ind. Inform. **9**(1), 28–42 (2013)
2. K. Solangi, M. Islam, R. Saidur, N. Rahim, H. Fayaz, A review on global solar energy policy. Renew. Sust. Energ Rev. **15**(4), 2149–2163 (2011)
3. K. Ishaque, Z. Salam, A. Shamsudin, M. Amjad, A direct control based maximum power point tracking method for photovoltaic system under partial shading conditions using particle swarm optimization algorithm. Appl. Energy **99**, 414–422 (2012)
4. R.A. Mastromauro, M. Liserre, A. Dell'Aquila, Control issues in single-stage photovoltaic systems: MPPT, current and voltage control. IEEE Trans. Ind. Inform. **8**(2), 241–254 (2012)
5. R. Kadri, J.P. Gaubert, G. Champenois, An improved maximum power point tracking for photovoltaic grid-connected inverter based on voltage-oriented control. IEEE Trans. Ind. Electron. **58**(1), 66–75 (2011)
6. K. Kobayashi, I. Takano, Y. Sawada, A study of a two stage maximum power point tracking control of a photovoltaic system under partially shaded insolation conditions. Sol. Energy Mater. Sol. Cells **90**(18–19), 2975–2988 (2006)
7. T. Esram, P.L. Chapman, Comparison of photovoltaic array maximum power point tracking techniques. IEEE Trans. Energy Convers. **22**(2), 439–449 (2007)
8. A.I. Dounis, P. Kofinas, C. Alafodimos, D. Tseles, Adaptive fuzzy gain scheduling PID controller for maximum power point tracking of photovoltaic system. Renew. Energy **60**, 202–214 (2013)
9. W. Xu, C. Mu, J. Jin, Novel linear iteration maximum power point tracking algorithm for photovoltaic power generation. IEEE Trans. Appl. Supercond. **24**(5), 1–6 (2014)
10. N. Kakimoto, S. Takayama, H. Satoh, K. Nakamura, Power modulation of photovoltaic generator for frequency control of power system. IEEE Trans. Energy Convers. **24**(4), 943–949 (2009)
11. N. Liu, M. Cheng, X. Yu, J. Zhong, J. Lei, Energy-sharing provider for PV prosumer clusters: a hybrid approach using stochastic programming and stackelberg game. IEEE Trans. Ind. Electron. **65**(8), 6740–6750 (2018)

12. H. Jia, X. Li, Y. Mu, C. Xu, Y. Jiang, X. Yu, J. Wu, C. Dong, Coordinated control for EV aggregators and power plants in frequency regulation considering time-varying delays. Appl. Energy **210**, 1363–1376 (2018)
13. E. Vittal, M. O'Malley, A. Keane, A steady-state voltage stability analysis of power systems with high penetrations of wind. IEEE Trans. Power Syst. **25**(1), 433–442 (2010)
14. R. Shah, N. Mithulananthan, R. Bansal, V. Ramachandaramurthy, A review of key power system stability challenges for large-scale PV integration. Renew. Sust. Energ Rev. **41**(Supplement C), 1423–1436 (2015)
15. F. Kennel, D. Görges, S. Liu, Energy management for smart grids with electric vehicles based on hierarchical MPC. IEEE Trans. Ind. Inform. **9**(3), 1528–1537 (2013)
16. C. Fernandes, P. Fras, J.M. Latorre, Impact of vehicle-to-grid on power system operation costs: the spanish case study. Appl. Energy **96**, 194–202 (2012)
17. S. Vachirasricirikul, I. Ngamroo, Robust LFC in a smart grid with wind power penetration by coordinated V2G control and frequency controller. IEEE Trans. Smart Grid **5**(1), 371–380 (2014)
18. V.P. Singh, N. Kishor, P. Samuel, Load frequency control with communication topology changes in smart grid. IEEE Trans. Ind. Inform. **12**(5), 1943–1952 (2016)
19. H. Bevrani, *Robust Power System Frequency Control* (Springer International Publishing, 2014)
20. P. Kundur, N.J. Balu, M.G. Lauby, *Power System Stability and Control*, vol. 7 (McGraw-Hill, New York, 1994)
21. Y. Tang, J. Yang, J. Yan, H. He, Intelligent load frequency controller using GrADP for island smart grid with electric vehicles and renewable resources. Neurocomputing **170**, 406–416 (2015)
22. S. Sukumar, M. Marsadek, A. Ramasamy, H. Mokhlis, S. Mekhilef, A fuzzy-based PI controller for power management of a grid-connected PV-SOFC hybrid system. Energies **10**(11), 1720 (2017)
23. K. Vrdoljak, N. Peri, I. Petrovi, Sliding mode based load-frequency control in power systems. Electr. Power Syst. Res. **80**(5), 514–527 (2010)
24. M. Klimontowicz, A. Al-Hinai, C.H. Peng, Optimal LFC SMC for three-area power system with high penetration of PV. J. Electr. Syst. **12**(1), 68–84 (2016)
25. C. Mu, Y. Tang, H. He, Improved sliding mode design for load frequency control of power system integrated an adaptive learning strategy. IEEE Trans. Ind. Electron. **64**(8), 6742–6751 (2017)
26. X. Li, Y.-J. Song, S.-B. Han, Frequency control in micro-grid power system combined with electrolyzer system and fuzzy PI controller. J. Power Sources **180**(1), 468–475 (2008)
27. M. Veerachary, T. Senjyu, K. Uezato, Neural-network-based maximum-power-point tracking of coupled-inductor interleaved-boost-converter-supplied PV system using fuzzy controller. IEEE Trans. Ind. Electron. **50**(4), 749–758 (2003)
28. M. Datta, T. Senjyu, A. Yona, T. Funabashi, C.H. Kim, A frequency-control approach by photovoltaic generator in a PV-Diesel hybrid power system. IEEE Trans. Energy Convers. **26**(2), 559–571 (2011)
29. C. Juang, C. Lu, Load-frequency control by hybrid evolutionary fuzzy PI controller. IEE Proc. Gener. Transm. Distrib. **153**(2), 196–204 (2006)
30. D. Rerkpreedapong, A. Hasanovic, A. Feliachi, Robust load frequency control using genetic algorithms and linear matrix inequalities. IEEE Trans. Power Syst. **18**(2), 855–861 (2003)
31. D. Qian, S. Tong, H. Liu, X. Liu, Load frequency control by neural-network-based integral sliding mode for nonlinear power systems with wind turbines. Neurocomputing **173**, 875–885 (2016)
32. P.J. Werbos, in *Approximate Dynamic Programming for Real-Time Control and Neural Modeling*. Handbook of Intelligent Control: Neural, Fuzzy, and Adaptive Approaches (Van Nostrand Reinhold, 1992)
33. J. Si, Y.T. Wang, Online learning control by association and reinforcement. IEEE Trans. Neural Netw. **12**(2), 264–276 (2001)

34. H. He, Z. Ni, J. Fu, A three-network architecture for on-line learning and optimization based on adaptive dynamic programming. Neurocomputing **78**(1), 3–13 (2012)
35. P.K. Patchaikani, L. Behera, G. Prasad, A single network adaptive critic-based redundancy resolution scheme for robot manipulators. IEEE Trans. Ind. Electron. **59**(8), 3241–3253 (2012)
36. C. Mu, Z. Ni, C. Sun, H. He, Air-breathing hypersonic vehicle tracking control based on adaptive dynamic programming. IEEE Trans. Neural Netw. Learn Syst. **28**(3), 584–598 (2017)
37. C. Mu, Y. Zhang, Learning-based robust tracking control of quadrotor with time-varying and coupling uncertainties. IEEE Trans. Neural Netw. Learn Syst. **31**(1), 259–273 (2020)
38. C. Mu, K. Wang, C. Sun, Learning control supported by dynamic event communication applying to industrial systems. IEEE Trans. Ind. Inform. **17**(4), 2325–2335 (2021)
39. Z. Ni, H. He, J. Wen, X. Xu, Goal representation heuristic dynamic programming on maze navigation. IEEE Trans. Neural Netw. Learn Syst. **24**(12), 2038–2050 (2013)
40. S. Mohagheghi, Y. Valle, G.K. Venayagamoorthy, R.G. Harley, A proportional-integrator type adaptive critic design-based neurocontroller for a static compensator in a multimachine power system. IEEE Trans. Ind. Electron. **54**(1), 86–96 (2007)
41. W. Guo, F. Liu, J. Si, D. He, R. Harley, S. Mei, Online supplementary ADP learning controller design and application to power system frequency control with large-scale wind energy integration. IEEE Trans. Neural Netw. Learn Syst. **27**(8), 1748–1761 (2016)
42. Y. Tang, H. He, J. Wen, J. Liu, Power system stability control for a wind farm based on adaptive dynamic programming. IEEE Trans. Smart Grid **6**(1), 166–177 (2015)
43. C. Mu, W. Liu, W. Xu, Hierarchically adaptive frequency control for an ev-integrated smart grid with renewable energy. IEEE Trans. Ind. Inform. **14**(9), 4254–4263 (2018)
44. C. Mu, Y. Zhang, H. Jia, H. He, Energy-storage-based intelligent frequency control of microgrid with stochastic model uncertainties. IEEE Trans. Smart Grid **11**(2), 1748–1758 (2020)
45. C. Mu, K. Wang, Z. Ni, C. Sun, Cooperative differential game-based optimal control and its application to power systems. IEEE Trans. Ind. Inform. **16**(8), 5169–5179 (2020)
46. J. Liang, G.K. Venayagamoorthy, R.G. Harley, Wide-area measurement based dynamic stochastic optimal power flow control for smart grids with high variability and uncertainty. IEEE Trans. Smart Grid **3**(1), 59–69 (2012)
47. H.J. Lee, J.B. Park, Y.H. Joo, Robust load-frequency control for uncertain nonlinear power systems: a fuzzy logic approach. Inf. Sci. **176**(23), 3520–3537 (2006)
48. R.K. Sahu, S. Panda, U.K. Rout, DE optimized parallel 2-DOF PID controller for load frequency control of power system with governor dead-band nonlinearity. Int. J. Electr. Power Energy Syst **49**, 19–33 (2013)
49. H. Asano, K. Yajima, Y. Kaya, Influence of photovoltaic power generation on required capacity for load frequency control. IEEE Trans. Energy Convers. **11**(1), 188–193 (1996)
50. G.Q. Zeng, X.Q. Xie, M.R. Chen, An adaptive model predictive load frequency control method for multi-area interconnected power systems with photovoltaic generations. Energies **10**(11), 1840 (2017)
51. X. Yu, Y. Xue, Smart grids: a cyber-physical systems perspective. Proc. IEEE **104**(5), 1058–1070 (2016)
52. G.O. Suvire, M.G. Molina, P.E. Mercado, Improving the integration of wind power generation into AC microgrids using flywheel energy storage. IEEE Trans. Smart Grid **3**(4), 1945–1954 (2012)
53. K. Takigawa, N. Okada, N. Kuwabara, A. Kitamura, F. Yamamoto, Development and performance test of smart power conditioner for value-added PV application. Sol. Energy Mater. Sol. Cells **75**(3–4), 547–555 (2003)
54. X. Li, D. Hui, X. Lai, Battery energy storage station (BESS)-based smoothing control of photovoltaic (PV) and wind power generation fluctuations. IEEE Trans. Sustain. Energy **4**(2), 464–473 (2013)
55. T. Zhao, Z. Ding, Cooperative optimal control of battery energy storage system under wind uncertainties in a microgrid. IEEE Trans. Power Syst. **33**(2), 2292–2300 (2018)
56. M.R. Aghamohammadi, H. Abdolahinia, A new approach for optimal sizing of battery energy storage system for primary frequency control of islanded microgrid. Int. J. Electr. Power Energy Syst. **54**, 325–333 (2014)

57. P.C. Sekhar, S. Mishra, Storage free smart energy management for frequency control in a Diesel-PV-Fuel cell-based hybrid AC microgrid. IEEE Trans. Neural Netw. Learn Syst. **27**(8), 1657–1671 (2016)
58. A. Oudalov, D. Chartouni, C. Ohler, Optimizing a battery energy storage system for primary frequency control. IEEE Trans. Power Syst. **22**(3), 1259–1266 (2007)
59. J.Y. Kim, J.H. Jeon, S.K. Kim, C. Cho, J.H. Park, H.M. Kim, K.Y. Nam, Cooperative control strategy of energy storage system and microsources for stabilizing the microgrid during islanded operation. IEEE Trans. Power Electron. **25**(12), 3037–3048 (2010)
60. B. Ge, W. Wang, D. Bi, C.B. Rogers, F.Z. Peng, A.T. Almeida, H. Abu-Rub, Energy storage system-based power control for grid connected wind power farm. Int. J. Electr. Power Energy Syst. **44**(1), 115–122 (2013)
61. L. Johnston, F. Díaz-González, O. Gomis-Bellmunt, C. Corchero-arcía, M. Cruz-Zambrano, Methodology for the economic optimisation of energy storage systems for frequency support in wind power plants. Appl. Energy **137**, 660–669 (2015)
62. D. Xu, J. Liu, X. Yan, W. Yan, A novel adaptive neural network constrained control for a multi-area interconnected power system with hybrid energy storage. IEEE Trans. Ind. Electron. **65**(8), 6625–6634 (2018)
63. L. Dong, Y. Zhang, Z. Gao, A robust decentralized load frequency controller for interconnected power systems. ISA Trans. **51**(3), 410–419 (2012)
64. C. Mu, Y. Zhang, Z. Gao, C. Sun, ADP-based robust tracking control for a class of nonlinear systems with unmatched uncertainties. IEEE Trans. Syst. Man Cybern. **50**(11), 4056–4067 (2020)

Hybrid Renewable Energy Systems for Future Power Grids

Rebecca Eager and Md. Rabiul Islam

Abstract Issues relating to the power quality and reliability of commercial grids are becoming an increasing concern as the penetration of renewable energy sources increases to meet future energy demands. This chapter outlines current single source generation systems, with particular emphasis given to wind, solar, tidal and wave energy. Issues with such systems are explored, with particular reference to the power generation fluctuations typical of solar farms. The potential impact of these problems to connected power grids is also explained, highlighting the need for compensating hybrid energy systems. Different models of hybrid renewable energy systems are included, with reference to onshore and offshore system structures. A review of current research relating to new technologies which have applications in energy storage, signal control and power transmission for hybrid systems was also undertaken. An alternative for DC or AC buses to interconnect multiple energy sources, a common magnetic bus is considered as an alternative solution for hybrid renewable energy systems. Although the hybridisation of energy sources reduces the intermittency in renewable generated power, it is still not as stable as traditional fossil fuel generation; requiring the development of additional technologies to achieve satisfactory stability for grid integration. A comprehensive summary of current research and developmental activities, and possible future avenues of research to develop a reliable and cost-effective hybrid renewable energy system are also presented in this chapter.

Keywords Micro grids · Hybrid · Renewable energy systems · Wind · Solar · Wave

R. Eager (✉) · M. R. Islam
Faculty of Engineering and Information Sciences, University of Wollongong, Wollongong, NSW 2522, Australia
e-mail: re291@uowmail.edu.au

M. R. Islam
e-mail: mrislam@uow.edu.au

S. K. Das et al. (eds.), *Advances in Control Techniques for Smart Grid Applications*,
https://doi.org/10.1007/978-981-16-9856-9_3

List of Acronyms

AC	Alternating current
DC	Direct current
DFIG	Doubly fed induction generator
Hz	Hertz
IGBT	Insulated-gate bipolar transistor
kW	Kilowatt
MW	Megawatt
PEMFC	Proton exchange membrane fuel cell
PI	Proportional integral

1 Introduction

Renewable energy is produced from natural resources which are constantly restored and will never be exhausted. The current predominant method of energy production in Australia uses coal as a fuel source and accounts for approximately 75% of domestic energy requirements [1]. As fossil fuels are a finite resource and are being depleted; renewable energy sources have been identified as the most important source of power to meet future energy demands. The currently available renewable resources include biomass, geothermal, hydro, marine current, solar, tidal, wave and wind power.

Many renewable energy sources are reliant on cyclic or stochastic weather sources for power generation, resulting in intermittent energy production from the system and decreasing its reliability as a power source. These issues are amplified in single source generation systems as there is no secondary energy source or compensating technology to mitigate the variability in energy production. Power fluctuations of this nature also decrease the power quality and stability of the system [2]. This is a significant problem when connecting renewable energy systems to existing power grids with day-ahead electricity markets, which are most common [3]. In day ahead markets, suppliers sell their electrical energy the day before it is used, and the quantities sold are based on forecasted loads for the next day. A variable and unreliable energy source is therefore not suited to connection to a power grid unless the energy production can be stabilised.

One of the methods in development to smooth the power fluctuations is creating hybrid renewable energy systems which combine one or more renewable energy generation technologies with other generation systems. These systems can consist of renewable and/or non-renewable energy generation with energy storage devices. An example of a common onshore system would be a hybrid wind and photovoltaic system where the complementary nature of their power production (solar generation is more prevalent during the day, whilst wind generation is more prevalent at night) achieves a more stable power output. The advanced state of development of the technologies employed to harness these resources is also a factor in their prominence.

The adaptability of hybrid systems is bolstered by incorporating an energy storage system. Battery energy storage systems are very common in solar applications and have been shown to stabilise systems by counteracting the intermittency of renewable power [4]. Combining energy technologies assists in alleviating the uncertainty associated with renewable power generation and improves the reliability of systems integrated with power grids.

Hybrid renewable energy systems can be adapted to fulfill different purpose and have varying energy generation capacity. They can exist as microgrids which act as an autonomous energy source for a specific location, or as larger distributed systems which are connected to domestic power grids. Microgrid systems must perform all power quality and energy management issues, therefore, systems utilising intermittent renewable energy sources usually include an energy storage system to provide a controllable energy source. Grid connected systems may incorporate energy storage systems but can also solely rely on control techniques and power electronics to stabilise the generated power.

Currently, wind power is the most cost-effective renewable energy source for large-scale implementation and has recently surpassed hydropower as the leading source of clean energy in Australia in 2019 [5]. Wind power involves using wind energy to provide the mechanical power to spin an electric generator, which produces electricity. As a result, many existing hybrid renewable energy generation systems incorporate wind power as a primary or secondary power source. Onshore hybrid energy systems which include wind power are often combined with solar power; examples of such systems are included in [4, 6–9].

Whilst the majority of installed renewable generation systems are located onshore, the limited onshore space means offshore wind farms are expected to become increasingly prevalent [10]. They are becoming a prominent research topic as they take advantage of open marine space and large availability of renewable energy sources. Hybrid offshore wind farms most often utilise wind energy as the primary energy source and different ocean energy sources as the secondary source; namely marine current, tidal or wave power. Marine current and tidal power are particularly advantageous as their cyclic nature makes them highly predictable and contributes greatly to the stability of the energy generation system. References [2, 11–16] are all examples of different offshore hybrid renewable energy systems involving wind power and an ocean energy source.

Offshore wind farms can produce high levels of power as offshore winds tend to be stronger than onshore winds. However, there are some issues related to the economic feasibility of these farms due to the need to install undersea transmission systems to transport power from the offshore substation to onshore power grids [17]. Systems being investigated include both AC and DC-based transmission; with their most suited applications varying based on cost and transmission distance.

The primary issues associated with current hybrid renewable energy system technologies are output power fluctuations and economic feasibility. Although utilising multiple energy sources reduces the intermittency in generated power, it is still not as stable as fossil fuel generation; requiring the development of additional technologies to satisfactorily stabilise the system for grid integration. Some of the strategies used

to mitigate this problem are connecting some form of energy storage system to the renewable energy generators or implementing sophisticated control schemes within the system to identify and negate voltage and current fluctuations in the power waveform. As many renewable energy systems are under constant re-development, some technologies are very expensive to implement, particularly on a large scale. Other high-cost factors are the supporting infrastructure for renewable energy generation plants.

The most common form of energy storage system used in hybrid renewable energy systems is a battery energy storage system. Suitable batteries include lithium-ion, lead acid and fuel cells. All these batteries allow any excess energy to be stored and later re-injected into the system to supplement the outgoing power supply during periods of reduced renewable electricity generation. There are advantages of using a battery energy storage system for personal and commercial energy systems as the ability to store and reuse excess power decreases reliance on distributed electricity for a standalone system; and increases the reliability and stability of a grid-connected renewable generation plant. The disadvantages of using batteries consist of a potentially high initial cost of the batteries, which is inflated by the need to also install a battery management system to control and manage any safety issues, as well as potentially negative environmental impacts if batteries are not appropriately disposed of.

As a result of research into energy storage systems to supplement hybrid renewable energy generation, alternative technologies to batteries include compressed air energy storage, molten salt, superconducting magnetic energy storage, supercapacitors, flywheels and undersea energy storage. Examples of the different forms of energy used by these technologies as a storage method include thermal, kinetic, electrostatic and magnetic energy. All these alternatives result in similar improvements in the stability of grid-connected systems compared to battery energy storage systems but offer reduced negative environmental effects.

The specific technologies selected for a hybrid system depend partially on the type of connection between the energy sources before transmission; this is in the form of a bus, but these can be AC or DC in nature. Systems which supply power to grids require transmission systems to transport the power from the generation site to grid substations. Traditional power lines carry high voltage AC electricity to minimise power losses, but research into alternative transmission technologies is being conducted; particularly with regards to offshore hybrid systems as these systems are placed on the seabed and have different demands. Alternative transmission systems include low frequency AC and high voltage DC.

2 Renewable Energy Technologies

The most commonly utilised renewable energy systems currently are hydropower, wind energy, solar energy, biomass and geothermal energy. The suitability of these systems for hybridisations varies depending on factors like flexibility in geographical

location and supporting infrastructure. As a result, the renewable energy sources most prominently featured in research related to hybridisation are solar, wind, tidal and wave energy. These technologies are outlined in more detail below.

2.1 Solar Energy

A photovoltaic system is comprised of numerous solar panels which form a solar array. The capacity of this type of renewable energy system is highly adjustable and can be connected to a power grid or act on its own.

A solar panel consists of smaller photovoltaic cells which are capable of transforming light energy into electricity [18]. Each cell contains a semiconductor layer which is surrounded on both sides by a conducting material. Within the semiconductor is a p-type and a n-type layer, forming a p–n junction, which creates an electric field forcing positively charged particles to move to the n-side and negatively charged particles to move to the p-side. When light strikes the cell, the energy from the photons is transferred to the electrons in the semiconductor, allowing them to move through the conductor and create an electrical current within the cell.

Efficiency is a concern for photovoltaic systems as there are numerous limiting factors. Most photovoltaic cells use silicon as the semiconducting material, which is incapable of converting some photons into electricity. Furthermore, the energy imparted to the electrons needs to exceed the band-gap energy of the semiconductor for them to conduct electricity. As light photons have varying energy levels, not all electrons receive enough energy to reach the conduction band and this energy is instead transformed into thermal energy. There are other factors affecting solar cell efficiency as well, with the estimated efficiency of silicon photovoltaic cells coming in around 33%.

There are methods of improving photovoltaic cell efficiency, but all of them increase costs. They include increasing the purity of the semiconductor and using a more efficient semiconducting material such as gallium. Another cost factor is the degradation of solar panels over time due to environmental factors, causing their output energy to decrease.

2.2 Wind Energy

Traditional wind energy systems first developed in the 1980s used fixed-speed wind turbines with squirrel cage induction generators. These systems had a slightly delayed response to changes in wind speed resulting in large power variations within the system. Power electronics were used to connect the generator to the power grid, which only required simple semiconductor devices. The fixed generator speeds placed high

mechanical stresses on system components which lead to more expensive construction costs and efficiency losses [19]. This reduced the energy yield from wind turbine systems.

In the 1990s, more advanced power electronics (e.g., diode bridges, choppers) were used for rotor resistance control of wound-rotor induction generator systems. This allowed for variation of generation within a certain range, relieving mechanical stresses within the wind turbine systems.

To further mitigate this problem, variable speed generators were developed in the 2000s. The advantages of these generators over fixed speed generators include:

- Allow for pitch control to limit maximum power production during periods of high wind speeds;
- Reduce mechanical stresses by absorbing the energy from wind gusts and storing it as mechanical torque within the turbine;
- Improve power quality by reducing torque pulsations in the system;
- Improve system efficiency by adjusting and optimising the turbine speed for the current wind conditions.

The introduction of variable speed systems like doubly fed induction generators also resulted in the development of more advanced power electronics. Devices like bidirectional voltage source converters have allowed for complete control of the rotational speed of the generator. This allows for the optimisation of generator efficiency within a wide range of wind speeds and the providing of some ancillary services to power grids.

Doubly fed induction generators (DFIGs) are the most common form of generator in modern wind turbines [20, 21]. Within a DFIG wind turbine system is the wind turbine, a gearbox, the DFIG and an AC/AC converter. The gearbox is used to increase the low rotational speed of the turbine to a much higher speed in the shaft connected to the generator. The generator itself consists of a three-phase stator winding and a three-phase rotor winding, the latter of which is fed by slip rings. The stator is connected directly to the power grid or transmission system whilst the rotor is connected to the AC/AC converter, which uses insulated-gate bipolar transistors (IGBTs). Power electronics assist with active and reactive power control in the system, and flexibly control rotor frequency and current. Whilst this maximises energy yield, the system had an insufficient ability to control power in the event of a grid or generator disturbance. However, DFIG systems are well suited to high-capacity wind turbines with output power ratings larger than 1 MW; making these wind turbine systems favourable for offshore applications.

2.3 Tidal Energy

Tidal energy is currently not in widespread use but poses great potential for meeting future energy demands. There are several permutations of tidal energy technology, but all involve transforming the kinetic energy from the rise and fall of the ocean into

usable electricity. Installing tidal energy systems is very costly, meaning it is only practical for large-scale commercial projects [22]. More widespread usage will not happen until costs decrease. The three main technologies used for harnessing tidal energy are tidal turbines, tidal barrages and tidal fences.

Tidal turbines have very similar operating principles to wind turbines. Placed below the water's surface, the turbines use the tidal currents to turn the turbine blades. The turbine is connected to a generator via a gearbox which is responsible for transforming the kinetic energy into electricity. As water is more dense than air, tidal turbines can produce more electricity than wind turbines, but the turbine blades need to be more robust which increase manufacturing costs. There is a risk of collision with marine life, but this is mitigated by the low rotational speed of the turbines.

Tidal barrages are low-walled dams which are normally installed in areas of high tidal current such as estuaries or coastal bars. The base of the barrage is bolted to the sea floor whilst the top just clears the surface of the water. Sluice gates are used to control the flow rate of the water to create a reservoir on one side of the barrage. Tidal turbines are also installed near the bottom of the barrage inside tunnels. They are turned with the incoming and outgoing tides to transform the energy into electricity. Tidal barrages are the most efficient method of generating electricity from tidal currents. However, the need for the construction of the supporting infrastructure for the dam wall dramatically increases the cost of the project. As they are also a physical barrier, they largely inhibit the ability for marine life to pass through which can negatively affect the local ecosystem.

Tidal fences are a combination of tidal turbines and barrages. Several vertical turnstiles are placed in narrow bodies of water with high velocity tidal currents, such as inlets and the mouths of rivers and streams. These form a fence-like structure where the water flow pushes the blades in a turnstile fashion rather than like a propeller. The turnstiles are still connected to a generator in a similar fashion to turbines and barrages. These systems don't require the large concrete structures like barrages and are installed completely underwater, so have a much smaller impact on the surrounding ecosystem.

2.4 Wave Energy

Wave energy conversion systems are currently at a fairly early stage of development [23, 24], and the primary areas of research surrounding wave energy systems are their potential for hybridisation. The possibility of incorporation with wind turbines is the most promising due to the ability of wave energy converters to suppress platform motion in offshore floating wind turbines [25]. However, wave energy implementation in offshore wind farms at this stage of development can result in significant increases in project costs.

The types of wave energy converters under development include those suited for near coast and offshore locations, as well as varying water depths. They primarily

fall into three categories: oscillating water columns, oscillating bodies and overtopping devices. An oscillating water column involves air trapped in a chamber which is compressed by the changing wave pressure. Oscillating bodies generate energy through its relative motion to a stable body. Overtopping devices use the potential energy of the water to power a low head turbine.

Two of the most notable hybrid wind and wave systems are W2Power and Poseidon Wave and Wind; both of these projects have produced a demonstration scale deployment in the ocean. The W2Power system involves a dual semisubmersible offshore wind turbine platform with two turbines. Numerous oscillating body wave energy converters are placed under the surface on the platform. The full scale system would produce 10 MW of power with 7.2 MW from the wind turbines and 2–3 MW from wave energy. Currently, a small-scale device has been tested with the wind turbines only. In comparison, the Poseidon Wave and Wind system has a buoyancy stabilised platform with multiple wind turbines and wave energy converters. A smaller–scale model has been tested and it featured three wind turbines and 10 wave energy converters. The full-scale version of the system would include 2.6 MW of power from the wave energy converters and 2.3–5 MW from the wind turbines. The Poseidon Wave and Wind system uses both oscillating body and oscillating water column wave energy converters, whereas the W2Power system only uses oscillating body converters.

Hybridising wind and wave energy on a common platform is ideal for maximising the amount of power generated whilst being efficient in the amount of marine space used. The other advantages of these types of systems include streamlining of maintenance and grid connections and the wave energy would allow for the smoothing of power fluctuations produced from wind energy. Most significant research surrounding this subject revolves around the ability of wave energy converters to suppress platform motion in offshore wind turbines as they absorb the energy from incoming waves. This is an important factor when considering the reduced system fatigue and efficiency improvement within the systems. This research is still in the early stages but shows promise for the future implementation of offshore hybrid wind and wave energy systems.

2.5 Issues with Single-Source System

As previously outlined, there are factors reducing the power quality and reliability of single-source renewable energy systems. Whilst they are a feature of most renewable energy sources, these issues are prominent and easily identifiable in solar farms. Solar power production is almost exclusively undertaken during daylight hours and is subject to fluctuation depending on weather factors like cloud cover and solar irradiance. This cyclic generation means solar farms are less capable of increasing or decreasing power production depending on present demand for energy. Specific fluctuations caused by environmental conditions are potentially more problematic for grids due to the higher unpredictably and rapid rate of change.

Issues related to this problem are exacerbated by the continued commissioning of large solar farms without accurate methods of predicting impacts on the power grid. It is likely additional infrastructure will be required to mitigate this problem in the future; namely large energy storage facilities to better control power distribution and delivery, and the introduction of compensating alternate energy sources.

3 Hybrid Energy Systems and Technologies

Hybrid renewable energy systems most commonly comprise of two or three energy sources and can be located on land or offshore. Whilst non-renewable power sources can be included in hybrid systems, the three examples of possible of hybrid energy systems given below only include renewable sources.

In addition to appropriate selection of renewable energy sources, developing and adapting current and new technologies for hybrid systems is a prominent area of research. The areas investigated for this report include specific technologies in the areas of energy storage systems, control strategies and transmission systems.

A new technology being investigated for potential applications as a link between renewable energy sources, or between hybrid energy systems and power grids is magnetic buses. Their inclusion in a power system removes the need for some supporting infrastructure like step up transformers and line filter circuits. The experiment conducted for this report investigates different forms of windings for transformers and evaluates their efficiency.

3.1 Structure of Hybrid Energy Systems

3.1.1 Two-Source Onshore System

Wind and solar power are two of the most developed renewable energy systems. As more solar energy is produced during the day whilst wind energy dominates during the night, the complementary nature of these energy sources is well suited to hybridisation. Hybrid wind and solar systems can be adapted for use as microgrids or grid integrated systems, and their capacity is highly flexible.

Renewable microgrid systems installed in remote areas often use energy storage systems to stabilise the power output. The system in Fig. 1 shows the basic structure of a hybrid wind and solar microgrid system with battery energy storage. This particular system feeds DC and AC loads so it has a DC and AC bus in parallel. As wind turbines produce AC power, it is converted into DC before going to the bus, whilst DC/DC converters are connected to the solar array and battery storage system to ensure the inbound voltage matches the DC bus voltage. The steady state bus voltages will vary depending on the capacity of the system, however the buses will almost always be

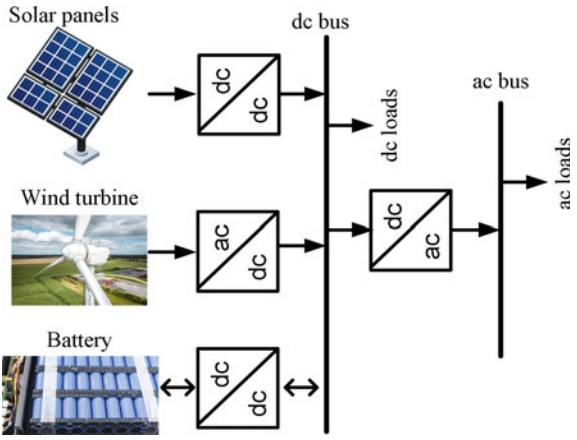

Fig. 1 Hybrid wind and solar microgrid system with AC and DC loads

rated for high voltages. Electricity is permitted to flow in both directions between the battery storage system and the DC bus to allow the battery to charge and discharge.

3.1.2 Two-Source Offshore System

One type of offshore hybrid renewable energy system that is being researched extensively is a wind and wave system. These two technologies are highly compatible and are able to be installed on the same offshore platform which promotes an efficient use of available marine space. The presence of wave energy conversion generators under the water's surface also aids in platform motion suppression of offshore wind turbines. The main factor preventing the commercial implementation of hybrid wind and wave systems is the high project costs.

Both wind and wave energy generation systems produce AC power, therefore, it is more efficient to use an AC bus to transfer power to the transmission system. As the tidal generation system will be located on or near the coast, it would be cost effective to locate the combined wind and wave platforms relatively close to the coast, depending on the specific geographical features of the chosen location. Generally, this suggests smaller transmission distances to onshore power, which current research suggests may be well suited to a high voltage DC transmission system. The basic structure of such a system is shown in Fig. 2.

3.1.3 Three-Source Offshore System

Another possible form of an offshore hybrid system is the combination of wind, tidal and marine current energy. In order to take maximum advantage of the available oceanic energy sources, this type of system is most beneficial as a near-coast installation. Marine current turbines, similar to wave energy conversion systems,

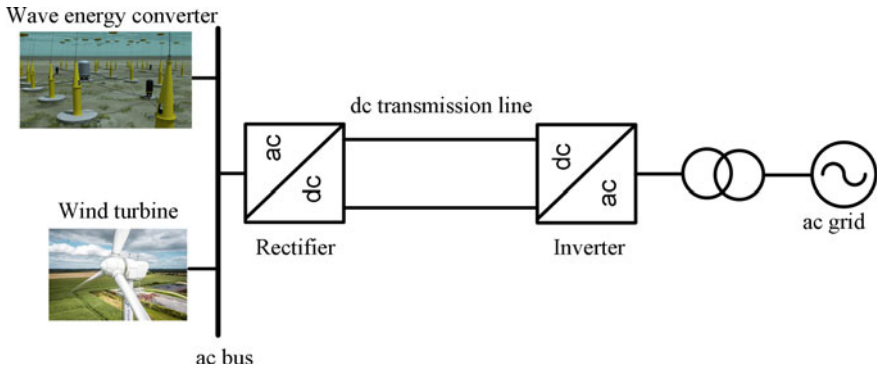

Fig. 2 Hybrid wind and wave offshore system with a DC transmission system

can be installed on the same offshore platform as wind turbines. The primary factor preventing the research on these types of systems to progressing to real-life testing is cost, particularly with regards to the tidal energy system.

Despite all three sources producing AC power, two AC buses have been used in the system. This is mainly due to geographical location as the tidal system will likely be located on the coast whilst the wind and marine current platforms will be off the coast. Due to the placement of the generation system, the transmission lines will likely need to traverse a smaller distance so a traditional high voltage AC transmission system was selected. This system is shown in Fig. 3.

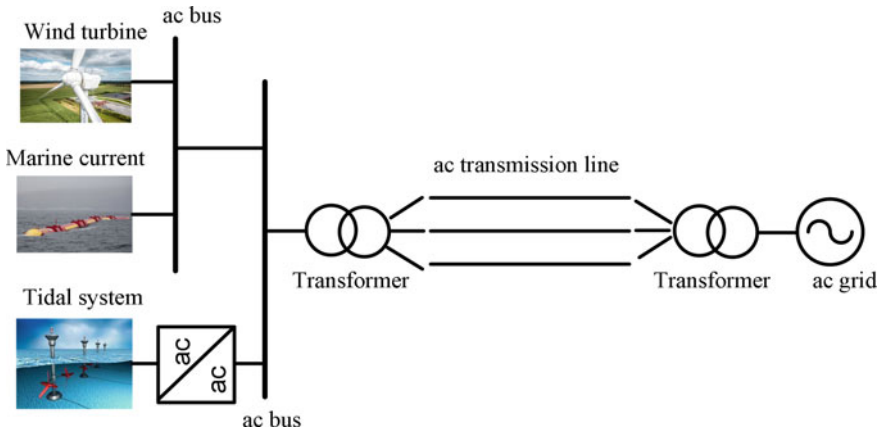

Fig. 3 Hybrid wind, marine current and tidal system with an AC transmission system

3.2 Hybrid Energy System Technologies

3.2.1 Energy Storage Systems

Battery Energy Storage for a Hybrid Wind and Photovoltaic System

Battery energy storage systems have multiple uses when applied to hybrid renewable energy systems. They have numerous applications which have benefits for commercial and residential purposes which are outlined below [26].

Residential

- Self-Consumption: allows excess renewable energy generated to be stored and used when needed (e.g., storing solar power during the day to use at night);
- Emergency Backup: used as an alternative to generators in the event of a power outage.

Commercial

- Peak Shaving: prevents businesses from drawing more than their predetermined threshold of grid power during peak periods;
- Load Shifting: can manipulate energy usage to decrease grid power used during more expensive periods, saving money on electricity bills;
- Emergency Backup: allows essential systems to operate in the event of a power outage;
- Microgrids: improve economic feasibility of grid-disconnected, remote microgrid energy systems;
- Renewable Integration: smooths output of renewable energy systems for more stable grid integration.

All energy storage systems contain one or more battery modules, sensors and control components, and an inverter [27]. They can be AC or DC coupled depending on the system application. Using multiple battery modules is advantageous in the event of a malfunction as the faulty module can be replaced without seriously affecting system operation. The introduction of control components into a storage system allows for constant monitoring of all technology to optimise efficiency, and analysis of energy consumption data to allow for discharge in peak periods. The inverter allows power to flow between the AC and DC system states; this promotes the ability of the batteries charge and discharge.

The battery energy storage systems modelled in Figs. 4 and 5 can be applied to a renewable system utilising solar energy for a commercial or residential application [28]. The DC coupled system directs excess power production to the batteries, and releases power through the inverter when required. This system stores power before it is converted to AC which saves costs by limiting the number of AC and DC conversions required and can be configured to supply power during a grid outage; but is unable to draw power from the grid for storage. AC coupled systems aren't as efficient as DC coupled systems, but are more common as they offer other benefits.

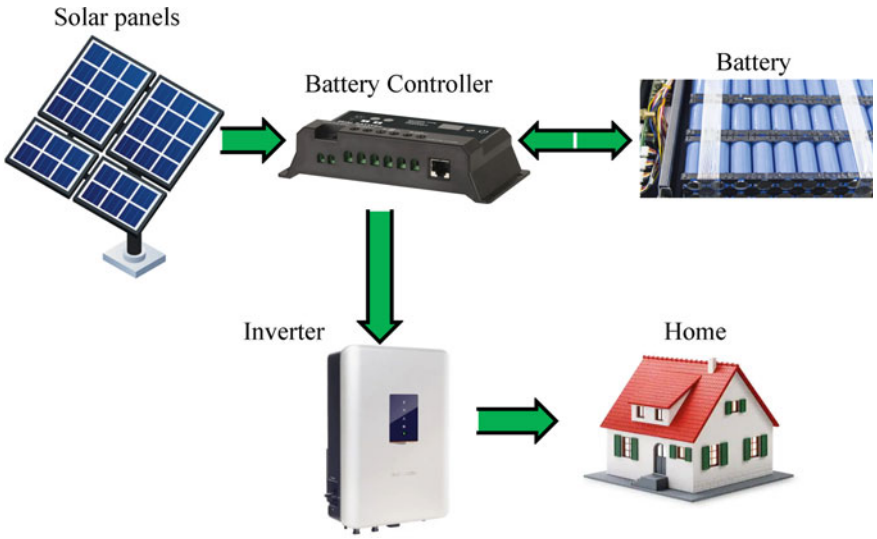

Fig. 4 DC coupled storage system

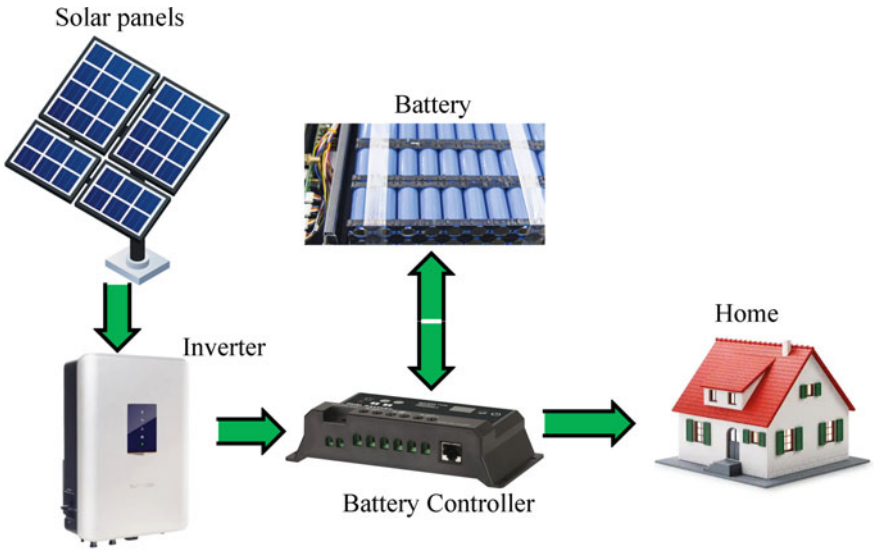

Fig. 5 AC coupled storage system

They can draw power from the grid, negating the need to use power from the grid during peak periods which reduce utility costs, as well as provide the emergency backup and storage of excess solar energy. They also operate independently of the

solar power system, so they can be retrofitted whilst power is being drawn from other sources.

The standalone microgrid system in [7] uses a wind turbine and solar array as primary energy sources with a battery energy storage system. The storage system consists of a proton exchange membrane fuel cell (PEMFC) and an energy management system which regulates the power flow within the system by monitoring and forecasting the renewable power availability and state of charge of the batteries. This system is self-sufficient under varying climatic conditions, designed for use in remote areas and can be connected to a power grid or acts as a microgrid system.

The different components of this hybrid system are all connected via a DC link. On the generation-side of the system, the following components are connected; a DC wind generator (5 kW capacity) and a DC/DC converter, photovoltaic modules (5 kW capacity) and a DC/DC converter, a lead-acid battery and a buck-boost DC/DC converter (includes a dumping load to dissipate battery overcharge) and a fuel cell (6.2 kW capacity with a unidirectional DC/DC converter). The load side of the system consisted of a three-phase inverter, LC filter and a resistive AC load.

The voltage level at the DC link is dependent on the generator outputs and the load impedance. The DC/AC converter operates with a three-phase proportional integral (PI)-based control system. A PEMFC was chosen as a power source due to its high efficiency in steady-state, reliable power generation, low operation noise and eco-friendliness [29]. However, its drawbacks include an unstable output voltage, slow response to variation in the load and high cost [30].

The system was tested experimentally using equipment which emulates real wind turbine and photovoltaic array behaviour. The test conducted begun with the wind emulator operating at a fixed speed with the batteries going into discharge mode to meet the power load requirements in the initial stages. Once the photovoltaic generator is activated, the batteries are no longer required and begin to charge as there is now excess power generation. The batteries go back into discharge mode when the load requirement is raised; the DC link voltage remained constant through the duration of the experiment. The obtained experimental results showed promised and this hybrid renewable energy system is recommended for future studies.

Superconducting Magnetic Energy Storage for a Hybrid Wind, Thermal and Nuclear System

In a wind farm connected to a grid with thermal and nuclear electricity generation plants, a superconducting magnetic energy storage system was developed as an alternative to batteries in [31]. It was developed to better maintain the stipulated voltage and frequency requirements for the grid during periods of dynamic disturbance. This system was chosen for short-term energy storage due to its faster response to compensate for wind power fluctuations when compared to batteries which have a slower discharging process. However, the drawbacks of this system include the high initial and maintenance costs, and significant supporting infrastructure.

Two of the most prevalent types of wind turbine generators are the variable speed double induction generator and fixed speed squirrel cage induction generator. The squirrel cage generator was selected for this wind farm due to the reduced maintenance, low cost and simplicity in operation. This is the justification for the selection of a superconducting magnetic energy storage system; it can provide the large reactive power and control of voltage and frequency variations that battery storage systems can't supply. Despite this, a new control strategy was implemented to further improve the performance of the energy storage system. It consisted of integrating dual parallel connected DC/DC chopper circuitry to assist the superconducting magnetic energy storage device with switching between charging and discharging modes.

The system was first modelled and tested using a traditional superconducting magnetic energy storage unit to stabilise the power network, later tests incorporated a single DC-DC chopper and a dual parallel DC-DC chopper. The same wind speed data was used for all experimental scenarios. The testing process showed a smaller dip in frequency during periods of wind speed change when the DC-DC choppers were connected compared to when they weren't. The dual parallel DC-DC chopper performed better than the single DC-DC chopper because it has increased current control in the voltage source converter circuitry and enhanced switching ability. This led to the conclusion this system provided satisfactory recovery periods for the grid frequency in times of dynamic disturbance to fulfill grid operator requirements.

Hybrid Supercapacitor and Undersea Energy Storage System for a Wave Energy System

The wave energy conversion system presented in [11] featured the renewable energy source operating in parallel with a hybrid energy storage system consisting of supercapacitors and an undersea energy storage system. The components of the storage system each have distinctive operating characteristics, so a sophisticated energy management system was introduced to more efficiently size components and optimise energy yield. The wave energy conversion portion of the system used a direct-drive linear generator-based system.

The design of the hybrid energy storage system was primarily dependent on the energy storage technology selection, power and energy capacity of the components and managing the power flow between storage components and the system. Supercapacitors, like batteries and fuel cells, are commonly featured in hybrid storage systems. The undersea energy storage system has been recently proposed as a potential alternative energy storage technology. It is placed on the seabed and consists of a concrete sphere containing a reversible pump-turbine unit, a permanent-magnet synchronous machine and steel pipe to allow for water flow. When the generated electricity exceeds current demand, water is pumped out of the device and water is permitted to flow back in when additional energy is required to meet demand.

Using components of optimal size in the hybrid energy storage system has numerous benefits for the specified renewable energy system. These include but aren't limited to reduction in cost and weight of the system and increasing energy

efficiency and yield. The relevant constraints on component sizing are the state of charge and the voltage, current and frequency ratings of devices. The approach taken in sizing the energy storage components involved implementing an optimisation-based energy management strategy. In particular, a reinforcement learning technique was used where the system takes into account the quality of power allocation within the system for various component sizes; from this the combination with the highest reward is selected. This method is highly adaptable, but the real-time implementation means the optimality suffers slightly.

The hybrid energy system was tested against supercapacitors and an undersea energy storage system on its own. It was determined the hybridisation of the two systems resulted in reduced capacity components. The proposed energy management strategy was also shown to adequately regulate power fluctuations within the system in real-time, meaning it would be viable to connect this renewable energy system to an onshore power grid.

3.2.2 Control Strategies

Power Fluctuation Compensation for a Hybrid Wind and Tidal System

The system proposed in [14] investigates a novel power fluctuation compensation system for a hybrid offshore wind and tidal turbine system. The adjustments made to the system aimed to mitigate generated power fluctuation and stabilise power quality issues such as voltage sags or frequency variations.

The offshore system used consisted of 2.3 MW capacity wind turbine generators with a 60 m rotor radius, and 1 MW capacity tidal turbines with a rotor radius of 25 m. The tidal generation system was connected in parallel to the wind system. After generation, the AC power was passed through a transformer to increase the voltage to 12 kV. It was then transformed into DC power by a converter before travelling more than 10 km to the onshore power grid through an undersea DC transmission cable. A DC/AC converter is also present on the grid-side of the transmission system to adequately integrate the power with the grid.

The output of the tidal generators is generally more stable than that of the wind turbines on account of the higher predictability of the renewable energy source. To stabilise the wind turbine output, the tidal generator is connected to an insulated-gate bipolar transistor (IGBT) bidirectional inverter system. Furthermore, the tidal induction motor can be mechanically isolated from the tidal turbine shaft by a one-way clutch when the rotational speed of the turbine is lower than that of the inverter's magnetic fields. This allows the turbine to act as a fly-wheel energy storage system by use of the IGBT inverter control. The stored energy can be extracted by decelerating the motor with the inverter control system.

The testing phase of the system was conducted experimentally under varying wind and tidal turbine generator speeds. Initially, the wind turbine model starts up to build the DC capacitor voltage before the grid-side DC/AC converter begins to operate. When the IGBT converter starts to drive the induction motor the one-way

clutch is off and the system is in fly-wheel mode. Finally, the modelled tidal turbine starts up and once its rotation speed exceeds that of the induction motor, the one-way clutch switches on and the system goes into generator mode and the power from the tidal turbine joins the wind power already being transmitted to the grid. The system shows satisfactory operation from the preliminary experimental results; but concerns related to the stability of the system call for a more advanced experimental study.

Advanced Power Output Forecasting for a Hybrid Wind and Marine Current System

The hybridisation of offshore wind turbines with a marine current system is beneficial in combating the characteristic power fluctuations of wind energy systems. This is due to marine current being highly predictable and subject to slow cyclic variation which is in direct contrast to the unpredictable and erratic nature of wind. In order to improve the prospects of grid integration in [13], advanced prediction methods were employed to ensure the power output of this renewable energy system would satisfy grid code requirements.

The characteristics of wind energy make it difficult to produce highly accurate forecasts, one such method involves artificial neural networks. These have outstanding approximation capabilities and can produce reasonably accurate predictions, but issues can arise if the training data is too chaotic or noisy, leading to errors in wind speed forecasting. Constructing prediction intervals is a good method to combat this issue is they establish upper and lower bounds for a prediction with a probability called a confidence interval. The bootstrap technique is the most common method used to form prediction intervals for artificial neural networks and achieves satisfactory performance. For this hybrid energy system, this is combined with a nonlinear auto-regressive exogenous neural network model to obtain point forecasts for wind speeds.

The highly predictable nature of marine current means prediction methods can be developed to predict currents at a particular location within a 98% accuracy. The harmonic analysis method is a complex prediction method as all tidal harmonic constituents need to be known for the given location but is very accurate and is the method selected to predict marine current speeds in this system.

To further improve this system's potential for grid integration, the wind and marine current turbines were integrated with a small battery energy storage system. The prediction methods employed allowed for small power fluctuations within a specified limit; these fluctuations were infrequent and can be eliminated using the battery energy storage system. The combination of these techniques resulted in a renewable energy system with reliable power dispatching, satisfying onshore power grid requirements. Furthermore, this power strategy is more economically feasible than traditional methods of simply injecting all available renewable energy power into the grid and can be adapted for other renewable energy systems.

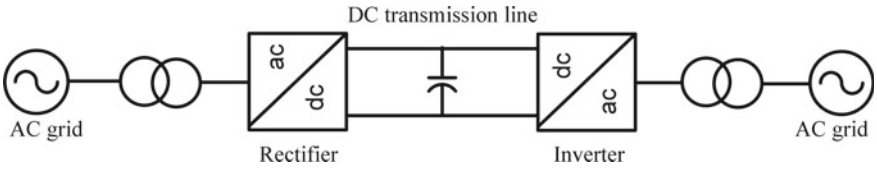

Fig. 6 Voltage source converter high voltage DC transmission system

3.2.3 Transmission Systems

High Voltage DC Transmission for a Hybrid Wind, Wave and Tidal System

Traditionally, undersea transmission systems are high voltage AC, but recent research into the feasibility of using a high voltage DC system for near-coast offshore systems is being conducted. The potential advantage of this system is an increased ability to control active and reactive power fluctuations within the system, improving stability for grid connection. The system has been tested with voltage source converter technology as the necessary control techniques can be efficiently implemented.

Voltage source converters are devices which allow for connection between high voltage AC and DC systems. In power generation, they are used to convert AC power into DC power, and vice versa, for integration with a high voltage DC transmission system. These devices can operate at high frequencies and turn on or off in a controlled manner through the use of insulated-gate bipolar transistors (IGBTs). A simplified voltage source converter-based DC transmission system is shown below in Fig. 6 [32].

The converters are connected to the AC system via transformers to change the AC voltage to the equivalent DC voltage level; the transformers are usually single-phase three-winding type to accommodate for the three-phase power required in large energy generation systems. Phase reactors and AC filters can also be connected to the voltage source converters; the phase reactors control active and reactive power and reduce high frequency harmonic currents, and the AC filters prevent voltage harmonics from entering the system. The voltage source converter devices themselves can be two-level or three-level, but both consist of a bank of IGBTs which serve as switches. The capacitor in the DC transmission line reduces voltage ripple, but also aids in power flow control by providing a low inductive path for current when the source converters are off. The control system in this type of transmission system utilises a pulse width modulation technique. This system produces the desired voltage signal from the voltage source converters by comparing it to a sinusoidal reference signal, which can be changed almost instantly in different ways to control active and reactive power. The cables used as the transmission line are usually made of a polymer as they are light, flexible and have high mechanical strength.

An offshore hybrid wind, tidal and wave renewable energy system was presented in [12]. The system was connected to an onshore power grid via a high voltage DC link based on voltage source converter technology. The wind and tidal turbines are both

modelled by a doubly fed induction generator system, whilst a permanent-magnet synchronous generator was used for wave energy conversion. A damping controller system was incorporated with the DC link and the ability of this technology to stabilise the microgrid system was assessed.

An undersea DC transmission system was selected due to its economic benefits when compared to an equivalent AC system for a near-coast renewable energy farm. Another benefit of this type of transmission link is its high-power capacity and responsive control ability. The DC link was rated for 200 MW, which is based on the capacity of the renewable energy generators; 80 MW capacity wind turbines, 60 MW capacity tidal turbines and 50 MW capacity waver generators. The wind and tidal turbines are connected in parallel to a bus which is connected to another bus via a short transmission line. This second bus also houses the connection to the wave generators and is the link to the high voltage DC transmission system. On the grid-side of the link, another bus connects the renewable energy power to the power grid. The control system integrated with the transmission line utilised a proportional integral derivative damping controller.

The tests conducted on an experimental model of this system showed the high voltage DC link with the damping controller provided the best response characteristics to reduce potentially large fluctuations in active and reactive power. When the transmission was replaced with an equivalent AC transmission line, the three-phase short circuit fault triggered in the power grid resulted in severe voltage fluctuations in the tidal and wave generators. This was considerably reduced with the DC transmission system. It was concluded the proposed voltage source converter-based high voltage DC link with a proportional integral derivative damping controller rendered adequate damping characteristics to stabilise the connected hybrid renewable energy generation system.

Low Frequency AC Transmission for an Offshore Wind Farm

The research in [10], investigated the feasibility of applying a low frequency AC transmission system over distances greater than 100 km to connect large offshore wind farms to power grids. The operation of this new system was compared to high frequency AC, and current commutated and voltage-source converter-based high voltage DC systems.

The supporting electrical devices needed for each transmission system are outlined below:

Conventional AC: transformers on the rotor-side and grid-side of the transmission lines to ensure the correct voltage are present for transmission and grid integration.

Low Frequency AC: similar transformers to the conventional AC system, but an additional AC/AC converter is placed after the transmission line to increase the frequency of the power to meet grid requirements.

High Voltage DC: as the power produced from the wind turbine generators and the power used in the grid is AC, AC/DC and DC/AC converters are placed before

and after the transmission line respectively. The transformers are still necessary to adjust the AC voltage levels.

The simulation of this system for testing included a doubly fed induction generator-based wind farm, transformers and a power cable. Three tests were conducted with the simulation; steady-state, variable wind speed and a short circuit fault. The results showed improved transmission capabilities at frequencies lower than 50–60 Hz (normal operating frequency for AC transmission), as well as better reactive power control during the short circuit fault. It was concluded this transmission technology showed potential but requires additional research to better understand its suitability for application in real systems.

4 Summary

Renewable energy sources have been identified as the most important alternative to fossil fuel-based electricity generation when considering future commercial and domestic energy requirements. Whilst many forms of renewable energy are available, this report focused on solar, wind, tidal and wave energy. Solar and wind energy are two of the most technologically mature renewable energy sources and are two of the most prevalent sources already in use. Tidal and wave energy are currently at earlier stages of development, but tidal power has the potential to generate large amounts of power for industrial usage and wave energy is widely available as an offshore energy source.

However single source renewable generation systems are reliant on intermittent weather sources, which introduce unreliable power into commercial electricity grids. The resulting power fluctuations decrease the power quality of the system, potentially destabilising power grids; which can cause widespread damage to power system infrastructure and grid connected loads. This issue is prominent in solar farms, where power generation is almost exclusively undertaken during daylight hours. Solar power is also subject to rapid changes in power due to unpredictable weather conditions. These specific problems require solutions such as large-scale energy storage or alternate energy sources to justify the continued commissioning of commercial solar farms. Hybrid renewable energy systems are currently being researched as a potential solution to the rising concerns related to single source systems.

Hybrid energy systems can be adapted to onshore or offshore applications and can combine two or more renewable energy sources. Depending on the specific circumstances, non-renewable source can also be included as part of a hybrid power system. The selection of renewable sources is generally based on the combination of their power generation windows; for example, wind and solar power are well suited as solar power will dominate during the day and wind energy will dominate at night. This inherently goes some way towards addressing the intermittent power production characteristic of single source systems.

Current research into hybrid systems is centred around further improving their power quality and reliability for power generation. The main focus areas centre

around technologies which have applications in energy storage, power signal control and transmission systems. One such technology in the early stages of development is a magnetic bus which may be a potential alternative to high voltage electric buses used to interconnect energy sources as well as connect generation systems to power grids [33–35].

The hybrid systems presented in this chapter show great potential for correcting issues associated with single source renewable energy systems. However, the majority of research into hybrid systems is still at an experimental stage and not ready for small-scale implementation yet. Hence, this chapter recommends making improvements to existing technologies and systems to better understand and predict power quality issues in power grids whilst waiting on the construction of new hybrid systems.

References

1. Geoscience Australia, in *Australia's Energy Production, Consumption and Exports*. Scientific Topics: Energy: Basics. Available https://www.ga.gov.au
2. S.K.S. Kushwaha, S.R. Mohanty, P. Samuel, Robust H∞ control for stability assessment in grid-connected offshore wind and marine current hybrid system. IET Renew. Power Gen. **13**(2), 318–329 (2019)
3. P. Hou, G. Yang, P. Enevoldsen, A.H. Nielsen, in *Cooperation of Offshore Wind Farm with Battery Storage in Multiple Electricity Markets*. 2018 53rd International Universities Power Engineering Conference (UPEC) (Glasgow, 4–7 September 2018), pp. 1–6. https://doi.org/10.1109/UPEC.2018.8541864
4. S. Najafi-Shad, S. Masoud Barakati, A. Yazdani, An effective hybrid wind-photovoltaic system including battery energy storage with reducing control loops and omitting PV converter. J. Energy Storage (2020). ISSN 2352-152X. https://doi.org/10.1016/j.est.2019.101088
5. Clean Energy Council, *Wind Energy Facts*. Technology: Wind, 2018. Available https://www.cleanenergycouncil.org.au
6. S. Marmouh, M. Boutoubat, L. Mokrami, Performance and power quality improvement based on DC-bus voltage regulation of a stand-alone hybrid energy system. Electr. Power Syst. Res. **163**(Part A), 73–84 (2018). ISSN 0378-7796. https://doi.org/10.1016/j.epsr.2018.06.004
7. B. Benlahbib, N. Bouarroudj, S. Mekhilef, D. Abdeldjalil, T. Abdelkrim, F. Bouchafaa, A. lakhdari, Experimental investigation of power management and control of a PV/wind/fuel cell/battery hybrid energy system microgrid. Int. J. Hydrogen Energy **45**(53), 29110–29122 (2010). ISSN 0360-3199. https://doi.org/10.1016/j.ijhydene.2020.07.251
8. A. Shaqour, H. Farzaneh, Y. Yoshida, T. Hinokuma, Power control and simulation of a building integrated stand-alone hybrid PV-wind-battery system in Kasuga City, Japan. Energy Rep. **6**, 1528–1544 (2020). ISSN 2352-4847. https://doi.org/10.1016/j.egyr.2020.06.003
9. K. Sarker, D. Chatterjee, S.K. Goswami, Grid integration of photovoltaic and wind based hybrid distributed generation system with low harmonic injection and power quality improvement using biogeography-based optimization. Renew. Energy Focus **22–23**, 38–56 (2017). ISSN 1755-0084. https://doi.org/10.1016/j.ref.2017.10.004
10. C.N. Mau, K. Rudion, A. Orths, P.B. Eriksen, H. Abildgaard, Z.A. Styczynski, in *Grid Connection of Offshore Wind Farm Based DFIG with Low Frequency AC Transmission System*. 2012 IEEE Power and Energy Society General Meeting (San Diego, CA, 22–26 July 2012), pp. 1–7
11. J. Nunez Forestieri, M. Farasat, Integrative sizing/real-time energy management of a hybrid supercapacitor/undersea energy storage system for grid integration of wave energy conversion

systems. IEEE J. Emerg. Sel. Top. Power Electron. 8(4), 3798–3810 (2020). https://doi.org/10.1109/JESTPE.2019.2926061
12. L. Wang, C. Lin, H. Wu, A.V. Prokhorov, Stability analysis of a microgrid system with a hybrid offshore wind and ocean energy farm fed to a power grid through an HVDC link. IEEE Trans. Ind. Appl. **54**(3), 2012–2022 (2018). https://doi.org/10.1109/TIA.2017.2787126
13. M.B. Anwar, M.S.E. Moursi, W. Xiao, Novel power smoothing and generation scheduling strategies for a hybrid wind and marine current turbine system. IEEE Trans. Power Syst. **32**(2), 1315–1326 (2017). https://doi.org/10.1109/TPWRS.2016.2591723
14. M.L. Rahman, S. Oka, Y. Shirai, Hybrid power generation system using offshore-wind turbine and tidal turbine for power fluctuation compensation (HOT-PC). IEEE Trans. Sustain. Energy **1**(2), 92–98 (2010). https://doi.org/10.1109/TSTE.2010.2050347
15. L.N. Ren, P. Zhang, Numerical investigation on the dynamic responses of three integrated concepts of offshore wind and wave energy converter. Ocean Eng. **217**, 107896 (2020). ISSN 0029-8018. https://doi.org/10.1016/j.oceaneng.2020.107896
16. K. Lu, C. Hong, Q. Xu, Recurrent wavelet-based Elman neural network with modified gravitational search algorithm control for integrated offshore wind and wave power generation systems. Energy **170**, 40–52 (2018). ISSN 0360-5442. https://doi.org/10.1016/j.energy.2018.12.084
17. E. Muljadi, M. Singh, V. Gevorgian, in *Doubly Fed Induction Generator in an Offshore Wind Power Plant Operated at Rated V/Hz*. 2012 IEEE Energy Conversion Congress and Exposition (ECCE) (Raleigh, North Carolina, 15 September 2012), pp. 779–786. https://doi.org/10.1109/ECCE.2012.6342740
18. J.M.K.C. Donev et al., Photovoltaic system. Energy Education (April 2020). Available https://energyeducation.ca
19. F. Blaabjerg, K. Ma, Wind energy systems. Proc. IEEE **105**(11), 2116–2131 (2017). https://doi.org/10.1109/JPROC.2017.2695485
20. S. Muller, M. Deicke, R.W. De Doncker, Doubly fed induction generator systems. IEEE Ind. Appl. Mag. (2002)
21. M.R. Islam, Y.G. Guo, J.G. Zhu, in Steady State Characteristic Simulation of DFIG for Wind Power System. International Conference on Electrical & Computer Engineering (ICECE 2010), (Dhaka, Bangladesh, 18–20 Dec. 2010), pp. 151–154
22. C. Lane, How does tidal power work? Solar reviews, 8 Dec 2020. Available https://www.solarreviews.com
23. O. Farrok, M.R. Islam, M.R.I. Sheikh, Y.G. Guo, J.G. Zhu, Design and analysis of a novel lightweight translator permanent magnet linear generator for oceanic wave energy conversion. IEEE Trans. Magn. **53**(11), 8207304 (2017)
24. O. Farrok, M.R. Islam, M.R.I. Sheikh, W. Xu, in *A New Optimization Methodology of the Linear Generator for Wave Energy Conversion Systems*. 2016 IEEE International Conference on Industrial Technology (ICIT) (Taipei, Taiwan, 14–17 March 2016), pp. 1412–1417
25. K.L. McTiernan, K.T. Sharman, Review of hybrid offshore wind and wave energy systems. J. Phys. Conf. Ser. (2020)
26. Ideal Energy, How battery energy storage works (2020). Available https://www.idealenergysolar.com
27. CPS National, *Battery Energy Storage Systems*. Medium and Large Scale Solar (2020). Available https://www.cpsnational.com.au.
28. Solar Gain, *How Battery Energy Storage Works*. Battery Storage (2021). Available https://www.solargain.com.au
29. H. Rezk, Comparison among various energy management strategies for reducing hydrogen consumption in a hybrid fuel cell/supercapacitor/battery system. Int. J. Hydrogen Energy (2019). https://doi.org/10.1016/j.ijhydene.2019.11.195
30. B. Bendjedia, Influence of secondary source technologies and energy management strategies on energy storage system sizing for fuel cell electric vehicles. Int. J. Hydrogen Energy (2017). https://doi.org/10.1016/j.ijhydene.2017.03.166

31. K.E. Okedu, Improving the dynamic performance of grid connected wind farm using new SMES switching technique. J. Renew. Sustain. Energy **10**, 043311 (2018). https://doi.org/10.1063/1.5040244
32. T. Kalitjuka, Control of voltage source converters for power system applications. Norw. Uni. Sci. Technol. (2011)
33. M.R. Islam, M.A. Rahman, K.M. Muttaqi, D. Sutanto, A new magnetic-linked converter for grid integration of offshore wind turbines through MVDC transmission. IEEE Trans. Appl. Supercond. **29**(2), 5400905 (2019)
34. M.R. Islam, O. Farrok, M.A. Rahman, M.R. Kiran, K.M. Muttaqi, D. Sutanto, Design and characterization of advanced magnetic material based core for isolated power converters used in wave energy generation systems. IET Electr. Power Appl. **14**(5), 733–741 (2020)
35. M.R. Islam, Y. Guo, J. Zhu, H. Lu, J.X. Jin, High-frequency magnetic-link medium-voltage converter for superconducting generator-based high-power density wind generation systems. IEEE Trans. Appl. Supercond. **24**(5), 5202605 (2014)

Operation of Renewable Energy and Energy Storage-Based Hybrid Remote Area Power Supply Systems: Challenges and State-of-the-Arts

Md. Nafiz Musarrat, Md. Rabiul Islam, Kashem M. Muttaqi, Danny Sutanto, and Afef Fekih

Abstract Remote Area Power Supply (RAPS) systems can play an effective role in supplying electric power to rural and remote communities. RAPS systems are traditionally powered by non-renewable sources. The growing environmental awareness and improved technology have led to the increased penetration of renewable sources into the grid. However, the intermittent nature of renewable sources reduces the overall reliability of the RAPS system. This chapter aims to present a comprehensive review of the renewable energy-based RAPS system, its dynamic performance, and different approaches to deal with the system instabilities. An overview of the RAPS systems and associated challenges has also been presented.

Keywords Remote area power supply system · Frequency regulation · System instability · Wind energy

List of Symbols

w	Word size
n	Number of points in raw data

M. R. Islam · K. M. Muttaqi · D. Sutanto
School of Electrical, Computer and Telecommunications Engineering, University of Wollongong, Wollongong, NSW 2522, Australia
e-mail: mrislam@uow.edu.au

K. M. Muttaqi
e-mail: kashem@uow.edu.au

D. Sutanto
e-mail: soetanto@uow.edu.au

M. N. Musarrat (✉) · A. Fekih
The University of Louisiana at Lafayette, Lafayette, LA 70504, USA
e-mail: md-nafiz.musarrat1@louisiana.edu

A. Fekih
e-mail: afef.fekih@louisiana.edu

S. K. Das et al. (eds.), *Advances in Control Techniques for Smart Grid Applications*,
https://doi.org/10.1007/978-981-16-9856-9_4

Ic	Capacitor current
C	Capacitor
ΔP	Difference in power
ΔP_h	High frequency component of change in power
ΔP_L	High frequency component of change in power
S	Raw time series
SW	SAX words
t	PAA coefficient
i, m, k	Sequence number

List of Acronyms

AC	Kilogram
AREN	Australian renewable energy agency
DC	Direct current
MPPT	Maximum power point tracking
PAA	Piecewise aggregate approximation
PMSG	Permanent magnet synchronous generator
RAPS	Remote area power supply systems
RoCoF	Rate of change of frequency
SAX	Superconducting magnetic energy storage
SMES	Superconducting magnetic energy storage
SOPPT	Suboptimal power point tracking
WECS	Wind energy conversion systems

1 Introduction

Electricity generation is one of the largest sources of carbon emission. Global warming and carbon emission have been accelerating at an alarming rate which calls for the need to reduce the use of fossil fuels, which are still the main source of energy. Underdeveloped countries are explicitly dependent on fossil fuels due to the lack of available infrastructure. Figure 1 shows that CO_2 emission has been significantly increasing over the years. The fastest growth of the emission comes from fossil fuels and industry, which is very alarming. Due to the serious environmental impact, renewable energy has drawn the attention of world leaders, and it has been recognized that renewable energy sources are an effective solution to these serious challenges [1–3]. Figure 2 shows that renewable sources are still showing significant growth in recent years. In the last few decades, wind energy has increased rapidly and has become the leading source of clean energy in Australia [4].

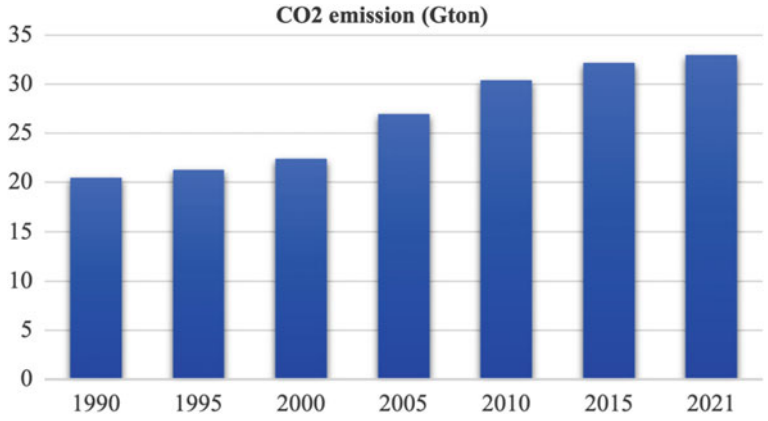

Fig. 1 Change in Carbon flux over the years [expressed in Gigaton (Gt)] [4]

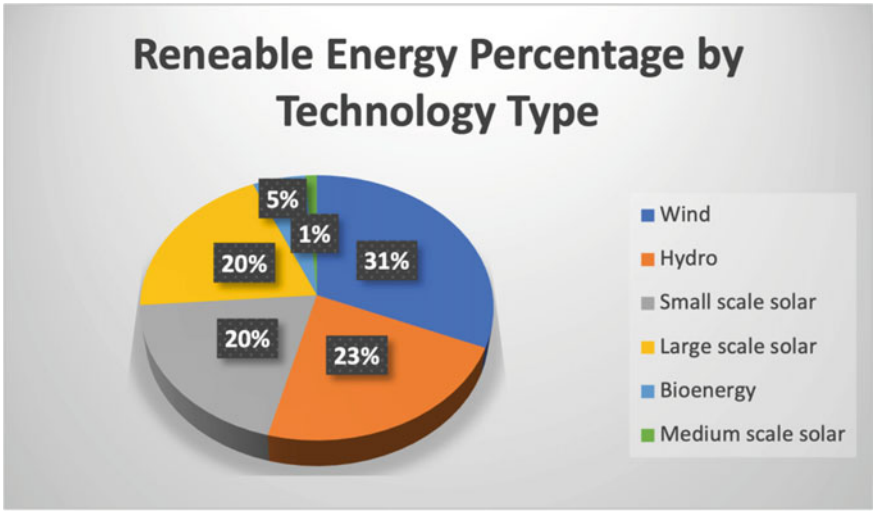

Fig. 2 Renewable energy generation in Australia by technology type [18]

The integration of renewable energy sources with the large grid is a popular topic of research; however, the rural and remote areas which are deprived of the central utility grid are often dependent on renewable sources. Instead of the large utility grid, the electrical power to the remote communities is usually supplied through a remote area power supply (RAPS) system. A RAPS system can be defined as a small electricity network that serves a group of households [5–10]. It is never connected to the utility grid, which means it never absorbs from or injects power to the grid. It is becoming increasingly popular as a feasible solution for rural areas to get access to electric power [11–17]. They can efficiently supply power without any

interruption to the consumers. In a large utility grid, the level of renewable energy penetration is usually limited. But, in a RAPS system, the system can be as high as a hundred percent renewable-based. With the higher penetration of renewable energy, the system resilience will be lower due to the intermittent nature of the renewable sources. Also, the load is highly fluctuating in a small network. Since there are energy sources of different characteristics, the coordination of them can be quite challenging. Nonlinear loads are more likely to occupy a large portion of the total load, which can compromise the power quality significantly.

RAPS system is an effective way to supply electric power to remote communities. A significant amount of the world population is without access to the utility grid, and the RAPS system is a convenient solution to this. It is even promoted rigorously by different non-governmental organizations (NGOs). Traditionally, the RAPS system is usually diesel generator/engine (DE) based. However, with the increasing concern for the environment, renewable energy options have been increasingly utilized. It seems unwise not to utilize renewable sources since one of the promising benefits of a remote area is abundant accommodation for renewable energy resources. Furthermore, fuel transfer to a remote area alone is extremely costly. Therefore, it is more economic to utilize the local renewable resources than import costly conventional fuel. The RAPS system can consist of a single energy source or a single energy storage. It also can be a hybrid of energy source and storage.

Australia is one of the countries that has rigorously adopted RAPS systems. There are several RAPS projects underway in Australia, and they are quite significant considering the local demand in those areas. A few examples are presented as follows. The power demand of Rottnest Island, Western Australia is supported by seven diesel engines and one wind turbine. Huge electric energy is needed to supply the desalination plant which produces drinkable water for that locality. The proposed hybrid RAPS project will add 600 kW of solar energy to increase its renewable energy capacity. Hydro Tasmania will introduce an advanced control management system with a dynamically controlled resistor. The controlled system will be working with a smart demand-management algorithm based on the demand of the desalination plant. This project aims to reduce diesel–fuel consumption by 45% and provide cheaper power [19].

So far, Hydro Tasmania has showcased some extraordinary results in the Bass Strait with increased renewable energy penetration. In the King Island project, they have been able to effectively lower down the fossil fuel usage by 45%, largely from the energy converted from the wind turbines. Currently, the wind turbines support 70% of the energy demand on the island resulting in reduced fuel consumption from around 4.5 million liters to 2.6 million liters per annum. Figure 3 shows the real-time energy support scenario from different sources for the Kings Island RAPS system [20].

The Australia Energy Research Agency (ARENA) plays a leading role in the development and growth of RAPS systems. Funded by ARENA, Windlab, and Eurus will develop the Kennedy Energy Park in partnership as a hybrid RAPS which is located in North Queensland. A 15 MW solar, 43.2 MW wind, and a 2 MW battery storage facility will support the community. Integration of battery storage with solar

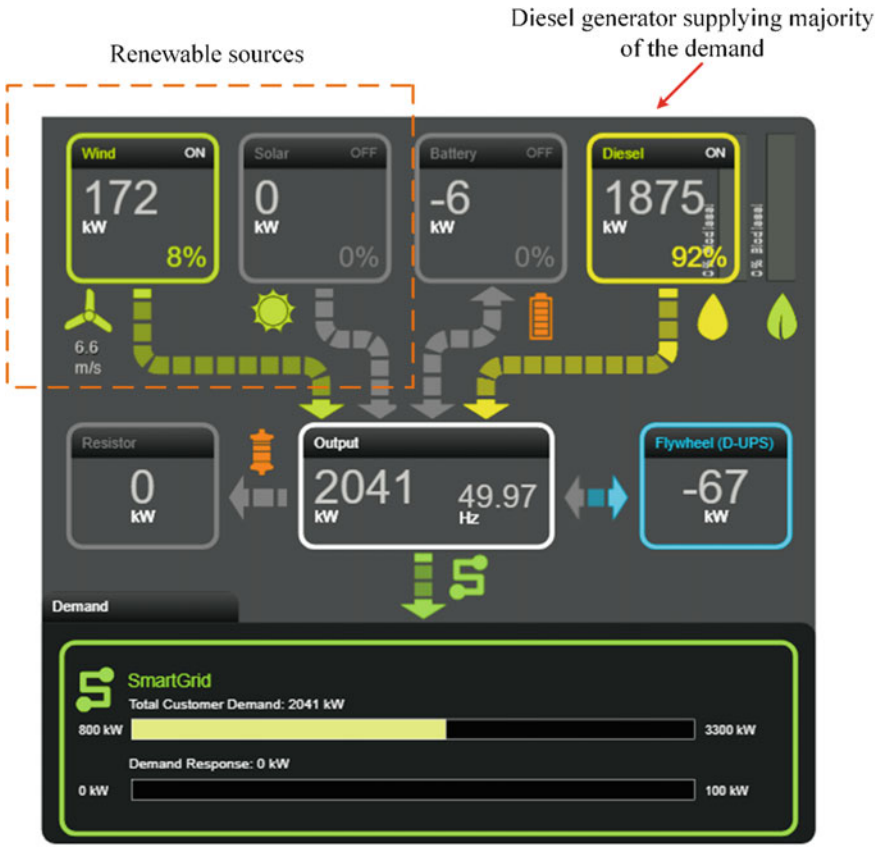

Fig. 3 Real-time energy utilization dashboard of Kings Island RAPS system [21]

and wind will allow renewable electricity to be stored for peak use. The battery will also mitigate any potential load fluctuations. It is expected that this system will be able to supply continuous electricity [22].

A diesel generator-based RAPS system is more reliable; however, its operating cost is very high. A renewable energy-based RAPS system is economically sound, but the system can become more unreliable. Also, the effect of load fluctuation in a RAPS system is very high. However, intermittency is an inherent nature of renewable sources. Control mechanisms are required to ensure the efficient operation of renewable generation systems. The controls in the renewables are usually optimized to extract the maximum power from renewable sources (wind, solar, etc.). For example, both PV and wind energy conversion systems (WECS) are operated by maximum power point tracking. Therefore, these techniques do not facilitate the network event ride-through capability [23, 24]. The renewable sources are interfaced with the network through a power electronic converter [5, 25]. Hence, the system

dynamics do not affect their controllability [21]. The RAPS can be a single energy resource-based, energy storage-based, or hybrid system.

Renewable sources do not have inherent inertia; and therefore, they do not have any resilience in case of any emergency event [26]. The grid-connected renewable sources have different operation strategies since any large utility grid is very stringent in maintaining the fundamental parameters [27, 28]. But RAPS system is a small network and it is non-stringent. All the generators are primary power suppliers and failure of any of them will cause a generation demand mismatch. To maintain the power quality, load-shedding will be needed which reduces the power system reliability. In a conventional generator, the power generation can be adjusted according to the demand by injecting more fossil fuels. But, for renewable sources, it is not possible to adjust the generation according to the demand. The maximum available renewable energy is fixed in any area with a given conversion system at its highest efficiency. The current environmental concern calls for increasing the level of renewable energy penetration. But, with the higher renewable penetration, the system reliability may be affected. Also, unlike large utility grids, there will be no advanced protection devices or control systems. The grid code is not maintained strictly in a RAPS system. Rather, a RAPS system is expected to incorporate cost-effective and efficient protection and control system. The main target of a RAPS system is end-user satisfaction. Since the high penetration of renewables produces unpredictable power generation; it also increases the probability of unplanned tripping and power outage. Also, the reliability measurement in a large grid is much rigorous and complex. On the other hand, in a RAPS system, customer satisfaction and meeting some primary standards are the main priorities.

Since it has been established that the RAPS systems are not robust enough to withstand network incidents, it is expected that the control becomes faster and more efficient. They also require continuous monitoring and rapid decision-making. The central control administrator needs to deal with a large number of data. Analyzing those data and making a quick decision will be extremely difficult if these data are processed in a conventional approach. Therefore, in this chapter, a symbolic aggregate approximation-based data mining tool is presented in this chapter for efficient and rapid processing of data and decision-making.

The structure of this chapter is organized as follows. In Sect. 2, the RAPS systems in Australia are reviewed. In Sect. 3, the support for frequency regulation from the WECS is discussed. Finally, in summary, the conclusion is presented.

2 Basic Topology of RAPS Systems

The RAPS system can be ac bus, dc bus, or hybrid-bus. However, the most common RAPS system in Australia is the ac bus. In a common ac bus RAPS system as shown in Fig. 4a, both the ac generator and dc generator are connected to the common ac bus. Therefore, inverters are used at the dc generator to convert the dc power

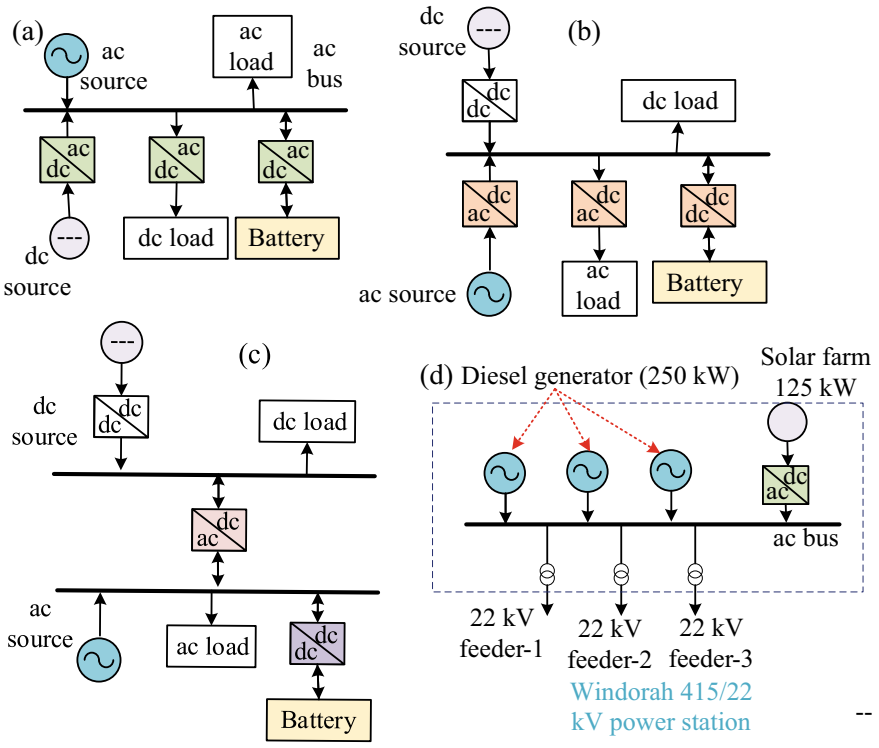

Fig. 4 Basic block diagram of an ac bus hybrid RAPS system: **a** a hypothetical ac bus RAPS system; **b** a hypothetical dc bus RAPS system; **c** a hypothetical hybrid-bus RAPS system; **d** Windorah RAPS system from Energy Queensland (Ergon Energy) [29]

to ac power. The ac load absorbs energy from the ac bus, and the dc load absorbs energy from the ac bus through ac/dc converters. If a storage system is installed in the system, it absorbs or injects power to achieve power balance between generation and load demand through bidirectional converters [5]. Figure 4b shows the dc bus system, where the ac sources are connected to the bus through an ac/dc converter. DC sources are directly connected to the bus. AC loads are supplied through an inverter. The dc loads are connected to the bus directly unlike an ac bus system. A hybrid-bus system is shown in Fig. 4c. In this system, all sources can be connected to the bus as their type. AC sources are connected to the ac bus whereas, dc sources are connected to the dc bus. In this case, unlike dc or ac bus systems, sources do not need to be connected through power converters. Similarly, the loads are connected to their respective types of buses. An example of the RAPS system is shown in Fig. 4d. It shows the solar power and diesel generator-based RAPS system in Windorah, north Queensland which is an ac bus system. It is worth mentioning that most of the RAPS systems in Australia are ac bus. Also, usually in a RAPS system, a conventional generator, e.g., diesel generator is responsible for maintaining the system voltage

and frequency level. Figure 4d shows that the power is mainly supported by diesel generators.

3 Dynamic Behavior of RAPS Systems with Renewable Energy Sources During Sudden Load Changes

3.1 Frequency Regulation Support from Variable-Speed WECS

Frequency events can occur for various reasons such as load rejection, load changes, motor starting, fault, etc. However, this section focuses on the impact of the high rate-of-change-of-frequency (RoCoF) as well as the voltage fluctuation in the dc-link. The sources and the causes of power system events must be known before appropriate mitigating actions are taken. A comparative analysis between two types of distributed generators (DG): (i) diesel generators and (ii) wind turbines has been examined under the steady-state and transient operation. Usually, a rapid load variation in a RAPS system causes RoCoF and causes the system to shut down. Besides load variations, high wind fluctuations too can cause the frequency event.

Although in a large grid, the system frequency does not change much; in a RAPS system, this is a very common cause of system failure. The conventional generators generally have natural inertia, and the governors also adjust the power outputs with respect to the power demand to regulate the system frequency. But the variable-speed WECS are isolated from the grid; and although the DFIG-based WECS has some natural inertia, it is not significant. That is why advanced management is needed for WECS-based RAPS [30]. To enhance the frequency support by utilizing the kinetic energy of the variable-speed WECS rotor, a power reserve was recommended in [31]. In [31–34], the frequency support from the wind turbines was investigated. In [31], the power fluctuation that causes the frequency excursion is mitigated using two approaches. The power fluctuations are passed through a high-pass filter with a pre-defined cut-off frequency as shown in Fig. 5. If the fluctuation rate is higher than

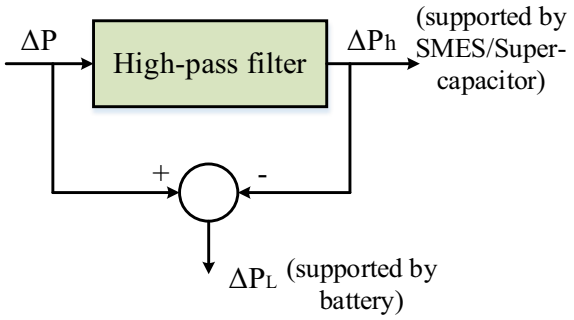

Fig. 5 High-pass filter to extract the high-frequency power fluctuations [31]

the cut-off limit, it would be mitigated through high power energy storage such as super-capacitor or superconducting magnetic energy storage (SMES) whereas, if the fluctuation is below the cut-off frequency, it would be mitigated by a conventional battery. Although SMES/super-capacitors have high power density, they have a very low energy density which means they cannot supply power for a long time. Therefore, it is expected that they can only support intermittent frequency regulation.

Since WECS are electronically controlled, they are faster in their response than conventional generators, and they can be controlled to respond to the rapid variation in network parameters. In [34], this feature has been exploited to explore the feasibility of a transient control. The proposed method in [34] utilized a fraction of the kinetic energy stored in the rotational masses to support the frequency regulation. Also, communication with the conventional diesel generator allowed the power imbalance to be handled efficiently. But, releasing kinetic energy would shift the operating point from the MPP which would cause a secondary frequency event. Also, after the operating point is shifted, it would take time to move back to the previous point.

For a permanent magnet synchronous generator-based wind turbine, the electromagnetic torque can be controlled by controlling the inductor current. However, a sudden change in the torque will cause significant torque stress on the drive train. Therefore, to improve the reliability for frequency regulation and to improve the stress on the drivetrain, an enhanced frequency response strategy using the ultra-capacitor for a PMSG based wind turbine has been proposed for the RAPS system in [35]. In [35], the super-capacitor mitigates the transient power imbalance to support the frequency. The reserved power by the suboptimal operation is utilized to charge the super-capacitor. The artificial inertia controller activates the super-capacitor to support the power imbalance. As super-capacitor can respond very fast, it improves the transient performance of the WECS significantly. However, the RoCoF is still significantly high as observed from the result presented in [35]. In [36], another frequency regulation technique has been proposed which further improves the frequency regulation support. But, in this case, the RoCoF has been managed to be within the limit. Figure 6 shows the basic topology of the integration of the different types of energy storage with the power conditioning system of WECS for frequency regulation support. Figure 7 shows the SMES available at the University of Wollongong.

3.2 Determination of Optimum Charging Power in Cases of Energy Storage with High Power Density

In [21], the suboptimal power point tracking (SOPPT) strategy with artificial inertia support has was discussed to reserve the power to charge the SMES. In this strategy, the WECS is deliberately operated away from the maximum power point tracking (MPPT) curve. Therefore, when the charging is necessary, the WECS shifts to the MPPT curve to supply the reserved power for SMES charging. Otherwise, if the

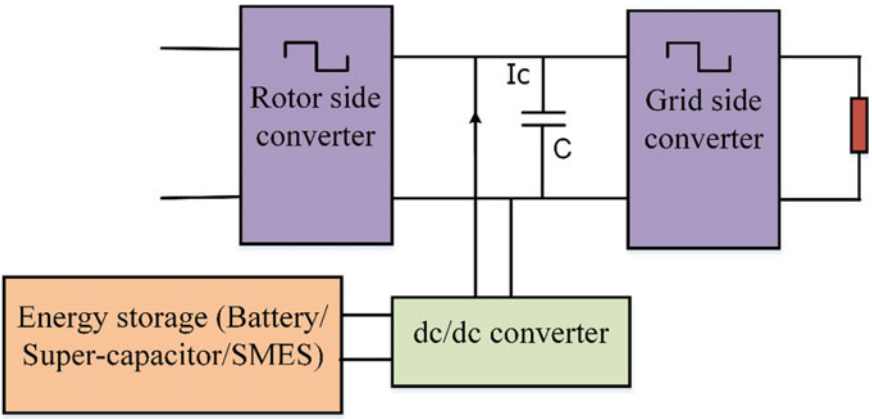

Fig. 6 Supplemental energy storage integration in a wind energy conversion system

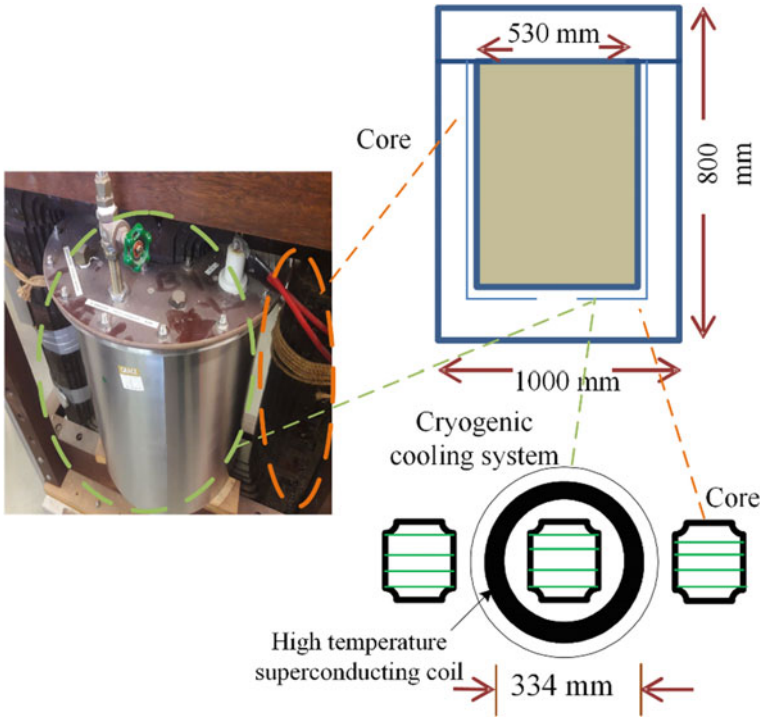

Fig. 7 The iron-cored high-temperature SMES coil at the University of Wollongong and its cross-sectional view from the top [36]

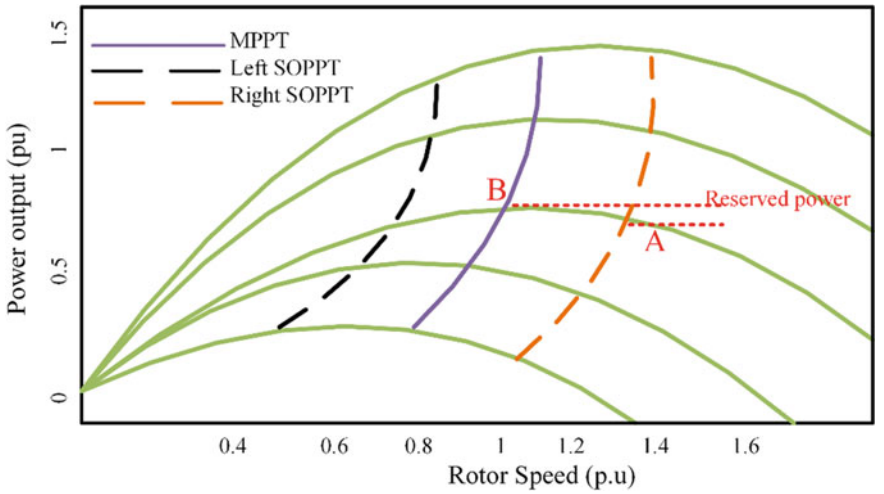

Fig. 8 Wind turbine power curves

WECS was operating along the MPPT curve, sudden load increase due to SMES charging would cause frequency excursion. The quantity of the reserved power is dependent on the SOPPT curve. Figure 8 shows the wind turbine power curves.

In [35], the frequency regulation support by an ultra-capacitor was proposed. In both cases, the charging is necessary which is supported by available wind power and suboptimal power point tracking (SOPPT). The SMES or ultra-capacitor can support significant power. However, in a small RAPS system, full power capacity is not required. But the power reserve should be enough to support the worst load fluctuation. However, due to the intermittent nature of the wind and the resulting unreliable power reserve, this SOPPT strategy is not the best solution to meet the sudden change in power demand. Also, continuous operating away from the MPPT curve is not economical. Also, the mechanical stress caused by the sudden torque increase is extremely detrimental to the drivetrain. The frequent mechanical stress will increase the maintenance cost of the mechanical counterparts. The frequency excursions are very common in a RAPS since system resilience is typically low in a small grid, unlike that of a large grid. Therefore, it is mandatory to design a resilient frequency regulation control approach to ensure system reliability. The SMES/ultra-capacitor charging power is supplied by the reserved power, P_{res} due to suboptimal power point tracking. But, continuously operating the wind turbine away from the MPP will cause significant stress as mentioned earlier. Also, a continuous operation in the suboptimal point might cause secondary frequency events. Therefore, it is necessary to predict how much power reserved in the SMES might be sufficient and when it would be needed. This latter can be estimated from the previously recorded load profiles of different households in a RAPS system, which could be a large number of data. Classifying load patterns and finding the relevant load profile could be very burdensome and inefficient. To solve this problem, a dimensionality reduction

is required, and SAX is a good solution for this problem. Also, partitioning around medoids (PAM) is an efficient algorithm for further classification or clustering of the profiles. A brief theory of SAX and PAM is discussed in Sects. 3.2.1 and 3.2.2.

3.2.1 A Brief Review of Symbolic Aggregate Approximation (SAX) *Algorithm*

An algorithm called SAX was proposed by Keogh to reduce the dimensionality of data and ease the burden of calculation [37]. Using the SAX algorithm, a time series is represented by characters, significantly reducing the dimensionality. Keogh also proposed a technique to find the most unusual time series subsequence. The brute force and the heuristic methods were used to discover the time series discord. This algorithm is used for the assessment of the solar PV impacts on low voltage (LV) and medium voltage (MV) networks. In this technique, the raw time series is converted to piecewise aggregate approximation (PAA) coefficients. Then, the PAA coefficients are converted to characters according to the level they are in as per Gaussian distribution. After that, the strings are grouped according to their pattern using a clustering algorithm. The cluster, containing the time series of interest, is separated and subject to the Brute force analysis. The profile with the largest non-self-match distance is detected as the most anomalous time series.

A time series, m is considered which is of length, n: $m = m_1, m_2, m_3 \ldots, m_n$. After normalizing the time series, it will be converted to a w-dimensional time series, such that $w < n$, using Piecewise Aggregate Approximation (PAA). The formula for calculating PAA is

$$t_i = \frac{w}{n} \sum_{k=\frac{n}{w}(i-1)+1}^{\frac{n}{w}i} S_k \tag{1}$$

If the PAA series is expected to be symbolized using k-alphabet, then the Gaussian distributed curve has to be divided into k-1 breakpoints. W is the word size. With the higher number of w, the resolution will be higher, but it would cause a computational burden. It is expected that the Euclidean distance between the raw time series is greater or equal to the Euclidean distance of the raw time series. If this condition is fulfilled, it will satisfy the "Lower Bounding" of the distance. The equation representing this is given by (2):

$$D(m_1, m_2, m_3, \ldots, m_n) \leq D(l_1, l_2, l_3, \ldots, l_n) \tag{2}$$

The lower bounding distance is calculated from the Gaussian breakpoints with the expression given as below:

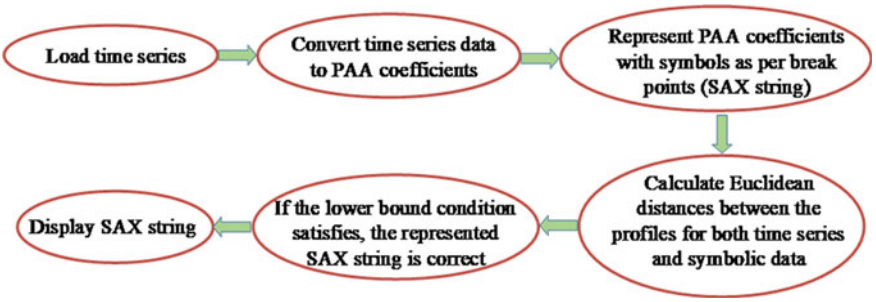

Fig. 9 SAX representation process

$$dist_{\min}(SW_1, SW_2) = \sqrt{\frac{n}{w}\sum_{k=1}^{w}[dist(sa_{1k}, sa_{2k})]^2} \tag{3}$$

where, sa_{1k}, sa_{2k} are the alphabets of the SAX words SW_1 and SW_2, respectively.

The right-hand side of the above equation represents the lower bounding distance of the SAX representation. Figure 9 shows the flow chart of the SAX representation process.

For illustration, the above-mentioned mathematical operation is applied to a wind profile data of 100 days as shown in Fig. 10. The Gaussian curve is divided into 4 breakpoints. The values of them are obtained from the Gaussian distribution table. The symbolization of the PAA series will be carried out in an ascending manner. Any value equal or less than the 1st level will be assigned the character "a," equal or less than the 2nd level will be assigned character "b," equal or less than the 3rd level will be assigned character "c," and so on. The dimensionality reduction of the raw time series using the SAX representation preserves its essential characteristics. The raw

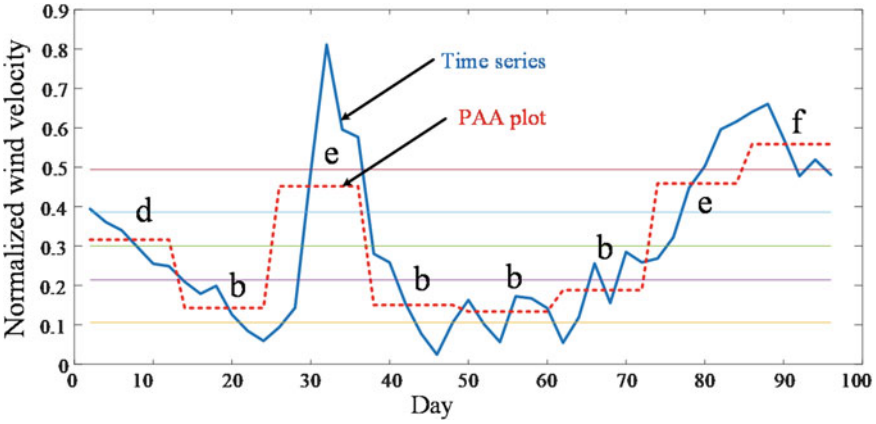

Fig. 10 Converting time series into SAX representation

time series is presented by the blue line, and the PAA approximation level is shown by the red line. The time series is presented by the 5 alphabets and the word size will be 8. The larger the value of the word length, the resolution will be higher, but this will increase the computational burden.

3.2.2 Demonstration of the *SAX-Based Clustering Technique for a Sample Set of Load Profiles*

Three loads have been considered which corresponds to three different households. To choose the appropriate amount of reserved power, the load profiles of those households need to be analyzed. The time series of a 24-h load profile with a 5 min interval for three consecutive days have been taken for analysis. They are collected from the Amy Close suburb of NSW state of Australia. These time series are converted to the PAA (piecewise aggregate approximation) coefficients. As per Gaussian distribution, the PAA coefficients will be converted to characters which will significantly reduce the dimensionality while preserving the essential features of the time series.

If the PAA series for the load profiles are expected to be symbolized using k-alphabet, then the Gaussian distributed curve has to be divided into $k - 1$ breakpoints. In this case, the alphabet size is considered to be 6. Therefore, there will be 5 levels of Gaussian distribution. Any values that are equal or less than the 1st level will be assigned "a," whereas the ones equal or less than the 2nd level will be assigned "b," and those equal or less than the 3rd level will be assigned "c," and so on. The SAX strings of the time series for the three days are shown in Table 1. Instead of 2880 data, the time series has been interpreted with only 8 data strings. The results are shown in Fig. 11.

Now the load profiles represented by SAX strings will be classified according to their characteristics to identify the most fluctuating load profile using a clustering algorithm. The K-means clustering has been used in this experiment to classify the load profiles. It has been observed that Cluster 1, which is shown in blue, shows the most fluctuating characteristic and a significant increase in demand from 2 to 6 pm. Cluster 1 belongs to load 3. After that, a brute force algorithm has been implemented for the load 3 clusters to find the most anomalous load profile among load 3 profiles. The profile with the highest Euclidean distance within the cluster is the most anomalous one and its peak demand will be the amount of the required

Table 1 SAX character strings

Day	Load 1	Load 2	Load 3
1	'b' 'a' 'd' 'c' 'b' 'c' 'f' 'f'	'a' 'e' 'e' 'd' 'c' 'e' 'd' 'a'	'c' 'a' 'a' 'b' 'e' 'f' 'e' 'f'
2	'b' 'a' 'b' 'c' 'd' 'd' 'f' 'f'	'a' 'e' 'e' 'd' 'c' 'e' 'd' 'a'	'b' 'a' 'b' 'e' 'e' 'f' 'e' 'd'
3	'a' 'a' 'd' 'c' 'c' 'e' 'f' 'e'	'a' 'e' 'e' 'd' 'c' 'e' 'd' 'a'	'b' 'b' 'c' 'b' 'e' 'f' 'd' 'c'

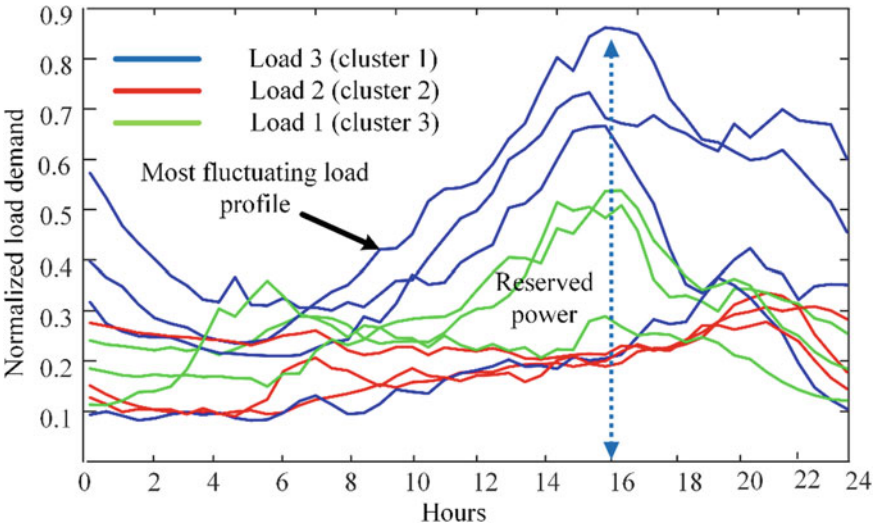

Fig. 11 Discriminated wind profile with SAX and clustering algorithm

reserved power. The peak demand of this profile will be taken as a reference for the power reserve in the wind turbine. It also shows that the peak demand continues from 2 to 6 pm, which means during that period, the PMSG based WECS will operate along a SOPPT curve so that there is a power reserve of the same amount. Therefore, in the worst-case scenario, if there is a sudden demand of the peak load, the WECS will be able to meet the generation demand gap through SMES.

4 Summary

The remote and rural areas can facilitate the deployment of renewable energy sources for power generation by providing the necessary geographical space. However, the most common challenge of renewable energy resources is their intermittent nature, which can reduce the overall system reliability. Also, the control of the RAPS system is complex, because, unlike large utility grids, RAPS systems are prone to network disturbances. The RAPS system needs to supply the demand on its own and cannot depend on the grid. Therefore, it is expected that each component of the RAPS system participates in supporting the network events. In this review, it is revealed that the improvement of dynamic performance, especially frequency regulation of the RAPS system is a major focus of many reported papers and several strategies have been proposed to improve its performance. Most of the effective techniques include external energy storage with a very high power density. A strategy has been discussed in this chapter to find the optimum reserved power for these storage devices. Also,

an efficient and advanced approach has been presented for automatic detection and characterization of voltage events in a RAPS network which would be beneficial to system planning and design.

References

1. M.R. Islam, M.F. Rahman, W. Xu (eds.), *Advances in Solar Photovoltaic Power Plants* (Springer-Verlag GmbH, Heidelberg, Germany, 2016)
2. M.R. Islam, N.K. Roy, S. Rahman (eds.) *Renewable Energy and the Environment* (Springer Nature, Singapore Pte Ltd., 2018)
3. M.R. Islam, S. Mekhilef, R. Saidur, Progress and recent trends of wind energy technology. Renew. Sustain. Energy Rev. **21**, 456–468 (2013)
4. IEA, Change in CO_2 emissions by fuel, *1990–2021*, IEA, Paris. https://www.iea.org/data-and-statistics/charts/change-in-co2-emissions-by-fuel-1990-2021
5. Y. Tan, L. Meegahapola, K.M. Muttaqi, A review of technical challenges in planning and operation of remote area power supply systems. Renew. Sustain. Energy Rev **38**, 876–889 (2014)
6. K. Presnell, Exporting Australia's remote area power supply industry. Renew. Energy **22**, 353–360 (2011)
7. T. Hirose, H. Matsuo, Standalone hybrid wind-solar power generation system applying dump power control without dump load. IEEE Trans. Industr. Electron. **59**, 988–997 (2012)
8. D.R. Thiam, Renewable decentralized in developing countries: Appraisal from microgrids project in Senegal. Renew. Energy **35**, 1615–1623 (2010)
9. E.S. Sreeraj, K. Chatterjee, S. Bandyopadhyay, Design of isolated renewable hybrid power systems. Sol. Energy **84**, 1124–1136 (2010)
10. A. Gupta, R.P. Saini, M.P. Sharma, Modelling of hybrid energy system—part iii: Case study with simulation results. Renew. Energy **36**, 474–481 (2011)
11. A.H. Mondal, M. Denich, Hybrid systems for decentralized power generation in Bangladesh. Energy Sustain. Dev. **14**, 48–55 (2010)
12. O.D. Mipoung, L.A.C. Lopes, P. Pillay, Frequency support from a fixed-pitch type-2 wind turbine in a diesel hybrid mini-grid. IEEE Trans. Sustain. Energy **5**, 1–9
13. G. Tzamalis, E.I. Zoulias, E. Stamatakis, E. Varkaraki, E. Lois, F. Zannikos, Techno-economic analysis of an autonomous power system integrating hydrogen technology as energy storage medium. Renew. Energy **36**, 118–124 (2011)
14. L. Ferrer-Martí, B. Domenech, A. García-Villoria, R. Pastor, A milp model to design hybrid wind–photovoltaic isolated rural electrification projects in developing countries. Eur. J. Oper. Res. **226**, 293–300 (2013)
15. S. Rolland, Switched on to mini grids. Renew. Energy Focus **12**, 10–12 (2011)
16. E.I. Zoulias, N. Lymberopoulos, *Hydrogen-Based Autonomous Power Systems: Techno-Economic Analysis of the Integration of Hydrogen in Autonomous Power* (Springer, London, 2008)
17. R. Lasseter, *White Paper on Integration of Distributed Energy Resources: The Certs Microgrid Concept* (2002)
18. Clean Energy Australia Report 2020. Available online: https://www.cleanenergycouncil.org.au/resources/resources-hub/clean-energy-australia-report
19. Kennedy energy park [Online] Available at: https://arena.gov.au/projects/kennedy-energy-park. Accessed on 05/10/21
20. Real time energy dashboard [Online] Available at: https://www.hydro.com.au/clean-energy/hybrid-energy-solutions/success-stories/king-island. Accessed on 05/06/19
21. Y. Tan, L. Meeghapola, K.M. Muttaqi, Suboptimal power-point-tracking based primary frequency response for DFIGs in hybrid RAPS. IEEE Trans. Ener. Conv. **31**, 93–105 (2016)

22. Rottnest WREN project [Online] Available at: https://arena.gov.au/projects/rottnest-island-water-and-renewable-energy-nexus-wren-project/. Accessed on 05/10/21
23. M.N. Musarrat, M.R. Islam, K.M. Muttaqi, D. Sutanto, Suboptimal power point tracking for frequency response of PMSG based wind turbines in remote area power supply systems, in *Proceedings of 2018 IEEE International Conference on Applied Superconductivity and Electromagnetic Devices (ASEMD)* (2018), pp. 1–2
24. M.R. Islam, M. Rakibuzzaman, M.H. Ali (eds.), *Emerging Power Converters for Renewable Energy and Electric Vehicles: Modelling, Design and Control* (CRC Press, Taylor and Francis Group, United Kingdom, 2021)
25. M.N. Musarrat, M.R. Islam, K.M. Muttaqi, D. Sutanto, Shunt active dc filter to reduce the dc-link ripple current caused by power converters to improve the lifetime of aluminum electrolytic capacitors. IEEE Trans. Ind. Appl. **57**, 4306–4315 (2021)
26. M.N. Musarrat, A. Fekih, M.R. Islam, An improved fault ride through scheme and control strategy for DFIG-based wind energy systems. IEEE Trans. Appl. Supercond. **31**, 1–6, Art no. 5401906 (2021)
27. J.A. Peas Lopes, C.L. Moreira, A.G. Madureira, Defining control strategies for microgrids islanded operation. IEEE Trans. Power Syst. **21**, 916–924 (2006)
28. R. Majumder, Some aspects of stability in microgrids. IEEE Trans. Power Syst. **28**, 3243–3252 (2013)
29. [Online] Available at: https://www.utas.edu.au/__data/assets/pdf_file/0008/778607/IPS-Connect-2015-Chris-Smith.pdf. Accessed on 05/10/21
30. R.H. Newnham, W.G.A. Baldsing, Advanced management strategies for remote-area power-supply systems. J. Power Sources **133**, 141–146 (2004)
31. J.M. Mauricio, A. Marano, A. Gomez-Exposito, J.L. Martinez-Ramos, Frequency regulation contribution through variable-speed wind energy conversion systems. IEEE Trans. Power Syst. **24**, 173–180 (2009)
32. O.D. Mipoung, L.A. Lopes, P. Pillay, Frequency support from a fixed-pitch type-2 wind turbine in a diesel hybrid mini-grid. IEEE Trans. Sustain. Energy **5**, 110–118 (2014)
33. G. Ramtharan, J.B. Ekanayake, N. Jenkins, Frequency support from doubly fed induction generator wind turbines. IET Renew. Power Gen **1**, 3–9 (2007)
34. N.R. Ullah, T. Thiringer, Karlsson, Temporary primary frequency control support by variable speed wind turbines: Potential and applications. IEEE Trans. Power Syst. **23**, 601–612 (2008)
35. Y. Tan, K.M. Muttaqi, Enhanced frequency response strategy for PMSG based wind energy conversion system using ultracapacitor in remote area power supply systems, in *Proceedings of the IEEE Industry Applications Society Annual Meeting 2013*, TX, USA (2015), pp. 1–8
36. M.N. Musarrat, M.R. Islam, K.M. Muttaqi, D. Sutanto, Enhanced frequency support from a PMSG-based wind energy conversion system integrated with a high temperature SMES in standalone power supply systems. IEEE Trans. Appl. Supercond. **29**, 1–6 (2019)
37. J. Lin, E. Keogh, S. Lonardi, B. Chiu, A symbolic representation of time series, with implications for streaming algorithms, in *Proceedings of the 8th ACM SIGMOD Workshop on Research Issues in Data Mining and Knowledge Discovery 2003*, San Diego, CA (2003), pp. 1–10

A Symbolic Aggregate Approximation-Based Data Mining Tool for the Detection and Classification of Power Grid Voltage Events

Md. Nafiz Musarrat, Md. Rabiul Islam, Kashem M. Muttaqi, Danny Sutanto, and Afef Fekih

Abstract Precise detection and classification of voltage events would require very detailed investigation from a very large pool of data. There exist several data mining and parametric analysis techniques to detect voltage events, however, they are computationally burdensome. In this chapter, a symbolic aggregate approximation (SAX)-based data mining tool is developed that can not only detect and classify voltage events accurately but also with considerably less computational effort. Instead of cycle-by-cycle analysis, a cluster-based analysis is proposed to classify the voltage events where the SAX algorithm is used for reducing the dimensionality of the raw time series. The proposed algorithm has been tested on a practical test network and results have been presented.

Keywords Voltage events · Symbolic aggregate approximation · Cluster · Voltage sag · Voltage swell

List of Symbols

V	Voltage

M. R. Islam · K. M. Muttaqi · D. Sutanto
School of Electrical, Computer and Telecommunications Engineering, University of Wollongong, Wollongong, NSW 2522, Australia
e-mail: mrislam@uow.edu.au

K. M. Muttaqi
e-mail: kashem@uow.edu.au

D. Sutanto
e-mail: soetanto@uow.edu.au

M. N. Musarrat (✉) · A. Fekih
The University of Louisiana at Lafayette, Lafayette, LA 70504, USA
e-mail: md-nafiz.musarrat1@louisiana.edu

A. Fekih
e-mail: afef.fekih@louisiana.edu

S. K. Das et al. (eds.), *Advances in Control Techniques for Smart Grid Applications*,
https://doi.org/10.1007/978-981-16-9856-9_5

V_α	α-component of three phase voltage
V_β	β-component of three phase voltage
A_{ma}	Major axis
A_{mi}	Minor axis
V''	Voltage during network event

List of Acronyms

DFT	Discrete Fourier transform
IEEE	Institute of Electrical and Electronic Engineers
PAA	Piecewise aggregate approximation
PAM	Partitioning around medoids
pu	Per unit
RMS	Root mean square
RVC	Rapid voltage changes
SAX	Symbolic aggregate approximation

1 Introduction

In the past, the power quality was ensured merely by establishing a continuous power supply. Now, the definition of power quality has become more sophisticated [1]. Several criteria need to be fulfilled to maintain the quality of supply power up to standard. Renewable energy sources have become very popular worldwide and have become mainstream sources of electricity [2–4]. With a large number of renewable energy sources network instability increases [5–7]. The voltage fluctuation is one of the major issues that need to be addressed. The evolvement of technology and the increased customer demand for improved service facilitated this need for fast detection of disturbance. According to IEEE, the voltage sag or swell would occur if the RMS voltage is less or more than 10% of the nominal value [8] for one-half cycle to one minute. The voltage sag or swell is not good for electric components. Often these electric components would trip if the voltage level falls below or rises above a certain limit. Therefore, the voltage sag or swell is often given equal importance as the short interruptions of the power supply. However, recently a new type of voltage event has been introduced which is named the rapid voltage (fluctuations or) changes (RVC). This is a fairly new idea. In the 3rd edition of IEC 61000-3-7, the definition and standard to detect the RVC were discussed [9]. According to this standard, if the RMS voltage at any instance falls below or rises above the nominal voltage and the deviation is more than the threshold but does not cross the sag or swell limit, then it will be categorized as an RVC event. RVC events are usually ignored, but they have a significant effect on flickers [10]. To mitigate the effect of flickering, the detection

and analysis of RVC have received much attention. An experiment conducted in [11] dictates that the flickering would be visible to more than 95% of the subjects if the RVC magnitude is equal to or below 4%. Therefore, in this chapter, a 4% deviation from the nominal voltage is taken as the threshold for the RVC detection.

To improve the power quality, it is needed to detect and analyze voltage events such as sag, swell, or RVC, and take initiative to mitigate these problems. The automatic analysis of voltage events has become a promising aspect [12]. Many techniques have been developed for the detection and analysis of different voltage events in distribution systems. Most of the available techniques to characterize voltage events are achieved by measuring the magnitude and the period [12–15]. These techniques require rigorous calculation and cause a heavy computational burden. Hence, the process becomes significantly slow. Therefore, it has become a necessity to develop a computational tool to detect and analyze voltage events without causing a heavy computational burden. It is also to be noted that, to detect a short duration (a cycle or two) voltage event, the data should be analyzed in the millisecond range and hence a huge database will be required. Analyzing the huge database through the conventional process is not efficient at all.

To overcome the huge computational burden, a new computational tool is developed in this chapter. The SAX algorithm is used in this chapter to reduce the dimensionality of the raw data. An elliptic parameter analysis is performed to classify voltage events. The rest of the chapter is structured as follows. In Sect. 2, a brief review of the present different algorithms and techniques is provided, and a comprehensive description of the proposed approach is given. In Sect. 3, the validity of the proposed approach is tested. Real power system data from the 230 V Swedish grid in Oslo is used in this chapter for analysis. The data is obtained from the data recording in PQube database available on PQube website [16]. Finally, Sect. 4 concludes the chapter.

2 Proposed Approach to Detect and Classify Voltage Events

As stated earlier, huge computations are usually required to observe and classify different voltage events precisely from a huge database. Usually, there is a huge number of data recorded every day through smart devices and meters placed at different points of the network. Modern meters can record data with a very high resolution. Although this feature can facilitate precise detection, it increases the computational burden. Analyzing the whole data series to classify the voltage events is not an efficient approach since only a specific number of time frames contain voltage events that occur only a few times a day. Some of the irregularities in voltage profiles are not significant and it is not worth analyzing every single piece of data. If the times and locations are identified for the most severe fluctuations, a more detailed analysis can be carried out later to investigate the cause.

To distinguish the time series of interest from a huge database that contains significant irregularities, the mining of data using pattern recognition tools is necessary.

However, performing those data mining algorithms on raw data series would cause an excessive computational burden. To reduce the computational stress, dimensionality reduction is necessary. There are several methods to reduce the dimensionality but in this chapter, the symbolic aggregate approximation (SAX) method is used. The SAX algorithm converts the raw time series into a symbolic string. The length of the string depends on the sampling window. The character strings are formulated in such a way that it preserves the basic features or characteristics of the original profile. After that, the clustering algorithm is performed on the strings. After identifying the clusters and time frames of interest, a more detailed analysis can be carried out to characterize them.

Characterizing voltage events from elliptic parameters has drawn much attention recently. However, analyzing the ellipses for every single cycle would require overwhelming resolution of data and it is not efficient at all for a long and high number of voltage profiles. Therefore, the elliptic analysis is proposed to be carried out only for the clusters of interest in this chapter. If an event is detected, the ellipse conversion is performed for a short-time frame around the events. Then those ellipses are classified into several clusters too as per their characteristics before parameter calculations to label those clusters for the specific type of voltage events.

2.1 SAX Algorithm

A brief review on the SAX algorithm [12] was provided in the chapter *Operation of Renewable Energy and Energy Storage-based Hybrid Remote-area Power Supply (RAPS) Systems: Challenges and State-of-the-arts.* Its application to efficiently find the anomaly among a set of time series due to computation in the reduced dimensionality [17, 18] can be utilized in detecting the events in the voltage profiles.

2.2 A Brief Review of Partitioning Around Medoids (PAM) Algorithm

The PAM algorithm groups n datasets into k clusters. This algorithm is used to minimize the dissimilarity between the representatives of each cluster and its members. The following equations representing the algorithm are used to solve this.

$$F(x) = \sum_{i=1}^{n} \sum_{k=1}^{n} d(i, j) z_{ij} \tag{1}$$

$$\sum_{i=1}^{n} z_{ij} = 1, \; j = 1, 2, 3, ...n \tag{2}$$

$$z_{ij} \leq y_i, \; j = 1, 2, 3, ...n \tag{3}$$

$$y_i, z_{ij} \in \{0, 1\}; i, j = 1, 2, .., n \tag{4}$$

where $F(x)$ is the main function that needs to be minimized. $d(i, j)$ is the matrix of estimated dissimilarities between i and j elements. z_{ij} is a variable to make sure that dissimilarities among the members of the same cluster are calculated in the main function [14]. Equation (2) dictates the assignment of one element to one cluster only. Also, Eq. (3) ensures the condition to be fulfilled so that the element is assigned to a medoid that corresponds to the cluster and the number of clusters is maintained at the predefined value. Equation (4) assigns the decision variable with just 0 or 1. The algorithm for PAM is shown in Fig. 1.

Fig. 1 PAM process

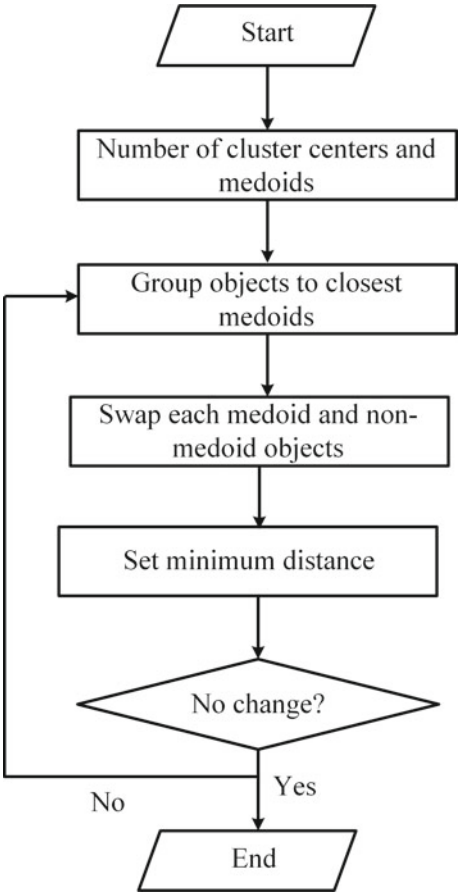

2.3 A Brief Review of Elliptic Parameter Analysis of Voltage Events

It is assumed that the phase difference between the three-phase voltages is 120°. Clarke's transformation maps the three-phase voltages into the alpha–beta domain. The matrix for evaluating Clarke's coefficients is shown in (5). The voltage components in the alpha–beta domain are obtained as given in (10)–(11) [18].

$$[c] = \sqrt{\frac{2}{3}} \begin{bmatrix} 1 & -\frac{1}{2} & -\frac{1}{2} \\ 0 & \sqrt{\frac{3}{2}} & -\sqrt{\frac{3}{2}} \\ \frac{\sqrt{2}}{2} & \frac{\sqrt{2}}{2} & \frac{\sqrt{2}}{2} \end{bmatrix} \tag{5}$$

$$V_{\alpha\beta 0} = C V_{abc} \tag{6}$$

$$V_{\alpha}(t) = \sqrt{\frac{2}{3}} \left(|V_a| - \frac{1}{2}|V_b| e^{-j\frac{2\pi}{3}} - \frac{1}{2}|V_c| e^{j\frac{2\pi}{3}} \right) \tag{7}$$

$$V_{\beta}(t) = \sqrt{\frac{2}{3}} \left(\frac{\sqrt{3}}{2} \left(|V_b| e^{-j\frac{2\pi}{3}} - |V_c| e^{j\frac{2\pi}{3}} \right) \right) \tag{8}$$

Figure 2 depicts the mapping of three-phase voltages into the alpha–beta domain under normal conditions. Note, the perfect unity circle in this case, which means that the major and minor axes are equal. However, for unsymmetrical voltage sag or swell, the three-phase voltages become ellipsoid in the alpha–beta domain. The eccentricity, inclination angle as well as major and minor axes depend on the severity of the sag or swell. The ellipses that correspond to the sag or downward RVC, will be inside the unit circle. On the contrary, the ellipses that correspond to the swell or upward RVC will be outside the unity circle [19]. In this chapter, the focus is on classifying the sag, swell, and RVC. Further classification of sag or swell is outside the scope of this chapter. Therefore, among all the elliptic parameters, only the major and minor axes are of interest. By analyzing the major and minor axis, different types of voltage events are identified.

The appropriate conditions for characterizing voltage events are as below. The following thresholds are determined from the formulas presented in the next section. However, the detailed graphical representation can be found in [20].

(a) Unsymmetrical voltage sag: $A_{mi}/A_{ma} < 0.933$, symmetrical voltage sag: $A_{mi} < 0.9$

(b) Unsymmetrical voltage swell: $A_{ma} > 1.06$, symmetrical voltage swell: $A_{ma} > 1.1$

(c) Unsymmetrical RVC events: $0.933 < A_{mi}/A_{ma} < 0.973$ (downward) or $1.026 < A_{ma} < 1.067$ (upward) Symmetrical RVC events: $0.9 < A_{mi} < 0.96$ (downward) or $1.04 < A_{ma} < 1.1$ (upward)

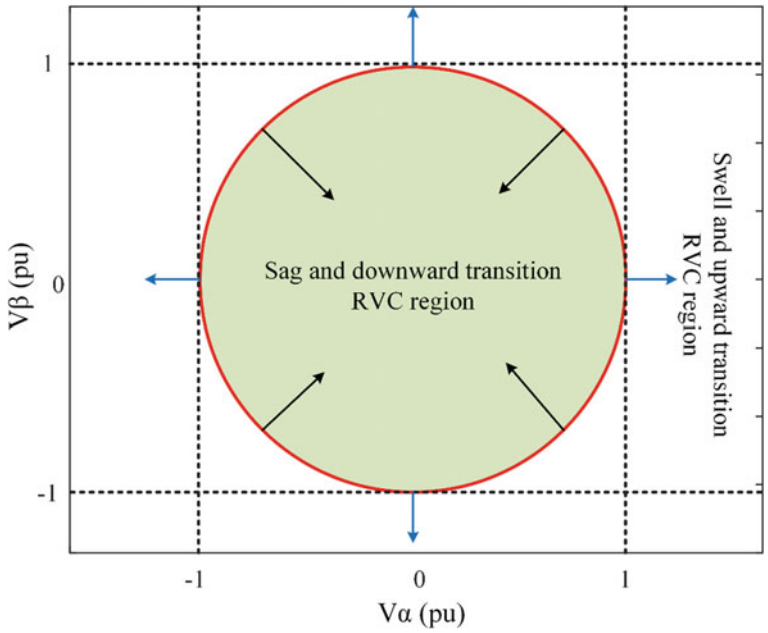

Fig. 2 Three-phase voltages mapped into the alpha–beta domain

2.4 Theoretical Approach for Calculating the Thresholds for Elliptic Parameters to Classify Voltage Events

The major and minor axes of the ellipses are obtained as given in (9)–(10).

$$A_{ma} = \left||V_\alpha| + |V_\beta|\right| \tag{9}$$

$$A_{mi} = \left||V_\alpha| - |V_\beta|\right| \tag{10}$$

The voltage magnitudes in normal conditions and during the event are denoted by V and V'', respectively.

As mentioned earlier, the sag, swell, RVC (downward), and RVC (upward) limits are taken as 0.9 pu, 1.1 pu, 0.96 pu, and 1.04 pu respectively.

The major and minor axis lengths during voltage events can be obtained by replacing $V\alpha$ and $V\beta$ in (9) and (10) from (7) and (8).

If the voltage event occurs in one phase, the thresholds of minor axis length and the length ratio of the minor axis to the major axis are calculated for different voltage limits from (11) and (12) [20, 21].

$$A_{ma} = V \tag{11}$$

$$A_{mi} = (2V'' + V)/3 \tag{12}$$

In this case, for any event, the major axis is unchanged. However, the minor axis length changes with the severity of voltage fluctuation.

If the voltage event occurs in two phases, the thresholds of major and minor axis length and their ratio are calculated for different voltage limits from (13) and (14) [20].

$$A_{mi} = V'' \tag{13}$$

$$A_{ma} = (2V + V'')/3 \tag{14}$$

In this case, major and minor axis length changes with different types of events.

If the event occurs in all three phases, the length of both major and minor axes will be V''.

Substituting the values of voltage limits for different voltage events in (11)–(14) yields the thresholds for major/minor axis length and their ratio. For example, putting the sag limit 0.9 in (12)–(14), the ratio of the major and minor axis length is found to be 0.933 for each case. This is considered as the threshold for detecting an unsymmetrical sag. Putting the downward RVC limit of 0.96, the threshold ratio of the minor axis to the major axis to detect the unsymmetrical downward RVC is found to be 0.973. In the same approach, thresholds can be evaluated for swell and upward RVC events.

2.5 Approximation of the Elliptic Parameters by Image Processing-Based Contour Fitting Approach

In [20], the DFT (discrete Fourier transformation) analysis is performed on the original voltage profiles to obtain the harmonics and extract the system frequency components by phasor analysis. However, performing Fourier analysis on that huge number of data set would require heavy computation. Therefore, an image processing-based approximation process is utilized in this chapter. In this process, the ellipse image is converted to a binary image. Then, a weighted average method is performed on the points of these binary images to estimate the centroids and the eccentricity. These data are used then to approximate a contour that would be the best fit for the given perimeter of the distorted ellipse or circle. This method is illustrated in Fig. 3 where an ellipse distorted with severe phase angle jump is shown. The heavily distorted shape of a normal ellipse makes it very complicated to measure the elliptic parameters. With the proposed contour fitting algorithm, the prospective ellipse is extracted (red marked) as shown in the figure. Now, the parameters can be approximated easily from this figure.

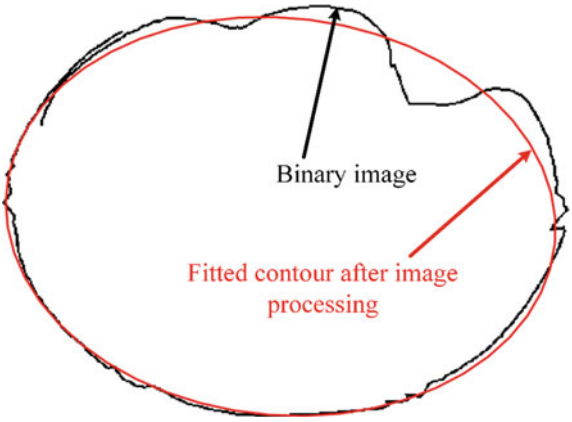

Fig. 3 Image processing-based contour fitting approach to approximate the elliptic parameters

2.6 Detection Algorithm of the Proposed Approach

The RMS voltage profiles are recorded for 24 h. Each of the time series will be then split into 24 1-h time series segments or sub-profiles. The dimensionality of these sub-profiles is reduced by SAX representation. After converting the time series into SAX strings, a PAM clustering algorithm is performed to classify them into 2 clusters: non-fluctuating and fluctuating sub-profiles. Most of the sub-profiles contain no fluctuations. The fluctuating profiles are of interest here.

In the previous step, the sub-profiles that contained fluctuations have been identified. Now, as explained in Sect. 2.2, the three-phase voltages of these profiles will be converted to an ellipse for each cycle. The orientation of all these ellipses will be converted to zero degrees. Hence, the clustering will be carried out solely based on their shape or perimeter; not their orientation. The elliptic parameters are approximated through a contour fitting approach discussed in Sect. 2.5. After that, these ellipses are again mapped into SAX strings and clustered into 5 groups: normal condition, sag, swell, and RVC (upward and downward) using the PAM algorithm. However, the ellipses that fit the criteria for normal conditions are automatically redacted from the record and not considered for further analysis. Figure 4 shows the complete process of the proposed approach.

An analysis of elliptic parameters is carried out to label each cluster. Using the Brute-force method, the ellipse with the lowest non-self-match distance in a specific cluster is determined. If the parameters of that ellipse satisfy the conditions of a voltage event, the whole cluster is labeled for that voltage event. The algorithm is shown in Fig. 5. This strategy effectively reduces the computational burden since parametric analysis is performed on only one ellipse for each cluster. Moreover, the SAX transformation reduces the dimensionality, notably.

The voltage sag/swell and RVC have a fine line to distinguish them from each other. Although these two different clusters (labeled as sag/swell and RVC) have sufficient distinctive features, the borderline ellipses should be checked if they are

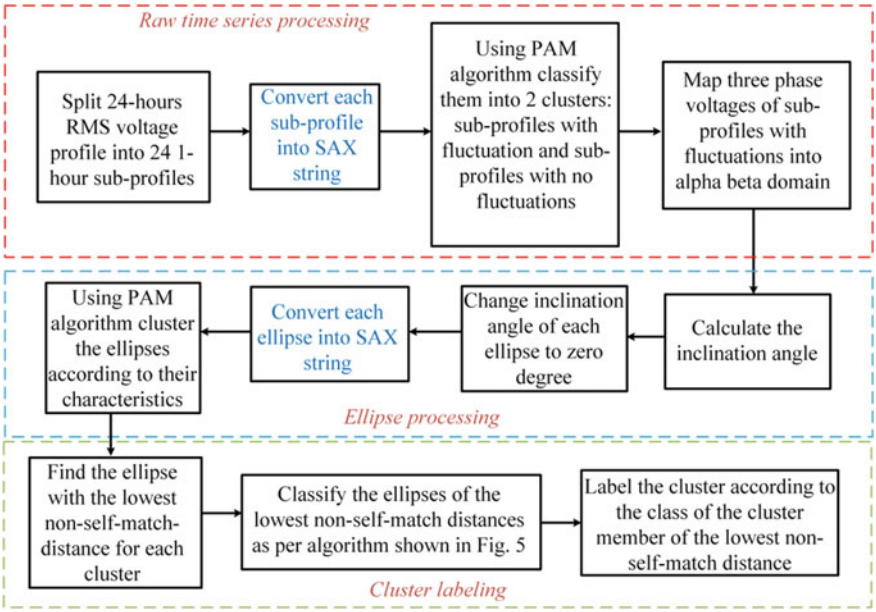

Fig. 4 Detection and classification algorithm of the proposed approach

in the right cluster. To achieve this, a Brute force method is performed between the downward RVC and sag clustered ellipses, and upward RVC and swell clustered ellipses. The lowest Euclidean distance between the members of two opposite clusters denotes which two ellipses are adjacent in borderline. Next, these two ellipses can be analyzed using the algorithm in Fig. 5 to check if they are in the right cluster.

3 Validation Test of the Proposed Approach

The validity of the proposed approach will be tested in this section. Real power system data is collected from the 230 V Swedish grid in Oslo. PQube meter provides the RMS data of every half cycle. For the validity test, the voltage data of a specific day (24 h) is taken.

The 24 h' data will be split into 24 sub-profiles in a 1-h interval. Figure 6 shows the RMS voltage profile for 24 h. The sudden spikes in the profile denote the voltage events. From the figure, the voltage events are observed between 3–4 h, 6–7 h, 16–17 h, 20–21 h, and 23–24 h timeframe.

Therefore, among 24 1-h sub-profiles, only 5 sub-profiles of the above-mentioned time frame should be separated for further analysis. The rest 19 sub-profiles should be deleted as they present normal conditions. This is carried out by converting the sub-profiles into SAX strings and performing a PAM clustering algorithm. For SAX

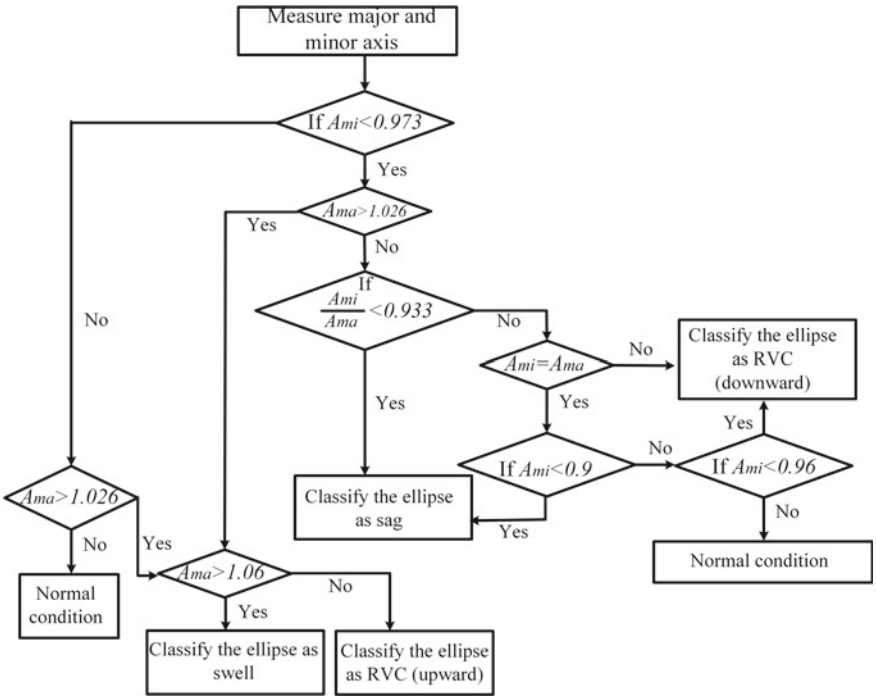

Fig. 5 Application of the proposed algorithm for event classification

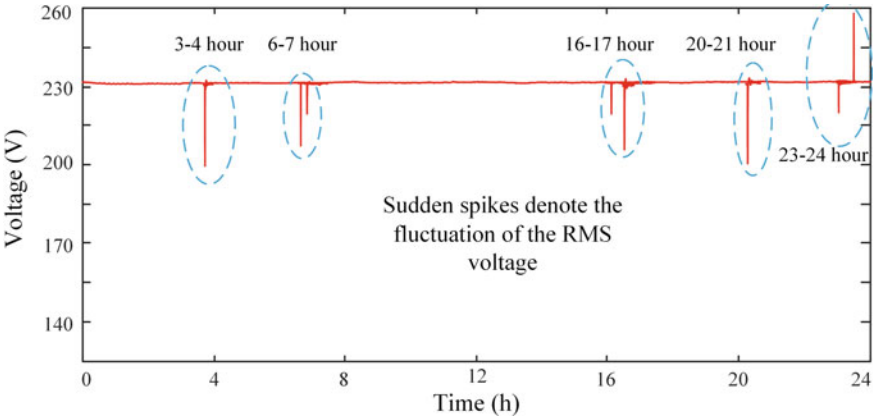

Fig. 6 RMS voltage profile of 24 h

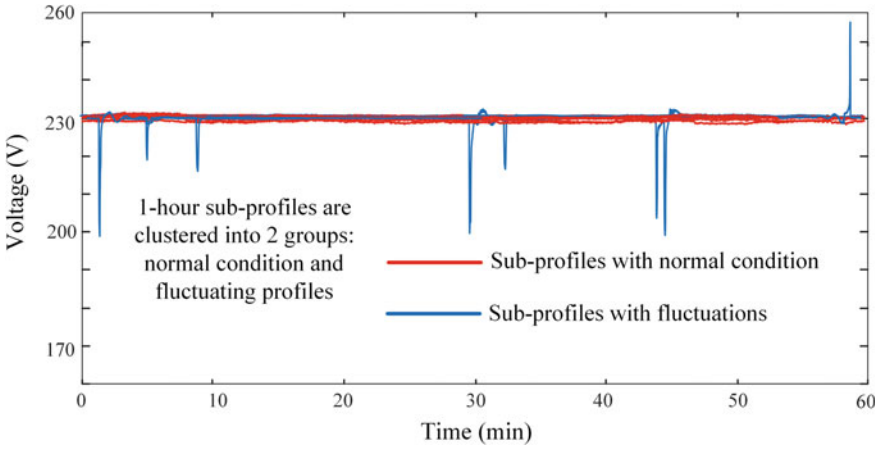

Fig. 7 1-h RMS voltage profiles grouped into 2 clusters

conversion, the alphabet size is taken as 5 and the word size is taken as 16. Figure 7 shows the clustered profiles. 19 of them are found to be normal conditions, whereas 5 of them contain voltage events.

The three-phase voltages corresponding to these 5 sub-profiles are mapped into the alpha–beta domain. Therefore, as explained earlier, the alpha–beta domain plot shows ellipses for each cycle. The inclination angle for each ellipse is changed to zero. The time series of these ellipses are clustered using the PAM algorithm again after converting the time series to SAX strings. To demonstrate and verify the proposed approach of ellipse processing (shown in Fig. 4) in detail, analysis is shown for events in 1-h voltage sub-profiles in a 20–24 h time frame. For SAX conversion, in this case, the alphabet size is taken 6 and the word size is taken 8. The proposed technique is implemented through MATLAB programming. The interface for MATLAB coding is shown in Fig. 8. A new script is needed to be opened in the "Editor" mode for writing the codes. Once the code is complete, clicking the "Run" button will compile the code and show outputs. If there is an error in the code, an error window will pop up detailing the type of error.

Figure 9 shows the MATLAB code for finding the PAA coefficients and breakpoints. The breakpoints are determined by the Gaussian distribution model. The number of breakpoints is dependent on the alphabet size.

Figure 10 shows the MATLAB code for the symbolic representation of the PAA coefficients. The symbols are assigned according to the breakpoints. The word size determines the number of symbols that will be used to represent the whole time series.

From Fig. 11, it is observed that there are 3 clusters. Cluster 1 and 2 are inside the unit circle and they correspond to voltage sag and downward RVC. Cluster (cluster 1, blue marked) with the smallest ellipses is supposed to correspond to the voltage sag events. The cluster which is between the unit circle and the sag cluster corresponds to

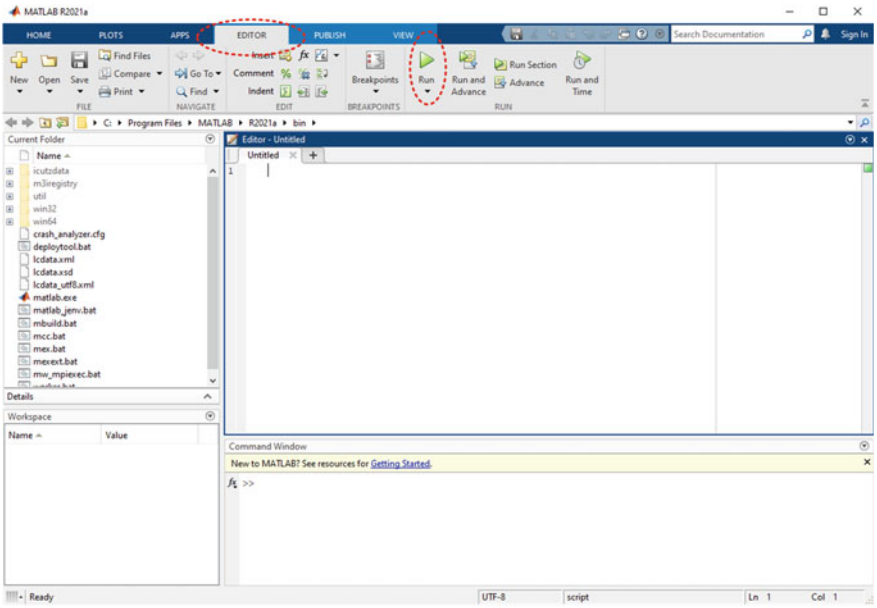

Fig. 8 MATLAB interface for coding

```
word_size=input('word size= ');
alphabet_size=input('alphabet size= ');
win_size=floor(length(data)/word_size);

data=(data-mean(data))/std(data);
plot(data);
hold on;

if (length(data)==word_size)
    PAA=data;
else
    PAA=mean(reshape(data,win_size,word_size));
end

PAA_plot = repmat(PAA', 1, win_size);
PAA_plot = reshape(PAA_plot', 1, length(data))';

plot(PAA_plot,'r');

string = zeros(1,length(PAA));

switch alphabet_size
        case 2, cut_points  = [-inf 0];
        case 3, cut_points  = [-inf -0.43 0.43];
        case 4, cut_points  = [-inf -0.67 0 0.67];
        case 5, cut_points  = [-inf -0.84 -0.25 0.25 0.84];
        case 6, cut_points  = [-inf -0.97 -0.43 0 0.43 0.97];
        case 7, cut_points  = [-inf -1.07 -0.57 -0.18 0.18 0.57 1.07];
        case 8, cut_points  = [-inf -1.15 -0.67 -0.32 0 0.32 0.67 1.15];
        case 9, cut_points  = [-inf -1.22 -0.76 -0.43 -0.14 0.14 0.43 0.76 1.22];
        case 10, cut_points = [-inf -1.28 -0.84 -0.52 -0.25 0. 0.25 0.52 0.84 1.28];
        case 11, cut_points = [-inf -1.34 -0.91 -0.6 -0.35 -0.11 0.11 0.35 0.6 0.91 1.34];
        case 12, cut_points = [-inf -1.38 -0.97 -0.67 -0.43 -0.21 0 0.21 0.43 0.67 0.97 1.38];
        case 13, cut_points = [-inf -1.43 -1.02 -0.74 -0.5 -0.29 -0.1 0.1 0.29 0.5 0.74 1.02 1.43];
        case 14, cut_points = [-inf -1.47 -1.07 -0.79 -0.57 -0.37 -0.18 0 0.18 0.37 0.57 0.79 1.07 1.47];
        case 15, cut_points = [-inf -1.5 -1.11 -0.84 -0.62 -0.43 -0.25 -0.08 0.08 0.25 0.43 0.62 0.84 1.11 1.5];
        case 16, cut_points = [-inf -1.53 -1.15 -0.89 -0.67 -0.49 -0.32 -0.16 0 0.16 0.32 0.49 0.67 0.89 1.15 1.53];
        case 17, cut_points = [-inf -1.56 -1.19 -0.93 -0.72 -0.54 -0.38 -0.22 -0.07 0.07 0.22 0.38 0.54 0.72 0.93 1.19 1.56];
```

Fig. 9 MATLAB code for finding PAA coefficients and breakpoints according to Gaussian distribution

```
symbols={'a', 'b', 'c', 'd', 'e', 'f', 'g', 'h', 'i', 'j','k','l','m','n','o','p','q','r','s'};

for i = 1 : length(PAA)
    string(i) = sum( (cut_points <= PAA(i)), 2 );
end


for i=1:length(PAA)
    sax_string(i)=symbols(string(i));
end

disp('SAX String: ')
disp(sax_string)


guidelines = repmat(cut_points', 1, length(data));
plot(guidelines');
hold on;


% get the x coordinates for the segments
for i = 1 : word_size
        x_start = (i-1) * win_size + 1;
        x_end   = x_start + win_size - 1;
        x_mid   = x_start + (x_end - x_start) / 2;

        % show symbols
        text(x_mid, PAA_plot(x_start), symbols{string(i)}, 'fontsize', 14);

end
```

Fig. 10 MATLAB code for symbolic representation of PAA coefficients which are assigned according to breakpoints

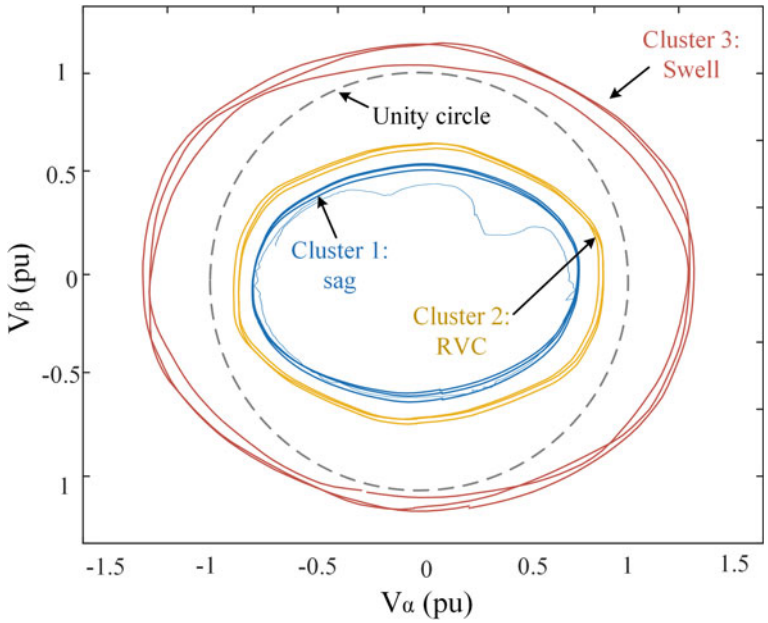

Fig. 11 Clustered ellipses corresponding to different voltage events

```
saxmat=cell2mat(sax_string);
k=3;
[idx]=kmedoids(saxmat,k);

for i=1:length(idx)
if (idx(i)==1)
    plot(df(i,:),'b')
    hold on;

elseif(idx(i)==2)
    plot(df(i,:),'g');
    hold on;
else
    plot(df(i,:),'r');
    hold on;
end
end

disp('cluster indices: ');
disp(idx);

indice=input('indice number: ');
num_ind=sum(idx(:)==indice);
anomaly=zeros(word_size,num_ind);

l=1;

for k=1:length(idx)
    if(idx(k)==indice)
        anomaly(:,l)=saxmat(k,:);
        l=l+1;
    end
end

anodist=dist(anomaly);
disp('non self match distances: ')
disp(anodist)
```

Fig. 12 MATLAB code for PAM clustering of SAX strings

the downward RVC (cluster 2, yellow marked). There is only one cluster outside the unit circle which should correspond to either RVC or the voltage swell (red marked).

Figure 12 shows the MATLAB code for PAM clustering. The SAX strings are clustered by assigning index numbers to SAX strings. SAX strings in a cluster have the same index numbers.

In this step, the non-self-match distances are calculated using the Brute-force method for each of the members of a cluster. As mentioned in Sect. 2.6 of the previous section, the ellipse with the lowest non-self-match distance in a cluster is identified. This ellipse is then analyzed with the algorithm shown in Fig. 3 to label the cluster for a specific voltage event.

Figure 13 shows the matrix of Euclidean distances among the ellipses of clusters 1 and 2. The top left box and the bottom right box in the matrix represent the non-self-match distances of the ellipses in cluster 1 and cluster 2 respectively. The rest of the area (shaded) represents the Euclidean distances of the ellipses in one cluster from the ellipses of another cluster.

Cluster 1: The matrix of the non-self-match distances for cluster 1 is shown in the top left box of Fig. 10. If the smallest value for each column is considered, it is observed from the matrix that column 2 of this sub-matrix has the lowest "minimum" value which is 2.23. Therefore, ellipse 2 has the highest non-self-match distance. Its parameters are analyzed. For ellipse 2, the minor axis length is 0.65, major axis length is 0.72. Therefore, their ratio is 0.902 which is below the threshold of 0.933 which makes it a sag event. Hence, it can be concluded that all other ellipses in that cluster present voltage sag events.

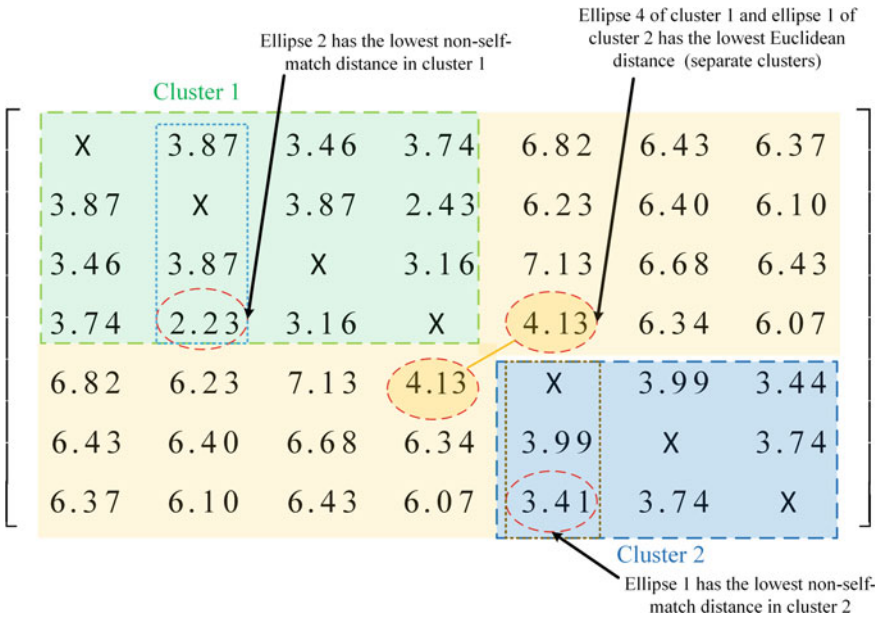

Fig. 13 Matrix of Euclidean distances among the ellipses of clusters 1 and 2

Cluster 2: Now for cluster 2, non-self-match distances are calculated which is shown in the bottom right box of Fig. 10 and it is observed that ellipse 1 has the lowest non-self-match distance. Therefore, its parameters are analyzed. For ellipse 1, the minor axis length is 0.75, major axis length is 0.79. Therefore, their ratio is 0.96 which is above the threshold of 0.933 but below the RVC limit of 0.95 which makes it an RVC event. Hence, it can be concluded that all other ellipses in that cluster present RVC events.

Cluster 3: There is only one cluster outside the unit circle. It corresponds to either upward RVC or voltage swell. Ellipse 2 is identified as the ellipse with the lowest non-self-match distance in the same process as used for clusters 1 and 2. For ellipse 2, the major and minor axis lengths are found to be 1.1 and 1.02, respectively. Since the length of the major axis is greater than the swell threshold of 1.067, this cluster presents a swell event.

As mentioned earlier in Sect. 2.6, the ellipses at the borderline of sag/swell and RVC clusters are separated by a fine line. From the shaded area of the matrix in Fig. 10, it is evident that ellipse 4 from cluster 1 and ellipse 1 from cluster 2 are adjacents since they have the lowest Euclidean distance. Ellipse 1 of cluster 2 has already been checked before. Now, ellipse 4 of cluster 1 needs to be checked. Ellipse 4: Minor axis length: 0.70, major axis length: 0.76. Therefore, their ratio is 0.92 which is below the threshold of 0.933 which confirms that it is a sag. Hence, it can be concluded that clustering has been done appropriately.

4 Summary

This chapter proposed a SAX-based computational tool that detects and characterizes different types of grid voltage events without causing a heavy computational burden. Dimensionality reduction of the time series by the SAX algorithm and cluster-based analysis for voltage event identification makes the process a lot faster. PAM algorithm has been used for clustering the same type of events. Since RVC and sag/swell sometimes show resemblance in the ellipse shape, a brute-force method-based strategy has been considered to ensure that they belong to the right cluster. Also, a contour fitting approach has been used to estimate the elliptic parameters. This technique has allowed the estimation of the parameters even if the ellipses have been severely distorted. The results presented in this chapter, show that the proposed SAX-based data mining technique can successfully detect voltage events from a huge database and correctly classify them.

References

1. M.H.J. Bollen, *Understanding Power Quality Problems—Voltage Sags and Interruptions* (IEEE Press, 1999)
2. M.R. Islam, Y. Guo, J. Zhu, A review of offshore wind turbine nacelle: Technical challenges, and research and developmental trends. Renew. Sustain. Energy Rev. **33**, 161–176 (2014)
3. M.R. Islam, P.C. Sarker, S.K. Ghosh, Prospect and advancement of solar irrigation in Bangladesh: A review. Renew. Sustain. Energy Rev. **77**, 406–422 (2017)
4. M.N. Musarrat, M.R. Islam, K.M. Muttaqi, D. Sutanto, Minimization of the thermal stress on the rotor side converter of DFIG while operating around synchronous speed, in *Proceedings of 2018 IEEE International Conference on Power Electronics, Drives and Energy Systems (PEDES)* (2018), pp. 1–6
5. M.N. Musarrat, M.R. Islam, K.M. Muttaqi, D. Sutanto, Enhanced frequency support from a PMSG-based wind energy conversion system integrated with a high temperature SMES in standalone power supply systems. IEEE Trans. Appl. Supercond. **29**, 1–6, Art no. 3800206 (2019)
6. V.T. Tran, M.R. Islam, D. Sutanto, K.M. Muttaqi, Mitigation of solar PV intermittency using ramp-rate control of energy buffer unit. IEEE Trans. Energy Convers. **34**, 435–445 (2019)
7. M.N. Musarrat, A. Fekih, M.R. Islam, FOSMC versus PI for the control of the grid side converter of a DFIG-based wind turbine, in *Proceedings of 2020 IEEE International Conference on Applied Superconductivity and Electromagnetic Devices (ASEMD)* (2020), pp. 1–2
8. M. McGranaghan, D. Mueller, M. Samotyj, Voltage sags in industrial systems. IEEE Trans. Ind. Appl. **29**, 397–403 (1993)
9. K. Brekke, H. Seljeseth, O. Mogstad, Rapid voltage changes —definition and minimum requirements. *Presented at International Conference and Exhibition on Electricity Distribution*, CIRED 2009, Prague, Czech Republic (2009)
10. J. Barros, J.J. Gutiérrez, M. de-Apráiz, P. Saiz, R.I. Diego, A. Lazkano, Rapid voltage changes in power system networks and their effect on flicker. IEEE Trans. Power Delivery **31**, 262–270 (2016)
11. J. Barros, M. de-Apráiz, R.I. Diego, J.J. Gutiérrez, P. Saiz, Azcarate, Minimum requirements for rapid voltage changes regulation based on their effect on flicker, in *Proceedings of the IEEE International Workshop on Applied Measurements for Power Systems (AMPS)*, Liverpool, UK (2017), pp. 1–5

12. Voltage Characteristics of the Electricity Supplied by Public Distribution Systems (1994) European/British Std. EN (EuroNorms) BS/EN 50160, CLC, BTTF 68-6
13. IEEE Recommended Practice for Monitoring Electrical Power Quality (1995), IEEE Std. 1159
14. International Electrotechnical Vocabulary (IEV) (1999), IEC Std. 60050
15. Electricity Supply—Quality Supply—Part 2: Minimum Standards (2002), South African Bureau of Std. NRS 048
16. [Online] Available at: http://map.pqube.com/sweden-orebro-pqube-3/html_event_page.htm. Accessed on 05/06/19
17. J. Lin, E. Keogh, S. Lonardi, B. Chiu, A symbolic representation of time series, with implications for streaming algorithm, in *Proceedings of the 8th ACM SIGMOD Workshop on Research Issues in Data Mining and Knowledge Discovery*, 2003, San Diego, CA (2003), pp. 1–10
18. J.E. Alam, K.M. Muttaqi, D. Sutanto, A SAX-based advanced computational tool for assessment of clustered rooftop solar PV impacts on LV and MV networks in smart grid. IEEE Trans. Smart Grid **4**, 577–585 (2013)
19. Data mining algorithms [Online] Available at: https://en.wikibooks.org/wiki/Data_Mining_Algorithms_In_R/Clustering/Partitioning_Around_Medoids_(PAM)
20. M.R. Alam, K.M. Muttaqi, A. Bouzerdoum, Characterizing voltage sags and swells using three-phase voltage ellipse parameters. IEEE Trans. Ind. App. **51**, 2780–2790 (2015)
21. J.R. Camarillo-Peñaranda, G. Ramos, Characterization of sags due to faults in radial systems using three-phase voltage ellipse parameters, in *Proceedings of the IEEE Industry Applications Society Annual Meeting*, Cincinnati, OH (2017), pp. 1–8

Identifying Hosting Capacity of Renewable DG Units in Smart Grids Considering Protection Systems

Hossam A. Abd el-Ghany, Essam M. Rashad, Ahmed M. Azmy, and Nagy I. Elkalashy

Abstract This chapter introduces a framework to define the optimal allocations and permissible hosting capacity of renewable distributed generations (DGs) using genetic algorithm (GA). The investigation is carried out considering inverter-based technologies such as the case of photovoltaic system. The inverter control is exploited to dynamically limit the DG contribution current during network faults. Accordingly, the DG penetration ratings can be significantly increased with avoiding their effects on the overcurrent protection coordination. To accomplish this task, a multi-objective function is established considering the overall maximum capacity of DGs, power loss reduction, voltage enhancement, and fault current limitation. In addition, the optimization process takes into account the protection coordination and voltage level as constraints. The constraints of coordination, including recloser-relay and fuse-recloser schemes, are inserted with the multi-objective function in an improved fitness function. The proposed framework is applied on an 11 kV overhead distribution feeder. Without replacement of the existing protection systems, the results confirm the large DGs integration possibility with significant loss reduction, improvement of voltage level, and fault current decrease. This is realized through the inverter control to limit DG contribution in fault currents.

Keyword Distributed generation · Fault current limitation · Optimization techniques · Protective devices coordination

H. A. Abd el-Ghany · E. M. Rashad (✉) · A. M. Azmy
Electrical Power and Machines Engineering Department, Faculty of Engineering, Tanta University, Tanta, Egypt
e-mail: emrashad@ieee.org

H. A. Abd el-Ghany
e-mail: hossam.saleh@f-eng.tanta.edu.eg

A. M. Azmy
e-mail: azmy@f-eng.tanta.edu.eg

N. I. Elkalashy
Electrical Engineering Department, Faculty of Engineering, Minoufiya University, Shebin Elkom 32511, Egypt
e-mail: nagy.elkalashy@sh-eng.menofia.edu.eg

S. K. Das et al. (eds.), *Advances in Control Techniques for Smart Grid Applications*,
https://doi.org/10.1007/978-981-16-9856-9_6

List of Symbols

C_2, C_3 and C_4	Scaling factors for maximization problem
DG_{C_i}	Capacity of the installed DGs (MW)
F_1, F_2, F_3, and F_4	Fault locations
(I_{fDG})	Fault currents from the DG (A)
(I_{fs})	Fault currents from the substation (A)
I_{rated}	IBDG rated current installed (A)
I_{SC}	Short circuit current (A)
K	Degree of limiting the fault current
K_m	Time multiplier
N_{DG}	Number of DGs
$\max\_\text{CM}_{\text{relay}_{\text{recl}}}$	Maximum coordination margins between recloser and relay (s)
$\min\_\text{CM}_{\text{fuse}_{\text{reclfast}}}$	Minimum coordination margin between recloser and fuse (s)
$\min\_\text{CM}_{\text{relay}_{\text{recl}}}$	Minimum coordination margins between recloser and relay (s)
P_{loss}	Active power losses (W)
Q_{loss}	Reactive power losses (VAR)
t_{fuse}	Fuse operating time (s)
$t_{\text{recl}_{\text{fast}}}$	Fast curve operating time of recloser (s)
$t_{\text{recl}_{\text{slow}}}$	Slow curve operating time of recloser (s)
t_{relay}	Relay operating time (s)
VDG-f	DG terminal voltage during fault (pu)
V_{j}	*j*th Bus voltage (pu)
V_{nom}	Nominal value of voltage (pu)
V_{max}	Maximum voltage limits (pu)
V_{min}	Ninimum voltage limits (pu)
W_1, W_2, W_3, W_4 and W_5	Positive constant weights
$\emptyset_{\text{CM}}$	Inequality constraints
$(\lvert\Delta \text{V}\rvert)$	Voltage deviations (pu

List of Acronyms

AC	Alternating Current,
ACSR	Aluminium Conductor Steel Reinforced,
CHP	Combined Heat and Power,
CM	Coordination Margin,
DC	Direct Current,
DG	Distributed Generation,
DS	Distribution System,

FC	Fuel cells,
FCL	Fault Current Limiter,
GA	Genetic Algorithm,
IBDG	Inverter-based distributed generations,
IEEE	The Institute of Electrical and Electronics Engineers,
LTC	Load tap changing transformers,
MFCL	Magnetic Fault Current Limiters,
MM	Minimum Melting,
MTG	Micro turbines generators,
MVA	Mega Volt Ampere,
MW	Mega Watt,
OPF	Optimal Power Flow,
PE	Power electronic,
PV	Photovoltaic,
RCGA	Real-Coded Genetic Algorithms,
RMS	Root Mean Square,
SFCL	Superconducting Fault Current Limiters,
SG	Synchronous generator,
SSFCL	Solid State Fault Current Limiter,
VAR	Volt Ampere Reactive,
WT	Wind turbines

1 Introduction

The connection and utilization of distributed generators in distribution systems (DS) have become a necessity all over the world. There are many economic, environmental and technical benefits of using DGs [1]. The higher efficiency and lower power losses are examples of economic aspects. In addition, the reduction of greenhouse gas emissions represents a main environmental benefit. Finally, DGs can support the network voltage and increase the reliability as technical advantages.

DGs can improve the voltage profile along the feeder due to the changes in direction and magnitude of real and reactive power flow [1, 2]. Also, the DGs interconnection will reduce the feeder losses since they supply local active and reactive powers according to their optimal locations within the network [3]. Regardless of these benefits, DGs have adverse influence on protection scheme, especially when they are used with high capacities. Generally, DGs cause variations in fault current level and direction causing false tripping due to the coordination mismatch [3–5]. Conventional distribution systems have radial structure with a single source, where the protection schemes depend on relay, reclosers, and fuses. For temporary faults, reclosers are used to protect the main feeders. In addition, the system is protected against permanent faults by connecting fuses in laterals and sub-laterals [2–6].

The current contribution of DGs may result in a miscoordination between recloser and fuse, which is commonly accomplished according to fuse-saving principles [4]. DGs also increase the short-circuit currents in distribution networks causing a possible trip to healthy lines. After DGs connection according to the smart grid concept, original protection system may still be valid when the power flow direction is maintained unchanged [4]. This could be accomplished based on hosting capacity strategy for the DG units.

The same problem is discussed in [5] including the impact on the fault current level, malfunctioning, and protection coordination. The use of directional recloser to solve these problems is assessed regarding various faults using real-time power system simulator [6]. According to IEEE standard 1457, DGs have to be disconnected under any abnormal conditions [7]. This is recommended since the classical protection system is not designed to clear DGs fault currents [7]. The DG optimal size has been determined based on optimal power flow (OPF) and regarding the coordination of recloser-fuse [8]. At each node of the distribution system, the DG maximum capacity has been determined by taking into account the coordination protection. At the first stage, a single DG in the distribution system has been considered. Then in the second stage, several DGs are considered at separated nodes [9]. However, the optimum DG capacities are not evaluated widely with the support of fault current limitation of DG contribution current.

Due to the rapid increase of DG penetration in DSs, the protection design and coordination exhibit more complication because of the mix between generation and load nodes. It is a must to consider several factors in this situation including number, size, location, and technology of the connected DGs. The reason is their effect on changing short circuit levels and protective devices coordination [10, 11]. Protective algorithms for radial DSs with multiple DGs are presented in [12, 13]. These algorithms consider the system topology by obtaining feedback about the circuit breakers status. Generally, the control system identifies the time–current curve (TCC) that should be adapted for a certain relay to guarantee suitable protection coordination of systems comprising DGs. Some algorithms depend on some calculations developed in Microsoft Excel, with TCC and operating cycle as inputs [12]. Other algorithms utilize the communication feasibility existing in modern relays [13]. Thus, adaptive protection algorithms can be effective for appropriate coordination and operations of inverse-time overcurrent relays (OCRs) even with load variations and/or insertion of DGs units. The execution of these algorithms requires microcontroller-based digital protection relays equipped with memory [14].

Fault current limiters (FCL) are commonly utilized to limit fault currents to acceptable levels. Regardless of their connection in series with power lines, they should provide low impedance and power losses under normal operation [15]. FCLs can also enhance system stability and fault-ride through capability and reduce the overall cost in the case of new installations [15]. The best location of FCLs in DSs comprising DGs is beside the DGs in order to effectively limit their effects on the protection coordination [2].

Recently, inverters are extensively utilized with renewable energy resources with continuous increase of their employment. The reasons of this trend are the price

drop of the photovoltaic modules manufacturing, better social acceptance of photovoltaic parks, and government support for renewable resources. Thus, grid-connected systems necessitate better understanding and development of photovoltaic inverters in both normal and abnormal conditions [15].

2 Motivation and Contribution

The previous discussion ensures the following facts:

- The integration of distributed generation (DG) in power systems is increasing dramatically every year
- The use of renewable energy-based DGs will be a must with increasing fuel costs of conventional power plants
- DGs can improve the power system reliability, since they are unlimited, and have less pollution effects
- Insertion of DGs in distribution systems has negative impacts on the existing protection scheme due to the miscoordination, where the contribution of DG fault current speeds up the downstream relay before the upstream relay.

The previous issues give special importance to deeply investigate the capacity limits of DG in DSs in order to maintain the traditional protection scheme. The impacts of DG penetration on overcurrent protection coordination including fuse-recloser and recloser-relay have also to be analyzed. These points represent the main motivations behind this research point.

In order to analyze the above framework, a typical 11 kV overhead distribution feeder is built in MATLAB/Simulink®. The simulation will be accomplished considering different types of distributed generators. The results will define DG capacity limits and location for different line faults without affecting the protection system coordination in the distribution system. The voltages profile, power losses, and total fault current, due to DG insertion in the DS, will be also studied.

3 Distributed Generation Technology

Distributed generation is defined as an electrical power source connected to a certain point in the power system, where this point is very close to consumer's location, while this source is small related to the centralized power plants [3, 16]. The most obvious effect of increasing generation from DG units is the reduction in the network loading [17, 18]. DG technologies may contain small/medium ratings, modular energy conversion units, that convert primary energy forms into electrical energy, and in certain cases, heat and cooling through combined heat and power (CHP) technology.

There are three basic types of distributed generation based on the machine type and the grid connection [19, 20]. Two types are conventional ones of DGs, which can be directly interconnected with the utility system. The first one uses induction generators, while the second is based on synchronous generators type. The inverter-based distributed generation (IBDG) is the third type.

Synchronous generators are used with most reciprocating engines and most high-power turbines (gas, steam, and hydro). They can be a source of both active and reactive power to the utility. Thus, these generators can provide sustainable fault current that affects the utility.

Induction generators are commonly used only with wind turbines and some low-head hydro applications [21]. They may be equipped with capacitors, or power electronic-based reactive compensators [22]. These generators can supply fault currents for only few cycles during three-phase faults on the utility side. Interconnection protection associated with induction generators typically requires only over/under voltage and frequency relaying.

Due to their continuous progress, the power electronic (PE) technologies are used extensively in converting most forms of electrical energy to desirable forms. One of the most important benefits of PE converters is their fast response, which is reflected on improving power quality. PE-based inverters are widely used in non-traditional, small dispersed generators, especially the micro turbines generators (MTG), fuel cells (FC), photovoltaic (PV), and fuel cell combined with an energy storage system like batteries. Conventionally, these devices are asynchronously connected to the power system using solid-state microprocessor-controlled devices. The output power can be regulated through digital control, which can also shut the unit down when the utility system is unavailable. Thus, these schemes can be used in high-reliability applications such as micro grids and may reduce fault currents of distributed generation that increases the hosting capacity of DG units [21–23].

The PE interface can provide protective functions with suitable flexibility for paralleling and disconnection according to the IEEE standard 1547 interconnection requirements [6]. However, it can be more sensitive depending on the situation and utility interconnection requirements.

4 Inverter-Based Distributed Generators (IBDG)

From protection point of view, DG connection schemes can be classified into two main types, namely rotating machine-based and inverter-based connection types. Regarding inverter-based DG, the generated voltage may be in a DC or an AC form depending on the nature of generating unit. In this case, the inverters are used with DG systems to convert their voltage into the nominal value at system frequency [24].

The use of a power electronic interface becomes mandatory between renewable energy source and power networks. Recently, there are two motivations for the rapid evolution of power electronic devices. The first one is the enhancement in power electronic capabilities regarding the speed and power capacity of these switches. On

the other hand, the implementation of advanced and complex control algorithms by real-time computer controllers is the second one. Therefore, the cost-effective and grid-friendly converters are greatly improved by these two expansions [25].

In the following section, a general overview about DG units will be discussed focusing on their potential impacts on the distribution networks. In addition, a summary of some aspects related to PV, wind turbine, fuel cells, and micro-turbine units as inverter-based DG sources is highlighted. The objective is to clarify some critical points about these technologies.

4.1 Wind Turbines

Wind farm is a group of wind turbines (WTs) that can be regarded as a single electricity source. Modern wind farms are installed either offshore or on land (onshore). The capacity and site of wind turbines is selected according to the load demand and the wind speed. The main power system problems associated with integrating wind energy into electric grid come from the lack of active and reactive powers control. The active and reactive powers control aims to keep the frequency and voltage stable within acceptable limits. Therefore, the voltage must be transferred to DC and back again to AC with the aid of inverters, due to the variable nature of wind speed. However, fixed-speed wind turbines are connected directly to the main grid system [26].

4.2 Photovoltaic Units

A photovoltaic system receives the sun light and converts its energy into electrical form. In this system, the construction of solar cells uses the semiconductor materials, which transform the collected photons' energy into electrical energy, when they are subjected to sunlight. The cells are arranged in an array that may be fixed or movable to track the sun to extract the maximum power [26].

Figure 1 shows the block diagram of the grid-connected PV generator. PV arrays are connected to main DC bus through a DC chopper of boost type. It is mandatory to use inverters to integrate between PV system and AC-grids. PV arrays consist of Nst parallel strings, while each string consists of certain number of series connected PV-modules. To extract the available power during different weather conditions, maximum power point tracking technique (perturb and observe) is used [27].

These systems are environmentally friendly without any kind of emissions. They are easy to be used with simple designs without the need for any other fuel sources. On the other hand, they need large spaces and their initial cost is relatively high. PV systems generate DC voltage, which is then transferred into AC form with the aid of inverters. Photovoltaic systems can be used with and without storage systems depending on the application.

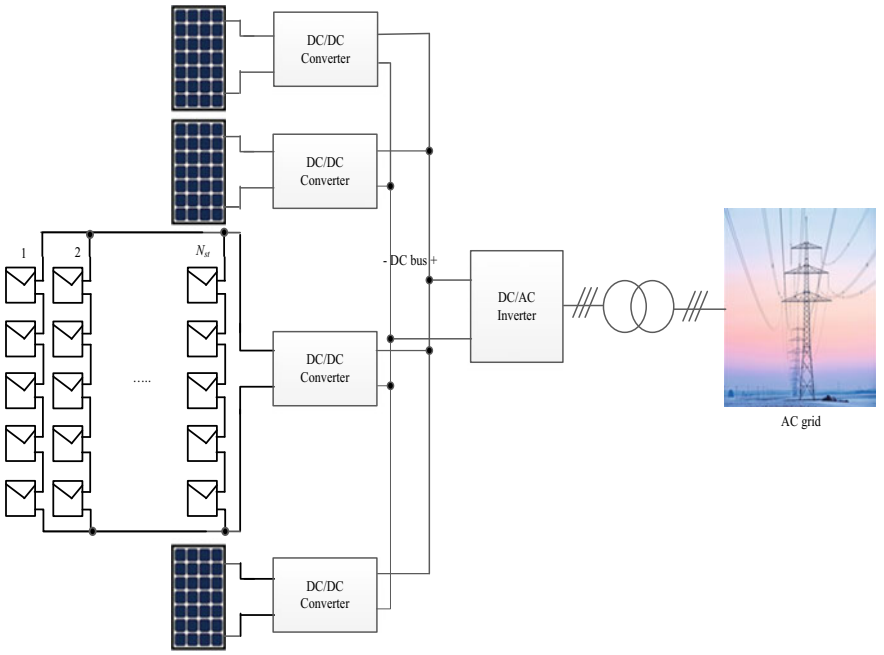

Fig. 1 Block diagram of the PV system assisted with one diode per each string [27]

4.3 Fuel Cells

Due to their modularity, high efficiency, environmental benefits, and power quality, the fuel cells have attracted high attention in several applications. The main principles of these systems are based on generating electricity using the electrotechnical process through converting oxygen (commonly from the air) and hydrogen (from a fuel source) into water. The oxygen is fed to the cathode and the hydrogen is directed to the anode. The electricity can be attained through the moving process of the charged particles toward each other (hydrogen and oxygen). Based on an inverter, the DC voltage generated from the fuel cells can be converted to obtain the AC voltage required for the load/grid sides. The function of electrolyte is to regulate the conduction process from the protons by providing low resistance to them and also force the electrons to be passed through the other electrode within the external circuit. The electrical power can be regulated by controlling the moving process of particles. A reformer is used in the fuel cell to get the hydrogen from hydrocarbon fuel such as methane, ethane, natural gas, and gasoline without any combustion, which ensures its cleanliness and efficiency. For the fuel cells with low temperatures, an external reformer is used. Conversely, for the cells with high temperatures, an internal reformer is used for a highly efficient operation [26]. Figure 2 explains the fuel cells principles of operation.

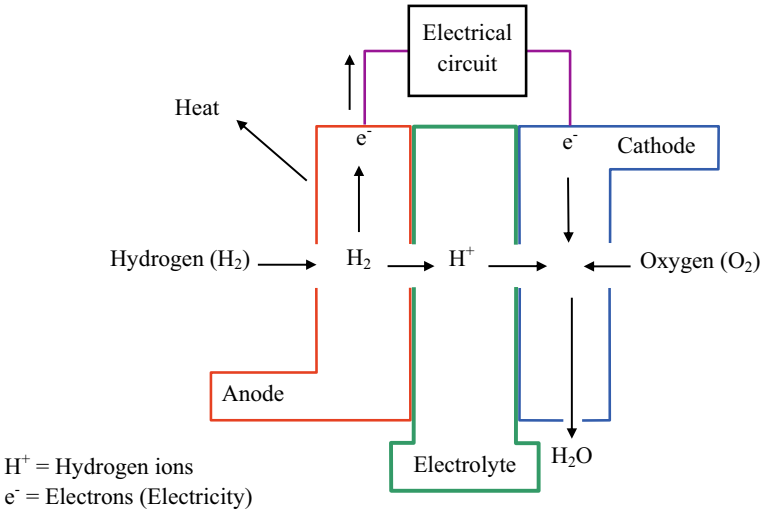

Fig. 2 Operation principles of fuel cells [24]

A main disadvantage of the fuel cell is that it also produces heat besides the electricity generation, which would increase the efficiency. However, the issue of electrolyte aging, and this impact on the lifetime and efficiency should be considered and studied [24].

4.4 Micro-turbines

The mechanism of a micro-turbine is to convert thermal energy into mechanical energy by using natural gas flow. The air is pumped by the compressor in the combustion chamber and is mixed with gas. When rotates, the turbine drives the generator and the compressor at the same time. In the most commonly-used designs, the compressor, turbine, and generator are connected to the same shaft as shown in Fig. 3. Due to the generator high speed, the obtained voltage has to be transferred to the DC form and then back to the AC form that can be provided for a suitable frequency and voltage.

The clean operation is the main merit of micro-turbines, and also the reduced size and high efficiency. The main drawback of micro-turbines is their high maintenance cost. In addition, selling the surplus energy and developing the dispatch and control methods for a large number of micro turbines have not been settled yet [24].

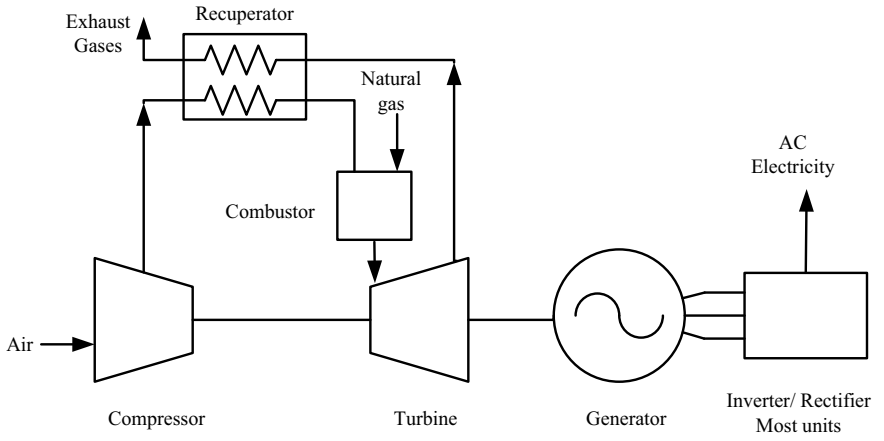

Fig. 3 Schematic diagram of a micro-turbine [24]

5 Distribution System Protection

The common distribution feeder's configuration has a radial form, where the loads are supplied from higher-voltage levels. The traditional distribution systems protection is an integration of simple overcurrent relays, reclosers, and fuses as protective devices [3, 28]. The objective of feeder protection structure is to guarantee the service continuity to the most of healthy users. This combination is used to clear temporary and permanent faults. The permanent fault along the main feeder is isolated by the main circuit breaker at the beginning of the feeder equipped with an (OC) relay. The time speed of OC relay is inversely proportional to the fault-current magnitude. The fuses are responsible for isolating permanent faults at laterals. The automatic recloser clears downstream temporary faults from its location.

6 Mitigating DG Impact for Increasing Hosting Capacity

Higher DG penetration levels increase the short circuit current (I_{SC}) in the distribution system [21, 29–31]. Regarding the coordination of protective devices, there are two ways to mitigate this increase. The first one is to modify the protective devices setting and/or characteristics. The second way is to use fault current limiters with the distributed generation in order to overcome its impact on the overcurrent protection without setting modification, protection replacement or using extra communication features.

6.1 Modified Recloser Characteristics

Based on proper coordination margin, the recloser has the priority for distribution system protection before fuse action. The high penetration of DGs into the recloser-fuse section badly affects the selectivity of the protection scheme between recloser and fuse. To overcome this problem, it is proposed to move the characteristic of the recloser slow curve to operate earlier the fuse melting.

6.2 Fault Current Limiters

Fault current limiter (FCL) devices are used to limit fault currents to an acceptable level. Although they are connected in series with power lines, they provide very small impedance and power losses under normal operation [32]. Normal operational losses, reliability, economics, and size should be considered when selecting these devices. FCLs can also improve the system stability and fault-ride through capability in addition to the reduction of cost in the case of new installations [33].

There are many types of FCLs with different strategies [34]. They can be classified into two main categories, i.e., passive and active, based on their ignition concept. According to the technology used to increase the series impedance, they are classified as superconducting fault current limiters (SFCL) [35], magnetic fault current limiters (MFCL) [36], and solid-state fault current limiters (SSFCL) [37]. Regarding their impedance seen by the fault current, these FCLs are generally classified as resistive and inductive types.

7 Fault Current Limiting Using Inverter Control

Since the current limiting scheme considered in this study depends on just controlling the DG inverter; the DG contribution fault current can be easily restricted without any additional hardware. Such a limiting concept can be categorized as another type of the passive FCLs. The objective of the limiting scheme is to reduce inverter output current during solid short circuits in the network area. This limitation can restrict the current value to the corresponding inverter rating power or to limit the current to certain values depending on the inverter terminal voltages. Lower voltage results in higher limiting currents and, thus, higher allowable DG size, i.e., higher hosting capacity. This can be achieved by developing a direct relation with the corresponding per unit terminal voltage.

To highlight the considered FCL technique, Fig. 4 depicts the inverter controller for limiting its contributing fault current [38]. The major variables that affect the current level are the direct and quadrature current components. If a voltage dip exists due to a fault situation, there would be a noticeable increase in the current level in

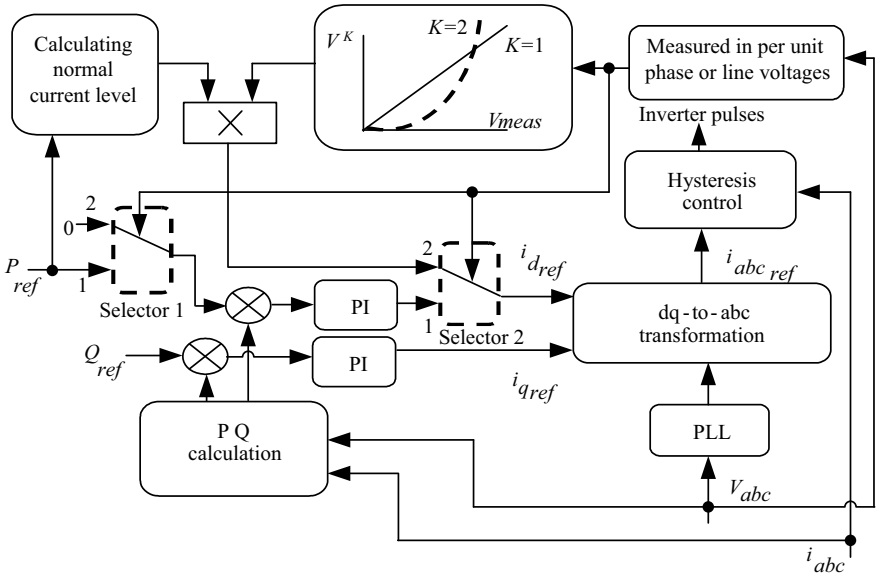

Fig. 4 Inverter control containing the fault current limitation scheme [38]

order to retrieve the value of the active power set point. This would be featured by a high value of the direct current component as control action consequences.

The basic idea behind the introduced methodology is to limit the direct current component during the fault. The limitation methodology is set such that the limited direct current component is proportional to the per unit voltage dip. This is accomplished with the aid of the selector in order to select the direct current either under normal control operation or under limiting control condition. As shown in the figure, there are two proposed selectors to choose between positions 1 and 2.

For the selector 2, position 1 represents the normal operation, where the inverter controls active and reactive power. On other hand, position 2 is selected during fault conditions and, accordingly, the modified control scheme is activated. The selectors change their positions based on the monitored voltage level. For example, if the voltage level is lower than 0.8 pu, indicating a fault condition, the selector is at position 2. The first selector, at the lift hand side in Fig. 4, is used to maintain the reference value of the active power at zero level during the fault. This is done to diminish the reference direct current component to provide a smooth voltage recovery after the fault clearance. In this case, the reference current will be low at the instant of recovery to provide a soft building up of the voltage waveforms after clearing the fault. This control concept is practically evaluated using laboratory setup addressed in [38]. In order to limit the fault current of IBDG, a factor k, representing the degree of limiting the fault current, is introduced and expressed by the following equation,

$$I_{fDG,i} = V_i^k \cdot I_{\text{rated},i} \tag{1}$$

where $I_{\text{rated},i}$ is the IBDG rated current installed at bus i, $I_{fDG,i}$ is the IBDG fault current contribution, V is the pu voltage, and $k = 0, 1, 2 \ldots$ etc. $k = 0$, refers to limiting the fault current to the rated current of IBDG, while $k = 1$ refers to limiting the fault current in proportional to the per unit voltage at IBDG bus multiplied by the rated current of IBDG. This proportional factor is depicted in the up middle box in Fig. 4 by a solid curve. For DG higher rating, this factor is suggested to be $k = 2$ that is proportional to the square of the measured per unit voltage as depicted by a dashed curve. Such a concept of limiting proportionality as a function of terminal per unit voltage will be evaluated later.

8 Technical Impacts of DG

The radial distribution system is characterized by the one-way energy flow nature. This leads to higher voltage regulation. At substations, the insertion of load tap changing transformers (LTC), line regulators into distribution feeders, and/or shunt capacitors into feeders or along the line regulates the system voltage [2]. The connection of DGs may lead to changing the direction and magnitude of real and reactive power flows. This affects the voltage profile along this feeder. At the customer's location, per unit voltage may exceed the primary-side voltage of the distribution transformer.

The DGs connection may reduce the power losses of the feeder since the DG provides active and reactive powers. The reduction of losses requires the determination of an appropriate DGs location in the system [9, 39].

9 Problem Formulation

Multi-objective optimization problems have a set of different optimal solutions. On the other hand, single-objective problems have a single optimal solution. The optimal solutions have to be utilized to avoid all terms of the multi-objective problems, which are instantaneously considered from the point of view of the decision-making. The decision-makers have resilience to compromise among these terms according to the system requirements and situation. The main objective of this problem is defining the hosting capacity of IBDGs according to the coordination margin of existing protective devices. In addition, the problem combines terms of various nature, such as maximizing voltage improvement, minimizing power losses, and minimizing fault current levels. In the following subsections, the terms of the multi-objective function and the main constraints will be addressed.

9.1 Terms of the Multi-objective Function

Mathematically, the proposed optimization problem can be described using four-term objective functions with three constraints. The four parts are the IBDG unit's hosting capacity (F_1), the voltage regulation (F_2), the total fault current level (F_3) for the distribution system, and the power loss (F_4).

The main goal of this chapter is to maximize the hosting capacity and number of DGs. To achieve this goal, the following function F_1 is defined:

$$F_1 = \sum_{i=1}^{N_{\mathrm{DG}}} \mathrm{DG}_{C_i} \tag{2}$$

where, DG_{C_i} is the capacity of the ith installed DG in MW and N_{DG} is the number of DGs.

The second goal of siting and capacity DGs is to improve the voltage level (F_2). It is required to reduce the voltage deviations ($|\Delta V|$) from the nominal value (V_{nom}). The value of the voltage deviations $|\Delta V|$ can be defined as:

$$F_2 = |\Delta V| = \sum_{j=1}^{\mathrm{N}} \frac{\left|V_{\mathrm{nom}} - V_j\right|}{V_{\mathrm{nom}}} \tag{3}$$

where, V_j is the jth bus voltage and N is the number of buses.

Fault current levels of the grid increase based on the DGs capacities and their location. The equivalent impedance, from the fault point of view, is decreased since the impedance of DG is represented in parallel with the impedance to the grid at its insertion point. Regarding the network fault current level, it increases due to DGs insertion. The related term is the summation of the fault currents from substation (I_{fs}) and the DG ($I_{f\mathrm{DG}}$) as follows:

$$F_3 = I_f = \sum_{i=1}^{N_{\mathrm{DG}}} \left(I_{f\mathrm{DG}}\right) + I_{fs} \tag{4}$$

On the contrary, the power losses may be reduced by decreasing lines power flow. This is achieved by locating the DG units optimally nearby load centers. The losses also can be decreased by reducing the reactive power flow. This is accomplished by controlling the generation and absorbed reactive power throughout the network. In addition, the voltage profile can be improved too. For the power loss term, F_4, the active power losses between ith and jth buses are defined as:

$$P_{\mathrm{loss}_{i-j}} + j\,Q_{\mathrm{loss}_{i-j}} = S_{i-j} + S_{j-i} \tag{5}$$

$$F_4 = \sum_{j=0}^{N} \sum_{i=1}^{N} \left(P_{\text{loss}_{i-j}}\right) \tag{6}$$

Then, the general multi-objective function can be given based on the four terms as follows:

$$\max(F) = \max(W_1 \cdot F_1 - W_2 \cdot (C_2 \cdot F_2) - W_3 \cdot (C_3 \cdot F_3) - W_4 \cdot (C_3 \cdot F_4)) \tag{7}$$

where W_1, W_2, … are weights of positive constants for maximization problem. C_2, C_3, and C_4 are scaling factors. These factors are assigned in terms of the objective function in order to obtain the same effect on fitness function [26]. The first part has to be maximized, while the other three parts have to be minimized.

To achieve the DGs capacity limits and location in radial systems, the multi-objective function (F) becomes:

$$\begin{aligned} F = {} & W_1 \sum_{i=1}^{N_{\text{DG}}} \text{DG}_{C_i} - W_2 \left(C_2 \cdot \sum_{i=1}^{N} \frac{|V_{\text{nom}} - V_i|}{V_{\text{nom}}} \right) \\ & - W_3 \left(C_3 . \left(\sum_{i=1}^{N_{\text{DG}}} \left(I_{f\text{DG}} \right) + I_{fs} \right) \right) - W_4 \left(C_4 \cdot \sum_{j=0}^{N} \sum_{i=1}^{N} \left(P_{\text{loss}_{i-j}} \right) \right) \end{aligned} \tag{8}$$

9.2 System Constraints

The first constraint is the Fuse-Recloser coordination margin given as:

$$t_{\text{fuse}} - t_{\text{recl}_{\text{fast}}} \geq \min \_\text{CM}_{\text{fuse}_{\text{reclfast}}} \tag{9}$$

where t_{fuse} is the operating time of fuse in seconds, $t_{\text{recl}_{\text{fast}}}$ is the recloser fast curve operating time, $\min \_\text{CM}_{\text{fuse}_{\text{reclfast}}}$ is the minimum margin between recloser and fuse. The second constraint is Relay-Recloser coordination that is given as:

$$\max \_\text{CM}_{\text{relay}_{\text{recl}}} \geq t_{\text{relay}} - t_{\text{recl}_{\text{slow}}} \geq \min \_\text{CM}_{\text{relay}_{\text{recl}}} \tag{10}$$

where t_{relay} is the relay operating time, $t_{\text{recl}_{\text{slow}}}$ is the slow curve operating time of recloser; $\min \_\text{CM}_{\text{relay}_{\text{recl}}}$ and $\max \_\text{CM}_{\text{relay}_{\text{recl}}}$ are minimum and maximum margins between recloser and relay. The third constraint is related to voltage limits. The voltages at buses depend on voltage regulation limits and should be within specified limits as [40]:

$$V_{\min} \leq V_i \leq V_{\max} \tag{11}$$

where, $V_{\min}$ and $V_{\max}$ are the minimum and maximum voltage limits, respectively. The allowable voltages are within 0.95–1.05 pu limits [41].

10 Solution of the Optimization Problem Using GA and Proposed Framework

The genetic algorithm (GA) is a numerical optimization algorithm that is inspired by both natural genetics and natural selection with the parallel searching method. For directing the population toward convergence to the global optimum solution, Real-Coded Genetic Algorithms (RCGA) are preferred [40]. The "initialization", "selection", "crossover and mutation", and "evaluation" processes are the main procedures in this algorithm.

Multi-population RCGA [18] leads the population to the global optimum solution. Moreover, the multi-population construction enhances the obtained results quality, which is employed in this chapter. Rendering this framework, the individuals migrate every population between subpopulations to interchange information among them. Other techniques as Particle Swarm Optimization (PSO) could be characterized by simple construction. The convergence of PSO speed is faster and, in addition, it needs less parameters identification. However, these techniques could easily fall into local-optimal solutions in the first iterations unlike GA. In general, GA is preferred compared to other techniques for highly constrained formulations such as the adopted problem.

In terms of a multi-objective function, the optimization problem can be formulated considering fault current limits, DGs penetration limits, voltage regulation, and power losses. Moreover, the inequality constraints ($\emptyset_{\mathrm{CM}}$) are considered with the coordination margin of protective devices. The formulation and declaration of the coordination margin for the recloser-relay and the constraints representing fuse-recloser are discussed in [42]. The fitness function can be formulated as:

$$\text{fitness} = F - W_5 \emptyset_{\mathrm{CM}}(x) \tag{12}$$

When the violation to protection constraint happens, the value W_5 takes a non-zero. For excluding a certain term from the objective function, the corresponding weight factor, i.e., W_2, W_3, and/or W_4, is set to zero, except the first term.

Attaining the final solution of the genetic model and creating new individuals are the main jobs of genetic operators. The framework is outlined as follows. For the population of chromosomes, the random initialization is the first stage. After that, the evaluation of fitness for all individuals (chromosomes) is performed in the population. Using an individual GA search, the selection is done with the conjecture of natural selection and genetics. The genitors are chosen as the chromosomes for

reproduction. Finally, by modifying and combining the genetic code of the operators (crossover and mutation), they could manipulate the selected individuals. For one generation, this cycle is defined and repeated until reaching the stop criterion. Figure 5 illustrates the outlines of the proposed framework. The genetic operators generate new individuals and provide the final solution of the genetic model.

The steps of the random initialization are presented as:

- Reading system data.
- Performing load flow, short circuit, and protection settings.
- Setting coordination margins among protective devices.
- Inserting DG and initializing chromosome population randomly.

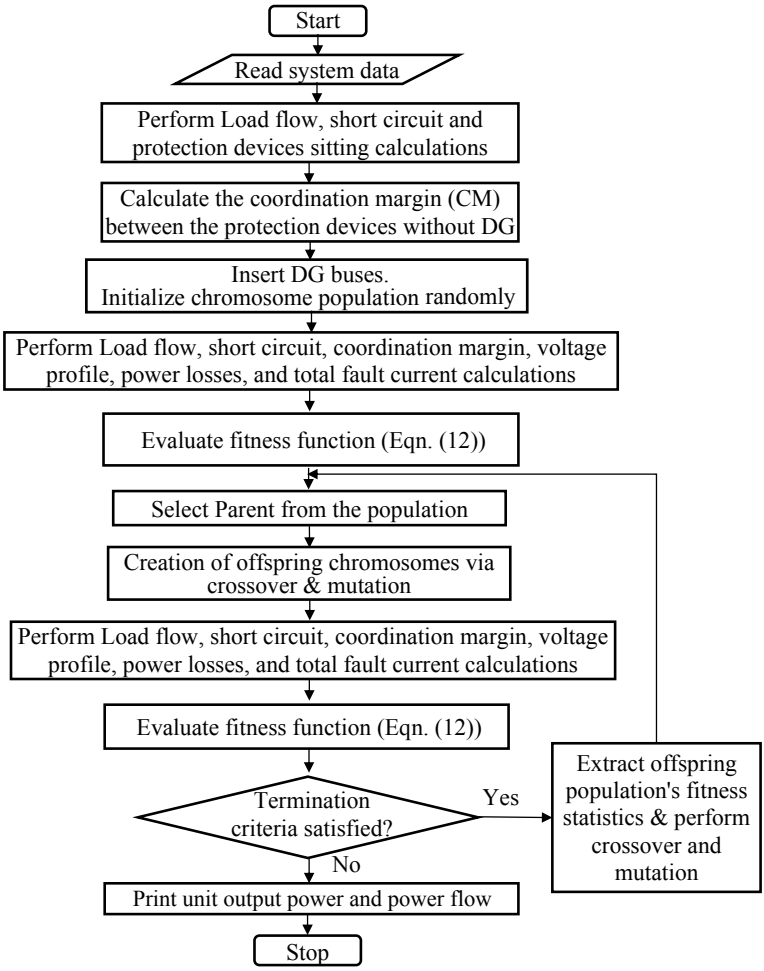

Fig. 5 Flowchart of GA evaluation process for the proposed framework

The steps of population evaluation are performed as follows:

- Performing load flow to calculate the voltage values, power losses, and voltage levels during fault.
- Performing short circuit calculations to obtain the coordination margin and total fault current.
- Calculating the coordination margin (CM) between the protection devices considering the DG penetration.
- Evaluating fitness function as given by (12).

Generally, for calculating the power losses, voltage values, and pre-fault voltage, the optimal power flow is developed for each individual. This step depends on updating the system data when inserting the DG units through cables and transformers.

11 Investigated Overhead Distribution System

Nediba feeder is selected as the case study, which represents a typical Egyptian overhead distribution system supplied from a substation 66/11 kV (Khairy). The adopted system one-line diagram is given in Fig. 6 containing one underground cable, 45 overhead sections, and 47 buses. The MATLAB® code is the simulation tool used for the adopted distribution system. A current of about 196 A is supplied through the feeder. A 16 km-Aluminum Conductor Steel Reinforced (ACSR 70/12) is presented as the overhead transmission line. With an impedance of 10%A, a delta/star transformer 25 MVA, 66/11 kV is used. A recloser and a fuse are put at 10.65 and 13.5 km, respectively. A detailed description of the system is given in [28].

In the main feeder and at arbitrary locations, a DG is connected with a transformer having a similar rating. The delta/star earthed 11/0.4 kV transformer is used, where the zero-sequence loop is opened using the delta winding on the utility side at transformer point in the distribution feeder during earth faults (phase to earth fault type). For a three-phase fault, the investigation is carried out due to the highest fault current.

For all fault places such as in the fuse section, the recloser has to be coordinated with the fuse on the main line, where the recloser and fuse currents are closed to each other. The corresponding time of operation for the recloser and fuse fault currents is illustrated in Fig. 7 [28]. On the fuse section and for the whole range of fault currents, both devices must be coordinated. Considering the characteristics of recloser curves, the coordination procedure can be obtained. For a fast recloser curve and aided with the characteristics given in [42], the current setting is selected as 140 A and the time multiplier (K_m) is set as 0.05.

For the slow recloser curve, the current setting is selected as 250 A and the time multiplier (K_m) is set as 0.15. For the whole range of fault currents in the fuse section, with the 100 A fuse characteristics (defined in [42]), the recloser setting is selected to get the coordination. In a similar manner, the setting current of the feeder relay curve

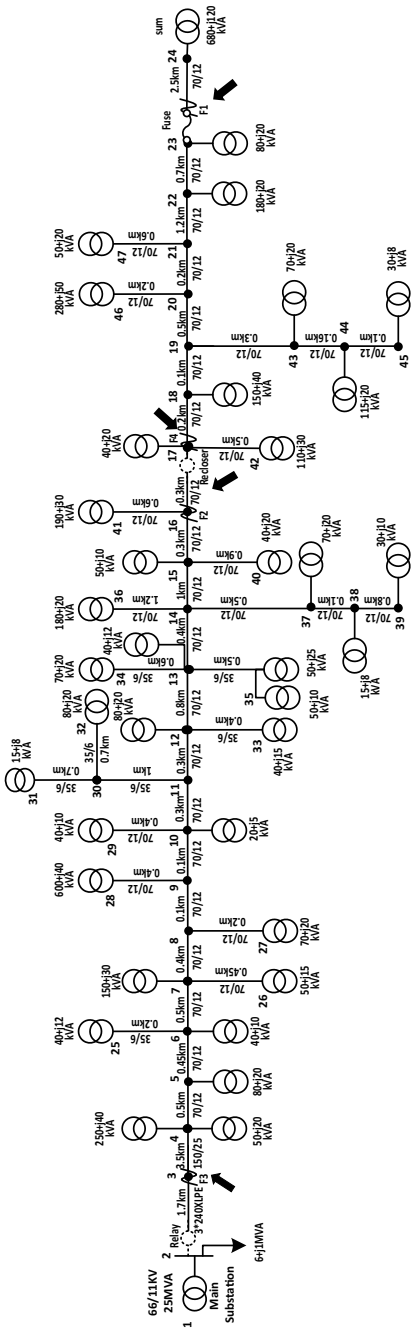

Fig. 6 Single line diagram of Egyptian Nediba distribution system with its protection scheme (47 bus system) [28]

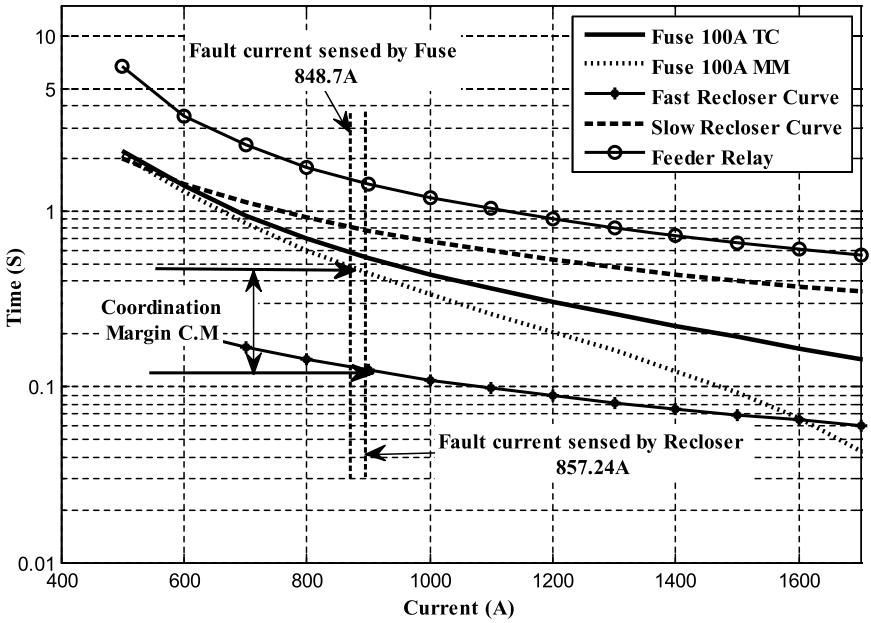

Fig. 7 Relay, recloser, and fuse characteristics [28]

is chosen as 390 A and the time multiplier (K_m) is set as 0.14. To get the coordination with the slow curve characteristics of the recloser, the relay setting is chosen. Due to the time difference allowed between the minimum melting (MM) of the fuse and the recloser fast curve, the minimum margin between fuse and recloser is obtained as 0.2 s. Without causing any effect for the protection coordination, the rating limits of DGs penetration should be studied.

12 Performance Analysis and Discussion

The siting and sizing problem of the DG units is solved using meta-heuristic optimization techniques. The GA is used to solve this problem regarding the following three cases. The first case is when the DG is located in recloser-fuse region, while it is located in feeder-relay-recloser region in the second case. In the third case, the DGs are located along the feeder. These cases are studied to evaluate the effect of DGs on the recloser-fuse coordination and feeder relay-recloser coordination. The fault locations (F_1 and F_4), shown in Fig. 6, refer to these cases.

Different weight values are assigned to objective function terms in order to obtain the same effect on fitness function. From experience, the proposed weight values are set as: summation of maximum limits of DGs ratings: $W_1 = 0.25$, voltage values:

$W_2 = 0.25$, total system fault current: $W_3 = 0.25$, power losses: $W_4 = 0.25$, and coordination margin constraint between protective devices: $W_5 = 1000$.

12.1 Case 1: DGs Located in Recloser-Fuse Region

As can be expected, the fuse operating time is reduced when the DGs capacity increases for faults at F_1. Conversely, the DGs capacity has almost no effect on the recloser operating time since the fault is simulated at the terminals of DGs. Generally, the network fault current is reduced with the higher terminal voltage of recloser. The coordination between recloser and feeder-relay is preserved for a wide range of DG capacities since their operating times are decreased at the same time. On the other hand, there will be no difference regarding the recloser and feeder-relay since they will have the same fault currents because DG is located at fuse terminals only.

Figure 8 shows the maximum hosting capacity of a single synchronous generator (SG) and IBDG based on FCL at different locations in recloser-fuse region with a fault at F_1. In case of SG, the maximum capacity of DG that can be installed in the recloser-fuse zone is 0.1483 MW at bus 23 alone. Alternatively, the maximum hosting capacity of DG unit at bus 17 alone is 0.4618 MW. This capacity satisfies the coordination between the recloser and fuse for conventional protection scheme.

Figure 9 shows the maximum limits of a single IBDG unit at different locations with a fault at worst condition, which is F_1 for a factor k equals to 0 and downstream fault for k equal to 1. The worst fault condition for $k > 0$ is that the fault occurs far from the DG location at the downstream direction. Since the line impedance produces

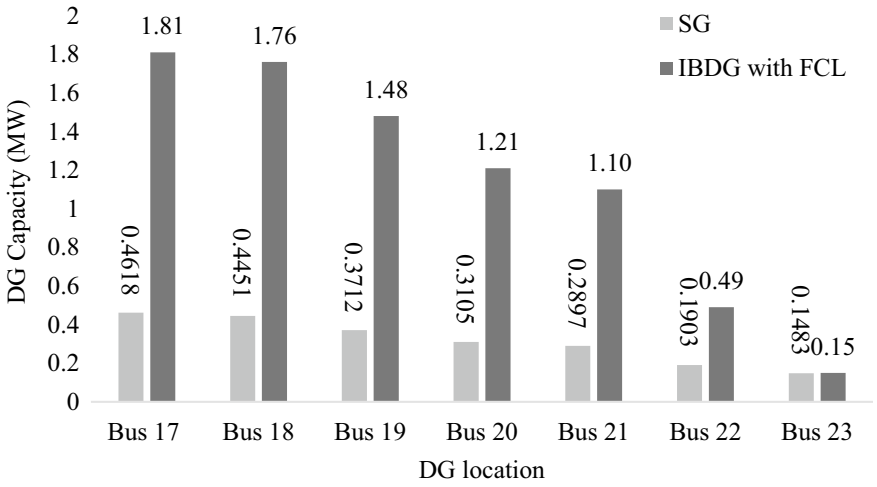

Fig. 8 Max limits of a single DG at different location with a fault at F_1 for synchronous generator (SG) and IBDG associated with FCL ($k = 0$)

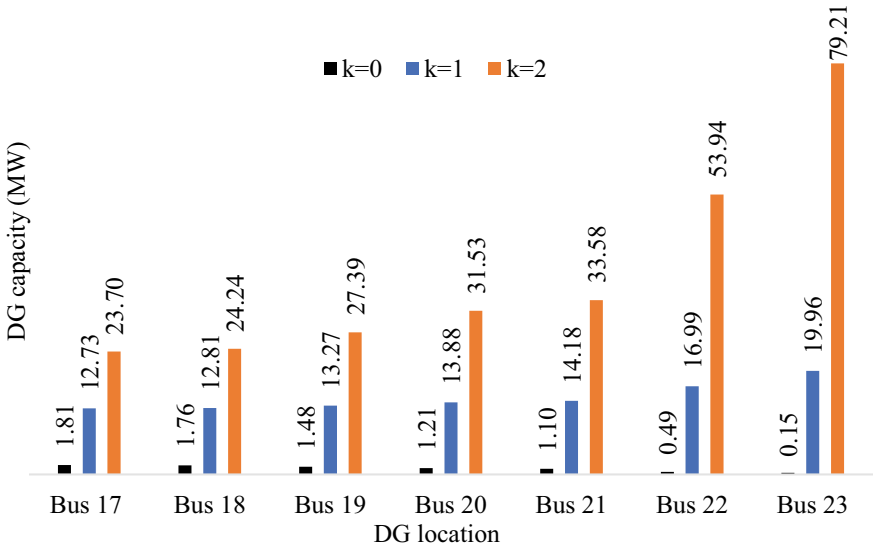

Fig. 9 Max limits of a single IBDG at different locations with a fault at worst condition of varying factor k

voltage at the DG location and the limitation current depends on the multiple of V^k and the IBDG rated current, this limitation value is decreased when the fault occurs at the far end.

When a fault occurs at the upstream section, the voltage is extremely reduced during the fault occurrence. Then, the maximum capacity of IBDG can be increased by increasing the level of fault current limitation, i.e., the decrease in the value of V^k. When a fault occurs at the extremely downstream location, the voltage is increased during the fault occurrence. The current limitation will not be high and miscoordination between protective devices occurs due to decreasing the level of fault current limitation.

Referring to the results in Fig. 9, the maximum capacity of the IBDG is recognized when located at bus 23 alone in two cases. In the first case, where $k = 0$, the unit current is limited to the rated value. In this case, the maximum capacity is found to be 0.15 MW. In the second case, where $k = 1$, the unit current is maintained proportional to the per unit terminal voltage. Accordingly, the maximum capacity is significantly increased to be 19.96 MW. Alternatively, the maximum capacities of IBDG with FCL unit at bus 17 alone for rated and proportional limits are, respectively, 1.81 and 12.73 MW. These results confirm that limiting the fault current of the DG has the ability to provide larger capacities. The maximum capacity of IBDG can be increased by increasing the level of fault current limitation, i.e., decreasing the value of V^k. This can be accomplished by increasing the factor k and/or decreasing the per unit terminal voltage by locating the IBDG closer to the fuse location.

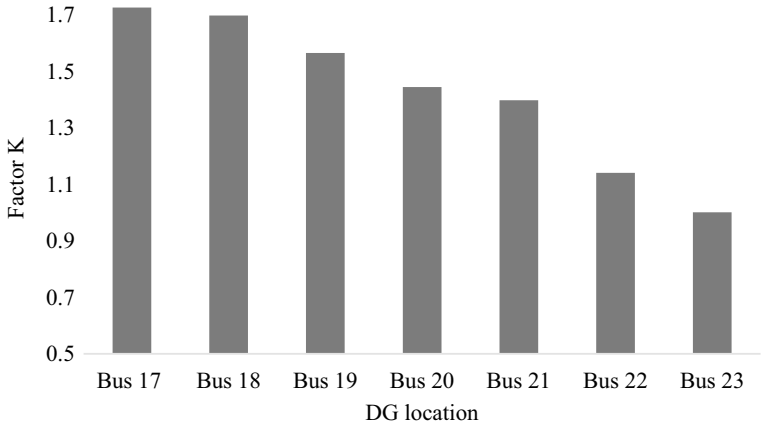

Fig. 10 Variation of factor k with different locations of a single IBDG with the same capacity

Figure 10 shows the variation of factor k with different locations of a single IBDG. This relation is obtained under the condition that all IBDG units have the same rating at all buses. The evaluation is carried out to limit the fault current according to the pu terminal voltage. Accordingly, the inverter mode of operation depends on the computation of rms values of phase and line voltages. Then, the computation of pu values is achieved in order to select the minimum one that limits the fault current. The voltage is extremely reduced during the fault occurrence, with the DG is located at downstream bus. Accordingly, the inverter current is increased as shown in Table 1. The factor k is computed depending on the selected current rating of IBDG, measured per unit voltage, and obtained fault current at this bus. The selected IBDG rating is 20 MW at bus 17 as shown in Table 1. The factor k has highest value of 1.73, where IBDG is located near recloser location, while it is decreased to 1 when IBDG is placed near the fuse location.

Table 2 shows the limits of IBDG rating for different locations in recloser-fuse region and different values of factor k for a fault under worst conditions. The best location and maximum hosting capacity of the IBDGs are achieved by the combination of DG units by saving the coordination margin between fuse and reclosure. In

Table 1 IBDG terminal voltage, minimum voltage, and power losses during normal operation and fault occurrence under worst conditions

DG location	Bus 17	Bus 18	Bus 19	Bus 20	Bus 21	Bus 22	Bus 23
VDG-f (pu)	0.54	0.53	0.48	0.44	0.42	0.31	0.25
Min. V (%)	97.71	97.78	97.64	97.39	97.28	96.7	96.4
P_{loss} (MW)	0.087	0.087	0.089	0.093	0.095	0.11	0.12
Q_{loss} (Mvar)	0.134	0.142	0.157	0.172	0.18	0.22	0.247

Table 2 IBDG penetration limits with different DG locations in recloser-fuse region with a fault under worst conditions based on FCL

DG location		Bus 17	Bus 18	Bus 19	Bus 20	Bus 21	Bus 22	Bus 23
P (MW)	$k = 0$	0	1.76	0	0	0	0	0
	$k = 1$	4.32	1.51	3.57	0.74	0.77	0.90	3.87
	$k = 2$	8.89	3.21	8.13	1.89	2.06	3.27	17.45
VDG-f (pu)		0.49	0.47	0.44	0.39	0.38	0.28	0.22
Min. V (%)		98						
P_{loss} (MW)		0.067						
Q_{loss} (Mvar)		0.126						

conclusion, $k = 2$ results in the maximum penetration level of DG and all relations are incorporated in the objective function as illustrated in Table 2.

The DG power generation enhances the voltage levels in the system as indicated by "min V (%)" in the table evaluated at different buses in most cases. This is attributed to the ability of IBDG to produce reactive power during normal operation. Furthermore, the increasing of IBDG penetration reduces active and reactive power losses in the feeder. The main reason of power losses reduction is the reduction of power flows through the system. Nevertheless, the fault current level is enlarged in the feeder with the IBDG penetration increase.

Table 2 illustrates the total fault at the faulty bus and the minimum value of the feeder voltages from substation to fuse location. Likewise, the voltage and fault current values under the best situation from the point of view of the multi-objective function are shown in this Table. Due to the consideration of a multi-objective function comprising different terms at the same time, all performance indices are enhanced with different degrees consistent with the weight factors.

To verify the validity of various cases concerning protection coordination, the fault currents of the fuse and recloser are investigated for a fault at F_1 after inserting a 0.15 MW IBDG unit at bus 23 as an example. Figure 11 shows the recloser-fuse coordination margin for a 0.15 MW IBDG unit at bus 23 with a fault at F_1, where the coordination margin is satisfied. The fault current values sensed by the recloser and fuse are 858.91 A and 970.8 A, respectively, where the IBDG injects a current of 7.85 A that is the critical current before the miscoordination. The per unit terminal voltage during the fault is 0.001 pu at bus 23. Hence, the rating current of the IBDG is proportional to the fault current contribution of DG for $k = 0$.

Similar results are obtained for different capacities and DG locations with higher values of factor k. For the case when k equals 1 to limit the fault current to 7.85 A, the maximum capacity is 19.96 MW, with a rated current of 1047.9 A. When k equals 2 and to limit the fault current to the same level, the maximum capacity can be increased to 79.21 MW with a rated current of 4158.5 A. The per unit terminal voltage during the fault (under the worst conditions) is 0.25 pu at bus 23 as shown in Fig. 6. Actually, the presented capacities of IBDG are not practical choices due to their high values. In both cases, i.e., $k = 1$ and $k = 2$, the high currents may activate the

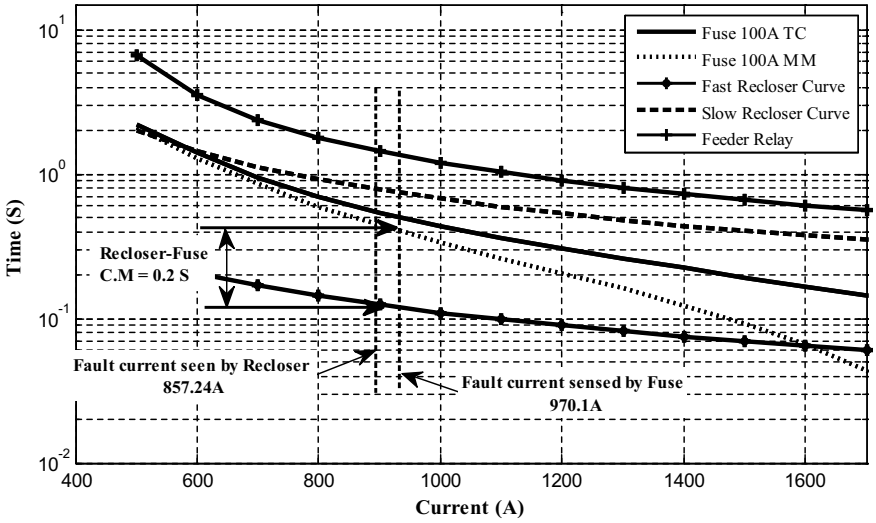

Fig. 11 Recloser-fuse coordination margin for a 0.15 MW IBDG unit (rated) at bus 23 with a fault at F_1

protective devices during the normal operation. In addition, the conductor capacity cannot withstand these values of currents. The analysis presented here is to ensure that very high capacities of IBDGs can be installed without affecting the protection coordination considering the proposed strategy. Thus, the capacity of these units can be chosen according to technical and economic aspects without any restrictions from the protection system.

The practical constraints, such as transmission line maximum limits, must be taken into consideration when defining appropriate size taking into account that the capacity of IBDG units is restricted by the network rated power. According to Fig. 12, the recloser-fuse CM is improved with increasing the factor k with the same capacity of IBDG unit located at bus 23. The most acceptable and commonly used coordination margin between protective devices is 0.35 *s*. This value is achieved at a factor "k" of 0.44 at IBDG capacity of 3.5 MW, which is about 33% of the total load. This value is selected since many researches recommend a level around 30% for the maximum contribution of DG units.

12.2 Case 2: DG Located in Relay-Recloser Region

Once the fault happens at F_1, the reclosure and fuse operating times are reduced with the IBDG rating increase when it is placed in the relay-recloser zone. The protective devices operating times are reduced when IBDG units are placed near the relay, and they are increased when IBDG units are positioned near the recloser. This is due to the

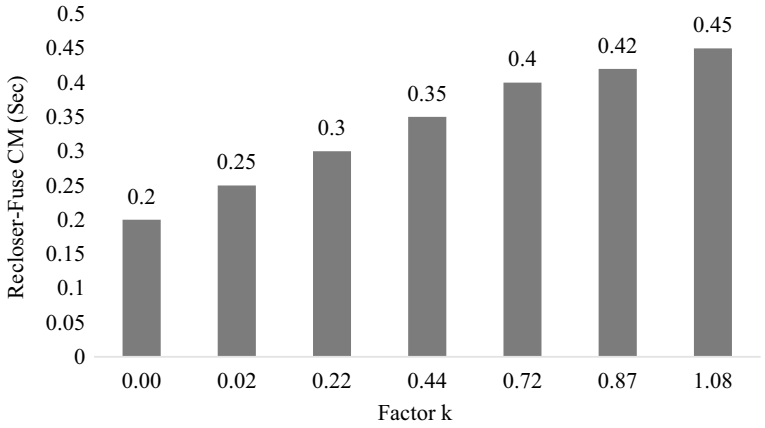

Fig. 12 Variation of the recloser-fuse CM with variation of factor k for the same capacity of IBDG unit located at bus 23

Table 3 Limits of DG penetration with different IBDG positions at one bus in relay-recloser region and fault locations at F_1

DG location		Bus 4	Bus 7	Bus 10	Bus 11	Bus 12	Bus 13	Bus 14	Bus 15	Bus 16
P (MW)	$k = 0$	9.48	5.96	4.73	4.30	3.94	3.54	2.77	2.57	2.38
	$k = 1$	11.57	9.13	8.07	7.76	7.53	7.33	7.21	7.23	7.29
	$k = 2$	14.11	13.98	13.77	13.99	14.39	15.20	18.75	20.36	22.32
VDG-f (pu)		0.82	0.65	0.59	0.55	0.52	0.48	0.38	0.36	0.33

lower fault current contribution from IBDG since the fault path is longer. According to Table 3, the DG rating maximum limit that fulfills the coordination between the recloser (fast curve) and fuse equals 9.48 MW for a factor k equals 0.

For any fault under the worst conditions (F_4 or downstream of this section), there is no change in the fault current through feeder-relay from the value without IBDG placed near recloser but the recloser fault current will rise. The IBDG rating maximum limit that fulfills the coordination between the relay and recloser (slow curve) is 3.54 MW for a factor k equals 0 as shown in Table 4. The maximum limit of IBDG rating is reduced from 9.48 MW to 3.54 MW to achieve all coordination margins. From these Tables, the best choice of the distributed generation is an IBDG unit in the relay-recloser section close to the relay.

The per unit voltage during fault is increased when IBDG is located near relay location as shown in Table 3. This occurs since the IBDG is located near the substation and the fault occurs after the fuse location. The IBDG siting is determined depending on the IBDG bus voltage during fault, since the inverter control implementation depends on the per unit voltage during fault. The allowable location for IBDG unit is restricted by the bus per unit voltage during fault. The IBDG can be located at all buses that have, during fault, voltage values lower than or equal to their voltage

Table 4 Limits of DG penetration with different IBDG locations at one bus in relay-recloser region and fault locations at F_4 based on FCL

DG location		Bus 4	Bus 7	Bus 10	Bus 11	Bus 12	Bus 13	Bus 14	Bus 15	Bus 16
P (MW)	$k = 0$	3.54	3.17	3.03	2.96	2.89	2.81	2.64	2.60	2.57
	$k = 1$	3.80	4.23	4.29	4.31	4.33	4.32	4.32	4.29	4.29
	$i = 2$	5.62	7.66	8.61	9.14	9.74	10.62	13.72	14.95	16.56
VDG-f (pu)		0.58	0.68	0.55	0.50	0.47	0.44	0.41	0.31	0.29
Min. V (%)		91.14	93.79	94.68	95.08	95.47	95.95	97.04	97.33	97.59
P_{loss} (MW)		0.27	0.27	0.24	0.24	0.23	0.23	0.23	0.22	0.22
Q_{loss} (Mvar)		0.49	0.49	0.51	0.52	0.52	0.52	0.52	0.53	0.51

setting. As shown in Table 3, if the voltage setting value is 0.8 pu, IBDG can be located at buses 7–16 since their voltages during fault are lower than the setting value. On the other hand, IBDG can be located at all buses if the setting voltage is 0.9 pu [19]. The setting voltage is determined by the system operator. The remaining results show the maximum capacity of IBDG without considering the pu voltage during fault.

Table 5 demonstrates the limits of IBDG penetration at different DG locations in the relay-recloser zone for a fault at F_4. Therefore, the best location and maximum sizing of the DGs are a group of IBDG units saving a suitable coordination margin between recloser and relay. Considering only the IBDG capacity and neglecting the voltage values, total fault current and power losses in the objective function result in locating the IBDG near the relay. Conversely, considering the voltage levels, total fault current and power losses cause the IBDG to be located near the recloser. Table 5 illustrates the active and reactive power loss, total fault current, and minimum voltages with different DG locations in the relay-recloser region and a fault at F_4.

Table 5 IBDG penetration limits with different DG positions in relay-recloser region with a fault under worst conditions of F_4 based on FCL

DG location		Bus 4	Bus 7	Bus 10	Bus 11	Bus 12	Bus 13	Bus 14	Bus 15	Bus 16
P (MW)	$k = 0$	0	0	0	0	0	0	0	0	2.57
	$k = 1$	0	0	0	0	0	0	0	0	4.29
	$k = 2$	0	0	0	0	0	0	0	0	16.56
VDG-f (pu)		–	–	–	–	–	–	–	–	0.26
Min. V (%)		98								
P_{loss} (MW)		0.22								
Q_{loss} (Mvar)		0.51								

12.3 Case 3: DG Located Along the Feeder

Limits of IBDG-capacity for different DG locations along the feeder for a fault at F_1 considering all objective function terms are illustrated in Table 6. The best alternative is the distribution of units at different buses saving coordination margin between fuse and reclosure. As in Table 6, maximum DG penetration is achieved when 3 units are connected at different buses around the recloser location. Conversely, the capacity of IBDG units is taken as a ratio of maximum capacity when located in the relay-recloser region. This ratio, which considers the coordination for the entire feeder, is attained from a single unit positioned at bus 16. Total fault current, the active and reactive power loss and voltage levels minimum value with different DG locations in the relay-recloser region and a fault at F_4 are also shown in Table 6.

The results show that, with IBDG units and maintaining the conventional protection scheme, the voltage values and power losses are improved in case 1 and case 3 compared to case 2. This is due to the insertion of DG units with high capacity beside load centers (along the feeder).

Table 7 summarizes the hosting capacity of a single and multi-IBDG compared with the conventional DG. As shown from this table, for conventional DG and IBDG, the hosting capacity is increased when moving closer to the upstream protective devices (bolded numbers for DG and IBDG). On the other hand, for a single proposed IBDG, the hosting capacity is increased when moving closer to the downstream protective devices (the bolded number for proposed IBDG). This can be achieved by increasing the degree of limitation by locating the IBDG closer to the fuse location. Accordingly, the optimal hosting capacity is defined along feeder regarding the multi-objective function as shown in the last row of Table 7, where the voltage values and power losses are improved.

Table 6 IBDG penetration limits with different DG positions along feeder

DG location		Bus 16	Bus 17	Bus 18	Bus 19	Bus 20	Bus 21	Bus 22	Bus 23
P (MW)	$k = 0$	2.21	0.26	0.10	0.16	0	0	0	0
	$k = 1$	4.14	2.22	2.66	3.00	0.86	1.09	1.86	1.11
	$k = 2$	7.99	4.39	5.30	6.48	2.09	2.78	6.38	4.91
VDG-f (pu)		0.52	0.51	0.50	0.46	0.41	0.39	0.29	0.23
Min. V (%)		98.09							
P_{loss} (MW)		0.068							
Q_{loss} (Mvar)		0.1246							

Table 7 Summary of DG hosting capacity at different locations with a fault at worst condition and $k = 2$ with different region

DG location	Bus16	Bus17	Bus18	Bus19	Bus20	Bus21	Bus22	Bus23	
For single DG									
SG	**1.14**	**0.4618**	0.4451	0.3712	0.3105	0.2897	0.1903	0.1483	
IBDG	**2.57**	**1.81**	1.76	1.48	1.21	1.1	0.49	0.15	
Proposed IBDG	**16.56**	23.7	24.24	27.39	31.33	33.58	53.94	**79.21**	
For multi-IBDG									Sum of max limits
Recloser-fuse	–	8.89	3.21	8.13	1.89	2.06	3.27	17.45	44.9
Along feeder	7.99	4.39	5.30	6.48	2.09	2.78	6.38	4.91	40.32

13 Summary

A new algorithm for optimal renewable energy locations is proposed to increase the hosting capacity of DG units. The algorithm is successfully established to determine the number, locations, and maximum capacity of the DGs for inserting DG-based inverter in distribution systems. This scheme is based on formulating a multi-objective function using both protection and technical considerations. Technical aspects include minimizing line loss, improving voltage levels, and maximizing capacity of inserting DG-based inverter without replacing the existing protection system. The analysis recommends that the maximum levels of IBDGs can be achieved when located near recloser location without considering other factors for low degree of limitation. On the other hand, for high degree of limitation, the IBDG maximum capacity location is close to the fuse location. The more limitation of IBDG fault current at a certain location, the more allowable IBDG capacity can be installed in this location. This is valid up to certain practical constraints that consider other technical and economic limits. The maximum capacity of IBDG can be increased by increasing the level of fault current limitation. This can be accomplished by increasing the degree of limitation and/or decreasing the per unit terminal voltage during fault by moving the IBDG closer to the fuse location, where the voltage level is lower.

References

1. H.A. Abdel-Ghany, A.E.F. Hamad, A.M. Azmy, Evaluating the effect of considering repairing-fault periods on calculating technical losses in medium-voltage feeders of ring distribution networks. Electr. Power Syst. Res. **196**, 107192 (2021)
2. N.I. Elkalashy, N.F. Sherbilla, A.I. Taalab, T.A. Kawady, Distributed generation with fault

current limiter impacts on recloser–fuse protection for distribution feeder, in Proceedings of the 15th International Middle East Power Systems Conference (MEPCON'12), Alexandria University, Egypt, pp. 23–25 (2012)
3. S.A.M. Javadian, M.R. Haghifam, S.M.T. Bathaee, M.F. Firoozabad, Adaptive centralized protection scheme for distribution systems with DG using risk analysis for protective devices placement. Int. J. Electr. Power Energy Syst. **44**(1), 337–345 (2013)
4. A. Kamel, M.A. Alaam, A.M. Azmy, A.Y. Abdelaziz, Protection coordination for distribution systems in presence of distributed generators. Electr. Power Compon. Syst. **41**(15), 1555–1566 (2013)
5. S. Kwon, C. Shin, W. Jung, Evaluation of protection coordination with distributed generation in distribution networks, in Proceedings of the 10th IET International Conference on Developments in Power System Protection (DPSP 2010), pp. 74–78 (2010)
6. A.F. Naiem, Y. Hegazy, A.Y. Abdelaziz, M.A. Elsharkawy, A classification technique for recloser-fuse coordination in distribution systems with distributed generation. IEEE Trans. Power Delivery **27**(1), 176–185 (2011)
7. IEEE Standard for Interconnecting Distributed Resources with Electric Power Systems, IEEE Std. 1547–2003, Jul. 2003
8. S. Katyara, L. Staszewski, Z. Leonowicz, Protection coordination of properly sized and placed distributed generations–methods, applications and future scope. Energies **11**(10), 2672 (2018)
9. M.A. Gana, U.O. Aliyu, G.A. Bakare, Integration and evaluation of the impact of distributed generation on the protection system of distribution network with DG Using Etap. Eng. Appl. Sci. **4**(2), 44–51 (2019)
10. H. Zayandehroodi, A. Mohamed, H. Shareef, M. Mohammadjafari, M. Farhoodnea, A novel protection coordination strategy using back tracking algorithm for distribution systems with high penetration of DG, in 2012 IEEE International Power Engineering and Optimization Conference Melaka, Malaysia, pp. 187–192. IEEE (2012)
11. P.T. Manditereza, R. Bansal, Renewable distributed generation: the hidden challenges—a review from the protection perspective. Renew. Sustain. Energy Rev. **58**, 1457–1465 (2016)
12. A.E. Momesso, W.M. Bernardes, E.N. Asada, Fuzzy-based non-communicating adaptive overcurrent relay. IFAC-PapersOnLine **51**(28), 315–320 (2018)
13. M. Chandran, S. Kumar, P. Somasundaram, Smart and adaptive over current protection for distribution system with distributed generation. Int. J0 Adv. Res. Electr. Electron. Instrument. Eng. **3**(2), 102–111 (2014)
14. S. Mitra, P. Chattopadhyay, Design and implementation of flexible numerical overcurrent relay on FPGA. Int. J. Electr. Power Energy Syst. **104**, 797–806 (2019)
15. M. Firouzi, G.B. Gharehpetian, Improving fault ride-through capability of fixed-speed wind turbine by using bridge-type fault current limiter. IEEE Trans. Energy Convers. **28**(2), 361–369 (2013)
16. J.C. Hernández, J. De la Cruz, B. Ogayar, Electrical protection for the grid-interconnection of photovoltaic-distributed generation. Electr. Power Syst. Res. **89**, 85–99 (2012)
17. M. Abedini, M.H. Moradi, S.M. Hosseinian, Optimal management of microgrids including renewable energy scources using GPSO-GM algorithm. Renew. Energy **90**, 430–439 (2016)
18. A.E.F. Hamad, H.A. Abdel-Ghany, A.M. Azmy, Switching strategy for DG optimal allocation during repairing fault periods on loop distribution networks. Int. Trans. Electr. Energy Syst. **27**(12), e2454 (2017)
19. G.A. Quiroga, C.F.M. Almeida, H. Kagan, N. Kagan, Protection system considerations in networks with distributed generation, in *Electric Distribution Network Management and Control* (Springer, Singapore, 2018), pp 255–280
20. Y. Mohammadi, R.C. Leborgne, Improved DR and CBM methods for finding relative location of voltage sag source at the PCC of distributed energy resources. Int. J. Electr. Power Energy Syst. **117**. 105664 (2020)
21. H.R. Baghaee, M. Mirsalim, G.B. Gharehpetian, H.A. Talebi, MOPSO/FDMT-based Pareto-optimal solution for coordination of overcurrent relays in interconnected networks and multi-DER microgrids. IET Gener. Transm. Distrib. **12**(12), 2871–2886 (2018)

22. A. Kadri, H. Marzougui, A. Aouiti, F. Bacha, Energy management and control strategy for a DFIG wind turbine/fuel cell hybrid system with super capacitor storage system. Energy, **192**, 116518 (2020)
23. IEEE guide for the operation, classification, application, and coordination of current-limiting fuses with rated voltages 1–38 kV, IEEE Std C37.48.1-2002
24. P. Basak, S. Chowdhury, S.H. nee Dey, S.P. Chowdhury, A literature review on integration of distributed energy resources in the perspective of control, protection and stability of microgrid. Renew. Sustain. Energy Rev. **16**(8), 5545–5556 (2012)
25. N. Femia, G. Petrone, G. Spagnuolo, M. Vitelli, *Power Electronics and Control Techniques for Maximum Energy Harvesting in Photovoltaic Systems* (CRC Press, 2017)
26. J.A. Smith, M.H. Nehrir, V. Gerez, S.R. Shaw, A broad look at the workings, types, and applications of fuel cells, in IEEE Power Engineering Society Summer Meeting, vol. 1, pp. 70–75. IEEE (2002)
27. H.A. Abdel-Ghany, A.E. ELGebaly, I.B. Taha, A new monitoring technique for fault detection and classification in PV systems based on rate of change of voltage-current trajectory. Int. J. Electr. Power Energy Syste. **133**, 107248 (2021)
28. H.A. Abdel-Ghany, A.M. Azmy, Defining the practical constraints of inserting DG units in distribution systems regarding protection schemes. Int. Trans. Electr. Energy Syst. **25**(12), 3618–3629 (2015)
29. D. Isle, M. Vaziri, M. Zarghami, S. Vadhva, Review of concepts to increase distributed generation into the distribution network, in 2014 Sixth Annual IEEE Green Technologies Conference, pp. 118–125. IEEE (2014)
30. M.Y. Shih, A. Conde, C. Ángeles-Camacho, E. Fernandez, Z. Leonowicz, F. Lezama, J. Chan, A two stage fault current limiter and directional overcurrent relay optimization for adaptive protection resetting using differential evolution multi-objective algorithm in presence of distributed generation. Electric Power Syst. Res. **190**, 106844 (2021)
31. M. Sadeghi, M. Abasi, Optimal placement and sizing of hybrid superconducting fault current limiter for protection coordination restoration of the distribution networks in the presence of simultaneous distributed generation. Electr. Power Syst. Res. **201**, 107541 (2021)
32. D. Baimel, N. Chowdhury, J. Belikov, Y. Levron, New type of bridge fault current limiter with reduced power losses for transient stability improvement of DFIG wind farm. Electr. Power Syst. Res. **197**, 107293 (2021)
33. B. Tipo, J. Li, B. Qin, Fault ride through capability enhancement of doubly fed wind generator using hybrid protection circuits, in 2019 IEEE 8th International Conference on Advanced Power System Automation and Protection (APAP), pp. 1200–1203. IEEE (2019)
34. J.H. Teng, C.N. Lu, Optimum fault current limiter placement with search space reduction technique. IET Gener. Transm. Distrib. **4**(4), 485–494 (2010)
35. H. Ge, K. Yang, M. Junaid, Y. Tan, Z. Liu, Y. Geng, J. Wang, A quenching recovery time test method for resistive type superconducting fault current limiters used in DC circuit, in 2017 4th International Conference on Electric Power Equipment-Switching Technology (ICEPE-ST), pp. 393–396. IEEE (2017)
36. J.R. Prigmore, J.A. Mendoza, G.G. Karady, Comparison of four different types of ferromagnetic materials for fault current limiter applications. IEEE Trans. Power Delivery **28**(3), 1491–1498 (2013)
37. H.T. Tseng, J.F. Chen, Quasi-bridge-type fault current limiter for mitigating fault transient phenomena. IET Gener. Transm. Distrib. **8**(8), 1377–1391 (2014)
38. M.S. Abbas, *Limiting Effects of Renewable Distributed Generation on the Performance of Protective Relaying* (Thesis, Faculty of Engineering, Minoufiya University, Egypt, M. Sc, 2014)
39. M.A. Abdelkader, M.A. Elshahed, Z.H. Osman, An analytical formula for multiple DGs allocations to reduce distribution system losses. Alex. Eng. J. **58**(4), 1265–1280 (2019)
40. A.H. Abdel-Ghany, A.M. Azmy, M. Saad, Optimal dg deployment based on technical and economic considerations with daily load variation. Int. J. Eng. Res. Africa Trans. Tech. Publications Ltd. **45**, 115–131 (2019)

41. S.A. Hosseini, S.S.K. Madahi, F. Razavi, M. Karami, A.A. Ghadimi, Optimal sizing and siting distributed generation resources using a multiobjective algorithm. Turk. J. Electr. Eng. Comput. Sci. **21**(3), 825–850 (2013)
42. H.A. Abdel-Ghany, A.M. Azmy, N.I. Elkalashy, E.M. Rashad, Optimizing DG penetration in distribution networks concerning protection schemes and technical impact. Electr. Power Syst. Res. **128**, 113–122 (2015)

Management of Distributed Generation for Smart Buildings

Ahmed M. Azmy

Abstract Small and modular Distributed Generation (DG), such as fuel cells, can be used for onsite service within smart buildings to cover a part of the electrical and thermal load demand. In this case, the optimal capacity and output from the used generating unit(s) can be calculated to supply a part of load demand, where the excess/lack of power is exported to/imported from the utility. Minimization of the energy price is a main target in this case to achieve win–win situation and to enable DG units to participate as a source of power with the utility. This can be achieved by the optimal management of the daily performance of the candidate DG unit(s), such as proton exchange membrane (PEM) fuel cells located in smart buildings. The process could be developed to include multi-DG units in the building in a cooperative manner. The simultaneous generation of electrical and thermal energy has to consider the load requirements in an economic framework. Smart meters are required to account for the surplus/shortage energy that is exported to/imported from the utility, respectively. The main challenge when using such units in residential applications is their high cost. Therefore, the management process depends on an accurate economic model to describe all operating costs considering both electrical and thermal relations. Due to the discontinuity and nonlinearity of the model, a robust optimization tool has to be utilized.

Keywords Performance management · Performance optimization · Proton exchange membrane (PEM) fuel cells · Smart buildings · Smart grids

List of Symbols

$C_{NGFC,i}$	Overall daily natural-gas cost for FC at home "*i*" ($/day)
$C_{NGRL,i}$	Overall daily natural-gas cost to feed remaining thermal load in home "*i*" ($/day)

A. M. Azmy (✉)
Electrical Power and Machines Engineering Department, Faculty of Engineering, Tanta University, Tanta, Egypt
e-mail: azmy@f-eng.tanta.edu.eg

S. K. Das et al. (eds.), *Advances in Control Techniques for Smart Grid Applications*,
https://doi.org/10.1007/978-981-16-9856-9_7

$C_{o\&m\mathrm{fc},i}$	Overall daily operating and maintenance cost of FC at home "i" ($/day)
$C_{\mathrm{purc},i}$	Overall daily cost of purchased electricity for home "i" ($/day)
$C_{\mathrm{sold},i}$	Overall daily revenue due to sold electricity by home "i" ($/day)
C_{TOTAL}	The overall daily operating cost of entire system ($/day)
DS	The data size (bytes)
$\mathrm{FC}_{o\&m}$	Daily operation and maintenance constant of PEMFC ($/kWh)
L	The required latency
$L_{\mathrm{el},J,i}$	Electrical load demand of home "i" at interval "J" (kW)
$L_{\mathrm{th},J,i}$	Thermal load demand of home "i" at interval "J" (kW)
MRT	The minimum running period of the FC (h)
MST	The minimum stop periods of the FC (h)
N	Number of FC units
N_C	The number of consumers (s)
$N_{\max,i}$	The maximum number of start and stops allowed for the FC at home "i" per day
NR	The network data rate (bps)
n	Number of residential homes included in the study
$n_{(\mathrm{start-stop}),i}$	The number of starts and stops of FC at home "i" per day
NU	The number of unknowns
$P_{\mathrm{aux},i}$	Electrical power consumed by auxiliary devices of FC at home "i" (kW)
$P_{\mathrm{el},J,i}$	Electric power produced by DG units at home "i" at interval "J" (kW)
P_{excess}	The surplus thermal power that is stored as hot water or dissipated (kW)
$P_{\mathrm{fc(elect)},i}$	Produced electric power in FC at home "i" (kW)
$P_{\mathrm{fc(therm)},i}$	Output thermal power from FC in home "i" (kW)
$P_{\mathrm{grid},i}$	Purchased/Sold electric power from/to the grid in home "i" (kW)
$P_{i,J-1}$	The power generated by the FC in home "i" at interval "$J-1$" (kW)
$P_{J,i}$	FC electrical power at home "i" at interval "J" (kW)
$P_{\mathrm{load(elect)},i}$	Electric load demand in home "i" (kW)
$P_{\mathrm{load(therm)},i}$	Thermal load demand of home "i" (kW)
$P_{\max,i}$	Maximum limit of generated power from FC at home "i" (kW)
$P_{\min,i}$	Minimum limit of generated power from FC at home "i" (kW)
$P_{\mathrm{ng},i}$	Thermal power through direct burning of natural gas in home "i" (kW)
$P_{\mathrm{th},J,i}$	FC thermal power in home "i" at interval "J" (kW)
SC_i	Daily start-up cost of the FC in home "i" ($/day)
$T_{\mathrm{el}-p}$	Sold electricity tariff ($/kWh)
$T_{\mathrm{el}-s}$	Purchased electricity Tariff ($/kWh)
$T_{\mathrm{ng-fc}}$	Natural gas tariff for supplying FCs ($/day)
$T_{\mathrm{ng-rl}}$	Natural gas tariff for supplying thermal loads ($/kWh)
T_{off}	The time duration, where the FC unit at home "i" is off (h)
$T_{\mathrm{t-1}}{}^{\mathrm{on}}$	The FC running period at time interval "$t-1$" (h)
$T_{\mathrm{t-1}}{}^{\mathrm{off}}$	The FC stop period at time interval "t_1" (h)
Us	The unit ON/OFF status: Us = 1 for running mode and 0 for stop mode
ΔP_D	The lower limit of the ramp rate (kW/h)

ΔP_u	The upper limit of the ramp rate (kW/h)
ΔT	Time interval between two successive settings of FC (h)
$\eta_{J,i}$	FC electrical efficiency in home "i" at interval "J"
$€_{\mathrm{i}}$	Hot start-up cost of FC at home "i" ($)
$€_i + \varphi_{\mathrm{i}}$	Cold start-up cost of FC at home "i" ($)
τ	The cooling time constant of the FC unit at home "i" (h

List of Acronyms

AMI	Advanced Metering Infrastructure
DG	*Distributed Generation*
FC	*Fuel Cell*
PEMFC	*Proton Exchange Membrane Fuel Cell*
PV	Photovoltaic

1 Introduction

Onsite service for residential applications is one of promising fields of fuel cells (FCs) and photovoltaic (PV) [1]. The capacity of distributed generating (DGs) units can be selected to cover a large part of electrical and thermal load demand in the building. A main requirement, which is essential in this regard to reduce energy price, is the optimal management of the DGs operation to bring them to competition with the main-grid system. The decrease in the operating cost will considerably contribute in reducing the cost of energy and increase the feasibility of using DGs. Proton exchange membrane FC (PEMFC) and PV units are candidate for this task due to their good features, especially for low-capacity applications [1].

The first step to achieve optimal management of DGs is the development of precise economic models considering essential electrical and thermal relations [2]. Due to the discontinuous nature of such models, the utilization of artificial intelligent optimization tool is required. The optimized settings of DGs depend on operating conditions and can be carried out for one day in advance.

Demand side management strategy could be applied to provide a bonus for customers who participate in this process and, hence, the customers can offset the initial cost of the DG system [3]. To maximize the benefits behind the proposed idea, a full automated system has to be considered with respect to the appliances control for energy conservation. The choice of a proper communication technology is essential to ensure a comprehensive solution that achieves a suitable data flow rate and accepted latency with flexibility and security [4].

In [5], the authors developed a hybrid energy system including heat and power that is used for a residential load. The energy management system depends on optimal

Pontryagin minimum principles to minimize fuel consumption. The authors in [6] introduced a peer-to-peer (P2P) management scheme to regulate the energy in buildings with the possibility of sharing energy between partners. A two-stage optimization approach is introduced in [7] based on a hybrid demand response program to reduce running costs considering uncertainty. In [8], home energy management systems are proposed for self-scheduling of assets for residential applications. The design of the management system considers dynamic pricing programs and it is developed based on a stochastic mixed-integer linear programming framework.

This chapter establishes an intelligent technique to manage DG performance for residential applications. This is accomplished through identifying the optimal settings of DGs, either a single unit or several units operating cooperatively, depending on the developed economic models. The optimal settings are identified for a single PEMFC and three identical PEMFCs in cooperative manner as examples of the proposed systems.

2 Motivation and Contribution

Based on the previous discussion and literature survey, customers will face many challenges when dealing with demand response programs. Examples are the poor communication with the grid without the possibility of sharing the decision-making or information. In addition, the use of DGs without coordination could not achieve the required benefits. Thus, sharing information between grid and customers and developing home automation and home energy management systems would achieve the win–win situation.

The contribution of this chapter is to introduce a general framework to maximize the benefits of utilizing DG units within smart homes in a cooperative manner. The developed approach focuses on automated procedures that do not require any experience from customers. The framework depends on two-way information flow with fully automated and remote control of DG units.

3 Residential System Construction

DGs can contribute electrical and thermal energy to residential loads [9]. The difference between generated and consumed powers is compensated by the main grid system. The tariffs of sold and purchased electricity could be the same or not according to the pool market prices. Generally, two energy meters are required to measure the purchased and the sold electricity. If a thermal energy is produced by the DGs, it can be utilized for water and space heating, where the load has a natural-gas source to compensate for expectable deficiencies. According to the natural-gas market, there may be different tariffs for each utilization, such as residential, commercial, and industrial applications [10]. In some cases, a special tariff is assigned for

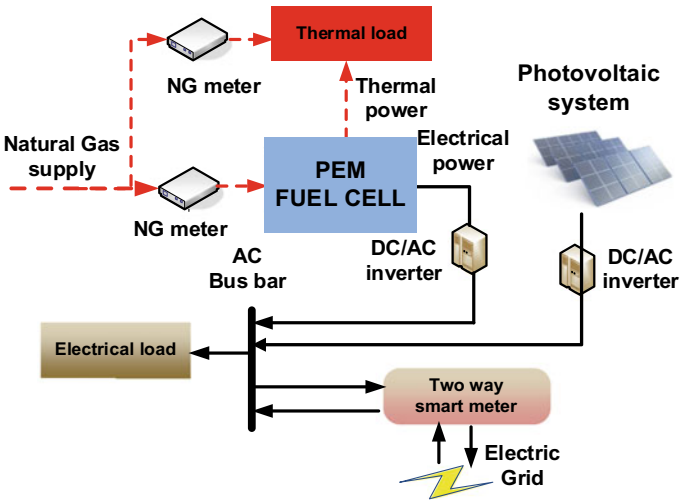

Fig. 1 Construction of a residential system with a fuel cell and PV for smart buildings with electrical and thermal flow

electric generation applications. Therefore, it is required to measure the consumptions of natural gas separately for the FCs and boilers to compute the cost of each consumption according to its own tariff.

Figure 1 illustrates the construction of a residential system with two candidate DGs, i.e., PV and PEMFC. This configuration assumes different supplementary devices used in the system such as pumps, fans… etc. that are not shown in the figure. If the PV system is used, an electrical storage battery will be considered. However, the concentration in this chapter is only to the utilization of a PEMFC that can provide both electrical and thermal power.

The thermal energy produced by PEMFC is used to supply the thermal load demand, including heating of both water and space if needed. With low thermal power from FC, the remaining thermal load demand could be supplied from either a neighbor home or by burning natural gas. There is a possibility of exchanging thermal energy between homes if they are close to each other. On the other hand, if the homes are far from each other, there will be no possibility for interchanging thermal power between them.

3.1 Selection of Communication System

It is possible to use a number of DGs in different locations within the smart building and, thus, communication infrastructure is required to connect DGs in cooperative manner to achieve higher benefits for participants [11, 12]. Figure 2 highlights the possible multi-layer architecture of communication system in smart buildings.

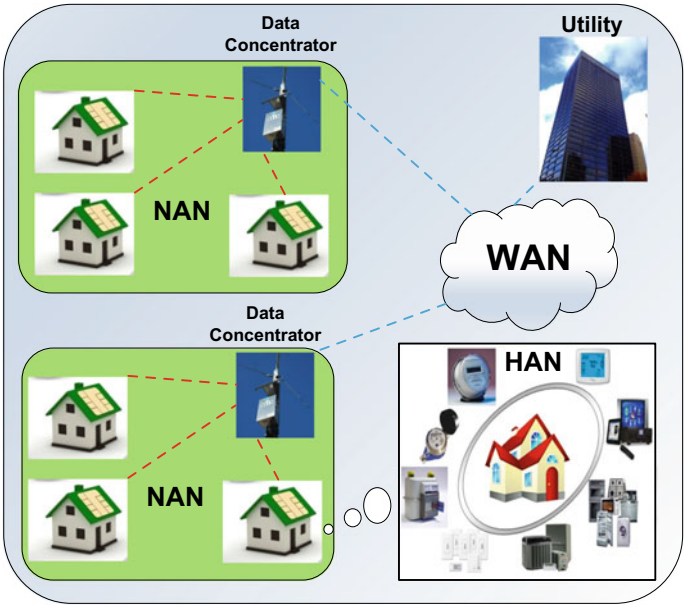

Fig. 2 Multi-layer architecture of smart grid communication system

The communication system has to achieve economic, efficient, reliable, and secure operation [13, 14].

To achieve complete, robust, reliable, and fast communication links between different homes, many requirements are needed. Depending on the nature of application, the communication network is selected. The main requirements needed for any communication network to link FCs are summarized in the following points:

Data rate

Data rate specifies the speed of data transmission between smart building components. Generally, the speed of communication data required for distributed automation and Advanced Metering Infrastructure (AMI) is relatively low.

Network latency

Network latency is defined as the minimum time taken by a message to travel from the transmitting point to the receiving one across the communications system [15]. However, for small distances and local signals, this requirement does not represent a critical issue.

Quality of Service

Quality of service is defined as the capability of performing required measurements with improved transmission rates, error rates, etc. [16]. This guarantees a certain degree of performance for data flow and represents an important issue for smart

building management. Thus, the quality of service has a high priority when selecting the proper communication system.

Frequency Ranges

It is required to have a low frequency range for smart building management to enable radio signals to overcome barriers, e.g., foliage, rains, and walls.

Reliability

Reliability clarifies the operational qualification and degree of instability for the system under study [4]. The use of smart communication and consistent control devices would help in improving grid reliability.

Security

Security represents the capability of the communication system to handle different physical and cyber-attacks to protect data [4]. This is achieved through many tools such as firewall, virtual private network, intrusion detection/prevention systems, and access control systems.

Scalability

Scalability is required due to the use of cooperative devices and services. The dependency on end-user interaction and real-time monitoring increases the importance of scalability [16].

Choice of an appropriate communication network to be compatible with smart buildings and satisfy system requirements is the beginning of the establishment of the infrastructure. The following steps should be applied to guarantee selecting a proper network:

- Investigating the system to identify the required data to be transmitted through communication system
- The number of bytes needed for different messages and the required latency are determent to define the size of data.
- The number of DG units and the number of customers served by the network have to be determined
- The network data rate for the system is calculated using the following relation:

$$\mathrm{DR} = \frac{\mathrm{DS} \times 8 \text{ bits/bytes} \times N_C}{L} \tag{1}$$

where:

NR is the network data rate (bps)
DS is the data size (bytes)
N_C is the number of consumers
L is the required latency (s).

- The required coverage area is determined according to the application

- The suitable network is designated according to the listed factors

3.2 *Distributed Generating Units*

The system may include many DGs in different homes. In addition, some homes may participate in the system without having DGs to purchase electricity and thermal power from neighboring participants. The general structure of any home is illustrated in Fig. 3. This system represents an example for smart homes, while other configurations are also applicable. The introduced methodology can be extended to include any number of homes with any number of DG units. As early mentioned, the use of PV units is out of the scope in this chapter.

PEMFCs are candidate as a type of DGs to be utilized within smart homes to produce heat and power simultaneously due to their advantages such as [17]:

- Low temperature operation (about 65–85 °C) enabling safe operation in residential homes in addition to fast start-up process [18]
- Suitability for hybrid configurations of renewable energy systems especially with wind and photovoltaic [19]
- Possibility of combined heat and power production [20]
- Providing a source for hot water that can be circulated and heated by the exhaust heat of the unit

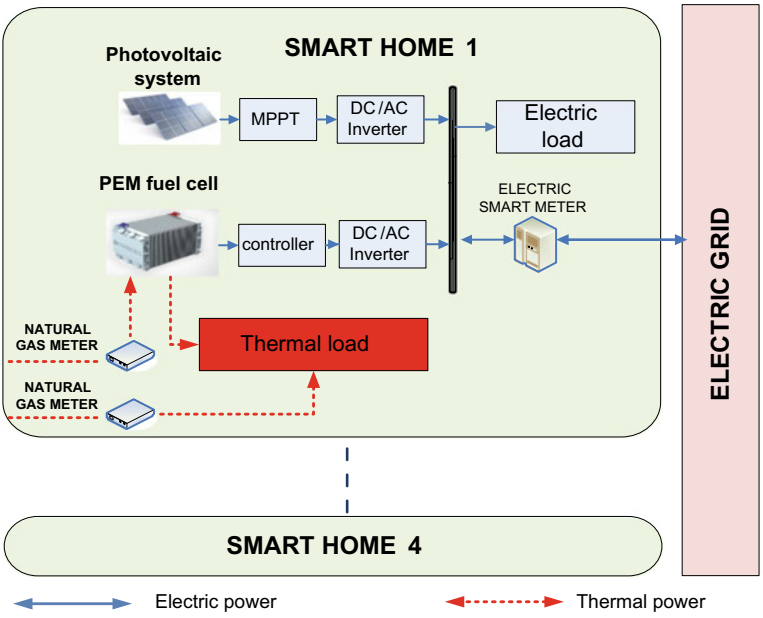

Fig. 3 Different technologies within smart homes

- The output of PEMFCs can vary quickly to meet the load demand, i.e., quick response to load variations
- There is a great development in manufacturing of reformer/PEMFC systems for residential applications
- PEMFCs have high power density, i.e., high power/volume compared to other types except for AFCs [21]
- They have high efficiency reaching 40% at rated current [20]
- Long operating life that can extend to about 40,000 operating hours [17]
- Modularity and potential for simple manufacturing [22]
- Silent operation, where a level of 60 dB at 1 m is recognized, which is suitable for indoor installation [23].

If a PV unit is used, it will depend on maximum power tracking technique for optimal utilization. Unlike PV unit, FCs can produce both electric and thermal energy. According to the shown configuration, the participant homes are connected at the same bus to exchange electric energy between them. On the other hand, adjacent homes can exchange thermal power as well.

4 The Proposed Methodology

This aim of this part is to identify the optimal operating setting of the FC if operated alone without PV modules. This would decrease total operating costs of DGs and provide economic benefits for utility as well as customers. For cooperative operation, it is intended to identify the optimal operating points for all units together. Thus, the optimal setting aims to reduce the overall daily operating cost of all DGs together. However, the algorithm will be applied for a single unit as well as several units. To identify the operating settings of DG units, the following steps are suggested:

- The master controller communicates with different appliances and smart meters to collect and store daily electric and thermal consumptions.
- The master controller sends the collected information to utility's control center to build a complete database of consumptions for all homes to be used in the forecast processes.
- The electricity tariffs in addition to natural-gas prices are received by control center from service vendors.
- The control center identifies the situation of all DG unit contributing in the system
- At the end of the day, the control center forecasts the electric and thermal demands for the next day.
- An optimization process is accomplished according to the objective function in order to obtain the optimal settings of FC units for minimizing the overall daily operating costs for the entire system.
- The optimal settings of FC units are used as reference set points within the smart home.

- The fore mentioned procedures are repeated periodically to update the settings to account for uncertainty.

For flexibility and general formulation, the following assumptions are stipulated:

- Each home has different daily load curves for electric and thermal demands
- The different FCs could have different ratings with their own characteristics and features
- There is a possibility for using different tariffs for purchasing and selling electricity
- There are different tariffs for purchasing natural gas to feed FC and thermal loads.

As a first step, it is assumed that each home operates individually without any communication or coordination with other homes. Generally, there are two obligatory balance equations representing total electrical and thermal power in each home as follows:

The balance equation of total electric power in each home is given as follows [24]:

$$P_{\text{fc(elect.)},i} = P_{\text{load(elect.)},i} + P_{\text{grid},i} \tag{2}$$

where:

$P_{\text{fc(elect.)},i}$: Produced electric power in FC unit at home "i" (kW)
$P_{\text{grid},i}$: Purchased/Sold electric energy from/to the utility in home "i" (kW)
$P_{\text{load(elect.)},i}$: Electric load demand in home "i" (kW).

The second balance equation belongs to total thermal power as follows:

$$P_{\text{fc(therm.)},i} + P_{\text{ng},i} = P_{\text{load(therm.)},i} + P_{\text{excess}} \tag{3}$$

where:

$P_{\text{fc(therm.)},i}$: Output thermal power from FC in home "i" (kW)
$P_{\text{ng},i}$: Thermal power through direct burning of natural gas in home "i" (kW)
$P_{\text{load(therm.)},i}$: Thermal power of home "i" (kW)
P_{excess}: The surplus thermal power that is stored as hot water or dissipated.

These conditions guarantee satisfying the load demands from either DGs or grid system and burners.

5 Development of PEMFC Economic Model

The problem has to be formulated in the form of an objective function that will be solved subject to a number of constraints.

5.1 Objective Function

In general, the objective function should consider all factors affecting the optimal decisions of the DG output power. It can be derived as a daily operating cost of the home through one day "$C_{(\mathrm{TOTAL})}$" that is developed in terms of costs and revenues. The costs include natural-gas price for feeding FC and thermal load, purchased electric energy from the utility, start-up cost of FC, and maintenance cost. On the other hand, revenues represent income due to sold electric energy to the utility. The overall daily operating cost is derived in the following form [25]:

$$C_{\mathrm{TOTAL}} = C_{\mathrm{NGFC},i} + C_{\mathrm{NGRL},i} + C_{\mathrm{purc},i} - C_{\mathrm{sold},i} + C_{\mathrm{o\&}m\mathrm{fc},i} + \mathrm{SC}_i \tag{4}$$

where:

C_{TOTAL}: The overall daily operating cost of home "i" ($/day)
$C_{\mathrm{NGFC},i}$: Overall daily natural-gas cost for FC at home "i" ($/day)
$C_{\mathrm{NGRL},i}$: Overall daily natural-gas cost to supply the remaining thermal power in home "i" ($/day)
$C_{\mathrm{purc},i}$: Overall daily cost of obtained electrical power for home "i" ($/day)
$C_{\mathrm{sold},i}$: Overall daily revenue due to sold electrical power from home "i" ($/day)
$C_{\mathrm{o\&}m\mathrm{fc},i}$: Overall daily operating and maintenance cost of FC at home "i" ($/day)
SC_i: Daily start-up cost of FC unit in home "i" ($/day).

The details of the objective function terms are described as follows:

$$C_{\mathrm{NGFC},i} = T_{\mathrm{ng-fc}} \times \Delta T \sum_{J=1}^{96} \frac{P_{J,i} + P_{\mathrm{aux},i}}{\eta_{J,i}} \tag{5}$$

$$C_{\mathrm{NGRL},i} = T_{\mathrm{ng-rl}} \times \Delta T \sum_{J=1}^{96} \max\left(L_{\mathrm{th},J,i} - p_{\mathrm{th},J,i}, 0\right) \tag{6}$$

where:

$T_{\mathrm{ng-fc}}$: Natural-gas tariff for supplying FC ($/kWh)
ΔT: Time interval between two sequential settings of FC (h)
$P_{J,i}$: FC electrical power in home "i" at interval "J" (kW)
$P_{\mathrm{aux},i}$: Electrical power consumed by auxiliary devices of FC at home "i" (kW)
$\eta_{J,i}$: FC electrical efficiency in home "i" at interval "J"
$T_{\mathrm{ng-rl}}$: Natural-gas tariff to feed thermal loads ($/kWh)
$L_{\mathrm{th},J,i}$: Thermal power of home "i" at interval "J" (kW)
$P_{\mathrm{th},J,i}$: FC thermal power in home "i" at interval "J"(kW).

$$C_{\text{sold},i} = T_{\text{el}-s} \times \Delta T \sum_{J=1}^{96} \max\left(P_{J,i} - L_{\text{el},J,i}, 0\right) \tag{7}$$

$$C_{\text{purc},i} = T_{\text{el}-p} \times \Delta T \sum_{J=1}^{96} \max\left(L_{\text{el},J,i} - P_{J,i}, 0\right) \tag{8}$$

where:

$T_{\text{el}-s}$: Purchased electricity Tariff ($/kWh)
$T_{\text{el}-p}$: Sold electricity tariff ($/kWh)
$P_{\text{el},J,i}$: Electric power supplied by DG units at home "i" at interval "J" (kW)
$L_{\text{el},J,i}$: Electrical power of home "i" at interval "J" (kW)
ΔT: Time interval between two successive settings of the FC; 15 min.

$$C_{o\&m\text{fc},i} = \text{FC}_{o\&m} \times \Delta T \sum_{J=1}^{96} P_{J,i} \tag{9}$$

$$\text{SC}_\text{i} = €_\text{i} + \varphi_\text{i}\left(1 - \text{e}^{\frac{-\text{T}_{\text{off,i}}}{\tau_\text{i}}}\right) \tag{10}$$

where:

FC $_{o\&m}$: Daily operation and maintenance constant of FC unit: 0.003$/kWh [17]
$€_i$: Hot start-up cost of FC at home "i"
$€_\text{I} + \varphi_i$: Cold start-up cost of FC at home "i"
T_{off}: The time duration, where the FC unit at home "i" is off (h)
τ: Cooling time constant of the FC at home "i" (h).

In the previous equations, the time interval between two successive FC settings is assumed to be 15 min. In addition, the O&M constant of PEMFC is taken as 0.003$/kWh [17].

The power needed to supply supplementary devices could be assumed constant in spite of the produced power because its variation is limited. Thus, it can be taken in the range of 4%–6% of the unit rated power in all cases. Conversely, the FC efficiency varies with the operating power. This efficiency is defined as the ratio between the produced power from the unit to the available energy contained in the natural gas. Generally, the FC efficiency is calculated in terms of two voltages in the cell. The first one is the actual operating voltage of a single cell that depends on the operating point, while the second is the reversible potential (with a standard value of 1.482 V) [26, 27]. On the other hand, the global efficiency of the FC takes into account the power required by supplementary devices such as pups that reduce the output power.

Figure 4 illustrates typical curves that characterize the FC efficiencies, i.e., the ideal theoretical and the actual efficiencies [26, 27]. In the following calculations, the typical actual efficiency curve is used in terms of the produced electric power,

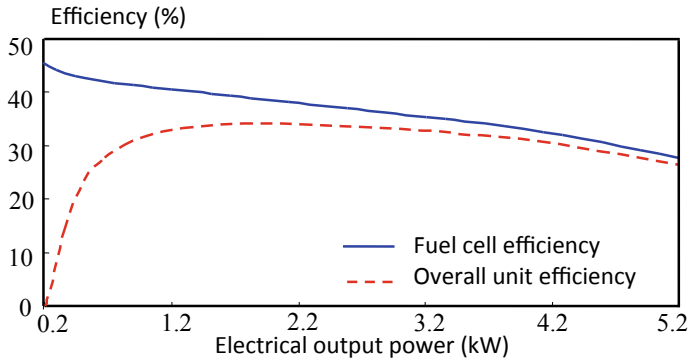

Fig. 4 Standard efficiency curves of FC system

where the efficiency is calculated depending on the electric power at the operating point.

The thermal energy produced in the FC units depends on the value of the produced electric energy. The electrochemical process in the stack produces thermal energy that can be extracted using, e.g., circulating water mechanism with suitable management system. The nature of the relation between thermal and electrical energy is almost linear for small generated power. However, there will be a curvature in the relation for higher produced power. The thermal power could be a little bit higher than the electrical power in some kinds of FCs [28]. For FCs operating at low temperatures such as PEMFC, the value of electrical efficiency is relatively lower than other high-temperature types, but more thermal power is obtained as shown in Fig. 5. On the other hand, for high-temperature FCs, this relation is reversed with thermal power lower than the produced electrical power.

Generally, the ratio between thermal power and the electrical produced power can reach 150% near the rated produced power [26–28]. To simulate this relation

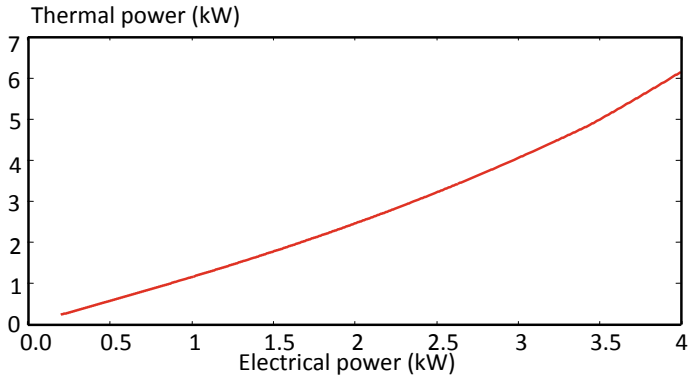

Fig. 5 Standard dependency of thermal power on electrical power of PEMFC

in the economic model, a nonlinear relation has to be developed according to any methodology such as curve fitting. Thus, the thermal output power could be obtained point-by-point at each time interval with the variation of the produced electrical power.

After calculating the thermal power at each time interval, it can be used directly in the equations describing the daily cost of obtained natural gas for residential burners as described by Eq. (6).

5.2 Constraints Formulation

The FC operation is restricted by many constraints. Generally, the following constraints can be activated to ensure proper operation of the system [29]:

$$\text{Upper and lower capacity constraint}: \quad P_{\min,i} \leq P_i \leq P_{\max,i} \tag{11}$$

$$\text{Constraint of up ramp rate}: \quad P_{J,i} - P_{J-1,i} \leq \Delta P_u \tag{12}$$

$$\text{Constraint of down ramp rate}: \quad P_{J-1,i} - P_{J,i} \leq \Delta P_D \tag{13}$$

When the FC unit is switched on, it is not allowed to be switched off before a certain minimum time and vice versa. These constraints can be derived in the form of continuous running/stop time constraint as follows:

$$\left(T_{t-1}^{\text{on}} - \text{MRT}\right) \cdot \left(U_{s,t-1} - U_{s,t}\right) \geq 0 \tag{14}$$

$$\left(T_{t-1}^{\text{off}} - \text{MST}\right) \cdot \left(U_{s,t} - U_{s,t-1}\right) \geq 0 \tag{15}$$

The maximum number of start/stop cycles per day of the PEMFC unit has to be maintained within an acceptable level as follows:

$$n_{(\text{start}-\text{stop}),i} \leq N_{\max,i} \tag{16}$$

where:

$P_{\min,i}$: Minimum value of produced power from PEMFC at home "i"
$P_{\max,i}$: Maximum value of produced power from PEMFC at home "i"
ΔP_u: The upper boundary of ramp rate
ΔP_D: The lower boundary of ramp rate
$P_{J-1,i}$: The power generated by the FC in home "i" at time interval "$J-1$"
$P_{J,i}$: The power generated by the FC unit in home "i" at time interval "J"

T_{t-1}^{on}, T_{t-1}^{off}: the durations of continuous PEMFC run and stop till time interval "$t-1$" respectively (h)
MRT, MST: minimum continuous run and stop durations of the PEMFC, respectively (h)
Us: the situation of unit operation, i.e., ON/OFF, where Us = 1 refers to running status, while Us = 0 refers to stop status
$n_{(\text{start}-\text{stop}),i}$: The number of start/stop cycles per day of the PEMFC unit at home "i"
$N_{\max,i}$: Maximum number of start/stop cycles per day permissible for the PEMFC unit at home "i".

The detailed parameters that can be used in the previous equations to develop the comprehensive economic model of the FC unit are summarized in Appendix A.

6 Selection of Optimization Technique and Results

For the purpose of solving the developed minimization problem in an optimization form and getting the required optimal settings of PEMFC unit, a robust metaheuristic algorithm is required. Examples of these algorithms are: Particle Swarm, shuffled frog leaping, Ant colony, and simulated annealing. The reason for using such algorithms is the discontinuous nature of the optimization problem. Regardless of the optimization tool, the obtained optimal settings of the FC will be sent through the master controller as reference values for the local controller(s) for the overall day. These settings will ensure minimum total daily operating cost for the whole system. Figure 6 shows the flowchart of the management process.

Figures 7 and 8 show two cases for the expected optimal output power from FC for two cases: For the first case, there is no possibility for selling electricity to the utility, while the extra power from the FC is sold to the grid in the second case.

In the first case, the FC does not produce electrical power that exceeds the load demand because the extra power cannot be sold to the grid. Contrary, the FC produces more electrical power in the second case that covers the load demand and the remaining is sold to the main grid system. The main idea here is to understand the effect of pool market and deregulation on the future homes and the need for customers encouragement to participate in electricity generation. However, this is conditioned by converting the classical grid into smart one and designing suitable tariffs through demand side management strategies.

For more understanding of the effect of these tariffs, the effect of changing selling electricity tariff is highlighted by illustrating an example. Figure 9 illustrates the impact of changing the tariff related to sold electricity alone with all other tariffs are maintained constant. As can be expected, the increase of sold electricity tariff causes the FC to increase its electricity production up to the rated value. For the case of a low value of sold-electricity tariff, the PEMFC unit tracks the electrical demand of the load. For intermediate rates of the sold-electricity tariff, the optimal output

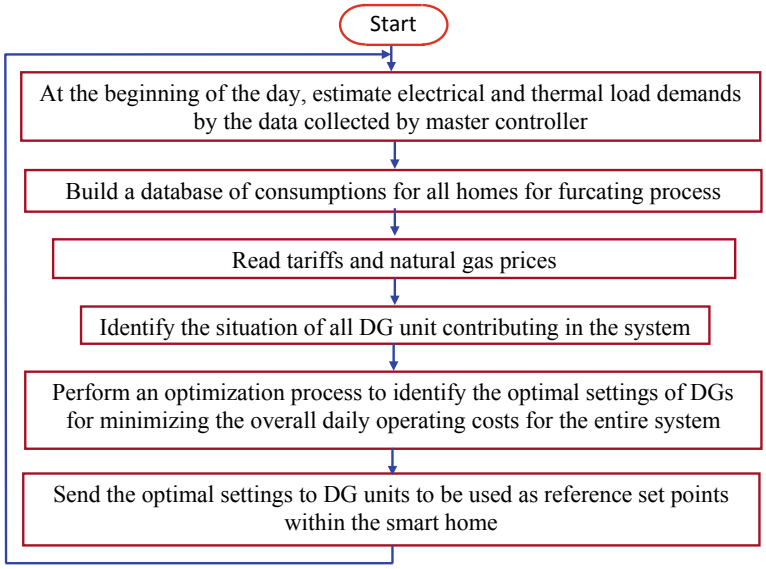

Fig. 6 Flowchart of the proposed management procedures

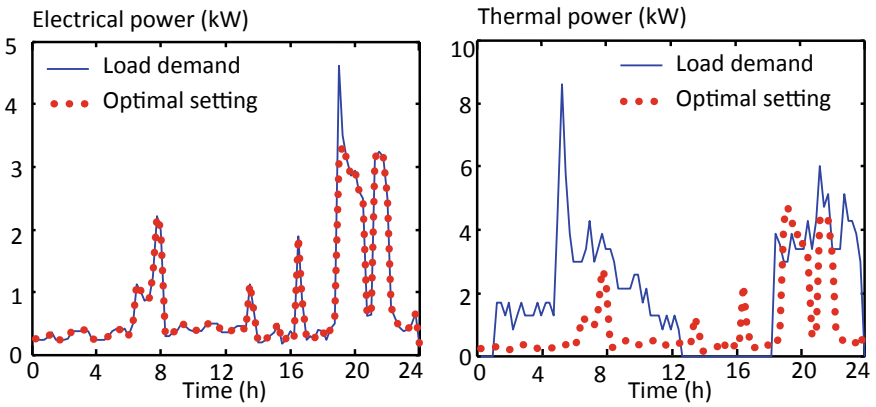

Fig. 7 Optimal produced power from the FC without selling electricity

power from the FC tracks the thermal load demand with the possibility of selling the excess of electrical power to the utility. For the case of high rates for sold-electricity tariff, the owners of the FC unit can achieve more profit for the sold electricity and, hence, high produced power is observed over the entire day. Even with the wasted thermal energy that exceeds the load demand, the sold electrical power compensates this loss and causes higher profits.

It is possible for the optimal setting of FC to prefer not to operate the unit during some periods of the day. This is clear through illustrating the following example with

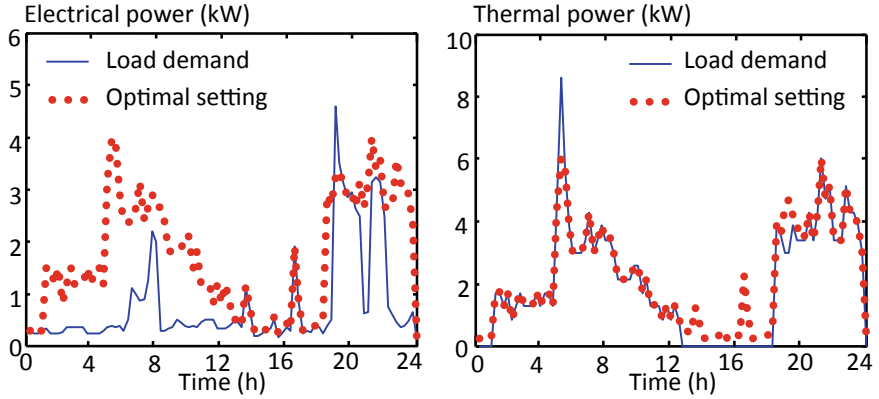

Fig. 8 Optimal produced power from the FC when selling electricity

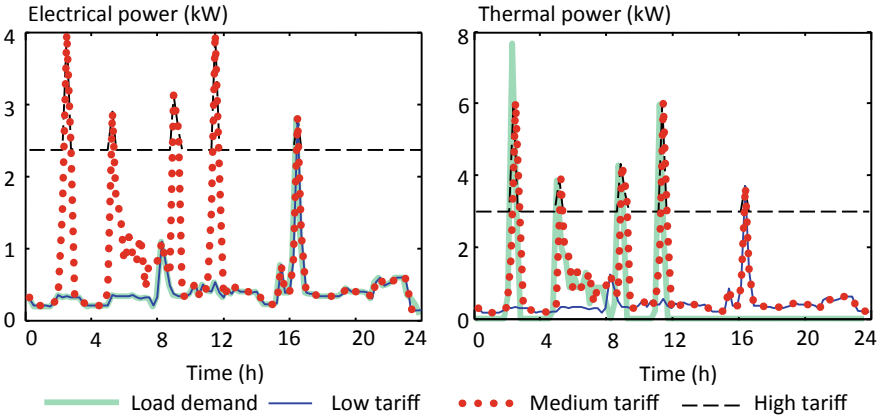

Fig. 9 Impact of changing the tariff of sold electricity

changing the natural-gas tariff. Varying the natural-gas tariff for feeding the FC has the impact confirmed in Fig. 10.

The successive start/stop cycles of FC cause higher stresses and, hence, these situations are avoided. The priority is given for running or shut down for certain periods as in the previous case, where the FC is switched off for 12 h in case of high natural-gas price, i.e., high tariff. Due to the high tariff of natural gas, it is not preferred to operate the FC for prolonged periods.

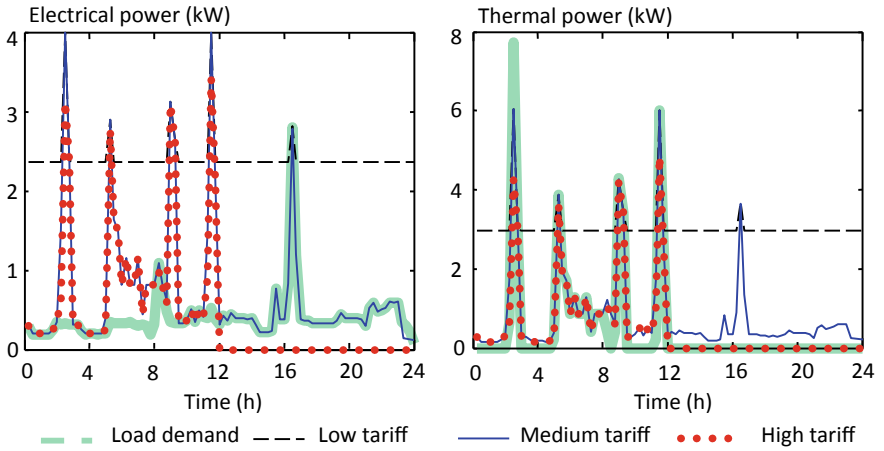

Fig. 10 Impact of changing tariff of natural gas for feeding FC

7 Management of Multi-DGs Simultaneously

It is possible for any FC to operate at partial load to provide low power for prolonged periods according to the economic situation. Although this decision is obtained from the optimization algorithm, better economic operation could be achieved with multi-DG units when operating in cooperation between them. Therefore, it is suitable to study the case of utilizing small units that could be installed in different homes in the smart building. The following case will consider three identical units with a total equivalent capacity similar to the required electric and thermal load demand. The configuration of the residential system when "*n*" units are used is shown in Fig. 11.

The idea behind this configuration can be explained as follows:

- One unit could be used when low power is required in the building and the other units are used when required.
- A communication system is used to regulate the performance of FC units according to the load demand and the tariffs of electricity and natural gas.
- A protocol is established between the customers to handle the energy exchange between them to achieve win–win situation.
- Smart meters are installed to account for the power consumed by each home to calculate the cost of both electrical and thermal energy.
- The generated electrical and thermal power from each FC is computed and the corresponding cost of energy is derived.

Some modifications are required to be implemented on the optimization mathematical model to handle the management process between "*n*" FC units. For instance, and as it is assumed that the time interval between two successive decisions for the FC output is 15 min, the number of unknowns in the case of a single FC is 96. For three units, this number will be 288 unknown variables, where 96 unknowns belong

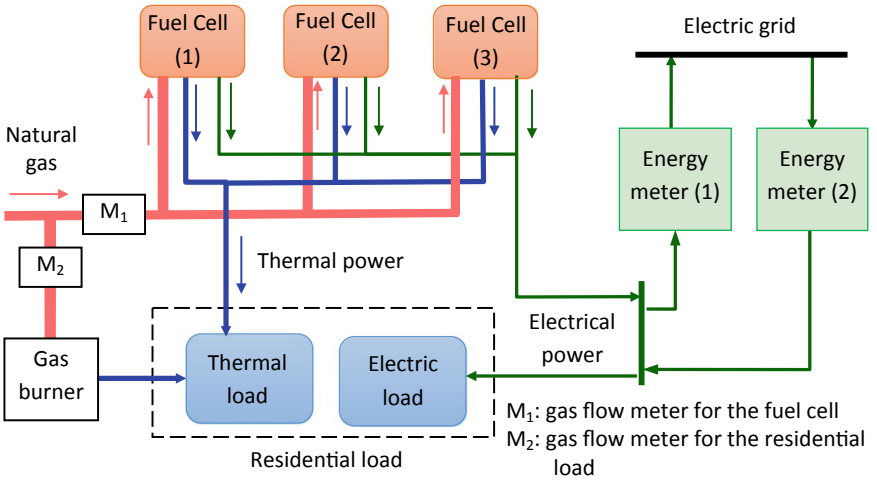

Fig. 11 Construction of a residential system supplied by (n) PEMFCs

to each unit. Generally, the total number of unknowns is given as:

$$\mathrm{NU} = \frac{24 \times 60}{\Delta T} \times N \tag{17}$$

where:

NU: is the number of unknowns
N: is the number of FC units
ΔT: is the time interval between two successive decision of FC output (min) 24 × 60 represents the total day time (min).

The balance equations representing total electrical and thermal power in the system are also modified as follows:

The balance equation of overall electric power in the entire system is given as:

$$\sum_{i=1}^{N} P_{\mathrm{fc(elect.)},i} = \sum_{i=1}^{n} \left(P_{\mathrm{load(elect.)},i} + P_{\mathrm{grid},i} \right) \tag{18}$$

where:

n: Number of residential homes included in the study.

The total thermal power in the system is given as:

$$\sum_{i=1}^{N} P_{\mathrm{fc(therm.)},i} + \sum_{i=1}^{n} P_{ng,i} = \sum_{i=1}^{N} P_{\mathrm{excess}} + \sum_{i=1}^{n} P_{\mathrm{load(therm.)},i} \tag{19}$$

Note that the number of FCs "N" may be different from the number of homes in the building "n".

The modification in the objective function is carried out as:

$$C_{\text{TOTAL}} = \sum_{i=1}^{N} \{C_{\text{NGFC},i} + C_{o\&m\text{fc},i} + SC_i\} + \sum_{i=1}^{n} \{C_{\text{NGRL},i} + C_{\text{purc},i} - C_{\text{sold},i}\} \tag{20}$$

The complete daily cost is obtained according to the sum of supplied electrical and also thermal power obtained from all FC units, the overall electrical and thermal demands by loads and the overall purchased and sold electric energy. According to this strategy, the target is directed to the overall costs and revenues rather that the values of individual units. Applying some cooperative strategies, such as game theory, can help in allocating the costs and revenues for each participant. The parameters used in the economic model for the case of multi-FCs used in the smart building are summarized in Appendix B.

In the following, some results will be illustrated for three different cases. The modification in the three cases is only in the operating tariffs to show their effects on the optimal decisions. Table 1 gives the values of tariffs used in the study in the three cases. In addition, the corresponding overall operating costs are given in case of feeding the load using a single FC unit to compare the results of this case with the case of using three FC units.

The optimization process can be carried out using various load-demand curves and different operating tariffs according to the market situation. Figures 12, 13 and 14 show the optimal produced electrical power from the three FC units, as an example, as well as the overall electrical and thermal power to feed a selected load curve in the three cases. The obtained values of electrical and thermal produced power, as obtained for the optimal settings of a single FC, are also depicted in the same figures.

Table 1 Various tariffs and the related overall operating costs with optimal settings of a single as well as three FCs to feed a residential load

	C_{NGFC}(\$/kWh)	C_{NGRL}(\$/kWh)	C_{purc}(\$/kWh)	C_{sold}(\$/kWh)	Overall operating cost (\$/day)	
					One unit	Three units
Case (1)	0.03	0.07	0.16	0.1	1.834	1.589
Case (2)	0.03	0.09	0.16	0.0	4.254	3.428
Case (3)	0.03	0.05	0.12	0.0	3.783	3.395

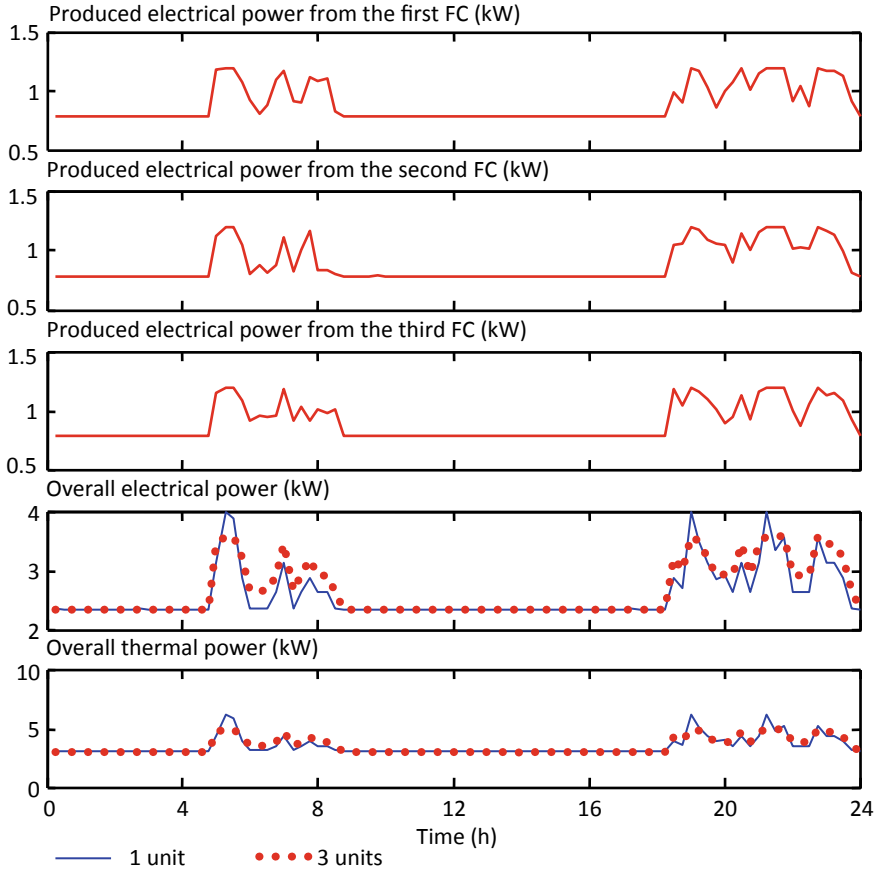

Fig. 12 Optimal performance of three and one fuel cells: first case

It is important to notice that the same load demands under identical operating conditions are used in the case of a single and three FC units. Thus, it will be easy to compare between the obtained results to evaluate the utilization of a single and a number of units in a cooperative manner.

The total electrical and thermal supplied powers from three FCs are similar to the produced power from a single FC with small differences. This reflects the tendency of the produced power under certain conditions to supply a certain load. In addition, the similarity proves the success of the optimization process to provide similar overall performance regardless of the number of DG units used to supply the load. However, it is clear that the production of each unit varies according to the variation of load demand during the day in addition to the operating tariffs. During some periods, one or two units are not operated, where the required power is obtained from one unit only. In other cases, some units operate for short periods to meet the load during peak-load time. In general, when using multi-units, they operate near rated values,

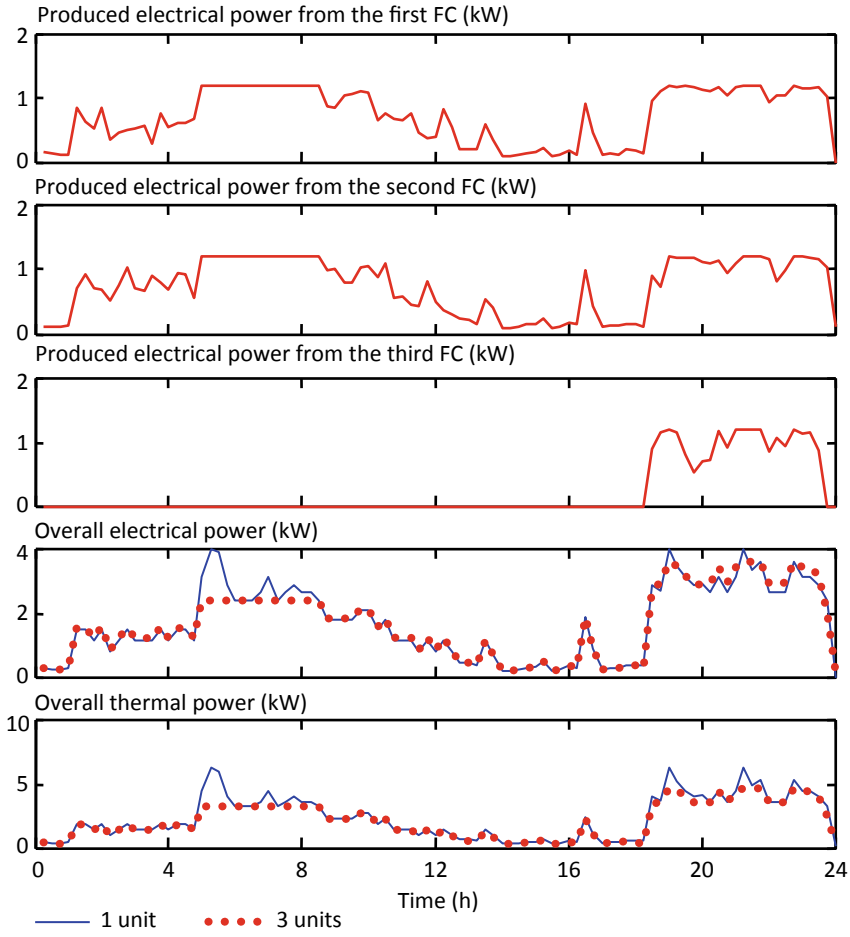

Fig. 13 Optimal performance of three and one fuel cells: case (2)

which provide a privilege for this strategy compared to the use of a single generating unit.

On the other hand, the operation of a single unit gives the possibility for operating at low power for long periods. For many DGs, this would shorten the life time of the unit and reduce the overall efficiency.

The overall daily operating costs of utilizing a single unit are higher than utilizing three FCs. This is attributed to the flexibility of operating one, two, or three units avoiding the production of thermal power when not required. Thus, the cooperation of the owners within same smart buildings can achieve more benefits and reduce the overall cost. However, a demand-side management strategy has to be followed to encourage participation for energy production in smart buildings.

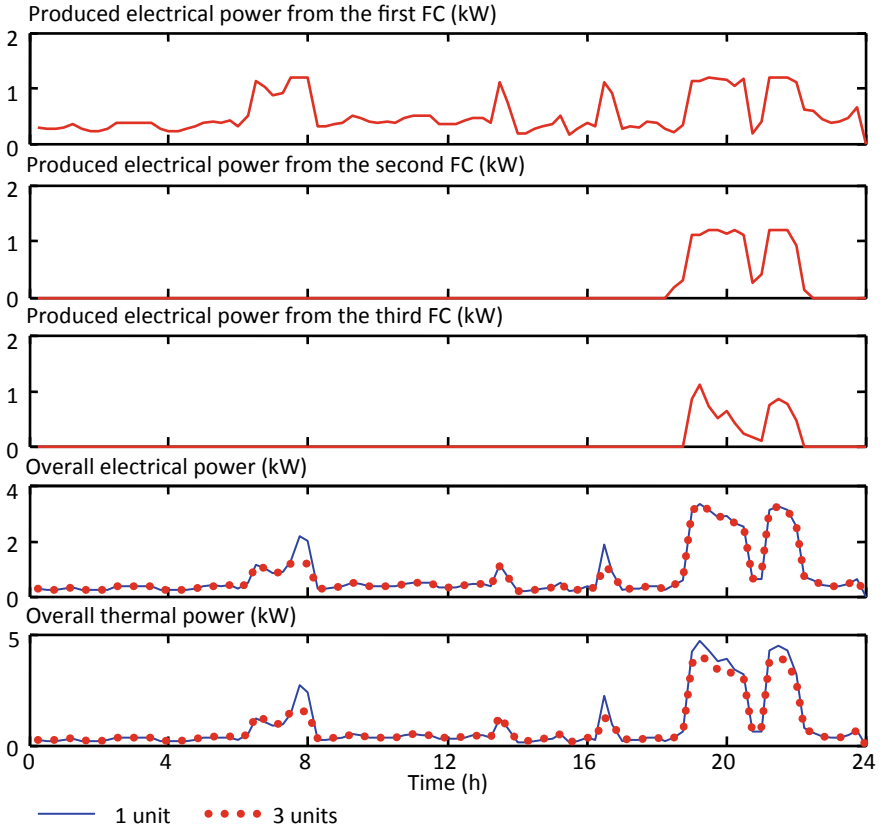

Fig. 14 Optimal performance of three and one fuel cells: case (3)

Another advantage of utilizing many DGs is avoiding the loss of thermal energy produced from a single unit. As seen from the results, the FC, as an example, produces thermal power more than the load requirement in many situations. This represents a loss for the system because the storage of thermal power is a difficult task. In the case of using many units, it is possible to exchange the surplus thermal power with adjusting customers that increases the energy utilization and reduces overall cost.

8 Summary

This chapter presented an approach for managing the operation of FCs for smart buildings. This step reinforces the demand-side management that will contribute in the near future in supporting the main grid system. The idea depends on minimizing the overall costs by optimizing the settings of PEMFCs for residential applications.

According to pool-market strategies, there will be possibility for purchasing or selling electric power for different tariffs. An optimization process is performed considering different operating tariffs and load curves to minimize the overall daily cost. The performances of a single and multi-FC units are managed optimally based on detailed economic models. Investigating the attained results confirmed a significant decrease in the daily operating costs after applying the management process. This would encourage customers to participate in demand-side management strategies after enhancing the economic feasibility of used DG units. The coordination between customers can help in achieving more benefits and win–win situations when applying management strategies for all DG units at the same time.

Appendix A

The following Table gives the Fuel cell parameters used in the economic model of a single unit.

	Value	Unit
$K_{O\&M}$	0.005	\$/kWh
MST	1.5	h
MRT	1.5	h
$N_{\max}$	4.0	–
P_a	0.2	kW
$P_{\max}$	4.0	kW
$P_{\min}$	0.2	kW
α_h	0.05	\$
β	0.15	\$
ΔP_U	8.0	kW/h
ΔP_D	10.0	kW/h
τ	0.75	h

The relationship linking FC efficiency with the produced electrical power is given as follows:

$$h_J = 0.4485 - 0.0536\ P_J + 0.0127\ P_J^2 - 0.001824\ P_J^3.$$

The relationship linking Fc thermal power with the produced electrical power is given as follows:

$$P_{\text{th},J} = -0.0714 + 1.152\ P_J - 0.0237\ P_J^2 + 0.0443\ P_J^3 - 0.00373\ P_J^4$$

Appendix B

Fuel cells parameters used in t economic model of three units

The parameters are the same for the three units assuming that they are identical.

	Value	Unit
$K_{O\&M}$	0.005	\$/kWh
MDT	1.5	h
MUT	1.5	h
$N_{\max}$	4.0	–
P_a	0.08	kW
$P_{\max}$	1.35	kW
$P_{\min}$	0.1	kW
α_h	0.02	\$
β	0.06	\$
ΔP_U	4.0	kW/h
ΔP_D	5.0	kW/h
τ	0.5	h

The relationship linking FC efficiency with the produced electrical power is given as follows:

$$\eta_J = 0.448 - 0.1608\ P_J + 0.114\ P_J^2 - 0.049073\ P_J^3$$

The relationship linking FC thermal power with the produced electrical power is given as follows:

$$P_{\text{th},J} = -0.02073 + 1.05\ P_J - 0.0617\ P_J^2 + 0.341\ P_J^3 - 0.08754 P_J^4$$

References

1. Y. Li, W. Gao, X. Zhang, Y. Ruan, Y. Ushifusa, F. Hiroatsu, Techno-economic performance analysis of zero energy house applications with home energy management system in Japan. Energy Build. **214**, 109862 (2020)
2. A. Mostafaeipour, H. Rezayat, M. Rezaei, A thorough investigation of solar-powered hydrogen potential and accurate location planning for big cities: a case study. Int. J. Hydrogen Energy **45**(56), 31599–31611 (2020)
3. M. Roozbeh, G.S. Thirunavukkarasu, M. Seyedmahmoudian, A. Stojcevski, R. Kowalczyk, A relaxed constrained decentralised demand side management system of a community-based residential microgrid with realistic appliance models. Appl. Energy **277**, 115626 (2020)

4. A. Azari, Survey of smart grid from power and communication aspects. Middle-East J. Sci. Res. **9**, 1512–1519 (2014)
5. O. Kai, W.W. Yuan, Y.B. Kim, Development of optimal energy management for a residential fuel cell hybrid power system with heat recovery. Energy **219**, 119499 (2021)
6. H. Mehrjerdi, Peer-to-peer home energy management incorporating hydrogen storage system and solar generating units. Renew. Energy **156**, 183–192 (2020)
7. H.S. Ryu, M.K. Kim, Article two-stage optimal microgrid operation with a risk-based hybrid demand response program considering uncertainty. Energies **13**, 6052 (2020)
8. M.S. Javadi, M. Gough, M. Lotfi, A.E. Nezhad, S.F. Santos, J.P.S. Catalão, Optimal self-scheduling of home energy management system in the presence of photovoltaic power generation and batteries. Energy **210**, 118568 (2020)
9. W. Chong, Z. Zhang, O. Abedinia, S.G. Farkoush, Modeling and analysis of a microgrid considering the uncertainty in renewable energy resources, energy storage systems and demand management in electrical retail market. J. Energy Storage **33**, 102111 (2021)
10. A. Jerzy, J. Lorenc, A. Weychan, Price-based demand side response programs and their effectiveness on the example of TOU electricity tariff for residential consumers. Energies **14**(2), 287 (2021)
11. W. Wang, Y. Xu, M. Khanna, A survey on the communication architectures in smart grid. Comput. Netw. **55**, 3604–3629 (2011)
12. S. Marzal, R. Salas, R.G. Medina, G. Garcerá, E. Figueres, Current challenges and future trends in the field of communication architectures for microgrids. Renew. Sustain. Energy Rev. **82**, 3610–3622 (2018)
13. A. Kailas, V. Cecchi, A. Mukherjee, A survey of communications and networking technologies for energy management in buildings and home automation. J. Comput. Netw. Commun. **6**, 2090–7141 (2012)
14. T.G. Mussi, L.B. Campos, C.E. Cugnasca, Home automation networks: a survey. Comput. Stand. Interf. **50**, 42–54 (2017)
15. V.C. Gungor, D. Sahin, T. Kocak, S. Ergut, C. Buccella, C. Cecati, G.P. Hancke, A survey on smart grid potential applications and communication requirements. IEEE Trans. Industr. Inf. **9**(1), 28–42 (2013)
16. N.M.R. Yaghoubi, H.H. Dezaki, A.H. Niasar, Optimal stochastic scenario-based allocation of smart grids' renewable and non-renewable distributed generation units and protective devices. Sustain. Energy Technol. Assess. **44**, 101033 (2021)
17. ONSITE SYCOM Energy Corporation, Review of Combined Heat and Technologies Power Technologies. The U.S. Department of Energy, Office of Energy Efficiency and Renewable Energy (1999)
18. D.H. Nguyen, T. Ishihara, Distributed peer-to-peer energy trading for residential fuel cell combined heat and power systems. Int. J. Electr. Power Energy Syst. **125**, 106533 (2021)
19. W Li, Modeling, control and simulation of a small photovoltaic fuel cell hybrid generation system. Int. Conf. Comput. Intell. Softw. Eng. 1–6 (2009)
20. Energy and Environmental Analysis Inc. group, Technology Characterization: Fuel Cells. Arlington, Virginia (2008)
21. A. Alaswad, A. Omran, J.R. Sodre, T. Wilberforce, G. Pignatelli, M. Dassisti, A. Baroutaji, A.G. Olabi, Technical and commercial challenges of proton-exchange membrane (PEM) fuel cells. Energies **14**(1), 144 (2021)
22. D. Nong, C. Wang, A.Q. Al-Amin, A critical review of energy resources, policies and scientific studies towards a cleaner and more sustainable economy in Vietnam. Renew. Sustain. Energy Rev. **134**, 110117 (2020)
23. FuelCells.org. fuel Cells 2000-Benfites. http://www.fuelcells.org/base.cgim?template=benefits (2015)
24. M.A. Mosa, A.A. Ali, Energy management system of low voltage dc microgrid using mixed-integer nonlinear programing and a global optimization technique. Electr. Power Syst. Res. **192**, 106971 (2021)

25. M. Ghorbanian, S.H. Dolatabadi, P. Siano, Game theory-based energy-management method considering autonomous demand response and distributed generation interactions in smart distribution systems. IEEE Syst. J. (2020)
26. H.Q. Nguyen, B. Shabani, Proton exchange membrane fuel cells heat recovery opportunities for combined heating/cooling and power applications. Energy Convers. Manage. **204**, 112328 (2020)
27. J. Wang, H. Wang, Y. Fan, Techno-economic challenges of fuel cell commercialization. Engineering, **4**(3), 352–60 (2018)
28. J. Renau, V. García, L. Domenech, P. Verdejo, A. Real, A. Giménez, F. Sánchez, A. Lozano, F. Barreras, Novel use of green hydrogen fuel cell-based combined heat and power systems to reduce primary energy intake and greenhouse emissions in the building sector. Sustainability **13**(4), 1776 (2021)
29. Y. Gad, H. Diab, M. Abdelsalam, Y. Galal, Smart energy management system of environmentally friendly microgrid based on grasshopper optimization technique. Energies **13**(19), 5000 (2020)

Smart Inverters and Controls for Grid-Connected Renewable Energy Sources

Mohd. Hasan Ali and Naga Lakshmi Thotakura

Abstract This chapter describes the concept of smart inverters and their control strategies for the integration of renewable energy sources (RES) such as solar photovoltaic (PV), wind turbine generators, and fuel cell (FC) systems into the power grid. The necessity of an inverter in RES systems and the types of inverters according to their operational roles in grid-connected mode are described. Mathematical modeling of RES systems is described. The selection parameters criteria of the inverter, its control technique, and switching techniques are discussed. The role of smart inverters in renewable applications with the grid-support functions is reviewed. Three types of grid-interacting inverters are compared, and their control schemes are discussed. Various inner-loop controllers used at the primary control level are classified, and their operating methods are discussed. The advantages and disadvantages of the described inner-loop control techniques are summarized. The simulation diagram and results of a three-phase grid-connected solar PV system are shown in the chapter.

Keywords Grid-connected renewable energy sources · Smart inverter · Distributed energy sources · Grid-feeding converters · Inner-loop current control · Voltage regulation · Frequency regulation

List of Symbols

V	Voltage (V)
f	Frequency (Hz)
P	Active power
Q	Reactive power
V_g	Grid voltage

M. H. Ali (✉) · N. L. Thotakura
The University of Memphis, Memphis, TN 38152, USA
e-mail: mhali@memphis.edu

N. L. Thotakura
e-mail: nlthtkra@memphis.edu

S. K. Das et al. (eds.), *Advances in Control Techniques for Smart Grid Applications*,
https://doi.org/10.1007/978-981-16-9856-9_8

I_{g}	Grid current
t	Time period (s)
$p.u$	Per unit
P_{rated}	Rated active power (KW)
P_{max}	Maximum power
V_{max}	Maximum voltage
P_{min}	Minimum active power (W)
I_{rms}	Root-mean-square of the DER current
I_{rated}	DER unit rated current capacity
I_{l}	Fundamental current measured at the reference point
h	Individual harmonic order
E_{mg}	Microgrid voltage measured at PCC
ω_{mg}	Microgrid frequency measured at PCC
ΔE	Error voltage
$E*$	Reference voltage of the microgrid
$\Delta\omega$	Error frequency
$\omega*$	Reference frequency of the microgrid
$u_{\mathrm{pi}}(t)$	Output response of the PI controller
$u_{\mathrm{pid}}(t)$	Output response of the PID controller
$u_{\mathrm{pR}}(t)$	Output response of the PR controller
K_{p}	Gain of the proportional controller
K_{i}	Gain of the integral controller
K_{d}	Gain of the derivative controller
$\mathrm{PE}_{\mathrm{pv}}$	Power error of the PV system
PE_{w}	Power error of the wind system
$\mathrm{CPE}_{\mathrm{pv}}$	Change in power error of the PV system
$\mathrm{CPE}_{\mathrm{w}}$	Change in power error of the wind system
P_{array}	Total power of the PV array
P_{m}	Power of each PV module
N_{p}	PV cells connected in parallel in an PV module
N_{s}	PV cells connected in series in an PV module
I_{ph}	Each PV module photo current
I_{scr}	Short circuit current of the cell
T	Temperature in Kelvins (K)
S_{irrd}	Solar irradiation on the cell (mW/cm^2)
K_i	Temperature coefficient of cell's short circuit current
I_{rs}	PV module reverse saturation current
q	Charge of an electron
E_g	Bandgap energy
A	Diode ideality factor
K	Boltzmann's constant [J/K]
T_{r}	Cell referred temperature
I_o	Module saturation current
I_{pv}	Output current of a PV cell
V_{pv}	Output voltage of a PV cell

P_{pv}	Power of a PV cell
T_{pv}	Temperature of a PV cell
R_{se}	Series resistance of a cell
R_{sh}	Shunt resistance of a cell
P_{w}	Mechanical power of a wind turbine
A_w	Rotor blades intercepting area (m^2)
V_{w}	Average wind speed (m/s)
ρ	Air density (kg/m^3)
λ	Tip speed ratio
C_p	Power coefficient (or) Betz's coefficient
ω_r	Angular speed (rad/s)
Q_{w}	Wind energy (KWh)
R_{w}	Radius of the wind turbine (m)
h_{ref}	Reference height of wind turbine (m)
h	Height of the turbine to be measured
h_o	Measure of surface roughness
$v(h)$	Wind speed at height h (m/s)
$v(h_{\text{ref}})$	Wind speed at reference height h (m/s)
V_{Cin}	Cut-in wind speed
V_{Cout}	Rated wind speed
V_{RCout}	Rated cut-out speed
k	Weibull form factor
ω_{opt}	Optimum rotor angular speed (rad/s)
λ_{opt}	Ideal tip speed ratio
V_{FC}	Output voltage of single fuel cell
E_{Nerst}	Standard reversible voltage
V_{Act}	Voltage drop due to anode and cathode activation
V_{Ohm}	Ohmic voltage drop
V_{Con}	Voltage drop due to concentration
V_{Cell}	Voltage of the fuel cell
n	Number of cells in series in a fuel cell stack
ΔG	Standard Gibbs energy change (J/mol)
F	Faraday constant
S	Change in entropy (J/mol)
P_{H_2}	Partial pressure of hydrogen (atm)
P_{O_2}	Partial pressure of oxygen (atm)
R	Universal gas constant (8.314 J/K mol)
T_{ref}	Reference temperature (K)
ξ_i	Parametric coefficients
I_{stack}	Cell operating current (A)
C_{O_2}	Oxygen concentration (mol/cm)
R_c	Resistance to protons passing through membrane
R_m	Resistance to the passage of electrons through membrane
ρ_m	Membrane specific resistivity for electron flow (cm)
C_o	Initial SOC point of the battery

C_{bat}	Battery capacity
I_{bat}	Battery current
η_{bat}	Battery efficiency of charging or discharging
σ	Self-discharge rate of a battery
T_{bat}	Battery Temperature
C'_{bat}	Nominal battery capacity
P_s	PV array's power
P_{w}	Wind turbine's power
P_{load}	Load power
η_{rect}	Rectifier efficiency
η_{inv}	Inverter efficiency
V_{o}	Output voltage
V_{s}	Input source voltage
$C_{\text{p-opt}}$	Optimal-wind turbine power coefficient
inc	Increment
$I_{\text{mppt}(k)}$	Current at MPPT at sample time k
$E_{\text{pv}}(k)$	Error output of PV system at sample time k
$\text{CE}_{\text{pv}}(k)$	Change in error of a PV system at sample time k
$E_{\text{w}}(k)$	Error output of wind system at sample time k
$\text{CE}_{\text{w}}(k)$	Change in error of a wind system at sample time k
$\mu(D)_i$	Duty cycle's aggregated membership function
$T_{\text{m-opt}}$	Optimum mechanical torque
K_{opt}	Constant
P_{dc}	Inverter DC input power
η_{MPPT}	Efficiency of the MPPT
f_{r}	Filter resonant frequency
f_{c}	Carrier frequency
L_{fg}	Filter inductor on the grid side
L_{fi}	Filter inductor on the inverter side
C_{fg}	Filter capacitance
V_{n}	Rated line-to-neutral grid voltage
$I_{\text{c,max}}$	Maximum AC current ripple
M_{amp}	Amplitude modulation
M_{freq}	Frequency modulation
A_{r}	Amplitude of the sinewave signal
A_{c}	Amplitude of carrier wave
fr	Frequency of the sinewave signal
abc	Natural reference frame
dq	Synchronous rotating reference
$\alpha\beta$	Stationary reference frame
V_d* (or) V_{tq1}	Reference voltage signal in d-coordinate
V_q* (or) V_{tq1}	Reference voltage signal in q-coordinate
i_d*(or) i_{dref}	Reference current signal in d-coordinate
i_q*(or) i_{qref}	Reference current signal in q-coordinate
i_q (or) i_{q1}	Measured current signal in q-coordinate

i_d (or) i_{d1}	Measured current signal in d-coordinate
V_d	Measured voltage signal in d-coordinate
V_q	Measured voltage signal in q-coordinate
$P*$	Active power reference
$Q*$	Reactive power reference
$V*$	Reference voltage
$\omega*$	Reference frequency
P_{gm}	Measured active power of the grid
Q_{gm}	Measured reactive power of the grid
P_g*	Grid active power reference
Q_g*	Grid reactive power reference

List of Acronyms

RES	Renewable energy sources
PV	Photovoltaic
FC	Fuel cell
DER	Distributed energy resources
BSS	Battery storage systems
EPS	Electrical power system
PCC	Point of common coupling
Hz	Hertz
f	Frequency
V	Voltage
p.u.	Per unit
RMS	Root mean square
THDs	Total harmonic distortions
KW	Kilo watt
VRT	Voltage ride through
FRT	Frequency ride through
UV	Under voltage
OV	Over voltage
OF	Over frequency
UF	Under frequency
DC	Direct current
SCC	Short circuit current
OCV	Open circuit voltage
PWM	Pulse width modulation
TRD	Total rated current distortion
AC	Alternating current
h	Individual harmonic order
ESS	Energy storage systems
MPPT	Maximum power point tracker

MPP	Maximum power point
P&O	Perturbation and Observation
INC	Incremental conductance
IGBTs	Insulated gate bipolar transistors
VSI	Voltage source inverter
CSI	Current source inverter
VV	Volt-Var
P–Q	Power-reactive power
V–f	Voltage-frequency
I–V	Current-Voltage
P–V	Power- Voltage
PI	Proportional-integral
PR	Proportional resonant
PID	Proportional-integral derivative
FLC	Fuzzy logic controller
ANFIS	Adaptive neuro-fuzzy inference system
NN (or) ANN	Artificial neural networks
MF	Membership functions
PLL	Phase locked loop
VBD	Voltage based droop
LQR	Linear quadratic regulator
LQI	Linear quadratic integrator
DB	Deadbeat controller
VSC	Voltage source converter
THD	Total harmonic distortion
RC	Repetitive controller
FL	Fuzzy logic
PE	Power error
CPE	Change in power error
PSF	Power signal feedback
OTC	Optimal torque control
PMSG	Permanent magnet synchronous generator
HSC	Hill climbing search
TSR	Tip speed ratio
SOC	State of charge
PEM	Proton exchange membrane
PEMFC	Proton exchange membrane fuel cell
SPWM	Sinusoidal Pulse width modulation
PMSG	Permanent pole magnet synchronous generator
D	Duty cycle
OTC	Optimum torque control
PSF	Power signal feedback
LF	Low frequency
HF	High frequency
MPC	Model predictive controller

H∞	H-infinity controller
FL	Fuzzy logic
SMC	Slider mode control

1 Motivation Behind Renewable Energy Sources (RES)

Fossil fuels are non-renewable energy sources and are unsustainable in nature. The generation of electricity using pertinent fossil fuels such as coal, oil, and natural gas can emit greenhouse gasses which will cause environmental pollution and global warming. However, the traditional fossil fuel sources and their required maintenance incur a high cost and generate power at low efficiencies. For example, a conventional thermal power plant operating with coal as a fuel source has an efficiency of around 32–36% [1]. Moreover, an increase in energy demand and technological advancements in renewable energy sources boost the usage of renewable energy sources to generate electrical power. Renewable energy is a reliable source of power because it replenishes itself over a while, never runs out, and it is free. RES such as solar, wind, tide and waves, hydroelectric plants, fuel cells produce clean energy with fewer pollutants or greenhouse gases. Among those, hydroelectric, solar, and wind power plants generate most of the power from renewable sources. The discovery of PV technology has become a promising solution for energy generation due to its inherent features such as no presence of moving parts, low maintenance, and operation costs. RES is now replacing the traditional power sources as they are abundant to produce electricity. Hybrid systems such as combining two or more power systems or a combination of power systems with energy storage systems are widely used for better output.

2 Grid-*C*onnection Requirements for RES

Renewable resources such as small hydro, solar power, wind power, biogas, geothermal power are various small electrical power generating sources connected to the grid or distribution system. These are referred to as distributed energy resources (DER) [2]. The DER systems and grid-connected storage systems play an essential role in the electrical power distribution system. The distributed systems comprise multiple generation systems and storage components that enable reliable power generation from multiple renewable sources and lower environmental impacts.

The principal standard requirements for interconnection and interoperability of DER's with the electrical power system or network (EPS) are discussed as per the IEEE 1547 standards. The criteria and requirements summarized in this chapter are based on a 60 Hz frequency system. All the DER technologies interconnected to EPSs at traditional main or secondary distribution voltage levels shall follow the IEEE

standards and specifications [3]. The specifications mentioned are lower and upper limits of the permitted voltage and frequency trip settings described in this standard for DER. These are not meant to limit the capabilities and settings of other devices on the area EPS. They may vary according to the local EPS and the respective DER's interconnected to the power network. Incorporating the DER with the main grid requires maintaining the grid characteristics such as frequency and voltage stability similar to traditional power plants by withstanding various disturbances and faults [4]. The interconnection point of RES to the main power grid is referred to as a point of common coupling (PCC). The operating voltage of the DER system is considered as 1.0 per unit (p.u). The major requirements in a continuous operating mode, such as voltage regulation, frequency regulation, active and reactive power supply capabilities, are summarized below.

The DER must operate within the specified ranges of applied voltage and device frequency to energize the new, standalone, or disconnected DER system back with the existing EPS network or power grid. The minimum and maximum applicable voltage ranges are $\geq$0.917 p.u. and $\leq$1.05 p.u., respectively. The frequency of the DER should be in the range of $\geq$59.5 to $\leq$60.1 Hz during interfacing. And it must wait until the permissible service setting is enabled. When the PCC is at medium voltage during synchronization, the DER must parallel with the Area EPS without triggering step changes in the RMS voltage at the PCC beyond 3% of nominal voltage. When operating at low voltages, it should not trigger step changes beyond 5% of nominal voltage at the PCC.

The DER must be capable of injecting (over-excited) and consuming (under-excited) reactive power for active power output levels greater than or equal to the DER's minimum steady-state active power capacity (P_{min}), or 5% of the DER's rated active power, P_{rated} (kW), whichever is greater. The voltage regulation capability of the DER will be provided by changing the reactive power. Voltage regulation using reactive power control function can be made using the following methods: Constant power factor mode, Voltage-reactive (Volt-Var) power mode, Active-reactive (Watt-Var) power mode, and Constant-reactive power mode. The DER is responsible for selecting one of these methods to regulate the voltage according to the reference voltage, and the operating limits are varied according to the chosen model. In common, the constant power factor mode with unity power factor is used in the EPS network. A maximum of 10 s can maintain the adjustable reference point. Similarly, the DER must limit its active power output to no more than the active power limit set point in less than 30 s, or in the time it takes the primary energy source to decrease its active power output to meet the active power limit set point's specifications, whichever is longer.

A set of technical capabilities of the DER system to operate in the abnormal operating mode (i.e., during disturbances or faults) are summarized below. During faults, the DER's have the capability to continuously operate within the system without tripping. Ride-through capability is the DER system's ability to remain connected and continue to operate as specified by withstanding the voltage and frequency disturbances inside the specified limits. In particular, the DERs should have voltage ride-through (VRT) and frequency ride-through (FRT) capabilities to operate during

minor disturbances in the grid-connected mode. The abnormal operating performance specified here is for very high DER penetration in the EPS. It is based on both bulk power system stability/reliability and distribution system reliability/power quality needs and are coordinated with existing interconnection requirements. The abnormal performance characteristics can be modified according to either of the operational requirements.

Two under-voltage trip functions, UV1(0.88 p.u.) and UV2(0.50 p.u.), and two overvoltage trip functions, OV1(1.10 p.u) and OV2(1.20 p.u), are specified with respect to maximum clearing times of 2.0 s for UV's and 0.16 s for OV's to trip. Similarly, two under-frequency limits, UF1(61.2) and UF2(62.0), and two over-frequency ranges OF1(58.5) and OF2(56.5), are specified with a clearing time of 300 s for the first limit (UF1 and OF1) and 0.16 s for the second limit (UF2 and OF2) violation [3]. These settings can be modified according to the EPS requirements for EPS protection coordination. In case of short circuit faults, the DER system shall cease to energize the EPS circuit and trip unless the EPS operator specifies it. During open phase conditions, the DER shall detect and cease to energize and trip all phases to which it is connected within 2.0 s of the open phase condition [3]. The DER shall cease to energize the EPS and trip during the respective clearing period as indicated above when any relevant voltage is less than an under-voltage threshold or greater than an over-voltage threshold and any frequency under and over-frequency threshold as specified above.

DER must be configured without exceeding DER capacities to provide the voltage disruption ride-through functionality and frequency ride-through functionality to provide the active power output during minor deviations. In voltage ride-through functionality, the DER remains in continuous operation when its operating voltage is in between UV1 and OV1 (i.e., $0.88 \leq V \leq 1.10$ p.u.). The DER voltages in between OV1 AND OV2 (i.e., $1.10 < V \leq 1.20$ p.u.) and $V < 0.50$ p.u. make the system operate in momentary cessation mode. The operating voltages in between $0.50 \leq V < 0.88$ p.u. make the ride-through functionality operate in mandatory mode to make the system voltage as close as to reference voltage. And the voltages above OV2 (i.e., $V > 1.20$ p.u.) make the DER cease to energize during abnormal conditions. Similarly, the DER remains in continuous operation during its operating frequency between UF1 and OF1 (i.e., $58.8 \leq f \leq 61.2$). The DER operating with a frequency range of $61.2 < f \leq 61.8$ Hz and $57.0 \leq f < 58.8$ Hz makes the frequency ride-through functionality operate in mandatory mode to recover the system frequency to the reference value. For the frequency disturbances, in which frequency falls outside the ranges OF2 and UF2 of ride-through capabilities, the ride-through capabilities shall not apply to restore the system output or the continuous ride-through operation [3].

The total rated current distortion (TRD) includes both the harmonic and inter-harmonic distortions. The TRD is calculated using the following Eq. 1 [3].

$$\%\text{TRD} = \frac{\sqrt{I_{\text{rms}}^2 - I_1^2}}{I_{\text{rated}}} \times 100\% \tag{1}$$

where I_{rms} is the root-mean-square of the DER current, including all frequency components. I_1 is the fundamental current measured at the reference point, and I_{rated} is the DER unit rated current capacity. All the current measurements are subjected to the reference point. The maximum total rated current distortion (TRD) of the DER unit at rated current capacity is 5.0% [3].

3 The Necessity of Inverters with RES

The most advanced solar PV system and wind generating systems are widely integrated with the main power grid among the RES. The non-linear, intermittent availability, and dependency of RES on weather conditions can impact the power grid's quality, reliability, and stability by causing voltage and frequency fluctuations. To reduce the source's erratic nature and automatically buffer the power difference between RES and the loads, energy storage systems (ESS) are widely incorporated into the system. ESS, such as batteries, flue cell systems, supercapacitors, provide the DC voltage regulation and frequency supporting functions [5]. All the RES and ESS systems are connected to the grid using power converters. These power converters act as an interfacing stage between the RES, ESS, and the grid loads to deliver the energy by ensuring stable, sustainable, and reliable operation. The dc–dc boost converters and ac–dc converters interface the RES and ESS to a dc bus in grid-connected mode. Simultaneously, the dc–ac inverters take charge to convert the standard dc supply from the source into ac supply to deliver reliable AC power to the grid. Therefore, the grid interconnection requires various standards and regulations to integrate with the power grid to ensure its proper operation and stability.

The inverter plays a vital role in the interfacing of renewable dc sources into the AC power grid. Inverters are a class of power electronic devices that rapidly switch action to change the direction of a DC input to regulate electrical power flow to the grid. Thus, an inverter converts the available DC supply from the sources into an AC supply to deliver the active and reactive power into the AC power grid. The filters and other electronics are also employed to inject the pure sinusoidal wave at desired frequency, voltage, and phase of the power grid. The basic block diagram of the grid-connected RES system is shown in Fig. 1, where the solar PV array, wind turbines, fuel cell, and a battery energy storage system are connected to the DC-Bus through DC–DC or AC–DC converters. The three-phase two-level DC–AC inverter is employed to convert the DC–AC supply, and the filter is used to remove the harmonics in the output. The three-phase controlled output is fed to the smart grid or the utility loads. The monitoring and control system is employed to control the inverter output. The grid voltage (V_g) and current (I_g) are taken from the point of common coupling (PCC) as a reference and given to the controller to control the inverter output according to reference values.

As the inverter stands between renewable sources and the power grid, it needs to act smartly to obtain the maximum output from the sources. It must comply with the grid codes with easy maintenance and cost-effective solutions. Furthermore,

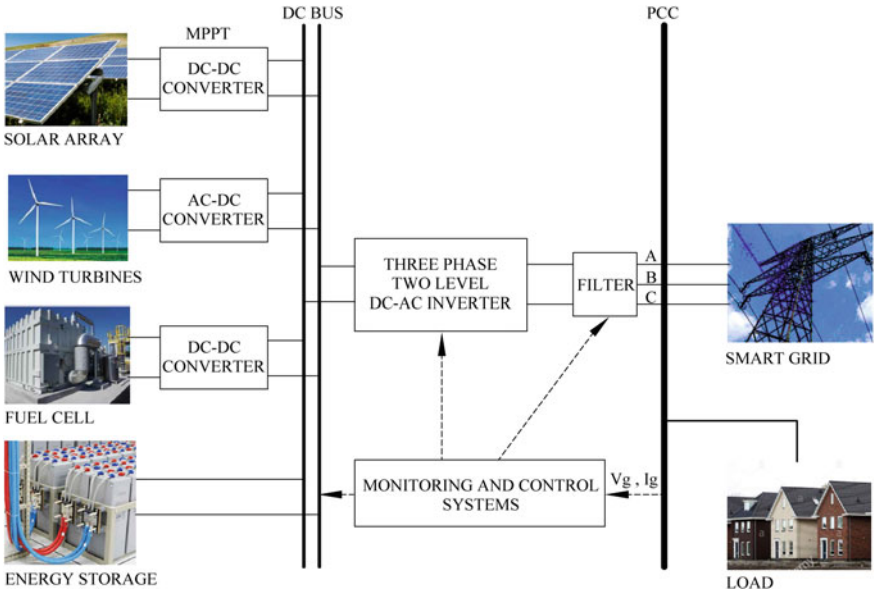

Fig. 1 Basic block diagram of grid-connected RES system

the inverter monitors the system and communicates with the computer networks to control the system parameters to regulate the injected output to the power grid.

According to the output voltage, power level, and applications, several types of inverters might be used in a RES system to accomplish the dc–ac conversion. For grid-tied interconnections, to achieve high functionality by reducing system fluctuations and bi-directional power flows, smart inverters have been introduced in the RES system with state-of-the-art communication protocols and control algorithms [6].

4 Mathematical Modeling of RES

The mathematical modeling of RES such as solar PV, wind power, fuel cell, and battery sources are described below.

4.1 Modeling of Solar PV Array

The solar cell is the fundamental component of a solar array. It is a *P–N* junction semiconductor that may generate electricity through the photovoltaic effect. A PV array is formed by connecting multiple PV cells in a series–parallel pattern. The total power of the PV array is determined as follows

$$P_{\text{array}} = N_{\text{p}} * N_{\text{s}} * P_{\text{m}} \tag{2}$$

where N_{s} and N_{p} are the numbers of PV cells connected in series and parallel, respectively, P_{m} is the power of each module.

The equivalent circuit of a single diode solar PV cell is shown in Fig. 2. Traditionally, a solar cell is represented by an equivalent circuit with a current source having a diode in parallel. The internal resistance of a cell represents the internal heating of each cell. A resistor in series with the current source defines the variation of the output voltage with the current of a cell.

The module photo current I_{ph} varies with irradiation and temperature of the cell and is given as follows

$$I_{\text{ph}} = \left[I_{\text{scr}} + K_{\text{i}}(T - 298) * \frac{S_{\text{irrd}}}{100} \right] \tag{3}$$

where I_{scr} is the short circuit current of the cell, K_{i} is the temperature coefficient of the cell's short circuit current, and T represents the cell temperature in kelvins (K). S_{irrd} stands for solar irradiation on the cell in (mW/cm^2).

Module reverse saturation current, I_{rs} is given as

$$I_{\text{rs}} = I_{\text{scr}} / \left[\exp\left(q * \frac{V}{N_s * AKT} \right) - 1 \right] \tag{4}$$

The cell temperature affects the module saturation current I_0, which is given by

$$I_o = I_{\text{rs}} \left[\frac{T}{T_r} \right]^3 * \exp\left[\frac{q * E_g}{AK} \left(\frac{1}{T_r} - \frac{1}{T} \right) \right] \tag{5}$$

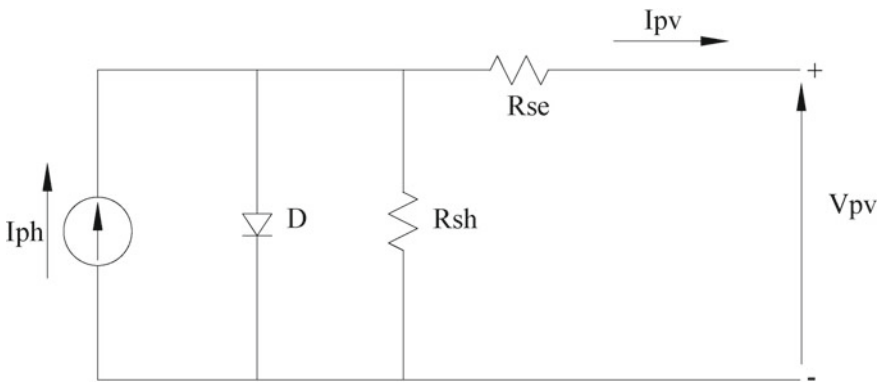

Fig. 2 Equivalent circuit of a single diode solar PV cell

The output current–voltage (I–V) characteristics of a PV cell is calculated by using the following Eq. 6 [7]

$$I_{\mathrm{pv}} = I_{\mathrm{ph}} - I_o\left[\exp\left(\frac{q * \left(V_{\mathrm{pv}} * I_{\mathrm{pv}} R_{\mathrm{se}}\right)}{A * K * T} - 1\right) - \frac{\left(V_{\mathrm{pv}} * I_{\mathrm{pv}} R_{\mathrm{se}}\right)}{R_{\mathrm{sh}}}\right] \tag{6}$$

where I_{ph} represents the current generated by the light incident on the solar cell, E_g denotes the bandgap energy, and A signifies the diode ideality factor. K indicates the Boltzmann's constant [J/K], T_{r} is the cell referred temperature, q represents the charge of an electron. R_{se} and R_{sh} are the series and shunt resistance of a cell. I_o is the reverse saturation current of the diode. Considering the requirement of energy, the number of series or parallel strings of solar cells are incorporated in the PV module to acquire the required power as per the application.

The output of the solar PV array depends on the irradiation and temperature of the cell. The weather conditions have a certain impact on the PV array output. The I–V characteristics of a solar PV array with different irradiation and temperature variations are shown in Figs. 3 and 4, respectively [8].

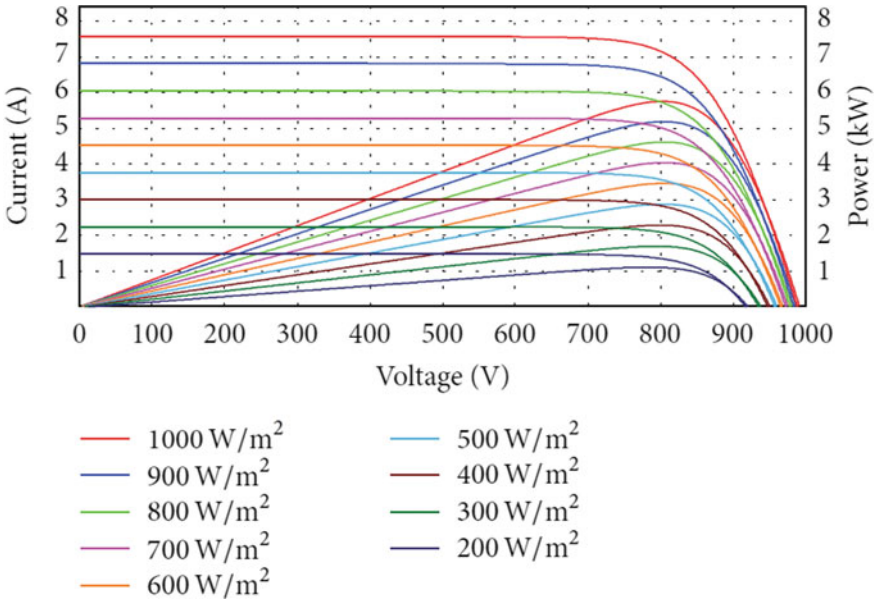

Fig. 3 The I–V and P–V curves of a solar PV array with different irradiation [8]

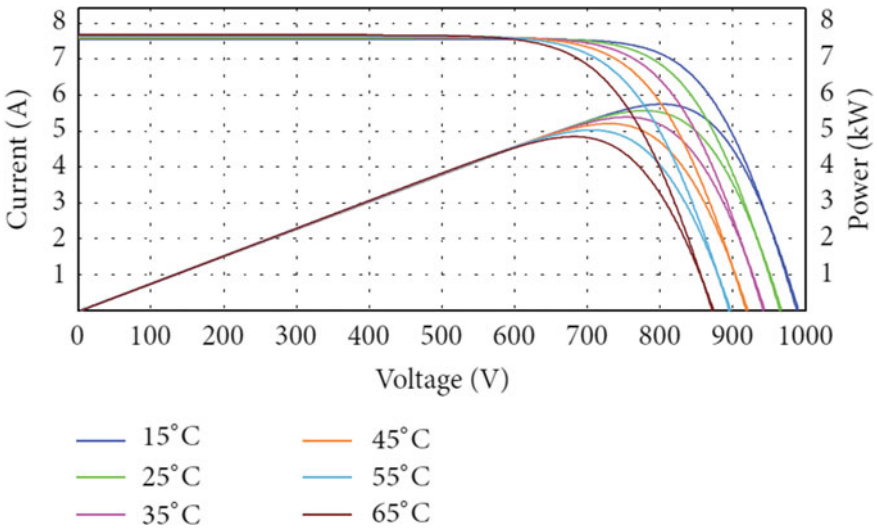

Fig. 4 The *I–V* and *P–V* curves of a solar PV array with temperature variation [8]

4.2 Modeling of Wind System

The wind turbine is the main component that turns the wind's kinetic energy into electricity in the wind generator system. Three major parameters can be used to assess a wind turbine's performance: power, torque, and thrust. The turbine power is usually chosen as the primary parameter because it controls how much energy is released by the turbine. The basic equation that governs the mechanical power of a wind turbine is as follows [9]:

$$P_w = \frac{1}{2} C_p(\lambda, \beta) \rho A_w V_{\mathrm{w}}^3 \tag{7}$$

where A_w is the rotor blades intercepting area (m^2), V_{w} is the average wind speed (m/s), and λ is the tip speed ratio (TSR). ρ is air density (Kg/m^3), C_p or also known as Betz's coefficient, is the power coefficient that has a theoretical maximum value of 0.593. The TSR is the ratio of a blade's tip's rotational speed to the wind turbine's wind velocity. Mathematically, it is defined as [10]

$$\lambda = \frac{R_{\mathrm{w}} \omega_{\mathrm{r}}}{V_{\mathrm{w}}} \tag{8}$$

where R_{w} is the radius of the turbine in meters, ω_{r} is the angular speed in radians per second (rad/s), and V_{w} is the average wind speed in meters per second (m/s). Wind energy in kWh can be obtained as follows:

$$Q_{\mathrm{w}} = P * t \tag{9}$$

where P refers to generated power and t is the time. The wind velocity at any given height can often be challenging to determine due to various reasons. In such cases, the data at any reference height can be interpolated or extrapolated to determine the wind speed at any given height. Because of vegetation, shadowing, and barriers in the area, measuring wind velocity at a lower altitude can be inaccurate [9].

$$v(h)\ln\left(\frac{h_{\mathrm{ref}}}{h_o}\right) = v(h_{\mathrm{ref}})\ln\left(\frac{h}{h_o}\right) \tag{10}$$

where h_{ref} is the reference height in meters (m), h is the height to be measured, h_o is the measure of surface roughness (0.1–0.25 for crop land), $v(h)$ is the wind speed at height h (m/s), and $v(h_{\mathrm{ref}})$ is the wind speed at reference height h (m/s).

Cut-in speed is the lowest wind speed at which the turbine begins to operate and generate electricity. Cut-out speed refers to the high wind speed at which the forces on the turbine assembly are high, posing a risk of rotor damage. To avoid damage, the rotor is brought to a halt using the braking mechanism. The wind speed between cut-in and cut-out at which the power output hits the highest limit that the electrical generator is capable of is referred to as rated output speed. It is possible to estimate the power output in terms of wind speed as follows:

$$P_{\mathrm{w}}(v) = \begin{cases} \left(\frac{v^k - v_C^k}{v_R^k - v_C^k}\right) * P_{\mathrm{Rated}} & v_{\mathrm{Cin}} \le v \le v_{\mathrm{Cout}} \\ P_{\mathrm{Rated}} & v_{\mathrm{Cout}} \le v \le v_{\mathrm{RCout}} \\ 0 & v \le v_{\mathrm{Cin}} \text{ and} v > v_{\mathrm{RCout}} \end{cases} \tag{11}$$

where P_{Rated} stands for rated power, v_{Cin} stands for cut-in wind speed, v_{Cout} stands for rated wind speed, v_{RCout} stands for rated cut-out speed, and k stands for the Weibull form factor—the value of k ranging from 1 to 3 in the existing literature according to the application.

The power generation changes with variations in wind velocity for a fixed rotor blade size. As a result, the best generator speed corresponding to maximum power should be found for the variable wind velocity. Maximum power point tracking (MPPT) is the process of changing the angular speed of the generator to extract the maximum power (MPP). MPPT is the subject of the next section. The power coefficient is maximized for an optimal TSR when zero blade pitches angle [9]. The optimum rotor speed is given by

$$\omega_{\mathrm{opt}} = \frac{\lambda_{\mathrm{opt}}}{R} * V_{\mathrm{w}} \tag{12}$$

Which can rephrase as

$$V_{\mathrm{w}} = \frac{R_{\mathrm{w}}\omega_{\mathrm{opt}}}{\lambda_{\mathrm{opt}}} \tag{13}$$

where ω_{opt} denotes the optimum rotor angular speed in rad/s, λ_{opt} denotes the ideal tip speed ratio, R_w denotes the radius of the turbine in meters (m), and V_w denotes the wind speed in meters per second (m/s).

4.3 Modeling of Fuel Cell

A fuel cell is an electrochemical cell that uses a pair of redox processes to transform the chemical energy of fuel, typically hydrogen and an oxidizing agent, commonly oxygen, into electricity. Fuel cells come in a variety of shapes and sizes, but they all have an anode, a cathode, and an electrolyte that allow ions to pass through. At the intersections of the three segments, two chemical reactions take place. Fuel is burned, water or carbon dioxide is produced, and an electric current is produced, which can be utilized to power electrical devices. There are several types of fuel cell technologies; all are designed for specific applications, but they all work on the same principle. Among several types, the Proton Exchange Membrane Fuel Cell (PEMFC) is a good choice for distributed energy sources to produce power.

PEMFC produces electrochemical energy with water as a by-product by combining hydrogen and oxygen over a platinum catalyst. The *I–V* parameters of a typical FC operating at ambient temperature and normal air pressure are depicted in Fig. 5 [11]. It shows the three different polarization characteristics of an FC cell.

The maximum cell voltage and various voltage drops are used to determine each cell voltage (losses) variance. A single cell's output voltage (V_{FC}) can be defined as [11]

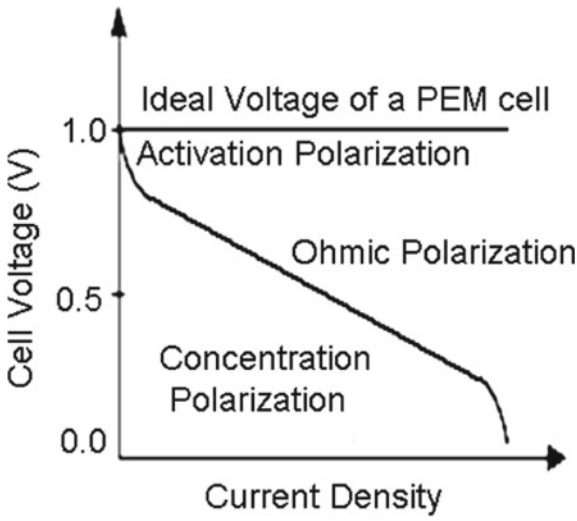

Fig. 5 Ideal *I–V* characteristics of a single PEMFC [11]

$$V_{\mathrm{FC}} = E_{\mathrm{Nerst}} - V_{\mathrm{Act}} - V_{\mathrm{Ohm}} - V_{\mathrm{Con}} \tag{14}$$

where E_{Nerst} is the standard reversible voltage, V_{Act} denotes the voltage drop caused by the anode and cathode activation, V_{Ohm} denotes the ohmic voltage drop caused by the conduction of protons through the solid electrolyte and electrons through internal electronic resistances; V_{Con} denotes the voltage drop caused by the concentration or mass transportation of the reactant. E_{Nerst} denotes the no-load voltage, whereas the other terms' total represents the drop in the usable voltage obtainable at the cell terminals. The voltage (V_{cell}) can be calculated for n cells connected in series and creating a stack as follows:

$$V_{\mathrm{Cell}} = n.V_{\mathrm{FC}} \tag{15}$$

From Fig. 5, the ideal voltage of a PEM cell is the maximum voltage produced by each cell in the stack at a given temperature with the known partial pressures of the reactants and products. It is supplied by and is calculated using Gibbs free energy as follows:

$$E_{\mathrm{nerst}} = \frac{\Delta G}{2F} + \frac{\Delta S}{2F}(T - T_{\mathrm{ref}}) + \frac{RT}{2F}\left[\ln\left(P_{\mathrm{H}_2}\right) + \frac{1}{2}\ln\left(P_{\mathrm{O}_2}\right)\right] \tag{16}$$

where ΔG denotes the standard free Gibbs energy change for the reaction in (J/mol); F denotes the Faraday constant (96.487 C). S denotes the change in entropy (J/mol); R denotes the universal gas constant (8.314 J/K mol). P_{H_2} and P_{O_2} denote the partial pressures of hydrogen and oxygen (atm), respectively; T_{ref} reference temperature and the T denotes the variable cell operation temperature (K). The voltage drop in a fuel cell is caused by several factors referred to as polarization. There are three causes of losses: (a) activation polarization, (b) ohmic polarization, and (c) concentration polarization [12]. Each of them is linked to a voltage drop and is prominent in a specific current density area. The voltage drop caused by the anode and cathode activation is known as activation over-voltage. It can be calculated using the following formula:

$$V_{\mathrm{Act}} = -\left[\xi_1 + \xi_2 * T + \xi_3 * T * \ln\left(C_{\mathrm{O}_2}\right) + \xi_4 * \ln(I_{\mathrm{stack}})\right] \tag{17}$$

The ξ_i's indicate parametric coefficients for each cell model, whose values are set based on theoretical equations having kinetic, thermodynamic, and electrochemical foundations, and I_{stack} is the cell operating current (A). C_{O_2} is the oxygen concentration in the catalytic interface of the cathode is measured in mol/cm.

The ohmic voltage drop is caused by the electrode's electrical resistance and the electrolyte's impedance to ion flow. It is given as

$$V_{\mathrm{ohm}} = I_{\mathrm{stack}} * (R_m + R_C) \tag{18}$$

where R_c is the resistance to protons passing through the membrane, which is usually constant, and R_m is the resistance to the passage of electrons through the membrane. R_m is obtained by multiplying membrane-specific resistivity (ρ_m) for the electron flow (cm) with the thickness of the membrane and is divided by active cell area (l) in cm. The concentration loss is due to a change in reactant concentration at the electrode surface when the fuel is utilized, resulting in a fall in the partial pressure of reactants, causing a decrease in voltage is given by

$$V_{\text{con}} = -\frac{RT}{n} * F * \ln\left(1 - \frac{i}{i_1}\right) \tag{19}$$

More fuel consumption reduces hydrogen and oxygen concentrations at various points in the PEM fuel cell gas channels while increasing concentrations of these reactants at the stack's input.

4.4 Modeling of Battery System

Renewable energy resources such as solar and wind are place- and weather-dependent. The battery storage systems (BSS) are widely integrated with RES to provide the increased energy demand without interruption of continuous power supply to the utility grid. The BSS can be modeled as a standalone system or hybrid system integrating with other RES. In hybrid systems, available excess power from the RES is stored in the battery systems. Cases where power demand is more than the power supply, the BSS discharge to meet the power demand. For the dynamic control of BSS in the system, estimating battery State of Charge (SOC) is essential. The ampere-hour counting approach is suggested as a good choice for estimating SOC calculations. The charging or discharging time, as well as the current expression, can be calculated using this model as follows:

$$\text{SOC} = C_o + \int_{t_o}^{t} \left(\frac{I_{\text{bat}}}{C_{\text{bat}}}\right) \mathrm{d}\tau \tag{20}$$

where C_o is the initial SOC point of the battery, C_{bat} is the battery capacity at temperature T_{bat}, and I_{bat} is the battery current. The charging and discharging behavior of the battery can be expressed using the SOC equation as follows [13]:

$$\text{SOC} = C_o\left[1 - \frac{\sigma}{24}(t - t_o)\right] + \int_{t_o}^{t} \left(\frac{I_{\text{bat}} * \eta_{\text{bat}}}{C_{\text{bat}}}\right) \mathrm{d}\tau \tag{21}$$

where σ is the self-discharge rate; η_{bat} is the battery efficiency of charging or discharging. The battery capacity is dependent on temperature, which is given as

$$C_{\text{bat}} = C'_{\text{bat}}(1 + \delta_c(T_{\text{bat}} - 298.15) \tag{22}$$

where the C'_{bat} is the nominal battery capacity. The equation for battery current in a hybrid grid with solar, wind, and BSS is given as follows [13]:

$$I_{\text{bat}} = \frac{P_S + P_{\text{w}} * \eta_{\text{rect}} - P_{\text{load}}/\eta_{\text{Inv}}}{V_{\text{bat}}} \tag{23}$$

where P_s is the PV array's power, P_{w} is the wind turbine's power, P_{load} is the load power, V_{bat} is the battery's voltage, η_{rect} is the rectifier's efficiency, and η_{inv} is the inverter's efficiency.

4.5 Modeling of DC–DC *Boost Converter*

The DC–DC boost converter is the most utilized converter on the DC side of the RES system. It is interfaced in between the DC power source such as solar, fuel cell, wind or battery system, and DC-link bus to convert the low input voltage into high output voltage on the DC side. In RES applications, it is designed to operate at its maximum power point by controlling its switching device such as MOSFET or IGBT transistors using a PWM signal and duty cycle of the controller. The equivalent circuit of a boost converter is shown in Fig. 6.

The boost converter boosts the input voltage by storing energy in an inductor for a set amount of time and then using that energy to raise the input voltage to a higher value. The input source charges up the inductor while switch *q* is closed, while diode *d* is reverse biased to provide isolation between the converter's input and output. The inductor's energy and the power supply are transmitted to the load when the switch

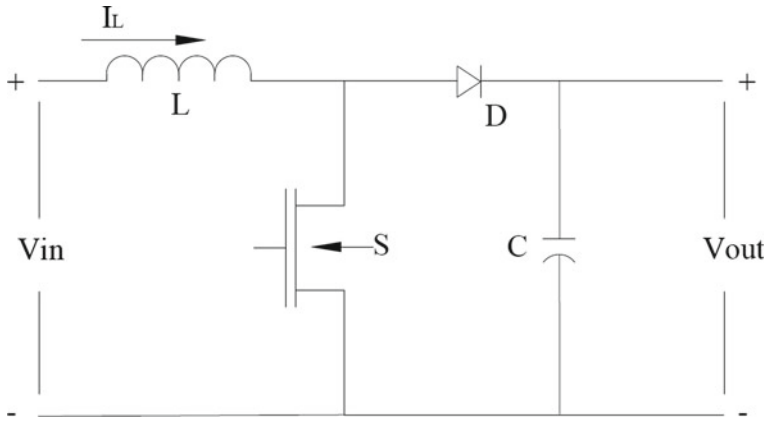

Fig. 6 Schematic diagram of the DC–DC boost converter

is opened. The following equation describes the relationship between the input and output voltages:

$$\frac{V_o}{V_s} = \frac{1}{1-D} \tag{24}$$

where V_o refers to the output voltage of the boost converter, V_s is the input source voltage from the RES source. D is the duty cycle.

5 MPPT Techniques

An essential function associated with the inverter system for wind and photovoltaic applications is the maximum power point tracking (MPPT) algorithm. The variable power output of solar PV and wind energy may not necessarily always correspond to the maximum power. A PV array's I–V and P–V characteristics with different irradiation and variable temperatures are shown in Fig. 4 [8]. To extract the maximum power point of the system under all conditions, the MPPT techniques are widely used in wind and PV systems. The MPPT algorithm aims to make the system operate at maximum peak power point in voltage versus current relationship of the connected PV array and wind turbine based on the characteristics of irradiance and temperature of the PV array and varying wind speed conditions of the wind system, respectively.

Several MPPT techniques such as perturbation and observation (P&O) technique [8], the incremental conductance (INC) technique [8, 14], ripple correlation technique, short circuit current (SCC) technique, and open-circuit voltage (OCV) technique, fuzzy logic (FL) method [15, 16], Adaptive neuro-fuzzy inference system (ANFIS)-based MPPT technique have been proposed in the literature. The complexity, cost, speed of convergence, sensors required, hardware implementation, and effectiveness of these techniques vary according to the application. Among all P&O and INC are the conventional methods widely used in practice because of their ability to track data in real-time under unvarying irradiation conditions and simple implementation structure. However, to track the non-linear nature of rapid irradiance changes and oscillations caused by adverse climatic conditions, intelligent methods like FL-based and artificial neural network (ANN)-based techniques were used in the literature. To obtain better efficiency by using the benefits of FL and ANN, ANFIS-based MPPT methods are proposed by the researchers [17].

In wind energy systems, the use of an MPPT controller in a wind system is vital, given its important role in extracting the maximum energy produced by the Permanent Magnet Synchronous Generator (PMSG) generator regardless of wind speed. Its principle is based on the execution of an MPPT algorithm that allows to reach and track the maximum power point.

In wind systems, there are numerous MPPT strategies that can be recognized. There are two types of methods: direct and indirect. Power Signal Feedback (PSF) and Optimal Torque Control (OTC) are the examples of indirect methods which

require prior knowledge of the wind turbine characteristics such as optimal-wind turbine power coefficient ($C_{p\text{-}opt}$) and optimal tip speed ratio (λ_{opt}) of the wind turbine [10]. Direct techniques such as Hill-Climbing Search (HSC) methods, FLC-based methods, on the other hand, do not necessitate prior knowledge of these concepts. Hence, various MPPT techniques, such as classical, optimization-based, and hybrid-based approaches, are summarized in the literature and used according to the applications [18].

5.1 Perturbation and Observation (P&O) Technique

The P&O algorithm is a simple technique and requires minimum sensors. In this technique, the MPPT controller adjusts the operating voltage from the PV array by a small amount in a specific direction and monitors power; if power increases, the controller tries more adjustments in that direction until power increases no longer. By using an algorithm, it samples dP/dV. If dP/dV is positive, the algorithm improves the voltage value toward MPP until dP/dV is negative [16]. This process is repeated until the algorithm reaches maximum power point (MPP). The power-voltage curve and flowchart of the P&O algorithm are shown in Fig. 7 [19] and Fig. 8 [8], respectively.

This approach is unsuitable when there is a considerable change in solar irradiation and/or temperature since the voltage fluctuates about the MPP, never reaching a precise value [16]. Although it is a simple and straightforward strategy, the performance deteriorates due to the trade-off between accuracy and speed when choosing the step size [8]. However, it lacks the speed and adaptability required for tracking quick transients according to the weather conditions.

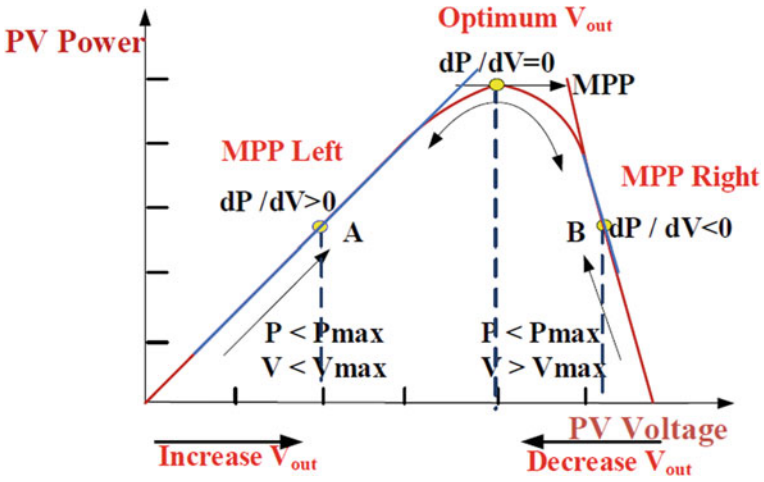

Fig. 7 P&O algorithm power-voltage curve [19]

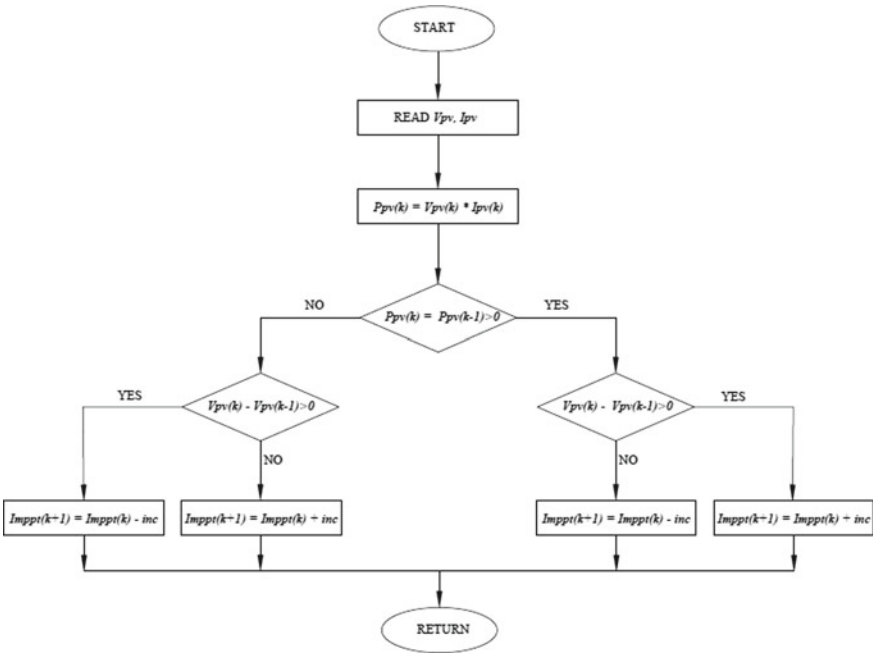

Fig. 8 Flowchart of the P&O algorithm [8]

5.2 Incremental Conductance (INC) Technique

The incremental conductance technique is based on the idea that at the MPP, the slope of the PV array power-voltage curve is equal to zero, so $dP/dV = 0$, and $P = VI$. Figure 9 shows the INC algorithm for power-voltage curve. The slope is positive in the area to the left of the MPP and negative in the area to the right. Summarizing that it is represented as:

$$\frac{dP}{dV} = 0, \quad \text{At MPP} \tag{25}$$

$$\frac{dP}{dV} > 0, \quad \text{left of MPP} \tag{26}$$

$$\frac{dP}{dV} < 0, \quad \text{right of MPP} \tag{27}$$

Substituting the PV array current as a function of voltage, $P = IV$, the equation can be approximated as

$$\frac{dP}{dV} = d(IV) = V\frac{dI}{dV} + I \tag{28}$$

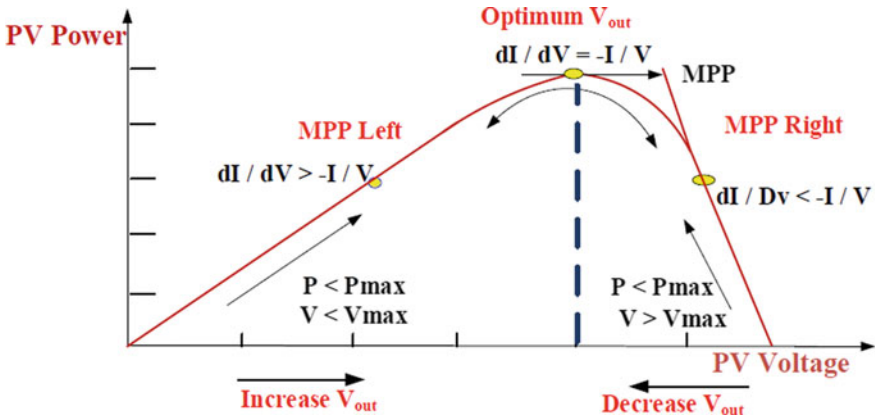

Fig. 9 INC algorithm power-voltage curve [19]

Setting the equation to zero, we will get

$$\frac{\mathrm{d}P}{\mathrm{d}V} = -\frac{I}{V}, \quad \text{At MPP} \tag{29}$$

$$\frac{\mathrm{d}P}{\mathrm{d}V} > -\frac{I}{V}, \quad \text{left of MPP} \tag{30}$$

$$\frac{\mathrm{d}P}{\mathrm{d}V} = -\frac{I}{V}, \quad \text{At MPP} \tag{31}$$

This technique uses the photovoltaic array's incremental conductance (I/V) to calculate the sign of the change in power with respect to voltage ($\mathrm{d}P/\mathrm{d}V$). It calculates the MPP by comparing the incremental conductance ($\mathrm{d}I/\mathrm{d}V$) with the array conductance (I/V). When these two are equal ($-I/V = \mathrm{d}I/\mathrm{d}V$), the output voltage is at MPP. The MPPT controller maintains the MPP voltage. When the irradiation changes, the procedure is repeated. This approach involves more processing in the controller, but it is faster at tracking changing circumstances than the perturb and observe method (P&O).

5.3 *Fuzzy* Logic (FL)-Based *MPPT*

The FL-based MPPT method is a dynamic control method used to track the MPP in solar PV and wind power systems by handling the non-linear nature of the inputs. This technique does not require the precise mathematical model of the system but necessitates the thorough knowledge, rule base, and membership functions of the system [16]. Two inputs of FL-based MPPT are error (E) and change in error (CE),

and the output variable is the duty cycle (D). The E and CE inputs of the PV and Wind systems, respectively, at a sampled time k, are defined as follows:

For PV system:

$$E_{\mathrm{pv}}(k) = \frac{P(k) - P(k+1)}{V(k) - V(k+1)} \tag{32}$$

$$\mathrm{CE}_{\mathrm{pv}}(k) = E_{\mathrm{pv}}(k) - E_{\mathrm{pv}}(k+1) \tag{33}$$

For Wind system:

$$E_{\mathrm{w}}(k) = \frac{P(k) - P(k+1)}{\omega(k) - \omega(k+1)} \tag{34}$$

$$\mathrm{CE}_{\mathrm{w}}(k) = E_{\mathrm{w}}(k) - E_{\mathrm{w}}(k+1) \tag{35}$$

The inputs $E_{\mathrm{pv}}(k)$ and $E_{\mathrm{w}}(k)$ denote the location of the operation point on the left or right side of MPP on the PV system's Power-Voltage characteristic curve and the wind turbine's Power-Wind velocity characteristic curve, respectively. The inputs $\mathrm{CE}_{\mathrm{pv}}(k)$ and $\mathrm{CE}_{\mathrm{w}}(k)$, respectively, describe the direction of movement of the operating point toward the MPP on the PV system's Power-Voltage Characteristic curve and the wind turbine's Power-Wind velocity Characteristic curve [15]. The structure of the rule base's membership functions (MF's) is one of the factors that influence an FLC's behavior. The controller structure of the fuzzy system is shown in Fig. 10. The MF's for the E, CE, and D are specified and given as inputs to the fuzzy system. The fuzzy inference rules are defined based on Mamdani's method [15]. The center of gravity approach is used to compute the D for the DC–DC Boost converter, as shown in eq. below.

$$D = \frac{\sum_{i=0}^{n} (\mu(D)_i).D_i}{\sum_{i=0}^{n} (\mu(D)_i)} \tag{36}$$

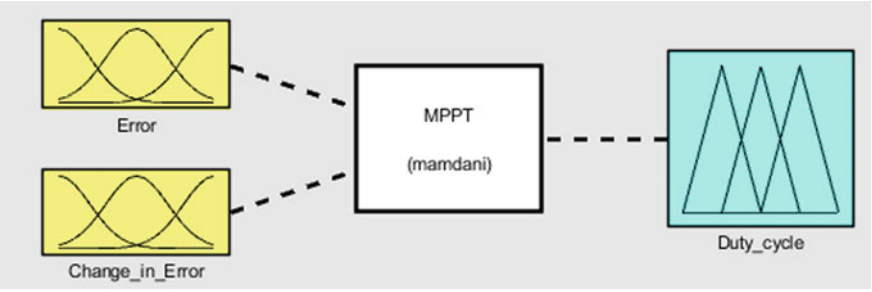

Fig. 10 Control structure of the fuzzy system

where $(\mu(D)_i)$ is the duty cycle's aggregated membership function, and D_i is the output variable.

For fuzzy logic MPPT rule configurations, a different number of subsets have been used. The tuning of rules provides more precision and dynamic response, but it is time-consuming. The flowchart of the FL-based MPPT algorithm is shown in Fig. 11.

Compared to traditional methods, fuzzy control algorithms can improve tracking performance for linear and non-linear loads. Because fuzzy logic does not rely on complicated mathematical equations, it is also suitable for non-linear control.

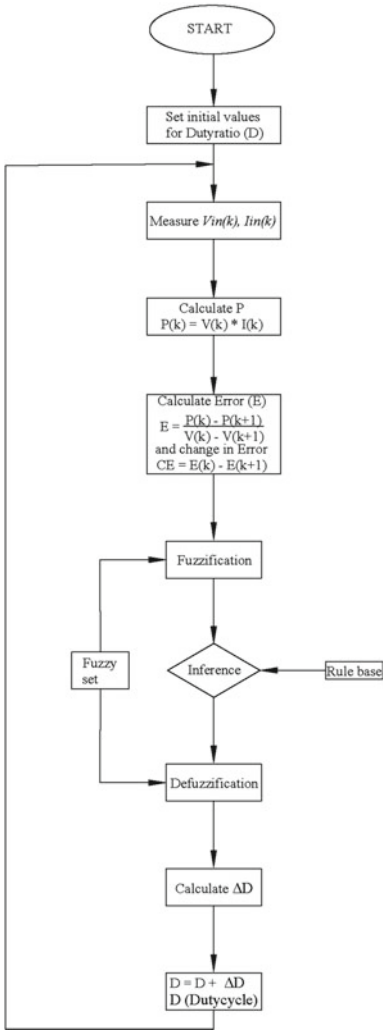

Fig. 11 The flowchart of the FL-based MPPT algorithm

5.4 *Adaptive* Neuro-Fuzzy *Inference System (ANFIS)-Based MPPT*

The ANFIS (adaptive network-based fuzzy inference system) is a hybrid method that combines the benefits of neural networks and FL systems. ANFIS is a fuzzy inference system with neural network optimization. Furthermore, ANFIS can automatically build fuzzy rules [20]. To achieve MPP, various ANFIS-based MPPT approaches have been proposed in the literature. From one configuration to another, the input and output variables are different. The irradiance and temperature (T_{pv}) of the PV array or V_{pv}, $I_{pv,}$ and T_{pv} of the PV array can be used as input variables for the MPPT. The output variable is the D for the DC–DC boost converter to keep tracking of MPP. A reference voltage is commonly calculated by providing the appropriate duty cycle to the converter's switches, causing the PV to function at its maximum efficiency. As a result, the PV's output voltage is operated close to the MPP voltage.

Fuzzification of input parameters from the input data is a term used to define the membership functions. The ANFIS controller generates the membership functions based on the prior knowledge received from the training dataset. The shape of the membership function changes during the training stage and the final shape is achieved after the training is completed. The learning power of the ANN is used for automatic fuzzy rule generation and self-adjustment of membership functions by the subsequent design of IF–THEN rules. The experimental data or an artificial set of data can be used to fuzzify and train the ANFIS model. The ANFIS-based MPPT structure with a five-layer network is shown in Fig. 12 [20]. For example, low, medium, and high are three generic bell-shaped-type membership functions for each input. The rule base defines the input and output membership functions relationship and mapping.

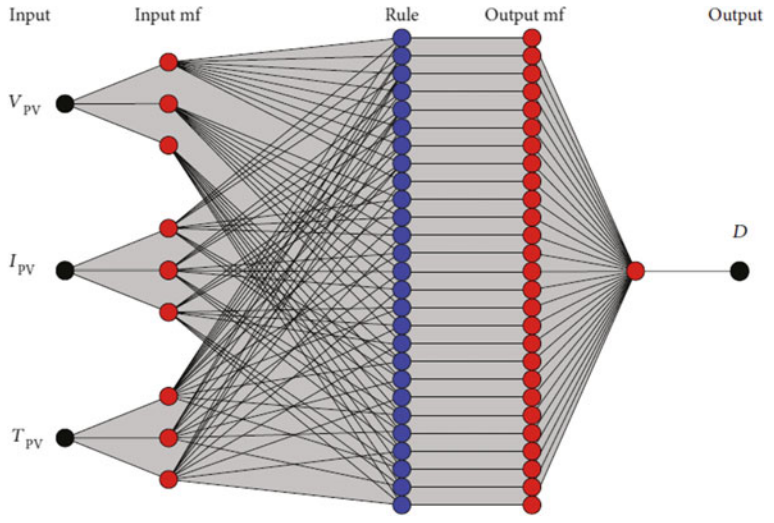

Fig. 12 The ANFIS model-based MPPT structure [20]

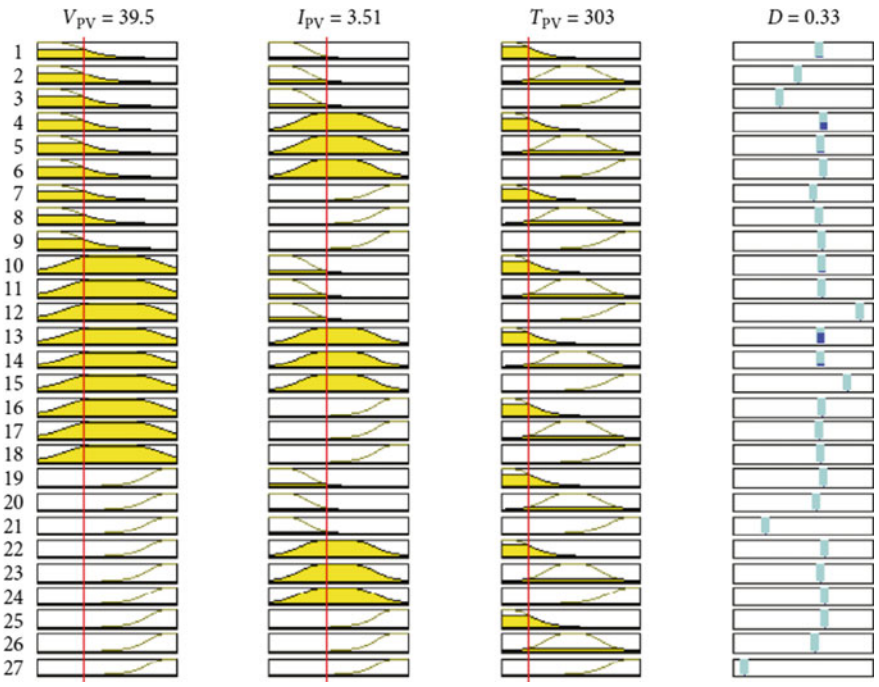

Fig. 13 Rule base of ANFIS based MPPT [20]

The ANFIS model can tune the red slider on the input and output variables according to the input parameter values. The output duty cycle of the ANFIS appears in the last column of Fig. 13 as the slider is moved. The experimental findings in the literature reveal that the ANFIS-based MPPT technique successfully tracks the MPP with a rapid response time, high tracking speed, and low oscillations. Under real-world steady and dynamic weather conditions, the ANFIS-based MPPT technique performs effectively. The maximum power tracking of PV modules can be improved with this strategy.

5.5 Optimal Torque Control (OTC) Method-Based MPPT

The Optimum Torque Control (OTC) control principle is to adjust the PMSG generator's torque to its reference torque for various wind speeds, and it necessitates knowledge of the optimal turbine parameters $C_{\text{p-opt}}$ and λ_{opt}. Considering the optimal wind speed equation, the optimum mechanical power can be represented as follows in the optimal case ($C_{\text{p-opt}}$ and λ_{opt}), using Eq. 7 [10]

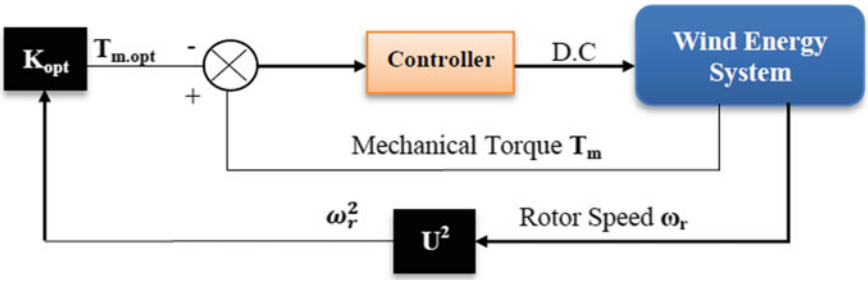

Fig. 14 The control structure of OTC method [10]

$$P_{\mathrm{m-opt}} = \frac{1}{2} C_{\mathrm{p-opt}}(\lambda, \beta) \rho \pi R_{\mathrm{w}}^2 V_{\mathrm{w}}^3 = K_{\mathrm{opt}} * \omega_{\mathrm{r-opt}}^3 \tag{37}$$

The optimum mechanical torque can be modeled as

$$T_{\mathrm{m-opt}} = \frac{P_{\mathrm{m-opt}}}{\omega_{\mathrm{r-opt}}} = K_{\mathrm{opt}} * \omega_{\mathrm{r-opt}}^2 \tag{38}$$

where K_{opt} is a constant dictated by the characteristics of the wind turbine and described by

$$K_{\mathrm{opt}} = \frac{1}{2} \frac{\rho \pi R_{\mathrm{w}}^2 * C_{\mathrm{p-opt}}}{\lambda_{\mathrm{opt}}^3} \tag{39}$$

The control structure of the OTC method is shown in Fig. 14. Where wind speed ω_r and mechanical torque T_m are obtained from the wind system and given as inputs to the closed-loop controller to obtain optimum output.

5.6 *Power Signal Feedback (PSF)* Method-Based *MPPT*

Using the Eq. 37 of the power optimum, the PSF approach may maximize the output power of a PMSG generator by computing the reference power for a given wind speed. The computed power is then compared to the current power to generate a control signal that is sent to the boost converter, ensuring that the power coefficient C_p and the tip speed ratio are always at their best values. The control structure of the PSF approach is illustrated in Fig. 15 [10]:

Thus, an MPPT controller associated with a DC–DC converter is widely preferred in RES power applications. In this case, the DC–DC converter handles the MPPT and provides some voltage amplification if needed. The DC–DC converter topologies are used in three categories which include

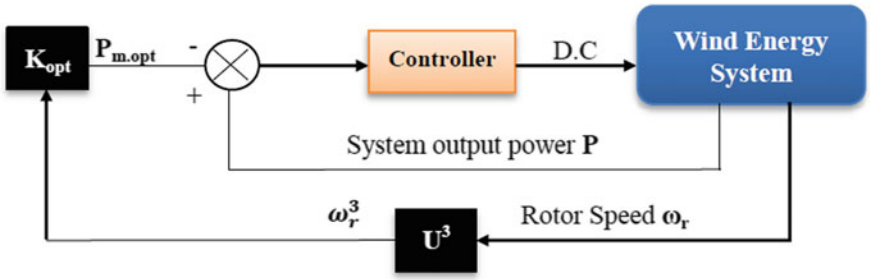

Fig. 15 The control structure of PSF method [10]

(i) The boost converter is also known as a step-up converter. It is used to increase the input voltage to a higher level as required.
(ii) The buck converter is also known as a step-down converter. It is used to reduce the output voltage than the input voltage level as required.
(iii) The buck-boost converter increases or decreases the voltage ratio with a unit gain for a duty ratio of 50%.

The DC–DC converter's duty ratio is adjusted according to the system output using a suitable inverter controller to obtain the sources' maximum input and maintain constant DC voltage at the DC link. A reasonable DC link capacitor is usually inserted after the DC–DC converter to minimize the DC voltage ripple present in the output and to enhance the input DC voltage to the inverter [21].

6 Inverters and *T*heir Selection Criteria

Inverters are power electronic devices that convert the DC energy produced by the RES into the AC power required by the grid. Inverters should produce AC energy of the required quality—with low total harmonic distortion of current, a high-power factor (close to unity), and a low level of electromagnetic interference. Inverters must also meet safety standards for users, equipment, and the grid.

The development in power electronics technology replaces the thyristors with insulated-gate-bipolar-transistor (IGBT) switches to increase the power capacity, response speed. Compared to the thyristor-based inverter, the IGBT-based converter does not require an external circuit to turn off the device. And the anti-parallel connection of the diode in the design adds the advantage of bi-directional power flows without affecting each leg's power rating. Based on the inverter operational control, the three-phase inverters are categorized into two types. They are Voltage Source Inverter (VSI) and Current Source Inverter (CSI). In VSI or CSI, the IGBT switches gate signals are the essential control parameters for the inverter systems.

VSI is a type of inverter which generates independently controlled AC output voltage as an output. In VSI, the DC source has negligible impedance and stiff

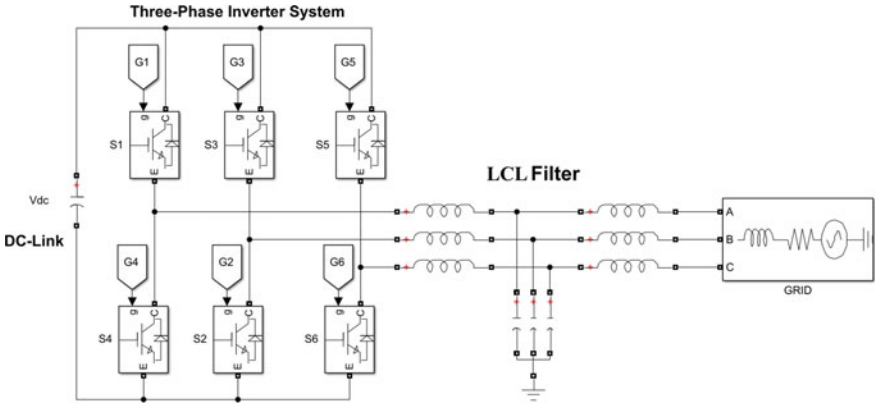

Fig. 16 Schematic diagram of three-phase bi-directional voltage source converter connected to the power grid using LCL filter

DC voltage at its input terminals. Its output voltage is mostly unaffected by the load variations. Due to these properties, the VSI is used in large power and industrial applications such as variable wind turbines, fuel cells, solar PV battery storage systems, adjustable speed drives [21]. The basic block diagram of three-phase bi-directional VSI is shown in Fig. 16. The DC-link voltage (V_{dc}) is given as input to the three-phase VSI. The signals G1, G2…G6 represent the gate signals to the IGBT switches of the inverter. The IGBT switches S1 and S4 constitute for phase-A, Switches S3 and S2 constitute for phase-B, and S5 and S6 are for phase-C. The switches are triggered accordingly with the help of gate pulses obtained from the inverter controller. The output of the inverter is connected to the LCL filter to remove the harmonics present in the output due to switching action. Further, the output of the filter is connected to the power grid.

In contrast, the CSI is a type of inverter which generates independently controlled AC output current waveform as an output. Similar to the VSI, the output current waveform mostly remains unaffected by the load if the CSI is fed with a stiff DC source. However, the CSI is usually fed through an adjustable current source from a high impedance DC source. It is mainly used in medium voltage industrial applications. Figure 17 shows an example of commercial inverters used for renewable power applications [22].

The three-phase grid-tied PV inverters range from >20 kW to 1 MW are shown from left to right. The inverters can be stacked together to operate for large-scale power applications to achieve the most robust, reliable, and efficient system. These are the scalable building blocks for multi-MW solar projects with state-of-the-art technology. They also offer advanced grid-support functions with low installation, operation, and maintenance costs compared to old ones.

Fig. 17 Photographs of the commercial inverters used for renewable power applications [22]

6.1 Selection Criteria for Inverters

The inverter is the main and essential component in the RES systems. The precise configuration and selection of an inverter are critical for the normal operation of a renewable power generation system. The inverter configuration should be determined using the technical indicators of the entire power system as well as the manufacturer's product sample handbook. In general, the selection criteria for the inverters are discussed as follows:

1. **Rated power**: The rated output power is the inverter's capacity to supply power to the load/grid. An inverter with a high-rated output power can handle a greater amount of power. When picking an inverter, it's important to make sure it has enough rated power to meet the equipment's requirements at maximum load, as well as the system's expansion and access to some temporary loads.
2. **DC–AC electrical machine efficiency**: The essential parameter for grid-connected RES power generation is the DC–AC electrical conversion efficiency, which is typical of different inverters. The inverter's efficiency has a significant impact on the power generation system's ability to generate adequate power

while lowering the cost of production. The use or lack of a galvanic insulation transformer has the most significant impact on the DC–AC conversion efficiency of all the design and construction parameters of inverters. Local regulations in several countries mandate galvanic insulation or its equivalent between the AC generated on the grid, and the DC generated on the PV side. This can be accomplished with either 50 Hz Low Frequency (LF) or High Frequency (HF) transformers [23]. The presence or absence of LF or HF transformers in inverters affects not only the size, weight, ease of installation, and material costs but also the earthing and safety measures to be implemented in the RES system, as well as the control of DC injection feed into the grid. Inverters using an LF transformer can achieve 92% DC–AC efficiency, whereas those with an HF transformer often achieve 94% [23]. Two percentage points can boost the efficiency by removing the insulating transformer. Inverters with HF insulation require more electronic components than inverters with LF insulation. Another aspect to consider is that inverters that use LF transformers always avoid injecting DC into the grid (by definition, an LF transformer does not allow DC current to pass through it). As a result, DC current measurement devices and related control for the injection of DC current are required for HF transformers.

In the recent market, inverters introduced can function at a wide range of DC voltages. For those inverters with high efficiency at partial loads, the DC input voltage has a small effect on the DC–AC conversion efficiency.

To improve efficiency-to-cost ratios, inverter manufacturers would rather raise the DC operating voltage and use low-current-carrying semiconductors to boost efficiency at partial loads. Inverters below the KW level should have an efficiency of 80–85% in general [23]. The efficiency of the 10 KW class should be between 85 and 90%,the efficiency of higher power should be between 90 and 95%. As a result, when choosing an inverter, as much as possible, it should be compared, and the product with the highest overall efficiency should be chosen.

3. **MPPT efficiency**: The DC power input to an inverter is determined by the point on the PV array's current–voltage (I–V) curve or wind characteristics at which it is operating. The inverter should ideally run at the maximum power point (MPP) in both systems. The MPP varies during the day, primarily due to environmental factors like irradiance, temperature, and wind speed, etc., but inverters directly connected to RES sources use an MPP tracking algorithm to maximize energy transfer.

   The MPPT tracking efficiency is defined as the ratio of the energy acquired by the inverter from a RES source to the energy obtained with optimum MPP tracking over a certain time period.

   This can be seen in the following equation [23]:

$$\eta_{\mathrm{MPPT}} = \frac{\int_0^t P_{\mathrm{dc}}\,\mathrm{d}t}{\int_0^t P_{\mathrm{m}}\,\mathrm{d}t} \tag{40}$$

   where P_{dc} is the inverter's DC input power and P_{m} is the MPP.

4. **Total Harmonic Distortion (THD) of the current**: The current generated by the PV inverter has its total harmonic distortion or THD. Grid-connected PV inverters must produce energy of defined quality. The harmonic spectrum of the current waveform (measured up to harmonic number 49) must have a THD of less than 5%, while the THD of the voltage must be less than 2% [23] according to IEC and IEEE standards. Inverters THD output current increases at power levels below nominal power.
5. **Power Factor**: In IGBT-based inverters, the power factor, which is also related to the quality of generated energy, is near to unity (0.999) for power operation levels above 20% of nominal power [23]. There are no technological hurdles to voluntarily controlling the power factor in order to generate or consume reactive energy. Improved grid quality (reactive power by phase displacement and harmonics control) has recently been explored and implemented in inverters for new, larger, centralized grid-connected PV systems.
6. **DC current Injection**: The DC current injection into the electrical grid via PV inverters is related to the THD of the generated current waveforms. Customers' DC injection into the general grid can cause the mains transformers' operating point to move toward probable saturation, resulting in a high primary current that can trip the fuses and create a power outage in that portion of the network. DC promotes cathodic corrosion of cabling, which reduces transformer lifetime and efficiency. A large, heavy 50 Hz LF transformer is commonly used in PV inverters, which prevents DC from being injected into the grid and also provides galvanic insulation. LF transformers account for about 15% of an inverter's total material cost and significantly increase the inverter's weight and diminish its DC–AC conversion efficiency [23]. As a result, in recent years, manufacturers have looked at ways to eliminate LF transformers. While the design of transformer-less inverters to minimize DC current injection has some technical complexities, they are being overcome using improved current sensing electronic control approaches.
7. **Prevention of Islanding**: The electrical phenomenon of islanding occurs when a segment of a power network is separated from the main supply, and PV systems exclusively power the loads. Islanding is undesirable in terms of public safety and that of the electricity distributor's staff, the quality of supply, and the potential damage to equipment in the event of automatic or manual re-closure of the distribution system to a power island. It is still a contentious subject in the international standardization of grid-connected PV systems. As a result, islanding protection is frequently integrated into the inverter. Active techniques (based on frequency shift, impedance monitoring by current injection, monitoring of phase jumps and harmonics, positive feedback methods, or unstable current amplification) should be combined with passive techniques (for detecting voltage and frequency changes) to prevent islanding under perfectly balanced load conditions in both active and reactive power cases. Many various preventative measures have been described and implemented, and they are continually improving. Several studies have been conducted to assess the likelihood of islanding and the danger associated with it, and they have concluded that

islanding is essentially impossible for low-density PV generation since load and generation never match. However, active islanding protection methods, in addition to voltage and frequency control, are required for grid sections with a high density of PV and wind generation to keep the risk of PV or wind introduction onto networks to a minimum.

8. **Output voltage adjustment**: The voltage stabilizing capacity of the output voltage of an inverter is represented by the adjustment performance of output voltage. When the dc input voltage is allowed to fluctuate within a certain range, the inverter output voltage fluctuates by a percentage of deviation, which is referred to as the voltage adjustment rate.

   When the load changes from zero to one hundred percent, the load adjustment rate, or deviation % of the output voltage of a high-performance solar inverter, should be delivered at the same time. Solar inverters with good performance should have a voltage adjustment rate of less than or equal to 3% and a load adjustment rate of less than or equal to 6%.
9. **Operation of Power Limitation**: In the literature, the ideal ratio between the nominal power of the RES and the inverter has been extensively studied. Because of the disparities between the nominal and operating power of the PV array or wind, inverters must be protected from the over-power operation. In cases when RES source power is greater than the inverter's maximum DC power input, inverters should have the internal algorithms essential to maintain maximum DC power input by diverting input power away from the MPP. For example, in circumstances when the PV array MPP is higher than the inverter's maximum input power might avoid power limitation losses if not considered in the PV system design and sizing.

The three-phase voltage source inverters with suitable inverter controllers are widely operated in the distribution networks or grid-connected operations to effectively optimize the inverter output and parameters [6]. The inverter control system aims to maintain the steady output voltage and frequency by achieving the minimum total harmonic content. The controller uses a suitable control strategy to maintain the voltage at a specific set point or reference input [24]. The duty cycle is the crucial control parameter in power electronic converters. It is controlled by the controller to enable the inverter output voltage to track the reference signal (Of and Power, [25]. Accurate tracking depends on the capability of the inverter controller. The output voltage harmonic content is maintained at a minimum point with a proper control strategy and design. Thus, smart inverters are designed and widely employed in the RES systems to control the system parameters according to the grid codes and provide state-of-art communication between the control networks. The comparison between conventional inverter and the smart inverter is shown in Table 1.

Table 1 Comparison between conventional inverter and the smart inverter [26]

Situation	Conventional inverter	Smart inverter
Ride-through utility fault	Avoid contribution to the fault	Involve in ride-through utility fault
Utility disturbance	Disconnect the PV system from the grid	Support and enhance grid V/F stability
Power generation	No capability to control power overproduction	Monitor and limit power generation
V/F variation	No contribution in supporting V/F. Only disconnected	Monitor V/F fluctuation and generate action stability
Anti-island detection	Not implemented yet	Investigate transient fault based on defined scheme
Flicker	No contribution	Mitigate voltage and frequency flicker
Power factor	No contribution	Active load balancing power factor and reactive power control

6.2 Selection Criteria of Filters

The filter is an essential component used at the inverter output. The inverter is coupled to a filter to connect to supply the power grid with a pure sinusoidal waveform without harmonic distortion. The non-sinusoidal nature of PWM voltages due to switching effects at these converters' outputs necessitates proper filtering to keep the current harmonics fed into the grid to a minimum [27]. The harmonic components of waveforms transmitted to the power grid are widely known to be highly dependent on the filter architecture and switching frequency [28]. First-order passive L-filter is usually connected between the inverter and utility grid to reduce the injection of current harmonics. The L filter has a simpler topology and is easy to design. However, this design is not viable for low switching frequencies (below a few kHz) [28]. Furthermore, the system's dynamic reactivity deteriorates. A large inductor is required to achieve the power quality standards under these conditions, reducing the transmission capabilities.

LC filters are another sort of second-order passive filter. An inductance in series with the inverter and a capacitance in parallel with the grid make up the filter. Compared to an L filter, the inductance can be lowered by using this parallel capacitance, resulting in lower costs and losses. Other issues arise from using a large capacitance, such as high inrush currents and high capacitance current at the fundamental frequency or the filter's reliance on the grid impedance for overall harmonic attenuation. Furthermore, LC filters have the drawbacks of time delay and resonance frequency [29].

To avoid activation of the filter resonance effect, the filter's resonant frequency should not coincide with frequencies of switching harmonics, which is perhaps the most significant consideration for selecting LCL filter parameters [30]. The filter

resonant frequency (f_r: $0.25 f_c < f_r < 0.5 f_c$) should be chosen so that it avoids resonance excitation and ensures the overall system's stability. The LCL filter resonant frequency f_r is given as follows:

$$f_r = \frac{1}{2\pi}\sqrt{\frac{L_{fg} + L_{fi}}{L_{fg} * L_{fi} * C_{fg}}} \tag{41}$$

where f_c is the carrier frequency (2–5 kHz), L_{fg} and L_{fi} are the LCL filter inductors on the grid side and inverter side, respectively. C_{fg} is the filter capacitance. The voltage drop at the rated load determines the combined filter inductance, typically between 5 and 20% of the rated line-to-neutral grid voltage (V_n). The converter side inductor is primarily responsible for limiting the converter AC current ripple. The maximum value of the converter AC current ripple ($I_{c,\,max}$) determines the minimum inductance value of the converter side inductor, which can be chosen as follows [30]:

$$L_{fi,min} = \frac{V_{dc}}{K * f_c * \Delta I_{c,max}} \tag{42}$$

where K is the coefficient that depends on the modulation technique, reactive power at f_n should be kept to a minimum when it comes to filtering capacitors. In this case, the maximum capacitance value is equal to [30]

$$C_{fd,max} = \frac{\lambda * P_{rated}}{2\pi f_n * \left(\sqrt{3} * U_n\right)^2} \tag{43}$$

where P_{rated} is the rated power of the inverter, and the coefficient λ is proportional to the maximum reactive power. Its value is commonly set between 0.05 and 0.1.

6.3 Control Technique of Inverter with a Switching Technique

The fundamental magnitude and frequency of an inverter's output voltage can be adjusted to be constant by exercising control within the inverter itself. Controlling the VSI and reducing harmonics can be accomplished using a variety of switching approaches. Pulse Width Modulation (PWM) control within the inverter is the most efficient way and widely used in the literature. The PWM method possesses the advantages of reducing lower-order harmonics while higher-order harmonics are eliminated using a filter and control of inverter output voltage without any additional control structure. However, this method has the disadvantage that the switching devices used in the inverter are expensive since they must have low turn-on and turn-off times; yet PWM is widely employed in industrial equipment.

The sinusoidal PWM (SPWM) method, also known as the triangulation, sub-harmonic, or sub-oscillation method, and has received substantial research. The Sinusoidal Pulse Width Modulation (SPWM) technique was explained to regulate the inverter because it can directly control the inverter output voltage and frequency using sine functions. The SPWM signal is generated by comparing the high-frequency (in the hundreds of kHz range) triangle carrier wave V_c with the three reference sinusoidal waves of the desired frequency at 120° phase shift. The modulated pulse's switching instants and commutation are determined by the intersection of waves. When the sine wave voltage exceeds the triangle voltage, the comparator generates a pulse, which is utilized to activate the inverter switches. The switches of any leg in the inverter cannot be turned off at the same time to avoid undefined switching states and undefined AC output line voltages in the VSI. The phase outputs are phase altered by 120°. The ratio of a triangle wave to a sine wave must be an integer N, the number of voltage pulses per half-cycle, so that $2N = \text{fc/fs}$. The SPWM is explained with reference to the single-phase in Fig. 18. The triangular carrier wave V_c is compared with one-phase sinusoidal reference $V_{\text{ref,}}$ for example. When $V_{\text{ref}} > V_c$, the output voltage to the IGBT S-1 in the phase-A of the figure—is $V_{\text{out}} = \frac{V_{\text{dc}}}{2}$. When $V_{\text{ref}} < V_c$, the output voltage to S-3 in the phase-A of figure—is $V_{\text{out}} = -\frac{V_{\text{dc}}}{2}$. Similarly, the

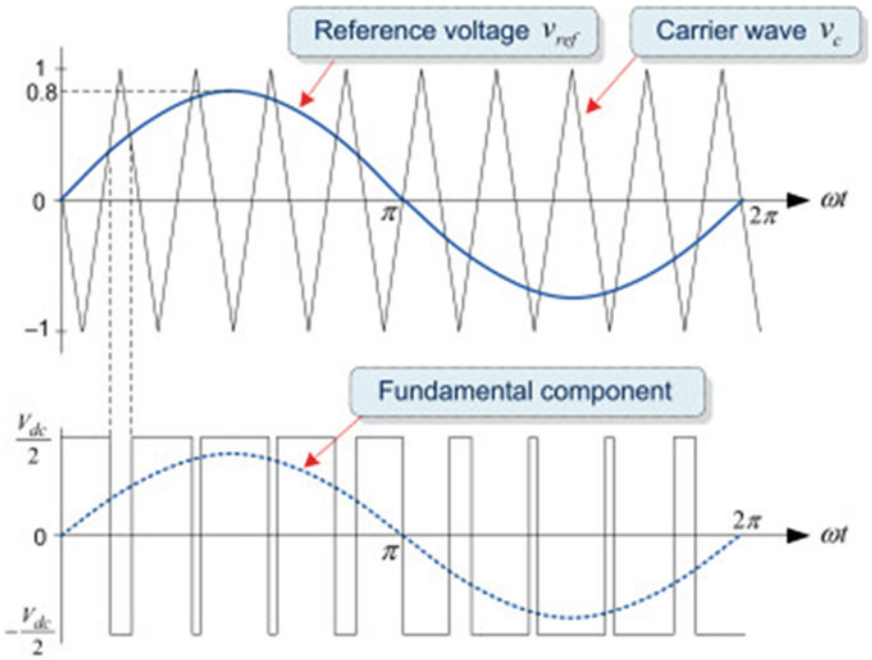

Fig. 18 The SPWM approach with single sine wave comparison with triangular wave (top) and respective modulation pulses to the switches in phase-A of a three-phase inverter is represented in the bottom [31]

other sine waves for phase-B and C are compared, and respective modulation pulse will be sent to the inverter IGBT switches in legs B and C.

The ratio of a triangle wave to a sine wave must be an integer N, the number of voltage pulses per half-cycle, so that $2N = fc/fs$. The amplitude (M_{amp}) and frequency modulation (M_{freq}) are defined as

$$M_{amp} = \frac{A_r}{A_c}; M_{freq} = \frac{f_r}{f_c} \tag{44}$$

where A_r and f_r are the amplitude and frequency of the sine wave signal, respectively, and A_c and f_c are the carrier wave signal amplitude and frequency, respectively.

Recent studies focus on the implementation of current control techniques of the inverter using various PWM modulation techniques. Current control is a high-status issue in three-phase grid-connected inverters that must be addressed. Current control's main purpose is to ensure that the measured signal is following the reference signal. Figure 19 depicts a basic three-phase grid-connected inverter with the current control technique.

In order to improve the quality of the current waveform, various current-control approaches have been used in the literature which are discussed in later section of the chapter. Current control in a three-phase system can be performed in a variety of ways, including the natural reference frame abc, the synchronous rotating reference frame dq, and the stationary reference frame $\alpha\beta$. The rotating synchronous reference frame (dq) coordinates are widely used in the research. The two current components

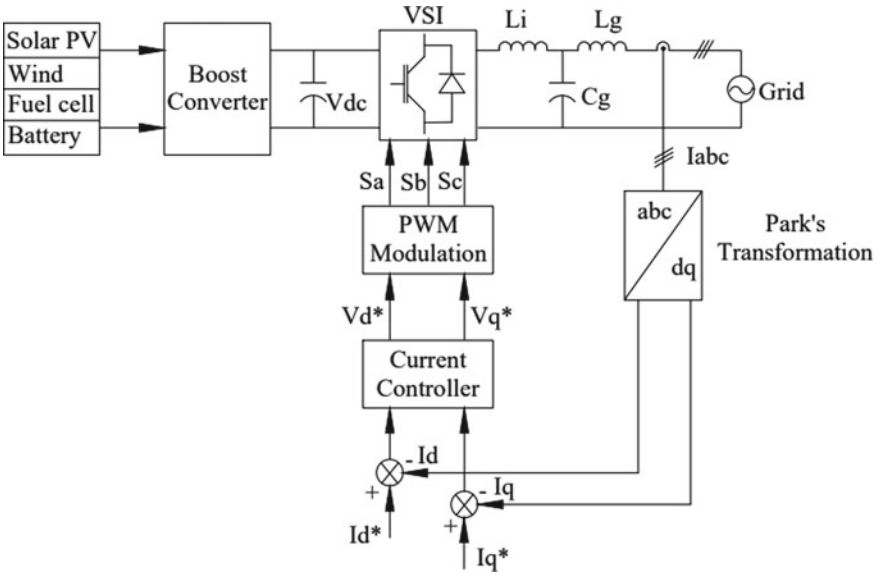

Fig. 19 Basic current control schematic for three-phase grid-connected inverter

appear as DC components. The direct component is represented by the d coordinate, whereas the q coordinate represents the quadrature component. Park's transformation transforms three-phase reference frame abc coordinates into dq synchronous coordinates in a rotating reference frame with angular frequency in the three-phase system. The measured i_d and i_q components are compared with the current controller's reference i_d* and i_q* values. The reference voltage signals V_d* and V_q* are fed to the PWM modulation. The reference dq signals are converted back to abc form using inverse park transform. The modulation pulses are generated according to the type of PWM technique to control the inverter output voltage.

6.4 *Power* Grid Synchronization Issues

To integrate renewable sources into the power grid, the grid connection requirements should be satisfied. Grid synchronization is an adaptive technique that is strongly related to grid monitoring. In the literature, many grid synchronization approaches such as the zero-crossing method (ZCM), phase-locked loop (PLL), and virtual flux have been presented (VF). Among those, PLL-based methods are most regularly used in the literature. Grid synchronous algorithm information is used at several levels of control of grid-connected inverters. As a result, grid synchronization technology, which detects grid conditions quickly and precisely, is a critical issue for power inverters that are connected to the grid in the distributed power generation system. A growing number of new energy-producing systems have been connected to the grid in recent years. This has a significant impact on grid stability, making it more difficult to connect inverters to the grid [32].

The modern power system is termed as a complex system. Due to the functioning of automatic adjustment devices and protection mechanisms or reclosing, the grid will suffer complicated transients when subjected to significant disturbances such as fast changes in load, primary component removal from or connection to the system, short circuit, or fault disconnection. Voltage unbalances, flashover, frequency shifting, and low and high order harmonic frequencies will arise at grid nodes close to the site of failure, as well as the electronic equipment linked to these nodes, during this time [32]. As a result, one of the most important difficulties in grid-connected inverter management is reliable detection of voltage frequency, positive and negative sequence components under complicated and unbalanced grid faults. Hence, accurate information of grid voltage is the basis for the control of inverter in grid-connected RES.

To detect the exact system voltage and phase-angle and to synchronize the system, the phase-locked loop (PLL)-based synchronous methods are widely implemented in the system. However, the current PLL techniques used in the system only control the voltage fluctuations caused by higher-order harmonics, eliminating the effects of lower-order harmonics in the system. The recent research advances in PLL-based techniques drive the control techniques to achieve better performance under all harmonics.

7 What is Smart Inverter?

In recent years, the advancement in power electronic devices leads to smart inverters development with smart features to operate autonomously with limited operator intervention. In addition to the standard DC–AC conversion, the smart inverter addresses the challenges associated with a highly variable RES system output integrated into the power grid network by allowing bi-directional power flow, sophisticated monitoring and communication with the associated grid status, self-awareness for fault detection, adaptability to the change of loads/working parameters, and the autonomous decision making to maintain the grid stability and reliability [33]. It can ride through minor frequency and voltage disturbances and provide a soft start after the power outages [6]. Also, it can inject or absorb power into or from the grid with principles of grid-serving and grid-feeding inverter. The smart features of a smart inverter are represented in Fig. 20 [34].

As mentioned before, incorporating the RES systems into the grid imposes the voltage and frequency fluctuations at the PCC. Typical inverters trip offline very quickly due to transient frequency or voltage fluctuations on the grid and do not return to their operation quickly, which causes vast power loss. Under grid unbalances and voltage fluctuations, the smart inverter should have the capability to remain connected to the grid for a specific duration based on the maximum and minimum

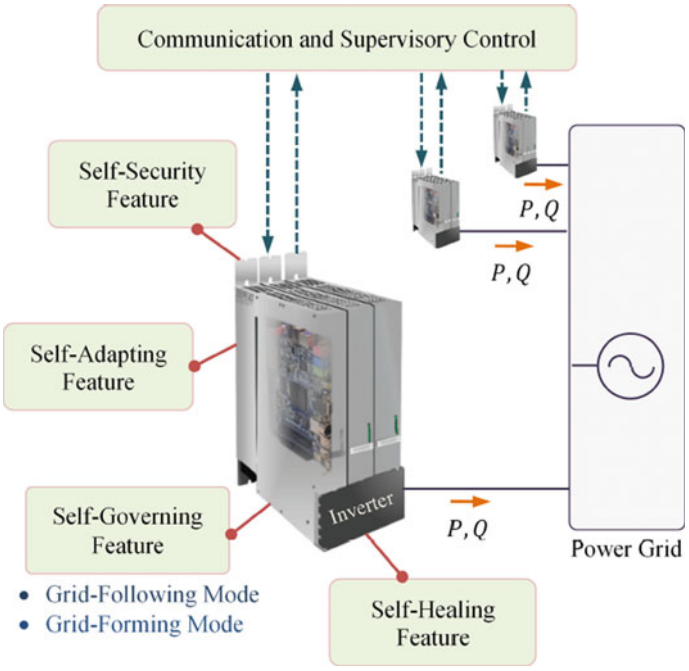

Fig. 20 Smart inverter with smart features connected to the power grid [34]

voltage deviation levels allowed by the system. It must trip (disconnect the system) when the limits are violated [35]. The smart inverter voltage ride-through capability supports the grid by providing reactive power support, negative sequence compensation, and stabilized grid voltage. To achieve the voltage ride-through capability under faults, voltage detection and synchronization schemes are usually employed in the RES system during integration. The frequency ride-through control scheme is also incorporated in the smart inverter to maintain the system frequency within the appropriate limits (60 ± 5 Hz). Furthermore, the smart inverter's voltage control features mitigate the power network's impact by using one of several operating-mode alternatives to modulate the real and reactive power profiles.

The power electronic devices such as converters, inverters contain various controlling and switching elements. The continuous operation of switching elements in the inverter and converter generates harmonic currents during non-linear loads. The injection of current distortions will cause power quality issues in the interconnected power network. IEEE standards limit the allowance of total harmonic distortions to 5% of the rated current level. However, the renewable systems connected to the grid suffer from harmonic distortions of the current due to unavoidable faults on a grid and operational modes. To control the harmonic distortion of injected current, various active and passive filters are widely used in the power system network. However, the filtering methods used in the system are sensitive to the system operating parameters and involve a high cost. To achieve power quality improvements and harmonic compensation, alternative control strategies were developed. Using the RES system capacity, the smart inverter's current controller is modified to achieve the system harmonic current compensation by using several controllers such as predictive controller, repetitive controller, or hybrid controller.

In the grid-connected system, the active power generation is greater than the grid power flow, and consumption leads to the reverse power flow in the power network. The reverse flow of the power leads to over-voltages and will cause problems to the coordinative protective devices, which disconnect the equipment for maintaining stability. The reactive power control strategies were proposed to achieve system stability and ensure the system voltage within the appropriate level. The renewable systems with energy storage systems and smart inverters supply the reactive power to the system or provide ancillary services for the low-voltage networks without any auxiliary equipment. The Volt-Var (VV) control method is implemented by the inverter to maintain the dynamic voltage regulation. To control the over-voltages during uncertain disturbances in the system, the inverter injects or absorbs reactive power to and from the system based on the voltage level at the inverter terminals.

8 Various Types of Smart Inverters and Their Control Methods

The grid-interactive smart inverters are classified into three types based on their operating role, namely: grid-feeding, grid-forming, and grid-supporting smart inverter [36]. In the case of a small islanded grid or microgrids operating with either PV or wind turbines, the inverter is controlled as an ideal AC voltage source with constant voltage and frequency [37]. This mode is called a grid-forming mode. The grid-forming inverter has a control approach to form the grid voltage. It can control its terminal voltage with respect to the changes in voltage phase angle at PCC with an instantaneous power response by considering its storage and reserve capacity [38]. In large power grids with synchronous generators and central inverters, the inverters feed the grid as an ideal current source. This mode is called grid-feeding mode. The grid-feeding current-controlled inverter has a control approach that injects the current into the grid to meet the given power set point independent of frequency and voltage deviations at the terminal [38]. It is designed to deliver active and reactive powers to the energized grid and does not contribute to power-sharing. In grid-supporting mode, neither grid-feeding nor grid-forming is an option. In inverter-dominated grids, the grid-supporting inverters play a key role in forming the voltage and frequency and adjust the active and reactive power setpoints during deviations either in interconnected mode or standalone grid [37]. The grid-supporting inverters are further divided into two types, namely grid-supportive grid-feeding and grid-supportive grid-forming inverter. The grid-supportive grid-forming inverter operates as a voltage source and regulates the voltage magnitude and frequency of the grid in either mode. In this operation, the voltage and frequency values are not fixed but operated as a function of active and reactive components of the droop equations. The grid-supportive grid-feeding inverter operates as a droop-controlled current source. The main objective of this inverter is to maintain the grid voltage, frequency, and amplitude under control by adjusting/regulating the exchange of active and reactive powers with the grid. The different behaviors of the grid-connected inverters are summarized in Table 2 [39, 37, 36].

An inverter's operation modes and control methods can vary based on the application and depend on the type of connected loads, modes of microgrids, etc. Currently, no standard operation and control strategies are standardized for inverter-interfaced operation. The majority of the literature focuses on the operation and control of renewable sources' primary control strategies due to their power-sharing challenges in a microgrid [40]. To ensure efficient power management, control, and coordinated operation of the renewable sources in power grids, a hierarchical control method with various control strategies has been developed and implemented in the power system. The main requirements of hierarchical control in a microgrid includes.

- Voltage regulation
- Frequency regulation
- Power flow control
- Power-sharing

Table 2 Electrical behavior of grid-connected inverters and their contribution to the grid [37]

Contribution to the grid	Grid-forming	Grid-feeding	Grid-supporting type	
			Grid-feeding	Gird-forming
Type of source	Ideal voltage source	Ideal current source	Droop-controlled current source	Droop-controlled voltage source
Type of control	Constant frequency/voltage. Provides *v-f* (ref)	Follows *P-Q* control	Adjusts *P-Q* (ref) (according to *v-f* level)	Provides *v-f* (ref) (according to *P-Q* level)
Output impedance	$Z = 0$	$Z = \infty$	Finite	Non-zero
Output frequency	Fixed frequency	Grid synchronized	Frequency droop	Frequency droop
Application	Island grid/isolated	Grid-connected	Grid-connected (or) isolated	Grid-connected (or) isolated

- Load sharing
- RES coordination
- Cost optimization
- Power generation and demand prediction

The hierarchical control is divided into three levels: primary control level, secondary control level, and tertiary control level. The hierarchical control of a microgrid with three-level controllers is shown in Fig. 21 [39].

The primary controller consists of inner voltage control and current control loops for instantaneous grid reference voltage and current tracking. It is responsible for stabilizing the local voltage level to the reference voltage and controlling the values by simultaneously adjusting frequency and output voltage magnitude [39]. As shown in Fig. 21, the difference (error signal) between active and reactive power reference (P^* and Q^*) and measured values (P_m and Q_m) is given to the reference voltage generator. It will generate the reference V_d^* and V_q^* components. The measured V_d

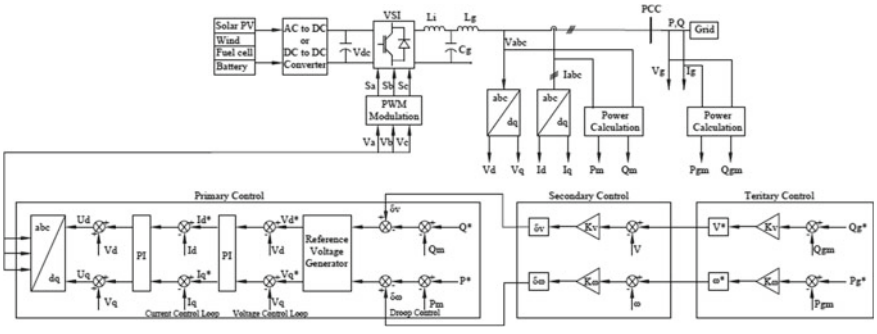

Fig. 21 Hierarchical architecture of a microgrid with primary, secondary, and tertiary control levels [40]

and V_q are compared with the reference V_d* and V_q* in the voltage control loop. The reference I_d* and I_q* are generated using the PI controller. The measured I_d and I_q are compared with the reference values (I_d* and I_q*) in the current control loop. The PI controller in the inner current loop will generate voltage signals which are given to the PWM method using inverse park transformation. The PWM technique uses the transformed abc voltage signals from *dq* axis to compute the gate pulse to the inverter switches based on the received reference signals. The secondary controller computes the δv and $\delta\omega$ by the difference between measured (V and ω) and a reference voltage and frequency ($V*$ and $\omega*$) values. At the same time, the territory controller provides the reference voltage and frequency ($V*$ and $\omega*$) values by computing the difference between measured (P_{gm} and Q_{gm}) and grid active and reactive power (P_g* and Q_g*) values.

The inner voltage and current regulation loops may operate using feedback, feed-forward, virtual impedance; linear and non-linear control loops to supervise and regulate the inductor and/or capacitor voltage of the filter to reach the fast dynamic response of the system while maintaining the system stability [39, 40]. The primary control is based only on local measurements and is responsible for improving the system's power quality, reliability, and performance.

The secondary controller plays a role in the grid synchronization of a microgrid with the main power grid. It is responsible for frequency and voltage restoration in case of deviations produced by virtual inertias and output impedances. The secondary control measures the microgrids voltage (E_{mg}) and frequency (ω_{mg}) and compares those with the set reference values $E*$ and $\omega*$ and sends the error values ($\Delta E = E* - E_{\text{mg}}$) and ($\Delta\omega = \omega* - \omega_{\text{mg}}$), respectively. The controller decouples the control parameters and sends the frequency and voltage restoration signals to maintain the set reference values. Similarly, the phase between grid and microgrid is also measured by the controller and sent to all the units to synchronize it to the power grid [39]. Thus, the secondary control enhances the system performance by maintaining voltage and frequency stability. The tertiary-level controller deals and regulates the power flows between the microgrid and main power grid at the PCC. It is also called a supervisory controller. This level maintains the load balancing by using optimal power flow algorithms. The active and reactive power flows can be injected or absorbed by adjusting the microgrid set points.

Numerous inner-loop control methods are developed to improve the system's performance by improving power quality, inverter output voltage or current tracking, and disturbance rejection by rejecting utility grid harmonics. From simple approaches to complex analytical controls, the different control strategies are mainly designed in accordance with the electrical grid conditions at the PCC. The developed methods are used according to the characteristics of the microgrid. These controllers are summarized in the following Fig. 22 [40].

Each inverter will have a droop control-based external power loop to allow each RES system's autonomous operation in a multi-connected or parallel-connected inverter system. The power control can be performed with or without communication with the main system. The power control techniques with communication are classified as Central control, Master/slave control, Peak values-based and Average

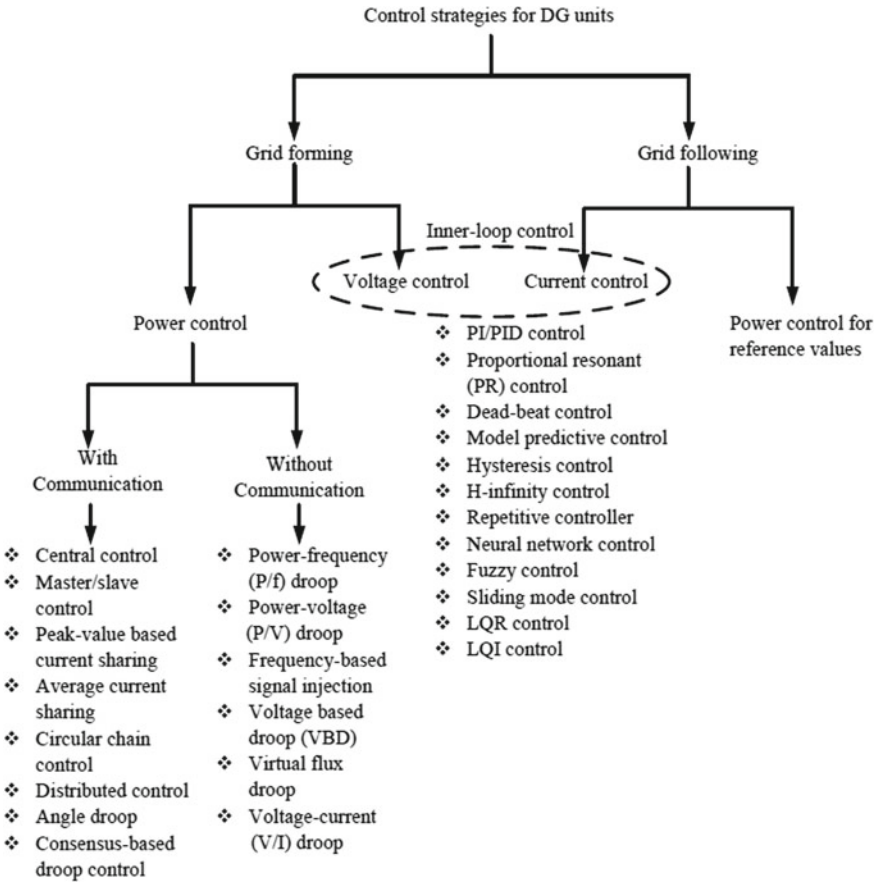

Fig. 22 Control techniques for inner-loop control in primary control [40]

current sharing based, Circular chain control, Distributed control, Angle droop, and Consensus-based droop control systems. The power–frequency (P/f) droop-based, Power-Voltage (P/V) droop-based, Frequency-based signal injection, Voltage-based droop, Virtual flux droop, and Voltage-Current (V/I) droop are the popular techniques used for power control without communication. In the literature, the power control techniques without communication are highly studied. Various inner-loop control methods are discussed briefly in the following sections.

8.1 Conventional PI and PID Controllers

The most commonly employed inverter controllers in RES systems are proportional-integral (PI) and proportional-integral-derivative (PID) controllers. The PI controller

algorithm in the time domain can be represented as Eq. 45.

$$u_{\mathrm{pi}}(t) = k_{\mathrm{p}} e(t) + K_{\mathrm{i}} \int_0^t e(t')\mathrm{d}t' \tag{45}$$

where $u(t)$ is the output of the PI controller, and K_{p} and K_{i} are the gains of the proportional and integral terms, respectively. The gain values given to the inverter IGBT switches determine the output behavior of the system. The block diagram of a three-phase inverter system using PI controller is shown in Fig. 23. The voltage V_{abc} and current I_{abc} are measured and are given to the PI controller. The PI controller compares the measured values with the reference voltage and current V_{abc}*, and I_{abc}* values, respectively. The output of the PI controllers is given to the PWM generator to generate the gate pulses to the generator.

The controller reduces the steady-state errors and generates the gains in such a way that the output voltage is regulated close to the reference voltage. The controller performance is achieved by executing a proper control strategy integrated with the Pulse Width Modulating (PWM) technique. Controlling the inverter switching scheme with PWM control techniques can significantly reduce the harmonics and distortions in the output voltage and produce the power at high efficiency. However,

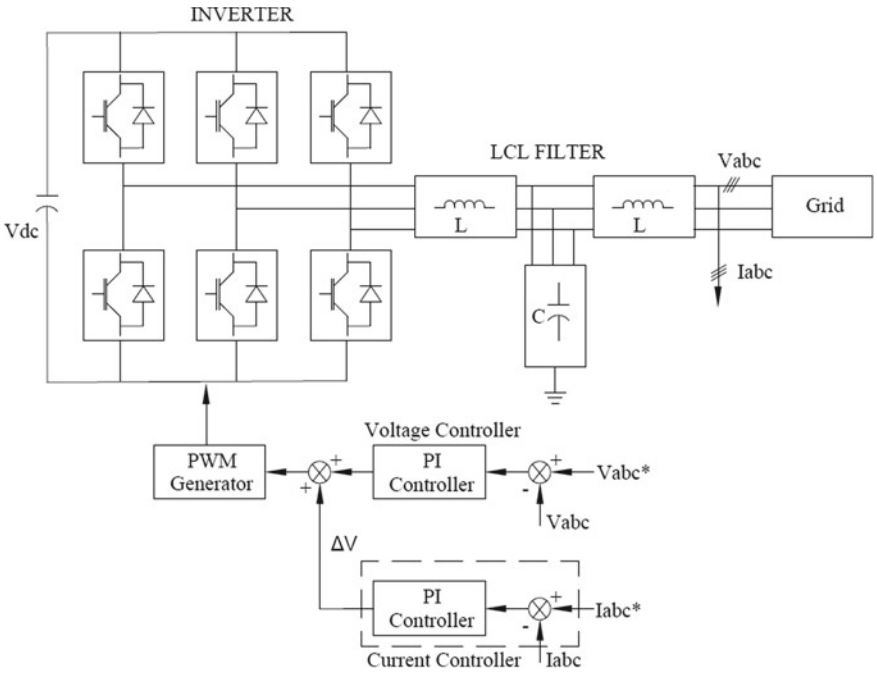

Fig. 23 Block diagram of three-phase inverter system with PI controller

there are various PWM techniques available for inverter control, and the control parameters such as computational speed, harmonic distortions, switching losses may vary according to the PWM techniques. The PI controllers are used for various applications in a power system, such as inner control loops, fault ride-through, using the optimal control algorithms to tune the control parameters. Although the system performance can be improved by optimal tuning of control parameters, the sensitivity to the operating conditions and long computational time will slow down the system response. Similar to the PI controller, the PID controller also widely employed in grid-connected RES systems. The PID controller algorithm in the time domain can be represented as Eq. 46.

$$u_{\mathrm{pid}}(t) = K_{\mathrm{p}} e(t) + K_{\mathrm{i}} \int_0^t e\left(t'\right) \mathrm{d}t' + K_{\mathrm{d}} \frac{\mathrm{d}e(t)}{\mathrm{d}t} \tag{46}$$

where $u(t)$ is the output of the PID controller, and K_{p}, K_{i}, and K_{d} are the gains of the proportional, integral, and derivative terms. Analogous to the PI controller, the conventional PID and other state machine controllers require an exact mathematical model of the system and are very sensitive to control parameter variations. They have demerits in terms of large-scale output filtering, intelligence application, and maintaining grid frequency. Considerable research has been conducted on inverter control issues such as power and voltage fluctuations, system non-linearity, harmonic distortion, internal power losses, unity power factor maintenance [41]. Increasing attention has been paid to developing an efficient inverter controller based on adaptive control techniques because of their fast dynamic response and self-tuning ability of control parameters [42]. The application of adaptive control algorithms in solar PV and wind systems allows the researchers to develop the controller's intelligence application based on fuzzy logic, neural network, neuro-fuzzy, and artificial intelligence-based control. A nonlinear-based adaptive supervisory control can be designed for three-phase smart grid inverter applications to generate and regulate the output voltage effectively. The intelligent controllers reduce the mathematical computation and analysis problems and avoid the complexity of handling system non-linearity. The fuzzy logic-based controller is the simplest controller among all the non-linear intelligent controllers for providing the control operation in smart inverter. Also, research shows that the fuzzy logic controller provides a superior response to the conventional PI or PID controllers in terms of sensitivity to load changes or parameters, settling time, and robustness [41]. Some of the non-linear controllers are discussed in the following section.

8.2 Proportional Resonant (PR) Controller

The Proportional Resonant (PR) controller is a combination of a proportional term and a resonant term and is commonly employed in both abc and $\alpha\beta$ reference frames

[40]. It is replaced with the conventional PI controller. Clark's transformation is used to convert from three-phase i_{abc} to $i_{\alpha\beta}$ coordinators within the control system to communicate the grid current to the stationary reference frame. As a result, PR controller variables have a sinusoidal shape. Near the resonant frequency, the PR controller has high gain and the capacity to eliminate steady-state error and attenuate particular harmonics. As an inner voltage controller, PR is an excellent solution for achieving the necessary results. It's an AC regulator/integrator, and it's similar to an integrator with infinite DC gain, which forces the error to zero [39]. In grid-connected applications, a low-order harmonics compensator can be simply added in parallel with the PR controller to increase the current controller's performance by restraining the distortion of grid current [12]. In PR controller, the resonant frequency determines controller performance by maintaining a consistent network frequency which can be modified in response to grid frequency variations. The transfer function of the PR controller in the Laplacian domain can be expressed as follows:

$$u_{PR}(s) = k_p + k_i \frac{s}{s^2 + \omega^2} \tag{47}$$

where k_p is the proportional gain, k_i is the integral gain, and ω represents the resonant frequency. The precise tuning and sensitivity to frequency fluctuations are the drawbacks of this method.

8.3 Model Predictive Controller (MPC)

The goal of the predictive control being developed is to reduce forecast error for precise current tracking without any error. MPC is appealing because it manages broad restrictions and non-linearities of a system with numerous input and output in a flexible control scheme. This technique employs current state control actions to forecast the behavior of the controlled variables in the future. The controller chooses the optimal switching states based on the cost function used as a criterion. MPC is based on iterative, finite-horizon plant model optimization [40]. The present plant state is sampled at time t, and a cost-minimizing control strategy is derived using a numerical minimization technique for a relatively short future time horizon: $[t, t + T]$. In particular, an online or on-the-fly calculation is utilized to investigate state trajectories that arise from the current state and discover a cost-minimizing control strategy until time $t + T$. Only the first step of the control strategy is executed, after which the plant state is sampled again, and the calculations are repeated from the new current state, resulting in new control and anticipated state route. The method's mathematical strategy demonstrates its sensitivity to parameter changes. The least-squares method can be used for parameter estimation to improve the accuracy of the control systems. Various methods based on PR controller have been proposed in the literature for achieving accuracy.

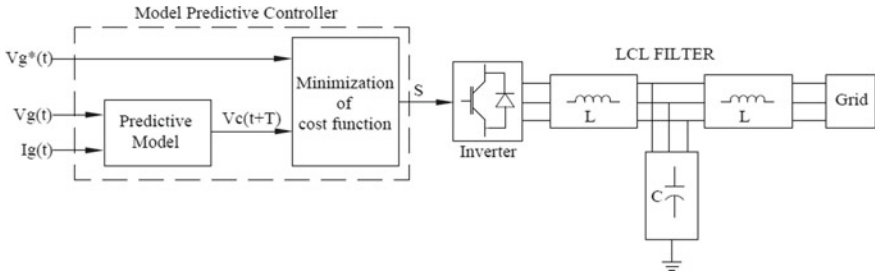

Fig. 24 Basic block diagram of a model predictive controller for a three-phase inverter system

Figure 24 shows the basic block diagram of a model predictive controller for a three-phase inverter system. The voltage and current signals V_g and I_g at sample time t are given as input to the predictive model, the output $V_c(t + T)$ and the reference signal V_g * (t) are given for the online calculation and to generate the cost minimization function. These calculations are repeated from the new current state. The output of the controller is used to generate the gate pulses to the inverter.

8.4 Dead-Beat (DB) Controller

The Dead-beat (DB) control is widely used for the current regulation of an inverter because of its effective dynamic performance in different applications [39]. DB belongs to the predictive controller family and is designed to predict the effect of current control action to reduce the forecast error. It has a very fast transient response and can track the reference current properly without any error. Because of its enormous bandwidth, the DB's instantaneous current tracking becomes appealing. The derivative of control parameters can be used to forecast future control actions. Because of its error correction, this control is well-known. The controller's main problem is that it is extremely sensitive to network factors. Although these methods improve the robustness of the deadbeat controller, they complicate the controller's structure in the event of parameter mismatches.

8.5 Hysteresis Controller

Hysteresis current controller has a non-linear controller loop and hysteresis comparators; an adaptive band of the controller must be constructed to achieve fixed frequency switching. It forces the grid-injected current to follow a reference current in a voltage source inverter. Each leg switching signal for an inverter is generated using the hysteresis control approach, which is highly simple and quick to respond. If the error

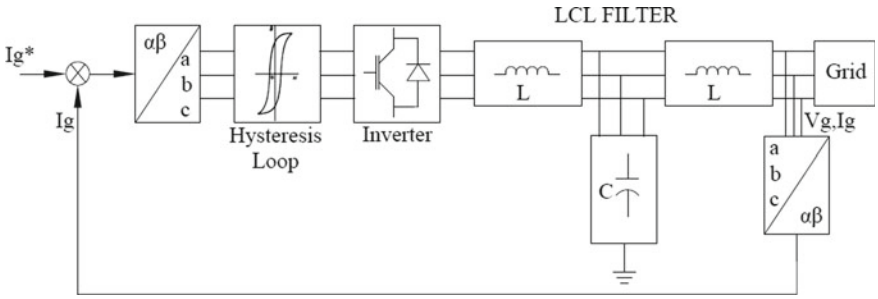

Fig. 25 Schematic diagram of a hysteresis controller for a three-phase inverter system

between the reference signal and the measured signal exceeds specific thresholds, the hysteresis controller generates a signal.

Figure 25 shows the schematic diagram of a hysteresis controller for a three-phase inverter system. In the hysteresis current controller, the measured current signals are transformed in $\alpha\beta$ frame and are used to compare with the reference value. The error generated is again transformed into abc frame and is given to the hysteresis loop in each phase to generate the gate pulses to each phase of the inverter.

8.6 Repetitive Controller (RC)

The repeated control (RC) is a simple learning control algorithm that uses the internal model principle to provide an alternative solution in case of periodic errors to eliminate the mistake in a dynamic system. The notion of repetitive feedback control (RC) was derived from iterative learning control, and it can be used to control utility converters with periodic reference signal disruptions. In these controllers, the difference between the reference value and the connected current of the feedback utility is used to generate a new reference for the following fundamental cycle. Within the RC, a low-pass filter is used to reduce high-frequency resonant peaks of gains in the controller without altering the low-frequency resonant peaks that correlate to substantial grid harmonics that must be rejected. As a result, the output voltage/current of the RC has very low harmonic distortion even when substantial non-linear loads are present.

8.7 H-infinity Controller

The H∞ controller approach's primary task is to reduce the output disturbance effect. It achieves a resilient performance in both parameter value changes and worst-case disturbances. The difficulties are first described in an optimization procedure, and

then the problems are solved using a controller. The design parameter's robustness and/or tracking performance are expressed as single values of various loop transfer functions. These loops can be shaped with the right weighting functions. The approach provides a number of benefits, including stable performance in the face of unbalanced loads, lower THD, lower tracking error, and ease of implementation in practice. The downsides of this controller are that it requires great mathematical comprehension and has rather slow dynamics.

8.8 Neural Network (NN) Controller

With the addition of a time delay, the neural network (NN) allows information to be processed in a systematic way that replicates the function of a human nerve system. The NN is a signal-transmission architecture composed of input, hidden, and output layers interconnected and operated in parallel mode to accomplish a specific processing task. The NN algorithm's self-learning characteristics make it feasible and simple to build for various operating situations and grid disturbances while also enhancing control performance.

Artificial Neural Networks (ANNs) are mathematical models that use computational neurons (non-linear cells) arranged in layers and linked to each other by weight factors to learn and process data in parallel. Because of their non-linear and adaptive structure, generalization capacity, and design independence from device parameters, ANNs are also used in microprocessor control systems. However, their "black box" existence has no rules for defining the structure (cells and layers) and the network instruction problem. In the design of intelligent control systems, FLCs and ANNs are complementary technologies. Neuro-fuzzy systems combine the fuzzy logic inference ability like a human with the learning and concurrent data processing abilities of ANNs to create neuro-fuzzy systems. The production time is cut in half, and the fuzzy model's accuracy is enhanced with these systems [43].

8.9 Fuzzy Logic (FL) Controller

Intelligent controllers such as fuzzy logic controllers (FLC), or neuro-fuzzy controllers, artificial neural network (ANN)-based controllers are more robust and efficient than the conventional techniques since they do not require the exact mathematical model of the system. FLC is a technique very often used in many control system applications. In a system, the FLC controller mimics the human brain to interpret the incoming information as imprecise terms. Fuzzy logic works on a rule basis (fuzzy sets), sets of IF–THEN fuzzy rules, linguistic variables, and associated membership functions (MF) for decision making. The logic is determined by the thought (trial-and-error based) that refers to the range of possible values regarded for fuzzy set members. The basic schematic diagram of fuzzy logic controller is shown

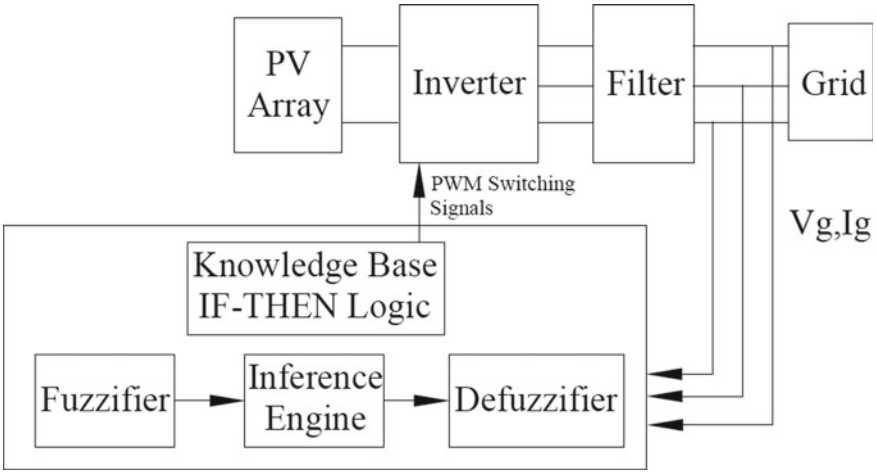

Fig. 26 Basic schematic diagram of fuzzy logic controller

in Fig. 26. The input variables V_g and I_g are measured and are given to the controller to control the process. In grid-connected mode, the error $e(t)$, the difference between the measured and reference values ($V_g * -V_g$; and $I_g * -I_g$), and its rate of change de/dt are given as an input to the FLC-based inverter controller. The fuzzifier will evaluate the inputs using the rule base in the inference engine and membership functions. The respective output corresponding to the inputs is obtained using defuzzifier. The output signals are used to generate the PWM switching pulses to the inverter switches.

The FLC is a suitable robust controller for controlling the grid-integrated inverter because of the power network's non-linear nature. The selection and development of system input and output variables, fuzzy rules, and MFs should be determined initially. The output $u(t)$ obtained from the controller is used to stabilize sinusoidal output without harmonics. The control algorithm may consist of different functional blocks such as Phase Locked Loop (PLL)-type frequency synchronization, voltage regulation, that utilize FLC controllers. However, a complex system with many non-linear controls can be designed easily with an FLC controller because of its simplicity. The FLC control system provides a reliable and high-quality output with better system response, but it is a trial-and-error method. Thus, it's a very time-consuming and error-prone process [41].

8.10 Adaptive Neuro-Fuzzy Inference System (ANFIS) Controller

Among the neuro-fuzzy controllers, the adaptive neuro-fuzzy inference system (ANFIS) controller is widely used in solar PV and/or wind energy systems as an MPPT controller and/or inverter controller of its fast convergence response compared to other neuro-fuzzy models. It consists of a fuzzy inference system based on the given dataset and applies neural learning rules to identify and tune the parameters. Its main features are easy implementation, fast and accurate learning, easy understanding of fuzzy rules, strong generalization skills, presence of both numeric knowledge and linguistics for problem-solving. A typical structure of the ANFIS system is shown in Fig. 27 [43–47]. Each circle represents a fixed node in the system, and the square box represents the adaptive node. It displays a multilayer feedforward network, with each layer performing a specific function on the input signals. The training data is required to tune the MF parameters.

An ANFIS controller is one of the control systems applied to control the grid interfaced inverter. The ANFIS controller can be used as an inverter control system to regulate the output power delivered to the grid, and/or it can also be used as a supervisory controller to supply and regulate the power flows into the grid from multiple grids connected sources. The inverter control system may consist of two ANFIS controllers operating to provide the grid's active and reactive powers. The ANFIS-based active power controller of an inverter uses an error signal determined as the difference between the active power demanded by the grid and the actual power delivered by the inverter into the grid as an input, and it determines the direct component of the current to be provided by the inverter to maintain the stability. The output current components are transformed into respective switching pulses of the

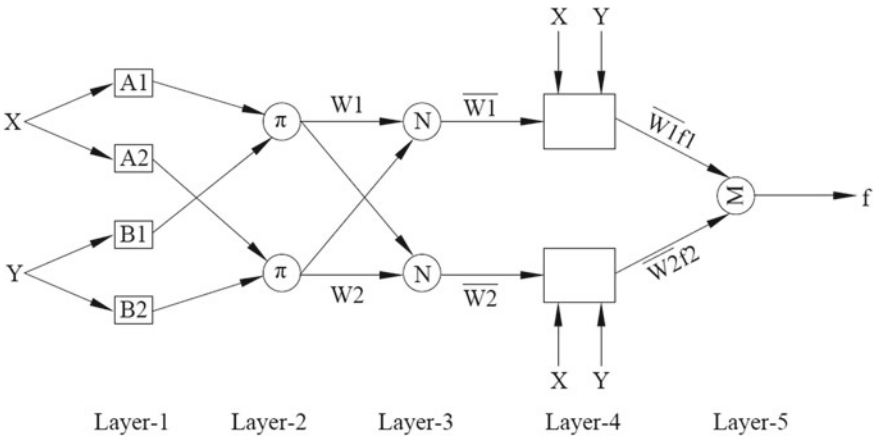

Fig. 27 Basic architecture of an ANFIS system [43–47]

inverter to supply the demanded power. The derivative of the given input error is used to interpret the prediction of future errors, which improves the controller's system stability and performance.

8.11 Slider Mode Control

The sliding mode controllers (SMCs) enable stable system parameter modification over a wide range of operating points. The controller responds with a powerful control action when a plant deviates from its typical operating points. Chattering is an issue with the controller. To address this issue, the SMC parameters are optimized using output ripple waves, and an additional integral term of the grid current is added to the sliding surface to eliminate tracking inaccuracies. The SMC approach has several advantages, including disturbance rejection, ease of implementation, and low sensitivity to changes in parameter values.

8.12 Linear Quadratic Regulator

The state-feedback of pole placement provides several advantages, including a high degree of flexibility and ease of application. In both steady-state and transient circumstances, the linear quadratic regulator (LQR) method performs well. The approach is intrinsically stable and can be used regardless of the order of the system. The accuracy of tracking during load changes is a downside of this strategy.

8.13 Linear Quadratic Integrator

To meet the quick dynamic response and nullify the steady-state voltage error between grid voltage and reference grid voltage during load changes, presents the linear quadratic integrator (LQI), which minimizes the system's cost function. In instantaneous reference voltage tracking, the integral term of the controller minimizes an error caused by outside disturbances. Finding the ideal increases that enable adequate tracking with 0% steady-state error is simple with this method.

In conclusion, the implementation of inner-loop control approaches is dependent on microgrid characteristics. For example, robust controllers are preferred to achieve effective performance when microgrid parameters are sensitive and uncertain. It is clear that a single controller will not be able to address all of the issues. However, more research into the design and implementation of these controllers for microgrid applications is necessary.

9 Advantages and Disadvantages of Various Control Approaches

The benefits and drawbacks of various conventional, linear, and non-linear inner-loop control techniques are summarized in Tables 3 and 4 [40].

Table 3 Merits and demerits of various conventional control techniques [40]

Control methods	Advantages	Disadvantages
Classical control PI	Simple control structures and easy implementation A zero steady-state error in *dq* frame	Performance degradation during disturbances Steady-state error in an unbalanced system
Proportional resonant (PR)	Improved performance with a robust inner current controller Almost zero steady-state error Low computational. Burden and implementation complexity	Sensitive to frequency variation Difficulty in controlling harmonics Require accurate tuning
Dead-beat controller (DB)	Suitable for harmonics control Fast transient response with low THD and harmonic noise	Require accurate filter model Sensitive to network parameters
Predictive control	Suitable for use in non-linear system Require less switching frequency Accurate current control with lower THD and harmonic noise	Require accurate filter model Require extensive calculations Sensitive to parameter variations
Hysteresis current control	Easy and simple implementation Fast transient response Inherent current protection	Resonance problems Limited to lower power levels Error in current tracking and harmonic issues
H controller	A very low THD and improved performance Robust performance in linear and non-linear/unbalance loads Reduced tracking error	Require deep mathematical understanding Relatively slow dynamics
Repetitive controller (RC)	Robust performance during periodic disturbances A zero steady-state error at all harmonic frequencies	Stabilizing problem Slow response during load fluctuations

Table 4 Merits and demerits of various non-conventional control techniques [40]

Control methods	Advantages	Disadvantages
Neural networks	Good performance in current control	A slow dynamic response Apply in static mode
Fuzzy control methods	Not influence by parameter variations and operational points Suitable for a large-scale non-linear system with easy design	Slow control method
ANFIS controller	Good performance during transients Efficient; minimum THD	Requires huge data. Requires long time for data training and learning. Complex computation
Adaptive fuzzy	Simpler than ANFIS Efficient	Poor performance during transients Complex control
Sliding mode control (SMC)	Reliable performance during transients Control over THD on design Good disturbance rejection	Chattering phenomenon in discrete implementation Difficulty in designing procedure
LQR&LQI controller	Fast dynamic response Easy design procedure Good tracking performance	Phase shift in voltage tracking during normal operation Voltage tracking error during disturbances Difficulty in extracting model

10 Case Study: *S*imulation Results

The simulation diagram shown in Fig. 28 consists of a three-phase grid-connected solar PV system with constant irradiance and temperature inputs. The P & O algorithm is used to track the MPP. The gate pulse of the MPPT algorithm is given to the boost converter to boost the input. The DC-link capacitor value is chosen in a way that the output voltage is constant, and pure DC is fed to the inverter without any ripples. The inverter system is designed using IGBT switches for each leg. The control structure explained in Fig. 21 is used to control the inverter. The inner-loop voltage and current control loops are shown in Fig. 29. The LCL filter is connected to the inverter to remove the harmonics in the inverter output. The filtered output is connected to the power grid.

The outer blocks in Fig. 29 represent the voltage control loop, while the inner-loop block represents the current control loop. The measured voltage and reactive power are compared with the reference values, and the error is passed through a PI controller. The output of the PI controller generates the I_{dref} and I_{qref} values. Again, the error is computed by taking the difference between the reference and measured values, then passing it to the PI controller. The Vtd1 and Vtq1 are the reference

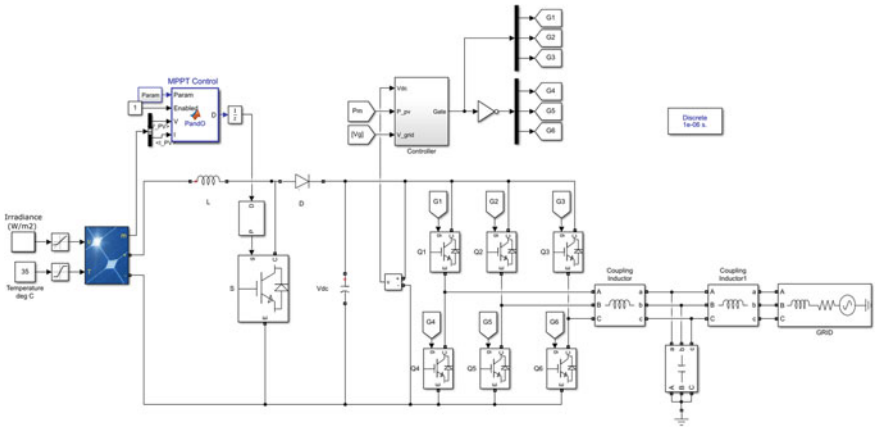

Fig. 28 Simulation diagram of three-phase grid-connected solar PV system

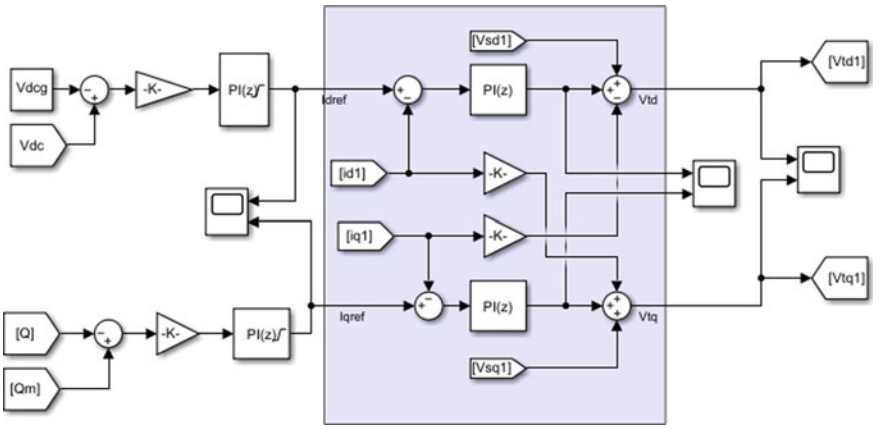

Fig. 29 Simulation diagram of inner voltage and current control loops

signals in the *dq* frame to be transformed into the abc reference frame for the PWM modulation.

Figure 30 shows the output voltage and current of a PV array with constant irradiance and temperature inputs. The input irradiance is maintained at 1000 W/m^2 and the temperature at 25 °C. The voltage output is obtained around 320 V and the current around 425 A.

Figure 31 shows the duty cycle (D) to the boost converter obtained using the P&O algorithm. This figure shows that the algorithm maintains around the reference value 0.725 when there is no input disturbance or variation.

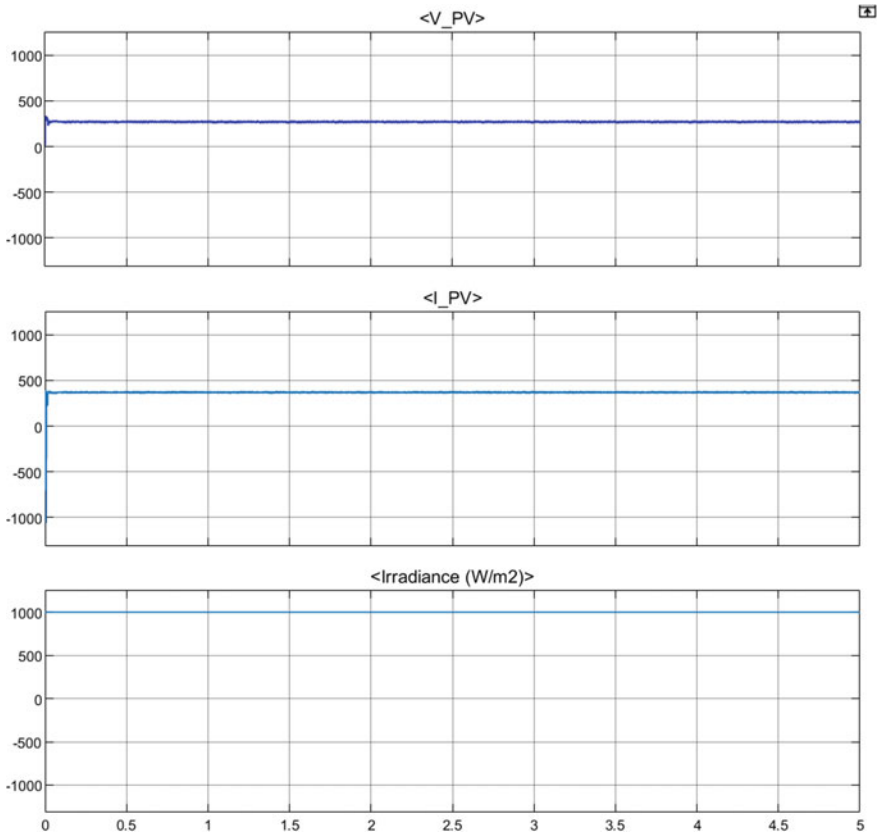

Fig. 30 The irradiance, voltage, and current outputs of PV array

Figure 32 shows the DC-link voltage output. The output voltage is maintained constant around 1000 V. The constant Dc voltage is provided to the inverter as an input.

Figure 33 shows the three-phase reference voltage input obtained using the control technique mentioned above. The reference voltage is limited between −1 and 1 V and is given to the PWM generator to control the inverter output according to the reference voltage.

Figure 34 shows the switching pulses given to a three-phase inverter. The switching pulses turn on and off the inverter switches accordingly to produce the three-phase AC output. The output voltage has a peak at the starting of the simulation. However, the system output is stabilized at 0.2 s and maintained constant throughout the simulation run time.

Figure 36 shows that the active power output obtained is close to 100 KW, and the reactive power is around 30 KW. The results of the PV system with other controllers

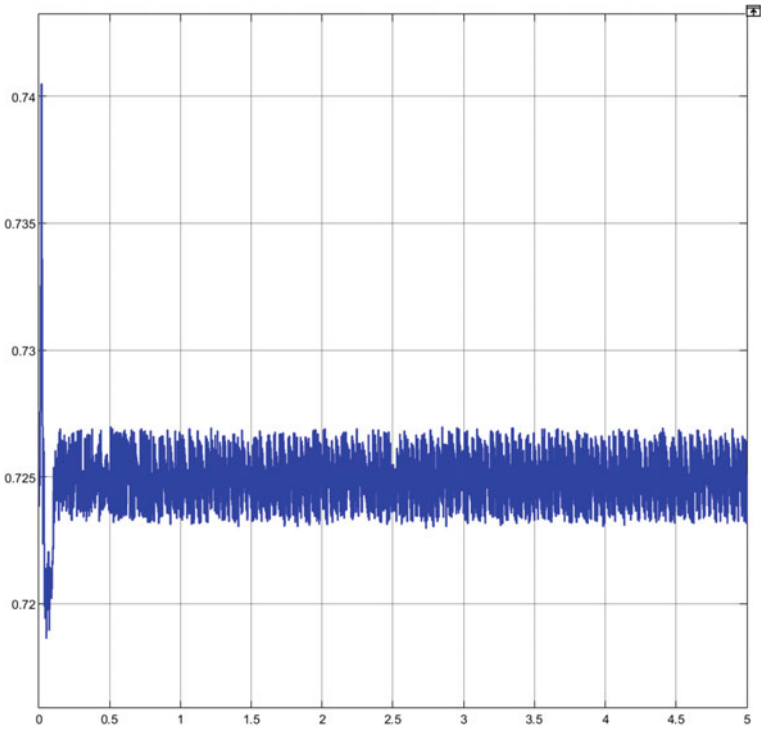

Fig. 31 The duty cycle of the MPPT algorithm to the boost converter using the P &O technique

such as fuzzy, ANFIS also follow a similar pattern. However, the power quality and stability of the system outputs are improved compared to the conventional control techniques.

11 Chapter Summary

The chapter presented and evaluated renewable sources motivation, such as solar PV systems, wind turbine systems, fuel cells, and storage systems in grid interfacing mode. According to the latest IEEE 2018 standards, the grid connection requirements for interfacing the renewable energy sources in the utility grid level are demonstrated. Mathematical modeling of RES such as solar, wind, fuel cells, and battery SOC calculations are studied in the chapter. The necessity and various types of MPPT techniques are discussed above. Power electronic devices such as inverters, DC–DC converters, and filters play a crucial role in renewable systems for power generation. The DC–DC and AC–DC converters are used to boost the input source voltage to interface to the DC bus. The inverters play a vital role in converting the DC into AC supply. Based on the operating role, the voltage source inverters are widely preferred in high-voltage

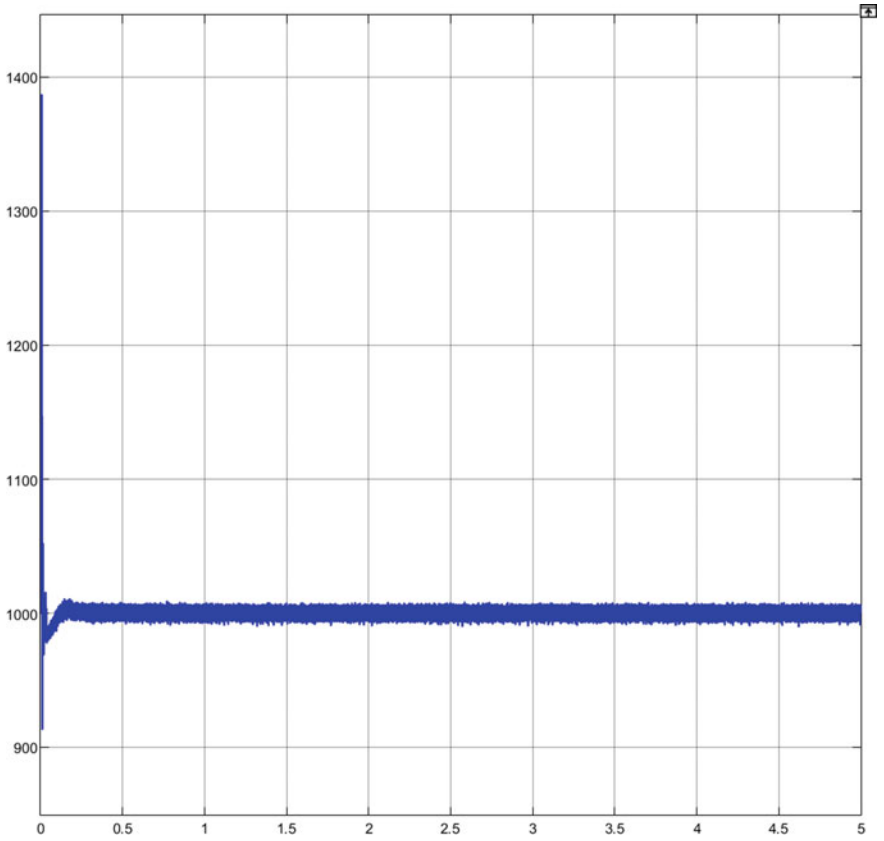

Fig. 32 DC-link voltage output

applications. The modeling of the DC–DC boost converter, inverter, and filters is discussed. The selection criteria for inverters are specified in the chapter. To improve the system stability under faults and to provide the grid-supportive functions, smart inverters can be developed with smart features. The smart inverter performs the standard DC–AC conversion. It provides the grid-support functions and ancillary services such as voltage and frequency regulation, fault ride-through, and dynamic current injection with high flexibility and reliability. The suitable controllers control the gate signals to the IGBT switches in VSI or CSI to achieve the reference output at the grid level. The inverter control technique and its switching methods using PWM modulation techniques are reviewed. The active power and reactive power compensation of the inverter can be achieved by changing the amplitude and phase of the inverter's output voltage. The hierarchical control scheme with three control levels is discussed, and various inner-loop control techniques are summarized for the grid-feeding and grid-forming mode inverters. Typically, conventional controllers such as PI or PID controllers are employed to maintain the steady output of the inverter. However, these

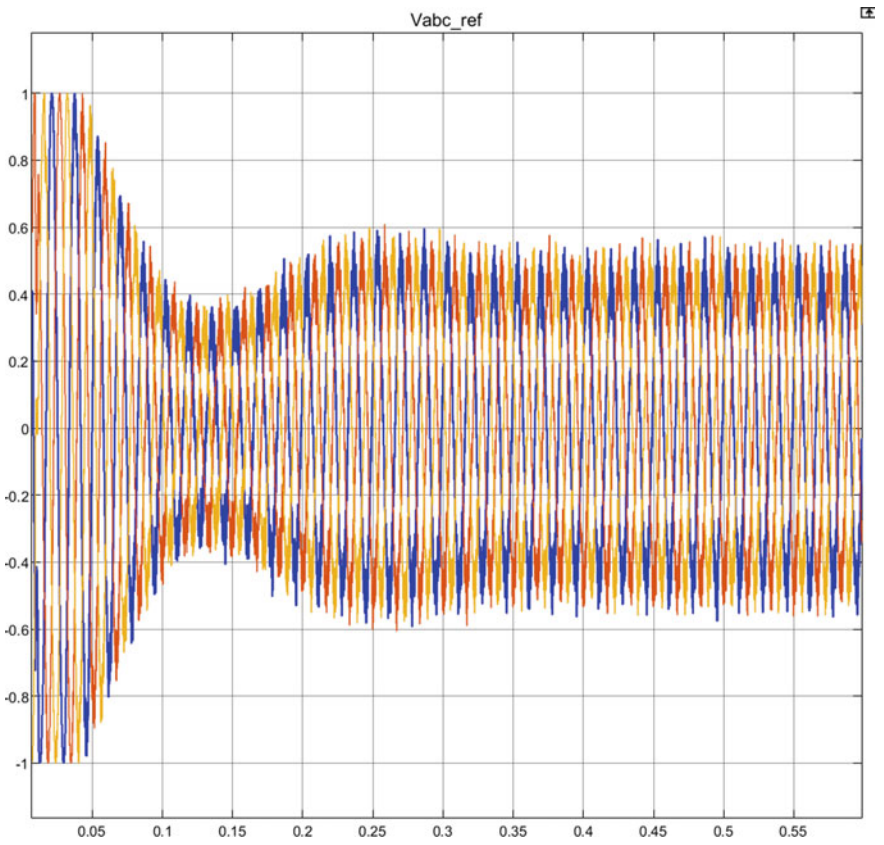

Fig. 33 Three-phase voltage reference obtained using the controller and is given to the inverter

traditional controllers involve time delays and are very sensitive to small voltage deviations in the system fluctuations. Non-linear controllers such as FLC, ANN, ANFIS provide the steady three-phase output of the inverter due to their non-linear nature and provide the effective output response. This chapter also summarizes the advantages and disadvantages of various inverter controllers for providing the stabilized sinusoidal output into the grid. The simulation results section shows the simulation diagram of the three-phase grid-connected solar PV system with inner voltage and the current control loop. The respective outputs such as PV array output voltage, duty cycle, dc-link voltage, inverter output, along with the controller reference signal are provided in the chapter.

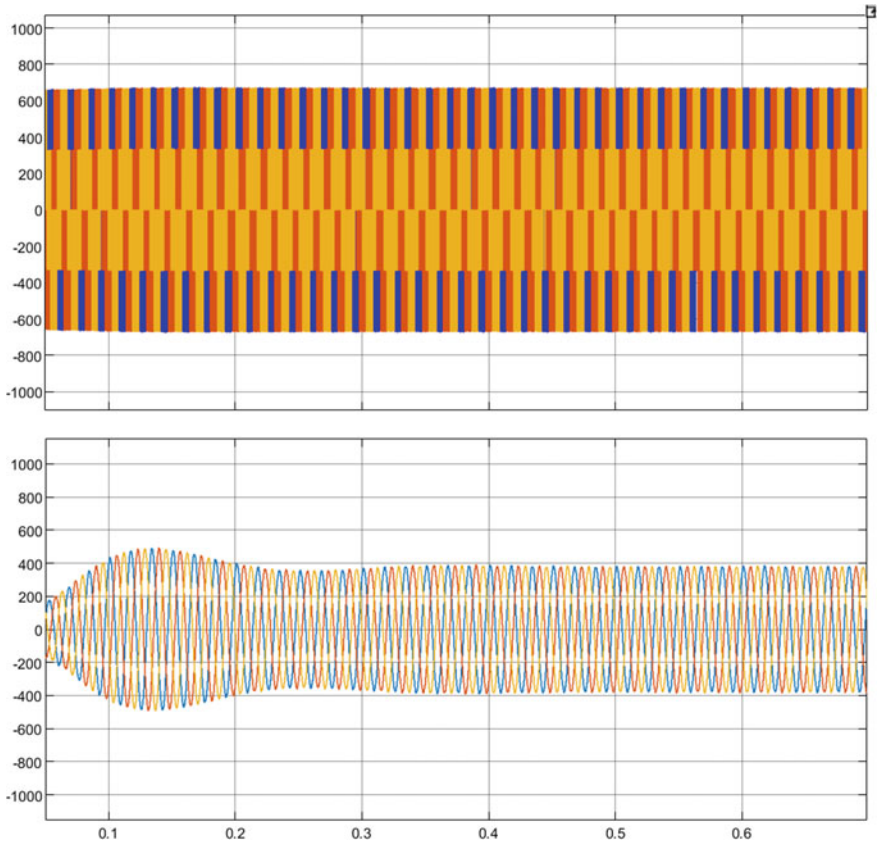

Fig. 34 Inverter pulses and corresponding output voltage

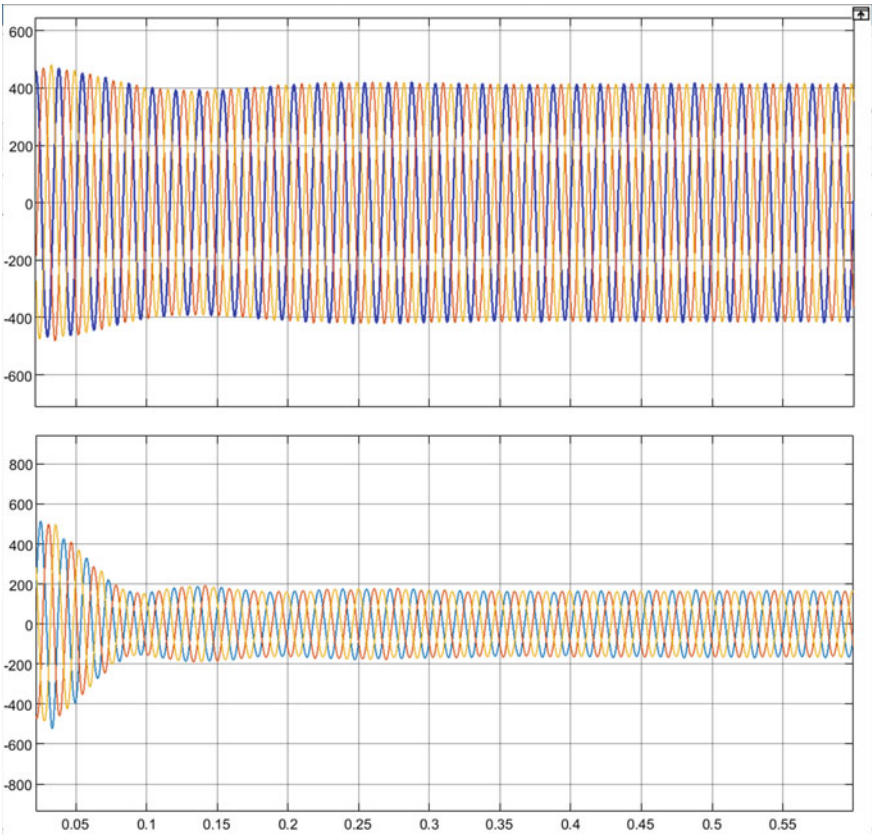

Fig. 35 Three-phase filtered output voltage and current waveforms supplied to the power grid. In this system, the three-phase output voltage of the PV system is maintained at 420 V, and the current is around 185 A.

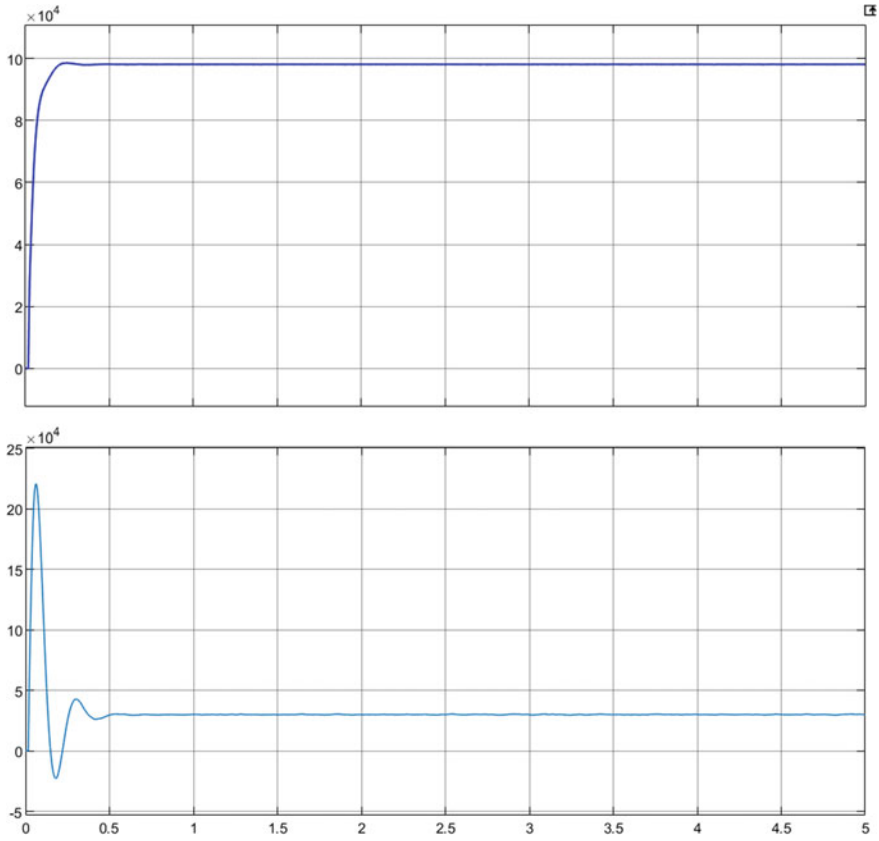

Fig. 36 The active and reactive power output of the PV system

References

1. R.J. Campbell, Increasing the efficiency of existing coal-fired power plants, in *Coal-Fired Power Plants: Efficiency Improvement Options* (2015), pp. 77–111
2. R.C. Dugan, T.E. Mcdermott, Distributed generation. IEEE Ind. Appl. Mag. **8**(2), 19–25 (2002). https://doi.org/10.1109/2943.985677
3. IEEE Standard Association, *IEEE Std. 1547–2018. Standard for Interconnection and Interoperability of Distributed Energy Resources with Associated Electric Power Systems Interfaces, IEEE Std 1547–2018 (Revision of IEEE Std 1547–2003)* (2018)
4. A.Q. Al-Shetwi et al., Grid-connected renewable energy sources: review of the recent integration requirements and control methods. J. Clean. Prod. **253**, 119831 (2020). https://doi.org/10.1016/j.jclepro.2019.119831
5. J. Rocabert et al., Control of energy storage system integrating electrochemical batteries and supercapacitors for grid-connected applications. IEEE Trans. Ind. Appl. **55**(2), 1853–1862 (2019). https://doi.org/10.1109/TIA.2018.2873534
6. B. Arbab-Zavar et al., Smart inverters for microgrid applications: a review. Energies **12**(5) (2019). https://doi.org/10.3390/en12050840

7. H. Patel, M. Gupta, A.K. Bohre, Mathematical modeling and performance analysis of MPPT based solar PV system. Int. Conf. Electr. Power Energy Syst. ICEPES **2016**, 157–162 (2017). https://doi.org/10.1109/ICEPES.2016.7915923
8. M. Hlaili, H. Mechergui, Comparison of different MPPT algorithms with a proposed one using a power estimator for grid connected PV systems. Int. J. Photoenergy(2016). https://doi.org/10.1155/2016/1728398
9. B. Bhandari et al., Mathematical modeling of hybrid renewable energy system: a review on small hydro-solar-wind power generation. Int. J. Precis. Eng. Manuf.- Green Tech. **1**(2), 157–173 (2014). https://doi.org/10.1007/s40684-014-0021-4
10. O. Zebraoui, M. Bouzi, Comparative study of different MPPT methods for wind energy conversion system. IOP Conf. Ser.: Earth Environ. Sci. **161**(1) (2018). https://doi.org/10.1088/1755-1315/161/1/012023
11. R. Seyezhai, B.L. Mathur, Mathematical modeling of proton exchange membrane fuel cell. Int. J. Comput. Appl. **20**(5), 1–6 (2011). https://doi.org/10.5120/2433-3272
12. A.O. Althobaiti, Proportional resonant control of three-phase grid-connected inverter during abnormal grid conditions (2017)
13. K. Sarita, R. Devarapalli, P. Rai, Modeling and control of dynamic battery storage system used in hybrid grid. Energy Storage **2**(3), 1–14 (2020). https://doi.org/10.1002/est2.146
14. A. Haddou et al., Comparative study of new MPPT control approaches for a photovoltaic system. Int. J. Power Electron. Drive Syst. **11**(1), 251–262 (2020). https://doi.org/10.11591/ijpeds.v11.i1.pp251-262
15. T. Bogaraj, J. Kanakaraj, J. Chelladurai, Modeling and simulation of stand-alone hybrid power system with fuzzy MPPT for remote load application. Arch. Electr. Eng. **64**(3), 487–504 (2015). https://doi.org/10.2478/aee-2015-0037
16. S. Samal, P.K. Barik, S.K. Sahu, Extraction of maximum power from a solar PV system using fuzzy controller based MPPT technique, in *International Conference on Technologies for Smart City Energy Security and Power: Smart Solutions for Smart Cities, ICSESP 2018—Proceedings* (2018) pp. 1–6. https://doi.org/10.1109/ICSESP.2018.8376721
17. K. Amara et al., Improved performance of a PV solar panel with adaptive neuro fuzzy inference system ANFIS based MPPT. in *7th International IEEE Conference on Renewable Energy Research and Applications, ICRERA 2018* (vol. 5, 2018), pp. 1098–1101. https://doi.org/10.1109/ICRERA.2018.8566818
18. Z.M.S. Elbarbary, M.A. Alranini, Review of maximum power point tracking algorithms of PV system. Front. Eng. Built Environ. **1**(1), 68–80 (2021). https://doi.org/10.1108/febe-03-2021-0019
19. S.A. Mohamed Abdelwahab, A.M. Hamada, W.S.E. Abdellatif, Comparative analysis of the modified perturb and observe with different MPPT techniques for PV grid connected systems. Int. J. Renew. Energy Res. **10**(1), 155–164 (2020)
20. A.M. Noman, K.E. Addoweesh, A.I. Alolah, Simulation and practical implementation of ANFIS-based MPPT method for PV applications using isolated Ćuk converter. Int. J. Photoenergy**2017** (2017). https://doi.org/10.1155/2017/3106734
21. H.B. Massawe, Grid connected photovoltaic systems with smartgrid functionality (2013) pp. 37–39
22. Utility-scale PV inverters—Yaskawa—Solectria Solar (no date). Available at: https://www.solectria.com/pv-inverters/utility-scale-inverters/ (Accessed: 3 November 2021)
23. M.A. Abella, (11) (PDF) Choosing the right inverter for grid-connected PV systems. Renew. Energy World **134** (2004)
24. M.J. Mnati, D.V. Bozalakov, A. den Van Bossche, PID control of a three phase photovoltaic inverter tied to a grid based on a 120-degree bus clamp PWM. IFAC-PapersOnLine **51**(4), 388–393 (2018). https://doi.org/10.1016/j.ifacol.2018.06.097
25. An improved PID and repetitive control for single phase inverters of photovoltaic power system (December 2018)
26. A.F. Tazay, Smart inverter control and operation for distributed energy resources (2017)

27. H.R. Karshenas, H. Saghafi, Basic criteria in designing LCL filters for grid connected converters. IEEE Int. Symp. Ind. Electron. **3**(1 c), 1996–2000 (2006). https://doi.org/10.1109/ISIE.2006.295879
28. C. Gurrola-Corral et al., Optimal LCL-filter design method for grid-connected renewable energy sources. Int. J. Electr. Power Energy Syst. **120**(8), 105998 (2020). https://doi.org/10.1016/j.ijepes.2020.105998
29. M. Hojabri, M. Hojabri, Design, application and comparison of passive filters for three-phase grid-connected renewable energy systems. ARPN J. Eng. Appl. Sci. **10**(22), 10691–10697 (2015)
30. G. Majic, M. Despalatovic, B. Terzic, LCL filter design method for grid-connected PWM-VSC. J. Electr. Eng. Technol. **12**(5), 1945–1954 (2017). https://doi.org/10.5370/JEET.2017.12.5.1945
31. S.-H. Kim, Pulse width modulation inverters, in *Electric Motor Control* (2017), pp. 265–340. https://doi.org/10.1016/B978-0-12-812138-2.00007-6
32. Y. Li et al., Grid synchronization technology for distributed power generation system, in *IEEE Transportation Electrification Conference and Expo, ITEC Asia-Pacific 2014—Conference Proceedings* (2014), pp. 1–6. https://doi.org/10.1109/ITEC-AP.2014.6941268
33. Y. Xue et al., On a future for smart inverters with integrated system functions, in *2018 9th IEEE International Symposium on Power Electronics for Distributed Generation Systems, PEDG 2018* (2018), pp. 1–8.https://doi.org/10.1109/PEDG.2018.8447750
34. B. Mirafzal, A. Adib, On grid-interactive smart inverters: features and advancements. IEEE Access **8**, 160526–160536 (2020). https://doi.org/10.1109/ACCESS.2020.3020965
35. K. Rahimi et al., Voltage regulation performance of smart inverters: power factor versus volt-VAR control, in *2017 North American Power Symposium, NAPS 2017* [Preprint] (2017). https://doi.org/10.1109/NAPS.2017.8107407
36. A. Vinayagam et al., PV based microgrid with grid-support grid-forming inverter control-(simulation and analysis). Smart Grid Renew. Energy **08**(01), 1–30 (2017). https://doi.org/10.4236/sgre.2017.81001
37. S. Reichert, G. Griepentrog, B. Stickan, Comparison between grid-feeding and grid-supporting inverters regarding power quality, in *2017 IEEE 8th International Symposium on Power Electronics for Distributed Generation Systems, PEDG 2017* (2017), pp. 1–4.https://doi.org/10.1109/PEDG.2017.7972536
38. P. Unruh et al., Overview on grid-forming inverter control methods. Energies **13**(10) (2020). https://doi.org/10.3390/en13102589
39. A.M. Bouzid et al., A survey on control of electric power distributed generation systems for microgrid applications. Renew. Sustain. Energy Rev. **44**, 751–766 (2015). https://doi.org/10.1016/j.rser.2015.01.016
40. M.A. Hossain et al., Overview of AC microgrid controls with inverter-interfaced generations. Energies **10**(9), 1–27 (2017). https://doi.org/10.3390/en10091300
41. M.A. Hannan et al., Fuzzy logic inverter controller in photovoltaic applications: issues and recommendations. IEEE Access **7**, 24934–24955 (2019). https://doi.org/10.1109/ACCESS.2019.2899610
42. A. Alhejji, M.I. Mosaad, Performance enhancement of grid-connected PV systems using adaptive reference PI controller. Ain Shams Eng. J. **12**, 541–554 (2020). https://doi.org/10.1016/j.asej.2020.08.006
43. P. García et al., ANFIS-based control of a grid-connected hybrid system integrating renewable energies, hydrogen and batteries. IEEE Trans. Industr. Inf. **10**(2), 1107–1117 (2014). https://doi.org/10.1109/TII.2013.2290069
44. J.R. Jang, Neuro-fuzzy modeling. **83**(3) (1995)
45. J.S. Jang, C.T. Sun, E. Mizutani, Neuro-fuzzy and soft computing (no date)
46. J.S.R. Jang, ANFIS: adaptive-network-based fuzzy inference system. IEEE Trans. Syst. Man Cybern. **23**(3), 665–685 (1993). https://doi.org/10.1109/21.256541
47. A. Taher, Adaptive neuro-fuzzy systems (2010)

Transformerless Three-Phase Solar Photovoltaic Power Conversion Systems

Deepak Ronanki and Harish Karneddi

Abstract Solar photovoltaic (SPV) energy is one of the promising and dominant renewable energy sources for clean and sustainable electricity production. Typically, a power conditioning unit (PCU) along with a low-frequency transformer on the AC side is utilized to integrate the photovoltaic (PV) source with the grid. However, they offer low efficiency, high cost, and low power density. Transformerless inverters gained more attention in grid-connected PV systems due to demands of power density, high efficiency, reliability, and low cost. However, leakage current is produced through the stray capacitances between the PV array and the ground. It is generated due to the fluctuation of common-mode voltages between PV neutral and grid. Also, it enhances DC injection into the grid due to the absence of galvanic isolation. Consequently, it causes fundamental safety problems and the degradation of the system's performance. This chapter aims to study and compare leakage current minimization approaches through converter topology modifications and pulse width modulation schemes in transformerless PV systems. The key performance of each inverter topology in terms of leakage current is holistically evaluated through simulation studies in MATLAB software. Finally, the merits and demerits of each power converter topology for transformerless solar systems are summarized in this chapter.

Keywords Common-mode voltage · Inverters · Leakage current · Modulation schemes · And solar power conversion systems

List of Symbols

P	Power (W)
D	Diode

D. Ronanki (✉) · H. Karneddi
Indian Institute of Technology Roorkee, Roorkee 247667, India
e-mail: dronanki@ieee.org

H. Karneddi
e-mail: harish_k@hre.iitr.ac.in

S. K. Das et al. (eds.), *Advances in Control Techniques for Smart Grid Applications*,
https://doi.org/10.1007/978-981-16-9856-9_9

S	Switching device
L	Inductor (mH)
I_{PV}	PV array output current (A)
V_{PV}	PV array output voltage (V)
C_{pv}	Stray capacitance of PV panel (μF)
V_{dc}	Input DC voltage (V)
V_{an}, V_{bn}, V_{cn}	Phase voltages of converter (V)
n	Neutral point
a, b, c	Terminals of a 3-phase system
V_0 *to* V_7	State vectors
$I_{leakage}$	Leakage current (A)
V_{CM}	Common-mode voltage (V)
R_g	Ground resistance (Ω

List of Acronyms

PV	Photovoltaic
PCU	Power conditioning unit
PVS	Photovoltaic systems
IEA	International Energy Agency
PVES	Photovoltaic energy systems
Hz	Hertz
LFT	Low-frequency transformer
HFT	High-frequency transformer
kWh	Kilowatt hour
THDs	Total harmonic distortions
EMI	Electromagnetic interference
CMV	Common-mode voltage
DC	Direct current
MPPT	Maximum power point tracking
CI	Central inverter
SI	String inverter
PWM	Pulse width modulation
UPS	Uninterrupted power supply
RMS	Root mean square
AC	Alternating current
kHz	Kilo Hertz
IGBTs	Insulated gate bipolar transistors
V	Volt
kW	Kilo watt
GW	Giga watt
VSI	Voltage source inverter
CSI	Current source inverter

MPPT	Maximum power point tracker
MPP	Maximum power point
I-V	Current versus voltage
P-V	Power versus voltage
A	Ampere
s	Seconds
MOSFET	Metal oxide semiconductor field-effect transistor
W	Watt
LC	Inductor-capacitor
SPWM	Sine pulse width modulation
SVM	Space vector modulation
NSPWM	Near-state PWM
AZPWM	Active zero state PWM
RSPWM	Remote state PWM
MSVPWM	Multilevel space vector pulse width modulation

1 Introduction

The generation of electricity from photovoltaic systems (PVS) is growing rapidly and has become one of the prominent among the distributed generation systems. International Energy Agency (IEA) has reported that more than least 627 GW of PV are installed worldwide, as 115 GW of PV were installed in 2019 [1]. The PVs are the third-most energy resource after hydro and wind energy in terms of cumulated installed capacity. Currently, strategic incentives and tariff schemes by federal governments in many countries are contributing to the widespread adoption of PVS. Last decade, the cost of PVS has dropped by 59% due to cutting-edge advances in materials, power electronics, and digital technologies along with the escalated manufacturing facilities by the industries. The power conditioning units (PCUs) are a part of PVS, which comprise of power electronic converters and their digital control mainly contribute to enhancing the energy yield from the sun and minimizing the cost, thereby offering convenient access to solar energy and cost-effective. Also, a smaller footprint, enhanced power quality, grid codes compliance, and improved reliability can be achieved through power electronic converters and their control [2].

PVS is mainly classified into grid-connected and off-grid (standalone) systems. The energy produced by grid-tied PVS is growing significantly, which feed power to the grid with sinusoidal currents and local loads. The standalone PVS are utilized in remote and rural areas where the grid connection is not available, complicated, and expensive. The local loads are fed by PVES with constant voltage and frequency in off-grid applications. Energy storage is employed with standalone systems, to supply continuous power supply in such a way that harvested PV power charges energy storage and gets utilized for supplying to the local loads [3]. However, grid-connected

PVS are preferred due to the existence of short-lived, costly, and bulky batteries in standalone applications. The PCU employing the voltage source converters with output filters is used for grid-connected and standalone systems. The output current and load voltage are regulated in on-grid and off-grid PVS, respectively. The main challenge associated with all PVS is the extraction of maximum power as the PV characteristic curve varies changes with environmental conditions, such as solar irradiation and core temperature [4].

To integrate solar PV with grid or AC loads, a PCU which converts the energy produced by PV panels from DC to AC while extracting maximum power from the solar PV system and is responsible to generate the required voltage and frequency for grid synchronization. This connection is achieved in two possible ways with and without galvanic isolation, as depicted in Fig. 1. Galvanic isolation between the PV source and grid is provided by using a transformer with an inverter connection. The most traditional way is the connection of the inverter along with a low-frequency transformer (LFT) on the AC side (Fig. 1a) or a high-frequency transformer (HFT) on the DC side (Fig. 1b). With the galvanic isolation, PVS is protected from hazardous voltages and avoids DC current injection into the grid [5]. However, LFTs (Fig. 1a) generates power loss in the windings, thereby reducing the system efficiency. Also, they are bulky, heavy, and expensive. One of the possible ways to enhance the power

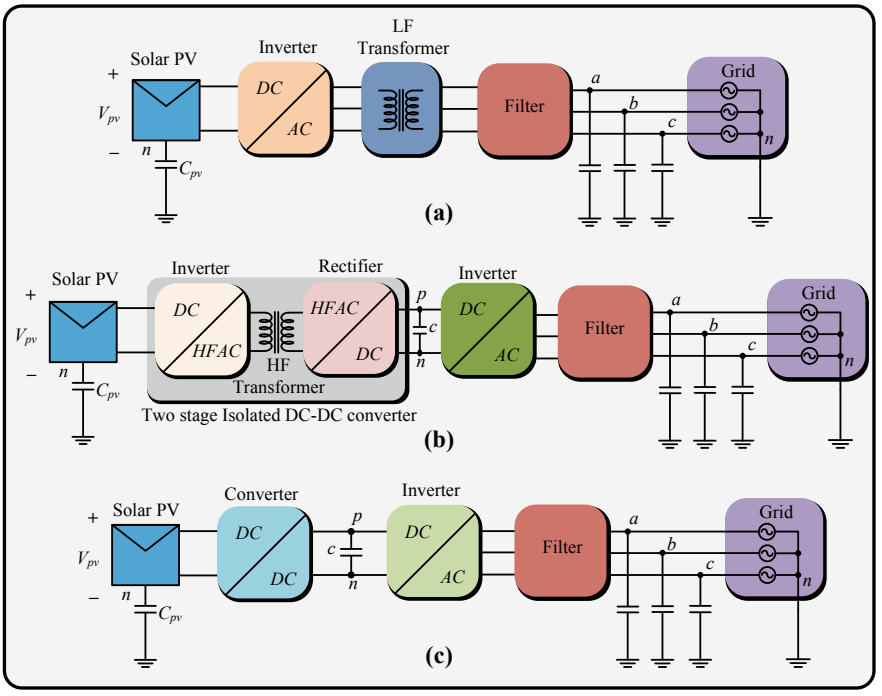

Fig. 1 Classification of grid-connected PVS: **a** LFT-based PCU, **b** HFT-based PCU, and **c** transformerless based PCU

density is the adoption of HFT, and their configuration is shown in Fig. 1b. However, the system efficiency is comparatively low due to multiple conversion stages.

Alternatively, transformerless PV grid-tied inverters (Fig. 1c) is introduced which can reach their efficiencies up to 97–98% with the high power density and low cost. However, several concerns such as safety issues, malfunction of sensors, and corrosion in underground equipment under the effects of the leakage current due to the absence of galvanic isolation between PV sources and the grid [6]. Also, the existence of the leakage current escalates the total harmonic distortion (THD), electromagnetic interference (EMI), and system losses.

Typically, the PV panels frame will be grounded (Fig. 2) to limit the leakage current as described in European and USA standards [7]. The intensity of leakage currents can be determined by the value of PV panel parasitic capacitance, converter topology, control technique, and switching frequency of converter operation [8]. Among them, inverter topologies and control strategies (pulse width modulation schemes) are proven to be the most dominant factors in determining the leakage current that flows from the PV source to the grid through parasitic capacitors formed between them. The intensity of these currents highly depends on the amplitude and frequency content of common-mode voltage (CMV) and parasitic capacitances [9]. Therefore, it is essential to understand the phenomenon of leakage current generation and methods to mitigate the generation of this phenomenon. Over the past years, sincere attempts have been made by the researchers to minimize the leakage current in the transformerless grid-tied PV inverters through advanced modulation techniques and power converter topology modifications. A holistic comparison among transformerless two-level converter topologies in terms of CMV and leakage current is also missing in the literature. This chapter mainly focuses on a review of transformerless inverter topologies, switching techniques, and control schemes are presented to limit the leakage current in PV systems.

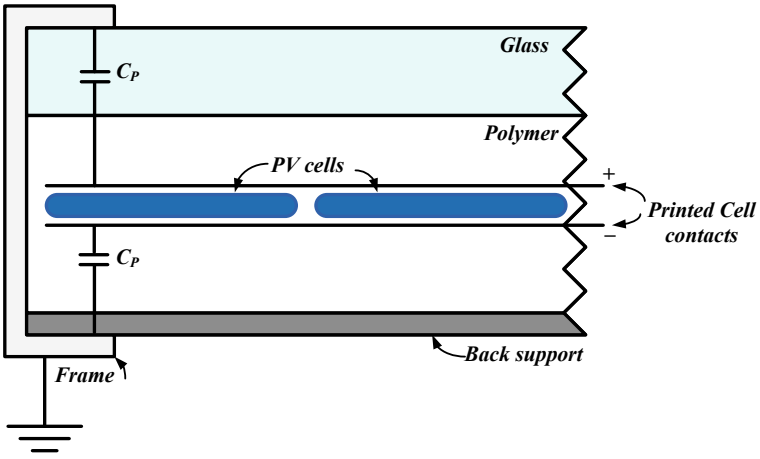

Fig. 2 Parasitic capacitance view of the solar PV panel

This chapter is organized as follows:

- The overview of power interface systems and their classification for grid-connected PV systems are presented in Sect. 2.
- The fundamental details of grid-tied inverters regarding leakage current generation and its minimization through control schemes are discussed in Sect. 3.
- The overview of transformerless three-phase grid-tied inverters and their operation principles are presented in Sect. 4.
- Comparison of various transformerless three-phase grid-tied inverters through simulation studies is illustrated in Sect. 5.
- Section 6 provides the concluding remarks of this chapter

2 Classification of Power Interface Systems

PV panel output is continuously varied concerning the irradiation and atmospheric temperature. Also, the partial shading and module age are considerable effects of PV system performance [10]. This mismatch of output leads to a reduction in output energy and the lifetime of the PV modules. Various maximum power point tracking (MPPT) techniques are proposed to extract the maximum energy from the PVS. The PCU extracts the maximum output from PVS and plays a vital role in maintaining the output at desired standards of load (for a standalone system) or grid (voltage and frequency) [11]. Based on the range of the output power, PVS are categorized under three regions [12, 13].

- Small-scale PVS (power rating <10 kW)
- Medium-scale PVS (power rating typically 10 kW–1 MW)
- Utility-scale PVS (typical power rating of 1–10 MW)

Based on the conversion stages, PVS can be interfaced with grid or load in two-stage or single-stage conversion. In two-stage, two sets of power conversion stage i.e. DC–DC and DC–AC conversion. The front-end DC–DC converter is accountable for yielding maximum power from PVS, whereas the DC–AC converter converts the DC power to AC with maintaining the grid standards. Two-stage conversion systems are mostly used for high power applications due to the maturity of the topological structures and their simplicity in control. However, conversion losses are more in the two-stage conversion. In single-stage conversion, both are maintained by the inverter alone and by the conversion losses are less as compared to the two-stage. However, the control of the system becomes complex.

Recently, the medium- and large-scale PV plants have gained great attention due to low maintenance and zero-emission. In general, the inverter is connected to the grid through the low-frequency transformer (LFT) to provide isolation, step-up operation, and minimize the leakage current. Because of the weight and size constraints of the LFT, the PV inverter system can be expensive and complex for installation and maintenance. To overcome the aforementioned short comes, transformerless inverter

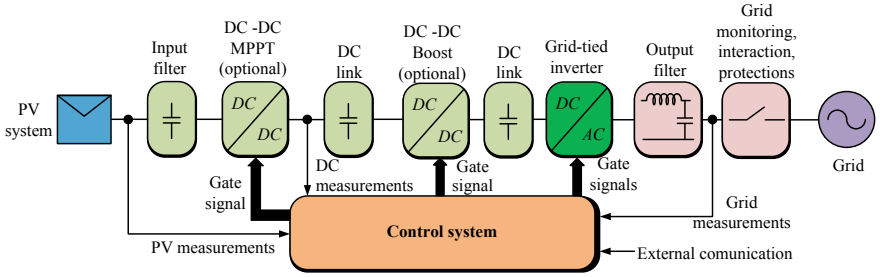

Fig. 3 A typical overview of grid-connected PVS

topologies are presented in this chapter. The block diagram of transformerless grid-connected PVS is illustrated in Fig. 3, which consists of several conversion stages and is followed by the filters [13]. PVS is connected through the DC/DC converter-1 and followed by one more DC/DC converter. The front-end DC/DC converters are placed to extract the maximum power from the PVS and a secondary DC/DC converter provides step-up or step-down based on the requirement. Usually, for grid-connected PVS step-up converter is equipped to deliver power to the medium voltage (MV) grids without using any step-up transformer and these DC/DC converters are optional. Finally, the inverter is placed at the output end to deliver AC power from the secondary DC/DC converter to the MV grid and in between filters are placed to suppress the voltage/current ripples.

The control system is shown in Fig. 3 monitor and controls all converters to extract maximum power from the PVS and to deliver power to the grid with the following predefined standards (Table 1). This block also controls the circuit breakers to make or break the PVS from the grid. During night-time, faulty condition or standalone operation control systems disconnects the PVS from the grid.

Grid interfaced solar PVs are categorized into four different (Fig. 4) types based on the configuration [2]. Central inverter (CI) based PV configuration illustrated in Fig. 4a is mostly adaptive configuration due to simple structure. CI configuration consists of a minimal component count for PCU, and one low-frequency transformer is sufficient to provide galvanic isolation. Therefore, the cost and the losses associated

Table 1 Standards associated with grid integration of PVS [12, 14, 15]

Standard	Voltage fluctuation	Power factor	DC current injection	Frequency tolerance (Hz)
IEEE 1547	5%	>0.9	<0.5%	59.3–60.5
IEEE929	–	>0.85	<0.5%	59.3–60.5
IEC 61,727	–	–	<1%	59–61
RULE 21	5%	>0.9	<0.5%	59.3–60.5
VDE-AR-4105	3%	>0.9	<1A	47.5–51.5
AS 4777	–	>0.5	<1%	45–55

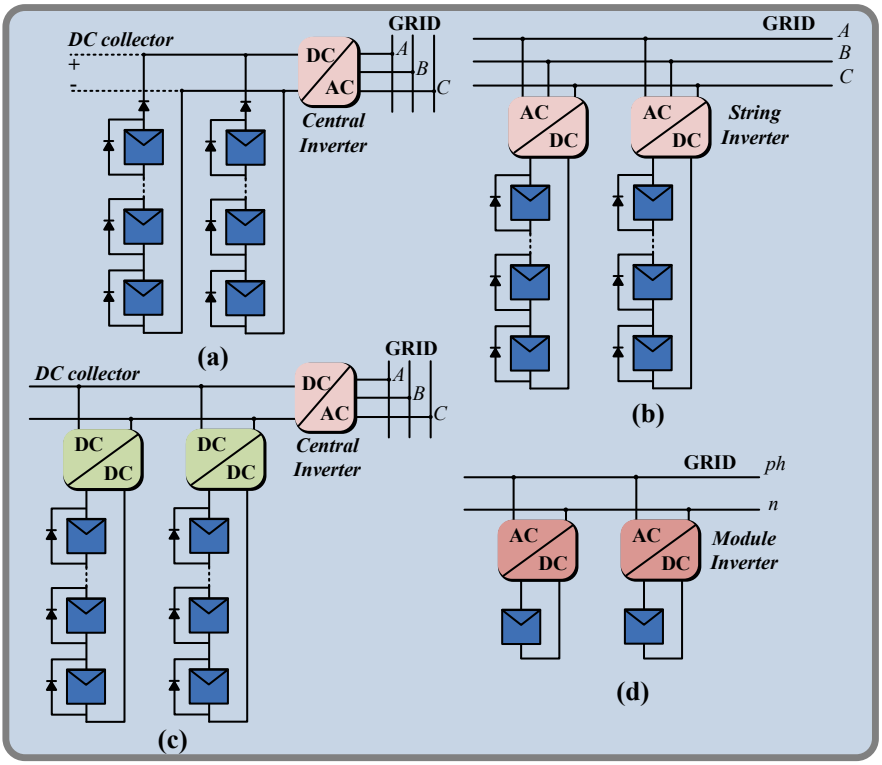

Fig. 4 Grid-tied PVS configurations, **a** central inverter configuration, **b** string inverter configuration, **c** multi-string inverter configuration, **d** module inverter configuration

with CI configurations are very less. Usually, these configurations are having an efficiency of typically 95–98% [16]. Because of the aforementioned benefits and ease of control, this configuration is more suitable for large-scale PVS. Apart from the benefits, CI configuration has poor MPPT tracking due to a single inverter for multiple strings. Multilevel inverter topologies are more suitable for CI-based PV systems. Over the past years, researchers have proposed various multilevel inverter topologies for transformerless grid interfaced PVS and which are consolidated in [17–21].

String inverter (SI) configuration illustrated in Fig. 4b consists of individual inverters for each string to improve MPPT (power yielding capability is increased by 1–3%) [22]. SI configuration consists of more conversion stages compared to the aforementioned configuration and also each string requires an individual LF transformer, which results in 60% expensive than CI configuration and increases the losses. Due to that SI configuration is preferable for medium-scale PVS.

The multi-string configuration in Fig. 4c combines the benefits of the CI configuration as well as the SI configuration. DC–DC converter yields the maximum output

from individual strings similar to SIs and forms DC bus and followed by CI to interface with the grid results reduction in transformer count to one. Therefore, improved efficiency and lower cost are achieved due to the reduction in the number of the transformers as compared to SI configuration, [2, 22]. Figure 4d shows the module inverter configuration; each module consists of individual inverter results increase in the power yielding capability. Due to a large number of component counts, these are suitable for small-scale applications [23].

Overall, transformerless inverters especially in string configuration have gained more attention due to demands of high efficiency, power density, and low cost. However, it causes fundamental safety problems and PV system degradation due to the existence of leakage current and DC injection into the grid. Therefore, this chapter mainly deals with the transformerless string inverter topological configurations to mitigate the leakage current to interconnect the PV plant with a grid.

3 Grid-Tied Inverters and Control Schemes

The inverter is used to convert the fixed DC voltage to the desired alternating voltage with the required frequency. These are used to interface the renewable energy sources with the grid or DC sources to the AC loads, and the block diagram of the inverter is shown in Fig. 5. Here, the DC input voltage is maybe from PVS (single-stage conversion) or the output terminals of DC–DC converter (two-stage conversion), and the output may be a single-phase or a three-phase based on the inverter topological configuration. Usually, inverters are used for various power controlling applications like speed control of motors, induction heating, uninterrupted power supply (UPS) for sophisticated loads.

Inverters are broadly classified into voltage source inverters (VSIs) and current source inverters (CSI) based on the input source. VSI converts the fixed DC voltage to the variable frequency AC voltage; its output voltage is independent of the load, and the current is depends on the impedance of the load. CSI converts the fixed DC voltage to the variable frequency AC current, the output current of the CSI is independent of the load but the voltage is dependent on the impudence of the load [9]. Based on a number of phases at output inverters are categorized into single-phase

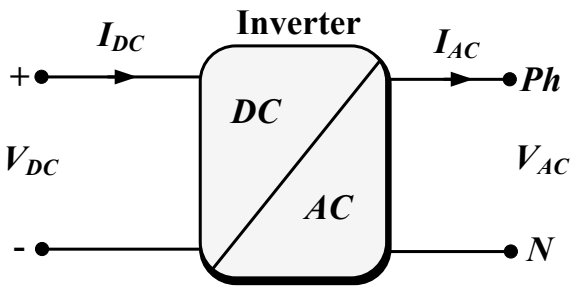

Fig. 5 Block diagram of the inverter

and three-phase inverters. Single-phase inverters are restricted to low power output and these inverters are popular for the UPS.

3.1 Three-Phase Inverter

Three-phase inverters are pretty popular in most applications due to their high power handling capabilities. The basic three-phase inverter is a six-switch inverter (H6 inverter), illustrated in Fig. 6. It consists of three arms with having two switches on each arm. These switches are operated in several states to obtain desired voltage and frequency at the output terminals, and this process of symmetrical switching is known as modulation [24]. The basic modulation techniques are 180° mode and 120° mode. During the 180° mode of operation, each switch operates for half of the period over a cycle, and switches corresponding to the same arm are operated in a complementary manner to avoid a dead short circuit of source terminals. The switching pattern of the 180° mode of operation is shown in Table 2. Due to the non-ideality of the switches, the outgoing switch goes to turn off slowly and leads to a dead short circuit of source terminals [25].

To eliminate the aforementioned problem, dead time is provided between the transitions of pole voltages. To achieve that 120° mode of operation is proposed. In this, each switch conducts for 120° over a period and 60° delay is provided in between the switching of the switches (Table 2) in the same leg but the major drawback with the 120° mode is output voltage decreases.

The output phase voltages of the VSI corresponding to the 180^0 mode of conduction are shown in Fig. 7. Irrespective of the load impudence the voltage remains

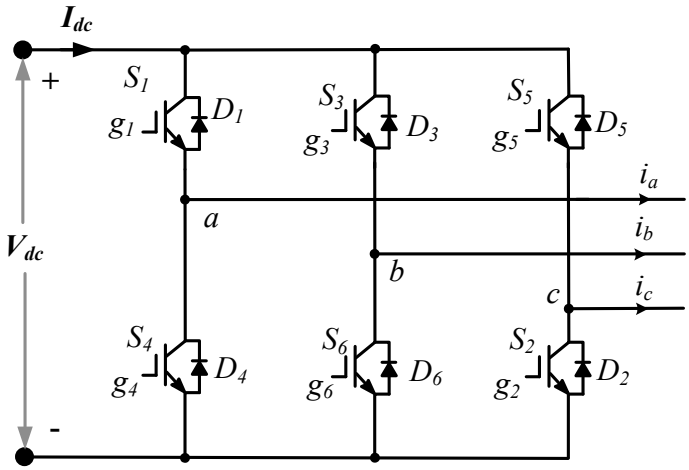

Fig. 6 Three-phase H6 inverter

Table 2 Switching pattern of VSI

Switching pattern for 180° mode of operation					
0–60°	60°–120°	120°–180°	180°–240°	240°–300°	300°–360°
S_1			S_4		
S_6		S_3			S_6
S_5	S_2			S_5	
Switching pattern for 120° mode of operation					
0–60°	60°–120°	120°–180°	180°–240°	240°–300°	300°–360°
S_1			S_4		
S_6		S_3			S_6
	S_2			S_5	

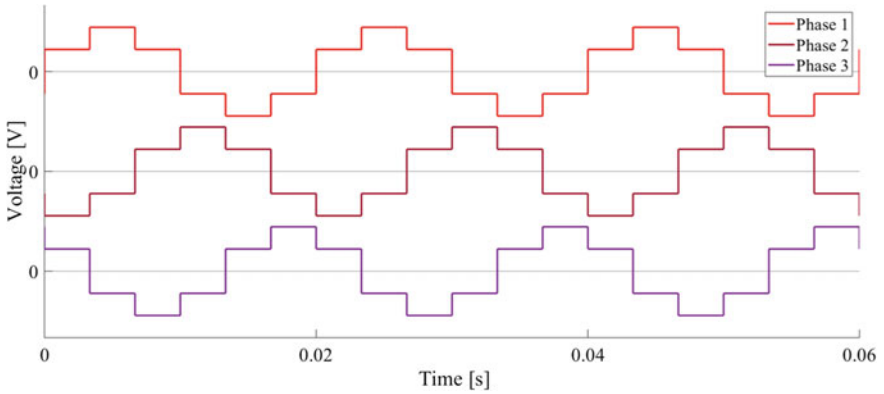

Fig. 7 The output voltage of three-phase H6 VSI in 180° operating mode

constant at 4 levels ($2*V_{dc}/3$, $V_{dc}/3$, $-V_{dc}/3$, $-2*V_{dc}/3$) with a 31% total harmonic distortion (THD).

3.2 Leakage Current and Common-Mode Voltage (CMV)

The CMV and the parasitic capacitance of the solar PV (Fig. 2) cause the leakage current. CMV can be determined by taking the mean of the pole voltages of the inverter (Eq. 1) [26]. Figure 8 shows the model diagram of the H6 inverter, where $V_a(t)$, $V_b(t)$, $V_c(t)$ are the instantaneous pole voltages and the V_{CM} is the common-mode voltage that appears in between the neutral point of the load and the source *–ve*, and C_{pv} is the stray capacitance of the solar PV panel.

$$V_{CM} = (V_a + V_b + V_c)/3 \tag{1}$$

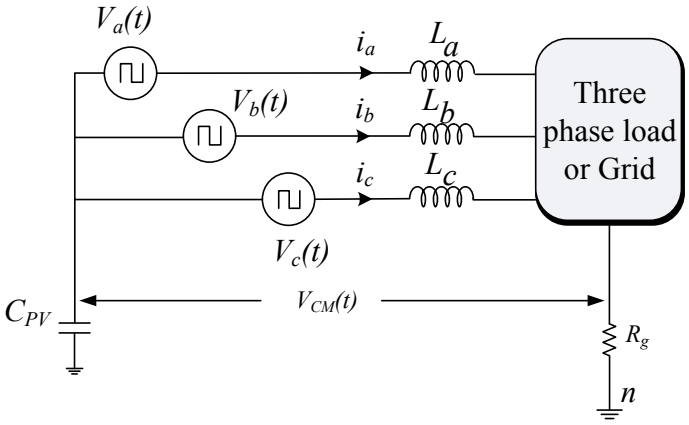

Fig. 8 CMV model of H6 inverter

$$I_{\text{leakage}} = C_{pv} * \mathrm{d}(V_{CM})/\mathrm{d}t \tag{2}$$

$$I_{\text{leakage}} \propto \mathrm{d}(V_{CM})/\mathrm{d}t \tag{3}$$

Therefore, the leakage current of the inverter can be minimized by suppressing the change in CMV (Eq. 3), and this must be within the standard limits of VDE-AR-N-4105 mentioned in Table 1 [27]. In this chapter, various modulation schemes and the inverter topologies are presented to minimize the leakage current by reducing the change in CMV.

3.3 Modulation Techniques to Minimize CMV

Change in CMV affects the leakage current of the inverter. This variation (peak-to-peak) can be minimized with the help of various modulation techniques. Peak-to-peak CMV of the H6 inverter in 180° conduction mode is V_{dc}, which results in more leakage currents, and in the following sub-sections, several modulation schemes are presented to minimize the CMV without changing the topological configuration.

3.3.1 Space *V*ector *M*odulation (SVM)

SVM is the most adopted modulation technique for controlling of H6 inverter to use the maximum DC bus of 91% without injecting any third harmonic component [28]. H6 inverter with the SVM technique forms 8 distinct states without causing any dead

Table 3 CMV at various states in SVM

S_1	S_3	S_5	Vector	CMV
0	0	0	V_0	0
1	0	0	V_1	$V_{dc}/3$
1	1	0	V_2	$2 * V_{dc}/3$
0	1	0	V_3	$V_{dc}/3$
0	1	1	V_4	$2 * V_{dc}/3$
0	0	1	V_5	$V_{dc}/3$
1	0	1	V_6	$2 * V_{dc}/3$
1	1	1	V_7	V_{dc}

Table 4 CMV at various states in NSPWM

S_1	S_3	S_5	Vector	CMV
1	0	0	V_1	$V_{dc}/3$
1	1	0	V_2	$2 * V_{dc}/3$
0	1	0	V_3	$V_{dc}/3$
0	1	1	V_4	$2 * V_{dc}/3$
0	0	1	V_5	$V_{dc}/3$
1	0	1	V_6	$2 * V_{dc}/3$

short circuit of DC source terminals. Each state is having different CMVs and are listed in Table 3.

From Table 3, it can be observed that with the SVM technique the variation of common-mode voltage is very high i.e. 0 to $V_{dc,}$ and results in a large leakage current.

3.3.2 Near *State* PWM (NSPWM)

The near-state pulse width modulation (NSPWM) method is similar to the SVM only. In this method, any output voltage vector is modelled with the neighbour three vectors of the reference voltage. Therefore, only the six active vectors (V_1 to V_6) are utilized to model any reference voltage [29]. From Table 4, it can be observed that the peak-to-peak voltage variation of the CMV is $V_{dc}/3$ i.e. from $V_{dc}/3$ to $2 * V_{dc}/3$. With the NSPWM method CMV variation is reduced to $V_{dc}/3$, and it minimizes the leakage current of the inverter.

3.3.3 Active *Zero State* PWM (AZPWM)

Extreme values of the CMVs are $0 * V_{dc}$ and V_{dc} occur at the time of zero vector instants. In the AZPWM scheme, a zero vector is produced by operating the two

Table 5 Switching pattern for AZPWM schemes

Modulation technique	Sector 1		Sector 2		Sector3	
SVPWM	7-2-1-0-1-2-7		7-2-3-0-3-2-7		7-4-3-0-3-4-7	
NSPWM	2-1-6-1-2		3-2-1-2-3		4-3-2-3-4	
AZPWM1	3-2-1-6-1-2-3		1-2-3-4-3-2-1		5-4-3-2-3-4-5	
AZPWM2	6-2-1-3-1-2-6		4-2-3-1-3-2-4		2-4-3-5-3-4-2	
RSPWM1	3-1-5-1-3		3-1-5-1-3		3-1-5-1-3	
RSPWM2B	4-2-6-2-4		4-2-6-2-4		2-4-6-4-2	
RSPWM3	0–π/6	π/6–π/3	π/3–π/2	π/3–π/2	π/2–2π/3	2π/3–5π/6
	3-1-5-1-3	4-2-6-2-4	4-2-6-2-4	3-1-5-1-3	3-1-5-1-3	2-4-6-4-2

opposite vectors with equal time. Based on the sequence of operation, AZPWM techniques are two types AZPWM1 and AZPWM2 mentioned in Table 5 [30].

In sector-1, the zero vector is implemented by operating vectors 3 and 6 with equal time and similarly for sector 2 vectors 1 and 4, and sector 3 vectors 2 and 5.

3.3.4 Remote *S*tate PWM (RSPWM)

RSPWM facilitates the elimination of high-frequency components from the CMV and in this modulation scheme only odd vector V_1, V_3, V_5, or only even vectors V_2, V_4, V_6 are used to produce the resultant vector. Based on the selection of vectors, RSPWM is classified into RSPWM1 (formed by only odd vectors) and RSPWM2B (formed by even vectors alone). RSPWM3 combines the RSPWM1 and RSPWM2B, and their switching sequences are mentioned in Table 3 [30].

3.4 Control Scheme of the Inverter Topologies

The closed-loop control is established based on active and reactive power control, as it is imperative to match the power demand. The control scheme consists of two cascaded loops in which the outer loop is to controls the power injection to the grid from PVS while the inner loop is to controls the grid current based on the outer power control loop. The current controller generates the voltage references for the PWM modulator. A carrier-based modulation scheme is utilized for the generation of the switching pulses for the active switches of the inverter topologies. In the carrier-based modulation method, switching pulses are generated according to the control logic and by comparing the carrier signals with the SVM modulation signals. SVM modulation signals are generated from the sinusoidal modulation signals by adding the zero-sequence component [31]. The block diagram of the control scheme is illustrated in Fig. 9.

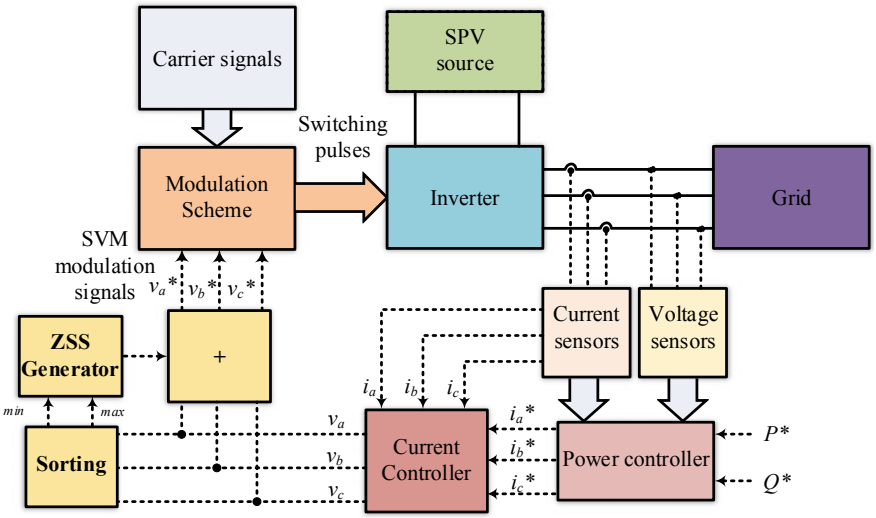

Fig. 9 Block diagram of transformerless inverter with a control structure

4 Transformerless Power Inverter Topologies

In the earlier section, the CMV of the H6 inverter is minimized by using various modulation techniques. In this section, the CMV of the inverter is going to be minimized by making topological changes to the inverter [31]. Among those inverter topologies, few are described in the following sub-sections.

4.1 H7 Inverter Topology

In the H6 inverter maximum and minimum values of the CMV, it appears at the zero vector states i.e. V_7 and V_0 states. H7 inverter shown in Fig. 10a is consists of power electronic semiconductor switch S_7 placed in its positive path [32]. During the zero vector V_7, the switch S_7 breaks the continuity of the circuit on the DC side of the inverter and results in zero CMV. The switching table of the converter corresponding to various states and its CMVs are listed in Table 6. The control strategy of the H7 inverter is modelled based on the lookup table (Table 6) and is illustrated in Fig. 10b [33]. From Table 6, it can be observed that the range of the CMV of H7 topology is 0 to $2 * V_{dc}/3$.

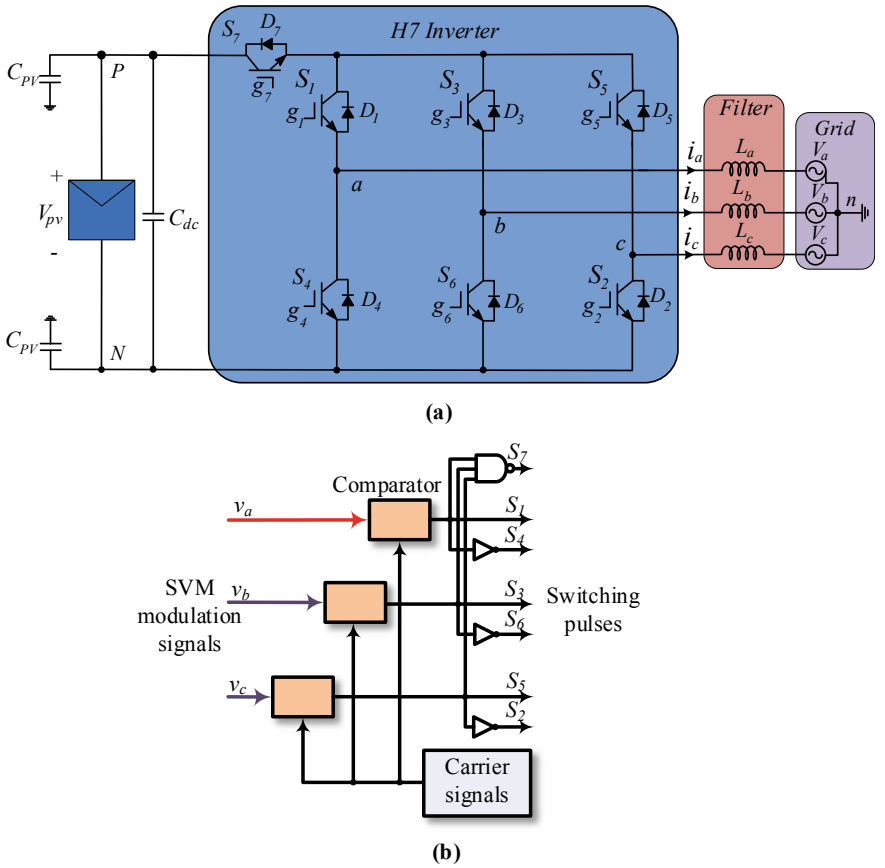

Fig. 10 H7 inverter **a** inverter topology **b** modulation scheme

Table 6 Switching states with CMVs of the H7 inverter

S_1	S_3	S_5	S_7	Vector	CMV
0	0	0	1	V_0	0
1	0	0	1	V_1	$V_{dc}/3$
1	1	0	1	V_2	$2 * V_{dc}/3$
0	1	0	1	V_3	$V_{dc}/3$
0	1	1	1	V_4	$2 * V_{dc}/3$
0	0	1	1	V_5	$V_{dc}/3$
1	0	1	1	V_6	$2 * V_{dc}/3$
1	1	1	0	V_7	0

4.2 *H8* Inverter Topology

H8 topology is similar to the H7, but in H8 both positive and negative paths are consisting of power electronic semiconductor devices illustrated in Fig. 11a. These switches isolate the DC supply from the load or grid at the time of both zero vector states i.e. at V_0 and V_7 [33].

During the vector V_7 the switch S_7 and at V_0 the switch S_8 breaks the conduction path on the DC side of the inverter. The switching states corresponding to various vectors are presented in Table 7. The modulation scheme (Fig. 11b) is developed according to the switching states. The range of CMV remains the same as the H7 inverter but the leakage current will reduce to approximately half due to discontinuous path during zero vector instant.

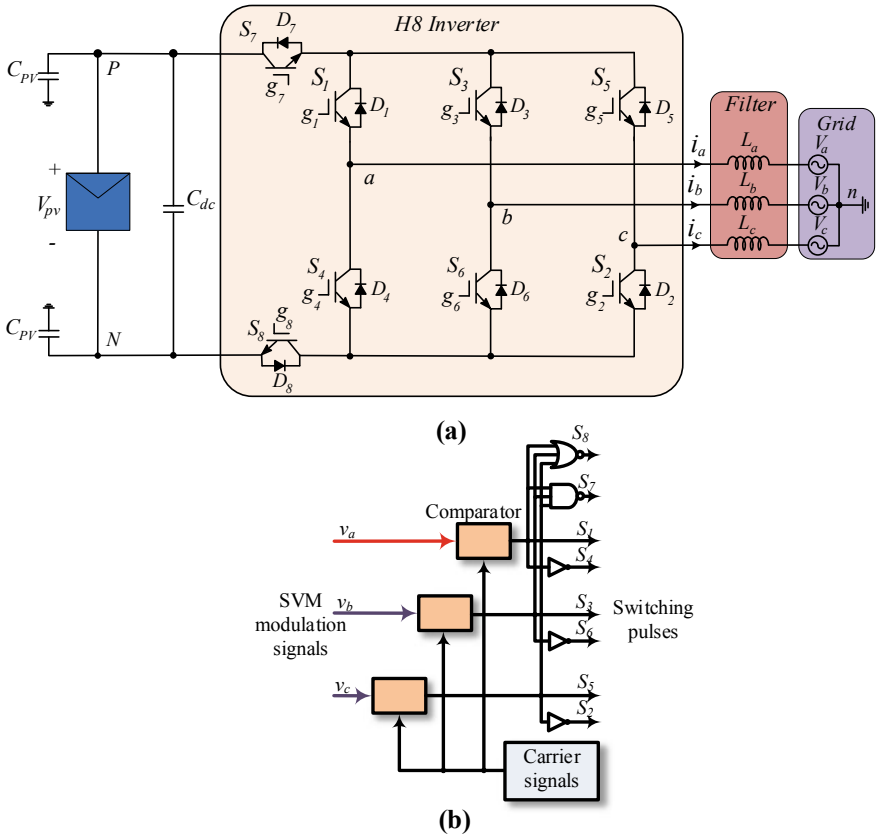

Fig. 11 H8 inverter **a** inverter topology **b** modulation scheme

Table 7 Switching states with CMVs of the H8 inverter

S_1	S_3	S_5	S_7	S_8	Vector	CMV
0	0	0	1	0	V_0	0
1	0	0	1	1	V_1	$V_{dc}/3$
1	1	0	1	1	V_2	$2 * V_{dc}/3$
0	1	0	1	1	V_3	$V_{dc}/3$
0	1	1	1	1	V_4	$2 * V_{dc}/3$
0	0	1	1	1	V_5	$V_{dc}/3$
1	0	1	1	1	V_6	$2 * V_{dc}/3$
1	1	1	0	1	V_7	0

4.3 *Three-Phase Seven Switch Inverter Topology*

The topology shown in Fig. 12a is similar to the H6 topology but the zero state V_0 and V_7 are provided by the seventh switch [34]. The 7th switch is connected to the

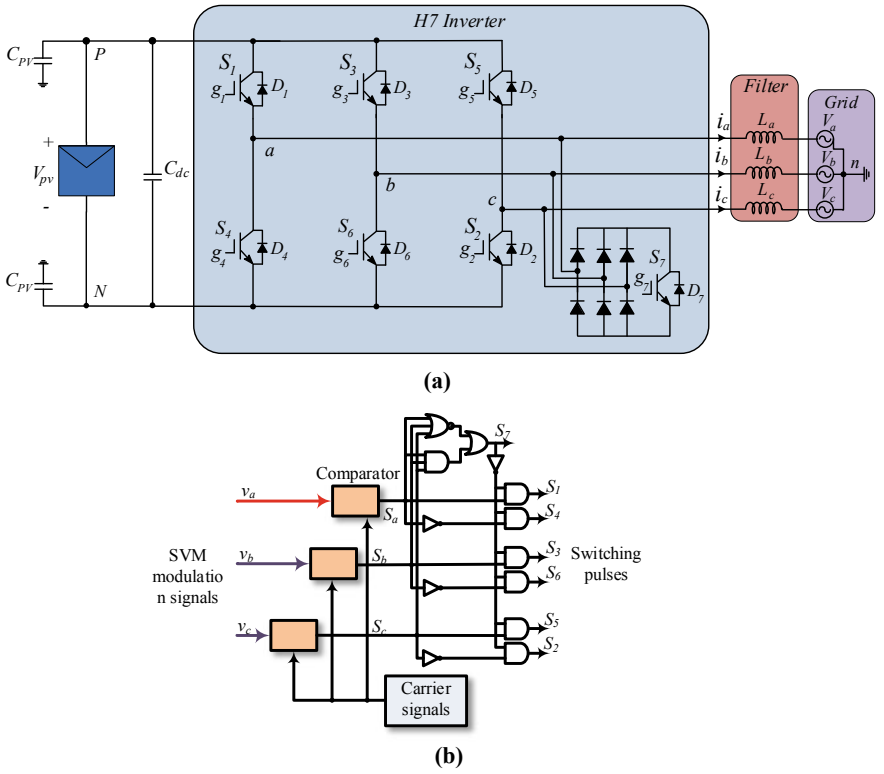

Fig. 12 Three-phase seven switch inverter **a** inverter topology **b** modulation scheme

Table 8 Switching sequence of three-phase seven switch inverter

Vector	Switching ($S_1S_3S_5S_7$)	V_{an}	V_{bn}	V_{cn}	CMV
V_1	1000	V_{dc}	0	0	$V_{dc}/3$
V_2	1100	V_{dc}	V_{dc}	0	$2 * V_{dc}/3$
V_3	0100	0	V_{dc}	0	$V_{dc}/3$
V_4	0110	0	V_{dc}	V_{dc}	$2 * V_{dc}/3$
V_5	0010	0	0	V_{dc}	$V_{dc}/3$
V_6	1010	V_{dc}	0	V_{dc}	$2 * V_{dc}/3$
V_0 & V_7	xxx1	$V_{dc}/2$	$V_{dc}/2$	$V_{dc}/2$	$V_{dc}/2$

inverter output terminals through a three-phase diode bridge rectifier. The switch S_7 is coming to conduction during zero states i.e. during V_0 and V_7 and the CMV during these states is $V_{dc}/2$.

The switching states and corresponding CMVs of this topology are listed in Table 8. The range of the CMV of this topology is $V_{dc}/3$ to $2 * V_{dc}/3$. According to the switching states presented in Table 8, modulation scheme is developed for seven switch inverters and it's illustrated in Fig. 12b.

4.4 *Three-Phase Eight Switch Inverter Topology*

This topology presented in Fig. 13a consists of eight switches (S_1 to S_8). S_1 to S_6 switch positions are similar to the H6 inverter, during the non-zero states the switching state of the switches S_1 to S_6 remains the same as the H6 inverter and S_7 is in on and S_8 is in off. S_7 and S_8 switches are operated in a complementary manner [36].

During zero vector states, both the switches on the leg-1 (S_1 and S_4) are in off, and switching states and CMV corresponding to all states are listed in Table 9. The modulation scheme for the 8-switch converter is modelled according to Table 9 and is illustrated in Fig. 13b. Therefore, during the non-zero vector instants, CMV is the same as the conventional H6 inverter i.e. either $V_{dc}/3$ or $2 * V_{dc}/3$ and at the zero vector instant CMV is $2 * V_{dc}/5$. The range of the CMV remains the same as the three-phase seven switch topology but the step-change in CMV is different.

4.5 *Four-Leg Inverter Topology*

The four-leg inverter shown in Fig. 14a consists of an auxiliary leg along with the H6 inverter. The auxiliary leg is operated such that it always maintains the constant CMV. Generally, the four-leg inverter is controlled with the carrier-based PWM method [37, 38]. The switching table of the four-leg inverter and corresponding CMV is presented

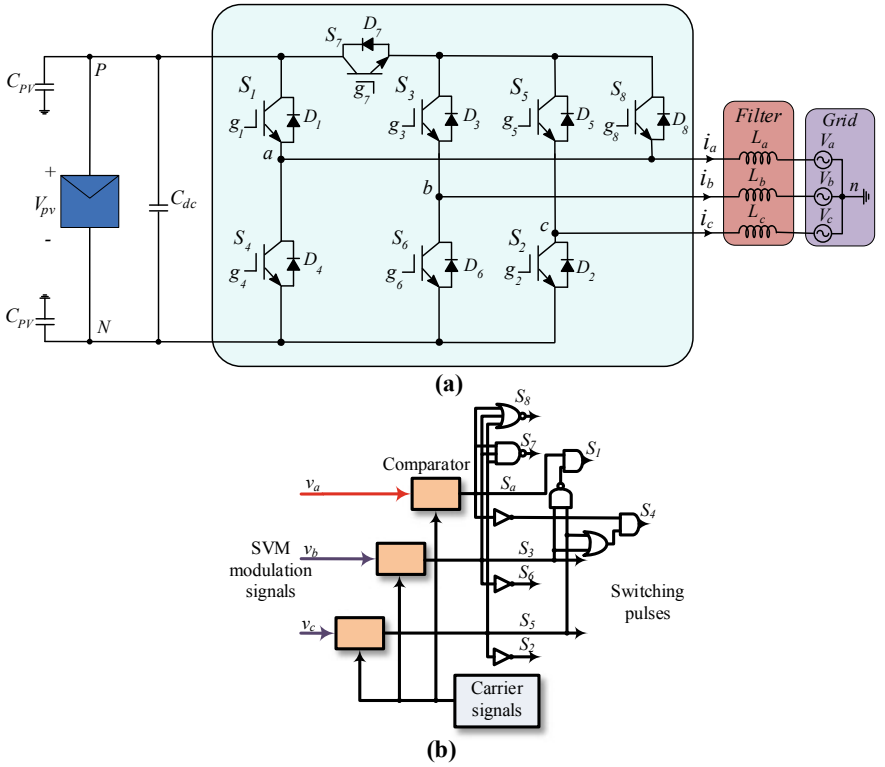

Fig. 13 Three-phase 8-switch inverter **a** inverter topology **b** modulation scheme

Table 9 Switching sequence of three-phase eight switch inverter

S_1	S_3	S_5	S_7	S_8	Vector	CMV
1	0	0	1	0	V_1	$V_{dc}/3$
1	1	0	1	0	V_2	$2 * V_{dc}/3$
0	1	0	1	0	V_3	$V_{dc}/3$
0	1	1	1	0	V_4	$2 * V_{dc}/3$
0	0	1	1	0	V_5	$V_{dc}/3$
1	0	1	1	0	V_6	$2 * V_{dc}/3$
S_1 & S_4 both *OFF*	1	1	0	1	V_7	$2 * V_{dc}/5$

in Table 10.

$$S_3 = \left(S'_a S_b + S_b S'_c + (S_a S_c)'\right) + S_b S'_{T2} = S'_4 \tag{4a}$$

$$S_5 = \left((S'_a S_c + S_c S'_b + (S_a S_b)\right)' + S_c S'_{T3} = S'_6 \tag{4b}$$

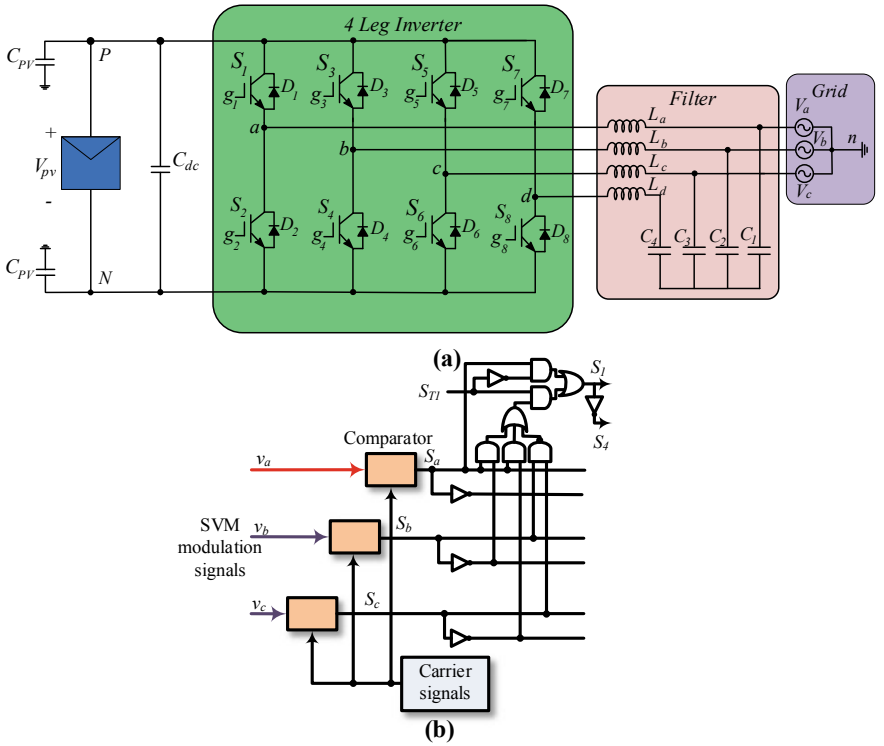

Fig. 14 Three-phase four-leg inverter **a** inverter topology **b** modulation scheme

Table 10 Switching sequence of three-phase four-leg inverter

S_1	S_3	S_5	S_7	Vector	CMV
1	0	0	1	V_1	$V_{dc}/2$
1	1	0	0	V_2	$V_{dc}/2$
0	1	0	1	V_3	$V_{dc}/2$
0	1	1	0	V_4	$V_{dc}/2$
0	0	1	1	V_5	$V_{dc}/2$
1	0	1	0	V_6	$V_{dc}/2$

$$S_7 = S_1 \oplus S_3 \oplus S_5 = S_8' \tag{4c}$$

The modulation scheme to generate switching pulse for S_1 and S_4 is illustrated in Fig. 14b and switching states corresponding to the each vector presented in Table 10. Similarly, algebraic expressions to generate switching pulses for the remaining switches are presented in Eq. (4a–c). Where S_{T1}, S_{T2}, and S_{T3} are the control signals having a pulse width of 33.33%. The zero states are obtained by operating opposite

Table 11 Switching table and capacitor voltages of DCM232 inverter

	S_1	S_3	S_5	$S_{7a} = S_{8a}$	$S_{7b} = S_{8b}$	V_{cpv1}	V_{cpv2}	V_{cpv3}	V_{cpv4}
V_1	1	0	0	1	0	$2 * V_{dc}/3$	$-V_{dc}/3$	$V_{dc}/3$	$-2 * V_{dc}/3$
V_3	0	1	0						
V_5	0	0	1						
V_2	1	1	0	0	1				
V_4	0	1	1						
V_6	1	0	1						
V_7	1	1	1	0	0				
V_0	0	0	0						

vectors at an equal time or the reference vector is generated by operating three closer vectors. The CMV of the four-leg inverter is constant at $V_{dc}/2$ irrespective of the reference vector. Due to the constant CMV across the parasitic capacitance, the change in CMV becomes zero, and results approximately zero leakage current.

4.6 DCM232 Three-Phase Inverter Topology

Generally, non-zero state vectors of the H6 inverter consist of two sets of CMVs either $V_{dc}/3$ or $2 * V_{dc}/3$, respectively. All odd vectors produce a common-mode voltage of $V_{dc}/3$ and all even vectors produce $2 * V_{dc}/3$. DCM232 is a topology that is proposed to separate these odd and even non-zero states, and power is delivered by two symmetrical isolated DC sources. DCM232 is modelled with 10 ($2 + 2 + 6$) switching devices and two isolated DC sources shown in Fig. 14a. The inner H6 operation remains the same as the conventional inverter [39].

For the odd non-zero vectors V_1, V_3, V_5, the upper voltage source V_{pv1} is connected to the H6 inverter by turn on the S_{7a} and $S_{8a;}$ and for the even non-zero vectors V_2, V_4, V_6, the lower voltage V_{pv2} is connected to the H6 inverter by turn on the S_{7b} and S_{8b}. During the zero states, S_7 and S_8 switches isolate both the sources from the load. The switching states and the voltage across the stray capacitors are listed in Table 11. The modulation scheme for this inverter corresponding to the various switching states is modelled (Fig. 15b) according to Table 11.

5 Simulation Results and Discussion

The aforementioned inverter topological configurations are simulated in MATLAB/SIMULINK software with identical parameters. For the simulation study, 480 V battery source is considered as an input, and a three-phase 2 kW resistive load is

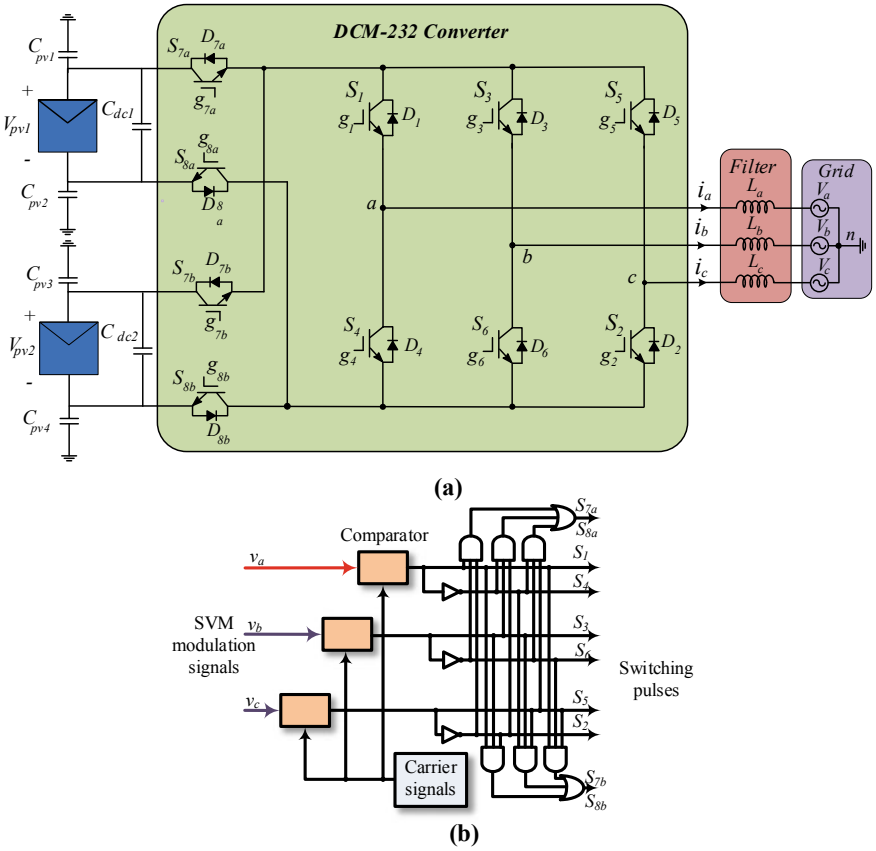

Fig. 15 Three-phase DCM232 inverter **a** inverter topology **b** modulation scheme

connected to the inverter terminals through a line inductance of 1 mH, and a 9 μF capacitor is considered as the stray capacitance of solar PV panel.

SVM-controlled H6 inverter is simulated and corresponding CMV and leakage currents are depicted in Fig. 16. H6 inverter CMV is varying from 0 to V_{dc} under the SVM modulation scheme (Fig. 16a) and the corresponding leakage current waveform and its RMS value (Red colour line) are shown in Fig. 16b. For the above specifications, the H6 inverter produces a 320-mA leakage current, thereby not within the standard limits of VDE-AR-N-4105.

A CMV and leakage current of modified SVPWM controlled H7 inverter are illustrated in Fig. 17. CMV of the inverter in Fig. 17a is varying in between 0 and 320 V (i.e. 0 to 2 * V_{dc}/3), and the leakage current corresponding to this CMV variation is shown in Fig. 17b which is having an RMS value of 230 mA. As compared to the H6 inverter, CMV variation and the leakage current of the H7 inverter are a bit lesser and within the standard limit (i.e. < 300 mA). Therefore, this topology is suitable for grid interface without using any transformer.

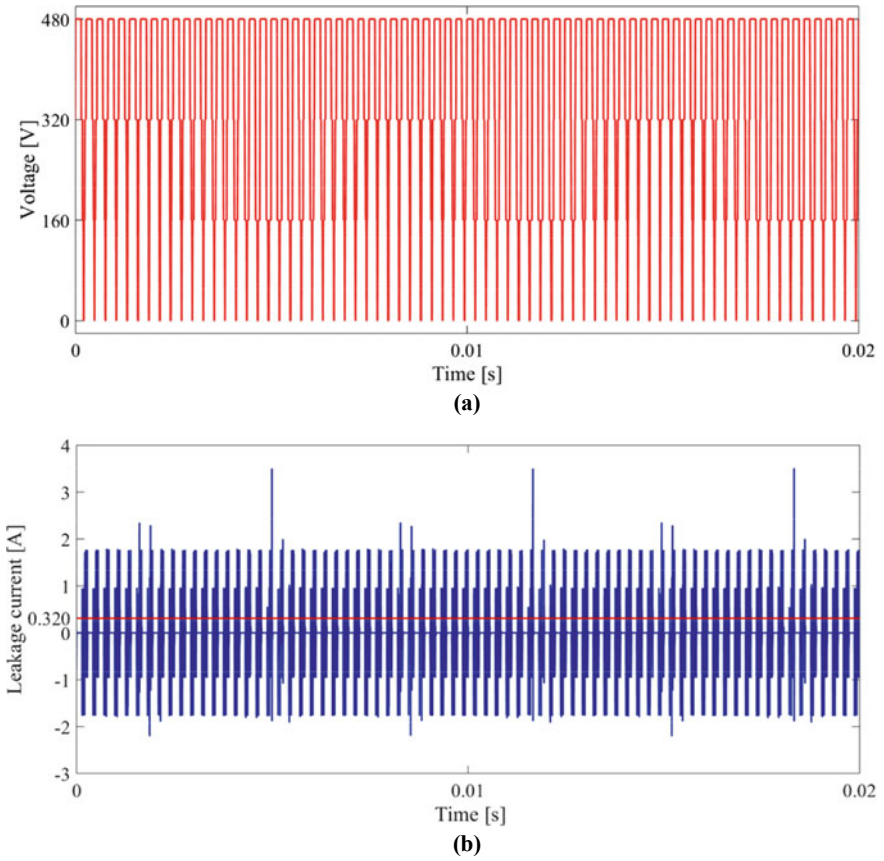

Fig. 16 Simulation results of H6 inverter using SVM **a** CMV, **b** leakage current

Similar to the H7 inverter, the H8 inverter is also simulated under the same modulation scheme and specifications. Obtained results with the H8 inverter are shown in Fig. 18. CMV (Fig. 18a) remains the same as the H7 inverter but the RMS value of the leakage current (Fig. 18b) is 165 mA; it is lesser than the H7 topology RMS leakage current i.e. 230 mA, due to the discontinuity of conduction in both the zero states.

CMV and leakage current corresponding to the three-phase seven switch inverter [30] are illustrated in Fig. 19. CMV of this inverter is varies from 160 V–240 V–320 V (i.e. $V_{dc}/3$–$V_{dc}/2$–$2 * V_{dc}/3$). It is observed that the CMV (Fig. 19a) is reduced in comparison to the earlier topologies. Therefore, leakage current is also reducing and the RMS value of the leakage current is 105 mA Fig. 19b), which complies with the VDE-AR-N-4105 standards.

Three-phase eight switch inverter CMV is depicted in Fig. 20a and is varying from 160 V–192 V–320 V ($V_{dc}/3$–$2 * V_{dc}/5$–$2 * V_{dc}/3$). The leakage current RMS

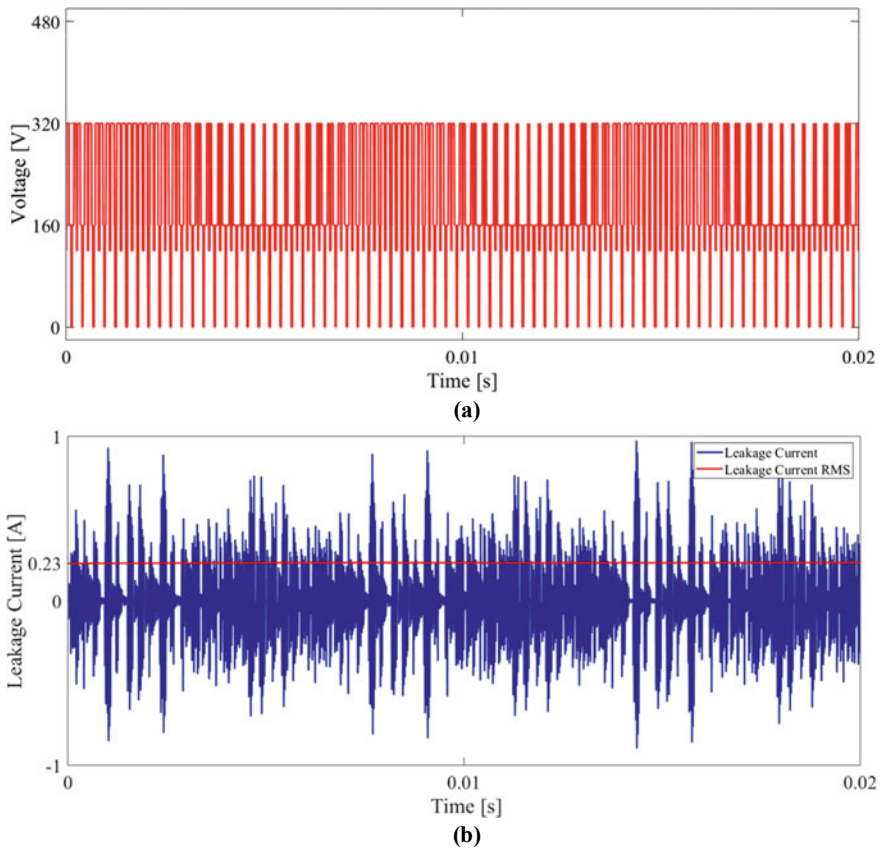

Fig. 17 Simulation results of H7 inverter **a** CMV, **b** leakage current

of the four-leg converter is shown in Fig. 20b; it was further reduced to 70 mA due to a reduction in the CMV variation across the stray capacitance.

The CMV generated by the four-leg inverter (Fig. 21a) is constant at 240 V ($V_{dc}/2$) irrespective of the state of operation. Due to the constant voltage across the parasitic capacitance, the leakage current is ideally zero. Because of the non-idealities, some amount of leakage current of 0.232 mA (RMS) is presented, and it is shown in Fig. 21b.

DCM232 inverter is having two isolated DC sources results in four stray capacitances illustrated in Fig. 15a. The voltage across these four capacitors is illustrated in Fig. 22. Due to the zero rate of change in the voltage across the stray capacitors, the leakage current associated with this topology is typically zero. The summary of the aforementioned inverter topologies is presented in Table 12.

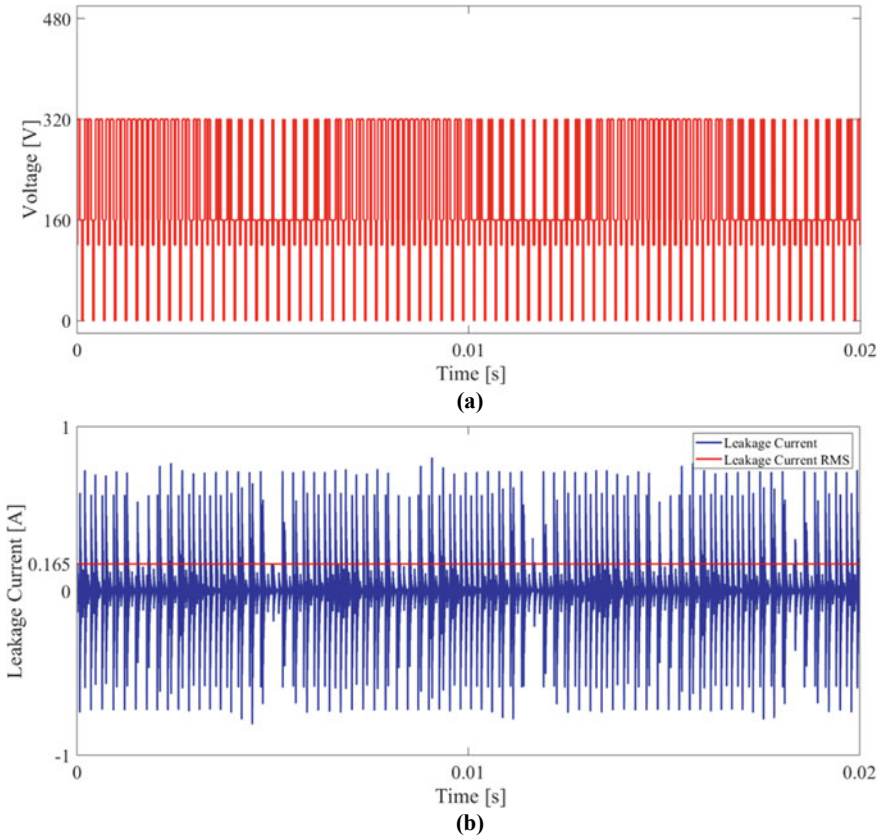

Fig. 18 Simulation results of H8 inverter **a** CMV, **b** leakage current

6 Concluding Remarks

This chapter exhaustively discussed the classification of power electronic interfaces and issues with transformerless three-phase grid-tied PV inverters. The operation and features of the leakage current minimization approaches such as advanced pulse width modulation techniques and power converter topology modifications in the transformerless grid-tied PV inverters are discussed in detail. In this chapter, a comprehensive analysis of state-of-the-art DC and AC bypass topologies derived from the conventional two-level inverter in terms of common-mode voltages and leakage currents is performed through MATLAB simulations. Most of the inverter topologies rely on the concept of disconnection of the inverter from the PV sources during zero states intervals, which enables breaking the leakage current conduction path. However, the CMV is not zero in such topologies. On the other hand, the DCM232 inverter and four-leg inverter can mitigate the leakage current with constant CMV by decoupling on DC and AC sides, respectively. It is anticipated that advanced

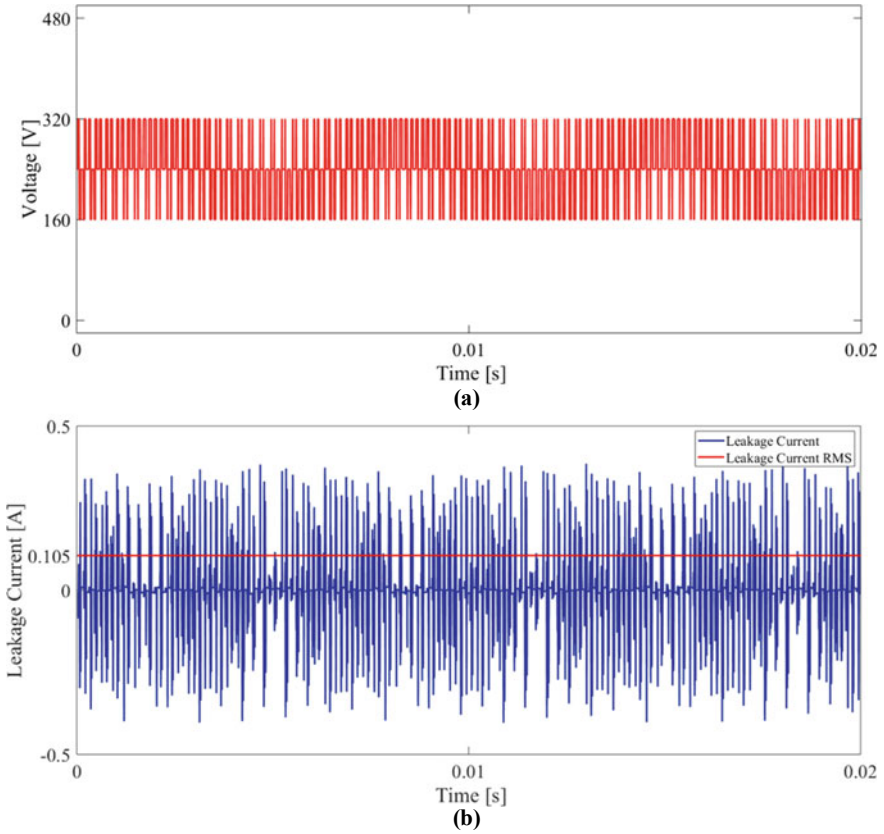

Fig. 19 Simulation results of Three-phase seven switch inverter **a** CMV, **b** leakage current

converter topologies with wideband gap devices will be dominantly used in the solar industry to achieve technical and economic benefits in near future.

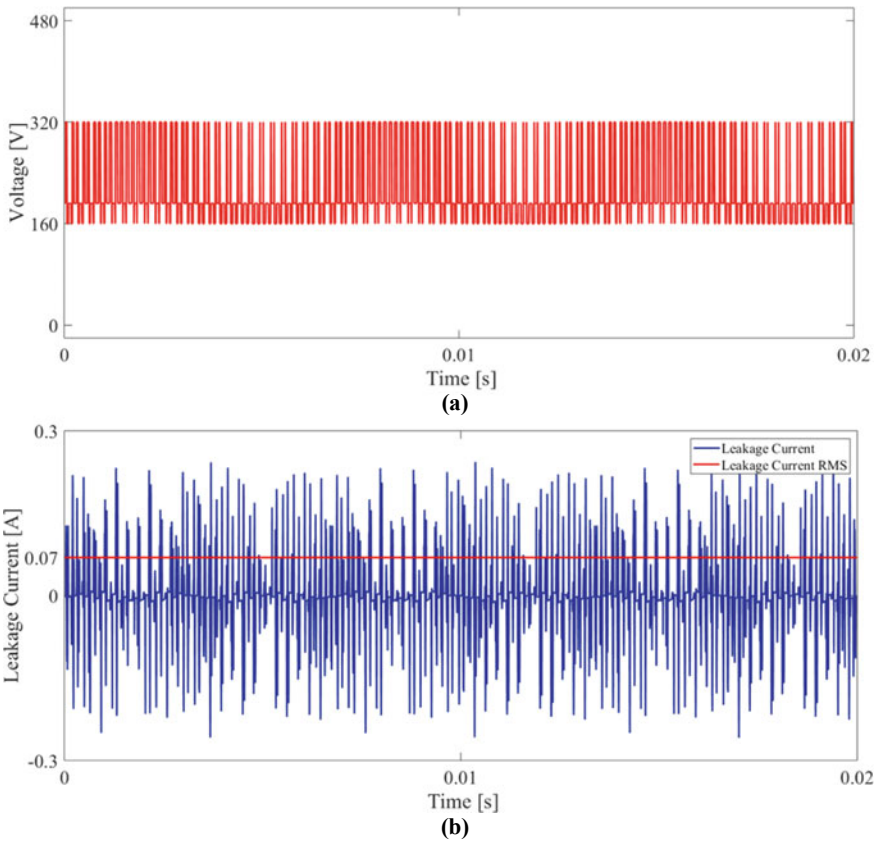

Fig. 20 Simulation results of three-phase eight switch inverter **a** CMV, **b** leakage current

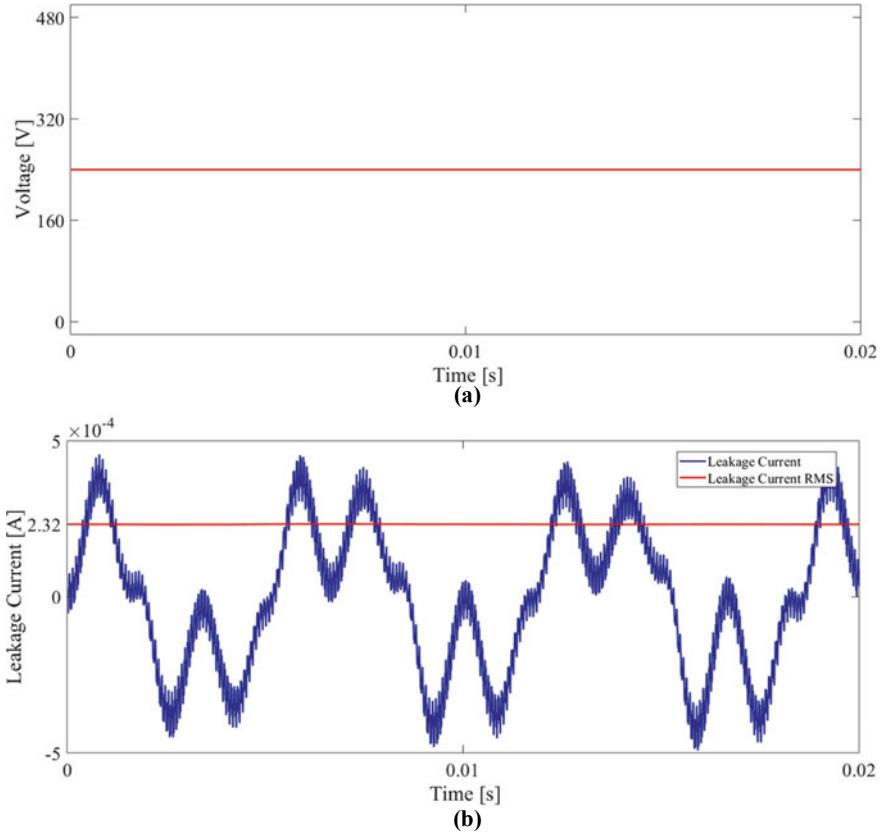

Fig. 21 Simulation results of Three-phase four-leg inverter **a** CMV, **b** leakage current

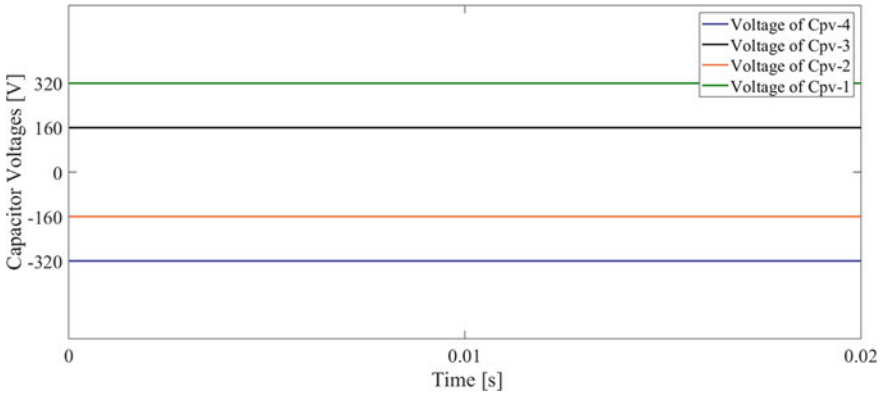

Fig. 22 Parasitic capacitance voltages of DCM232 inverter

Table 12 Summary of transformerless PV grid-tied systems

	Topology	Number of switches + Diodes	Overall variation in CMV	RMS value of leakage current (mA)	Voltage stress across the inductor	Decoupling side
1	H6 (SPWM)	6 + 0	0 to V_{dc}	343.5	V_{dc}	–
2	H6 (SVPWM)	6 + 0	0 to V_{dc}	340	V_{dc}	–
3	H7 topology [32]	7 + 0	0 to 2 * $V_{dc}/3$	238.5	V_{dc}	DC side
4	H8 topology [34]	8 + 0	0 to 2*$V_{dc}/3$	168	V_{dc}	DC side
5	7-switch inverters [35]	7 + 6	$V_{dc}/3$ to $2V_{dc}/3$	106.9	V_{dc}	AC side
6	8-switch inverters [36]	8 + 0	$V_{dc}/3$ to $2V_{dc}/3$	69.3	V_{dc}	AC side
7	Four-leg inverter [37, 38]	8 + 0	Constant	0.00626	V_{dc}	AC side
8	DCM232 3-ϕ inverter [39]	10 + 0	Constant	0	V_{dc}	DC side

References

1. International Energy Agency. Snapshot of global photovoltaic markets. Technical report, 2018 [online]. Available https://iea-pvps.org/snapshot-reports/snapshot-2020/
2. S. Kouro, J.I. Leon, D. Vinnikov, L.G. Franquelo, Grid-connected photovoltaic systems: an overview of recent research and emerging PV converter technology. IEEE Ind. Electron. Mag. **9**(1), 47–61 (2015)
3. R. Panigrahi, S.K. Mishra, S.C. Srivastava, A.K. Srivastava, N.N. Schulz, Grid integration of small-scale photovoltaic systems in secondary distribution network—a review. IEEE Trans. Ind. Appl. **56**(3), 3178–3195 (2020)
4. J. Young-Hyok, J. Doo-Yong, K. Jun-Gu, K. Jae-Hyung, L. Tae-Won, W. Chung-Yuen, A real maximum power point tracking method for mismatching compensation in PV array under partially shaded conditions. IEEE Trans. Power Electron. **26**(4), 1001–1009 (2011)
5. R.M. Hudson, M.R. Behnke, R. West, S. Gonzalez, J. Ginn, Design considerations for three-phase grid-connected photovoltaic inverters, in *Proceedings of photovoltaic specialists conference* (2002), pp. 1396–1401
6. Q. Yan, X. Wu, X. Yuan, Y. Geng, Q. Zhang, Minimization of the DC component in transformerless three-phase grid-connected photovoltaic inverters. IEEE Trans. Power Electron. **30**(7), 3984–3997 (2015)
7. O. Lopez et al., Eliminating ground current in a transformerless photovoltaic application. IEEE Trans. Energy Convers. **25**(1), 140–147 (2010)
8. S. Essakiappan, P. Enjeti, R.S. Balog, S. Ahmed, Analysis and mitigation of common-mode voltages in photovoltaic power systems, in *Proceedings of IEEE Energy Conversion Congress and Exposition*, Phoenix, AZ (2011), pp. 28–35
9. H.I. Yunus, R.M. Bass, Comparison of VSI and CSI topologies for single-phase active power filters, in *PESC Record. 27th Annual IEEE Power Electronics Specialists Conference*, vol. 2 (1996), pp. 1892–1898
10. R.J. Mustafa, M.R. Gomaa, M. Al-Dhaifallah, H. Rezk, Environmental impacts on the performance of solar photovoltaic systems. Sustainability **12**(2), 608 (2020)

11. F. Spertino, G. Graditi, Power conditioning units in grid-connected photovoltaic systems: a comparison with different technologies and wide range of power ratings. Sol. Energy **108**, 219–229 (2014)
12. R. Panigrahi, S.K. Mishra, S.C. Srivastava, A.K. Srivastava, N.N. Schulz, Grid integration of small-scale photovoltaic systems in secondary distribution network—a review. IEEE Trans. Ind. App. **56**(3), 3178–3195 (2020)
13. S. Kouro, C. Fuentes, M. Perez, J. Rodriguez,Single DC-link cascaded H-bridge multilevel multi-string photovoltaic energy conversion system with inherent balanced operation, in *IECON 2012–38th Annual Conference on IEEE Industrial Electronics Society* (IEEE, 2012), pp. 4998–5005
14. IEEE standard for interconnecting distributed resources with electric power systems, in *IEEE Std 1547–2003* (2003), pp.1–28
15. IEEE recommended practice for utility interface of photovoltaic (PV) systems, in *IEEE Std 929–2000* (2000), pp. i
16. A.B. Acharya, M. Ricco, D. Sera, R. Teoderscu, L.E. Norum, Performance analysis of medium-voltage grid integration of PV plant using modular multilevel converter. IEEE Trans. Energy Convers. **34**(4), 1731–1740 (2019)
17. M.R. Islam, Y. Guo, J. Zhu, A multilevel medium-voltage inverter for step-up-transformer-less grid connection of photovoltaic power plants. IEEE J. Photovoltaics **4**(3), 881–889 (2014)
18. M. Rabiul Islam, A.M. Mahfuz-Ur-Rahman, K.M. Muttaqi, D. Sutanto, State-of-the-art of the medium-voltage power converter technologies for grid integration of solar photovoltaic power plants. IEEE Trans. Energy Convers. **34**(1), 372–384 (2019)
19. M.R. Islam, Y. Guo, J. Zhu, A high-frequency link multilevel cascaded medium-voltage converter for direct grid integration of renewable energy systems. IEEE Trans. Power Electron. **29**(8), 4167–4182 (2014)
20. M.R. Islam, Y. Guo, J. Zhu, Multilevel converters for step-up-transformer-less direct integration of renewable generation units with medium voltage smart microgrids, in *Large Scale Renewable Power Generation* (Springer, Singapore, 2014), pp. 127–149
21. P.C. Sarker, et al., Solar photovoltaic power plants: necessity and techno-economical development, in *Renewable Energy and the Environment* (Springer, Singapore, 2018), pp. 41–69
22. A.M. Pavan, S. Castellan, S. Quaia, S. Roitti, G. Sulligoi, Power electronic conditioning systems for industrial photovoltaic fields: centralized or string inverters?, in *2007 International Conference on Clean Electrical Power* (2007), pp. 208–214
23. J. Imhoff, J.R. Pinheiro, J.L. Russi, D. Brum, R. Gules, H.L. Hey, DC-DC converters in a multi-string configuration for stand-alone photovoltaic systems, in *2008 IEEE Power Electronics Specialists Conference* (2008), pp. 2806–2812
24. D. Leuenberger, J. Biela, PV-module-integrated AC inverters (AC modules) With subpanel MPP tracking. IEEE Trans. Power Electron. **32**(8), 6105–6118 (2017)
25. K.K. Gupta, P. Bhatnagar, H. Vahedi, K. Al-Haddad, Carrier based PWM for even power distribution in cascaded H-bridge multilevel inverters within single power cycle, in *IECON 2016—42nd Annual Conference of the IEEE Industrial Electronics Society* (2016), pp. 6470–6475
26. R.W. Erickson, D. Maksimovic, *Fundamentals of Power Electronics* (Springer Science & Business Media, 2007)
27. İ Çolak, E. Kabalcı, G. Keven, Conventional H-bridge and recent multilevel inverter topologies, *Multilevel Inverters* (Academic Press, 2021), pp. 57–110
28. S. Kouro, C. Fuentes, M. Perez, J. Rodriguez, Single DC-link cascaded H-bridge multilevel multi-string photovoltaic energy conversion system with inherent balanced operation, in *IECON 2012—38th Annual Conference on IEEE Industrial Electronics Society* (2012), pp. 4998–5005
29. K. Zhou, D. Wang, Relationship between space-vector modulation and three-phase carrier-based PWM: a comprehensive analysis [three-phase inverters]. IEEE Trans. Ind. Elec. **49**(1), 186–196 (2002)
30. E. Un, A.M. Hava, A near state PWM method with reduced switching frequency and reduced common mode voltage for three-phase voltage source inverters, in *2007 IEEE International Electric Machines & Drives Conference* (2007), pp. 235–240

31. M.C. Cavalcanti, K.C. de Oliveira, A.M. de Farias, F.A.S. Neves, G.M.S. Azevedo, F.C. Camboim, Modulation techniques to eliminate leakage currents in transformerless three-phase photovoltaic systems. IEEE Trans. on Ind. Elec. **57**(4), 1360–1368 (2010)
32. D. Ronanki, P.H. Sang, V. Sood, S.S. Williamson, Comparative assessment of three-phase transformerless grid-connected solar inverters, in *2017 IEEE International Conference on Industrial Technology (ICIT)*, Toronto, ON, Canada (2017), pp. 66–71
33. T.K.S. Freddy, N.A. Rahim, W. Hew, H.S. Che, Modulation techniques to reduce leakage current in three-phase transformerless H7 photovoltaic inverter. IEEE Trans. on Ind. Elec. **62**(1), 322–331 (2015)
34. R. Rahimi, S. Farhangi, B. Farhangi, G.R. Moradi, E. Afshari, F. Blaabjerg, H8 inverter to reduce leakage current in transformerless three-phase grid-connected photovoltaic systems. IEEE J Emerg Sel Topics Power Electron **6**(2), 910–918 (2018)
35. X. Guo, D. Xu, B. Wu, Three-phase seven-switch inverter with common-mode voltage reduction for transformerless photovoltaic system, in *IECON 2014—40th Annual Conference of the IEEE Industrial Electronics Society*, Dallas, TX, USA (2014), pp. 2279–2284
36. A.K. Gupta, H. Agrawal, V. Agarwal, A novel three-phase transformerless H-8 topology with reduced leakage current for grid-tied solar PV applications, IEEE Trans. Ind. App. **55**(2), 1765–1774 (2019)
37. X. Guo, R. He, J. Jian, Z. Lu, X. Sun, J.M. Guerrero, Leakage current elimination of four-leg inverter for transformerless three-phase PV systems. IEEE Trans. Power Electron. **31**(3), 1841–1846 (2016)
38. D. Han, S. Li, W. Choi, B. Sarlioglu, Design, implementation, and evaluation of a GaN-based four-leg inverter with minimal common-mode voltage generation, in *2017 IEEE Energy Conversion Congress and Exposition (ECCE)* (2017), pp. 5383–5388
39. X. Guo, D. Xu, B. Wu, New control strategy for DCM-232 three-phase PV inverter with constant common-mode voltage and anti-islanding capability, in *2014 IEEE Energy Conversion Congress and Exposition (ECCE)*, Pittsburgh, PA, USA (2014), pp. 5613–5617

Sensorless Control Technologies for Stand-Alone and Grid-Connected Operation of Brushless Doubly-Fed Induction Generators in Smart Grid

Yi Liu, Mohamed G. Hussien, and Wei Xu

Abstract This chapter handles the investigation of various proposed sensorless schemes of rotor position observer for brushless doubly-fed induction generator (BDFIG) systems based on both schemes of the model reference adaptive system (MRAS) and the high-frequency signal (HFS) injection methodology. The algorithm of MRAS is implemented with the functional quantity of CW reactive power (Q-MRAS) which can eliminate the integration process for the flux estimation and reduce the required sensors used to achieve the effective estimation of rotor position signal for BDFIGs. On the other side, the proposed methodology of CW-HFS injection approach is realized through the injection of HFS into the CW side while the resulted induced signal detected from the PW side will observe the information of rotor position. The proposed new position observer of CW-HFS injection offers a high-performance operation with a good tracking for the actual rotor position during various states of operation with any need for the machine parameters which would assure its reliability and strong robustness.

Keywords Brushless doubly-fed induction generator (BDFIG) · Rotor position observer · MRAS based on CW reactive power · High-frequency signal injection

List of Symbols

L_{1r}	Inductance of coupling between the rotor side and the PW
L_{2r}	Inductance of coupling between the rotor side and the CW

Y. Liu · W. Xu
Huazhong University of Science and Technology, Wuhan 430074, China
e-mail: liuyi82@hust.edu.cn

W. Xu
e-mail: weixu@hust.edu.cn

M. G. Hussien (✉)
Department of Electrical Power and Machines Engineering, Faculty of Engineering, Tanta University, Tanta, Egypt
e-mail: mohamed.hussien3@f-eng.tanta.edu.eg

S. K. Das et al. (eds.), *Advances in Control Techniques for Smart Grid Applications*,
https://doi.org/10.1007/978-981-16-9856-9_10

L_1	Self-inductance of the PW
L_2	Self-inductance of the CW
L_r	Self-inductance of the rotor-side
ω_1	Angular frequency of the PW
ω_2	Angular frequency of the CW
R_1	Resistance of the PW
R_2	Resistance of the CW
R_r	Resistance of the rotor side
Ψ_{1dq}	Flux linkages of the dq-axis for the PW
Ψ_{2dq}	Flux linkages of the dq-axis for the CW
Ψ_{rdq}	Flux linkages of the dq-axis for the rotor side
i_{1dq}	*dq*-axis components of the PW
i_{2dq}	*dq*-axis components of the CW
i_{rdq}	*dq*-axis components of the rotor side
s	The differential operator, *d/dt*
u_{1dq}	*dq*-axis voltages of PW
u_{2dq}	*dq*-axis voltages of CW
ω_{hf}	The frequency of the injected HFS
$U_{2_{hf}}$	The magnitude of the injected HFS
$k_{p_{MRAS}}$	Proportion parameter of the PI controller for the proposed observer
$k_{i_{MRAS}}$	Integration parameter of the PI controller for the proposed observer

List of Acronyms

BDFIG	Brushless doubly-fed induction generator
PW	Power winding
CW	Cower winding
DVC	Direct voltage control
MRAS	Model reference adaptive system
HFS	High-frequency signal
PMSMs	Permanent-magnet synchronous machines
IMs	Induction machines
DFIGs	Doubly-fed induction generators
PLL	Phase-locked-loop

1 Introduction

Recently, the adjustable drive application based on the brushless doubly-fed induction generator (BDFIG) has impressed a good interest for its reliable structure. The stator side of the promising BDFIG can be represented with two separated windings with

pole pairs different from each other to avoid the direct coupling [1]. The windings of generator are denoted as the side of power-winding (PW) and the other side of control-winding (CW). On the other side, the rotor side of the BDFIG has various configurations over the years. However, the type of wound-rotor is preferred in this study due to its high efficiency of using the rotor windings and the great reduction of the harmonics and leakage reactance [2].

The shaft generator in the ship applications which is driven by the main engine can achieve a great reduction of the consumed fuel and consequently attain the efficient operation [1]. Hence, the essential part in the ship has been represented in the role of shaft generator for generating electricity with a highly system efficiency and reliability.

Due to the high structural reliability of BDFIG, its superior behavior has been increased day-by-day for various applications such as the wind energy systems [3] and the ship power generation systems [4]. As a result, involving the BDFIG in the ship applications has achieved a great research area [1].

The connection mode of the ship power-generating systems is categorized into two states with both the grid and the isolated loads. In the mode of grid cone connection, the desired control purpose is to regulate the power flow in terms of the reactive/active power using different topologies such as the vector-control method [3, 5]. For the operating mode of stand-alone, the essential purpose of control is to investigate the load voltage regulation with the principles of direct voltage control (DVC) strategy.

Over the years, the literatures have handled many control topologies of the promising BDFIG [6–8]. These methodologies of control are dependent on the signal of mechanical position/speed to obtain the intended frame angle of the CW dq-axis quantities. Therefore, a mechanical encoder is needed to realize the speed/position signal which would present a drawback for the control system due to the requirements of maintenance, arranging the sensors and the high system cost. For increasing the reliability of control system and reducing the overall cost, a sensorless position/speed estimation method is required for a better behavior of the isolated system-based BDFIG [1, 8–12].

Many various sensorless schemes to detect the speed signal have been discussed in literatures with both principles of the model and signal-injection methods. The scheme of model reference adaptive system (MRAS) has assured a better dynamic behavior under both mid/high-speed operation [13, 14]. However, the sensorless MRAS observers have some accuracy defects under the low-speed operation and also its full dependence on the machine parameters.

In order to eliminate these issues, the injection methodologies of high-frequency signal (HFS) have been reported over the years for induction machine (IMs) and permanent-magnet synchronous machines (PMSMs) [15, 16]. However, the implementation of this method for IMs and PMSMs is fully dependent on the saliencies of the rotor side. In other words, the modulation between the injected HFS and the rotor saliencies produces a high-frequency current which can be processed to obtain the signal of generator position.

On the other hand, the application of sensorless control based on HFS injection approach for doubly-fed induction generators (DFIGs) has been outlined with a

different concept without the need for rotor saliences [17, 18]. In these systems, the rotor position can be realized from the processed current of high frequency resulted from the modulation between the accessible rotor and stator windings by injecting the HFS into either the rotor side or the stator side.

In this chapter, the application of sensorless observer based on the HFS injection approach is not handled and investigated for the promising BDFIG. Aided with the indirect relationship between the CW and PW sides of BDFIG through the modulation effect of mechanical position for the flux, the concept of sensorless strategies depending on the HFS injections approach can be implemented without any need for the rotor saliency information [19].

2 Structure and Modeling of BDFIG

2.1 Construction and Operation

The system configuration of the stand-alone BDFIG is given in Fig. 1 with the main engine as a prime mover. The BDFIG contains two separated stator windings, the PW with p_1 pair-pole and connected directly to the load, and the CW with p_2 pair-pole and connected to the load via a bi-directional converter. Furthermore, the wound-rotor configuration is the main distinguished structure for its high efficacy in comparison with other types of rotor design [2].

The speed formula of the promising BDFIG is given as [1]

$$\omega_{rm} = \frac{\omega_1 + \omega_2}{p_1 + p_2} \tag{1}$$

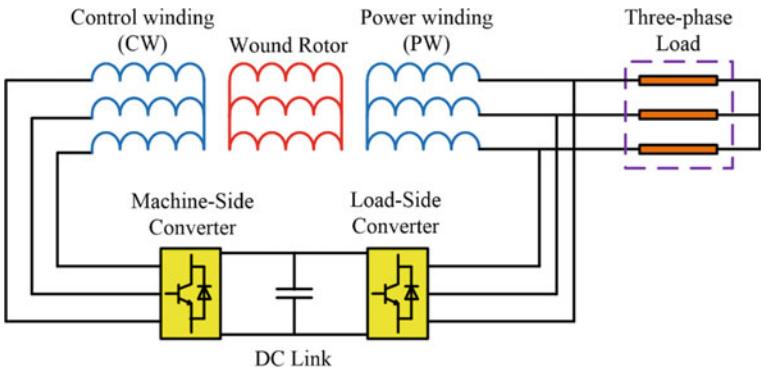

Fig. 1 System construction of the BDFIG based ship shaft system

where ω_1 and ω_2 represent the angular frequency of both the PW and CW, respectively.

The state of operation for BDFIGs can be explained as follows. The synchronous mode is for the operation under the natural speed, ω_N, at which ω_2 is equal to zero. Moreover, the sub-synchronous represents the operation of low speed (under the synchronous speed), and the super-synchronous refers to the high-speed operation (above its synchronous value). According to (1), the frequency of PW side can be controlled, with the changes of rotor speed, by varying the frequency of CW, ω_2 using the following expression

$$\omega_2 = (p_1 + p_2)\omega_{rm} - \omega_1 \tag{2}$$

2.2 DQ-axis Model of BDFIG

The dq-axis voltages, in the arbitrary frame ω_a, are given as

$$\left.\begin{aligned} u_{1_d} &= R_1 i_{1_d} + s\Psi_{1_d} - \omega_a \Psi_{1_q} \\ u_{1_q} &= R_1 i_{1_q} + s\Psi_{1_q} + \omega_a \Psi_{1_d} \\ u_{2_d} &= R_2 i_{2_d} + s\Psi_{2_d} - (\omega_a - (p_1 + p_2)\omega_{rm})\Psi_{2_q} \\ u_{2_q} &= R_2 i_{2_q} + s\Psi_{2_q} + (\omega_a - (p_1 + p_2)\omega_{rm})\Psi_{2_d} \\ 0 &= R_r i_{r_d} + s\Psi_{r_d} - (\omega_a - p_1\omega_{rm})\Psi_{r_q} \\ 0 &= R_r i_{r_q} + s\Psi_{r_q} + (\omega_a - p_1\omega_{rm})\Psi_{r_d} \end{aligned}\right\} \tag{3}$$

where s mentions the differential operator, d/dt. The dq-axis voltages of both PW and CW are expressed as u_{1dq} and u_{2dq}. In addition, the currents i_{1dq}, i_{2dq} and i_{rdq} are the dq-axis components of the PW, CW and rotor side. Moreover, Ψ_{1dq}, Ψ_{2dq} and Ψ_{rdq} are the flux linkages of the dq-axis for the PW, CW and rotor side. Also, R_1, R_2 and R_r are the resistances of the PW, CW and rotor side, respectively.

Moreover, the dq-axis flux linkages are represented as

$$\left.\begin{aligned} \Psi_{1_d} &= L_1 i_{1_d} + L_{1r} i_{r_d} \\ \Psi_{1_q} &= L_1 i_{1_q} + L_{1r} i_{r_q} \\ \Psi_{2_d} &= L_2 i_{2_d} + L_{2r} i_{r_d} \\ \Psi_{2_q} &= L_2 i_{2_q} + L_{2r} i_{r_q} \\ \Psi_{r_d} &= L_r i_{r_d} + L_{1r} i_{1_d} + L_{2r} i_{2_d} \\ \Psi_{r_q} &= L_r i_{r_q} + L_{1r} i_{1_q} + L_{2r} i_{2_q} \end{aligned}\right\} \tag{4}$$

where L_1, L_2 and L_r are the self-inductance of the PW, CW and rotor side. Furthermore, L_{1r} and L_{2r} are the inductance of coupling between the rotor side and both of the PW and CW, respectively.

3 Sensorless Control of BDFIGs with CW Reactive-Power MRAS Observer

3.1 Overall Voltage Control System Based on PW Field-Oriented Vector Control

Due to the efficient performance of the of the vector-control technique, the PW flux-oriented scheme is applied in this study for the sensorless voltage control target. Figure 2 gives the detailed relations of the machine phase axes under this orientation topology. In this scheme, the flux of PW in the d-axis is directed to the overall vector of PW flux and hence, the flux component in the q-axis is set to be equals zero. In Fig. 3, the complete system of the proposed sensorless voltage control based on CW reactive-power MRAS is presented.

Aided with the actual quantities of the PW voltages and currents, the associated components in *dq*-axis can be obtained. From which and for detecting the desired frame angle of the intended orientation scheme θ_1, the *dq*-axis flux linkages of PW can be attained, with a complete elimination for the integration process, as

$$\left.\begin{aligned} \Psi_{1_d} &= \left(u_{1_q} - R_1 i_{1_q}\right)/\omega_1 \\ \Psi_{1_q} &= \left(-u_{1_d} + R_1 i_{1_d}\right)/\omega_1 \end{aligned}\right\} \tag{5}$$

In the obtained procedure, the vector of flux for PW side adjusts its *d*-axis component, Ψ_{1d}, for attaining the reference voltage set for PW terminals ($\Psi_1{}^* = U_1{}^*/\omega_1{}^*$),

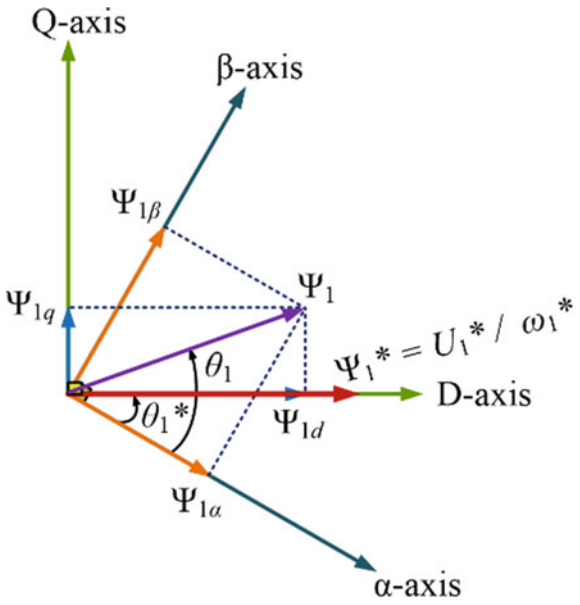

Fig. 2 BDFIG phase-axis relationship for the voltage control method

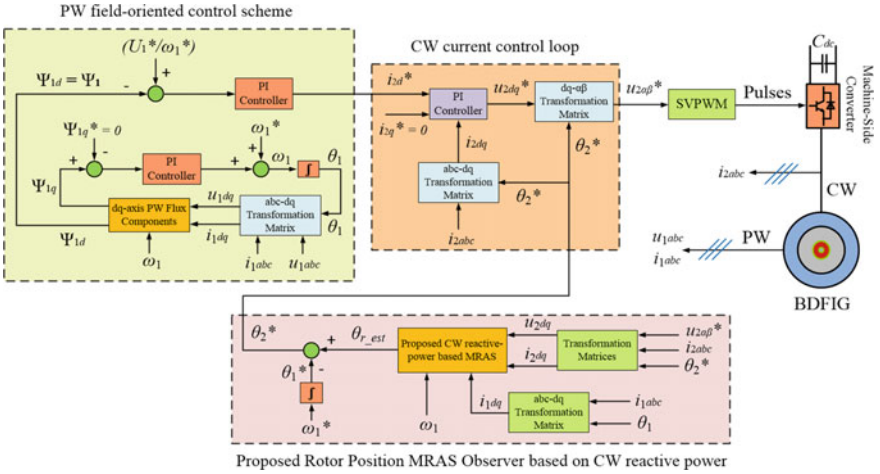

Fig. 3 Block diagram of the proposed sensorless DVC system for the adopted BDFIG system

as illustrated in Fig. 3. By adjusting the CW *d*-axis current, $i_{2d}{}^{*}$ through a PI controller, the amplitude of PW voltage can be maintained at its desired set value. Furthermore, the CW *q*-axis current $i_{2q}{}^{*}$ is directed to be equal to zero through the current loop for a better performance, as given in Fig. 3.

Finally, the current angle of CW side can be realized with the aid of the detected rotor position, θ_{r_est} (given from the proposed new observer-based CW reactive-power MRAS methodology) and the angle, $\theta_1{}^{*}$ (obtained by integrating the desired frequency of PW side). From which, the required pulses of the machine-side converter can be attained.

3.2 *Design Procedure of the Proposed MRAS Method-Based CW Reactive Power*

Generally, the principle of the MRAS observer is based on the two models of adaptive and reference with the suggested functional quantity. Then, the error between the two models is controlled using a PI adaptation to attain the estimated position signal. In this chapter, a proposed MRAS method is implemented with a new functional quantity of the CW reactive power for BDFIGs [14].

The computation of the proposed new MRAS observer based on CW reactive power as a functional quantity, as shown in Fig. 4, can be summarized as follows.

The instantaneous reactive power of BDFIG CW side is given by

$$Q_2 = \frac{3}{2}\left(u_{2_q} i_{2_d} - u_{2_d} i_{2_q}\right) \tag{6}$$

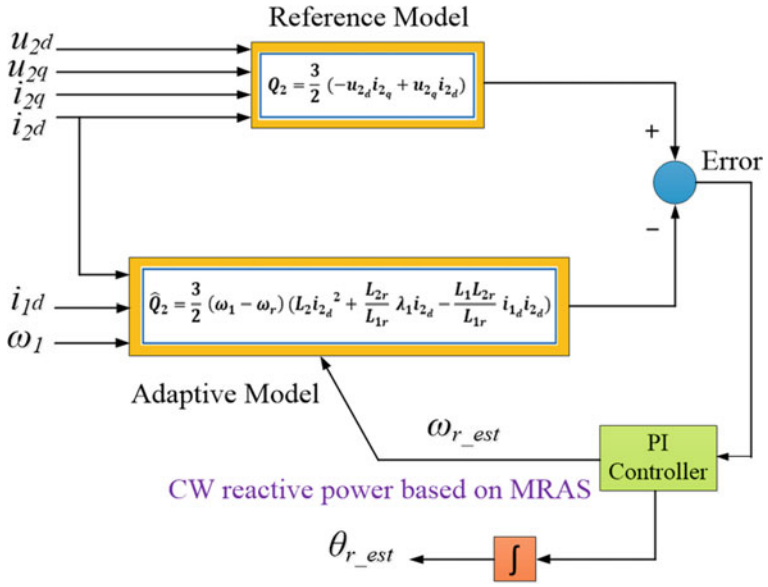

Fig. 4 Main block diagram of the adopted CW reactive-power MRAS observer

The relation in (6) can be rewritten, aided with the *dq*-axis expressions in (3) and (4), as

$$\hat{Q}_2 = \frac{3}{2}\left(R_2 i_{2_q} i_{2_d} + \frac{d\Psi_{2_q}}{dt} i_{2_d} + (\omega_1 - \omega_r)\Psi_{2_d} i_{2_d}\right) - \frac{3}{2}\left(R_2 i_{2_d} i_{2_q} + \frac{d\Psi_{2_d}}{dt} i_{2_q} - (\omega_1 - \omega_r)\Psi_{2_q} i_{2_q}\right) \tag{7}$$

From which,

$$\hat{Q}_2 = \frac{3}{2}(\omega_1 - \omega_r)\left(L_2\left(i_{2_d}^2 + i_{2_q}^2\right) + L_{2r}\left(i_{r_d} i_{2_d} + i_{r_q} i_{2_q}\right)\right) \tag{8}$$

With the principle of the orientation scheme for PW side, the rotor *dq*-axis currents are obtained as:

The *q*-axis quantity of the rotor current is given as

$$\Psi_{1_q} = L_1 i_{1_q} + L_{1r} i_{r_q} = 0 \tag{9}$$

$$i_{r_q} = -\frac{L_1}{L_{1r}} i_{1_q} \tag{10}$$

In addition, the associated d-axis quantity of the rotor current is realized as

$$\Psi_{1_d} = L_1 i_{1_d} + L_{1r} i_{r_d} = \Psi_1 \tag{11}$$

$$i_{r_d} = \frac{\Psi_1 - L_1 i_{1_d}}{L_{1r}} \tag{12}$$

Using the current-control loop of CW side ($i_{2q} = 0$) and aided with (10) and (12), the formula in (8) is given by

$$\hat{Q}_2 = \frac{3}{2}(\omega_1 - \omega_r)\left(L_2 i_{2_d}^2 + \frac{L_{2r}}{L_{1r}}\Psi_1 i_{2_d} - \frac{L_1 L_{2r}}{L_{1r}} i_{1_d} i_{2_d}\right) \tag{13}$$

It is well known that from the principles of MRAS topology, the adaptive model is the formula which depends on the speed signal of the machine and vice versa for the reference model. Therefore, the relation in (6) can be realized as the reference model and the expression in (13) represents the adaptive model of the proposed CW reactive-power MRAS observer.

3.3 Stability Analysis of the Proposed MRAS Observer

It is an important key for the proposed design procedure of the adopted new MRAS observer to fully satisfy the stability issue. For this aim, the practical synthesis technique for MRAS structures which is based on the concept of Landau hyperstability [20] is used in this paper. To guarantee this method, a non-linear time-varying feedback model is obtained aided with the proposed MRAS model as shown in Fig. 5. Landau hyperstability is satisfied when the feed-forward path is strictly positive real, and the time variant feedback path fulfills the Popov's integral inequality criteria. In

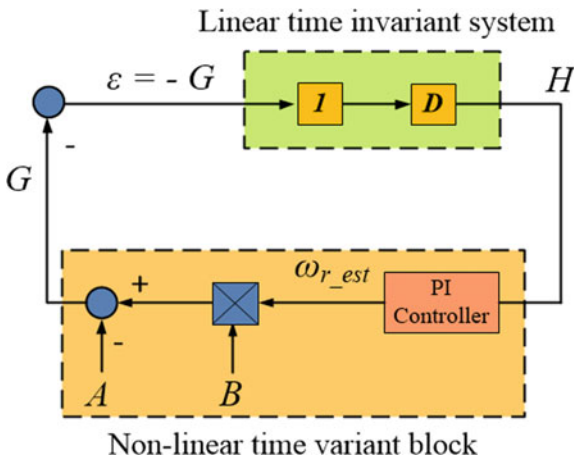

Fig. 5 Proposed MRAS system with the time-varying feedback model

order to make feed-forward path a strictly positive real, the error compensation block 'D' is realized as shown in Fig. 5. In this section, the stability issue of the proposed MRAS observer for sensorless DVC is completely studied and confirmed as follows.

By considering the error equation as

$$\varepsilon = Q_2 - \hat{Q}_2 \tag{14}$$

From which and aided with (6) and (13), the following can be expressed as

$$\begin{aligned}\varepsilon = &\frac{3}{2}\left(u_{2_q} i_{2_d} - u_{2_d} i_{2_q}\right) \\ &- \frac{3}{2}(\omega_1 - \omega_r)\left(L_2 i_{2_d}^2 + \frac{L_{2r}}{L_{1r}}\Psi_1 i_{2_d} - \frac{L_1 L_{2r}}{L_{1r}} i_{1_d} i_{2_d}\right)\end{aligned} \tag{15}$$

Aided with Fig. 5, the proposed procedure of MRAS observer based on CW reactive power in Fig. 4 can be represented as a time variant feedback path. From which and aided with the error expression in (15), the following model for the adopted feedback path can be expressed as

$$\begin{cases} G = -A + B\omega_{r_{est}}(\varepsilon, t) = f(t) \\ \varepsilon = -G \end{cases} \tag{16}$$

The expression for A and B can be represented, aided with (15), as

$$\begin{aligned} A &= \frac{3}{2}\left(u_{2_q} i_{2_d} - u_{2_d} i_{2_q}\right) + \frac{3}{2}\omega_1\left(i_{2_d}^2 + \frac{L_{2r}}{L_{1r}}\Psi_1 i_{2_d} - \frac{L_1 L_{2r}}{L_{1r}} i_{1_d} i_{2_d}\right) \\ B &= -\frac{3}{2}\left(L_2 i_{2_d}^2 + \frac{L_{2r}}{L_{1r}}\Psi_1 i_{2_d} - \frac{L_1 L_{2r}}{L_{1r}} i_{1_d} i_{2_d}\right) \end{aligned}$$

Furthermore, the estimated speed is obtain
ed as

$$\omega_{r_{est}}(\varepsilon, t) = \left(k_{p_{\mathrm{MRAS}}} + \frac{k_{i_{\mathrm{MRAS}}}}{s}\right) H \tag{17}$$

where, $k_{p_{\mathrm{MRAS}}}$ and $k_{i_{\mathrm{MRAS}}}$ are the control parameters of the adopted PI controller for the proposed observer which can be defined in this paper and tuned based on Ref. [21].

Aided with (16) and (17), the following expression can be obtained as

$$\begin{cases} \dot{f}(t) = B k_{i_{\mathrm{MRAS}}} H \\ H = \dfrac{\dot{f}(t)}{B k_{i_{\mathrm{MRAS}}}} \end{cases} \tag{18}$$

It can be shown that the feed-forward path is strictly positive real, whose proof is omitted here. Hence, and according to the adopted Landau hyperstability concept, the stability confirmation for the proposed MRAS observer can be satisfied when the time variant feedback path fulfills the Popov's integral inequality criteria.

The Popov's criterion for stability realization of the adopted sensorless system requires, aided with Fig. 5, that

$$\int_0^{t_1} H^T G \mathrm{d}t \geq -\gamma_o^2, \quad \forall t_1 > 0 \tag{19}$$

where, H and G are the input and output of the non-linear time variant block, respectively, as illustrated in Fig. 5, and γ_0^2 is a positive real constant.

By using (16) and (18), the expression in (19) is considered as

$$\int_0^{t_1} \frac{\dot{f}(t)}{B k_{i_{\mathrm{MRAS}}}} f(t) \mathrm{d}t \geq -\gamma_o^2 \tag{20}$$

Aided with (20), the obtained inequality (19) resembles the following inequality expression [29]

$$\int_0^{t_1} \dot{f}_1(t) k f_2(t) \mathrm{d}t \geq -\frac{k}{2} f_1^2(0), \quad \forall k > 0 \tag{21}$$

The derived inequality (19) follows the functional inequality (21) for Popov's criterion method. Therefore, the obtained analysis in this section confirms that the proposed MRAS using the CW reactive power as a functional quantity is stable.

3.4 Simulation Results

In this section, the simulation analysis is carried out to ensure the functionality of the proposed sensorless control strategy for DVC based on the presented new rotor position observer. The obtained results are provided aided with a 30-kVA wound-rotor BDFIG which has detailed complete parameters as illustrated in Table 1, [1]. Moreover, the intended set values of the PW voltage magnitude and frequency are adjusted at 311 V and 50 Hz, respectively.

3.4.1 Performance Test

This subsection aims at confirming the capability of the proposed new observer for sensorless DVC of the adopted BDFIG in the stand-alone ship shaft applications

Table 1 Main parameters of BDFIG in experiments [1]

Parameter	Value
Capacity	30 kVA
Range of speed	600–1200 rpm
p_1, p_2	1, 3
PW rated voltage and current	380 V, 45 A
CW voltage range	0–350 V
CW current range	0–40 A
R_1, R_2, R_r	0.4034 Ω, 0.2680 Ω, 0.3339 Ω
L_1, L_2, L_r	0.4749 H, 0.03216 H, 0.2252 H
L_{1r}, L_{2r}	0.3069 H, 0.02584 H

under both speed and load variations. During the first operating condition, the load is kept constant and the generator speed is varied from its synchronous speed to the low speed (sub-synchronous mode) and then returned to the synchronous mode and finally increased to the high speed (super-synchronous mode). The second operating condition is then applied to study the dynamic behavior of the adopted BDFIG while the load is changed under a constant speed.

The operation of the adopted BDFIG is started under the synchronous speed with 750 rpm and then decreased to the low-speed condition (sub-synchronous mode) with 600 rpm at $t = 1$ s while the applied resistive load is 11.6 kW as shown in Fig. 6. Finally, the generator speed accelerates to the synchronous mode at $t = 2$

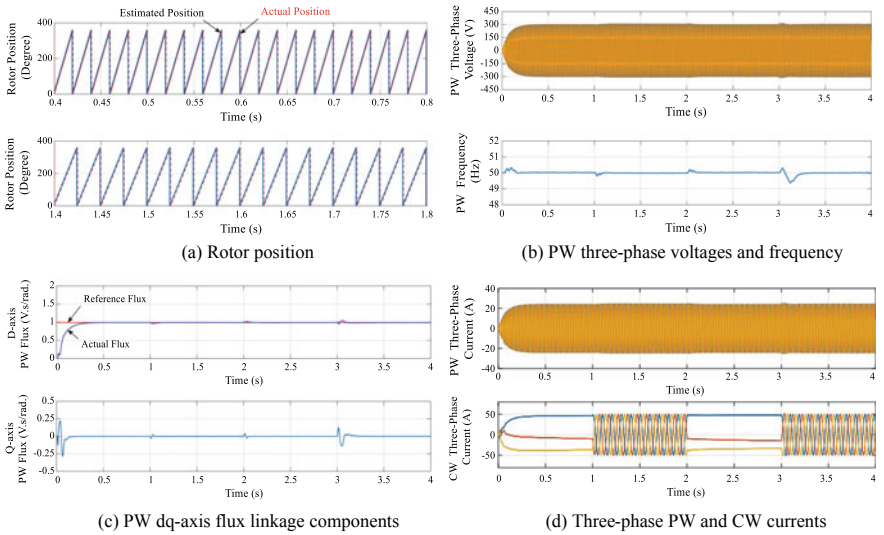

(a) Rotor position

(b) PW three-phase voltages and frequency

(c) PW dq-axis flux linkage components

(d) Three-phase PW and CW currents

Fig. 6 Performance test of the proposed sensorless control strategy based on CW reactive-power MRAS observer for DVC

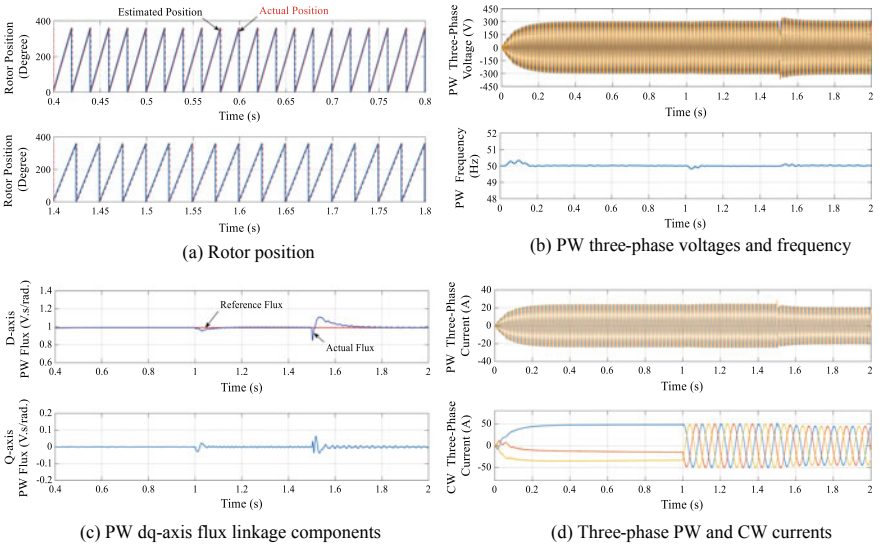

Fig. 7 The proposed sensorless system based on CW reactive-power MRAS observer for DVC under load change to be reduced from 11.6 to 9.7 kW

s with 750 rpm and then increased to the high-speed condition (super-synchronous mode) with 900 rpm at $t = 3$ s while the load is the same. On the other hand, Fig. 7 illustrates the dynamic performance of the proposed sensorless control system under load change condition to be decreased from 11.6 to 9.7 kW with the same speed of 600 rpm at $t = 1.5$ s.

It is observed from Figs. 6b and 7b that the PW voltage (in terms of magnitude and frequency) successfully tracks the intended quantities for DVC purpose ($U_1{}^* = 311$ V and $f_1{}^* = 50$ Hz).

In addition, it is obvious from Figs. 6c and 7c that the PW *dq*-axis flux linkage is kept constant to attain the desired quantities [$(\Psi_{1d}{}^* = \Psi_1{}^* = U_1{}^*/\omega_1{}^*)$ and $(\Psi_{1q}{}^* = 0)$] adjusted for the intended orientation of the PW flux.

Moreover, the results verify that the estimated rotor position is in a good accordance with the actual value as shown in Figs. 6a and 7a. This ensures the capability of the proposed MRAS observer based on CW reactive power to effectively estimate the rotor position of the adopted BDFIG.

3.4.2 Robustness Against Parameter Uncertainty

It can be observed from (13) that the proposed rotor position observer is dependent in its calculations on the parameters of the adopted BDFIG. Therefore, the BDFIG parameter sensitivity is more important to confirm the robustness of the proposed new

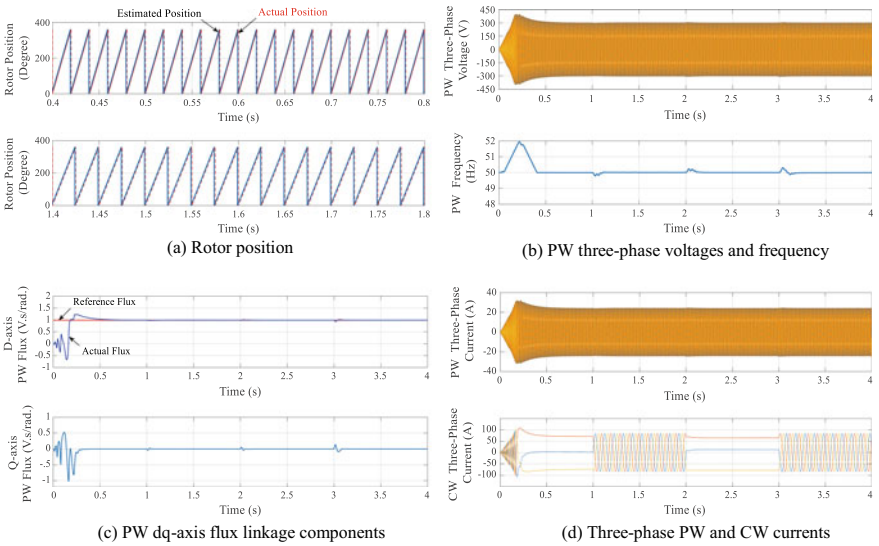

(a) Rotor position

(b) PW three-phase voltages and frequency

(c) PW dq-axis flux linkage components

(d) Three-phase PW and CW currents

Fig. 8 Proposed sensorless system based on CW reactive-power MRAS observer for DVC under 10% reduction in the machine inductances (L_1, L_2, L_{1r}, L_{2r})

rotor position observer and its effectiveness for sensorless DVC of the stand-alone ship shaft BDFIG under parameter uncertainty issue.

In this subsection, the variation effect of the adopted machine inductances (L_1, L_2, L_{1r}, L_{2r}) on the proposed MRAS observer is checked by assuming a change of 10% reduction in this parameter which in turn means the same change percentage in the value of each of all these inductances as shown in Fig. 8.

It can be concluded from Figs. 6, 7 and 8 that the efficacy of the suggested observer and its capability for sensorless DVC strategy is not affected by any change in the adopted generator inductances and also the CW resistance for the whole allowable limits of winding temperature.

This confirms and proves the functionality and robustness of the new rotor position MRAS observer based on CW reactive power for sensorless DVC of the adopted ship shaft stand-alone BDFIG system. All the given results confirm the simplicity and capability of the proposed sensorless control system to track the desired values of the PW voltage for the promising BDFIG in stand-alone applications.

3.5 Experimental Analysis

To validate the functionality of the proposed control strategy, the progress toward the experimental work is completely outlined in this section. In addition, comprehensive results of experiments to investigate the proposed sensorless control strategy are also presented which ensures the effectiveness of the suggested rotor position observer.

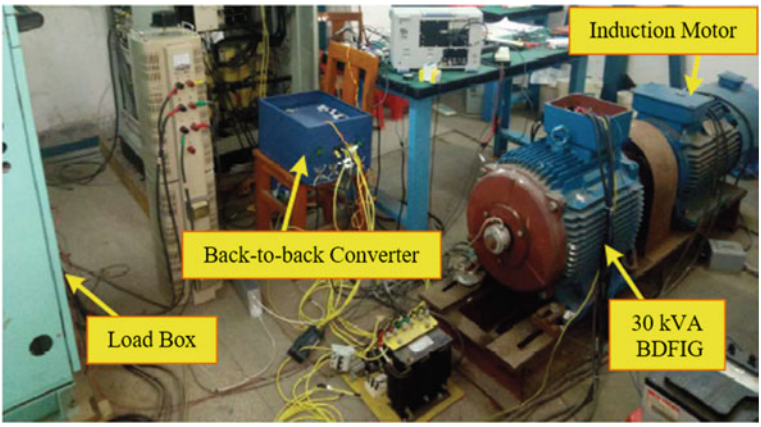

Fig. 9 A photograph of the test platform

For this purpose, the preparation of the BDFIG setup and the control system is shown in Fig. 9.

In Table 1, the detailed parameters are listed for the BDFIG prototype. In addition, an induction motor with a power rating of 37 kW is used to drive the BDFIG and fed from a Siemens MM430 inverter. Moreover, all voltage and current signals required for implementing the proposed sensorless control system are provided by LEM LV 100 and LEM LT 208-S7/SP1 sensors, respectively. As shown in Fig. 9, the back-to-back converter comprises of two main converters, the machine-side converter (MSC) and the load-side converter (LSC). The MSC provides excitation current to the control winding with variable frequency. Moreover, to regulate the dc-link voltage and to provide a bi-directional operation of CW side, the LSC with a suitable filter is energized.

3.5.1 Performance Test

In this subsection, experimental results are introduced to ensure the effectiveness of the proposed rotor position observer under the start-up operation of the stand-alone BDFIG. In addition, the capability of the proposed observer for sensorless DVC is also confirmed under the whole operation period of the presented generating system through starting, speed variation and load change conditions. In the experiments, the desired PW voltage in terms of the rms value and frequency is 150 V and 50 Hz, respectively.

Firstly, the BDFIG is started at a mechanical rotor speed of 600 rpm and with a balanced three-phase resistive load of 25 Ω per phase. Then, at $t = 14$ s, the generator speed is increased to 700 rpm until $t = 28$ s at which the speed is again reduced to 600 rpm. On the other hand, in order to confirm the effect of load change, the generator is started at 600 rpm with the balanced three-phase resistive load and then the balanced

load is suddenly increased to its double power in each phase at $t = 4.95$ s. Figs. 10 and 11 show the experimental results with the proposed rotor position observer under the start-up operation with the dynamic and steady-state behavior of the estimated rotor position, the speed variation and load change conditions, respectively.

It is observed from Figs. 10 and 11 that the PW voltage tracks successfully the desired values for DVC under the whole operation period. In addition, the results verify that the estimated rotor position is in a good accordance with the actual value as shown in Figs. 10a–d and 11a for both the starting condition speed variation state and load change condition, respectively. This ensures the effectiveness of the proposed new rotor position observer for sensorless DVC of the adopted stand-alone BDFIG system.

Moreover, Fig. 10f illustrates that the q-axis CW current tracks the desired value ($i_{2q}{}^{*} = 0$) to attain the intended current-orientation of the CW side which confirms the capability and efficacy of the presented CW current controller.

Furthermore, more additional experimental results to consider the performance of the proposed observer under the speed variation condition with the natural speed, and the effect of increasing the load change situation, according to the rated conditions, on the adopted estimation procedure are illustrated in Figs. 12 and 13, respectively. The speed change condition considering the operation under natural speed, as shown in Fig. 12, confirms the efficacy of the proposed observer to efficiently estimate the rotor position of the BDFIG under different situations of speed variations. In addition, it is obvious from Fig. 13 that the presented sensorless control system is not affected by the load changes with increasing the load condition to be doubled of the load case in Fig. 11 under the speed operation of 600 rpm. This proves the functionality of the proposed rotor position observer based on CW reactive-power MRAS for sensorless DVC of BDFIGs.

3.5.2 Robustness Against Parameter Uncertainty

To investigate the efficacy of the suggested position observer against the BDFIG parameter change, e.g., variation of inductances, some of the experimental results are introduced as shown in Fig. 14 including the estimation error of the proposed position observer. Furthermore, the CW reactive-power observation error, $\varepsilon = Q_2 - \hat{Q}_2$, has been also considered as shown in Fig. 14c.

In practical experimental operation, the actual parameters of BDFIG are not easy to be changed because of the generator structure. Hence, to verify the robustness of the proposed rotor position observer under the case of parameter variation, the experiments are carried out with 130% uncertainties of the whole parameters that affect the calculations of the suggested algorithm for the proposed new observer (13) by modifying the generator parameters in the controller instead of the actual generator parameters. In this paper, a change of 30% increasing in the generator parameters considered in (13) is carried out in the experiments as illustrated in Fig. 14.

It is obvious from Fig. 14 that the maximum rotor position error is around 1.11° and also the maximum observation error of CW reactive power using the presented

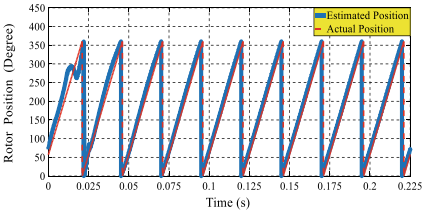

(a) Rotor position under the start-up stage

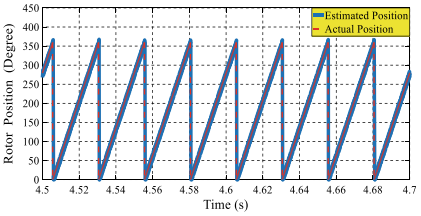

(b) Rotor position at 600 rpm

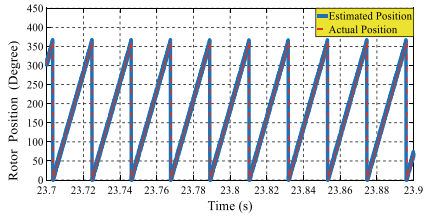

(c) Rotor position at 700 rpm

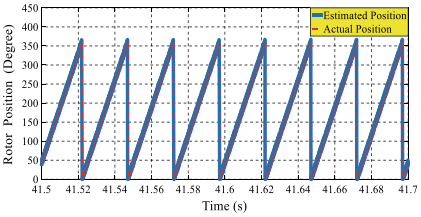

(d) Rotor position at 600 rpm

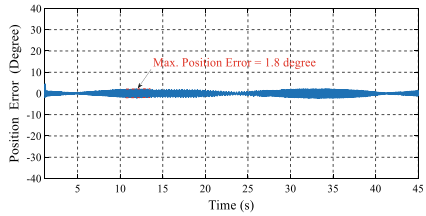

(e) Rotor position error

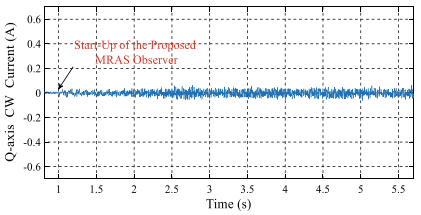

(f) Q-axis CW current

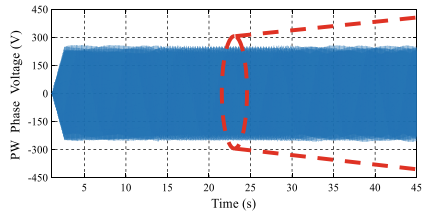

(g) PW phase voltage

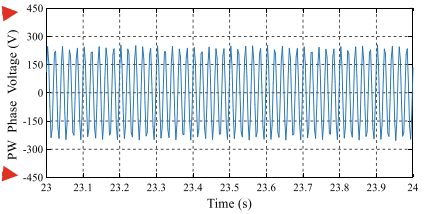

(h) Extended view of (g)

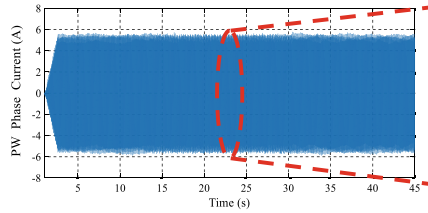

(i) PW phase current

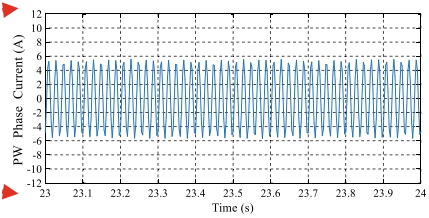

(j) Extended view of (i)

Fig. 10 Experimental results under the start-up operation and speed variation condition (600 rpm–700 rpm–600 rpm)

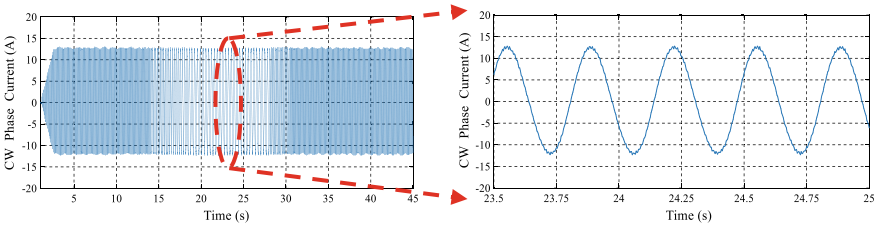

(k) CW phase current (l) Extended view of (k) at 700 rpm

Fig. 10 (continued)

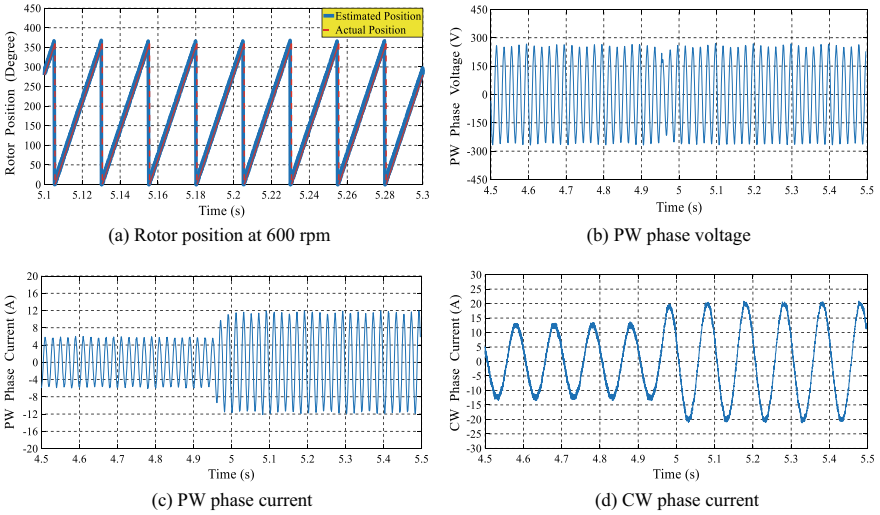

(a) Rotor position at 600 rpm (b) PW phase voltage

(c) PW phase current (d) CW phase current

Fig. 11 Experimental results under the load change condition (100% increasing)

MRAS observer is approximately 0.025 p.u as shown in Fig. 14b, c, respectively. This ensures that the performance of the proposed position observer and its capability for sensorless DVC is not affected by the uncertainty issue of the adopted BDFIG parameter, e.g., the generator inductances. This confirms and proves the functionality and robustness of the proposed rotor position observer for sensorless DVC of the stand-alone BDFIG. All presented experimental results ensure the functionality of the proposed sensorless DVC strategy based a suggested position observer for the promising BDFIG in stand-alone applications.

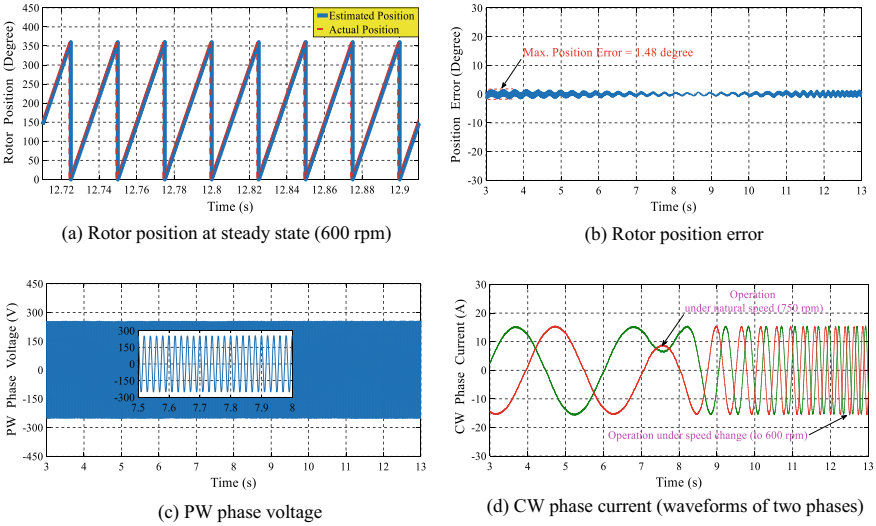

(a) Rotor position at steady state (600 rpm)

(b) Rotor position error

(c) PW phase voltage

(d) CW phase current (waveforms of two phases)

Fig. 12 Experimental results considering the natural speed operation

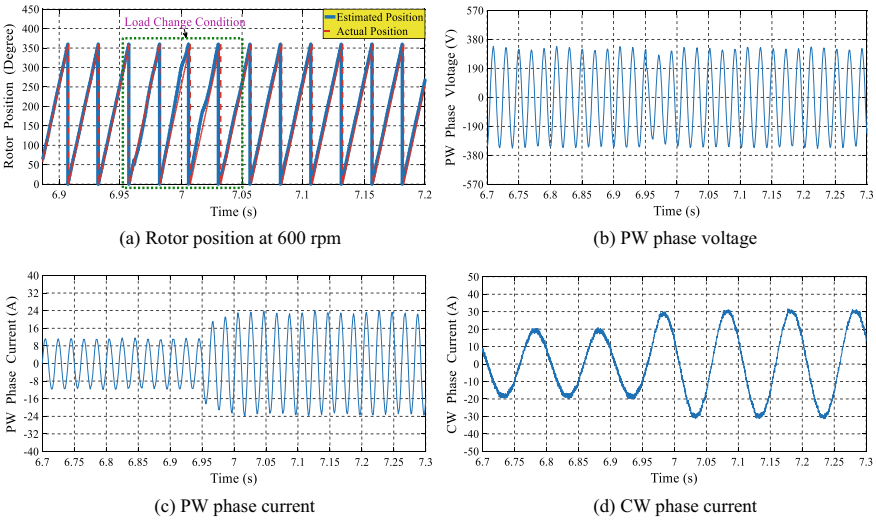

(a) Rotor position at 600 rpm

(b) PW phase voltage

(c) PW phase current

(d) CW phase current

Fig. 13 Experimental results with increasing the load change situation according to the rated conditions

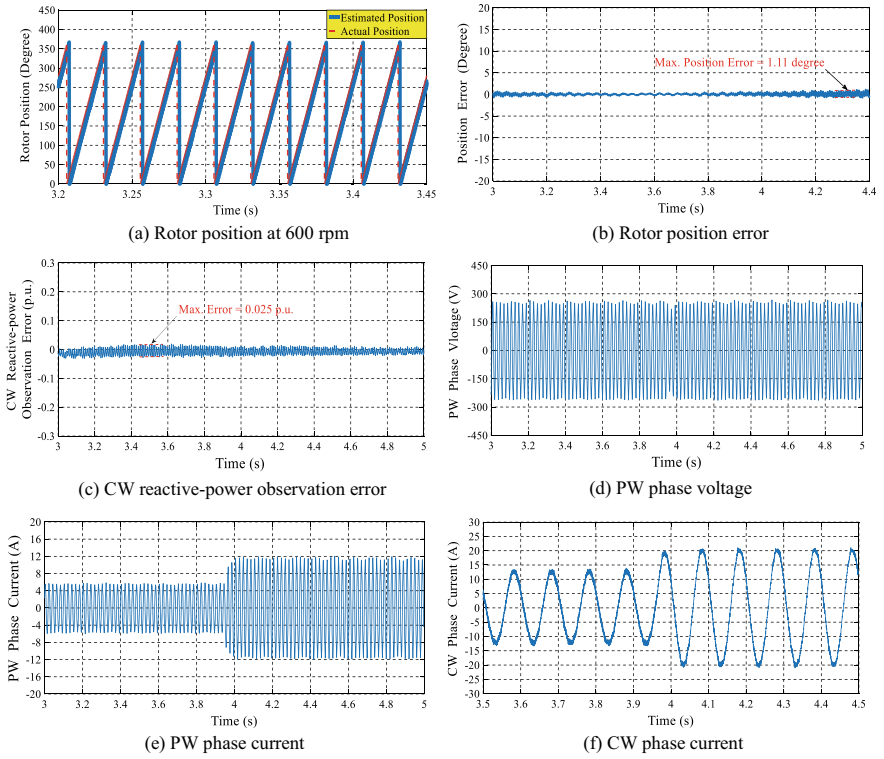

(a) Rotor position at 600 rpm

(b) Rotor position error

(c) CW reactive-power observation error

(d) PW phase voltage

(e) PW phase current

(f) CW phase current

Fig. 14 Experimental results under the case of BDFIG parameter change (130% uncertainty)

4 A New Rotor Position Observer of BDFIGs Based on Control-Winding High-Frequency Signal Injection

4.1 High-Frequency Model of BDFIG

Aided with the dynamic model of BDFIG in (3) and (4), in the PW frame ω_1, if the CW side of BDFIG is fed with HFS and considering an injected signal with a higher frequency than the generator speed (i.e., $\omega_{hf} \succ \omega_r$, where $\omega_r = (P_1 + P_2)\omega_{rm}$), the terms in (3) related to the rotor speed can be approximately neglected.

From which, the high-frequency dq model of BDFIG in the stationary frame of PW side can be represented as illustrated in Fig. 15 aided with the equivalent T-type circuit of BDFIG [8, 19] and expressed as

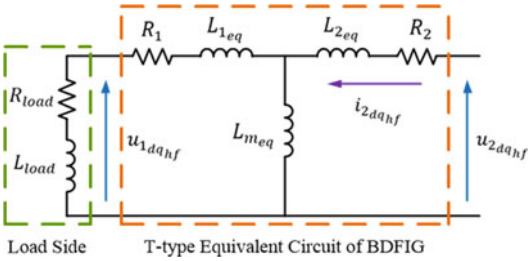

Fig. 15 High-frequency model of BDFIG based T-type equivalent circuit

$$\left.\begin{aligned} u_{1_d}^{st} &= R_1 i_{1_d}^{st} + \left(L_{1_{eq}} + L_{m_{eq}}\right) s i_{1_d}^{st} + \left(L_{m_{eq}}\right) s i_{2_d}^{st} \\ u_{1_q}^{st} &= R_1 i_{1_q}^{st} + \left(L_{1_{eq}} + L_{m_{eq}}\right) s i_{1_q}^{st} + \left(L_{m_{eq}}\right) s i_{2_q}^{st} \\ u_{2_d}^{st} &= R_2 i_{2_d}^{st} + \left(L_{2_{eq}} + L_{m_{eq}}\right) s i_{2_d}^{st} + \left(L_{m_{eq}}\right) s i_{1_d}^{st} \\ u_{2_q}^{st} &= R_2 i_{2_q}^{st} + \left(L_{2_{eq}} + L_{m_{eq}}\right) s i_{2_q}^{st} + \left(L_{m_{eq}}\right) s i_{1_q}^{st} \end{aligned}\right\} \tag{22}$$

where

$$L_{1_{eq}} = L_1 - \frac{\left(L_{1r}^2 + L_{1r} L_{2r}\right)}{L_r}, L_{m_{eq}} = \frac{L_{1r} L_{2r}}{L_r}$$
$$L_{2_{eq}} = L_2 - \frac{\left(L_{2r}^2 + L_{1r} L_{2r}\right)}{L_r}$$

4.2 Design of the Proposed Rotor Position Observer Based CW High-Frequency Signal Injection

As a result of the indirect relation between the PW and CW sides of BDFIG through the flux modulation by the rotor position, the concept of sensorless control strategies based on the HFS injections approach can be implemented without any need for the rotor saliency information. In this paper, a predefined HFS is injected into the CW side while the obtained induced signal detected from the PW side will observe the rotor position information. Different types of the injected HFS have been reported in the literatures [15–18]. Among these types, the rotating signal is preferred for its simplicity which will be investigated in this study as follows.

The injected CW high-frequency signal can be given as

$$u_{2_{dqhf}} = U_{2_{hf}} \mathrm{e}^{j\omega_{hf} t} \tag{23}$$

where ω_{hf} and $U_{2_{hf}}$ define the frequency and magnitude of the injected HFS, respectively.

Aided with the concept that the excitation of fundamental frequency and the rotor speed is relatively changed in a slowly manner with respect to the frequency of the injected HFS, therefore the steady-state operation of BDFIG can be assumed and then the resulted high-frequency CW current can be expressed as in (24) with the equivalent high-frequency CW impedance, as given in (25) and from which, the induced high-frequency PW voltage can be realized as in (26).

$$i_{2_{dqhf}} = \frac{U_{2_{hf}}}{\left|Z_{2_{hf}}\right|} e^{j\left(\omega_{hf} t - \varphi_{Z_{2hf}}\right)} \tag{24}$$

$$Z_{2_{hf}} = \left(R_2 + j\omega_{hf} L_{2_{eq}}\right) + Z_E = \left|Z_{2_{hf}}\right| \angle \varphi_{Z_{2hf}} \tag{25}$$

where

$$Z_E = \frac{j\left(\omega_{hf} \pm \omega_r\right) L_{m_{eq}} \left[\left(R_1 + R_{\text{load}}\right) + j\left(\omega_{hf} \pm \omega_r\right)\left(L_{1_{eq}} + L_{\text{load}}\right)\right]}{\left(R_1 + R_{\text{load}}\right) + j\left(\omega_{hf} \pm \omega_r\right)\left(L_{1_{eq}} + L_{\text{load}} + L_{m_{eq}}\right)}$$

Then,

$$u_{1_{dqhf}} = \frac{U_{2_{hf}}}{\left|Z_{2_{hf}}\right|} \left[R_{\text{load}} + j\left(\omega_{hf} \pm \omega_r\right) L_{\text{load}}\right] Z_M e^{j\left(\omega_{hf} t \pm \theta_r - \varphi_{Z_{2_{hf}}}\right)} \tag{26}$$

where

$$Z_M = \frac{j\left(\omega_{hf} \pm \omega_r\right) L_{m_{eq}}}{\left(R_1 + R_{\text{load}}\right) + j\left(\omega_{hf} \pm \omega_r\right)\left(L_{1_{eq}} + L_{\text{load}} + L_{m_{eq}}\right)}$$

With the assumption that $R_{\text{load}} < \left(\omega_{hf} \pm \omega_r\right) L_{\text{load}}$ and $\left(R_1 + R_{\text{load}}\right) < \left(\omega_{hf} \pm \omega_r\right)\left(L_{1_{eq}} + L_{\text{load}} + L_{m_{eq}}\right)$, due to the high level of ω_{hf}, the induced voltage of PW side with the high frequency is rewritten as

$$u_{1_{dqhf}} = \frac{U_{2_{hf}}}{\left|Z_{2_{hf}}\right|} \left(\omega_{hf} \pm \omega_r\right) \times L_{\text{load}} \frac{L_{m_{eq}}}{\left(L_{1_{eq}} + L_{\text{load}} + L_{m_{eq}}\right)} e^{j\left(\omega_{hf} t \pm \theta_r - \varphi_{Z_{2_{hf}}} + \frac{\pi}{2}\right)} \tag{27}$$

It is noticed from (24) and (27) that the angle of phase with both the resulted current of CW side with the high frequency, $i_{2_{dqhf}}$ and the induced voltage of PW side with the high frequency, $u_{1_{dqhf}}$ is determined by $\left(\frac{\pi}{2} \pm \theta_r\right)$. Therefore, the desired position of rotor side, $\theta_{r_{est}}$ is detected with the aid of these two quantities.

The main conceptual diagram of the new position observer based on the injection approach using CW-HFS is illustrated in Fig. 16. Aided with measured CW current and PW voltage quantities, the high-frequency components of the CW current, $\left(i^{hf}_{2_{dqhf}}\right)$ as given in (28), and the corresponding PW voltage, $\left(u^{hf}_{1_{dqhf}}\right)$ as expressed in (29), can be given after a filtering process (band-rejection filters), by removing the

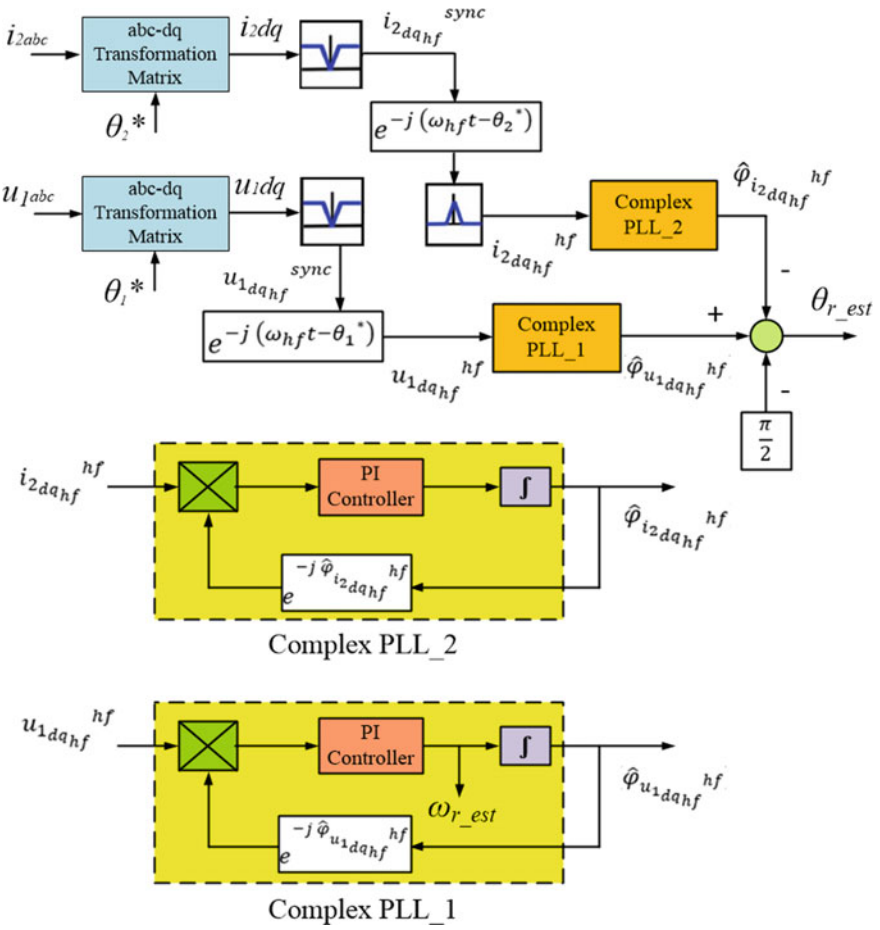

Fig. 16 Conceptual diagram of the novel position observer based on the injection approach using CW-HFS [19]

fundamental components, as shown in Fig. 16.

$$i_{2_{dqhf}}^{hf} = \frac{U_{2_{hf}}}{\left|Z_{2_{hf}}\right|} e^{j\left(-\varphi_{Z_{2_{hf}}}\right)} \tag{28}$$

$$u_{1_{dqhf}}^{hf} = \frac{U_{2_{hf}}}{\left|Z_{2_{hf}}\right|}\left(\omega_{hf} \pm \omega_r\right) \times L_{\text{load}} \frac{L_{m_{eq}}}{\left(L_{1_{eq}} + L_{\text{load}} + L_{m_{eq}}\right)} e^{j\left(\pm\theta_r - \varphi_{Z_{2_{hf}}} + \frac{\pi}{2}\right)} \tag{29}$$

Then, the resulted high-frequency current and voltage quantities are rotated to its corresponding synchronous frame of the HFS. From which, the error signal of a complex phase-locked-loop (PLL) can be determined using (28) for the current of CW and (29) for the voltage of PW.

Then, the regulation of the resulted error is realized aided with a PI-controller to attain the estimated phase angle of both the CW current, $\left(\hat{\varphi}^{hf}_{i_{2_{dqhf}}}\right)$ and the corresponding PW voltage, $\left(\hat{\varphi}^{hf}_{u_{1_{dqhf}}}\right)$ as illustrated in Fig. 16. In this paper, the estimated rotor speed in electrical quantity, $\omega_{r_{est}}$ is directed to the PI-controller output of the complex PLL_1 for the PW voltage, $\left(\hat{\omega}^{hf}_{u_{1_{dqhf}}}\right)$, as shown in Fig. 16.

The main defects of the presented sensorless methods based HFS injection approach reported in the literatures [17, 18] for ac machines and for DFIGs are the saturation effects and the requirements of the high-frequency impedance phase angle, $\varphi_{Z_{2hf}}$ and the equivalent of the load impedance, respectively. These issues are completely eliminated in this study with the suggested position observer based on the injection approach using CW-HFS.

4.3 Sensorless Voltage Control Topology with the Proposed Novel Position Observer

The essential control target for the stand-alone BDFIGs is to effectively regulate the load voltage with the principles of direct voltage control (DVC) scheme including a sensorless position detection procedure for a high performance [8, 19]. The main structure of the proposed control system for voltage regulation of BDFIGs aided with the new observer for rotational-position estimation using the concept of CW-HFS injection approach is given in Fig. 17.

The procedure of DVC method shown in Fig. 17 includes various loops of control such as the current-control loop of CW side, the voltage control loop of PW side and the realization loop of CW current frequency.

By adjusting the CW d-axis current, i^*_{2d} through a PI controller, the amplitude of PW voltage is to be kept constant at the reference set level. Furthermore, the CW q-axis current, i^*_{2q} is directed to zero value through the loop of current control for a better performance, as given in Fig. 17.

At final stage, the current angle of CW can be realized aided with the detected rotational position, $\theta_{r_{est}}$ (given from the proposed new observer-based CW-HFS injection methodology) and the angle, ${\theta_1}^*$ (obtained by integrating the reference set level of PW frequency). From which, the required gating signals of the machine-side converter are attained.

4.4 Analysis and Discussion

To validate the efficient behavior of the novel position observer, comprehensive simulation results are presented with a prototype of 30-kVA BDFIG whose detailed parameters specified in Ref. [14]. The obtained analysis and discussion are given to

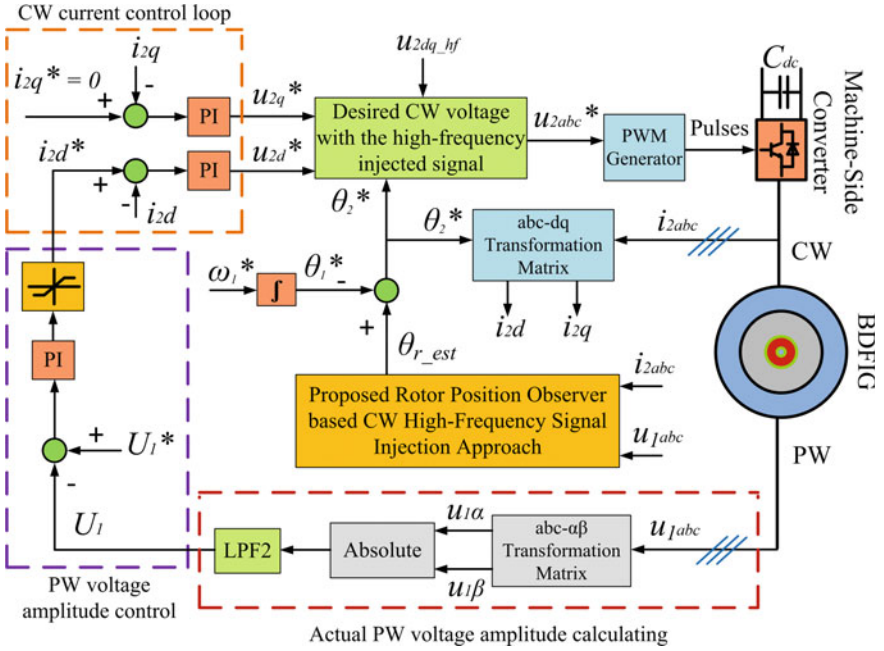

Fig. 17 Schematic diagram of the proposed control system for voltage regulation of BDFIGs with the new observer for position estimation

confirm the effective performance of the new position observer with various states of operation considering the start-up, change condition of speed and the variation state of load. The main target of the presented voltage control system is to attain a reference profile of PW voltage set at 311 V and 50 Hz.

The operation of BDFIG is initiated considering a resistive load of 11.6 kW and a 600 rpm of rotational speed. Then, at $t = 1.5$ s, the generator speed is increased until $t = 2$ s with a ramp change to 900 rpm as obtained in Fig. 18. Finally, a sudden variation in the load side is applied, at $t = 3.5$ s, to be reduced to 9.7 kW as illustrated in Fig. 19.

The obtained results in Figs. 18 and 19 assure the close coloration between the detected position signal and its real value with a good tracking behavior and a better realization for the desired voltage profiles of PW side with the presented sensorless DVC scheme considering various states of operation.

This would confirm the effectiveness of the novel procedure for the rotational-position estimation of BDFIGs based on the injection concept of CW-HFS. Moreover, the response of CW q-axis current, illustrated in Fig. 18e, validates the capability of the control loop for CW current to maintain the q-axis current at its intended value ($i_{2q}^* = 0$).

All the introduced results validate the capability and efficacy of the suggested sensorless voltage control system aided with the new observation methodology for

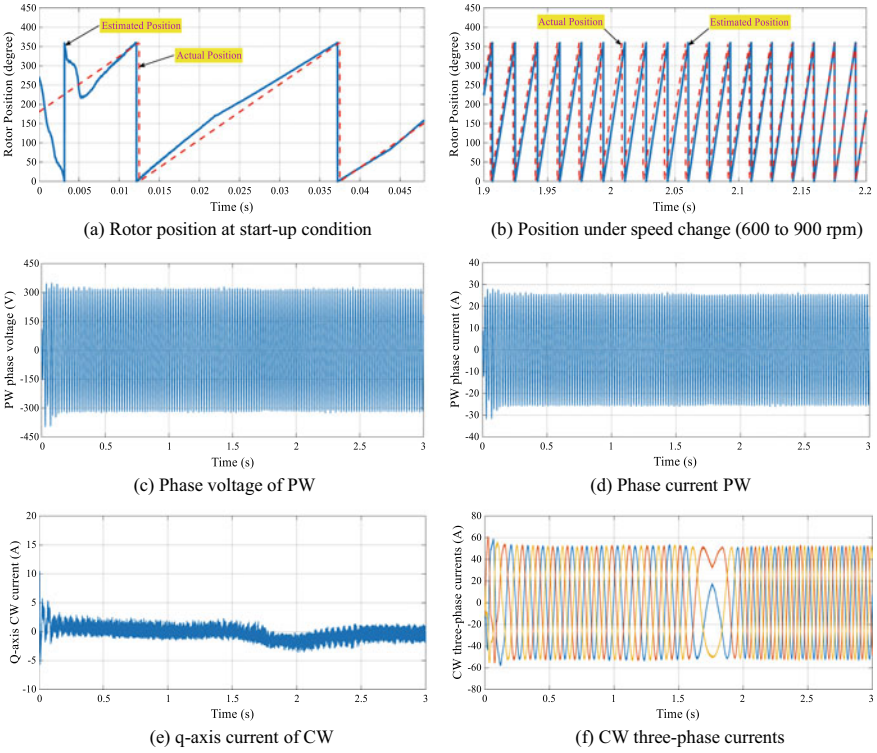

Fig. 18 Performance test with the operating conditions of the start-up and speed changes from 600 to 900 rpm

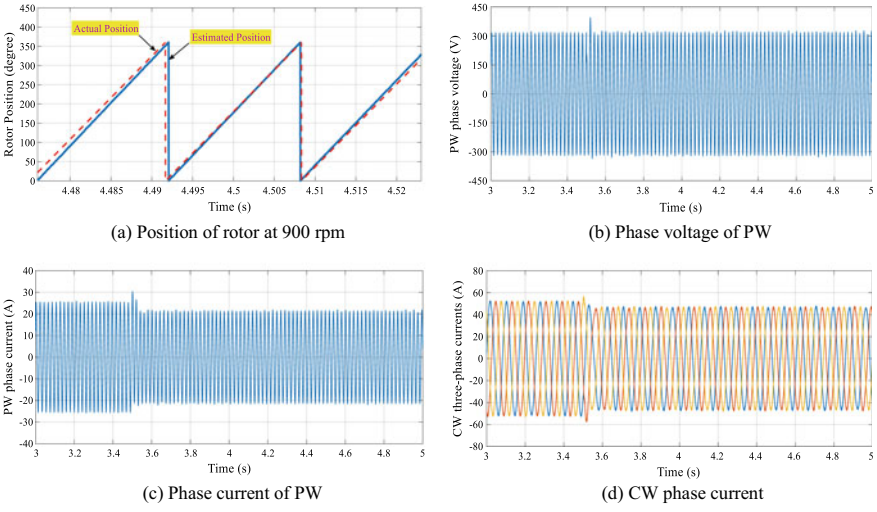

Fig. 19 Analysis under the load variation from 11.6 to 9.7 kW

rotor position detection with the concept of CW-HFS injection for the stand-alone generating system-based BDFIGs.

5 Summary

This chapter has handled the recent methodologies of sensorless position observers based on either the model or injected methods for the promising BDFIG in the ship power generation systems. The presented method based on the model principle has relied on the PW flux-orientation technique and the criteria of MRAS procedure for rotor position estimation algorithm with the functional quantity of CW reactive power. The obtained results of both simulation and experimental have confirmed the capability of the proposed sensorless control strategy for DVC. Moreover, the results have verified the efficacy of the proposed MRAS observer for sensorless DVC strategy of stand-alone BDFIGs under both cases of speed and load variations. Furthermore, the results have ensured the robustness against parameter uncertainty.

On the other side, this chapter has investigated a sensorless DVC methodology based on the injection approach of a high-frequency signal (HFS) for BDFIG in the stand-alone ship shaft applications. The proposed new observer has relied on the injection of HFS into the CW side while the induced signal detected from the PW side will observe the information of rotor position. The new proposed sensorless observer has not needed any saliencies in the rotor side for the rotational-position estimation, which has ensured the efficacy and simplicity of the new method. The obtained analysis has verified the efficiency of the proposed new observer-based HFS injection approach for the desired sensorless scheme for voltage control considering various states of operation such as the load and speed changes.

References

1. Y. Liu, W. Xu, J. Zhu, F. Blaabjerg, Sensorless control of standalone brushless doubly fed induction generator feeding unbalanced loads in a ship shaft power generation system. IEEE Trans. Ind. Electron. **66**(1), 739–749 (2019)
2. F. Xiong, X. Wang, Design of a low-harmonic-content wound rotor for the brushless doubly fed generator. IEEE Trans. Energy Convers. **29**(1), 158–168 (2014)
3. J. Chen, W. Zhang, B. Chen, Y. Ma, Improved vector control of brushless doubly fed induction generator under unbalanced grid conditions for offshore wind power generation. IEEE Trans. Energy Convers. **31**(1), 293–302 (2016)
4. M.G. Hussien, Y. Liu, W. Xu, M. Dong, in *Sensorless Position Control Based on Active Power MRAS for Ship Shaft Stand-Alone BDFIGs*. 2020 International Conference on Electrical Machines (ICEM), Gothenburg, Sweden, pp. 2209–2215 (2020)
5. S. Shao, E. Abdi, F. Barati, R.A. McMahon, Stator-flux-oriented vector control for brushless doubly-fed induction generator. IEEE Trans. Ind. Electron. **56**(10), 4220–4228 (2009)
6. Y. Liu, W. Ai, B. Chen, K. Chen, G. Luo, Control design and experimental verification of the brushless doubly-fed machine for stand-alone power generation applications. IET Elect. Power Appl. **10**(1), 25–35 (2016)

7. M.G. Hussien, Y. Liu, W. Xu, A.K. Junejo, S. Allam, Improved MRAS rotor position observer based on control winding power factor for stand-alone brushless doubly-fed induction generators. IEEE Trans. Energy Convers. (2021). https://doi.org/10.1109/TEC.2021.3110776
8. Y. Liu, W. Xu, G. Zhi, J. Zhang, Performance analysis of a stand-alone brushless doubly-fed induction generator using a new T-type steady-state model. J. Power Electron. **17**(4), 1027–1036 (2017)
9. W. Xu, M.G. Hussien, Y. Liu, M.R. Islam, S.M. Allam, Sensorless voltage control schemes for brushless doubly-fed induction generators in stand-alone and grid-connected applications. IEEE Trans. Energy Convers. **35**(4), 1781–1795 (2020)
10. M.G. Hussien, Y. Liu, W. Xu, Robust position observer for sensorless direct voltage control of stand-alone ship shaft brushless doubly-fed induction generators. CES Trans. Electr. Mach. Syst. **3**(4), 363–376 (2019)
11. Y. Liu, W. Xu, T. Long, F. Blaabjerg, An improved rotor speed observer for standalone brushless doubly-fed induction generator under unbalanced and nonlinear loads. IEEE Trans. Power Electron. **35**(1), 775–788 (2020)
12. M.G. Hussien, Y. Liu, W. Xu, J. Rodriguez, in *Fictitious Power Based MRAS Observer for Sensorless Control of Stand-Alone Brushless Doubly-Fed Induction Generators*. 2020 IEEE 9th International Power Electronics and Motion Control Conference (IPEMC2020-ECCE Asia), Nanjing, China, pp. 3511–3518 (2020)
13. M.G. Hussien, W. Xu, Y. Liu, S.M. Allam, Rotor speed observer with extended current estimator for sensorless control of induction motor drive systems. Energies **12**, 3613 (2019)
14. W. Xu, M.G. Hussien, Y. Liu, S.M. Allam, Sensorless control of ship shaft stand-alone BDFIGs based on reactive-power MRAS observer. IEEE J. Emerg. Sel. Topics Power Electron. **9**(2), 1518–1531 (2021)
15. C. Caruana, G.M. Asher, M. Sumner, Performance of HF signal injection techniques for zero-low-frequency vector control of induction machines under sensorless conditions. IEEE Trans. Ind. Electron. **53**(1), 225–238 (2006)
16. P.P. Acarnely, J.F. Watson, Review of position-sensorless operation of brushless permanent-magnet machines. IEEE Trans. Ind. Electron. **53**(2), 352–362 (2006)
17. Y. Liu, M.G. Hussien, W. Xu, S. Shao, E.M. Rashad, Recent advances of control technologies for brushless doubly-fed generators. IEEE Access **9**, 123324–123347 (2021)
18. D.D. Reigosa, F. Briz, C. Blanco, J.M. Guerrero, Sensorless control of doubly fed induction generators based on stator high-frequency signal injection. IEEE Trans. Ind. Appl. **50**(5), 3382–3391 (2014)
19. M.G. Hussien, Y. Liu, W. Xu, in A *New Rotor Position Observer of Brushless Doubly-Fed Induction Generators Based on Control-Winding High-Frequency Signal Injection*. 2021 IEEE 4th International Electrical and Energy Conference (CIEEC2021), China, pp. 1–6 (2021)
20. Y.D. Landau, Adaptive control: The model reference approach. IEEE Trans. Syst., Man, Cybern. **14**(1), 169–170 (1984)
21. I. Boldea et al., Fractional kVA rating PWM converter doubly fed variable speed electric generator systems: An overview in 2020. IEEE Access **9**, pp. 117957–117968 (2021)

Control and Observation of Induction Motors Based on Full-Order Terminal Sliding-Mode Technique

Minghao Zhou, Siwei Cheng, Wei Xu, Yong Feng, and Hongyu Su

Abstract This chapter proposes full-order terminal sliding-mode (FOTSM) based observation and control approaches for the sensorless speed control system of the induction motor (IM) with the full consideration of the unmatched uncertainties. The sensorless field orientation control (FOC) system for the IM is based on the accurately observing of the speed and the flux of the motor using the full-order terminal sliding-mode observer (FOTSMO). With the feedback of the precise estimated speed/flux, the FOTSM based controllers for the speed-, flux- and current-loops are designed to strengthen the robustness, accuracy and rapidness of the FOC system for the IM. By means of the virtual control technique in the outer-loop, the unmatched uncertainties including the parameter perturbation and the external disturbance can be thoroughly compensated. The proposed adaptive gain avoids overestimating the upper bound of the uncertainties in the FOC system for the IM. Due to the integral-type control law, the current references are smoothed and the chattering in the conventional SMC is eliminated. In the inner-loop controllers, the actual voltage control signals can force the tracking errors of the currents to converge to their equilibrium points in a finite time. Finally, the simulation and experimental results have demonstrated the effectiveness and feasibility of the proposed FOTSM based controllers and observers for the sensorless speed control of the IM.

M. Zhou · S. Cheng · H. Su
Harbin University of Science and Technology, Harbin 150080, China
e-mail: zhouminghao@aliyun.com

S. Cheng
e-mail: a2781056293@163.com

H. Su
e-mail: suzuhys@163.com

W. Xu (✉)
Huazhong University of Science and Technology, Wuhan 430074, China
e-mail: weixu@hust.edu.cn

Y. Feng
Harbin Institute of Technology, Harbin 150001, China
e-mail: yfeng@hit.edu.cn

S. K. Das et al. (eds.), *Advances in Control Techniques for Smart Grid Applications*,
https://doi.org/10.1007/978-981-16-9856-9_11

Keywords Sliding-mode control · Terminal sliding-mode · Observer · FOC system · Induction motor

List of Symbols

u, $\boldsymbol{u}$	The voltage and voltage vector
i, $\boldsymbol{i}$	The current and current vector
ϕ, $\boldsymbol{\phi}$	The flux and flux vector
θ	The rotor electrical angle
ω	The rotor electric angular velocity
ω_m	The rotor mechanical angular velocity
ω_s	The slip angle velocity
ω_1	The synchronous angle velocity with $\omega_1 = \omega + \omega_s$
J	The moment of inertia
R_s	The stator resistance
R_r	The rotor resistance
L_s	The stator inductance
L_r	The rotor inductance
L_m	The mutual inductance between the stator and rotor windings
T_e	The electrical torque
T_L	The load torque
n	The rotation speed
$\hat{}$	The estimated value
$-$	The error value
$[]_0$	The nominal value
$[]_{\text{ref}}$	The reference value
$[]_s$, $[]_r$	Stator and rotor parameters
$[]_{ABC}$, $[]_{abc}$	States in *abc*-axis
$[]_\alpha$, $[]_\beta$	States in α- and β-axis
$[]_q$, $[]_d$	States in q- and d-axis
n_p	The number of pole pairs of the stator
L_{sl}, L_{rl}	The stator and rotor leakage inductance
L_{sm}, L_{rm}	The mutual inductance between the stator and rotor windings
T_r	The rotor time constant $T_r = L_r/R_r$
σ	The leakage coefficient $\sigma = 1 - L_m^2/(L_s L_r)$
K	$K = 1/(\sigma_{Ls})$
ξ	$\xi = K(L_m/L_s)$
λ	$\lambda = K(R_s + R_r L_m^2/L_r^2)$

List of Acronyms

ADRC	Active disturbance reject control
AFO	Adaptive full-order observer
DTC	Direct torque control
EKF	Extended kalman filter
FOC	Field-oriented control
FOTSM	Full-order terminal sliding-mode
FOTSMO	Full-order terminal sliding-mode observer
IM	Induction motor
LSM	Linear sliding-mode
LSMO	Linear sliding-mode observer
MIMO	Multiply inputs multiply outputs
MPC	Model predictive control
MRAC	Model reference adaptive control
PI	Proportion-integral
SMC	Sliding-mode control
SMO	Sliding-mode observer
SVPWM	Space vector pulse width modulation

1 Introduction

Due to the advantages of simple structure, fast dynamic response, low moment of inertia, low-torque ripple, high reliability, and low costs of manufacture, repair and maintenance, the induction motor (IM) has been widely applied in many industrial applications, such as machine tools, steel mills, paper machines, etc. [1]. IMs are generally used in rough applications, such as mining industry, cranes, etc. Meanwhile, the IMs are applied in electrical vehicles, such as tesla model3, etc. Thus, the control performance needs to be improved. Control strategies for IMs mainly include V/F, direct torque control (DTC) and field-oriented control (FOC) [2, 3]. The DTC control strategy was first proposed by Depenrock in the 1950s. Combined with the bang-bang control strategies, the DTC can regulate the stator flux and the torque respectively. However, it could cause the torque ripple and the performance of the IM under the control strategy would become worse at a low speed. The FOC control strategy was mentioned by Hasse in the early 1970s and is extensively used in the IM control system to implement the decoupled control of currents.

In the traditional IM speed control system, the speed signal of the IM is detected by the sensors, such as optical encoder, rotary transformer, etc., and used as the feedback to implement the FOC system of the IM. The change of the temperature, humidity and so on will decrease the reliability of the sensors. Therefore, the sensorless control (also noted as self-sensing) has become a hot topic to deal with the aforementioned problems. Compared to the IM control system with sensor, the sensorless control

has advantages in motor drives due to cost reduction, system downsizing and reliability enhancement for motor drives. To realize the sensorless control of the IM, the accurate estimation for the rotor flux and observation of speed are indispensable, which means the observation algorithm of the speed and the rotor flux require high precision and strong robustness. The general observations of the rotor flux and speed include extended Kalman filter (EKF), adaptive full-order observer (AFO), sliding-mode observer (SMO), etc. The sliding-mode observer has been widely used in the observation of motors owing to its simple structure, easy implementation and strong robustness.

The linear sliding-mode observer (LSMO) processes the observation signal with low-pass filtering. This results in the phase lag of the observation and reduces the observer's accuracy, which is more serious especially at a low speed [4]. In [5–7], a speed/flux SMO is designed for the IM, but the estimation error in the conventional reduced-order sliding manifold is not convergent in a finite time. Moreover, the adopted boundary layer method would reduce the accuracy of the observer. In [8], a super-twisting based speed observer is proposed to obtain precise estimated speed with a twisting convergence trajectory. However, the high order sliding-mode reaches the sliding surface non-monotonically with a large overshoot. In [4], a low-pass filter is applied to deal with the chattering, but it causes the phase lag of the estimated speed. It can be seen that the output injections in existing SMOs are mainly switching signals, which would reduce the accuracy of the observers. Therefore, in this chapter, a full-order terminal SMO is proposed to implement a high-performance sensorless control for the IM system to strengthen the precision and anti-disturbance against the uncertainties.

Additionally, to improve the dynamic performance of the IMs in robustness, rapidness and accuracy, many methods have been proposed, such as PI control [9], adaptive control [10], model reference adaptive control (MRAC) [11], linear quadratic regulator (LQR) [12, 13], H_∞ control [14], model predictive control (MPC) [15, 16], backstepping control [17, 18], fuzzy control [19–22], neural network control [22], active disturbance rejection control (ADRC) [23] and sliding-mode control (SMC), etc. The model of the IMs is a class of nonlinear multi-inputs multi-outputs (MIMO) system with unmatched uncertainties. As a 2-order MIMO nonlinear system, the IM in the FOC system has various uncertainties including the matched and unmatched uncertainties. The matched uncertainties are those existing in the control channel, and the uncertainties that exist in the non-control channel are the so-called unmatched uncertainties. The matched uncertainties made up by the parameter perturbation in the inner-loop of the IM system can be directly compensated by the voltage control signals. However, the unmatched uncertainties are composed of the external disturbance and parameter variations in the outer-loop of the FOC system, which means the uncertainties cannot be compensated by the voltage control signals straightforwardly. With the appropriate design of the current controllers, the current error dynamics can be forced to converge to zero. Whereas, the speed error dynamics may converge to the neighborhood around zero due to the unmatched uncertainties. The general designs of the controllers for the FOC system of the IMs are based on the reduced-order mathematical model of the IMs, which means the controllers for the outer-loop and

inner-loop are separately designed and the influence of the unmatched uncertainties is ignored. This could lead the decrease in the dynamic performance of the IMs. Therefore, it is necessary to adequately consider both the matched and unmatched uncertainties in the IM control system.

SMC is recognized as an excellent controller design method for the FOC system for motors, due to its advantages of low sensitivity to inner parameter variations and strong robustness to external disturbances. However, the traditional SMC can only compensate for the matched uncertainties satisfying the so-called match condition. Therefore, with the development of the control theory, some improved SMC combined with other advanced control methods have been proposed to address the problem mentioned above. To implement the decoupled control of torque and flux, a nonlinear feedback linearization is adopted for the IM system in [24]. In [25], an online learning algorithm using adaptive sliding-mode training algorithm and type-2 neuro-fuzzy method is proposed to compensate the parametric uncertainties and disturbances in control of the IM. To enhance the dynamic performance of the current-loop in the control system of the IM, a disturbance rejection 2-order SMC is utilized in [26]. However, all of the above methods strictly depend on the accurate modeling of the IMs. To address the disturbance-observer errors and the uncertainty in the ADRC gains, an SMC component is proposed in [27], but the high-frequency switching noise in the voltage cannot be attenuated. It would lead to large noise in the space vector pulse width modulation (SVPWM) signal. A speed/flux observer based on twisting algorithm is designed to improve the robustness of the sensorless control system for IMs with core loss in [28]. However, a singularity would appear because of introducing the derivative of the current references with high-frequency switching signals into the voltages. In [29], to implement the real-time high-performance applications of IMs, an adaptive SMC based position tracking control is proposed, while the tracking error in the current-loop is not fully considered.

Furthermore, the chattering phenomenon, as an inherent feature of the SMC, is caused by the high-frequency switching control law in an SMC controller and may excite unmodeled dynamics in the closed loop. It extremely hinders the application of the SMC. The research of the control strategies attenuating chattering becomes a hot topic in recent years. Many methods have been proposed to attenuate the chattering [30–33]. In [34], a speed observer utilizing the 2-order sliding-mode based MRAC is proposed for sensorless six-phase IM to overcome the chattering in the classical SMC. However, the quasi-sliding mode method eliminates the chattering at the cost of control accuracy. Disturbance-observer based SMC can only weaken the chattering but not eliminate it. Super-twisting is non-monotonically convergent to the sliding manifold with a large overshoot. Therefore, the chattering-free performance of SMC method needs to be further improved [35].

In the existing sensorless control algorithm for the IMs based on the SMC, the challenges can be summarized as:

(a) The anti-disturbance performance and dynamic response of the observer need to be further improved;

(b) The chattering in the SMC signal would lead to large noise in the *d*-*q* current references, which could excite the unmodeled dynamics and reduces the stability of the system;
(c) The effect of parameter variation on the design of controllers cannot be adequately taken into consideration, and the SMC based existing works cannot compensate the unmatched uncertainties;
(d) The singularity problem may occur because the inputs of SVPWM contain the derivative of the current references. Meanwhile, there are high-frequency switching terms in the current references formed by the traditional SMC.

In the SMC based existing works, the unmatched uncertainties in the MIMO systems are not fully considered, and the existing SMC cannot overcome the unmatched uncertainties completely [22–31]. Therefore, a novel full-order terminal sliding-mode (FOTSM) [36–38] algorithm based controller and observer design method is proposed. Hence, the disturbance rejection capacity to unmatched uncertainties in the speed-loop is improved, and the dynamic performance and robustness of the current-loop are enhanced. So, the high-performance of the sensorless control system can be obtained. In this chapter, the model of IM is regarded as a second-order MIMO system with unmatched disturbance, and an adaptive method for the switching control gain design is established to address the influence of the parametric uncertainties on the controller design. Additionally, to eliminate the singularity caused by the derivative of the current references existing in the inputs of SVPWM, the current references are designed into derivable signals based on FOTSM instead of the reduced-order SMC in the chapter. The chattering phenomenon can be reduced without the conventional boundary layer method or low-pass filters. The chattering is eliminated, and outputs of controllers and observers can be smoothed. The performance of the sensorless control system is enhanced in the aspects of accuracy and rapidness.

The rest of this chapter is organized into the following sections. In Sect. 2, the mathematical model of the IM in different coordinates and the FOC system of the IM with unmatched uncertainties are introduced. In Sects. 3 and 4, the FOTSM based observers and controllers are presented respectively. Some conclusions are given in Sect. 5.

2 Mathematical Model of IMs

Some assumptions are given to simplify the analysis in the front:

1. the effect of magnetic saturation is neglected.
2. three-phase windings have the same structure and ignoring the fringe effect.
3. the effect of the slot is ignored.
4. the iron core loss is not taken into account.

All the notations in the control system of the IM are shown in the Table 1.

Table 1 Notations in the control system of the IM

Variables	Meaning of notations
u, $\boldsymbol{u}$	The voltage and voltage vector
i, $\boldsymbol{i}$	The current and current vector
ϕ, $\boldsymbol{\phi}$	The flux and flux vector
θ	The rotor electrical angle position
ω	The rotor electrical angular velocity
ω_m	The rotor mechanical angular velocity
ω_s	The slip angle velocity
ω_1	The synchronous angle velocity with $\omega_1 = \omega + \omega_s$
J	The moment of inertia
R_s	The stator resistance
R_r	The rotor resistance
L_s	The stator inductance
L_r	The rotor inductance
L_m	The mutual inductance between the stator and rotor windings
T_e	The electrical torque
T_L	The load torque
N	The rotation speed
$\hat{}$	The estimated value
$\bar{}$	The error value
$[]_0$	The nominal value
$[]_{\text{ref}}$	The reference value
$[]_s$, $[]_r$	Stator and rotor parameters
$[]_{ABC}$, $[]_{abc}$	States in abc-axis
$[]_\alpha$, $[]_\beta$	States in α- and β-axis
$[]_q$, $[]_d$	States in d- and q-axis
n_p	The number of pole pairs of the stator
L_{sl}, L_{rl}	The stator and rotor leakage inductance
L_{sm}, L_{rm}	The mutual inductance between the stator and rotor windings
T_r	The rotor time constant $T_r = L_r/R_r$
σ	The leakage coefficient $\sigma = 1 - L_m^2/(L_s L_r)$
K	$K = 1/(\sigma L_s)$
ξ	$\xi = K(L_m/L_s)$
λ	$\lambda = K(R_s + R_r L_m^2/L_r^2)$

2.1 *Mathematical Model of IMs in* a-b-c *Coordinate*

The mathematical model of an IM is generally composed of voltage, flux and motion equations. Based on the assumptions mentioned above, the voltage equation of the IM in *a-b-c* coordinate is expressed as follows [39]:

$$\boldsymbol{u} = \boldsymbol{R}\boldsymbol{i} + \frac{\mathrm{d}\boldsymbol{\phi}}{\mathrm{d}t} \tag{1}$$

where $\boldsymbol{u} = [u_s, u_r]^{\mathrm{T}} = [u_{sA}, u_{sB}, u_{sC}, u_{ra}, u_{rb}, u_{rc}]^{\mathrm{T}}$, $\boldsymbol{i} = [i_s, i_r]^{\mathrm{T}} = [i_{sA}, i_{sB}, i_{sC}, i_{ra}, i_{rb}, i_{rc}]^{\mathrm{T}}$, $\boldsymbol{\phi} = [\phi_s, \phi_r]^{\mathrm{T}} = [\phi_{sA}, \phi_{sB}, \phi_{sC}, \phi_{ra}, \phi_{rb}, \phi_{rc}]^{\mathrm{T}}$ and $\boldsymbol{R} = \mathrm{diag}(R_s, R_s, R_s, R_r, R_r, R_r)$.

The flux equation of the IM in the *a-b-c* coordinate is expressed as follows:

$$\boldsymbol{\phi} = \boldsymbol{L}\boldsymbol{i} \tag{2}$$

with

$$L_{ss} = \begin{bmatrix} L_{sm}+L_{sl} & -\frac{1}{2}L_{sm} & -\frac{1}{2}L_{sm} \\ -\frac{1}{2}L_{sm} & L_{sm}+L_{sl} & -\frac{1}{2}L_{sm} \\ -\frac{1}{2}L_{sm} & -\frac{1}{2}L_{sm} & L_{sm}+L_{sl} \end{bmatrix},$$

$$L_{rr} = \begin{bmatrix} L_{sm}+L_{rl} & -\frac{1}{2}L_{sm} & -\frac{1}{2}L_{sm} \\ -\frac{1}{2}L_{sm} & L_{sm}+L_{rl} & -\frac{1}{2}L_{sm} \\ -\frac{1}{2}L_{sm} & -\frac{1}{2}L_{sm} & L_{sm}+L_{rl} \end{bmatrix},$$

$$L_{sr} = L_{rs}^{T} = L_{sm}\begin{bmatrix} \cos\theta & \cos(\theta-120^\circ) & \cos(\theta+120^\circ) \\ \cos(\theta+120^\circ) & \cos\theta & \cos(\theta-120^\circ) \\ \cos(\theta-120^\circ) & \cos(\theta+120^\circ) & \cos\theta \end{bmatrix}$$

where $\boldsymbol{L} = [L_{ss}, L_{sr}; L_{rs}, L_{rr}]$.

The torque equation of the IM can be described by

$$T_e = n_p L_{sm}\begin{bmatrix} (i_{sa}i_{ra}+i_{sb}i_{rb}+i_{sc}i_{rc})\sin\theta \\ +(i_{sa}i_{ra}+i_{sb}i_{rb}+i_{sc}i_{rc})\sin(\theta+120^\circ) \\ +(i_{sa}i_{ra}+i_{sb}i_{rb}+i_{sc}i_{rc})\sin(\theta-120^\circ) \end{bmatrix}. \tag{3}$$

Finally, the motion equation of the IM can be expressed as:

$$T_e = T_L + \frac{J}{n_p}\frac{\mathrm{d}\omega}{\mathrm{d}t} \tag{4}$$

Therefore, Eqs. (1)–(4) can describe the mathematical model of the IM in the *a-b-c* coordinate.

2.2 Mathematical Model of IMs in α-β Coordinate

To derive the mathematical model of the IM in the α-β coordinate, the Clarke transformation is utilized as [40]:

$$\boldsymbol{C}_{3/2} = \sqrt{\frac{2}{3}}\begin{bmatrix} 1 & -\frac{1}{2} & -\frac{1}{2} \\ 0 & \frac{\sqrt{3}}{2} & -\frac{\sqrt{3}}{2} \end{bmatrix}. \tag{5}$$

Then the voltage equations of the IM in α-β coordinate can be described as:

$$\begin{cases} \boldsymbol{u}_{s\alpha\beta} = R_s \boldsymbol{i}_{s\alpha\beta} + p\boldsymbol{\phi}_{s\alpha\beta} \\ \boldsymbol{u}_{r\alpha\beta} = R_r \boldsymbol{i}_{r\alpha\beta} + (p+\omega)\boldsymbol{\phi}_{r\alpha\beta} \end{cases}, \begin{cases} \boldsymbol{\phi}_{s\alpha\beta} = L_s \boldsymbol{i}_{s\alpha\beta} + L_m \boldsymbol{i}_{r\alpha\beta} \\ \boldsymbol{\phi}_{r\alpha\beta} = L_m \boldsymbol{i}_{s\alpha\beta} + L_r \boldsymbol{i}_{r\alpha\beta} \end{cases} \tag{6}$$

where $\boldsymbol{u}_{s\alpha\beta} = [u_{s\alpha}, u_{s\beta}]^{\mathrm{T}}$, $\boldsymbol{u}_{r\alpha\beta} = [u_{r\alpha}, u_{r\beta}]^{\mathrm{T}}$, $\boldsymbol{i}_{s\alpha\beta} = [i_{s\alpha}, i_{s\beta}]^{\mathrm{T}}$, $\boldsymbol{i}_{r\alpha\beta} = [i_{r\alpha}, i_{r\beta}]^{\mathrm{T}}$, $\boldsymbol{\phi}_{s\alpha\beta} = [\phi_{s\alpha}, \phi_{s\beta}]^{\mathrm{T}}$ and $p = \mathrm{d}/\mathrm{d}t$.

Hence, the torque equation of the IM in α-β coordinate is given as:

$$T_e = n_p L_m (i_{s\beta} i_{r\alpha} - i_{s\alpha} i_{r\beta}) \tag{7}$$

In summary, Eqs. (4), (6) and (7) make up the IM model in α-β coordinate.

2.3 Mathematical Model of IMs in d-q Coordinate

The transformation among *a-b-c*, α-β and *d-q* coordinates is shown in Fig. 1. The rotating velocity of the *d-q* axis equals to the synchronous electrical angle velocity ω_1, and the Park matrix is given by

$$\boldsymbol{C}_{2s/2r} = \begin{bmatrix} \cos\theta & \sin\theta \\ -\sin\theta & \cos\theta \end{bmatrix}. \tag{8}$$

Then the voltage and flux equations of the IMs in the *d-q* coordinate can be described as follows [41]:

$$\begin{cases} \boldsymbol{u}_{sdq} = R_s \boldsymbol{i}_{sdq} + \begin{bmatrix} p & -\omega_1 \\ \omega_1 & p \end{bmatrix} \boldsymbol{\phi}_{sdq} \\ \boldsymbol{u}_{rdq} = R_r \boldsymbol{i}_{rdq} + \begin{bmatrix} p & -\omega_s \\ \omega_s & p \end{bmatrix} \boldsymbol{\phi}_{rdq} \end{cases}, \begin{cases} \boldsymbol{\phi}_{sdq} = L_s \boldsymbol{i}_{sdq} + L_m \boldsymbol{i}_{rdq} \\ \boldsymbol{\phi}_{rdq} = L_m \boldsymbol{i}_{sdq} + L_r \boldsymbol{i}_{rdq} \end{cases} \tag{9}$$

where $\boldsymbol{u}_{sdq} = [u_{sd}, u_{sq}]^{\mathrm{T}}$, $\boldsymbol{u}_{rdq} = [u_{rd}, u_{rq}]^{\mathrm{T}}$, $\boldsymbol{i}_{sdq} = [i_{sd}, i_{sq}]^{\mathrm{T}}$, $\boldsymbol{i}_{rdq} = [i_{rd}, i_{rq}]^{\mathrm{T}}$, $\boldsymbol{\phi}_{sdq} = [\phi_{sd}, \phi_{sq}]^{\mathrm{T}}$, $\boldsymbol{\phi}_{rdq} = [\phi_{rd}, \phi_{rq}]^{\mathrm{T}}$.

The torque equation of IMs in *d-q* coordinate is as follows:

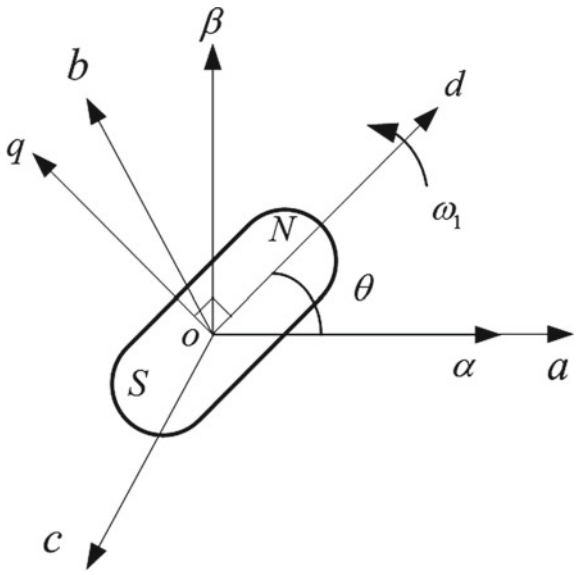

Fig. 1 The transformation among *a-b-c*, α-β and *d-q* coordinates

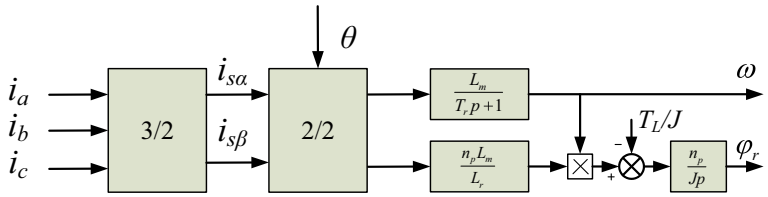

Fig. 2 The transformation and the decoupled mathematical model of the IM

$$T_e = \frac{n_p L_m}{L_r}(i_{sq}\phi_{rd} - i_{sd}\phi_{rq}) \tag{10}$$

According to the mentioned above, the mathematical model of IMS in the three coordinates (*a-b-c*, α-β and *d-q*). By the Clark transformation (5), the model of IMs in *a-b-c* coordinate (1)–(4) can be transferred into the model in α-β coordinate. Equations (4), (9) and (10) make up the model of IM in *d-q* coordinate with the Park transformation (8) (Fig. 2).

2.4 FOC System for the IMs with Unmatched Uncertainties

According to (9), the mathematical model of the IM in the *d-q* coordinate is described by:

$$\dot{\omega}_m = \frac{1}{J}\left(\frac{n_p L_m \phi_r}{J L_r} i_q - T_L\right) \tag{11a}$$

$$\dot{\phi}_r = -\frac{1}{T_r}\phi_r + \frac{L_m}{T_r} i_d \tag{11b}$$

$$\dot{i}_q = -\xi\omega\phi_r - \left(\omega + \frac{L_m i_q}{T_r \phi_r}\right) i_d - \lambda i_q + K u_q \tag{11c}$$

$$\dot{i}_d = \xi \frac{1}{T_r}\phi_r - \lambda i_d + \left(\omega + \frac{L_m i_q}{T_r \phi_r}\right) i_q + K u_d \tag{11d}$$

It can be seen from Eq. (11c) that the IM model consists of the outer- and inner-subsystems, where the outer-subsystem includes the speed- and flux-loop and the inner-subsystem includes the current-loops. To further analyze the dynamic process of the IM, the matched and unmatched uncertainties must be considered adequately in the outer- and inner-subsystems.

1. *Outer-Loop Subsystem of FOC System*

The tracking errors of the speed and rotor flux are defined by $e_\omega = \omega_{m\text{ref}} - \omega_m$ and $e_\phi = \phi_{m\text{ref}} - \phi_m$, with $\boldsymbol{e}_o = [e_\omega, e_\phi]^{\mathrm{T}}$ representing tracking error vector in the outer-loop. From the model (11), the outer-loop tracking error dynamics can be obtained as:

$$\begin{cases} \dot{e}_\omega = \dot{\omega}_{m\,\text{ref}} - \frac{n_p L_m \phi_r}{J^2 L_r} i_q + \frac{T_L}{J} \\ \dot{e}_\phi = \dot{\phi}_{r\,\text{ref}} + \frac{1}{T_r}\phi_r - \frac{L_m}{T_r} i_d \end{cases} \tag{12}$$

Due to the influence of the temperature and frequency, the values of the resistance and inductance may be changed as follows:

$$\begin{cases} R_j = R_{j0} + \Delta R_j,\ j = s, r \\ L_k = L_{k0} + \Delta L_k,\ k = s, r, m \end{cases} \tag{13}$$

Further

$$\begin{aligned} &\sigma = \sigma_0 + \Delta\sigma,\ K = K_0 + \Delta K,\ \xi = \xi_0 + \Delta\xi \\ &T_r = T_{r0} + \Delta T_r,\ \lambda = \lambda_0 + \Delta\lambda,\ J = J_0 + \Delta J \end{aligned} \tag{14}$$

The aforementioned uncertainties are assumed to be Lipschitz and bounded where the upper bounds can be assumed as follows:

$$\begin{cases} \left|\Delta R_j\right| \le M_{R_j},\ j = s, r \\ \left|\Delta L_k\right| \le M_{L_k},\ k = s, r, m \end{cases} \tag{15}$$

Further

$$|\Delta\sigma| \le M_\sigma, |\Delta K| \le M_K, |\Delta\xi| \le M_\xi,$$
$$|\Delta T_r| \le M_{T_r}, |\Delta\lambda| \le M_\lambda, |\Delta J| \le M_J. \tag{16}$$

where $M_{R_j}, M_{L_k}, M_s, M_K, M_x, M_{Tr}, M_\lambda > 0$ are known constants.

Therefore, considering the unmatched uncertainties, the error dynamics in the outer-loop can be rewritten by:

$$\begin{cases} \dot{e}_\omega = \dot{\omega}_{mref} - \frac{n_p\phi_r(L_{m0}+\Delta L_m)}{(\hat{J}+\Delta J)(L_{r0}+\Delta L_r)} i_q + \frac{T_L}{J} \\ \dot{e}_\phi = \frac{1}{T_{r0}+\Delta T_r}\phi_r - \frac{L_{m0}+\Delta L_m}{T_{r0}+\Delta T_r} i_d \end{cases} \tag{17}$$

The virtual control law is defined by

$$\tilde{\boldsymbol{u}} = \boldsymbol{g}_1 \boldsymbol{i}_{\text{ref}} = \left[u_\omega, u_\phi\right]^{\text{T}} = [n_p\phi_r F_{L_m/JL_r} i_{q\text{ref}}, (L_{m0}/T_{r0}) i_{d\text{ref}}]^{\text{T}} \tag{18}$$

where $\boldsymbol{g}_1 = \text{diag}\left(n_p\phi_r F_{L_m/JL_r},\ L_{m0}/T_{r0}\right)$, $\boldsymbol{i}_{\text{ref}} = [u_\omega/(n_p\phi_r F_{L_m/JL_r}), u_\phi T_{r0}/L_{m0}]^{\text{T}}$, $F_{L_m/JL_r} = L_{m0}/J_0 L_{r0}$.

It is defined that the tracking error of the stator current in the inner-loop stator is expressed as

$$\boldsymbol{e}_i = \boldsymbol{i}_{\text{ref}} - \boldsymbol{i} = \boldsymbol{g}_1^{-1}\tilde{\boldsymbol{u}} - \boldsymbol{i} = [e_{iq},\ e_{id}]^{\text{T}} \tag{19}$$

Let $\boldsymbol{f}_1(t, \boldsymbol{x}_o) = [\dot{\omega}_{m\text{ref}}, \phi_r/T_{r0}]^{\text{T}}$, then tracking error dynamics (17) in the outer-loop is expressed as:

$$\dot{\boldsymbol{e}}_o = \boldsymbol{f}_1(t, \boldsymbol{e}_o) - \tilde{\boldsymbol{u}} + \boldsymbol{\rho}_o(t, \boldsymbol{e}_o, \tilde{\boldsymbol{u}}) + \boldsymbol{g}_1\boldsymbol{e}_i \tag{20}$$

where $\boldsymbol{\rho}_o(t, \boldsymbol{e}_o, \tilde{\boldsymbol{u}}) = \boldsymbol{\rho} - \boldsymbol{\delta}\tilde{\boldsymbol{u}}$ is defined as the lumped unmatched uncertainty in the FOC system of the IM.

To further describe $\boldsymbol{\rho}_o(t, \boldsymbol{e}_o, \tilde{\boldsymbol{u}})$, the following uncertainties are calculated by (12) and (17) as follow:

$$\delta_\omega = \Delta F_{L_m/JL_r}/F_{L_m/JL_r} \tag{21a}$$

$$\delta_\phi = \Delta F_{L_m/T_r}/(L_{m0}/T_{r0}) \tag{21b}$$

$$\Delta F_{1/T_r} = \Delta T_r/(T_{r0}(T_{r0}+\Delta T_r)) \tag{21c}$$

$$\Delta F_{L_m/T_r} = (T_{r0}\Delta L_m - L_{m0}\Delta T_r)/(T_{r0}(T_{r0}+\Delta T_r)) \tag{21d}$$

$\Delta F_{L_m/JL_r} =$

$$[J_0 L_{r0}\Delta L_m - L_{m0}(J_0\Delta L_r + L_{r0}\Delta J + \Delta J\Delta L_r)]/J_0 L_{r0}(J_0 + \Delta J)(L_{r0} + \Delta L_r) \tag{21e}$$

Considering (15) and (16), the upper bound of the uncertainties is assumed as:

$$\begin{aligned} &|T_L/J| \le M_{T_L/J}, |i_d| \le i_{d\max}, \left|\dot{T}_L/J\right| \le G_{d(T_L/J)}, \\ &|\delta_\omega| \le M_{\delta_\omega} < 1, \left|\Delta F_{1/T_r}(t)\right| \le M_{1/T_r}, \left|\Delta F_{L_m/T_r}(t)\right| \le M_{L_m/T_r}, \\ &\left|\delta_\phi\right| \le M_{\delta_\phi} < 1, \left|i_q\right| \le i_{q\max}, \left|\Delta F_{L_m/JL_r}\right| \le M_{L_m/JL_r}. \end{aligned} \tag{22}$$

where $M_{T_L/J}$, M_{L_m/JL_r}, $G_{T_L/J}$, $G_{d(T_L/J)}$, $M_{\delta_\omega}, M_{1/T_r}, M_{L_m/T_r}$ and M_{δ_ϕ} are positive constants, $i_{d\max} = i_{q\max} = \sqrt{1.5}I_e$ and I_e is rated current of the IM.

Hence, the coefficient of the uncertain control gain can be assumed as:

$$\|\boldsymbol{\delta}\| \le M_\delta < 1 \tag{23}$$

where $M_\delta = \max\left(M_{\delta_\omega}, M_{\delta_\phi}\right)$.

Based on (21), (22) and (23), $\rho_\omega(t) = T_L/J$ and $\rho_\phi = \Delta F_{1/Tr}\phi_r$ are assumed to be Lipschitz and satisfy the boundary conditions as

$$|\rho_\omega(t)| \le M_{T_L/J}, \quad \left|\rho_\phi(t)\right| \le M_{\rho_\phi}(t) \tag{24}$$

where $M_{\rho_\phi}(t) = M_{1/T_r}|\phi_r|$ is a known positive function.

The lumped uncertainty matrix $\boldsymbol{\rho}$ is upper bounded in following form:

$$\|\boldsymbol{\rho}\| \le M_\rho = \sqrt{M_{T_L/J}^2 + M_{\rho_\phi}^2} \tag{25}$$

Proposition 1 *The derivative of the lumped uncertainty matrix* $\boldsymbol{\rho}$ *is bounded as*

$$\|\dot{\boldsymbol{\rho}}\| \le M_{d\rho} = \sqrt{G_{d(T_L/J)}^2 + M_{d\rho_\phi}^2} \tag{26}$$

where

$$M_{d\rho_\phi}(t) = M_{1/T_r}\left(\frac{1}{T_{r0}} + M_{1/T_r}\right)|\phi_r| + \frac{M_{1/T_r}L_{m0}}{T_{r0}}\left(1 + M_{\delta_\phi}\right)i_{d\max} \tag{27}$$

Proof The derivative of $\rho\phi$(t) is satisfied as

$$\begin{aligned} \left|\dot{\rho}_\phi(t)\right| &\le \left|\Delta F_{1/T_r}\right|\left((1/T_{r0})|\phi_r| + (L_{m0}/T_{r0})\left(1 + \left|\delta_\phi\right|\right)|i_d| + \left|\rho_\phi\right|\right) \\ &\le M_{1/T_r}\left((1/T_{r0})|\phi_r| + (L_{m0}/T_{r0})\left(1 + M_{\delta_\phi}\right)i_{d\max} + M_{1/T_r}|\phi_r|\right) \\ &\le M_{1/T_r}\left((1/T_{r0}) + M_{1/T_r}\right)|\phi_r| + M_{1/T_r}(L_{m0}/T_{r0})\left(1 + M_{\delta_\phi}\right)i_{d\max} \end{aligned} \tag{28}$$

Then it can be obtained that $\left|\dot{\rho}_\phi(t)\right| \le M_{d\rho_\phi}(t)$. Hence, the proof is completed.

2. *Inner-Loop Subsystem of FOC System*

Owing to (11), it can be seen that the *d-q* current dynamics are coupled, which illustrates that the *d-q* current dynamic would influence each other and lead to the torque ripple. Furthermore, in the high-speed domain, the coupling of the *d-q* currents will get worse. Therefore, the *d-q* currents need to be decoupled for the independent dynamic characteristics.

Without external disturbance in the inner-loop, the parameter variation representing the matched uncertainties exists. The current controllers for the inner-loop subsystem utilize $\boldsymbol{i}_{\text{ref}}$ as the input and $\boldsymbol{u}_{dq}$ as the output to generate the SVPWM modulation signals. Based on model (11), the inner-loop subsystem can be expressed by

$$\dot{\boldsymbol{i}} = \boldsymbol{F}(t, \boldsymbol{x}_o, \boldsymbol{i})\boldsymbol{i} + \boldsymbol{G}(\boldsymbol{u}_s + \boldsymbol{H}(t, \boldsymbol{x}_o)) \tag{29}$$

where $\boldsymbol{u}_s = [u_{qs}, u_{ds}]^{\mathrm{T}}$, $\boldsymbol{F} = \boldsymbol{F}_0 + \Delta\boldsymbol{F}$, $\boldsymbol{G} = \boldsymbol{G}_0 + \Delta\boldsymbol{G}$, $\boldsymbol{H} = \boldsymbol{H}_0 + \Delta\boldsymbol{H}$,

$$\begin{aligned}
\boldsymbol{G}_0 &= \begin{bmatrix} K_0 & 0 \\ 0 & K_0 \end{bmatrix}, \boldsymbol{F}_0 = \begin{bmatrix} -\lambda_0 & \omega_1 \\ -\omega_1 & -\lambda_0 \end{bmatrix}, \boldsymbol{H}_0 = \begin{bmatrix} \frac{\xi_0 \phi_r}{K_0 T_{r0}} & -\frac{\xi_0 \omega \phi_r}{K_0} \end{bmatrix}^{\mathrm{T}}, \\
\Delta\boldsymbol{F} &= \begin{bmatrix} -\Delta\lambda & \omega_1 \\ -\omega_1 & -\Delta\lambda \end{bmatrix}, \Delta\boldsymbol{G} = \begin{bmatrix} \Delta K & 0 \\ 0 & \Delta K \end{bmatrix}, \\
\Delta\boldsymbol{H} &= \left[\phi_r \left(\frac{\xi K_0 T_{r0} - \xi_0 K T_r}{K T_r K_0 T_{r0}} \right) \; -\omega \phi_r \left(\frac{\xi K_0 - \xi_0 K}{K K_0} \right) \right]^{\mathrm{T}}.
\end{aligned}$$

and the upper bounds of the uncertainties in (29) can be given as:

$$\begin{aligned}
&\|\Delta\boldsymbol{F}\| = |\Delta\lambda| \le M_\lambda, \|\Delta\boldsymbol{G}\| = |\Delta K| \le M_K, \left\|\Delta\dot{\boldsymbol{F}}\right\| \le M_{dA}, \\
&\|\boldsymbol{G}_0\| \le M_{D_0}, \left\|\Delta\dot{\boldsymbol{G}}\right\| \le M_{dD}, \|\boldsymbol{u}_s\| \le \sqrt{2}u_e
\end{aligned} \tag{30}$$

where M_{dA}, M_{D_0} and M_{dD} are positive constant, and u_e is the rated voltage.

Taking the parametric variation into account, the current inner-loop subsystem can be rewritten as

$$\dot{\boldsymbol{i}} = \boldsymbol{F}_0(t, \boldsymbol{x}_o, \boldsymbol{i})\boldsymbol{i} + (\boldsymbol{G}_0 + \Delta\boldsymbol{G})(\boldsymbol{u}_s + \boldsymbol{H}_0(t, \boldsymbol{x}_o)) + \boldsymbol{\rho}_{i0}(t) \tag{31}$$

where the inner-loop lumped uncertainty $\boldsymbol{\rho}_{i0}(t) = \Delta\boldsymbol{F}\boldsymbol{i}_s + (\boldsymbol{G}_0 + \Delta\boldsymbol{G})\Delta\boldsymbol{H}$.

The coupled *d-q* currents are presented in the matrix $\boldsymbol{F}$. For achieving decoupling of stator *d-q* currents, the feedforward compensation $\boldsymbol{Pi}$ is introduced for the *d-q* stator voltages $\boldsymbol{u}_s$

$$\boldsymbol{u}_s = \boldsymbol{P}\boldsymbol{i} - \boldsymbol{H}_0 + \boldsymbol{u} \tag{32}$$

where $\boldsymbol{u} = [u_q, u_d]^{\mathrm{T}}$ and feedforward compensation matrix $\boldsymbol{P}$ is expressed by $\boldsymbol{P} = [0, -\omega_1/K_0; \omega_1/K_0, 0]$.

The inner-loop subsystem is rewritten as follows by substituting (32) to (31)

$$\dot{\boldsymbol{i}} = (\boldsymbol{F}_0(t, \boldsymbol{x}_o, \boldsymbol{i}) + \boldsymbol{G}_0\boldsymbol{P})\boldsymbol{i} + \boldsymbol{G}_0\boldsymbol{u} + \Delta\boldsymbol{G}\boldsymbol{u} + \boldsymbol{\rho}_i(t, \boldsymbol{x}_o, \boldsymbol{i}) \tag{33}$$

where the lumped matched uncertainty $\boldsymbol{\rho}_i(t) = \Delta\boldsymbol{G}\boldsymbol{P}\boldsymbol{i} + \boldsymbol{\rho}_{i0}(t)$.

Considering $\boldsymbol{F}_0 + \boldsymbol{G}_0\boldsymbol{P} = \mathrm{diag}(-\lambda_0, -\lambda_0)$, the *d*-*q* currents can be dynamically decoupled.

Proposition 2 *$\boldsymbol{\rho}_i(t, \boldsymbol{x}_o, \boldsymbol{i}) = \Delta\boldsymbol{G}\boldsymbol{P}\boldsymbol{i} + \boldsymbol{\rho}_{i0}(t, \boldsymbol{x}_o, \boldsymbol{i})$ and its derivative are upper bounded and satisfy the following conditions:*

$$\left\|\boldsymbol{\rho}_i(t)\right\| \le M_{\rho_i}(t), \left\|\dot{\boldsymbol{\rho}}_i(t)\right\| \le M_{d\rho_i}(t) \tag{34}$$

where $M_{\rho_i}(t)$ and $M_{d\rho_i}(t)$ are positive functions:

$$M_{\rho_i}(t) = (\omega_1 M_K/K_0 + M_\lambda)\|\boldsymbol{i}\| + (K_0 + M_K)M_D \tag{35}$$

$$\begin{aligned} M_{d\rho_i}(t) = {} & (\omega_1 M_K/K_0 + M_\lambda)\Big((K_0 + M_K)\Big(\sqrt{2}u_{\max} + M_{D_0}\Big) + M_{\rho_i}\Big) + K_0 M_{dD} \\ & + M_K M_{dD} + (M_{dA} + (\omega_1 M_K/K_0 + M_\lambda)(\|\boldsymbol{F}_0\| + \omega_1 M_K/K_0))\|\boldsymbol{x}_2\| \end{aligned} \tag{36}$$

This proof follows straightforwardly from the proof of Proposition 1.

Let $\boldsymbol{G}_0\boldsymbol{u} = \boldsymbol{u}_i$ and from the outer-loop subsystem (20) and the inner-loop decoupled subsystem (33), it can be obtained that the mathematical model of the IM in FOC system is a 2-order nonlinear MIMO system with matched and unmatched uncertainties expressed as:

$$\dot{\boldsymbol{e}}_o = \boldsymbol{f}_1(t, \boldsymbol{e}_o) - \tilde{\boldsymbol{u}} + \boldsymbol{g}_1\boldsymbol{e}_i + \boldsymbol{\rho}_o(t, \boldsymbol{x}_o, \boldsymbol{i}) \tag{37a}$$

$$\dot{\boldsymbol{i}} = (\boldsymbol{F}_0(t, \boldsymbol{x}_o, \boldsymbol{i}) + \boldsymbol{G}_0\boldsymbol{P})\boldsymbol{i} + \boldsymbol{u}_i + \Delta\boldsymbol{G}\boldsymbol{G}_0^{-1}\boldsymbol{u}_i + \boldsymbol{\rho}_i(t, \boldsymbol{x}_o, \boldsymbol{i}) \tag{37b}$$

where $\tilde{\boldsymbol{u}} = \boldsymbol{g}_1\boldsymbol{i}_{\mathrm{ref}} = \boldsymbol{g}_1(\boldsymbol{i} + \boldsymbol{e}_i)$ is the virtual control vector in the outer-loop speed-subsystem (Fig. 3).

3 Full-Order Terminal Sliding-Mode Observation of IMs

This section introduces the designs of the sliding-mode observers including the conventional LSMO and the proposed FOTSMO to obtain the estimated rotor flux and speed signals and implement the FOC system of the IMs. By selecting the full-order sliding manifold and designing the output injections of the observer, the dynamic performance of the observer can be improved. The simple diagram of the sensorless control for the IM system is shown in Fig. 4.

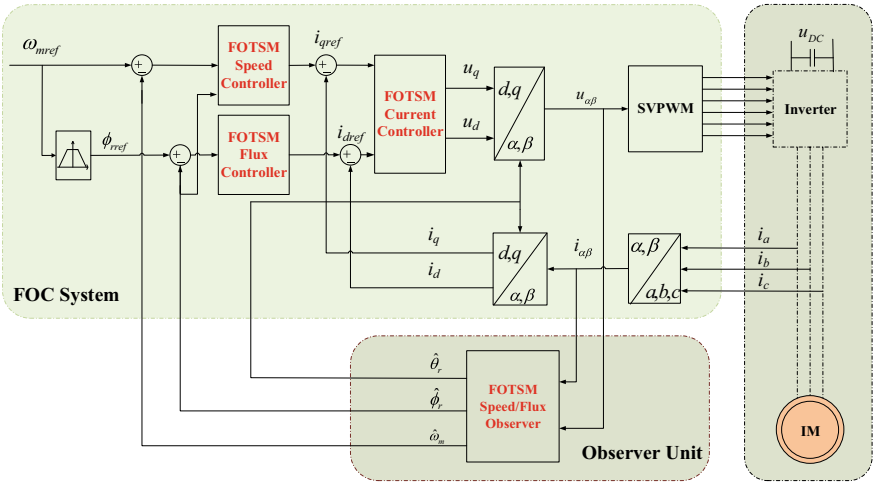

Fig. 3 Block diagram of the sensorless FOC system for the IM

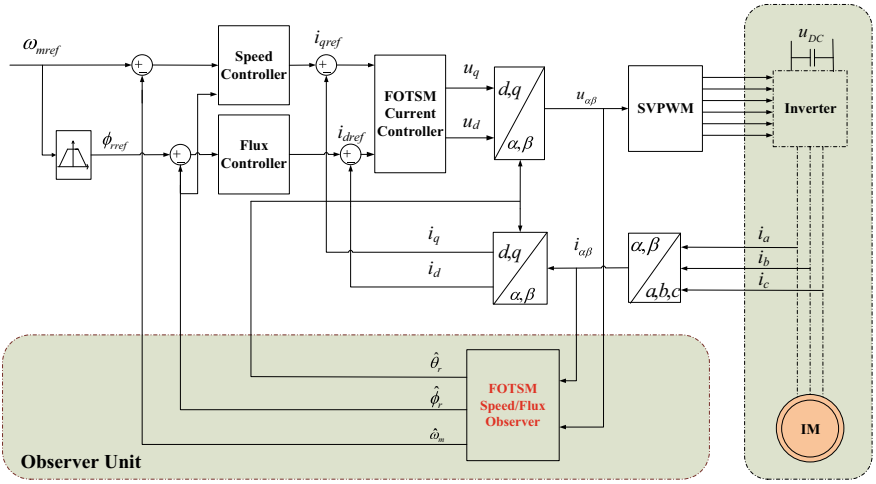

Fig. 4 Simple diagram of the sensorless control for the IM system

3.1 Linear Sliding-Mode Observer

The model of the IM in α-β coordinate can be expressed by:

$$\begin{cases} \dot{\boldsymbol{\phi}}_{r\alpha\beta} = -\boldsymbol{M} + \frac{L_m}{T_r}\boldsymbol{i}_{s\alpha\beta} \\ \dot{\boldsymbol{i}}_{\alpha\beta} = \xi \boldsymbol{M} - \lambda \boldsymbol{i}_{s\alpha\beta} + K\boldsymbol{u}_{s\alpha\beta} \end{cases} \tag{38}$$

where the matrix $\boldsymbol{M}$ contains the information of the speed, rotor flux and the rotor time constant as follows:

$$\boldsymbol{M} = \begin{bmatrix} 1/T_r & \omega \\ -\omega & 1/T_r \end{bmatrix} \begin{bmatrix} \phi_{\alpha r} \\ \phi_{\beta r} \end{bmatrix}. \tag{39}$$

For estimating the speed and rotor flux, a speed/flux observer based on FOTSM is proposed as follows by obtaining the matrix $\boldsymbol{M}$.

$$\begin{cases} \dot{\hat{\boldsymbol{\phi}}}_{r\alpha\beta} = -\frac{1}{\xi}\boldsymbol{w}_{\alpha\beta} + \frac{L_m}{T_r}\hat{\boldsymbol{i}}_{\alpha\beta} \\ \dot{\hat{\boldsymbol{i}}}_{\alpha\beta} = \boldsymbol{w}_{\alpha\beta} - \lambda\hat{\boldsymbol{i}}_{\alpha\beta} + K\boldsymbol{u}_{\alpha\beta} \end{cases} \tag{40}$$

where $\boldsymbol{w}_{\alpha\beta} = [w_\alpha, w_\beta]^{\mathrm{T}}$ is the output injection of the observer.

Owing to (38) and (40), the current error dynamics is given as:

$$\dot{\bar{\boldsymbol{i}}}_{\alpha\beta} = \boldsymbol{w}_{\alpha\beta} - \xi\boldsymbol{M} - \lambda\bar{\boldsymbol{i}}_{\alpha\beta} \tag{41}$$

where the matched uncertain matrix of the error dynamics can be assumed to be upper bounded as follows

$$\|\xi\boldsymbol{M}\| \le F_\omega, \ \left\|\xi\dot{\boldsymbol{M}}\right\| \le F_{d\omega} \tag{42}$$

where $F_\omega > 0$ and $F_{d\omega} > 0$ are known constants.

A linear sliding manifold is constructed as

$$\boldsymbol{s}_{LSM} = \bar{\boldsymbol{i}}_{\alpha\beta} \tag{43}$$

Theorem 1 *If a linear sliding manifold is adopted as (43) and the output injection can be designed, where the estimated current error can be forced to converge to zero asymptotically in the stator current error dynamics. Related equations are given by:*

$$\boldsymbol{w} = \boldsymbol{w}_{eq} + \boldsymbol{w}_n \tag{44a}$$

$$\boldsymbol{w}_{eq} = \lambda\bar{\boldsymbol{i}} \tag{44b}$$

$$\boldsymbol{w}_n = -k_1 \mathrm{sgn}(\boldsymbol{s}_{\mathrm{LSM}}) \tag{44c}$$

where $k_1 = F_{\omega 1} + \eta_1$, and η_1 is a positive constant.

Proof Choosing a Lyapunov function $V = 0.5\boldsymbol{s}^T\boldsymbol{s}$ and taking the time derivative of V yields

$$\dot{V} = \boldsymbol{s}^T\dot{\boldsymbol{s}} = \boldsymbol{s}^T\left(\boldsymbol{w}_{\alpha\beta} - \xi\boldsymbol{M} - \lambda\bar{\boldsymbol{i}}_{\alpha\beta}\right)$$

$$= \boldsymbol{s}^T\left(\boldsymbol{w}_{\alpha\beta n} - \xi \boldsymbol{M}\right) \tag{45}$$

Combining with (44c) gives:

$$\dot{V} = \boldsymbol{s}^T(-k_1 \mathrm{sgn}(\boldsymbol{s}_{\mathrm{LSM}}) - \xi \boldsymbol{M}) \leq \boldsymbol{s}^T(-k_1 \mathrm{sgn}(\boldsymbol{s}_{\mathrm{LSM}}) + \|\xi \boldsymbol{M}\|) \tag{46}$$

then it will get

$$\dot{V} \leq -\eta_1 \|\boldsymbol{s}\| < 0, \|\boldsymbol{s}\| \neq 0 \tag{47}$$

which implies the error dynamics of the stator current observer (41) will reach to zero asymptotically. On $\boldsymbol{s}(t) = 0$, it can be seen from (43) that the stator current error of the LSMO can be also forced to converge to zero asymptotically. Hence, the proof is completed.

Then the error dynamics Eq. (41) can be rewritten as:

$$\boldsymbol{w}_{\alpha\beta} = \xi \boldsymbol{M} = \xi \begin{bmatrix} -1/T_r & -\omega \\ \omega & -1/T_r \end{bmatrix} \boldsymbol{\phi}_{r\alpha\beta} \tag{48}$$

Combined with the observer (40), the rotor flux can be calculated by:

$$\hat{\boldsymbol{\phi}}_{r\alpha\beta} = \int_0^t \left(-\frac{1}{\xi}\boldsymbol{w}_{\alpha\beta} + \frac{L_m}{T_r}\hat{\boldsymbol{i}}_{\alpha\beta}\right)\mathrm{d}t \tag{49}$$

Then the rotor flux angle and the speed can be estimated in the following form, which provides the necessary condition of the FOC system.

$$\hat{\theta}_1 = \arctan(\hat{\phi}_{r\beta}/\hat{\phi}_{r\alpha}) \tag{50a}$$

$$\hat{\omega} = \left(\hat{\phi}_{r\beta} w_\alpha - \hat{\phi}_{r\alpha} w_\beta\right) / \left(\xi \left\|\boldsymbol{\phi}_{r\alpha\beta}\right\|^2\right) \tag{50b}$$

3.2 *Full-Order Sliding-Mode Observer*

A full-order fast terminal sliding manifold is proposed as

$$\boldsymbol{s} = \dot{\bar{\boldsymbol{i}}}_{s\alpha\beta} + \boldsymbol{C}_1 \bar{\boldsymbol{i}}_{s\alpha\beta} + \boldsymbol{C}_2 \bar{\boldsymbol{i}}_{s\alpha\beta}^{p/q} \tag{51}$$

where q and p are odds, and $0 < q/p < 1$, positive diagonal matrixes $\boldsymbol{C}_1 = \text{diag}(c_{\alpha 1}, c_{\beta 1})$ and $\boldsymbol{C}_2 = \text{diag}(c_{\alpha 2}, c_{\beta 2})$.

Theorem 2 *The error dynamics (41) can be forced to reach the ideal full-order fast sliding motion $\boldsymbol{s}(t) = 0$ within a finite time, $t \geq t_r$, $t_r \leq \ln(2\varepsilon V^{1/2}(\boldsymbol{s}(0))/\sqrt{2}\eta + 1)/\varepsilon$, thereafter remain on it and then converge to the equilibrium point along the $\boldsymbol{s}(t) = 0$ in a finite time t_s, $t_s \leq \max_{j=\alpha,\beta}(\ln(c_{j1}|i_{sj}(t_r)|^{(p-q)/p}/c_{j2} + 1)/(c_{j1}(p-q)/p))$, if the full-order fast terminal sliding manifold is selected as (51) and an integral-type output injection can be designed. Related equations can be found by*

$$\boldsymbol{w}_{s\alpha\beta} = \boldsymbol{w}_{s\alpha\beta eq} + \boldsymbol{w}_{s\alpha\beta n} \tag{52a}$$

$$\boldsymbol{w}_{s\alpha\beta eq} = \lambda \bar{\boldsymbol{i}}_{s\alpha\beta} - \boldsymbol{C}_1 \bar{\boldsymbol{i}}_{s\alpha\beta} - \boldsymbol{C}_2 \bar{\boldsymbol{i}}_{s\alpha\beta}^{p/q} \tag{52b}$$

$$\boldsymbol{w}_{s\alpha\beta n} = -\int_0^t (\varepsilon \boldsymbol{s} + k_2 \text{sgn}(\boldsymbol{s}))\text{d}t \tag{52c}$$

where $k_2 = F_{\omega 2} + \eta_2$ is the switching gain, η_2 is a positive constant and ε is used to accelerate the reaching stage.

Proof based on (41), the full-order fast terminal sliding manifold (51) can be rewritten as

$$\boldsymbol{s} = \boldsymbol{w}_{\alpha\beta} - \xi \boldsymbol{M} - \lambda \bar{\boldsymbol{i}}_{\alpha\beta} + \boldsymbol{C}_1 \bar{\boldsymbol{i}}_{\alpha\beta} + \boldsymbol{C}_2 \bar{\boldsymbol{i}}_{\alpha\beta}^{p/q} \tag{53}$$

Taking the derivative of the above $\boldsymbol{s}$ with respect to time t and substituting the output injection (52a) and (52b), it can get

$$\dot{\boldsymbol{s}} = \dot{\boldsymbol{w}}_{\alpha\beta n} - \xi \dot{\boldsymbol{M}} \tag{54}$$

Define a Lyapunov function $V = 0.5\boldsymbol{s}^T\boldsymbol{s}$. Taking the derivative of V to time t gives

$$\dot{V} = \boldsymbol{s}^T\left(\dot{\boldsymbol{w}}_{\alpha\beta n} - \xi \dot{\boldsymbol{M}}\right) \tag{55}$$

Owing to (52c), it will get:

$$\dot{V} = \boldsymbol{s}^T\left(-\varepsilon \boldsymbol{s} - k_2 \text{sgn}(\boldsymbol{s}) - \xi \dot{\boldsymbol{M}}\right) \leq -\|\boldsymbol{s}\|\left(\varepsilon\|\boldsymbol{s}\| + k_2 - \left\|\xi \dot{\boldsymbol{M}}\right\|\right) \tag{56}$$

then

$$\dot{V} + 2\varepsilon V + \sqrt{2}\eta V^{1/2} \leq 0 \tag{57}$$

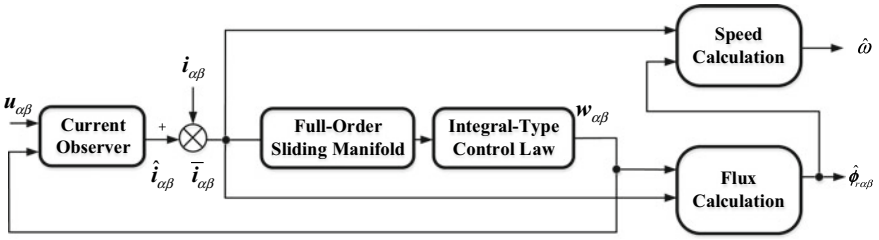

Fig. 5 Algorithm diagram speed and flux observer based on FOTSM

which means that the error dynamics of the observer (41) will converge to zero in a finite time [42]. On the sliding manifold $\boldsymbol{s}(t) = 0$, it is clear that from (51) the error dynamics (41) will behave in an ideal sliding motion:

$$\dot{\bar{\boldsymbol{i}}}_{\alpha\beta} + \boldsymbol{C}_1 \bar{\boldsymbol{i}}_{\alpha\beta} + \boldsymbol{C}_2 \bar{\boldsymbol{i}}_{\alpha\beta}^{p/q} = 0 \tag{58}$$

which is finite convergent. During the ideal sliding motion, the estimation error $\bar{\boldsymbol{i}}_{\alpha\beta}$ and its derivative will converge to zero. Hence, the proof is completed.

Similar to the derivation procedure of the linear sliding-mode (LSM) based speed/flux observer, the estimated speed/flux and the rotor flux angle can be expressed as

$$\hat{\boldsymbol{\phi}}_{r\alpha\beta} = \int_0^t \left(-\frac{1}{\xi} \boldsymbol{w}_{\alpha\beta} + \frac{L_m}{T_r} \hat{\boldsymbol{i}}_{\alpha\beta} \right) \mathrm{d}t \tag{59}$$

$$\hat{\theta}_1 = \arctan(\hat{\phi}_{r\beta} / \hat{\phi}_{r\alpha}) \tag{60a}$$

$$\hat{\omega} = \left(\hat{\phi}_{r\beta} w_\alpha - \hat{\phi}_{r\alpha} w_\beta \right) / \left(\xi \left\| \boldsymbol{\phi}_{r\alpha\beta} \right\|^2 \right) \tag{60b}$$

Remark 1 It is obvious that the output injection in the conventional LSMO is a switching signal, which can generate significant noise in the estimated $\boldsymbol{M}$. The proposed method makes the output injection of observer $\boldsymbol{w}_{\alpha\beta}$ continuous, which means the estimated speed can be smoothed. The algorithm block diagram of the proposed speed/flux observer based on FOTSM is shown in Fig. 5.

3.3 Simulation and Experimental Results

The related simulations have been carried out in Matlab/Simulink to demonstrate the effectiveness of the proposed observer. The parameters of the IM for the simulations are same as those of the related experiments, as depicted in Table 2. The observer

Table 2 Parameters of the IM

Symbol	Mean	Value
P	Rated power	3 kW
n	Rated speed	1435 rpm
n_p	Polar logarithm	2
R_s	Stator resistance	1.6 Ω
R_r	Rotor resistance	0.9 Ω
L_s	Stator inductance	163 mH
L_r	Rotor inductance	163 mH
L_m	Mutual inductance	153 mH
J	Moment of inertia	0.003 kg m^2
B	Friction factor	0.001
ϕ_{ref}	Given rotor flux	0.918 Wb

Table 3 Observer design parameters

Name	Value
LSM observer	$k = 15{,}000$
FOTSM observer	$q = 3, p = 5, \varepsilon = 200, k = 300, C_1 = \text{diag}(20,20), C_2 = \text{diag}(100,100)$

design parameters are shown in Table 3. The simulation results of the different methods (LSM and FOTSM) are shown in Figs. 6 and 7. It can be seen that the speed and flux under FOTSM can converge to the reference speed value faster and more accurately than the observer based on the LSM. Meanwhile, the speed under the LSM has a larger ripple than the FOTSM. The estimated flux angle under FOTSM tracks the actual flux angle more precisely.

To further validate the effectiveness of the proposed method, some related experiments have been carried out in an IM experimental platform based on TMS320F28335, which is loaded by one permanent magnet synchronous motor (PMSM), as shown in Fig. 8. The parameters of SPMSM have been given in Table 1, and the speed- and current-controllers parameters based on the three methods are listed in Table 3. Figures 9, 10 and 11 show the results of the observation experiments. It can be seen from Figs. 9 and 10 that the estimated speed/flux can quickly track the actual speed/flux under FOTSMO without using any low-pass filters. Figure 11 shows that the comparisons of rotor flux phase and amplitude estimation. It can be concluded that the FOTSM has a more precise estimation in phase. As depicted in Fig. 11b, the observation of the amplitude estimation under DC has 0.1 Wb steady-state error. However, the flux estimation under the FOTSM is smoother than that under the LSM, which further indicates the FOTSM based speed/flux observer has better accuracy than the LSM.

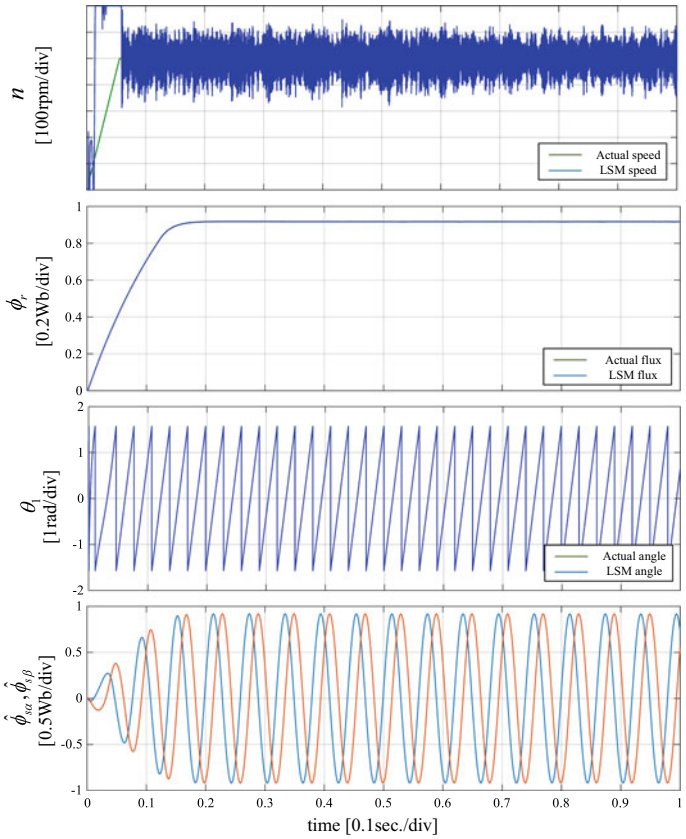

Fig. 6 LSM based speed estimation under parameters variations in simulation

4 Full-Order Terminal Sliding-Mode Control of IM

This section introduces the design and the stability proof of the novel backstepping based chattering-free FOTSM controllers proposed for the IM sensorless control system. The control objective is to force both the outer-loop tracking error $\boldsymbol{e}_o$ and the inner-loop current tracking error $\boldsymbol{e}_i$ to converge to zero rapidly rather than the neighborhood around zero. By designing the virtual control law $\tilde{\boldsymbol{u}}$, the unmatched uncertainties in the outer-loop can be completely compensated. And the actual control law $\boldsymbol{u}_i$ is used to deal with the matched uncertainty $\boldsymbol{\rho}_i(t,\ \boldsymbol{x}_o,\ \boldsymbol{i})$. The simple diagram of the control method for the IM system is shown in Fig. 12.

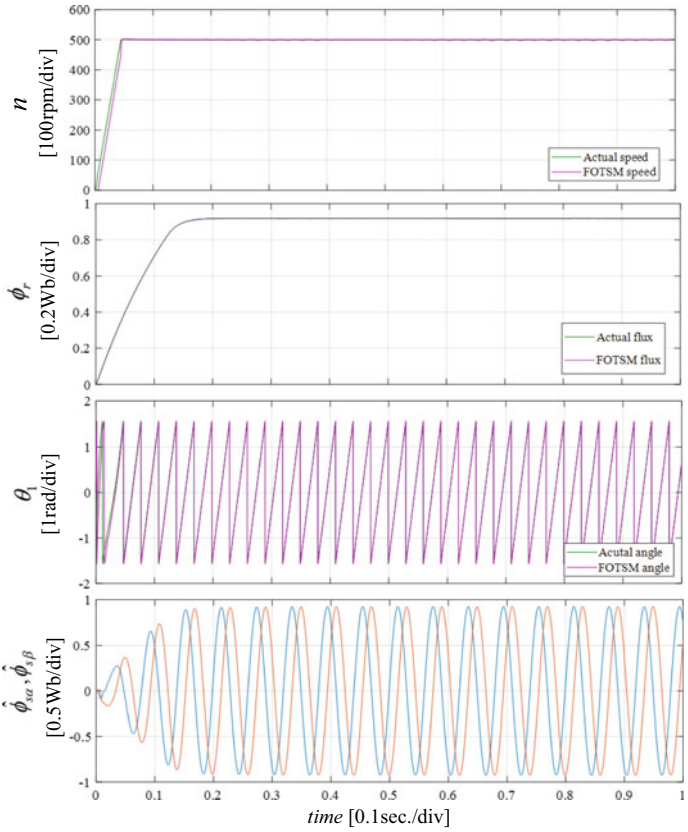

Fig. 7 FOTSM based speed estimation under parameters variations in simulation

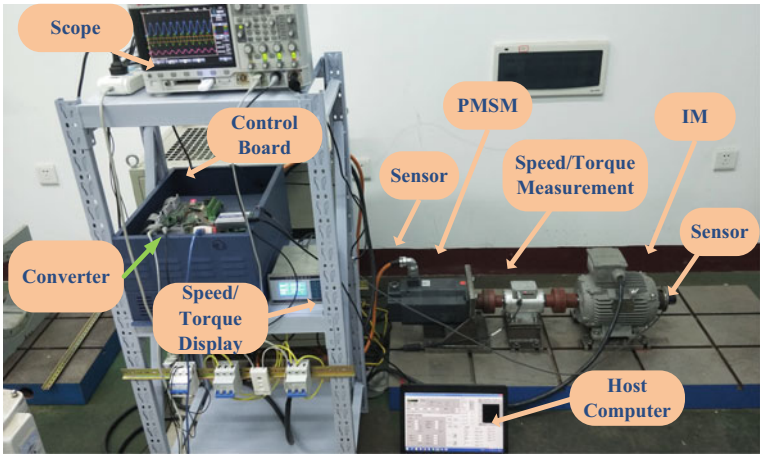

Fig. 8 The IM-PMSM experiment platform

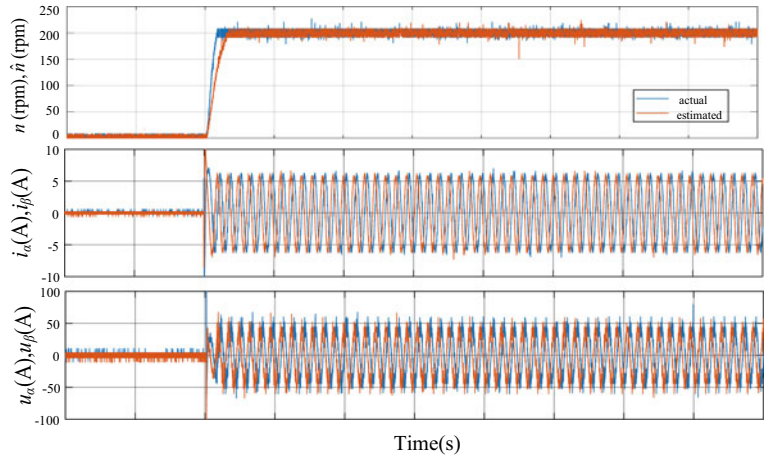

Fig. 9 FOTSM based speed estimation under parameter variations in experiment

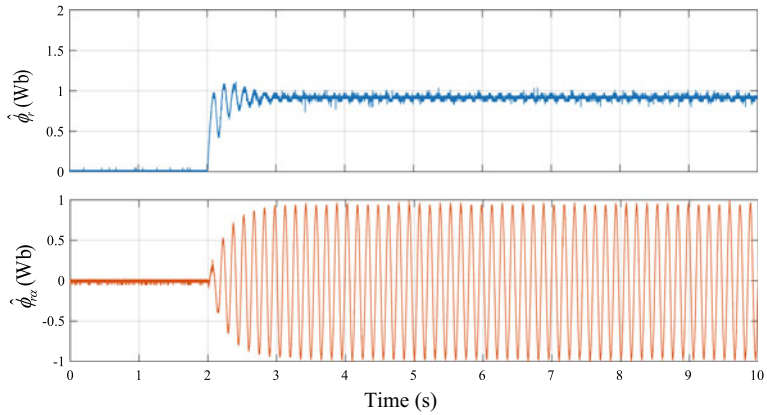

Fig. 10 FOTSM based rotor flux estimation under parameter variations in experiment

4.1 Outer-Loop Speed/Flux Controllers Design

A full-order liner sliding manifold $\boldsymbol{s}_o \in R^2$ is designed for the outer-loop speed/flux error dynamics (37a):

$$\boldsymbol{s}_o = \dot{\boldsymbol{e}}_o + \boldsymbol{C}_1 \boldsymbol{e}_o \tag{61}$$

where $\boldsymbol{C}_1 = \text{diag}(c_{11}, c_{12})$ is positive diagonal matrix.

Proposition 3 *The speed/flux error dynamics of the outer-loop subsystem* (37a) *can be forced to converge to zero after the current tracking error* e_i *and its derivative* $\dot{\boldsymbol{e}}_i$

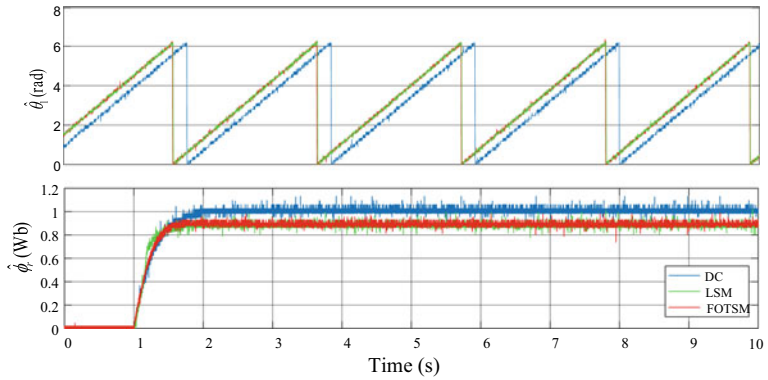

Fig. 11 Comparison of rotor flux amplitude and phase estimation

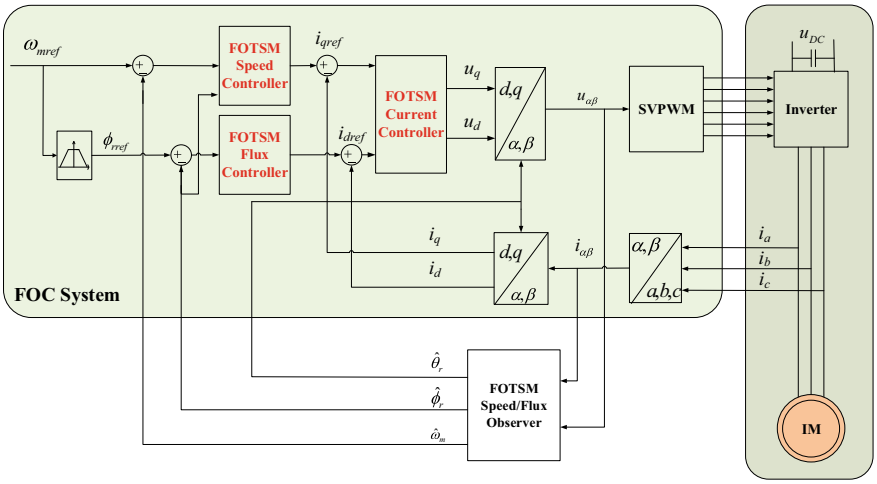

Fig. 12 Simple diagram of the control method for the IM system

reach its equilibrium point, if the full-order sliding manifold (61) is selected and an integral virtual control law with its related adaptive gain can be designed. Related equations can be found by

$$\tilde{\boldsymbol{u}}=\tilde{\boldsymbol{u}}_{eq}+\tilde{\boldsymbol{u}}_{n} \tag{62a}$$

$$\tilde{\boldsymbol{u}}_{eq} = \boldsymbol{f}_1(t, \boldsymbol{e}_o) + \boldsymbol{C}_1\boldsymbol{e}_o \tag{62b}$$

$$\tilde{\boldsymbol{u}}_n = \int_0^t k_o \mathrm{sgn}(\boldsymbol{s}_o)\mathrm{d}t \tag{62c}$$

$$k_o(t) = \frac{M_\delta M_{deq}(t) + M_{d\rho}(t) + \eta_o}{1 - M_\delta} \tag{62d}$$

where M_δ and $M_{d\rho}$ are defined by (23) and (26), and M_{deq} is the upper bound of the derivative of the equivalent control law, and $\eta_o > 0$ a constant.

Proof Considering the control law (62a) and (62b), the full-order linear sliding manifold (61) is rewritten as

$$\begin{aligned} \boldsymbol{s}_o &= \dot{\boldsymbol{e}}_o + \boldsymbol{C}_1 \boldsymbol{e}_o = \boldsymbol{f}_1(t, \boldsymbol{e}_o) - \tilde{\boldsymbol{u}} + \boldsymbol{g}_1 \boldsymbol{e}_i + \boldsymbol{\rho}_o(t, \boldsymbol{x}_o, \boldsymbol{i}) + \boldsymbol{C}_1 \boldsymbol{e}_o \\ &= -\tilde{\boldsymbol{u}}_n - \boldsymbol{\delta}\tilde{\boldsymbol{u}} + \boldsymbol{g}_1 \boldsymbol{e}_i + \boldsymbol{\rho}_o(t, \boldsymbol{x}_o, \boldsymbol{i}) \end{aligned} \tag{63}$$

Define a Lyapunov function $V = 0.5\boldsymbol{s}_o^T \dot{\boldsymbol{s}}_o$. Taking the derivative of V to time t gives

$$\begin{aligned} \dot{V} &= \boldsymbol{s}_o^T \dot{\boldsymbol{s}}_o = -\boldsymbol{s}_o^T \dot{\tilde{\boldsymbol{u}}}_n - \boldsymbol{s}_o^T \delta\dot{\tilde{\boldsymbol{u}}} + \boldsymbol{s}_o^T \dot{\boldsymbol{\rho}} + \boldsymbol{s}_o^T \boldsymbol{g}_1 \dot{\boldsymbol{e}}_i \\ &= -\boldsymbol{s}_o^T \dot{\tilde{\boldsymbol{u}}}_n - \boldsymbol{s}_o^T \dot{\tilde{\boldsymbol{u}}}_n - \boldsymbol{s}_o^T \delta\dot{\tilde{\boldsymbol{u}}}_{eq} + \boldsymbol{s}_o^T \dot{\boldsymbol{\rho}} + \boldsymbol{s}_o^T \boldsymbol{g}_1 \dot{\boldsymbol{e}}_i \end{aligned} \tag{64}$$

Considering the integral switching control law (62c) gives

$$\begin{aligned} \dot{V} &\le -k_o \|\boldsymbol{s}_o\| + k_o \|\boldsymbol{s}_o\| \|\boldsymbol{\delta}\| + \|\boldsymbol{s}_o\| \|\boldsymbol{\delta}\| \left\| \dot{\tilde{\boldsymbol{u}}}_{eq} \right\| + \|\boldsymbol{s}_o\| \|\dot{\boldsymbol{\rho}}\| + \boldsymbol{s}_o^T \boldsymbol{g}_1 \dot{\boldsymbol{e}}_i \\ &\le -k_o(1 - M_\delta)\|\boldsymbol{s}_o\| + M_\delta \|\boldsymbol{s}_o\| \left\| \dot{\tilde{\boldsymbol{u}}}_{eq} \right\| + \|\boldsymbol{s}_1\| M_{d\rho} + \boldsymbol{s}_o^T \boldsymbol{g}_o \dot{\boldsymbol{e}}_i \end{aligned} \tag{65}$$

Based on (62b), taking the derivative of the equivalent virtual control law yields

$$\dot{\tilde{\boldsymbol{u}}}_{eq} = \begin{bmatrix} \ddot{\omega}_{m\,\mathrm{ref}} + c_{11}\dot{e}_\omega \\ (1/T_{r0})\dot{\phi}_r + c_{12}\dot{e}_\phi \end{bmatrix} \tag{66}$$

then the upper bound of the equivalent virtual control law can be obtained

$$\left\| \dot{\tilde{\boldsymbol{u}}}_{eq} \right\| \le M_{deq} = \sqrt{M_{du_{\omega eq}}^2 + M_{du_{\phi eq}}^2} \tag{67}$$

where $M_{du_{\omega eq}}$ and $M_{du_{\phi eq}}$ are positive known functions:

$$\begin{aligned} M_{du_{\omega eq}}(t) = {} & c_{11} n_p F_{Lm/JLr} \phi_r \left(1 + M_{\delta_\omega}\right) i_{q\,\max} + |\ddot{\omega}_{m\,\mathrm{ref}}| \\ & + G_{d(T_L/J)} + c_{11}\left(|\dot{\omega}_{m\,\mathrm{ref}}| + G_{T_L/J} + M_{\rho_\omega}\right) \end{aligned} \tag{68}$$

$$M_{du_{\phi eq}}(t) = \left|\left(\frac{1}{T_{r0}}\right) - c_{12}\right|\left(\left(\frac{1}{T_{r0}} + M_{1/T_r}\right)|\phi_r| + \frac{L_{m0}}{T_{r0}}\left(1 + M_{\delta_\phi}\right)i_{d\max}\right) \quad (69)$$

then the derivative of V satisfies

$$\dot{V} \leq -\|\boldsymbol{s}_o\|\left(k_o(1 - M_\delta) - M_\delta M_{deq} - M_{d\rho}\right) + \boldsymbol{s}_o^T \boldsymbol{g}\dot{\boldsymbol{e}}_i \quad (70)$$

Substituting the adaptive gain (62d) into the above gives

$$\dot{V} = \boldsymbol{s}_o^T \dot{\boldsymbol{s}}_o \leq -\eta_o\|\boldsymbol{s}_o\| + \boldsymbol{s}_o^T \boldsymbol{g}\dot{\boldsymbol{e}}_i \leq -\eta_o\sqrt{2}V^{1/2} + \boldsymbol{s}_o^T \boldsymbol{g}\dot{\boldsymbol{e}}_i \quad (71)$$

Considering that it will be proofed $\dot{\boldsymbol{e}}_i$ can converge to zero by the following Theorem 3, it can be obtained that.

$$\dot{V} \leq -\sqrt{2}\eta_o V^{1/2} < 0, \quad \text{for } V \neq 0. \quad (72)$$

which illustrates that under the virtual control law $\tilde{\boldsymbol{u}}$ in (62) compensating the unmatched uncertainty completely, the outer-loop tracking error dynamics in the subsystem (37a) can reach the full-order linear sliding manifold $\boldsymbol{s}_o = 0$ in a finite time t_r, $t_r \leq \|\boldsymbol{s}_o(0)\|/\eta$, and remain on it thereafter. Then $\boldsymbol{e}_o$ can converge to zero. Hence, the proof is completed.

Remark 2 The virtual control law designed in Proposition 3 is smoothed by integral-type switching law, so $\boldsymbol{i}_{\text{ref}}$ are smooth signals. It is clear that the chattering in the $\boldsymbol{i}_{\text{ref}}$ is eliminated, which ensures the fast and accurate current tracking in the inner-loop, and avoids the singularity caused by the derivation of $\boldsymbol{i}_{\text{ref}}$ in the actual control law.

4.2 Inner-Loop Currents Controllers Design

Let the tracking error vector of the currents $\boldsymbol{e}_i = \boldsymbol{i}_{\text{ref}} - \boldsymbol{i}$, then according to the current subsystem (37b), the current error dynamics can be given as:

$$\dot{\boldsymbol{e}}_i = \dot{\boldsymbol{i}}_{\text{ref}} - (\boldsymbol{F}_0(t, \boldsymbol{x}_o, \boldsymbol{i}) + \boldsymbol{G}_0\boldsymbol{P})\boldsymbol{i} - \boldsymbol{u}_i - \Delta\boldsymbol{G}\boldsymbol{G}_0^{-1}\boldsymbol{u}_i - \boldsymbol{\rho}_i(t, \boldsymbol{x}_o, \boldsymbol{i}) \quad (73)$$

If the traditional reduced-order SMC is utilized to design the control law for the inner-loop current tracking error subsystem (37b), $\boldsymbol{e}_i$ can only be guaranteed to converge to zero, but its derivative $\dot{\boldsymbol{e}}_i$ cannot. Therefore, to implement Proposition 3, i.e., $\boldsymbol{e}_i$ and $\dot{\boldsymbol{e}}_i$ can be forced to converge to their equilibrium in a finite time, a full-order terminal sliding manifold $\boldsymbol{s}_i \in R^2$ is designed as

$$\boldsymbol{s}_i = \dot{\boldsymbol{e}}_i + \boldsymbol{C}_2\boldsymbol{e}_i^{q/p} \quad (74)$$

where $\boldsymbol{C}_2 = \text{diag}\,(c_{21}, c_{22})$ is a positive diagonal matrix, and q and p are odds and satisfy $0<q/p<1$.

Theorem 3 *The error dynamics (73) can be forced to reach the terminal sliding manifold $\boldsymbol{s}_i(t) = 0$ in a finite time from any nonzero initial condition $\boldsymbol{s}_i(0) \neq 0$, $t \geq t_r$, $t_r \leq \|\boldsymbol{s}_i(0)\|/\eta_i$, and then $\boldsymbol{e}_i$ and $\dot{\boldsymbol{e}}_i$ can converge to zero along sliding manifold $\boldsymbol{s}_i = 0$, in a finite time t_s, $t_s \leq \max(p/(c_{21}(p-q))|e_{id}(t_{rd})|^{1-q/p},\ p/(c_{22}(p-q))\left|e_{iq}(t_{rq})\right|^{1-q/p})$, i.e., $\boldsymbol{i}_s$ can track its reference $\boldsymbol{i}_{ref}$ within a finite time, if the full-order terminal sliding manifold $\boldsymbol{s}_i$ is chosen as (74), virtual control law $\tilde{\boldsymbol{u}}_2$ in Proposition 3 is adopted, and an integral-type actual control law $\boldsymbol{u}_i$ is designed. Related equations can be found by*

$$\boldsymbol{u}_i = \boldsymbol{u}_{ieq} + \boldsymbol{u}_{in} \tag{75a}$$

$$\boldsymbol{u}_{ieq} = -(\boldsymbol{F}_0(t,\ \boldsymbol{x}_o,\ \boldsymbol{i}) + \boldsymbol{G}_0\boldsymbol{P})\boldsymbol{i} + \boldsymbol{C}_2\boldsymbol{e}_i^{q/p} + \boldsymbol{g}^{-1}\left(\boldsymbol{C}_1\boldsymbol{f}_1(t, \boldsymbol{e}_o) - \boldsymbol{C}_1\boldsymbol{g}_1\boldsymbol{i} + k_o\text{sgn}(\boldsymbol{s}_o)\right) \tag{75b}$$

$$\boldsymbol{u}_{in} = \int_0^t k_i(t)\text{sgn}(\boldsymbol{s}_2)\text{d}t \tag{75c}$$

$$k_i(t) = \frac{(M_K/K_0)M_{du_{ieq}}(t) + M_{d\rho_i}(t) + \left\|\boldsymbol{g}^{-1}\right\|\|\boldsymbol{C}_1\|M_{d\rho}(t) + \eta_i}{1 - (M_K/K_0)} \tag{75d}$$

where K_0, M_K and $M_{d\rho i}$ are defined by (14), (16) and (34) in the adaptive gain, $M_{du_{ieq}}$ represents the upper bound of the derivative of $\boldsymbol{u}_{ieq}$ satisfying $\left|\dot{\boldsymbol{u}}_{ieq}\right| \leq M_{du_{ieq}}$,

$$\begin{aligned} M_{du_{ieq}}(t) = {} & (\lambda_0 + \max(c_{21}, c_{22}))(K_0 + M_K)\left(\sqrt{2}u_{\max} + \|\boldsymbol{D}_0\| + \frac{\omega_1}{K_0}\|\boldsymbol{i}\|\right) \\ & + (\lambda_0 + \max(c_{21}, c_{22}))\left(\lambda_0\|\boldsymbol{i}\| + M_{\rho_i}\right) \end{aligned} \tag{76}$$

and $\eta_i > 0$ is a positive constant.

Proof From the inner-loop current tracking error dynamics (73), the full-order terminal sliding manifold (74) can be reformed into

$$\boldsymbol{s}_i = \dot{\boldsymbol{i}}_{\text{ref}} - (\boldsymbol{F}_0(t, \boldsymbol{x}_o, \boldsymbol{i}) + \boldsymbol{G}_0\boldsymbol{P})\boldsymbol{i} - \boldsymbol{u}_i - \Delta\boldsymbol{G}\boldsymbol{G}_0^{-1}\boldsymbol{u}_i - \boldsymbol{\rho}_i(t, \boldsymbol{x}_o, \boldsymbol{i}) + \boldsymbol{C}_2\boldsymbol{e}_i^{q/p} \tag{77}$$

With the virtual control law (62), it can get

$$\begin{aligned} \boldsymbol{s}_i = {} & \boldsymbol{g}_1^{-1}\left(\dot{\boldsymbol{f}}_1(t, \boldsymbol{e}_o) + k_o\text{sgn}(\boldsymbol{s}_o) + \boldsymbol{C}_1\dot{\boldsymbol{e}}_o\right) - (\boldsymbol{F}_0(t, \boldsymbol{x}_o, \boldsymbol{i}) + \boldsymbol{G}_0\boldsymbol{P})\boldsymbol{i} \\ & - \boldsymbol{u}_i - \Delta\boldsymbol{G}\boldsymbol{G}_0^{-1}\boldsymbol{u}_i - \boldsymbol{\rho}_i(t, \boldsymbol{x}_o, \boldsymbol{i}) + \boldsymbol{C}_2\boldsymbol{e}_i^{q/p} \end{aligned} \tag{78}$$

Substituting (37b) into the above yields

$$\begin{aligned} \boldsymbol{s}_i = \boldsymbol{g}_1^{-1}\big(\dot{\boldsymbol{f}}_1(t,\boldsymbol{e}_o) + k_o \mathrm{sgn}(\boldsymbol{s}_o) + \boldsymbol{C}_1\big(\boldsymbol{f}_1(t,\boldsymbol{e}_o) - \boldsymbol{g}_1\boldsymbol{i} + \boldsymbol{\rho}_o(t,\boldsymbol{x}_o,\boldsymbol{i})\big)\big) \\ - (\boldsymbol{F}_0(t,\boldsymbol{x}_o,\boldsymbol{i}) + \boldsymbol{G}_0\boldsymbol{P})\boldsymbol{i} - \boldsymbol{u}_i - \Delta\boldsymbol{G}\boldsymbol{G}_0^{-1}\boldsymbol{u}_i - \boldsymbol{\rho}_i(t,\boldsymbol{x}_o,\boldsymbol{i}) + \boldsymbol{C}_2\boldsymbol{e}_i^{q/p} \end{aligned} \tag{79}$$

Considering the actual control law (75a) and (75b), it can get

$$\boldsymbol{s}_i = -\boldsymbol{u}_{in} - \Delta\boldsymbol{G}\boldsymbol{G}_0^{-1}\boldsymbol{u}_i - \boldsymbol{\rho}_i(t,\ \boldsymbol{x}_o,\ \boldsymbol{i}) + \boldsymbol{g}_1^{-1}\dot{\boldsymbol{f}}_1(t,\boldsymbol{e}_o) + \boldsymbol{g}_1^{-1}\boldsymbol{C}_1\boldsymbol{\rho}_o(t,\ \boldsymbol{x}_o,\ \boldsymbol{i}) \tag{80}$$

Consider a Lyapunov function $V = 0.5\boldsymbol{s}_i^T\dot{\boldsymbol{s}}_i$. Taking the derivative of V to time t yields

$$\dot{V} = \boldsymbol{s}_i^T\dot{\boldsymbol{s}}_i = -\boldsymbol{s}_i^T\dot{\boldsymbol{u}}_{in} - \boldsymbol{s}_i^T\Delta\boldsymbol{G}\boldsymbol{G}_0^{-1}\dot{\boldsymbol{u}}_i - \boldsymbol{s}_i^T\dot{\boldsymbol{\rho}}_i + \boldsymbol{s}_i^T\boldsymbol{g}^{-1}\ddot{\boldsymbol{f}}_1 + \boldsymbol{s}_i^T\boldsymbol{g}^{-1}\boldsymbol{C}_1\dot{\boldsymbol{\rho}}_o \tag{81}$$

then based on (37b), it will get

$$\dot{V} = -\boldsymbol{s}_i^T\dot{\boldsymbol{u}}_{in} - \boldsymbol{s}_i^T\Delta\boldsymbol{G}\boldsymbol{G}_0^{-1}\dot{\boldsymbol{u}}_i - \boldsymbol{s}_i^T\dot{\boldsymbol{\rho}}_i + \boldsymbol{s}_i^T\boldsymbol{g}^{-1}\ddot{\boldsymbol{f}}_1 + \boldsymbol{s}_i^T\boldsymbol{g}^{-1}\boldsymbol{C}_1\Big(\dot{\boldsymbol{\rho}} - \delta\dot{\tilde{\boldsymbol{u}}}\Big) \tag{82}$$

From (75a) it can be obtained:

$$\begin{aligned} \dot{V} &= -\boldsymbol{s}_i^T\Big(\dot{\boldsymbol{u}}_{in} + \Delta\boldsymbol{G}\boldsymbol{G}_0^{-1}\dot{\boldsymbol{u}}_{in} + \Delta\boldsymbol{G}\boldsymbol{G}_0^{-1}\dot{\boldsymbol{u}}_{ieq} + \dot{\boldsymbol{\rho}} - \boldsymbol{g}^{-1}\ddot{\boldsymbol{f}}_1 - \boldsymbol{g}^{-1}\boldsymbol{C}_1\Big(\dot{\boldsymbol{\rho}} - \delta\dot{\tilde{\boldsymbol{u}}}\Big)\Big) \\ &\le \|\boldsymbol{s}_i\|\big(-k_i + k_i\|\Delta\boldsymbol{G}\|\big\|\boldsymbol{G}_0^{-1}\big\| + \|\Delta\boldsymbol{G}\|\big\|\boldsymbol{G}_0^{-1}\big\|\big\|\dot{\boldsymbol{u}}_{ieq}\big\| \\ &\quad + \big\|\dot{\boldsymbol{\rho}}_i\big\| + \big\|\boldsymbol{g}_1^{-1}\big\|\big\|\ddot{\boldsymbol{f}}\big\| + \big\|\boldsymbol{g}^{-1}\big\|\|\boldsymbol{C}_1\|\Big(\|\delta\|\Big\|\dot{\tilde{\boldsymbol{u}}}\Big\| + \|\dot{\boldsymbol{\rho}}\|\Big)\Big) \end{aligned} \tag{83}$$

then it can be assumed that

$$\Big\|\dot{\tilde{\boldsymbol{u}}}\Big\| \le \Big\|\dot{\tilde{\boldsymbol{u}}}_{eq}\Big\| + \Big\|\dot{\tilde{\boldsymbol{u}}}_n\Big\| \le M_{deq} + \sqrt{2}k_i \tag{84}$$

With the adaptive switching gain (75d), then

$$\dot{V} \le -\sqrt{2}\eta_2 V^{1/2} < 0 \quad \text{for} \quad V \ne 0. \tag{85}$$

Similar to the proof of Theorem 2, it can be seen that the current tracking error dynamics in the inner-loop (73) can reach the ideal sliding-mode $\boldsymbol{s}_i(t) = 0$ in a finite time $t_r \le \|\boldsymbol{s}_2(0)\|/\eta_i$. Hence, $\boldsymbol{e}_i$ and $\dot{\boldsymbol{e}}_i$ will converge to zero in a finite time, and the tracking error $\boldsymbol{e}_o$ in the outer-loop can converge to zero owing to Propositions 3. The diagram of FOTSM method for the IM control system is shown in Fig. 13.

Remark 3 The proposed chattering-free FOTSM method can continuously make the high-frequency switching signal using the integral control law. Therefore, this method ensures that the control system has a strong disturbance rejection capability

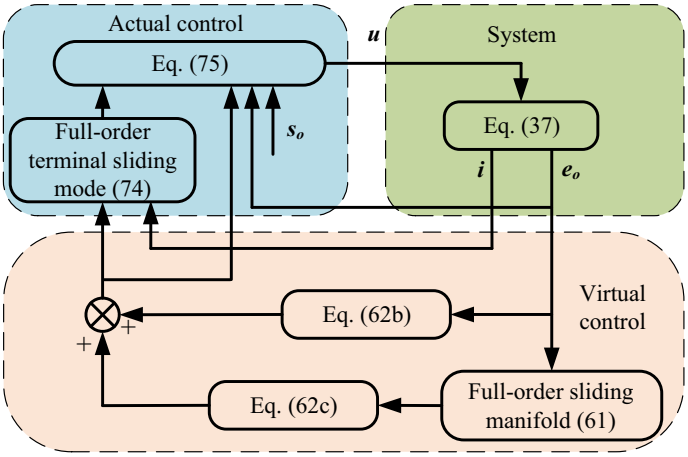

Fig. 13 The diagram of FOTSM method for the IM control system

to match uncertainties and finite-time convergence. Due to the smooth actual control signal $\boldsymbol{u}_{dq}$, the high sinusoidal actual PWM voltage signal $\boldsymbol{u}_{ABC}$ can be generated.

4.3 Simulation and Experimental Results

To validate the feasibility of the proposed controllers, the related simulations have been done. The parameters of the IM are shown in Table 2 and the controller design parameters are shown in Table 4. The simulation results of the three control methods (PI, LSM and FOTSM) are shown in Figs. 14, 15 and 16. It can be seen that the speed under the FOTSM nearly has no overshoot and the speed ripple is much shorter than that under LSM. The settling time of the speed under FOTSM is smaller than those under the other two methods, which indicates that the FOTSM has a

Table 4 Controller design parameters

Control	Sliding manifold	Switching control gain
Speed LSM	$s = 10e_{\omega}$	$k = 1100$
Flux LSM	$s = 10e_{\phi}$	$k = 50$
i_q LSM	$s = 5e_{iq}$	$k = 3000$
i_q LSM	$s = 5e_{id}$	$k = 3000$
Outer-loop FOTSM	$s = \dot{e}_o + C_1 e_o$	$C_1 = \text{diag}(600,60)$, $\eta_o = 1$
Inner-loop FOTSM	$s = \dot{e}_i + C_2 e_i^{p/q}$	$C_2 = \text{diag}(500,10)$, $q = 5$, $p = 7$, $\eta_i = 10$

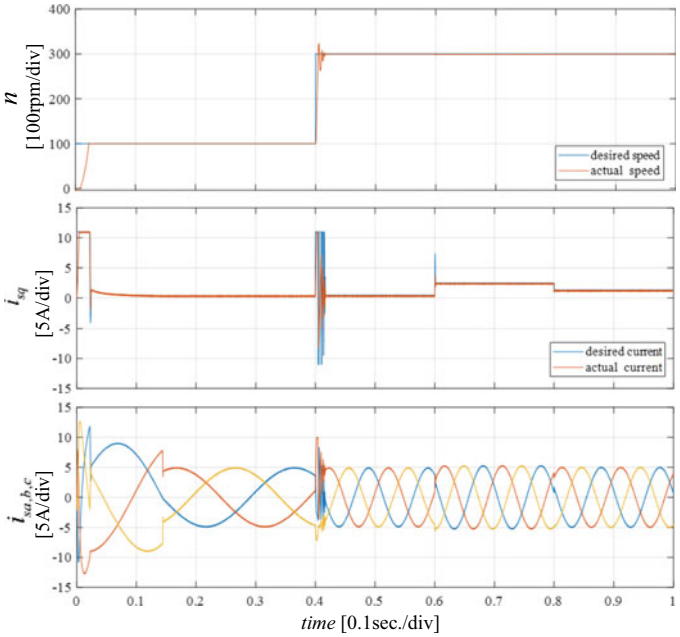

Fig. 14 Dynamic response of PI controllers based *q*-subsystem under external disturbance and parameter variations

Fig. 15 Dynamic response of LSM controllers based *q*-subsystem under external disturbance and parameter variations

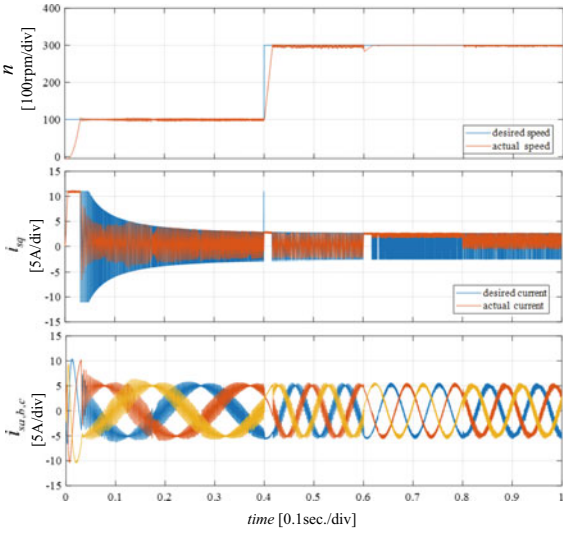

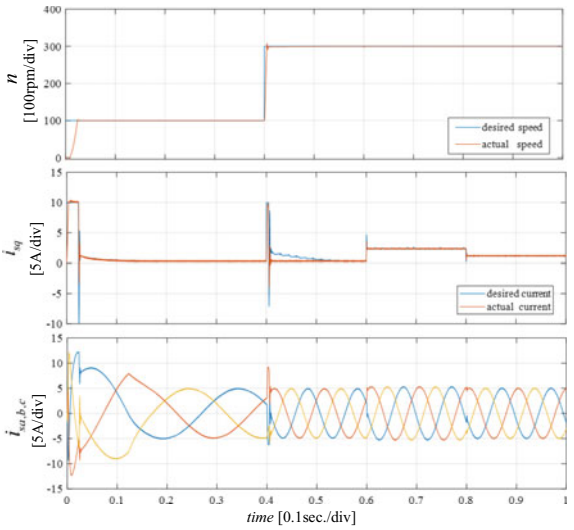

Fig. 16 Dynamic response of FOTSM controllers based *q*-subsystem under external disturbance and parameter variations

better anti-disturbance and accuracy. Meanwhile, the current ripple under FOTSM is significantly smaller than LSM, which means the chattering is eliminated under the control of the FOTSM. Moreover, some related experiments have been done in the IM-PMSM experimental platform to demonstrate the superiority of the proposed method. The speed and *q*-axis current responses under the three control methods during the process of the start-up and load adding are shown in Figs. 17, 18 and 19. It can be seen that only the PI has a 25% overshoot while the other two methods have little and the proposed method has the fastest settling time among the three methods. Meanwhile, the ripple of the current and voltage under FOTSM is much smaller than those under LSM, which indicates that the chattering is attenuated. The load (1Nm) is loaded at 2 s and removed at 10 s. It can be seen that the speed fluctuation under FOTSM is much smaller than those under the other two methods. From the above all, it can be concluded that the FOTSM has a better dynamic performance in accuracy, rapidness and anti-disturbance.

5 Summary

In the chapter, a novel integral-type FOTSM control method has been proposed to implement high precision and strong anti-disturbance sensorless speed control for the FOC system of the IM. The influences of parameter perturbations and external disturbance on the controllers are adequately analyzed. The accurate speed and rotor flux observations enhance the robustness and dynamic response of the IM sensorless control system under FOTSMO. With the accurate feedback of the speed and rotor flux, the FOTSM based speed, flux- and current controllers are designed to

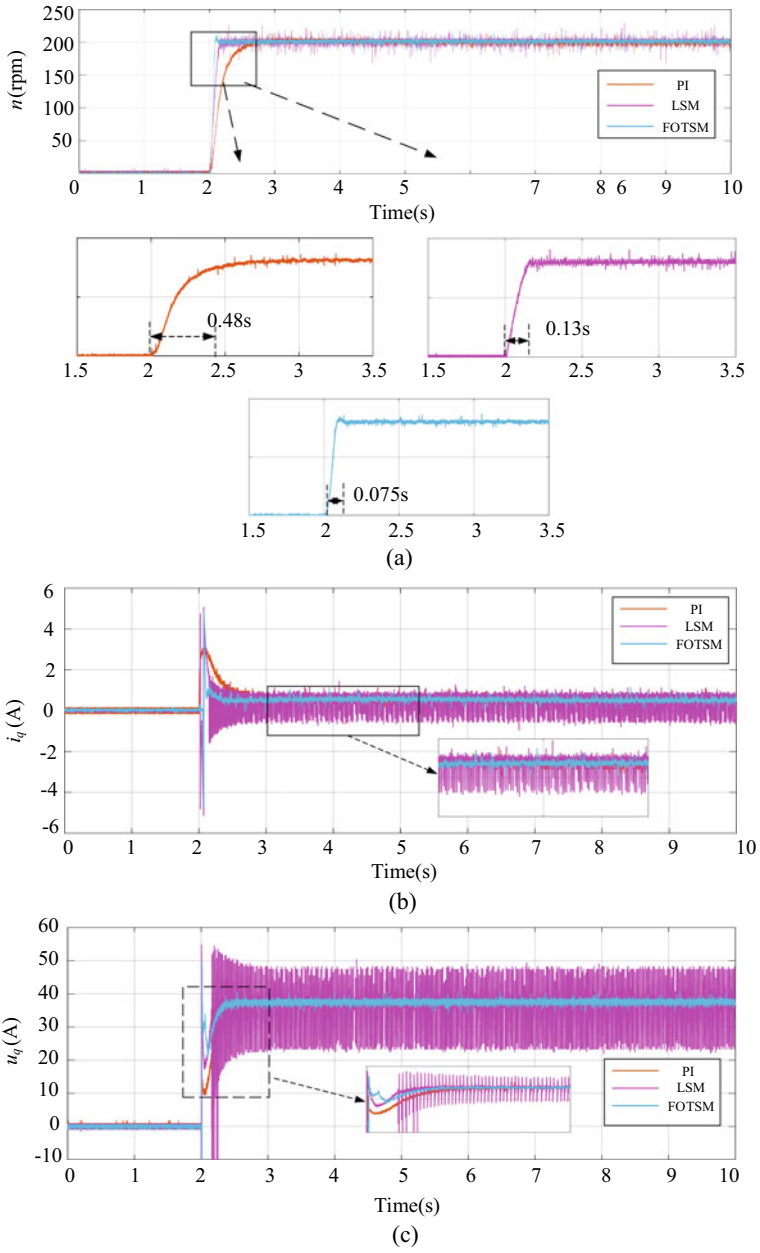

Fig. 17 The speed and q-axis current responses under PI, LSM and FOTSM during the start-up process. **a** Speed, **b** q-axis current, **c** q-axis voltage

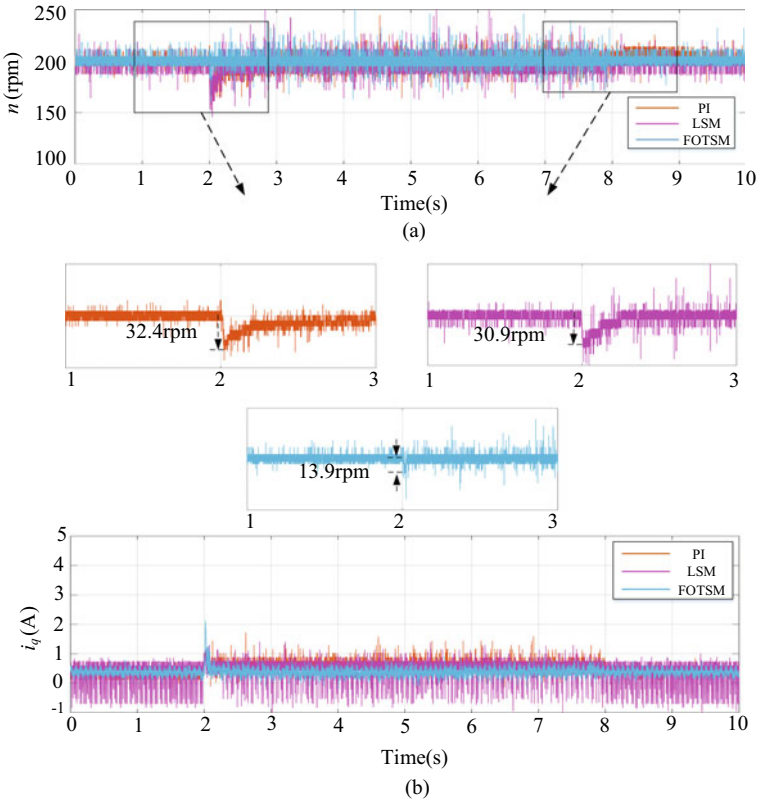

Fig. 18 The speed and q-axis current responses under PI, LSM and FOTSM with the load (1Nm). **a** Speed, **b** q-axis current

improve the accuracy, robustness and rapidness of the FOC system for the IM. By the use of the virtual control technique, the unmatched uncertainties can be thoroughly compensated. Owing to the integral-type control law and the adaptive gain, the overestimation of the upper bound for the uncertainties can be avoided and the chattering can be eliminated. Simulation and experimental results have validated the effectiveness and feasibility of the proposed method.

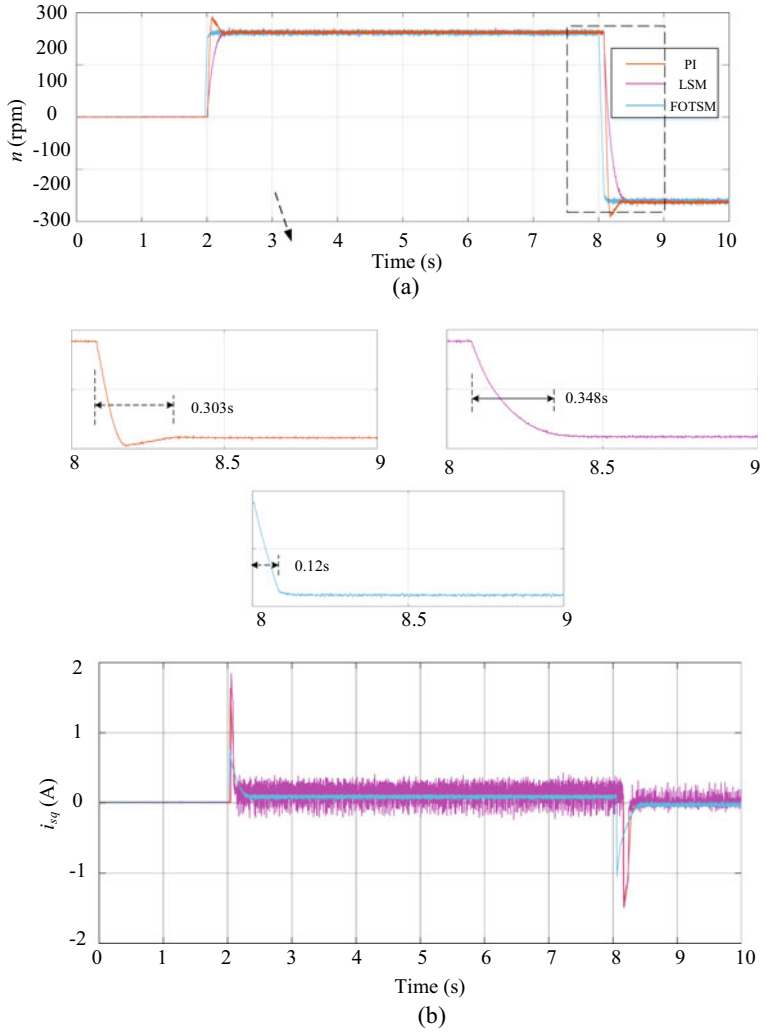

Fig. 19 The speed and q-axis current responses under PI, LSM and FOTSM during the speed-reverse process. **a** Speed, **b** q-axis current

References

1. C. Luo, B. Wang, Y. Yu, C. Chen, Z. Huo, D. Xu, Decoupled stator resistance estimation for speed-sensorless induction motor drives considering speed and load torque variations. IEEE J. Emerg. Sel. Top. Power Electron. **8**(2), 1193–1207 (2020)
2. A. Datta, G. Poddar, Improved low-frequency operation of hybrid inverter for medium-voltage induction motor drive under V/F and vector control mode of operation. IEEE J. Emerg. Sel. Top. Power Electron. **8**(2), 1248–1257 (2020)
3. F. Zhang, A new high power factor AC-AC inverter. IEEE Power Electron Lett. **1**(5), 10–13 (2000)

4. Y. Feng, J. Zheng, X. Yu, N.V. Truong, Hybrid terminal sliding-mode observer design method for a permanent-magnet synchronous motor control system. IEEE Trans. Ind. Electron. **56**(9), 3424–3431 (2009)
5. A. Ammar, A. Bourek, A. Benakcha, Sensorless SVM-direct torque control for induction motor drive using sliding-mode observers. J. Control Autom. Electr. Syst. **28**(2), 189–202 (2017)
6. M.S. Zaky, M.K. Metwaly, H.Z. Azazi, S.A. Deraz, A new adaptive SMO for speed estimation of sensorless induction motor drives at zero and very low frequencies. IEEE Trans. Ind. Electron. **65**(9), 6901–6911 (2018)
7. O. Barambones, P. Alkorta, Position control of the induction motor using an adaptive sliding-mode controller and observers. IEEE Trans. Ind. Electron. **61**(12), 6556–6565 (2014)
8. M. Morawiec, A. Lewicki, Speed observer structure of induction machine based on sliding super-twisting and backstepping techniques. IEEE Trans. Ind. Info. **17**(2), 1122–1131 (2021)
9. L. Shen, L. Emil, J. Martin, FCS-MPC-based current control of a five-phase induction motor and its comparison with PI-PWM control. IEEE Trans. Ind. Electron. **61**(1), 149–163 (2014)
10. T. Jakub, L.V. Quoc, S. Vaclav, P. Zdenek, Adaptive speed control of induction motor drive with inaccurate model. IEEE Trans. Ind. Electron. **65**(11), 8532–8542 (2018)
11. A. Abdelkarim, B. Abdelhamid, B. Amor, Adaptive MRAC-based direct torque control with SVM for sensorless induction motor using adaptive observer. Int. J. Adv. Manuf. Technol. **91**(5–8), 1631–1641 (2017)
12. T. Murata, T. Tsuchiya, I. Takeda, Vector control for induction machine on the application of optimal control theory. IEEE Trans. Ind. Electron. **37**(4), 283–290 (1990)
13. A. Matsushita, T. Tsuchiya, Decoupled preview control system and its application to induction motor drive. IEEE Trans. Ind. Electron. **42**(1), 50–57 (1995)
14. R. Gerasimos, B. Krishna, S. Dimitrios, Nonlinear optimal control for ship propulsion with the use of an induction motor and a drivetrain. *MATEC Web Conf*, vol. 188, no. 1, (2018)
15. H. Yang, Y. Zhang, P.D. Walker, A method to start rotating induction motor based on speed sensorless model-predictive control. IEEE Trans. Energy Convers. **32**(1), 359–368 (2017)
16. H. Gao, B. Wu, D. Xu, M. Pande, R.P. Aguilera, Common-mode-voltage-reduced model-predictive control scheme for current-source-converter-fed induction motor drives. IEEE Trans. Power Electron. **32**(6), 4891–4904 (2017)
17. F. Mehazzem, A. Reama, Comparative study of integral and classical backstepping controllers in IFOC of induction motor fed by voltage source inverter. Int. J. Hydrogen Energy **42**(28), 17953–17964 (2017)
18. B.R. Chiheb, F. Fethi, Z. Abderrahmen, C. Abdelkader, A novel adaptive control method for induction motor based on backstepping approach using dSpace DS 1104 control board. Mech. Syst. Signal Process **100**, 466–481 (2018)
19. R. Christian, R. Jose, K. Samir, V. Felipe, Multiobjective fuzzy-decision-making predictive torque control for an induction motor drive, in *IEEE Transaction on Power Electron*, vol. 32, no. 8 (2017), pp. 6245–6260
20. D. Xu, J. Huang, X. Su, P. Shi, Adaptive command-filtered fuzzy backstepping control for linear induction motor with unknown end effect. Inf. Sci. **477**, 118–131 (2019)
21. Z. Mohamed, K. Mohamed, A performance investigation of a four-switch three-phase inverter-fed IM drives at low speeds using fuzzy logic and PI controllers, in *IEEE Transaction on Power Electron*, vol. 32, no. 5 (2017), pp. 3741–3753
22. H. Sathishkumar, S. S. Parthasarathy, A novel neural network intelligent controller for vector controlled induction motor drive, *Energy Procedia*, vol. 138, no. 1.1 (2017), pp. 692–697
23. Z. Yin, C. Du, J. Liu, Research on autodisturbance-rejection control of induction motors based on an ant colony optimization algorithm. IEEE Trans. Ind. Electron **65**(4), 3077–3094 (2018)
24. A. Abdelkarim, B. Amor, B. Abdelhamid, Nonlinear SVM-DTC for induction motor drive using input-output feedback linearization and high order sliding-mode control. ISA Trans. **67**, 428–442 (2017)
25. M. Saleh, Y. Hamid, A.K.Mojtaba, Adaptive sliding-mode type-2 neuro-fuzzy control of an induction motor, *Expert Sys. Appl.* **42**(19), 6635–6647 (2015)

26. T.A.V. Ravi, C. Chandan, P. Bikash, Disturbance rejection analysis and FPGA-based implementation of a second-order sliding-mode controller fed induction motor drive, *IEEE Trans. Energy Convers.* **33**(3), 1453–1462 (2018)
27. A. Francesco, C. Maurizio, D. Filippo, Robust active disturbance rejection control of induction motor systems based on additional sliding-mode component. IEEE Trans. Ind Electron. **64**(7), 5608–5621 (2017)
28. D.G. Stefano, R.D. Jorge, M.M. Antonio, Sensorless high order sliding-mode control of induction motors with core loss. IEEE Trans. Ind. Electron. **61**(6), 2678–2689 (2014)
29. B. Oscar, A. Patxi, Position control of the induction motor using an adaptive sliding-mode controller and observers. IEEE Trans. Ind Electron. **61**(12), 6556–6565 (2014)
30. C. Edwards, S. Spurgeon, *Sliding-Mode Control: Theory and Applications* (Crc Press, 1998)
31. Y. Shtessel, C. Edwards, L. Fridman, *Sliding-Mode Control and Observation* (Springer, New York, 2014), pp. 213–249
32. B. Zheng, J.H. Park, Sliding-mode control design for linear systems subject to quantization parameter mismatch. J. Franklin Inst. **353**(1), 37–53 (2016)
33. A. Ahmadreza, L. Li, S. Su, N. Hung, On LMI-based sliding-mode control for uncertain discrete-time systems. J. Franklin Inst. **353**(15), 3857–3875 (2016)
34. H.M. Hosein, O. Mansour, T. Asghar, Modified DTC of a six-phase induction motor with a second-order sliding-mode MRAS-based speed estimator. IEEE Trans. Power Electron. **34**(1), 600–611 (2019)
35. S. Ouchen, M. Benbouzid, F. Blaabjerg, A. Betka, H. Steinhart, Direct power control of shunt active power filter using space vector modulation based on super twisting sliding-mode control, IEEE J. Emerg. Sel. Top. Power. Electron. (2020)
36. Y. Feng, M. Zhou, Q. Han, F. Han, Z. Cao, S. Ding, Integral-type sliding-mode control for a class of mechatronic systems with gain adaptation. IEEE Trans. Ind. Info. **16**(8), 5357–5368 (2020)
37. Y. Feng, M. Zhou, X. Zheng, F. Han, X. Yu, Full-order terminal sliding-mode control of MIMO systems with unmatched uncertainties. J. Franklin Inst. **355**(2), 653–674 (2018)
38. M. Zhou, Y. Feng, C. Xue, F. Han, Deep convolutional neural network based fractional-order terminal sliding-mode control for robotic manipulators. Neurocomputing (2019)
39. B.K. Bose, *Power Electronics and AC Drives* (Englewood Cliffs, 1986)
40. H.-J. Shieh, K.-K. Shyu, Nonlinear sliding-mode torque control with adaptive backstepping approach for induction motor drive. IEEE Trans. Ind. Electron. **46**(2), 380–389 (1999)
41. J. Xu, R. Yi, B. Chen, Stator-flux-orientated slip frequency control for induction motor, IPEMC, vol. 1 (2004), pp. 401–404
42. S. Bhat, D. Bernstein, Finite-time stability of continuous autonomous systems. SIAM J. Control Optim. **38**(3), 751–766 (2000)